# AN INVESTIGATION OF THE BOUNDARY LAYER BEHAVIOUR ON THE BLADING OF A SINGLE-STAGE AXIAL-FLOW COMPRESSOR

by

G.J. WALKER, B.Sc., B.E. (Hons.), M.I.E. Aust.

Submitted in partial fulfilment of the requirements
for the degree of

Doctor of Philosophy in the
Faculty of Engineering

UNIVERSITY OF TASMANIA
AUSTRALIA

November, 1971

CONTENTS

ACKNOWLEDGEMENTS

The work described in this thesis was carried out under the supervision of Professor A.R. Oliver, whose continued guidance and stimulus is deeply appreciated. The author also wishes to thank the staff of the Engineering Workshops, University of Tasmania, for their technical assistance ; he is particularly indebted to Mr. A. Robinson, whose skill and ingenuity in constructing and maintaining much of the apparatus contributed significantly to the success of the experimental program.

During the course of this work, the author has benefited greatly from his close association with personnel of the Australian Defence Scientific Service. The following people have assisted at different times through discussion or criticism of various aspects of the work embodied in this thesis:

Messrs. T.S. Keeble, W. Howard, D.G. Stewart, D.A. Frith and R.A. Wallis (now with C.S.I.R.O), and Dr. W.H. Schofield, Aeronautical Research Laboratories, Melbourne ;

Messrs. M.L. Robinson and K.D. Thomson, Weapons Research Establishment, Adelaide.

The preceding list is, however, by no means exhaustive.

The author has also received assistance in the form of personal discussion from Professor J.H. Horlock, Cambridge University, England, and Professor P.T. Fink, University of New South Wales, Australia.

Thanks are due to Miss. N. Lazenby for typing this thesis, and to Miss. A. Clark for typing earlier papers associated with this work.

The support of the Australian Department of Supply and the Australian Research Grants Committee for research into compressor aerodynamics at the University of Tasmania is gratefully acknowledged.

## ABSTRACT

Observations of the boundary layer behaviour on the blading of a single-stage axial-flow compressor are described : detailed measurements were carried out with hot wire, surface visualisation, and surface pitot tube techniques, and the presence of extensive regions of laminar flow was established. The behaviour of the laminar and turbulent boundary layers, and of separated laminar flow regions are reported. A new correlation is developed to describe the boundary layer transition behaviour, and the effects of pressure gradient, Reynolds number, and free stream turbulence on transition are discussed. A new turbulent skin friction law for conditions of large positive pressure gradient is developed, and the problem of the minimum Reynolds number for turbulent flow under a pressure gradient is re-examined. Various existing methods of calculating the turbulent boundary layer are examined and their success in predicting the boundary layer development on a stationary blade of the research compressor is evaluated. The application of the experimental results to the design and performance analysis of axial-flow turbo-machine blading is discussed. A family of surface velocity distributions giving unseparated flow over the suction surface of an axial-flow compressor blade is derived, and their computed performance is analysed. In conclusion, problems needing further investigation are outlined.


---

I hereby declare that, except as stated herein, this thesis contains no material which has been accepted for the award of any other degree or diploma in any University, and that, to the best of my knowledge or belief, this thesis contains no copy or paraphrase of material previously published or written by any other person, except when due reference is made in the text of this thesis.

G.J. Walker

## PREFACE

While present methods of designing axial flow compressors are able to produce machines having a generally satisfactory level of overall performance, it is often found that the pressure rise and efficiency actually achieved at the design flow are significantly different from the values estimated during design. Although much of this inaccuracy in performance prediction arises from errors in determining the flow conditions between blade rows, there is undoubtedly an appreciable contribution from the empirical methods used for selecting the compressor blade sections themselves.

The choice of blade sections for this type of machine is much more difficult than the design of an isolated aerofoil section because of the greater range of blade profiles involved and the additional variables of blade spacing and stagger. The complexity of the problem has forced the design and performance analysis of axial flow compressor blading to be based largely on the results of systematic tests of a limited number of basic profiles in two-dimensional cascades, for example the British work of Howell (1) and the American NACA work described by Johnsen and Bullock (2).

Because of this empirical approach it is not yet possible to predict the off-design performance of an arbitrary blade row with any great accuracy, nor is it certain that the standard blade sections in current use are yielding the optimum attainable performance. There is also considerable doubt about the design of blade configurations for which reliable cascade data is either scarce or unavailable; the cases of very high stagger, extremely low spacing, and non-standard blade profiles are notable examples.

It would be highly desirable to replace the existing procedures for blade selection and performance analysis with more accurate analytical methods making less use of empirical data. However, the development of sufficiently realistic mathematical flow models is being delayed by a lack of detailed information about the boundary layer and wake behaviour in compressors.

The analytical design of compressor blading commences with the specification of a blade surface pressure distribution which will produce a lift coefficient compatible with the required inlet conditions and degree of turning, without causing any unnecessary thickening or separation of the boundary layer. Potential flow theory is then used to determine the blade geometry corresponding to the chosen pressure distribution; this calculation must take into account the displacement effects of the blade boundary layer and wake, which effectively change both the blade shape and incidence and so alter the blade circulation and profile losses.

The theoretical performance analysis of a given blading configuration involves first the potential flow calculation of the blade surface pressure distribution from the specified blade geometry and inlet conditions, and

secondly the prediction of the boundary layer and wake development to give the blade profile losses. As with the design problem it is again necessary to modify the potential flow solution to allow for the viscous flow effects.

Clearly, there can be little hope of success with either of these problems until the viscous flow behaviour is properly understood, and this can only be achieved by making measurements of the boundary layers and wakes of an actual compressor blade row. It is most important that these measurements be obtained in a real compressor where the blades are subject to various secondary flows and unsteady flow effects not present in the idealised physical model provided by a two-dimensional cascade.

This thesis describes the results of a detailed survey of the boundary layer behaviour on the blading of a single stage axial flow compressor. The investigation was carried out with the aim of improving knowledge about the viscous flow behaviour in axial flow turbomachinery. The results obtained have been applied to the problems of predicting the boundary layer development on machine blades having known surface pressure distributions, and to the problem of choosing blade surface pressure distributions giving unseparated boundary layer flow. The use of potential flow theory to determine the surface pressure distribution from the blade geometry, or vice versa, is not dealt with specifically; although there are at present significant differences between the calculated and measured pressure distributions for compressor blades, it is believed that these arise mainly from errors in allowing for the viscous flow effects, rather than from shortcomings in the available methods of potential flow calculation.

# CHAPTER 1

## INTRODUCTION

The work described in this thesis forms part of a continuing investigation of compressor aerodynamics being carried out by the University of Tasmania and the Australian Department of Supply's Aeronautical Research Laboratories (A.R.L.), Melbourne. This research was initiated at A.R.L. under the leadership of Mr. F.G. Blight in the late 1940's, and personnel of the University of Tasmania have been participating in it since the early 1950's.

The broad aim of this project, as first visualised, was to use the latest potential flow theories to design axial flow compressor blade sections having specified surface pressure distributions; it was hoped that improved performance could be obtained by choosing a pressure distribution which made conditions more favourable for the boundary layers developing on the blade surface. Blade sections designed by this method were to be tested first in two-dimensional cascades at both low and high speeds, and then under three-dimensional flow conditions in a single stage compressor. The building of a multi-stage compressor utilising the new blade profiles was ultimately envisaged.

During the period 1952-1954, several compressor blade sections were designed by the method of Lighthill (3). Since little was known at that time about boundary layers in compressors, a number of different surface pressure distributions were chosen for these designs so that the effect of pressure distribution on the boundary layer could be evaluated. These blades were tested at low speed in a two-dimensional cascade by Blight and Howard (4) and Crooks and Howard (5), and a standard blade of British C4 section was also tested for comparison. The best of the new blades, section L5, had a slightly better low speed performance than the C4 blade over a wide range of incidence. Qualitative boundary layer studies using surface oil-film, surface pitot, and hot wire techniques indicated the presence of extensive laminar flow regions on all the cascades tested.

A single stage compressor or "Vortex Wind Tunnel" was designed and built at A.R.L. in 1954; a description of this machine and its overall performance characteristics is given in Chapter 2. Preliminary tests by Crooks and Howard (6), using the china clay visualisation technique, suggested the presence of long regions of laminar flow, followed by laminar separation, on both rotor and stator blades of this compressor. Their existence was quite unexpected since it was widely supposed in the literature, e.g. by Hawthorne (7), that the high level of free stream turbulence always present in turbomachinery would invariably result in transition to

turbulence occurring very close to the leading edge of a turbomachine blade.

The Vortex Wind Tunnel was subsequently transferred to the University of Tasmania, where investigations of the blade boundary layers were continued. Close (8) and Salter (9) used the method of Thwaites (10) to calculate the theoretical separation points for laminar boundary layers subject to the same pressure distributions as had been measured on the compressor blades, and found that these points agreed reasonably well with the commencement of the separation regions observed in surface visualisation tests. This greatly strengthened the belief that the compressor blade boundary layers were laminar prior to separation. It was also noted that the locations of separated flow regions on the blade surfaces in the single stage compressor were closely similar to those observed previously on identical blade sections in two-dimensional cascade tests.

It became obvious at this stage that an accurate model of the boundary layer development on a machine blade could not be obtained without a reasonable estimate of the location of transition to turbulence. With this problem in mind a more detailed quantitative survey of the boundary layer on a stator blade in the Vortex Wind Tunnel was carried out by the author, and the present thesis is based largely on the results of this investigation. The experimental techniques used are described in detail in Chapter 3, and a general discussion of the observed boundary layer behaviour follows in Chapter 4. Various detailed aspects of the boundary layer behaviour are treated in Chapters 5 - 7.

In Chapter 5 it is shown that extensive areas of laminar flow were indeed present on the blading of the research compressor under certain conditions ; the measured boundary layer development in these regions is compared with the theoretical predictions of Thwaites's method. The behaviour of separated laminar flow regions is also discussed in detail; it is suggested that the sudden drag rise of axial compressor blades at low Reynolds numbers is due to separation bubble bursting.

Chapter 6 commences by reviewing previous work on the physical nature of the boundary layer transition process. A new empirical correlation is derived to describe the transition behaviour on the compressor blades, and the influence of pressure gradient and free stream turbulence on transition is discussed. Some observations concerning the effects of passing blade wakes on the time-space distribution of laminar and turbulent flow during transition in the stator blade boundary layer are also presented.

Chapter 7 examines the flow behaviour in turbulent boundary layer regions on the stator blade. The familiar logarithmic wall similarity region is shown to be entirely absent from the measured velocity profiles. A new skin friction law is proposed to allow for the very large pressure gradients found on the compressor blade. The minimum Reynolds number

required to sustain a fully developed turbulent boundary layer under a pressure gradient is discussed. Various methods of predicting the turbulent boundary layer are reviewed, and the calculated boundary layer development is compared with the experimental measurements.

Chapter 8 discusses the application of the preceding experimental results to the design and performance analysis of axial flow turbomachine blading. First, the probable accuracy of performance estimates obtained from present boundary layer calculation methods is assessed. A family of surface velocity distributions giving unseparated flow over the suction surface of a compressor blade is then derived, and the computed performance of blades having the model velocity distribution is examined. In conclusion, some problem areas requiring further research are outlined.

# CHAPTER 2

## DESCRIPTION OF RESEARCH COMPRESSOR

### 2.1 Tunnel Layout

A longitudinal section of the Vortex Wind Tunnel is shown in Fig. 2.1 (a). Various external and internal details of the tunnel can be seen from the photographs in Figs. 2.1 (b) - 2.1 (f).

Air enters the tunnel almost radially through an opening 7 ft. diameter and 2 ft. wide which is covered with wire gauze (18 meshes per inch of 24 S.W.G. wire) to promote uniformity of flow conditions. A flared bend made of plywood then turns the flow through $90^{\circ}$ into an annulus with 45 in. outside diameter and 27 in. inside diameter. The velocity ratio through the entrance bend is approximately 7 to 1. The whole entrance section can be wheeled back on tracks to give access to the compressor blade rows.

The three compressor blade rows are contained in a parallel section one diameter (45 in.) long. The outer shell of the working section is made of aluminium and has several flanged joints allowing it to be broken in different places. The aluminium shell also contains three perspex windows (each about 4 in. square) which permit a limited amount of visual inspection while running, and horizontal instrument slots which allow traversing of measuring probes in a horizontal radial plane of the machine.

The working section is followed by a further parallel section about $1\frac{1}{4}$ diameters long and made of plywood, after which there is a diffusing section also of plywood. The diffuser is about 4 diameters long with a cylindrical core and a conical outer shell having an included whole angle of $7^{\circ}$. The inner wall of the diffuser is flared outwards at the downstream end to give nearly radial exit flow through a cylindrical opening 7 ft. in diameter. The air then recirculates through the room before returning to the tunnel inlet.

The outlet opening is controlled by a cylindrical throttle running on rails and driven by three symmetrically placed screws which carry sprockets connected by a single chain. This arrangement keeps the throttle cylinder parallel to the longitudinal axis of the tunnel, and allows repetition of the opening width to within about 0.02 in. Oliver (11) found the variation in flow for the same nominal throttle position to be generally less than 1% from the mean of several settings, except near surge where the flow varied from the mean by about $1\frac{1}{2}\%$. Only part of this variation was due to errors in throttle setting, however, as there were equally important effects arising from variations in Reynolds number with changes in atmospheric conditions, and from changes in density of the alcohol in the manometer which were not taken into account.

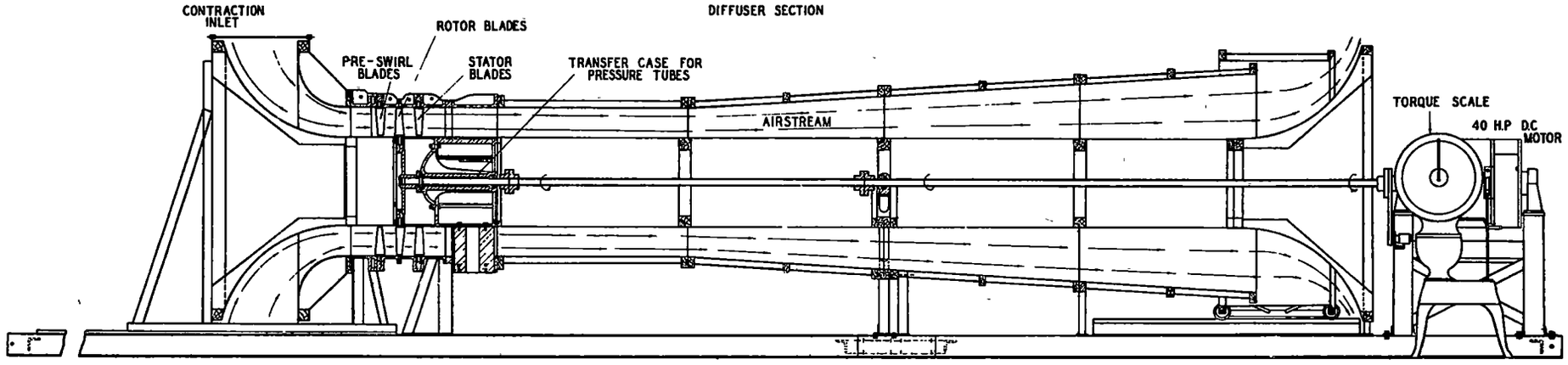


LONGITUDINAL SECTION OF TUNNEL

Scale: $\frac{1}{4}$ in. = 1 ft.

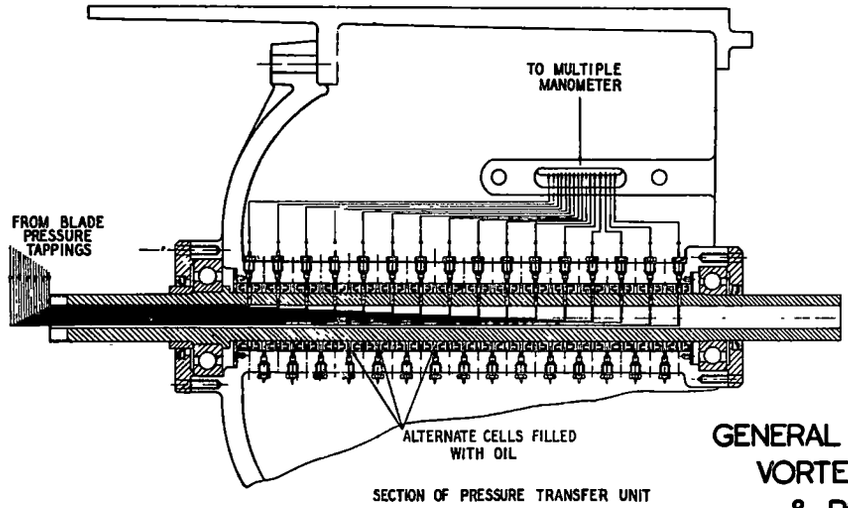


SECTION OF PRESSURE TRANSFER UNIT

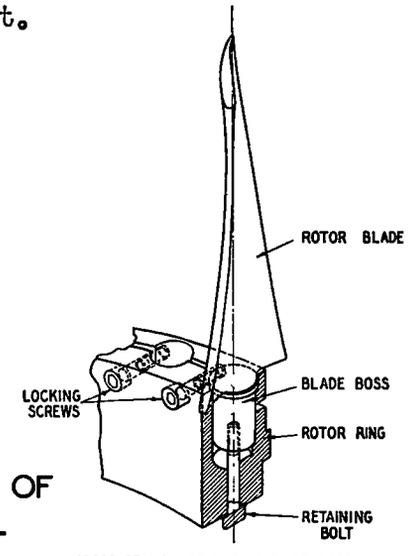


CROSS SECTION OF VARIABLE-STAGGER ROTOR BLADE ASSEMBLY

## GENERAL ARRANGEMENT OF VORTEX WIND TUNNEL & PART SECTIONS

Fig. 2.1(a)

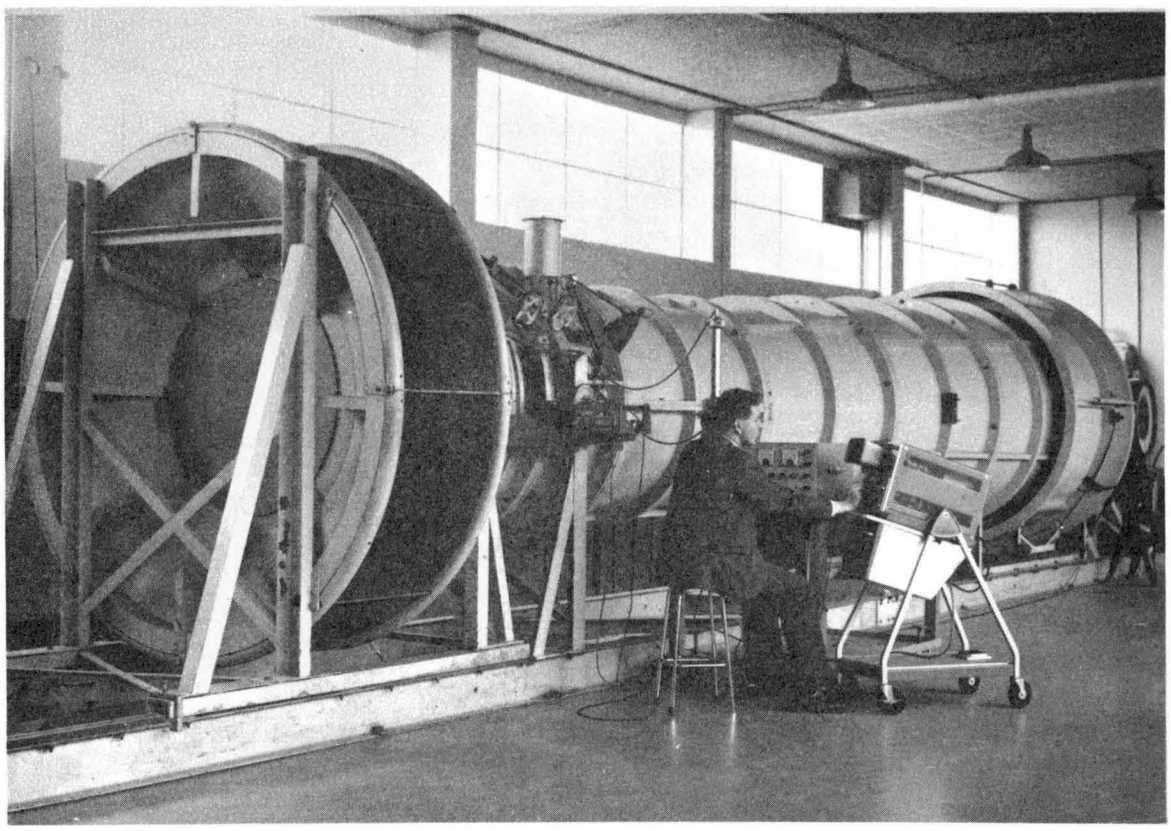

Fig. 2.1(b) Vortex Wind Tunnel - General View

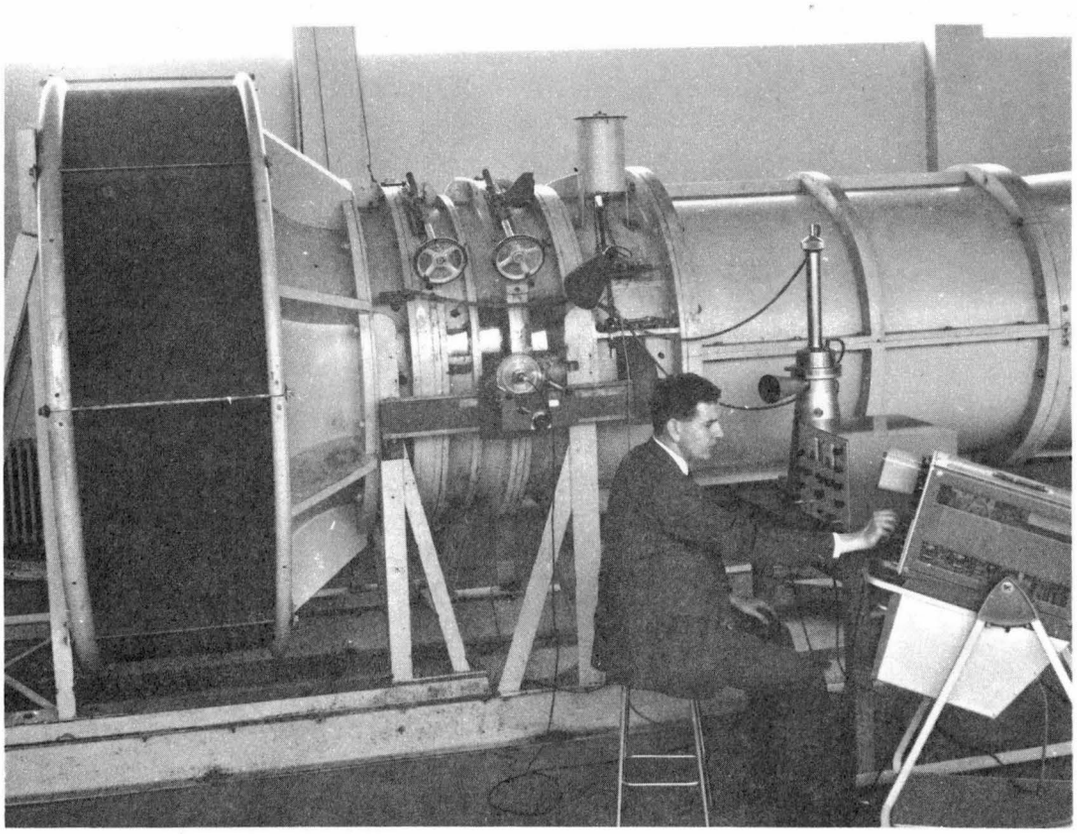

Fig. 2.1(c) Vortex Wind Tunnel - Inlet and Compressor Casing

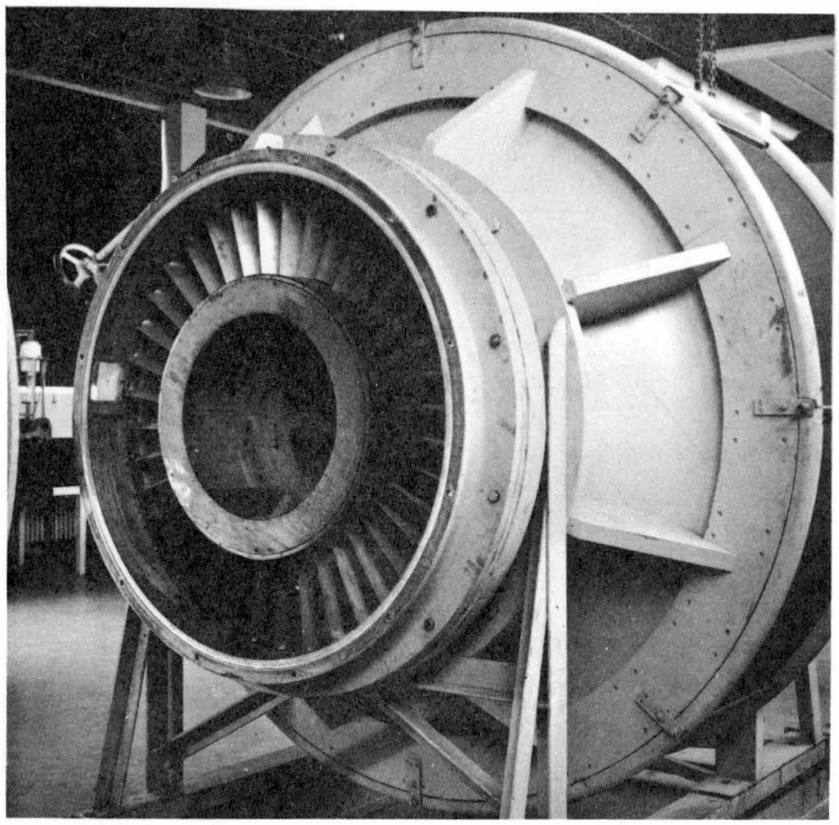

Fig. 2.1(d) Vortex Wind Tunnel - Inlet Section Wheeled Back to Show Compressor Inlet Guide Vanes

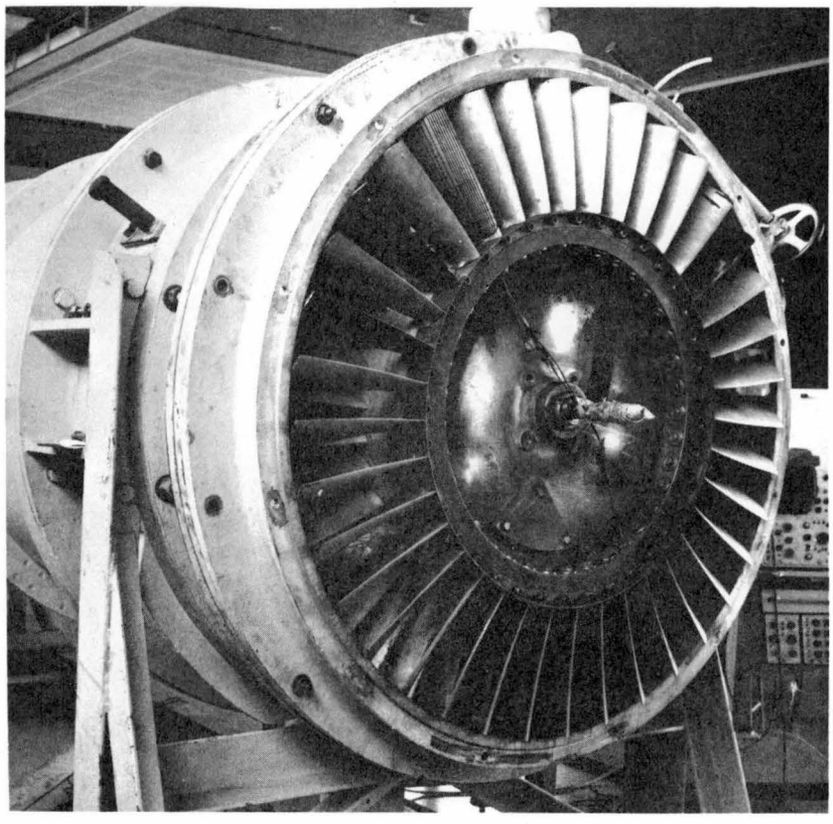

Fig. 2.1(e) Vortex Wind Tunnel - Inlet Section Removed to Show Compressor Rotor

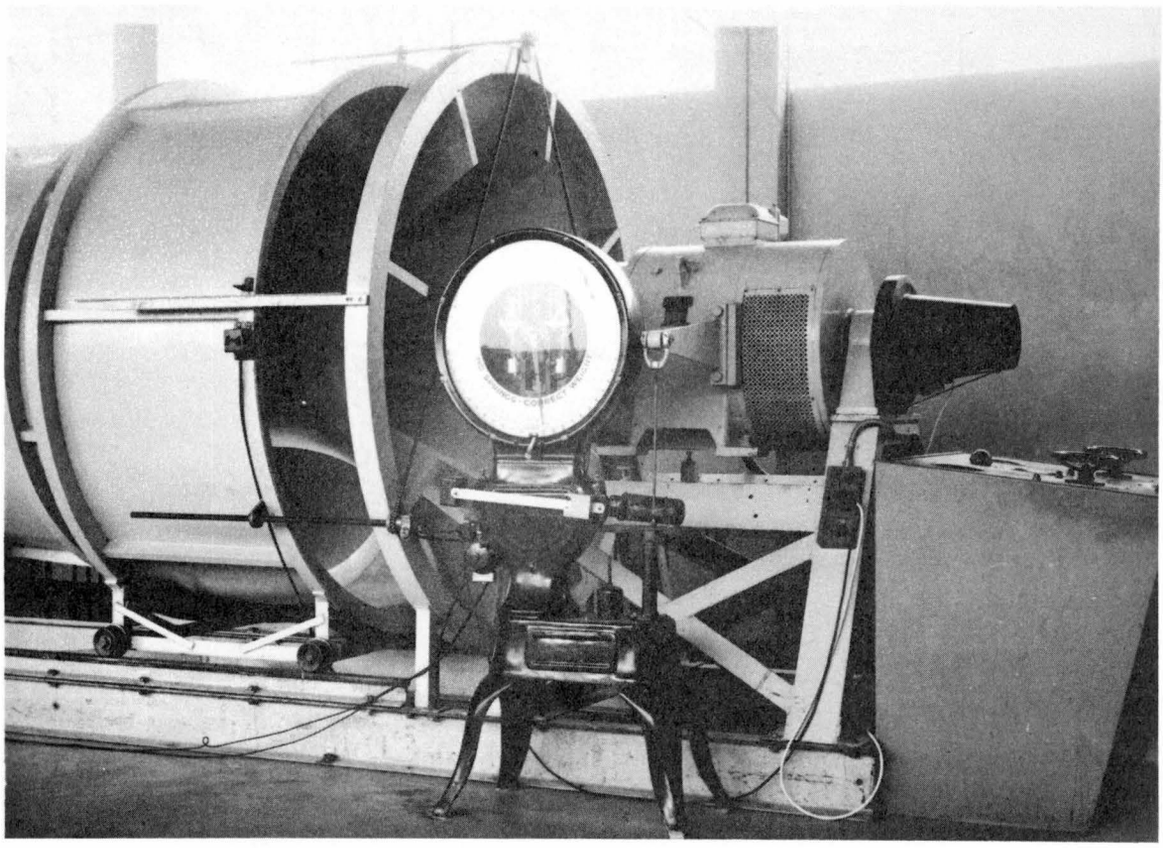

Fig. 2.1(f) Vortex Wind Tunnel - Drive Motor and Outlet Throttle

The compressor is driven by a 40 horsepower D.C. motor supplied from a Ward-Leonard set which allows manual control of speed up to 750 rpm. The motor is swung on bearings and its stator torque reaction can be measured by a lever arm connected to a modified platform scale. The driving motor is situated at the outlet with a rather long driving shaft in the centre of the cylindrical core; this arrangement stems from the requirement to provide easy access to the blade rows by rolling back the inlet section. A pressure transfer case (detailed in Fig. 2.1(a)) surrounding the shaft near the rotor support bearing enables the measurement of pressures on the rotating blades. The transfer case and main bearing are supported by three radial faired struts, each of 12 in. chord and 3 in. maximum thickness, with the longitudinal axis parallel to the tunnel centre-line. As there is some $22^{\circ}$ of swirl in the outlet flow at mid blade height, the supporting struts are at an appreciable angle to the local flow direction; but this did not appear to upset any of the pressure readings obtained by previous workers, except for measurements of tunnel wall static pressure downstream of the struts.

The tunnel inlet conditions were investigated by Close (12) who found the variation in axial velocity around the circumference to be generally less than 1% from the mean of readings taken at four different circumferential positions. There is a general trend for more flow to pass through the sides of the tunnel than through the top or bottom, probably due to the proximity of the floor to the bottom of the entry lip (as shown in Fig. 2.2). The radial variation in inlet conditions is also small, there being an increase in total head from the

outer wall (shell) to the inner wall (hub) of about 1% of the compressor inlet dynamic pressure, with correspondingly small variations in velocity and static pressure. The wall boundary layers upstream of the inlet guide vanes appear to be less than $\frac{1}{4}$ inch thick.

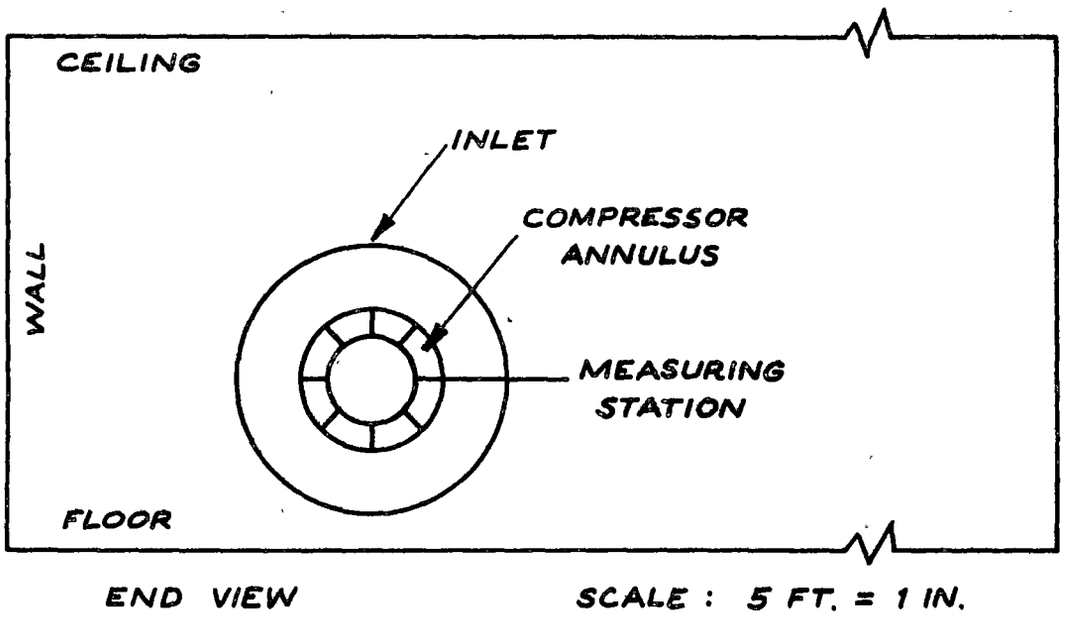


Fig. 2.2 Location of Research Compressor in Room

2.2 Details of Compressor

The single stage compressor has three blade rows, namely inlet guide vanes, rotor, and stator, which all have a tip diameter of 45 in. and a hub diameter of 27 in. The blades have cylindrical bosses at one end so that their angles can be set individually and then clamped into position. The stationary blades are clamped between two rings and have their bosses at the outer end; the rotor blades are held by radial retaining bolts through the rim of the rotor disc, the outer part of which is split and tightened onto the blade bosses by locking screws, as detailed in Fig. 2.1(a). The stationary blade supporting rings can be rotated to traverse the blades past a stationary measuring probe.

The blades are 9 in. long, giving a hub/tip ratio of 0.6, and have a chord length of 3 in., giving an aspect ratio of 3. The chord length is the same at all blade radii. All blades have clearances at each end to allow for movement past the stationary walls and to give some freedom in setting the angle. The average clearance is about 0.030" (about 0.3% of the blade height). The blade Reynolds number ($Re_c$) based on chord length and vector mean velocity varies from about $3 \times 10^4$ at a rotational speed of 150 rpm to about $2 \times 10^5$ at 750 rpm.

Each of the guide vane rows has 38 blades, giving a mean space/chord ratio of 0.99, and the rotor has 37 blades with a mean space/chord ratio of 1.02. The axial distance between blade rows may be varied by removing sections of the outer casing of the compressor and replacing them with sections of different length, thus altering the position of the fixed blade rows relative to the rotor. In the present series of investigations the axial distance between the centres of neighbouring blade rows was kept constant at two chord lengths. This gave

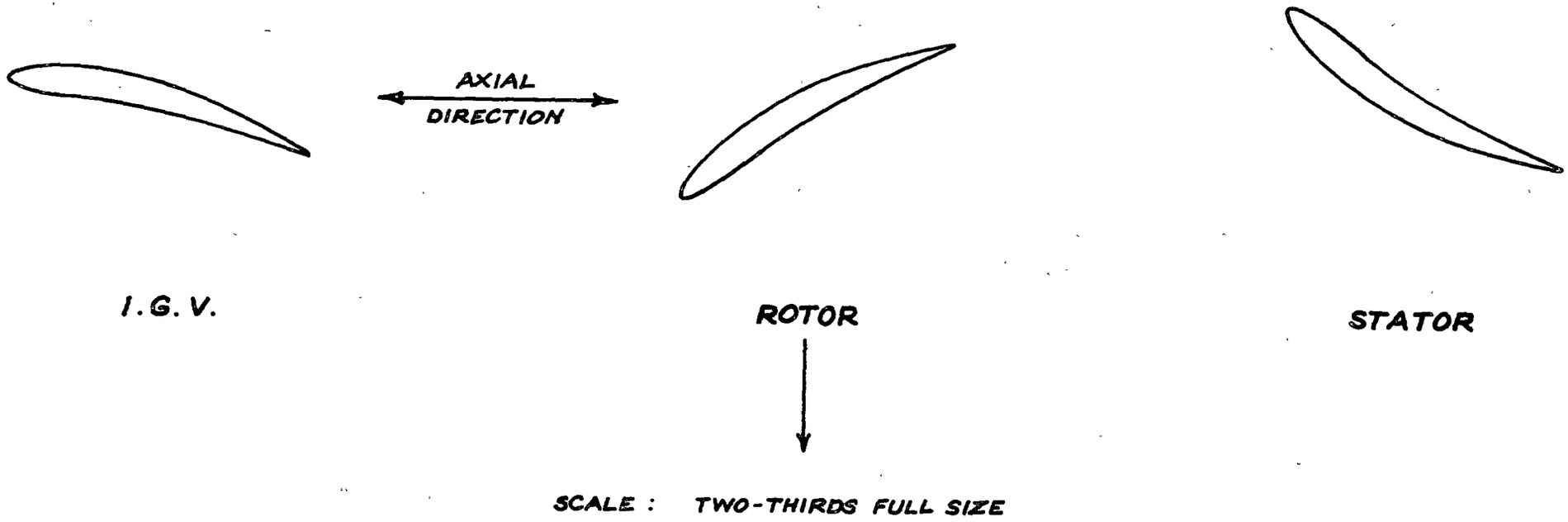


Fig. 2.3 Section of Compressor Blading at Mid-Blade Height

an axial clearance between blade rows of a little over one chord length (as shown in Fig. 2.3), which is rather more than is usally adopted in practical compressor designs; the extra spacing was used because it facilitated the insertion of measuring probes.

The blades are all of British C4 section with a nominal maximum thickness/chord ratio of 10%, wrapped around circular arc camber lines and twisted about a radial straight line close to the middle of the camber lines of all sections. They were machined from aluminium to within a tolerance of 0.001 inches per inch of chord. The blade sections were designed on the data of Howell (1) to give nominally free vortex flow conditions with 50% reaction at mid blade height at the nominal design flow, $\phi = 0.76$. This gives simple radial equilibrium with uniform axial velocity (and hence small radial flows) at the design point, which was expected to give ideal conditions for comparing the behaviour of the (identical) rotor and stator mid blade sections in the compressor with the performance of a similar section (designated S1) tested previously at low speed in a two-dimensional cascade tunnel (4). The design deflection of the rotor and stator blades was chosen to be roughly 85% of the nominal deflection defined by Howell, so that the incidence range of the compressor blades would roughly match the design incidence range of the Lighthill sections investigated in Refs. 4, 5.

General details of the compressor blading are summarised in Table 2.1, and the blade cross-sections at mid blade height are shown in Fig. 2.3.

Table 2.1

Blade Details - General

| | I.G.V. | Rotor | Stator |
|---|---|---|---|
| No. of blades | 38 | 37 | 38 |
| Core diameter (in.) | 27.0 | 27.0 | 27.0 |
| Shell diameter (in.) | 45.0 | 45.0 | 45.0 |
| Clearance at core (in.) | 0.020 - 0.060 | 0.030 | 0.030 |
| Clearance at shell (in.) | 0.025 | 0.033 | 0.020 |
| Hub stagger ($^{o}$) | 17.2 | 4.2 | 37.2 |
| Mid blade stagger ($^{o}$) | 13.9 | 29.5 | 29.5 |
| Tip stagger ($^{o}$) | 11.25 | 42.15 | 25.1 |
| Hub camber ($^{o}$) | 34.4 | 52.5 | 32.9 |
| Mid blade camber ($^{o}$) | 27.8 | 31.1 | 31.1 |
| Tip camber ($^{o}$) | 24.25 | 19.1 | 29.4 |
| Mid blade s/c | 0.99 | 1.02 | 0.99 |

Two blades from the rotor row and two blades from the stator row have been tapped so that surface pressure readings can be obtained from both the pressure and suction surfaces at the five different radial stations indicated below:

| Station | 1 | 2 | 3 | 4 | 5 |
|---|---|---|---|---|---|
| $R/R_T$ | 0.65 | 0.7 | 0.8 | 0.9 | 0.95 |

The tappings are at 5% intervals of chord for the first 40% of chord, and at 10% intervals of chord thereafter up to 90% of chord. Details of blade angles at the five measuring stations are given in Table 2.2

Table 2.2

Blade Details - Angles at Measuring Stations

| Station | 1 | 2 | 3 | 4 | 5 |
|---|---|---|---|---|---|
| $R/R_T$ | 0.65 | 0.7 | 0.8 | 0.9 | 0.95 |
| Stator stagger (°) | 35.0 | 33.0 | 29.5 | 26.5 | 25.3 |
| Stator camber (°) | 32.5 | 32.2 | 31.1 | 30.0 | 29.3 |
| Rotor stagger (°) | 9.6 | 18.3 | 29.5 | 38.3 | 42.1 |
| Rotor camber (°) | 47.0 | 41.2 | 31.1 | 22.9 | 20.0 |

## 2.3 Overall Performance Characteristics

The overall performance characteristics of the compressor as measured by Oliver (11) downstream of the rotor and downstream of the stator at a speed of 750 rpm are shown in Fig. 2.4. The values of total pressure rise were obtained by averaging the measured total pressures over a sector of the annulus one blade spacing in width, and subtracting the total pressure measured by a pitot tube at a point upstream of the inlet guide vanes. The pressures were made non-dimensional with respect to $\frac{1}{2}\rho U_{mb}^2$, which is the dynamic pressure based on the peripheral speed of the rotor blades at mid blade height. Fig. 2.4 also shows curves of compressor efficiency based on the measured values of motor torque reaction after allowing for the friction of the shaft rotating without blades. Both total pressure rise coefficients and efficiences are plotted against averaged values of flow coefficient $\phi = V_a/U_{mb}$.

Oliver (11) suggests that the total pressures measured downstream of the rotor are 1% higher than actual due to flow fluctuations arising from the rotor blade wakes. The measured efficiencies downstream of the rotor are thought to be up to two percentage points high due to the expected high total pressure readings, the favorable position (region of highest flow around the circumference) of the measuring station, and suspected errors in torque readings.

Stalling of the compressor commences at the rotor tip and the stator hub. In the latter case the separation of flow is more from the hub wall of the annulus than from the stator blades themselves. Surging begins at a flow coefficient of 0.55, which is very slightly below the lowest flow reading in the performance characteristics of Fig. 2.4. The surge is initially manifest as a slight audible buffeting and oscillation of the manometer readings; it is thought to be initiated by separation of the hub wall boundary layer downstream of the stator.

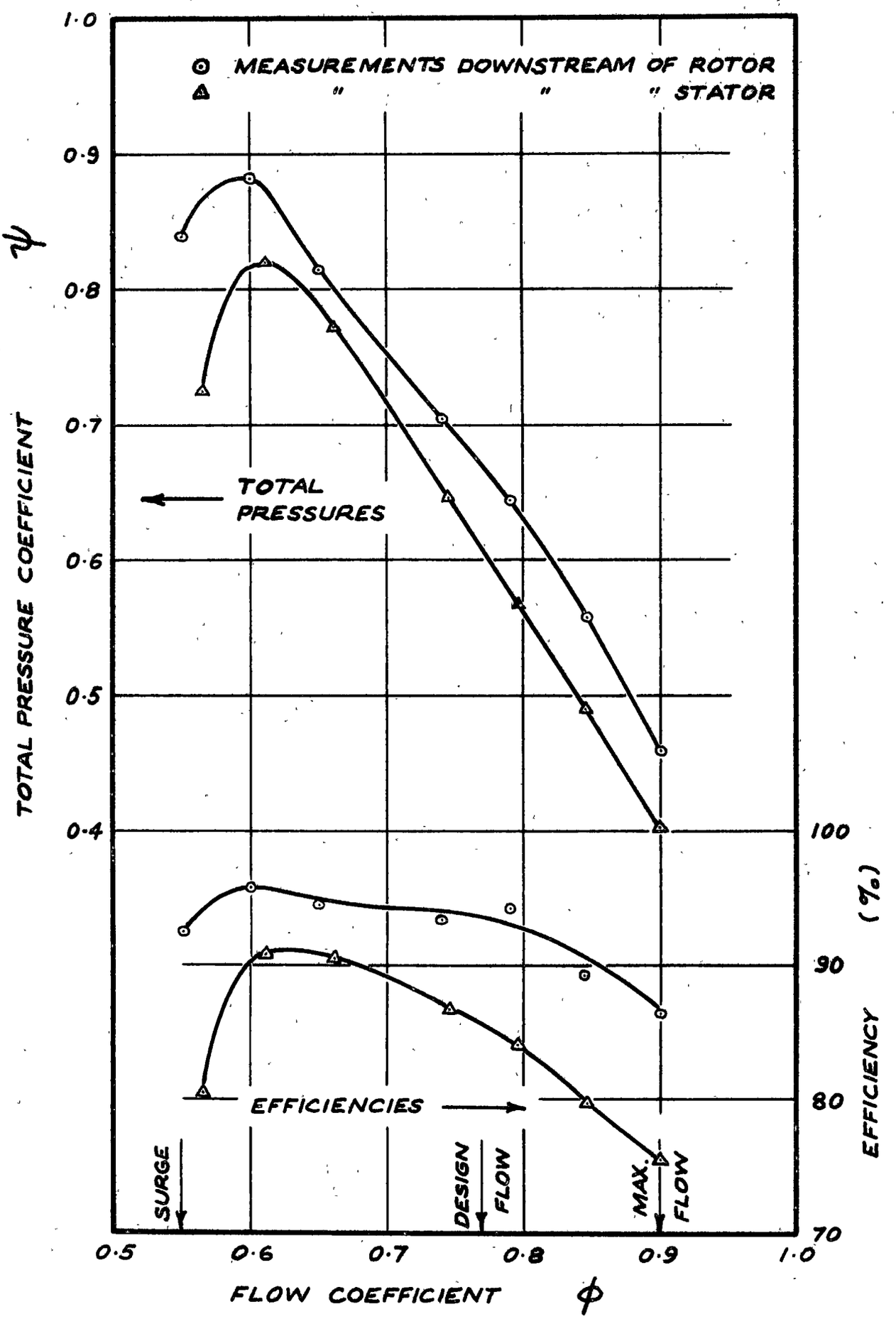


Fig. 2.4 Compressor Performance Characteristics at 750 rpm
- from Oliver (11)

# CHAPTER 3

## EXPERIMENTAL DETAIL AND PRESENTATION OF RESULTS

### 3.1 Range of Experimental Investigation

The purpose of the experimental investigation was to observe the boundary layer behaviour on the blades of an axial flow compressor over the widest possible range of external flow conditions. The most important factors influencing incompressible boundary layer development are the blade surface pressure distribution, blade chord Reynolds number ($Re_c$), and the level and type of disturbances in the free stream outside the boundary layer.

Variations in Reynolds number were obtained by altering the rotational speed of the compressor. Four standard speed settings were used during the present investigation, namely 750, 500, 250, and 150 rpm. This gave values of $Re_c$ for the stator blades in the range of $2 \times 10^5$ to $3 \times 10^4$, which covers the so-called "critical region" where reduction of Reynolds number causes a significant increase in compressor blade losses due to the development of separated flow regions on the blade surfaces.

Changes in blade surface pressure distribution were produced by altering the flow through the compressor so as to vary the blade incidence. Observations were made at seven standard throttle openings which had been used by other workers during previous investigations of the compressor performance. These throttle settings gave a range of flows from just above surge up to the maximum obtainable flow. Corresponding values of throttle opening, mean flow coefficient, and incidence at mid-blade height (where most of the measurements of the present investigation were obtained) are presented in Appendix B. The radial variation of air angle, axial velocity, and blade incidence at the standard throttle openings are indicated in Appendix C.

At mid-blade height, the stator incidence varied from about $-11^\circ$ to $+5^\circ$, and the rotor incidence ranged from about $-11^\circ$ to $+9^\circ$. The maximum positive incidence achieved on the stator was rather lower than that on the rotor due to the flow deviation downstream of the rotor changing with incidence, and to the separation of the hub wall boundary layer through the stator row at low values of flow coefficient.

The blade surface pressure distribution in an axial-flow machine is also influenced by the boundary layer growth on the annulus walls, and an overall measure of the magnitude of this effect is provided by the ratio of the axial velocities upstream and downstream of a blade row. The axial velocity ratio (A.V.R. = $V_{a_2}/V_{a_1}$) is a significant parameter in the problem of determining the blade surface pressure distribution from the blade and annulus geometry. But this particular problem does not arise in the present work, which is concerned only with predicting the blade boundary layer development when the surface pressure distribution is known; here the effects of axial

velocity changes are implicitly taken into account by using the actual blade pressure distribution measured from the surface tappings. Nevertheless, the A.V.R. is still relevant in the present context as it gives some indication of the degree of convergence or divergence in the bulk flow and the departures from two-dimensional flow in the blade boundary layers which this might produce (see also Section 4.5). Some typical values of A.V.R. in the research compressor are presented in Table 3.1; they are probably accurate to no better than 3% because of the effects of the rotor wakes on the pressure probe measurements.

Table 3.1

Axial Velocity Ratios: mid blade height, 750 rpm

From measurements of Oliver (11)

| Flow coeff. $\phi$ | 0.55 | 0.60 | 0.65 | 0.75 | 0.80 | 0.85 | 0.90 |
|---|---|---|---|---|---|---|---|
| A.V.R. (rotor) | 1.05 | 1.03 | 0.995 | 0.995 | 0.995 | 0.985 | 0.995 |
| A.V.R. (stator) | 1.065 | 1.035 | 1.05 | 1.04 | 1.02 | 1.025 | 1.02 |

Although no direct attempt was made to vary the level of free stream turbulence in the compressor during the present investigation, there was a considerable change in the level of disturbance with variations in compressor speed. Measurements of streamwise velocity fluctuations close to the plane of the stator leading edge indicated average values of 2% turbulence at 750 rpm, rising to 6% turbulence at 150 rpm. This increase in turbulence arose from the thickening of the rotor blade wakes as speed and Reynolds number were reduced. The highest turbulence level observed, close to stall at 150 rpm, was almost 10%.

The experimental program commenced by using the china clay visualisation technique to indicate the location of separated flow regions and boundary layer transition on both rotor and stator blades of the research compressor. A constant current hot wire anemometer was then used to measure the mean velocity profiles in the boundary layer of a stator blade. Some further observations of boundary layer transition on the stator blades were made with a stethoscope connected to a total head tube, and with a constant temperature hot wire anemometer which was used to record velocity fluctuations in the transition region. The compressor blade surface pressure distributions were measured from the surface tappings so that the theoretical boundary layer development could be calculated and compared with experimental results.

## 3.2 China Clay Visualisation Technique

### 3.2.1 General Remarks

The china clay technique provides a visual indication of the variation in fluid shear stress over a solid boundary; it depends on the rate of evaporation of a liquid film from the surface being a function of the wall shear

stress, $\tau_w = \mu(\partial u/\partial y)_{y=0}$. The surface is first prepared with a layer of white china clay on top of a black base coat, and is then sprayed with an oil such as methyl salicylate which has the same refractive index as the china clay particles. The liquid film renders the china clay particles transparent, so that the wetted surface takes the colour of the black base coat. Drying of the oil film is more rapid in regions of higher wall shear stress, so that after a period of running these areas become white, whilst areas of lower shear stress which are still wet appear black. This technique gives useful indications of the extent of separated flow regions on a surface, and the location of laminar-turbulent transition in the boundary layer can often be determined from the sudden increase in wall shear stress which accompanies the onset of turbulent flow.

3.2.2 Experimental Detail

The china clay visualisation technique was applied to the suction surfaces of both rotor and stator blades of the research compressor over the entire blade height. Four neighbouring blades from each of these rows were prepared for testing. A base coat consisting of 2 to 3 parts vegetable black to one part aircraft dope, with thinners added to give the required consistency, was applied to the blade surfaces by spraying. When the base had dried, the surface coat of china clay, consisting of 3 parts levigated kaolin to one part aircraft dope with thinners added, was sprayed over the base coat. Irregularities in the sprayed surface due to large particles of kaolin were removed by a light sanding with fine emery paper. The thickness of the finished coating was 0.001 - 0.002 in., which should have been insufficient to cause any significant distortion of the blade profiles.

Some small isolated roughness elements were usually allowed to remain on the surface because they were useful in providing information about the amount of cross flow in the blade boundary layers. The scarf vortices and subsequent turbulent flow wedge trailing downstream from these elements generated a high local wall shear stress which increased the drying rate in their vicinity. This caused the appearance of drying lines whose direction gave an approximate indication of the limiting streamlines at the blade surface.

Methyl salicylate was sprayed onto the blades immediately before each run, the evenness of the oil film being judged by the degree of colour removal from the china clay layer, and the apparent wetness of the surface. It was found important not to wet the rotor blade surfaces too much, as this resulted in excess liquid and some of the coating being thrown off by centrifugal forces. When the blade preparation had been completed, the tunnel was quickly closed and the compressor was run for a short period. The length of time needed to give distinct drying patterns depended on the compressor speed, thickness of the china clay layer, ambient temperature, and initial wetness of the surface, but the average drying time required was about 4 minutes. After some experience had been gained, the drying time needed could be estimated fairly closely.

Tests were carried out at the four standard speeds and seven standard throttle settings specified in Section 3.1, and the drying patterns obtained were recorded photographically. The position of the jump in wall shear stress following laminar-turbulent transition (where clearly defined) was measured with a flexible tape hooked onto the blade trailing edge and wrapped around the surface. Measurements were taken at the same radial stations as those of the blade pressure tappings.

Little attention was paid to the point of laminar flow separation as this had been investigated previously by Salter (9) and Close (8), who found that its location could be predicted moderately well by Thwaites's method (10).

### 3.2.3 Presentation of Results

The points of apparent turbulent reattachment measured in the china clay tests are tabulated in Appendix E, and photographs of typical drying patterns are shown in Figs. 4.2 - 6. The experimental results are described in detail in Section 4.2, and further discussion on their physical significance can be found in Sections 5.6.4.2 and 6.3.3.

## 3.3 Hot Wire Anemometry Techniques

### 3.3.1 General Remarks

Observations of flow in turbomachinery are always made difficult by the fluctuations in velocity arising from the wakes and circulation fields of other blade rows moving past a stationary probe. In this unsteady flow situation, the hot wire anemometer provides generally more accurate mean velocity measurements than conventional pressure probes, whose response to velocity fluctuations cannot be predicted with confidence; but in cases (especially at very low velocities) where the velocity fluctuations are relatively large, so that non-linearity of probe response becomes significant, even hot wire measurements must be regarded with suspicion. When measurements are required in very thin boundary layers, however, the hot wire anemometer is probably the only instrument available which provides the required spatial discrimination without causing a significant distortion of the local flow pattern.

### 3.3.2 Experimental Detail

A hot wire probe operated at constant current was used to measure mean velocity profiles at mid blade height in the boundary layer on a stator blade of the research compressor. In all, the development of 27 different boundary layers was investigated. Measurements were taken at all of the four standard speeds and seven standard throttle openings specified in Section 3.1, with the single exception of 750 rpm, 4.8 in. throttle ($\phi \simeq 0.55$), where the blade vibration was severe enough to make any measurements of doubtful accuracy, and might also have led to damaging of the probe. The

boundary layer traverses were obtained at 10% intervals of chord from x/c = 40% to x/c = 90%. No measurements were taken forward of 40% chord as the boundary layers were very thin in this region and were, in any case, predicted quite well by theoretical methods (see Section 5.4.2). The measurements were confined to the mid blade height position because it was thought that the smaller radial flows there would lead to a better comparison between the experimental results and the predictions of two-dimensional boundary layer theory.

The hot wire probe was mounted at a fixed axial and circumferential position in the compressor, and the stator blade was moved relative to it by rotating the whole stator row. This meant that the boundary layer traverses were not taken normal to the blade surface, but rather at a slight angle to it in the circumferential direction of the compressor. The change in longitudinal position during a traverse reached a maximum value of 2% chord for the thickest profiles measured at the lowest Reynolds numbers (150 rpm). However, the effect of this shift on the measured boundary layer parameters is not considered to have been very significant in the large majority of cases.

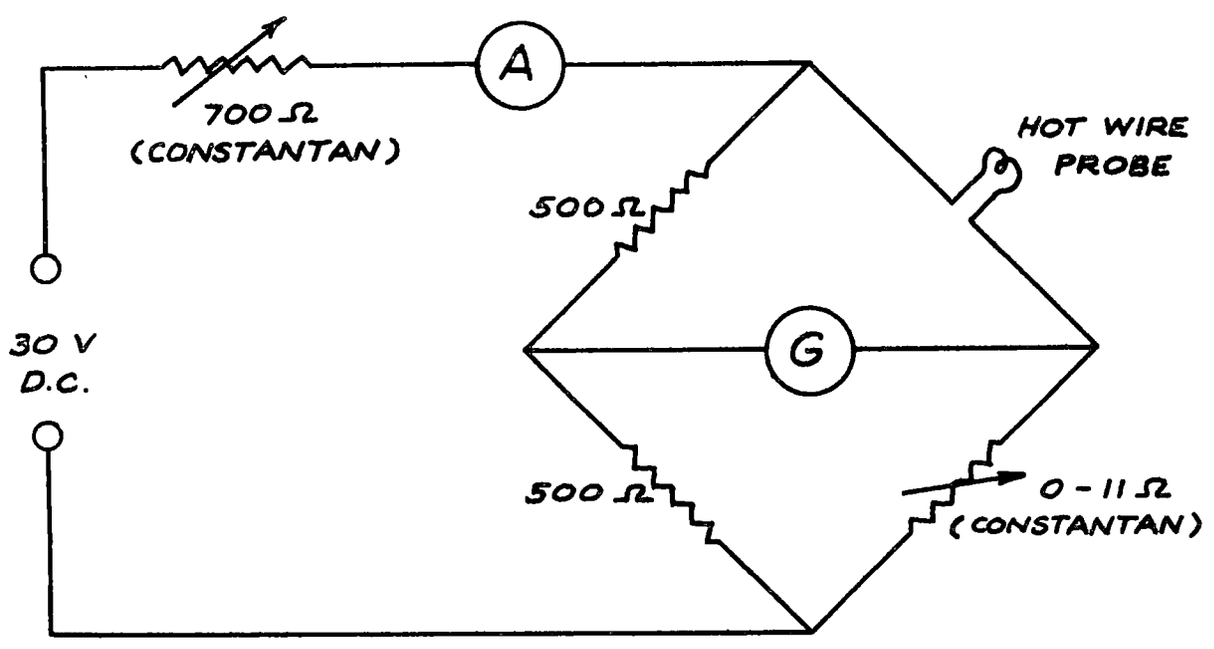


Fig. 3.1 Electrical Circuit for Constant Current Hot Wire Anemometer

A diagram of the electrical circuit used for the mean velocity measurements is shown in Fig. 3.1. The hot wire probe was operated at very nearly constant current by using a high stability constant voltage supply and a series resistance which was large compared with that of the probe. A simple Wheatstone bridge balanced with the aid of a spot galvanometer was used to measure the probe resistance, which was usually in the range 7 to 10 ohm. The balancing resistance could be read to 0.001 ohm, but measurements were

often of lower accuracy than this in unsteady flow situations such as transition boundary layers where it was necessary to average quite large fluctuations of the galvanometer spot. A probe current of about 65 ma was used for velocity measurements in the range 30 - 160 ft/sec; below 30 ft/sec a current of about 40 ma was found to be more suitable, as the probe became too sensitive to velocity fluctuations when operated at the higher current setting. The change from one value of current to the other was effected by the switching in or out of a fixed resistance in series with the constant voltage supply.

As the total boundary layer thickness on the compressor blades was sometimes as low as 0.030 in. it was necessary to develop special techniques for manufacturing and positioning the hot wire probes, and these are discussed in detail in Sections 3.3.3 and 3.3.6. Another major problem that arose in measuring such thin layers was the additional heat loss from the wire due to its proximity to the blade surface; a method of correcting for this effect, suggested by Wills (13), is discussed in Section 3.3.8. The possibility of the velocity measurements also being affected by the supporting prongs is noted in Section 3.3.9.

The calibration of hot wire probes, and the problems of allowing for calibration drift and changes in atmospheric conditions, are dealt with in Sections 3.3.4, 3.3.5 and 3.3.7, respectively. Finally, the overall accuracy of the hot wire mean velocity measurements is assessed in Section 3.3.10, and the methods of data reduction and presentation of results are described in Section 3.3.12.

Some time after the mean velocity traverses had been completed a DISA Constant Temperature Anemometer unit was acquired. Although no further quantitative measurements were obtained with this equipment, it was found extremely useful in observing velocity fluctuations during boundary layer transition on the stator blade. The experimental techniques used in obtaining these observations are discussed in Section 3.3.11.

### 3.3.3 Details of Probe Construction

#### 3.3.3.1 General remarks

The hot wire probes consisted of 0.0003 in. dia. tungsten wire spot-welded to 0.020 in. dia. nickel supports which had been flattened and sharpened at the tips. The average wire length used was 0.18 in. which gave a length/diameter ratio of about 600. Tungsten was chosen as the wire material because of its good mechanical properties, which allowed a certain amount of rough handling when positioning the probe. The use of spot-welding facilitated the accurate positioning of wires on their supporting prongs, an essential requirement when manufacturing probes for use in very thin boundary layers. Details of a typical probe are shown in Figs. 3.2 and 3.3.

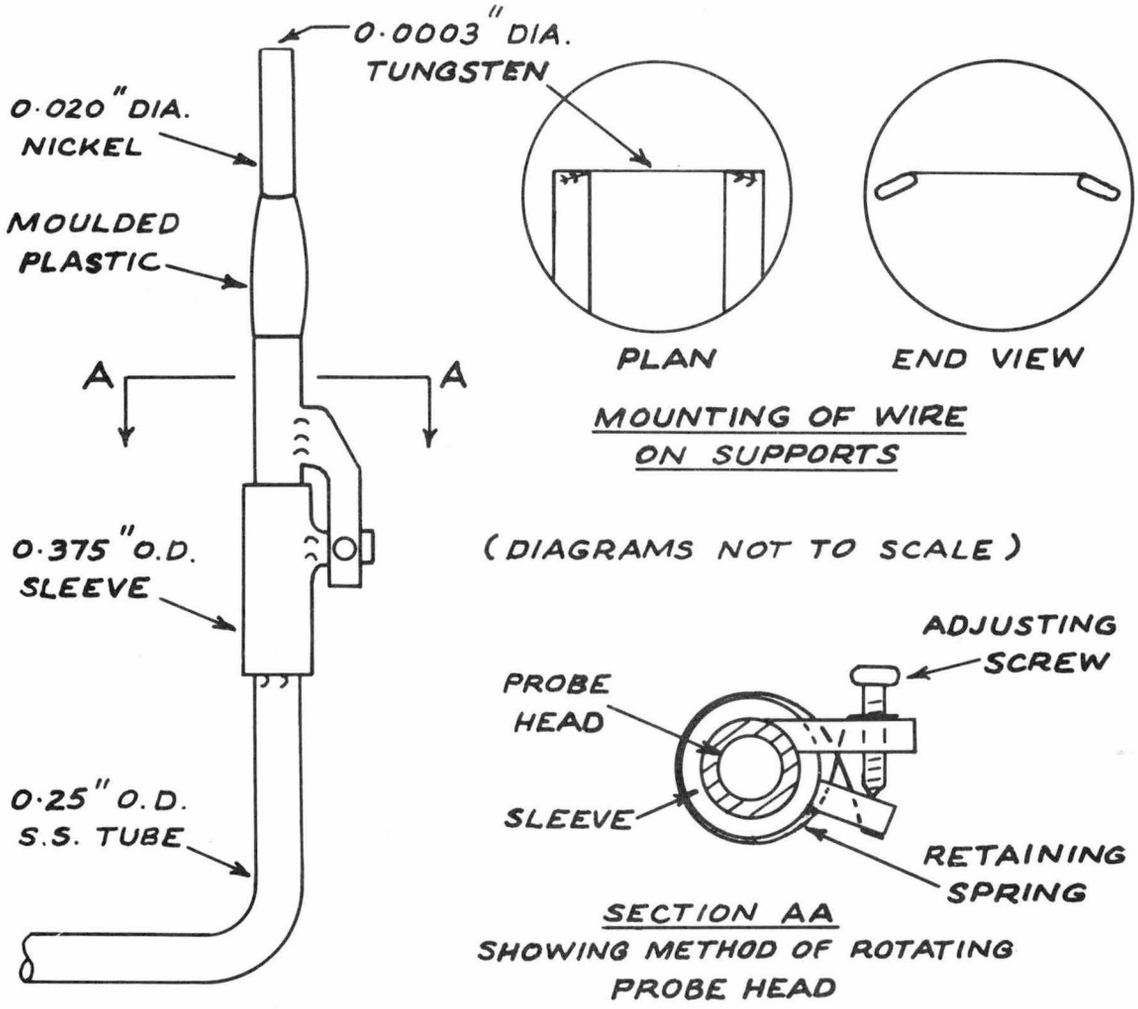


Fig. 3.2 Hot Wire Probe - Details of Measuring Head

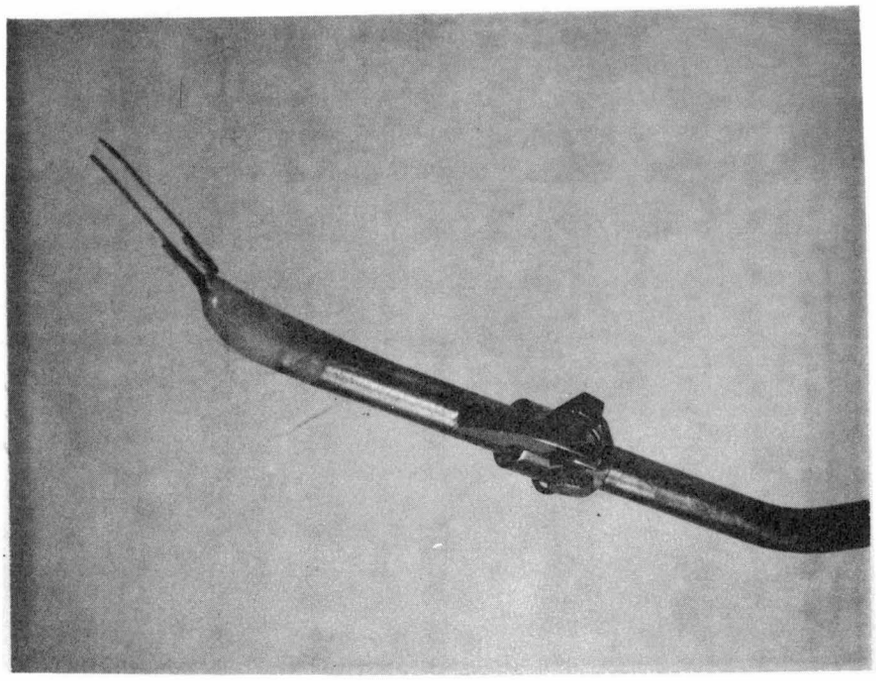

Fig. 3.3 Typical Hot Wire Probe

3.3.3.2 Construction of probe support

The probe support consisted of 0.250 in. O.D. stainless steel tubing of 18 S.W.G. thickness (approximate I.D. 0.154 in.). A connecting plug was soldered to one end to provide for connection to the anemometer unit through a co-axial cable. The probe support was connected to the outer conductor of the cable to ensure that the wire connecting leads inside the support were shielded from external electrical interference. At the other end of this tube the wire supporting prongs were fixed in a commercially available rapid setting plastic moulding compound which was worked to the desired shape by hand.

The wire supports were made of nickel because of its resistance to corrosion, and the ease with which all the commonly used hot wire probe materials could be welded to it. Both the supporting tube and the supporting prongs were bent as required so that the wire supports would be aligned roughly parallel to the local mean flow direction in the situation to be investigated.

When carrying out boundary layer measurements on the compressor blade it was necessary to have some means of rotating the probe head so that the wire could be accurately aligned parallel to the blade surface. This was done by fitting the probe head into a cylindrical sleeve on the end of the probe support, and using a screw adjustment against a retaining spring to rotate the probe. Details of this arrangement can be seen from Figs. 3.2 and 3.3.

3.3.3.3 Welding of wires to supporting prongs

The attachment of the tungsten wire to the nickel supports is not a true welding process because there is actually little fusion of the two metals. To effect a joining of these two metals, the nickel is first melted and the tungsten wire is then forced into it; after cooling, the tungsten wire is held in place by the nickel which has flowed around it and solidified.

A small spot-welding apparatus with copper electrodes was specially constructed for the purpose of mounting the wires on their supports, and a binocular microscope was mounted over it to give the operator a magnified view of the work, as shown in Fig. 3.4. The welding current was provided from a 240 volt A.C. supply through a variable A.C. transformer in series with a fixed A.C. transformer (250 volt : 2.5 volt, 300 volt amps). A foot-operated switch was used to initiate the welding pulse, and a timer in the circuit allowed the pulse duration to be pre-set to the desired value.

The correct welding current for a particular job was easily determined by trial and error setting of the variable transformer. The acceptable range of voltage settings was found to be fairly low; too high a voltage caused arcing, with subsequent cratering or disintegration of the wire supports,

whilst too low a voltage gave insufficient heating to effect a weld. Typical values of current required for joining tungsten to nickel were about 150 amps at 1.5 volts across the electrodes.

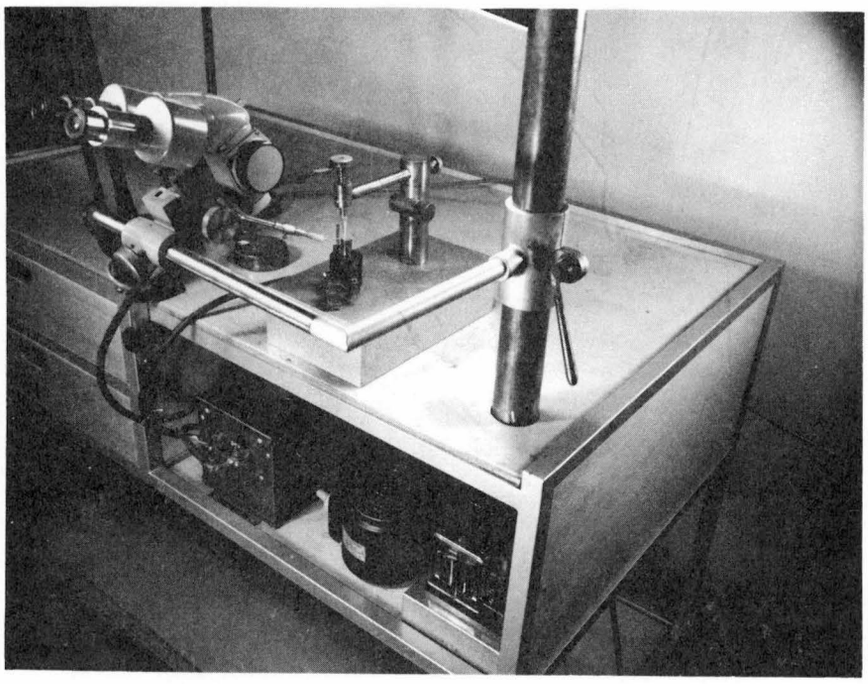

Fig. 3.4 Spot-Welding Apparatus for Constructing Hot Wire Probes

After placing the wire support on the lower electrode and correctly positioning the wire to be welded, the manually operated upper electrode was brought into contact with the work and the circuit closed with the foot switch. Heating the wire support to an orange heat was found to give the best results with tungsten wires. A large degree of control over the temperature of the work was obtained by varying the pressure applied to the upper electrode; this presumably altered both the contact resistance and the amount of arcing between electrode and work. After the weld was completed, the unwanted section of wire was removed by breaking it off with a pair of tweezers. In order to effect a reliable join between tungsten and nickel it was found essential to remove all dirt and oxide film from the work and electrodes before attempting a weld.

When manufacturing probes for use in the compressor blade boundary layers, it was necessary to locate the wire precisely on the prong tips because of the electrical contact method of determining the wire position relative to the blade surface (described in Section 3.3.6). This was more easily achieved when the prong tips were slightly flattened and bent so that they made a slight angle to the surface as shown in Fig. 3.2. Since the wire had to be as straight as possible for measuring in thin boundary layers, the supports were forced together by a small amount before effecting the final weld. On releasing the supports a small amount of tension was introduced into the wire to straighten it out. No attempt was made to electroplate

the ends of the wire in order to reduce the interference effects of the supports, as this would have made the determination of probe position more difficult.

3.3.3.4 Precautions taken before using probes

After the welding process had been completed, the wires were sprayed from a pressurised container with an electrical contact cleaning compound to remove any grease or dust which had accumulated on the wire during manufacture of the probe. The wires were then annealed for a short period by passing a large heating current through them, the maximum permissible current being determined by the temperature at which oxidation of the wire material commenced.

All probes used for obtaining turbulence level measurements or making observations of velocity fluctuations were first examined to see whether any noticeable vibration was present over the working range of flow velocities. The detection and elimination of wire vibration is discussed in Section 3.3.11.

3.3.4 Probe Calibration

The hot wire probes were calibrated in air over the velocity range 5 to 160 ft/sec. The velocity head from the pitot-static tube used as a standard was read on a Betz projection micro-manometer graduated to 0.1 mm water. The only calibration facility available while the mean velocity measurements were being obtained was a 16 in. square open circuit wind tunnel. This was a rather unsatisfactory arrangement because of the unsteadiness of the flow and the danger of collecting dust and fluff on the wire during running. Nevertheless, it was possible with extreme care to repeat calibration curves to within 1% of velocity even under these adverse conditions. (The later introduction of a closed circuit tunnel with a 9 in. square working section greatly simplified calibration because of the steadier and cleaner airstream achieved .)

The calibration curves were initially plotted dimensionally as wire resistance against velocity for constant current operation, (or bridge voltage against velocity for constant temperature operation) after making suitable corrections for changes in atmospheric conditions as shown in Section 3.3.7. This enabled any gross errors in calibration points to be detected immediately. For more refined smoothing of the calibration curves, however, it is better to plot the heat loss from the wire non-dimensionally in terms of Nusselt number and Reynolds number. King (14) originally suggested a relation of the form

$$Nu = A + B\,Re_w^{0.5} \qquad (3.1)$$

but the later work of Collis and Williams (15) indicated that the heat loss from cylindrical wires of infinite length in air could be better correlated by a relation of the form

$$Nu(T_m/T_a)^{-0.17} = 0.24 + 0.56\ Re_w^{0.45} \qquad (3.2)$$

where $T_m = \frac{1}{2}(T_w + T_a)$ is the arithmetic mean film temperature. The factor $(T_m/T_a)^{-0.17}$ was introduced to allow for Prandtl number variation and other temperature loading effects. Equation (3.2) is valid for incompressible flow up to $Re_w = 44$, where eddy shedding into the wake of the wire commences; its lower limit of validity is determined by the onset of free convection when buoyancy effects become large. Collis and Williams gave an approximate expression for the Reynolds number at which free convection becomes significant as

$$(Re_w)_a = 1.85\ (Gr)_a^{0.39}\ (T_m/T_a)^{0.76} \qquad (3.3)$$

where the subscript "a" indicates that the fluid properties are to be evaluated at the ambient temperature, $T_a$.

For all the hot wire calibrations obtained in the present investigation, a plot of $Nu(T_m/T_a)^{-0.17}$ against $Re_w^{0.45}$ was found to be a better approximation to a straight line than Nu against $Re_w^{0.5}$. But for wires of $l/d = 600$ there was always some residual curvature in the graph of $Nu(T_m/T_a)^{-0.17}$ against $Re_w^{0.45}$, and the best straight line fit to the results differed markedly from Equation (3.2). This difference is probably explained by the conduction of heat to the wire supports, which becomes comparable with the heat loss to the airstream for wires of low l/d. Equation (3.2) correlates the heat loss for wires of infinite l/d, in which case the amount of heat conducted to the supports is negligible compared with the heat transferred to the airstream by forced convection.

The proportion of heat lost to the supports is a function of the thermal conductivity of the wire material, the l/d ratio of the wire, and the temperature distribution along the wire, which varies with the wire Reynolds number and is also influenced by the flow around the supports. It is hardly surprising, therefore, to find that the Nusselt number based on the total rate of heat loss from the wire is significantly different from the value predicted by Equation (3.2) when the l/d ratio of the wire is small. It is noted that the tungsten wires used in the present investigation had a rather higher thermal conductivity than other commonly used wire materials and this undoubtedly helped to produce the large conduction loss observed; the conductivity of tungsten is about 2.5 times that of platinum.

It is very desirable to obtain an accurate analytical approximation to the heat transfer relation for a hot wire probe as an aid to smoothing calibration measurements. Even though individual quantities such as ambient conditions, wire resistance, bridge voltage, and velocity head can be read to a reasonably high accuracy, it must be expected that small random errors in their measurement will occasionally accumulate to produce a significant deviation from the true heat transfer relation. Another use of the smoothing curve is in the extrapolation of the wire calibration to velocities lower than those which can be directly measured with sufficient accuracy by a pitot-static tube. When using a projection micro-manometer

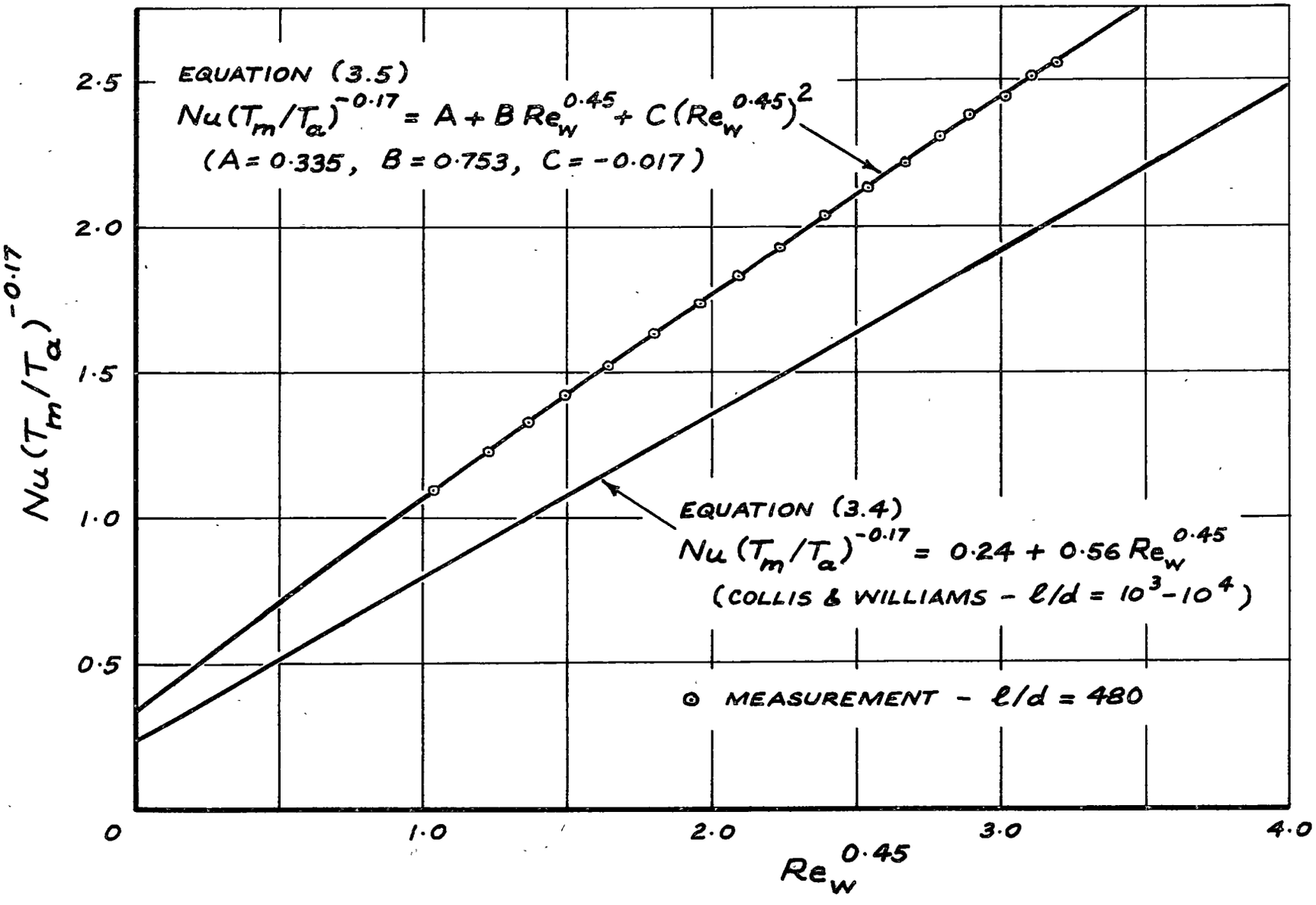


Fig. 3.5 Typical Hot Wire Probe Calibration

reading velocity head to 0.01 mm water, the possible reading errors exceed 1% of velocity at speeds less than about 10 ft/sec in air at normal pressure. Rather than obtaining the calibration at lower velocities by measurement in more complicated calibration facilities or by use of more sensitive manometers, it is far easier and probably just as accurate to extrapolate the smoothed curve fitted to the higher velocity calibration. The validity of this process for hot wire probes of small l/d ratio has been adequately demonstrated by Almquist and Legath (16).

Fig. 3.5 shows a typical calibration curve obtained from a tungsten wire 0.0003 in. diam. with l/d = 480; this probe was calibrated at constant current, I = 54 ma, over a range of air velocities from 7 to 75 ft/sec. The measured points show systematic deviations from a straight line

$$Nu(T_m/T_a)^{-0.17} = A + B\,Re_w^{0.45} \qquad (3.4)$$

In this case, the use of the linear relation, Equation (3.4), as the smoothed calibration curve would lead to errors of up to 3% of local velocity in the range of the experimental data; greater errors would result from extrapolation beyond this range.

To make some allowance for the curvature of the measured heat transfer relation shown in Fig. 3.5, it was decided to fit a parabolic relation of the form

$$Nu(T_m/T_a)^{-0.17} = A + B\,Re_w^{0.45} + C(Re_w^{0.45})^2 \qquad (3.5)$$

Fortunately, Equation (3.5) is a fairly good fit, and the measured calibration points in Fig. 3.5 deviate from it by amounts corresponding to velocity variations generally less than 0.5% of local velocity; furthermore, there is no longer any systematic trend discernible in the deviations, which appear to be distributed randomly. Since these differences are no greater than the possible experimental error, it appears that Equation (3.5) can be used with some confidence to represent the heat loss from "finite" wires (i.e. those of small l/d ratio).

A least squares fit to the data shown in Fig. 3.5 gave values of A = 0.335, B = 0.753 and C = -0.017 for the constants in Equation (3.5). It can be seen that the measured heat loss in this case differs greatly from that given by Collis and Williams in Equation (3.2). The above values for the parameters A, B, and C should not be taken as universal, since they are expected to be functions of l/d, the wire conductivity, the shape of the wire supports, and the manner of mounting the wire; they will therefore need to be determined individually for each wire calibration.

### 3.3.5 Correction for Calibration Drift

Calibration drift during running was minimised by annealing the wires after manufacture, and by spraying them with cleaning fluid at regular intervals to remove small dust particles. However, there was usually some residual calibration drift due to tarry deposits accumulating on the wire, or from impacts of large dirt particles straining the wire. Calibration

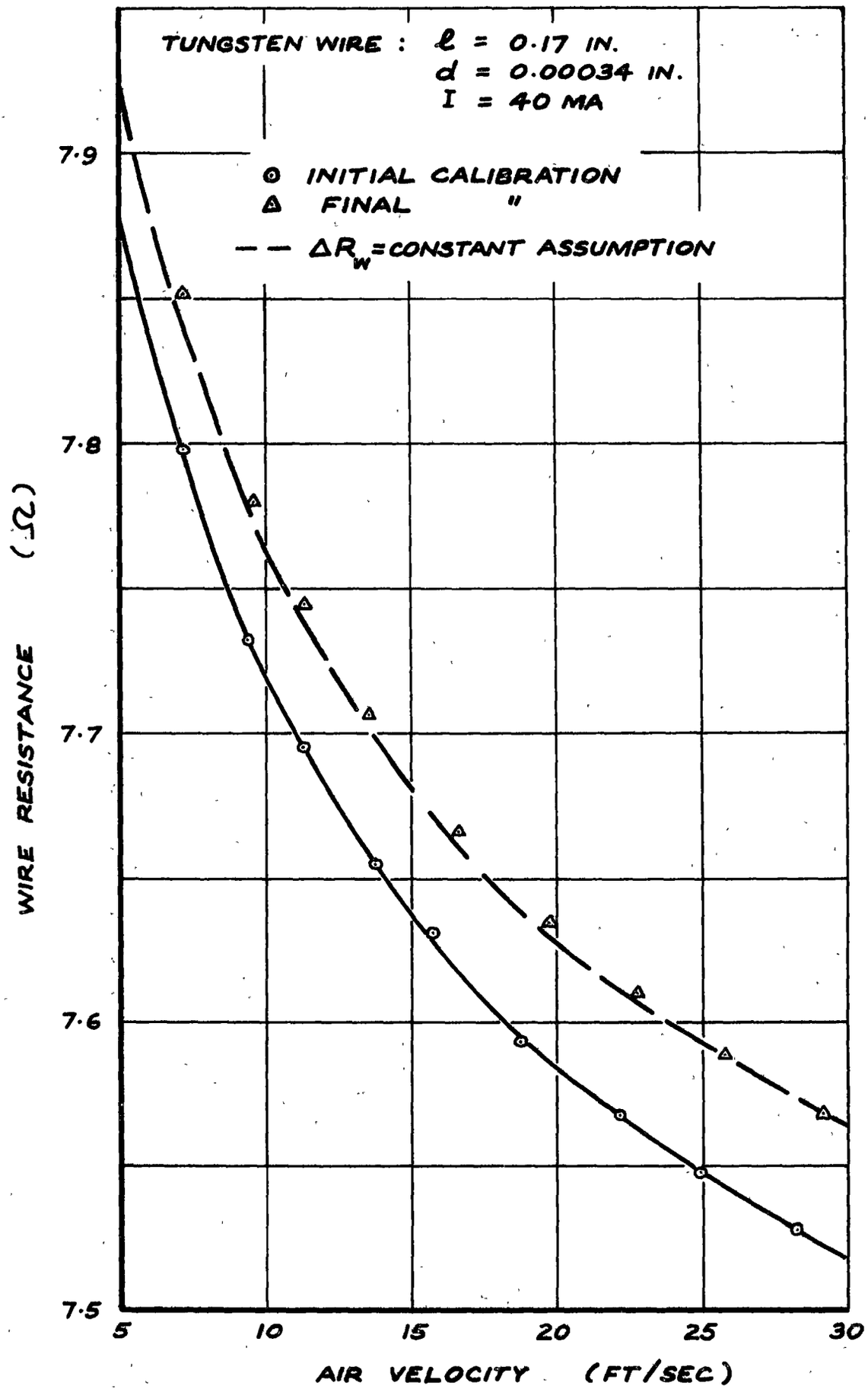


Fig. 3.6 Allowance for Drift in Hot Wire Probe Calibration

shifts of 5 to 10% of velocity after 20 hours running were fairly typical in the present investigation. Because positioning the hot wire probes in the compressor was a fairly difficult process, it was decided to obtain a measure of the calibration drift at any particular time and to apply a suitable correction for it, rather than to remove the probes from the compressor at frequent intervals for recalibration.

The procedure adopted was to place the hot wire probe at a fixed chordwise position on the stator blade and then to make all the boundary layer traverses at that position for the various standard compressor speeds and throttle openings before shifting the probe. In this case it was convenient to use the outer edge of each boundary layer measured as a reference point for checking calibration drift. The velocities at all these positions were measured immediately after a probe had been placed in the compressor, and immediately before its removal for recalibration. This process should have established the reference velocities to a reasonable accuracy, as any calibration change over the short interval required to measure them would have been negligible. Some care was taken to minimise other possible sources of error in determining the reference velocities, such as changes in compressor speed or Reynolds number.

For hot wire probes operated at constant current it was found that small calibration changes could usually be approximated with sufficient accuracy by a constant change in resistance over the whole speed range, as shown in Fig. 3.6. The resistance change was selected to make the velocity at the outer edge of each boundary layer equal to its accurately determined reference value. As the calibration shift was not exactly constant with speed, this process led to increasing errors in resistance at lower velocities; however, the corresponding errors in velocity measurement were usually tolerable because of the higher probe sensitivity at lower speeds.

This simple model would be too inaccurate for large calibration drifts, which would require an allowance for changes in slope of the calibration curve as well; at least two reference points would be needed in such cases. The ideal way of allowing for large movements in a hot wire calibration would be to completely recalibrate the probe in situ. But this is impracticable in a compressor because of the limited space available, the large spatial variation in the flow velocity, and the unsteady nature of the flow which has an uncertain effect on pressure probes.

### 3.3.6 Positioning and Alignment of Hot Wire Probes

The accurate alignment of the sensing wire with the wall, and the determination of its position relative to the wall, are of obvious importance when measuring in very thin boundary layers. Any errors in performing these tasks can produce quite large changes in measured values of wall shear stress and boundary layer thickness. The likely error in displacement thickness is

about the same as the error in determining the probe position relative to the wall; fortunately, the momentum thickness value is much less sensitive to errors of this kind. As the measured boundary layers on the stator blade of the research compressor had values of displacement thickness as low as 0.006 in., corresponding to a total thickness of about 0.030 in., it was necessary to position the hot wire probe to 0.0005 in. or better in order to obtain useful measurements.

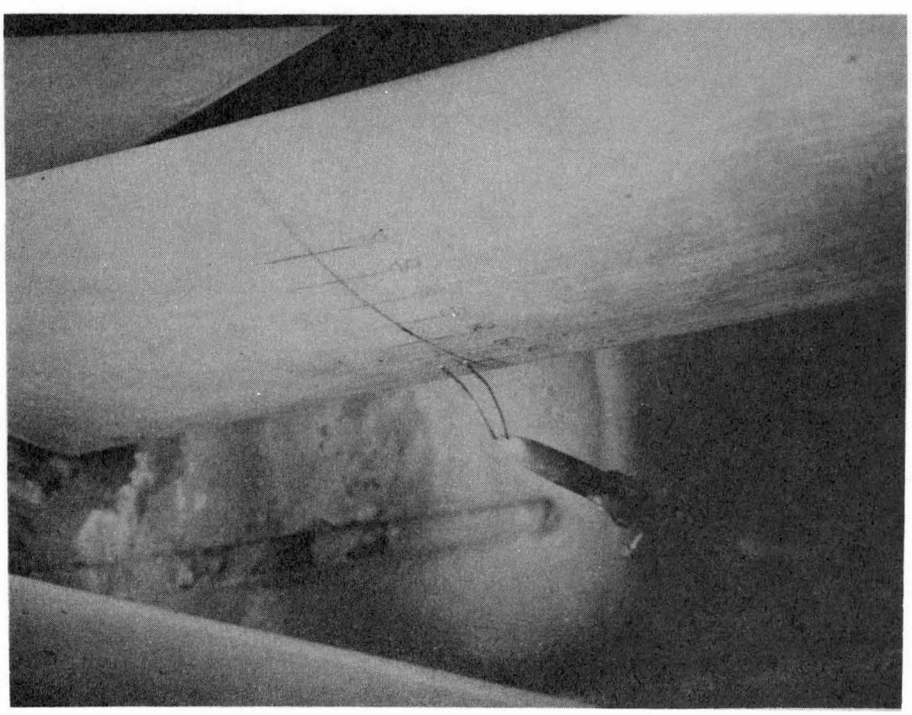

Fig. 3.7 Hot Wire Probe Mounted in Compressor

A photograph of a hot wire probe mounted in the compressor is shown above in Fig. 3.7. The probe holder was clamped firmly at the point where it passed through the instrument slot in the outer shell of the compressor, so that the probe was effectively supported by a cantilever only 5 in. long. A calculation of the likely deflection of the probe support under aerodynamic forces showed it to be only 0.0001 in. at the maximum flow velocity obtainable. Thus it was concluded that any movements of the probe itself would be negligible.

Movement of the stator blade due to its bending and twisting under aerodynamic forces while the compressor was running was also considered as a possible source of error in determining the probe position. The blade surface displacement at 10%, 50%, and 90% chord was checked with a dial gauge clamped inside the compressor as shown in Fig. 3.8. A typical set of deflection measurements is shown in Fig. 3.9; the accuracy of these readings is thought to be about 0.0001 in. The maximum displacement observed, about 0.002 in.,

was obviously significant; a suitable correction to the probe position was therefore applied in each boundary layer traverse to allow for the blade movements.

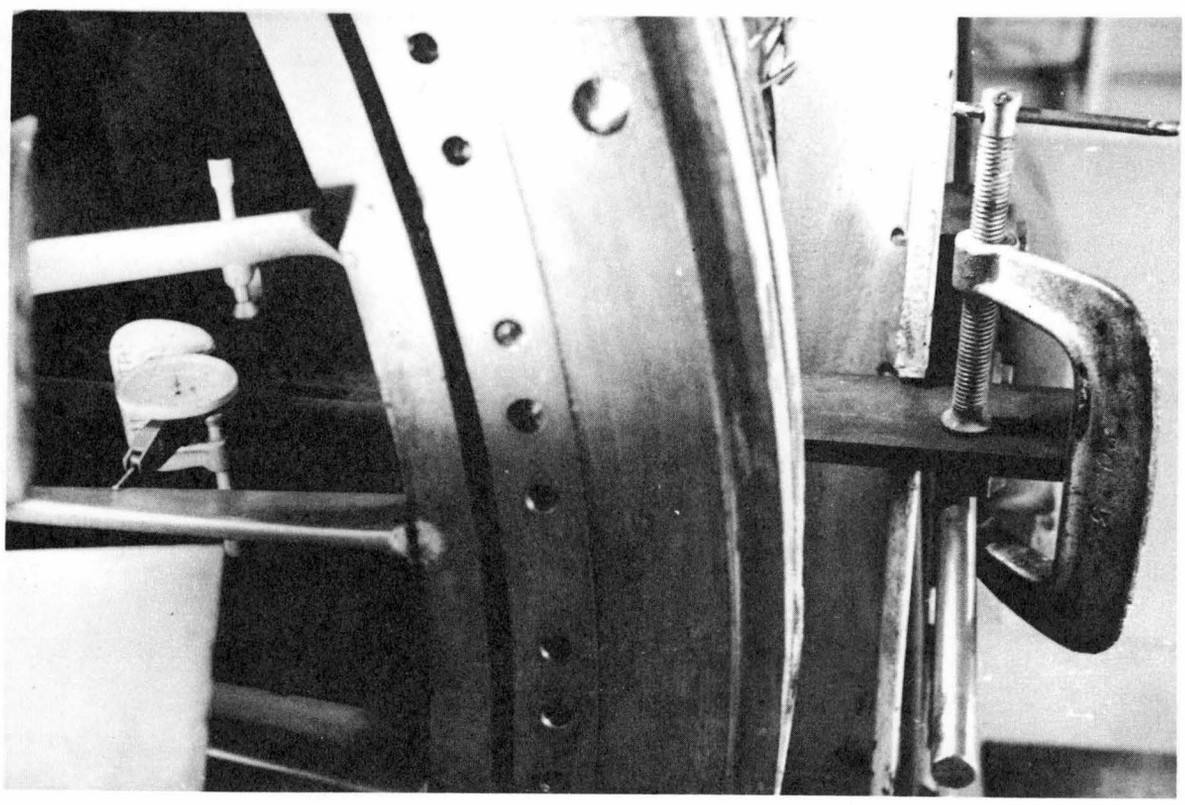

Fig. 3.8 Arrangement for Measuring Stator Blade Deflection

For the purpose of aligning the wire, the stator blade was traversed to within a few wire diameters of the probe, which was then viewed through a watchmaker's loupe along a line tangent to the blade surface. Back-lighting was provided so that the gap between the wire and the surface was clearly visible. The probe head was then rotated until the wire appeared parallel to the surface; any misalignment was readily discernible with the wire this close to the blade, and the accuracy of alignment achieved was probably better than one wire diameter over the length of the wire.

Movement of the hot wire probe relative to the blade surface was achieved by rotating the whole stator row. Displacements of the stator blade supporting ring were measured by a dial gauge graduated to 0.0001 in. which was clamped to the outer shell of the compressor. The position reading corresponding to the wire touching the blade surface was determined by electrical means; a resistance meter was connected between the probe leads and the stator supporting ring, and the blade was then traversed towards the wire until a sudden drop from open circuit to a finite resistance indicated that the wire had contacted the blade surface. (This method is only practicable if the probe is constructed as shown in Fig. 3.2 so that the sensing wire touches the surface before its supporting prongs). It was necessary to use extreme care

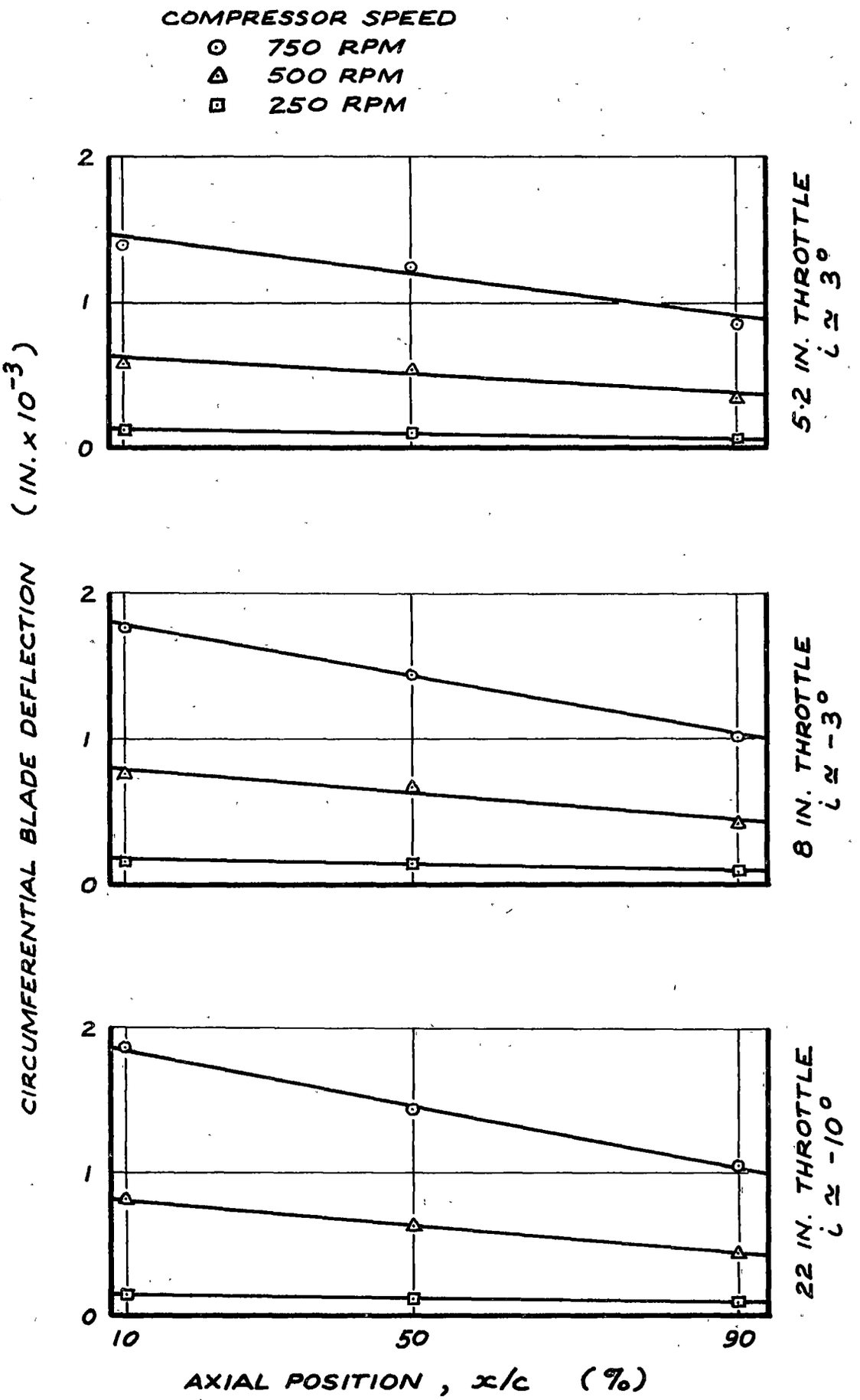


Fig. 3.9 Typical Measurements of Stator Blade Deflection at Mid-Blade Height

in this process as too sudden a contact would have given an inaccurate reading of the contact position, and might also have caused a significant calibration change by straining the wire. Where any small calibration changes did occur, they were corrected for by the method of Section 3.3.5.

Any method of determining the probe position relative to the blade which did not involve as great a risk of straining the wire would certainly have been more preferable. A traversing microscope might be suitable in some situations but it was considered impracticable in this investigation because of the small amount of space available between the compressor blade rows.

### 3.3.7 Correcting Hot Wire Readings for Changes in Atmospheric Conditions

When the heat transfer from a hot wire anemometer probe is plotted non-dimensionally as $Nu(T_m/T_a)^{-0.17}$ against $Re_w$, the results all collapse onto a single curve which is independent of atmospheric conditions. However, it is often convenient or desirable to plot the calibration curve dimensionally as wire resistance against velocity for constant current operation, or bridge voltage against velocity for constant temperature operation; in this case, a family of curves is obtained for different atmospheric conditions, and the measured resistance or voltage must be corrected to some standard atmospheric pressure and temperature before the flow velocity can be determined.

Correction formulae suitable for the relatively small variations in ambient pressure and temperature normally encountered in practice will now be summarised. Their derivation is set out in detail in Appendix A.

(a) Constant current operation

The change in wire resistance, $dR_w$, for small changes in atmospheric temperature and pressure of $dT_a$ and dP, respectively, is given by

$$\frac{dR_w}{R_w} = \left(1 - 0.606\,\frac{\theta}{T_m}\right)\frac{R_o \alpha\, dT_a}{R_a} + 0.36\left(1 - \frac{R_w}{R_a}\right)\frac{dP}{P} \qquad (3.6)$$

where $\alpha$ is the temperature coefficient of resistance of the wire at temperature $T_o$, $R_o$ is the wire resistance at temperature $T_o$, and $R_a$ is the wire resistance at ambient temperature $T_a$.

(b) Constant temperature operation

The corresponding change in bridge voltage, dV, for this mode of operation is given by

$$\frac{dV}{V} = -\left(1 - 0.303\,\frac{\theta}{T_m}\right)\frac{R_o \alpha\, dT_a}{2(R_w - R_a)} + 0.18\,\frac{dP}{P} \qquad (3.7)$$

It is interesting to note that for constant temperature operation the effects of pressure changes can easily equal those due to ambient temperature

variations. The sensitivity to pressure changes is independent of the overheating ratio for constant temperature operation, but becomes directly proportional to the overheating ratio for constant current operation.

In both modes of operation the sensitivity to ambient temperature variations is decreased as the overheating ratio, $T_w/T_a$, becomes larger.

### 3.3.8 Correction of Hot Wire Readings for Proximity to a Solid Boundary

#### 3.3.8.1 Introduction

The presence of a solid boundary close to a hot wire probe can produce significant changes in the rate of heat loss from the wire for a given local velocity. In this case, the use of a calibration obtained with the wire remote from any boundary is inappropriate, and can lead to appreciable errors in calculating the flow velocity from the measured wire resistance or anemometer bridge voltage.

The problem of correcting hot wire readings to allow for proximity to a solid boundary at ambient temperature was examined in detail by Wills (13). It was found that the rate of heat loss from a cylindrical wire close to a plane wall in incompressible laminar flow was given by

$$Nu(T_w/T_a)^{-0.17} = A + 0.56\, Re_w^{0.45} \qquad (3.8)$$

where the parameter A depended only on b/a, the ratio of the distance of the wire from the wall to the wire radius. For very large values of b/a, where the effect of the wall is negligible, Equation (3.6) becomes almost identical to Equation (3.2) given by Collis and Williams (15) (except that Wills used $T_w$ instead of $T_m$ in the temperature loading factor, but this difference does not appear to be greatly significant).

This fortuitous result provides a very simple means of correcting hot wire readings in laminar flow, since the only effect of a wall at ambient temperature is to cause an extra heat loss which remains constant (i.e. is independent of $Re_w$) when the wire is at a fixed distance from the wall. Wills's measurements of this additional heat loss are plotted as $Nu(T_w/T_a)^{-0.17}$ against b/a in Fig. 3.10, and are also given numerically in Table 3.3. It is noted that the relation shown in Fig. 3.10 was only verified for a limited range of wire Reynolds number due to the requirement of maintaining laminar flow; the maximum values of $Re_w$ achieved by Wills ranged from $Re_w = 0.2$ for b/a = 10, to $Re_w = 1.0$ for b/a = 100, as shown in Fig. 3.11.

The correction required when the flow near the wall was turbulent was found by Wills to differ markedly from the laminar flow correction. On the basis of measurements of turbulent flow in a two-dimensional channel of constant width, Wills suggested that the extra heat loss to the wall in this case should be of the same sign as that occurring in laminar flow, but smaller in magnitude by a factor of $0.5 \pm 0.1$. He was unable to explain why this factor was less than unity, except to suggest that the turbulent

motion would convect heat away from the wall on the average to a greater extent than the laminar motion, and might thereby reduce the total heat loss to the wall. Wills only expected the turbulent flow correction to apply within the viscous sub-layer, where the laminar and turbulent velocity profiles are generally similar.

Table 3.3

Effect of Wall Proximity on Heat Loss from Cylindrical Wires in Incompressible Laminar Flow near a Solid Boundary (from Wills (13))

| Distance from Wall b/a | Additional Heat Loss $Nu(T_w/T_a)^{-0.17}$ |
|---|---|
| 10 | 0.228 |
| 15 | 0.160 |
| 20 | 0.122 |
| 30 | 0.078 |
| 40 | 0.056 |
| 50 | 0.041 |
| 60 | 0.030 |
| 70 | 0.022 |
| 80 | 0.017 |
| 90 | 0.013 |
| 100 | 0.010 |

3.3.8.2 Correction of hot wire readings in laminar flow regions on the compressor blade

In the present investigation, many of the laminar boundary layer regions on the stator blade suction surface were so thin that the effect of the wall on the heat transfer from the hot wire probe was significant over most of the boundary layer height. The outer edge of the thinnest layer measured corresponded to b/a = 130 with the 0.0003 in. diameter wires used. Clearly, few useful experimental results could have been obtained in such cases without first applying a reasonably accurate correction to allow for the wall proximity effects.

Although the range of wire Reynolds number obtained in the compressor blade measurements was much greater than that of Wills's investigation, it was decided to apply the heat loss correction of Fig. 3.10 to see whether it yielded useful results. To minimise errors in determining b/a, which could have led to large errors in the applied correction for b/a small, the wire radius, a, was measured to ± 0.00001 in. using a microscope with an image-splitting eyepiece; variations of ± 10% in diameter were observed in wire nominally the same size, and in one isolated instance a length of 0.0005 in.

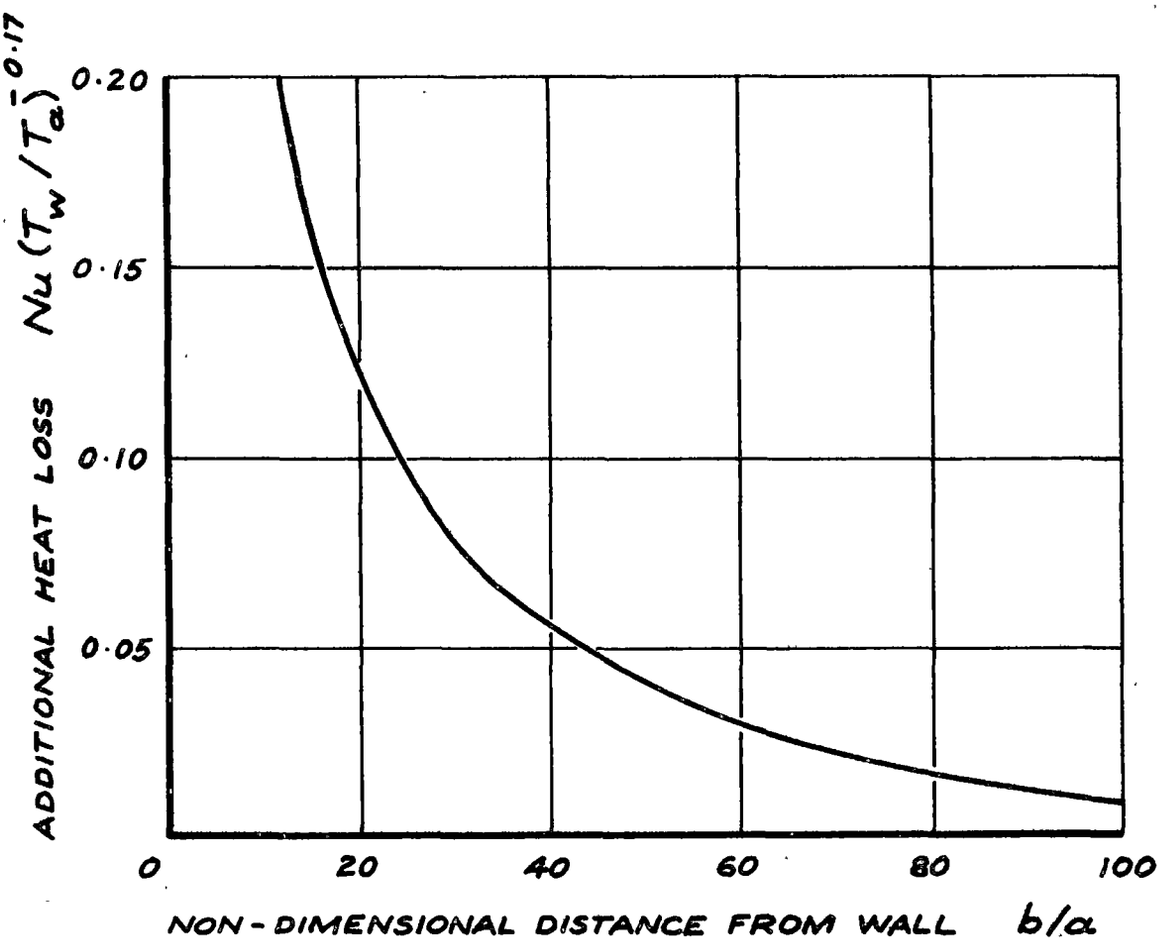


Fig. 3.10 Effect of Wall Proximity on Heat Loss from Cylindrical Wires in Laminar Flow - from Wills (13)

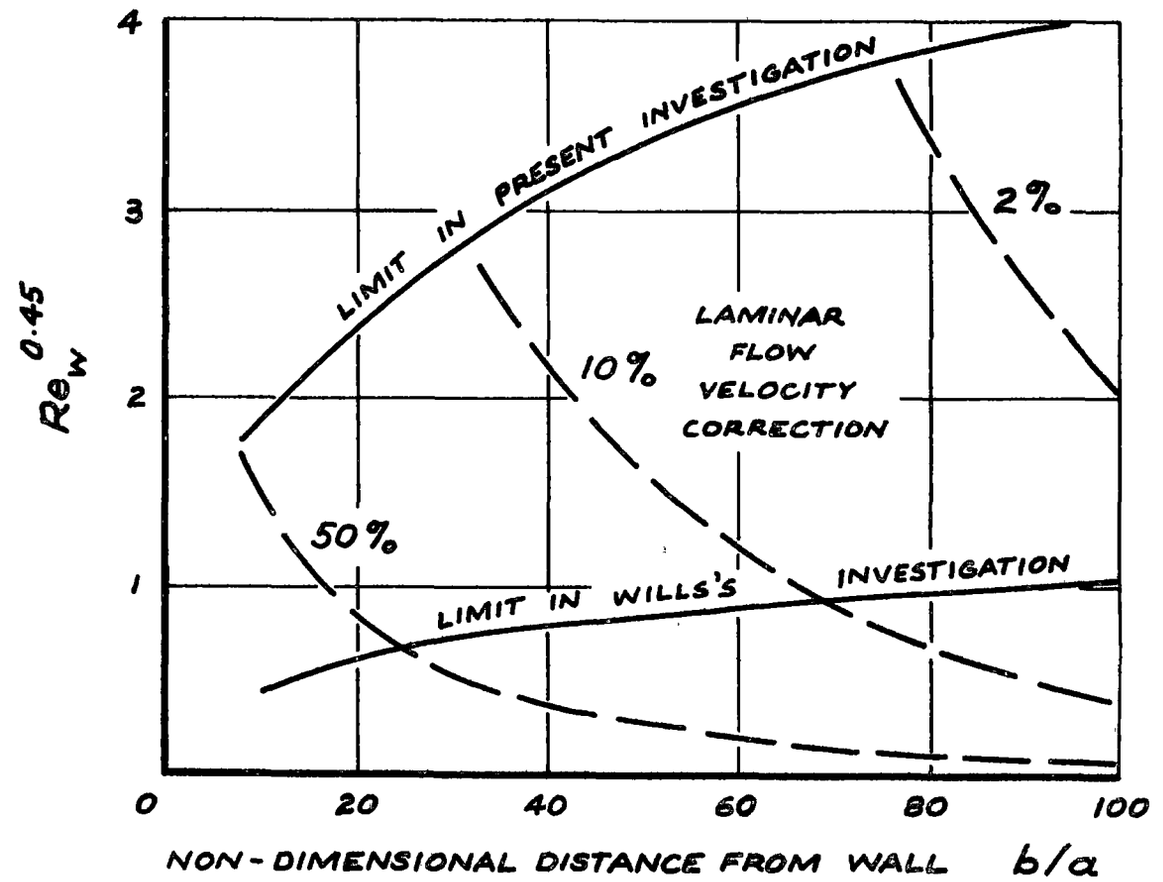


Fig. 3.11 Range of Conditions for which Wall Proximity Correction was Applied to Hot Wire Readings

diameter wire was found amongst wire nominally 0.0003 in. diameter. For all the laminar boundary layers measured, the corrected velocity profiles were smooth curves passing quite close to zero velocity on extrapolation to the measured wall position, $y = 0$. A comparison of the corrected velocity profiles with the theoretical velocity distributions for a laminar boundary layer in the same pressure gradient gave very reasonable agreement. (See, for example, Fig. 5.1 which is discussed in detail in Section 5.2 .)

It was therefore concluded that Wills's correction gave quite an adequate description of the wall proximity effects in the laminar boundary layer regions on the compressor blades. This result implied that Wills's correction was valid for a rather greater range of wire Reynolds number than was covered in his original investigation. The range of values of $Re_w$ covered in the compressor blade measurements is shown in Fig. 3.11; the maximum values varied from $Re_w \simeq 4$ for $b/a = 10$, to $Re_w \simeq 16$ for $b/a = 100$.

To give some idea of the possible magnitude of errors arising from wall effects on hot wire readings, a comparison between the corrected and uncorrected velocity profiles for a typical laminar boundary layer traverse on the stator blade has been made in Fig. 3.12. In this case, the total boundary layer thickness, $\delta$, was about 0.030 in., and the measuring wire was about 0.0003 in. diameter. At a distance of 0.002 in. from the wall ($y/\delta \simeq 0.06$) the error in mean velocity due to neglecting the extra heat loss near the wall is about 10% of the free stream velocity (or about 100% of the local mean velocity), which leads to an error of about 100% in the wall shear stress. The uncorrected velocity profile gives values of boundary layer displacement thickness and momentum thickness which are too low by 8%, and too high by 5%, respectively.

The importance of measuring the origin for y by some independent means when wall effect is significant, rather than by extrapolating the measured velocity profile to zero velocity, can easily be seen from Fig. 3.12. In this case, extrapolation of the uncorrected velocity profile gives an error of about $0.1\delta$ in locating the wall position; furthermore, there would be a strong possibility of breaking the wire by touching it on the wall, since the apparent origin is at $y = -0.1\delta$. It would be rather impracticable to proceed by assuming an origin, making an approximate wall correction, extrapolating the corrected profile to the origin, and then iterating, since this process is at best tedious and might not converge on the true origin. In any case, it is desirable to measure the origin for y independently, as the redundant information thus gained allows a better estimation of the accuracy of velocity profile measurements.

3.3.8.3 Correction of hot wire readings in turbulent flow regions on the compressor blade

The wall proximity correction to the hot wire readings usually influenced only the inner part of the measured velocity profiles in

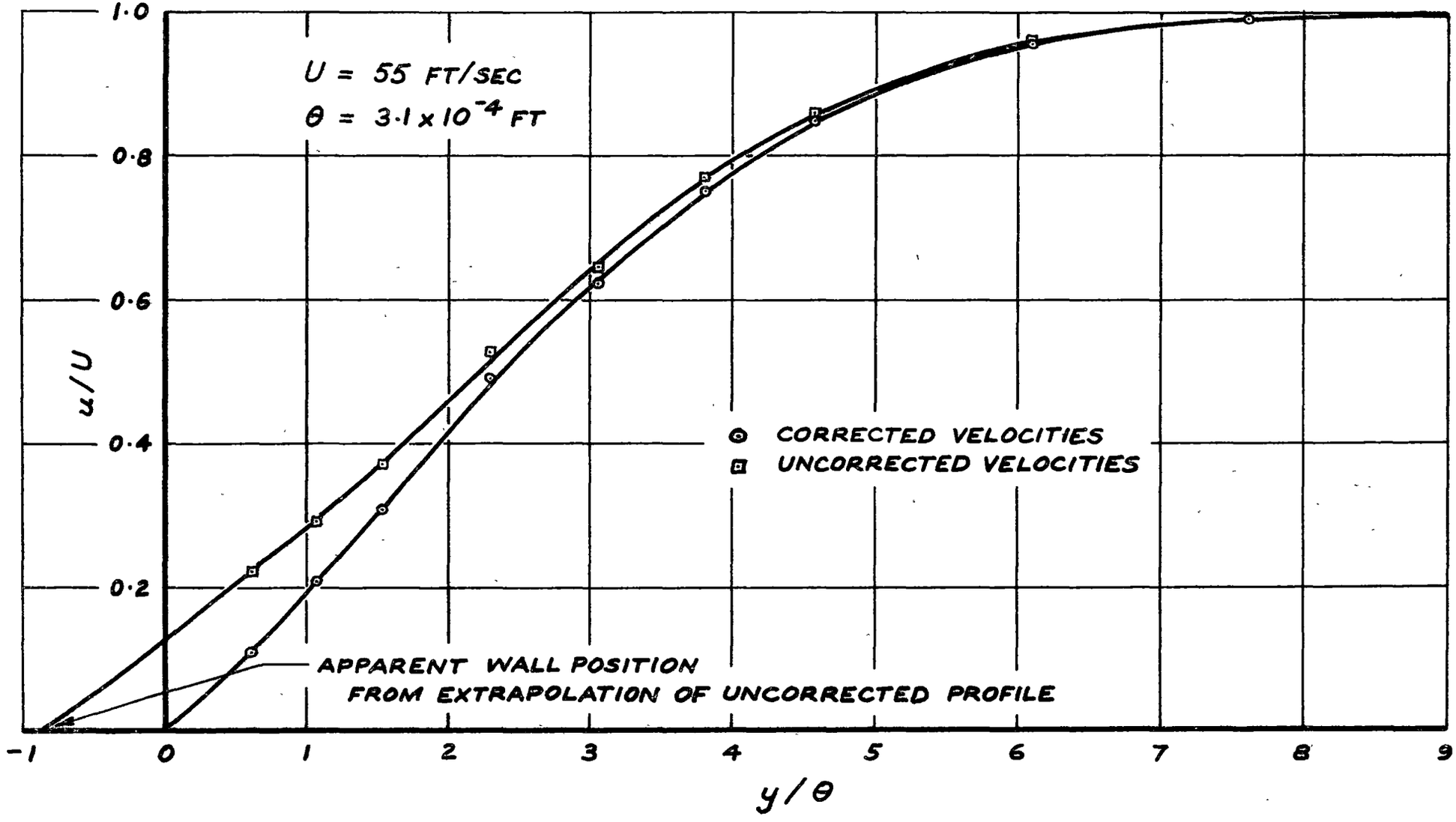


Fig. 3.12 Effect of Wall Proximity on Hot Wire Readings in a Laminar Boundary Layer

the turbulent flow regions on the stator blade suction surface, because of the relatively greater boundary layer thickness in these areas. At x/c = 90%, for example, the wall effect became insignificant for $y > 0.1\delta$, approximately, and use of the uncorrected velocity profiles would have caused errors in the displacement and momentum thickness values of only 1 - 3% and 1 - 2%, respectively. Nevertheless, the wall correction still affected the measured wall shear stress value at 90% chord by some 20 - 100%, depending on the Reynolds number. Thus it was still essential to apply a wall proximity correction to hot wire readings in the turbulent flow regions in order to obtain a useful description of the wall layer behaviour, and to provide reasonably accurate values of non-dimensional parameters involving the wall friction velocity, $u_\tau = \sqrt{\tau_w/\rho}$.

Following Wills's suggestion, all hot wire readings in the turbulent boundary layer regions were initially corrected by assuming the additional heat loss due to the wall to be half of that occurring in laminar flow. However, the corrected velocity profiles obtained did not appear physically reasonable, particularly with regard to the variation of the mean vorticity, $\zeta = \partial u/\partial y$, through the viscous sub-layer. The results were then reprocessed using the full laminar flow wall correction to see whether this would be more satisfactory. In this case, the corrected velocity profiles appeared to behave rather more reasonably, and there was a greater degree of consistency between the non-dimensional plots of the various velocity profiles measured in fully developed turbulent flow regions. It was therefore decided to adopt the results obtained by using the full laminar flow heat loss correction. (A detailed discussion of the physical reasoning behind this decision is left until Section 7.2, which examines the behaviour of the measured velocity profiles in turbulent flow regions.)

Since the above decision implied that the use of half the laminar flow wall correction in turbulent flow was either not general or incorrect, a separate experiment was designed to check the validity of Wills's original results. This was done by measuring the mean velocity profile of a turbulent boundary layer on a smooth metal plate, with a hot wire probe similar to those used previously in the compressor blade boundary layer measurements. The plate was placed parallel to one wall of the 9 in. square working section of a closed circuit wind tunnel, as shown in Fig. 3.13. At the measuring station, which was situated about 2.0 ft. from the leading edge of the plate, the free stream velocity was about 65 ft/sec, and the pressure gradient was zero, apart from a slight flow acceleration resulting from wall boundary layer growth; it was therefore expected that a well developed logarithmic similarity region would exist near the wall at this position. The boundary layer was sufficiently thick ($\delta \simeq 0.45$in.) for the wall proximity correction to be negligible in the logarithmic part of the velocity distribution. However, the wall effect still exerted a considerable influence on the hot wire readings in the viscous sublayer, which determined the wall shear stress,

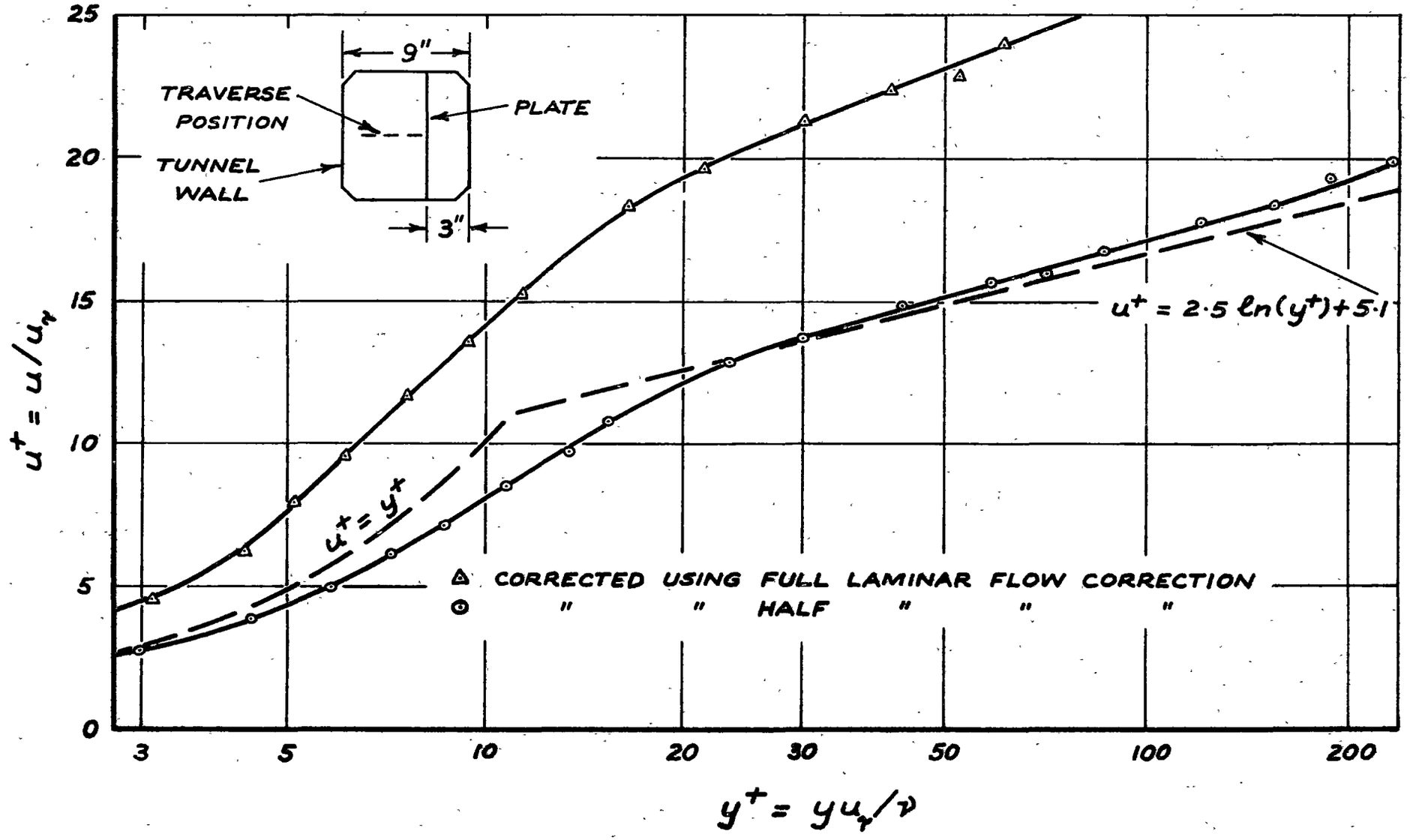


Fig. 3.13 Correction of Hot Wire Readings for Wall Proximity Effect in Turbulent Boundary Layer on Flat Plate
(U = 66 fps, $Re_\theta$ = 1590, H = 1.43)

$\tau_w = \mu(\partial u/\partial y)_{y=0}$. Thus any errors in allowing for wall effect were expected to give an incorrect value of $\tau_w$, which would in turn result in a plot of $(u/u_\tau)\sim(yu_\tau/\nu)$ deviating from the accepted law of the wall in the logarithmic region, given by Spangenberg et al.(19) as

$$u/u_\tau = 2.5\ln(yu_\tau/\nu)+5.1 \quad (yu_\tau/\nu>30) \qquad (3.9)$$

The experimental results are plotted in Fig. 3.13, and it is seen that the corrected velocity profile based on half the laminar flow wall correction is in excellent agreement with the law of the wall, Equation (3.7), whereas the use of the full correction results in considerable deviations from this relation. The use of half the laminar flow wall correction therefore appears justified for the case of turbulent flow in zero pressure gradient, but unjustified for the turbulent flow regions on the compressor blades.

The major difference between the boundary layer on the plate and the boundary layers on the compressor blade was that the latter were subjected to strong positive pressure gradients. It could be concluded, therefore, that for $dp/dx>0$ the extra heat loss from a hot wire near a solid boundary in turbulent flow varies between 0.5 and 1.0 times the corresponding heat loss in laminar flow, depending on the magnitude of the streamwise pressure gradient. This variation might also be explained in terms of Wills's suggestion that the mean heat transfer path from the wire in turbulent flow is altered by the fluctuating component of velocity normal to the wall, v'. Since the values of v' near the wall are much lower in an adverse pressure gradient (see, for example, the results of Spangenberg et al.(19)) it would be reasonable to expect a smaller amount of heat to be convected away from the wall on the average in this case; this would presumably result in a smaller difference between the laminar and turbulent flow wall proximity corrections.

In conclusion, it is stressed that the experimental results of the present investigation cover only a limited range of boundary layer Reynolds number, $200<Re_\theta<1100$, and a single wire diameter, 0.0003 in. These results might not be applicable to turbulent boundary layer measurements in cases where the Reynolds number is higher, or where a larger diameter wire is used, as the region over which the wall effect is significant could then extend well outside the viscous sub-layer.

### 3.3.9 Effect of the Wire Supports on Velocity Measurements

There is a growing body of experimental evidence indicating that the interference from the supports of a hot wire anemometer probe is not always negligible, and can be an important source of error in hot wire measurements under certain conditions. Hoole and Calvert (20) found that the inclination, $\alpha$, of the supporting prongs to the local flow direction had a significant effect on the heat transfer from a commercially manufactured hot wire probe. A calibration of this probe in steady flow indicated

that the heat loss from the wire increased with $\alpha$ up to $\alpha = 105^{\circ}$, where it reached a maximum value which was 10% greater than the heat loss for $\alpha = 0^{\circ}$, when the prongs were parallel to the local flow. In this case, an error of some 20% in mean velocity would have been obtained by using the calibration for $\alpha = 0^{\circ}$ when the actual value of $\alpha$ was $105^{\circ}$. Other probes examined by these workers showed a similar behaviour, but with different numerical values.

Van Thinh (21) found that measurements of both the mean velocity and fluctuating velocity components were affected by the inclination of the wire supports, and that this effect could be decreased by increasing the length/diameter ratio of the wire. Although it is not made clear in his paper, it seems probable that the ratio of the wire length to the diameter of the supporting prongs would also be an important quantity. Tritton (22) has also noted the effect of neighbouring bodies on hot wire measurements and suggested that the presence of another probe, or a probe's own supports, might alter the local intensity of turbulence as well as affecting the probe response.

These observations are supported by some measurements of mean velocity profiles in the turbulent boundary layer on the hub wall of the Vortex Wind Tunnel compressor by Merrington (23). Using a wire of $l/d \simeq 200$ with supports at $90^{\circ}$ to the local mean flow direction gave a mean velocity profile which differed considerably from the accepted law of the wall, Equation (3.9); the measured value of wall shear stress was about twice that predicted from empirical skin friction laws. When the probe design was altered to align the probe support tips parallel to the local flow, much better agreement with the law of the wall and theoretical skin friction values was obtained.

To summarise, it seems likely that errors in measurement arising from inclination of the probe support to the local flow direction will be minimised by increasing the wire length/diameter ratio, decreasing the diameter of the supports, and aligning the supports parallel to the local mean flow.

In the present investigation the hot wire probe supports were kept closely parallel to the local mean flow, both during calibration and in measurements of the compressor blade boundary layers. For this reason it is considered unlikely that probe support interference caused any significant errors in mean velocity measurements, except perhaps in the wall regions of turbulent boundary layers where the turbulence components were comparable with the local mean velocity.

### 3.3.10 Overall Accuracy of Hot Wire Mean Velocity Measurements

Although the hot wire calibrations obtained in the present investigation could be repeated to 1% of velocity, another 2% error may have arisen from approximations in correcting for calibration drift. Thus the best accuracy that could be claimed for mean velocity measurements in steady

flow would be about 3%. It is possible that some further error could have arisen from the unsteady flow situation in the compressor, where the streamwise turbulence intensity near the stator varies from about 2% at a rotor speed of 750 rpm to about 6% at 150 rpm. As the rotor wake passing frequency seen by the hot wire probe varied from 462.5 c/s at 750 rpm to 92.5 c/s at 150 rpm, it is rather doubtful whether the constant current anemometer would have registered the true mean velocity, since no compensation was provided for the thermal inertia of the wire and the mechanical inertia of the galvanometer used in the Wheatstone bridge. Because of the nature of the velocity variation (roughly constant, apart from periodic sharp downward spikes due to the rotor wake defects) it is most probable that the mean velocity measurements in the compressor were too high by an amount which was of the same order of magnitude as the freestream turbulence level.

The non-dimensional velocity profiles in the laminar boundary layer regions agree with the corresponding theoretical solutions to within $\pm$ 0.01 (in u/U) so consistently that it appears reasonable to claim this order of accuracy for them. This is surprisingly good, considering all the experimental difficulties; it is certainly much better than was expected when the measurement program was initiated. Evidently the non-dimensionalising process eliminates a proportion of the errors due to calibration drift and unsteady flow effects.

Velocity measurements obtained in turbulent boundary layers were probably of the same general accuracy as those in laminar flow, except in the wall regions where some additional errors could have arisen from non-linear probe response to the fluctuating flow, and from uncertainties in correcting the hot wire readings for wall proximity effects. As readings obtained at a fixed distance from the wall are corrected by subtracting an approximately constant amount from the measured value of $Re_w^{0.45}$, where $Re_w$ is the wire Reynolds number, the wall proximity correction becomes relatively larger as the absolute velocity decreases, as shown in Fig. 3.11. Hence any errors from this source would have been greatest for measurements obtained at the lowest compressor speed of 150 rpm.

### 3.3.11 Observations of Boundary Layer Velocity Fluctuations

Some time after the mean velocity measurements in the stator blade boundary layer had been completed, a DISA Constant Temperature Anomometer was acquired. This equipment was used to make qualitative observations of velocity fluctuations in the stator blade suction surface boundary layer at the 50% chord position at mid blade height. By changing the compressor throttle setting, and hence altering the blade incidence, the boundary layer transition region was moved relative to the hot wire probe so that the boundary layer behaviour at various stages of the transition process could be observed and the effects of free stream disturbances noted. Observations were made

at a compressor speed of 250 rpm with throttle openings of 4.8, 6.0, 8.0, and 22.0 in., giving blade incidences of $5.2^{\circ}$, $0.5^{\circ}$, $-3.2^{\circ}$, and $-10.1^{\circ}$, respectively.

The hot wire probes used in this investigation were identical to those used for the mean velocity measurements, but extra care was taken to eliminate any vibration of the wire or its supports. It is well known that such vibrations produce a relative motion between the wire and the air, and so cause fluctuations in bridge voltage which add to those produced by variations in the flow velocity.

The checking of probes for vibration was carried out in the 9 in. square working section of a closed circuit wind tunnel. Fluctuations in anemometer bridge voltage were monitored with a cathode ray oscilloscope. Any vibration of the probe was clearly visible as a regular sinusoidal signal superimposed on the random background fluctuations from the free stream turbulence in the tunnel, which varied from about 0.1% to 0.4% depending on the mean velocity. It was found that probe vibrations could generally be eliminated by reducing the amount of tension in the sensing wire, and this was achieved by gentle bending of the supporting prongs; however, it was considered desirable to have some small residual tension in the wire to minimise its movements in response to sudden changes in flow speed or direction.

The anemometer bridge voltage fluctuations produced by the velocity fluctuations in the compressor blade boundary layer were recorded photographically with a camera attached to the oscilloscope. The oscilloscope sweep was triggered once per revolution of the rotor by a light shining onto a photo-transistor through a radial slit in a disc attached to the compressor drive shaft. This ensured that the wakes of the same rotor blades were observed on each successive sweep, and eliminated any variation in the observed rotor wake velocity defect which could have arisen from differences in setting angle or shape of individual rotor blades. As the sweep was always triggered at the same time relative to the rotor wake passing, it was possible to superimpose photographically a number of successive traces and so gain some idea of the time variation in R.M.S. intensity of the velocity fluctuations during the rotor wake passage. It was usually found convenient to superimpose about 30 such traces; a smaller number did not give a very clear indication of the mean velocity variation, while a much larger number tended to clutter the photograph so much that some detail was lost.

Photographs of single traces of bridge voltage fluctuations were also obtained at each measuring position. These showed more clearly the frequency and shape of individual disturbances, which were usually masked to some extent in the multiple-trace records.

The hot wire signal was monitored continuously with the oscilloscope during these observations in case the probe started to vibrate whilst in the compressor. It was noticed on rare occasions that an initially vibration-free

probe would commence to oscillate after a large dust particle from the air-stream had impacted on the wire.

### 3.3.12 Data Reduction and Presentation of Results

#### 3.3.12.1 Mean velocity measurements

All of the data reduction from the hot wire mean velocity measurements was done by digital computer. A least-squares fit was used to determine the coefficients in the calibration curve, Equation (3.5); values of velocity less than 5 ft/sec were obtained by extrapolation of this curve. Data points for which free convection was significant, as defined by Equation (3.3), were discarded. Calibration drift during running was corrected for by the method of Section 3.3.5, and allowance for movement of the blade surface was made as described in Section 3.3.6. Effects of wall proximity were corrected by using Wills's laminar flow correction (Table 3.3) in all cases, including turbulent boundary layers (with the single exception of the data presented in Appendix I, where half the laminar flow correction was used).

The various boundary layer thicknesses were obtained by numerical integration of the corrected velocity profile. A parabola was fitted through the point (y = 0, u = 0) and the two data points nearest the wall; the slope of this curve at the wall, i.e. $(\partial u/\partial y)_{y=0}$, was then used to calculate the experimental value of the wall shear stress, $\tau_w = \mu(\partial u/\partial y)_{y=0}$. The value of vorticity, $\zeta = \partial u/\partial y$, at each data point was taken as the slope of a parabola fitted through that point and the next one on each side.

Values of momentum thickness, $\theta$, shape factor $H = \delta^*/\theta$, and skin friction coefficient, $C_f$, obtained from the hot wire measurements of the boundary layers on the stator blade suction surface have been tabulated in Appendix F. The variation of $\theta$ and H is also shown graphically in Figs. 4.7 (a-d), which are discussed in Section 4.4.

Because of space limitations it is only possible to present a representative sample of the detailed boundary layer velocity profile measurements. It was decided to use the data obtained at a compressor speed of 500 rpm, as this provided the best general compromise between detail of measurement and overall experimental accuracy. The detailed reasoning behind this choice was as follows:

(i) at the highest speed investigated, i.e. 750 rpm, fewer points were obtained on the experimental velocity profiles due to the relatively smaller boundary layer thickness;

(ii) much less detail was available in the wall region of profiles measured at 750 rpm because the markedly higher level of vibration at this speed made it inadvisable to measure very close to the blade surface. In addition, there was some uncertainty about the possible effects of blade vibration on the boundary layer flow;

(iii) the measurements at 750 rpm were prone to greater errors than those at 500 rpm, because of the reduced sensitivity of the hot wire anemometer at higher speeds;
(iv) while rather more detail was available from measurements in the thicker boundary layers produced at 250 and 150 rpm, the values of measured wall shear stress at the lower speeds were expected to be less accurate because of the wall proximity correction to the hot wire readings becoming increasingly large as the flow velocity was reduced (see Section 3.3.8 and Fig. 3.11). Additional uncertainties in these measurements arose from possible errors in extrapolating the hot wire calibration for velocities below about 5 ft/sec, and from non-linear probe response to large velocity fluctuations.

The boundary layer mean velocity profile measurements on the stator blade suction surface at a compressor speed of 500 rpm are tabulated in Appendix H and plotted in Figs. H.1-6. All of the velocity values in Appendix H were obtained by applying the full laminar flow wall proximity correction of Wills (13) to the hot wire readings.

Because of the doubts concerning the wall proximity corrections to be applied in turbulent flow, some velocity profiles obtained by using half the laminar flow correction have been given in Appendix I. This data, which was obtained at the 90% chord station on the stator blade suction surface at a compressor speed of 500 rpm, can be compared with that in Appendix H to gain some idea of the magnitude of the wall proximity effects, and the possible errors arising from them.

A discussion of the mean velocity profiles measured during various stages of the boundary layer development can be found in Sections 5.2, 5.6.6.3 and 7.3.

#### 3.3.12.2 Observations of velocity fluctuations

Some typical records of streamwise velocity fluctuations in the stator blade boundary layer are shown in Figs. 6.10 - 6.12.

## 3.4 Measurement of Blade Surface Pressure Distribution and Calculation of Surface Velocities

### 3.4.1 Experimental Detail

The surface pressure distributions at mid-blade height on the stator blade suction surface were measured from the blade surface pressure tappings for all of the standard compressor speeds and throttle settings specified in Section 3.1.

At each chordwise measuring station on the pressure-tapped blades there are five different holes (at the radial positions given in Section 2.2) all opening into the same connecting tube. In order to measure the surface pressure distribution at one particular radial station it was first necessary

to seal off the other four sets of tappings by means of adhesive tape placed on the blade surface. The pressures were measured on a multi-tube manometer filled with methyl alcohol (specific gravity $\simeq$ 0.80). The nominal manometer slope was arsin 1/10 for all measurements except those obtained at 750 rpm, where a nominal slope of arsin $\frac{1}{4}$ was used. Each manometer tube used was calibrated against a Betz projection micro-manometer to determine the product of tube slope and alcohol density. The manometer tube levels were read to $\pm$ 0.01 in. alcohol, and the Betz micro-manometer was read to $\pm$ 0.01 mm water.

The total pressure at mid-blade height in a plane about 1 in. forward of the stator leading edge was measured with a Conrad-type yawmeter. The static pressures measured on the blade were then subtracted from the appropriate total pressure values to obtain an estimate of the free-stream dynamic pressure at the location of the blade pressure tappings. In calculating the free-stream velocities from the dynamic pressures, due allowance was made for the effect of humidity on the air density. No separate allowance was made for variations in the density of methyl alcohol with temperature, which did not change by more than $4^{\circ}$C from the temperature at which the manometer tubes were calibrated.

Each pressure measurement was subject to possible errors from the effect of velocity fluctuations on the mean pressure observed by the probe or tapping, and from the way in which the resulting pressure fluctuations were transmitted to the manometer through the connecting tubes. The actual magnitude of the total error cannot be predicted with any confidence, but it would have to be of the same order as the free stream turbulence level. The values of dynamic pressure could be even less accurate that the individual pressure measurements, as they are determined from the difference of two experimental results.

At compressor speeds of 750 and 500 rpm, the free stream velocities calculated from the stator blade surface pressure measurements were on the average about 4 - 5% lower than the velocities obtained from the hot wire measurements at the same nominal positions; slightly larger average variations were observed at the lower speeds of 250 and 150 rpm. Because the hot wire traverses were not carried out along a line normal to the blade surface, the measurements in the outer part of the boundary layer were obtained at positions rearward of the corresponding pressure tappings by up to 2% of chord; thus the real differences between the hot wire and pressure tapping measurements are in most cases a little greater than the nominal differences quoted above.

Up to 40% of the observed differences (i.e. 2% of velocity) could have resulted from circumferential variations in axial velocity around the machine; the hot wire readings were obtained at the position of highest flow in the annulus, while the stator blade with the surface pressure tappings was some $60^{\circ}$ further around the circumference near the position of lowest flow. It is also possible that the blade surface pressure distributions at the two

measuring stations were not exactly similar because of small incidence variations around the circumference. As the various sets of readings were obtained at widely different times, changes in atmospheric conditions may have caused significant Reynolds number effects in a number of cases, particularly in measurements at the lower speeds. The balance of the variations between the two sets of velocity measurements might have arisen from differences in response of the respective probes and measuring equipment to the unsteady flow in the compressor; other measurements in this machine with the Conrad probe have given values of velocity which appear too low by about 3%.

However, another possibility is that the differences between the hot wire and pressure tapping measurements could have been partly caused by changes in the circumferential position of the inlet guide vane ring. Later measurements in the research compressor by Johnston and Lockhart (24) showed that rotation of the inlet guide vane ring could produce variations of some 5% in the flow velocity near the stator row. The setting of the inlet guide vane ring was not always recorded in the present investigation, as it was not considered to be such a significant parameter at the time the measurements were obtained; although it was normal practice to use the same settings throughout all the measurements, the possibility that a different guide vane position was used in some cases cannot be entirely discounted.

### 3.4.2 Presentation of Results

The surface velocity distributions obtained from the blade pressure tapping measurements are presented numerically in Appendix D, and graphically in Figs. 4.1 (a-e). Values of velocity have all been made non-dimensional with respect to $U_{mb}$, the peripheral speed of the rotor at mid-blade height.

## 3.5 Stethoscope Investigations of the Stator Blade Boundary Layer

### 3.5.1 Experimental Detail

A total head tube of 0.081 in. outside diameter connected to a stethoscope provided an additional means of determining the location of boundary layer transition on the stator blade. The tube was traversed along the suction surface at mid-blade height, and characteristically different sounds could be heard depending on the regime of flow in which the mouth of the tube was immersed.

With the tube mouth in a laminar flow region, only background noise from the rotor wakes and the mechanical noise of the machine were audible. When boundary layer transition commenced, the violent velocity and pressure fluctuations associated with the transition process produced a distinct crackling or rattling turbulent flow noise. As the total head tube was moved downstream through the transition region, both the level and pitch of the boundary layer noise increased steadily until a fairly well defined plateau of noise level

was finally reached. The position at which the turbulent noise first appeared, and the position at which the noise level plateau was reached, were taken as defining the limits of the transition region.

The total head tube was observed through the perspex windows in the compressor shell, and its chordwise position could be determined to ± 1%c by reference to a grid marked on the stator blade surface. The location of the transition region was recorded for as many of the standard speeds and throttle settings as possible; no measurements could be obtained at 150 rpm because the turbulent noise became almost inaudible at this speed.

### 3.5.2 Presentation of Results

The limits of the transition region obtained from the stethoscope survey are presented numerically in Table 6.2, and graphically in Fig. 4.6. These measurements are discussed further in Sections 4.3 and 6.2.

## 3.6 Measurement of Compressor Speed

The compressor speed was set by reference to a strobodisc mounted on the end of the rotor drive shaft. This disc was illuminated by a stroboscopic light whose flashing was synchronised with a 50 c/s signal from a crystal controlled oscillator reputed to be accurate to 1 part in $10^6$.

An alternative means of measuring the rotor speed was provided by a light source shining onto a photo-transistor through a radial slit in a disc mounted on the drive shaft. Once per revolution of the rotor, the transistor produced a voltage pulse which was amplified and used to drive an electronic counter located at the measuring station. The pulses were counted for one minute as measured by the crystal clock, and the total number, representing the average compressor speed over this interval, was then displayed for a further minute before counting recommenced.

After an initial warm-up period of about 15 minutes, only slow variations in speed were observed, in general, and it was quite easy to maintain speed to within ± 1 rpm when operating at 500 rpm. Although some larger fluctuations in speed did occasionaly occur as a result of sudden voltage surges in the power supply mains, they were usually confined to particular times of the day, and were immediately obvious to the ear because of the change in frequency of the compressor whine. The accuracy of speed control was mostly better than ± ¼% at 750 rpm, falling to ± ½% at 150 rpm.

# CHAPTER 4

## GENERAL BOUNDARY LAYER BEHAVIOUR

### 4.1 Introduction

This chapter discusses the overall behaviour of the compressor blade boundary layers, as indicated by the china clay visualisation tests, stethoscope observations, and the variation of integral parameters obtained from the hot wire measurements. It is intended as a brief introduction to the more detailed examination of various aspects of boundary layer behaviour which follows in Chapters 5 - 7.

The experimental observations all suggested the presence, at negative incidence, of extensive regions of laminar flow on the suction surfaces of both rotor and stator blades. These laminar flow regions contracted in length as the blade incidence became positive, until they occupied only a small fraction of the blade chord at incidences near positive stall.

The blade surface velocity distributions obtained from the surface pressure tapping measurements have been plotted in Figs. 4.1 (a - e) to assist in interpreting the various boundary layer observations.

### 4.2 Observations from China Clay Visualisation Tests

A total of 56 different china clay drying patterns from the rotor and stator blade suction surfaces were examined. Apart from minor differences between the behaviour on the rotor and stator blades, it was found that all of the drying patterns obtained could be broadly classified according to the blade incidence. A representative sample of these observations will now be discussed.

Fig. 4.2 shows the result of a test on the suction surface of a stator blade at moderately high negative incidence ($i = -6.2^{\circ}$ at mid-blade). A white drying zone near the leading edge extends to about 30% chord; it is followed by a dark region over the central part of the blade where drying is incomplete; finally, there is another more intense drying zone over the rearward part of the blade. This drying pattern indicates the presence, near the leading edge, of a region of accelerating laminar flow with a moderately high wall shear stress; this is followed by a region of decelerating laminar flow, where the wall shear stress is much lower and laminar separation probably occurs; the sudden increase in wall shear stress at the rear of the separation zone is due to the reattachment of a turbulent shear layer, following transition in the separated shear layer.

The line of turbulent reattachment in Fig. 4.2 is quite sharply defined, and runs almost parallel to the stator trailing edge over most of the blade height, probably because the blade incidence varies little with radial

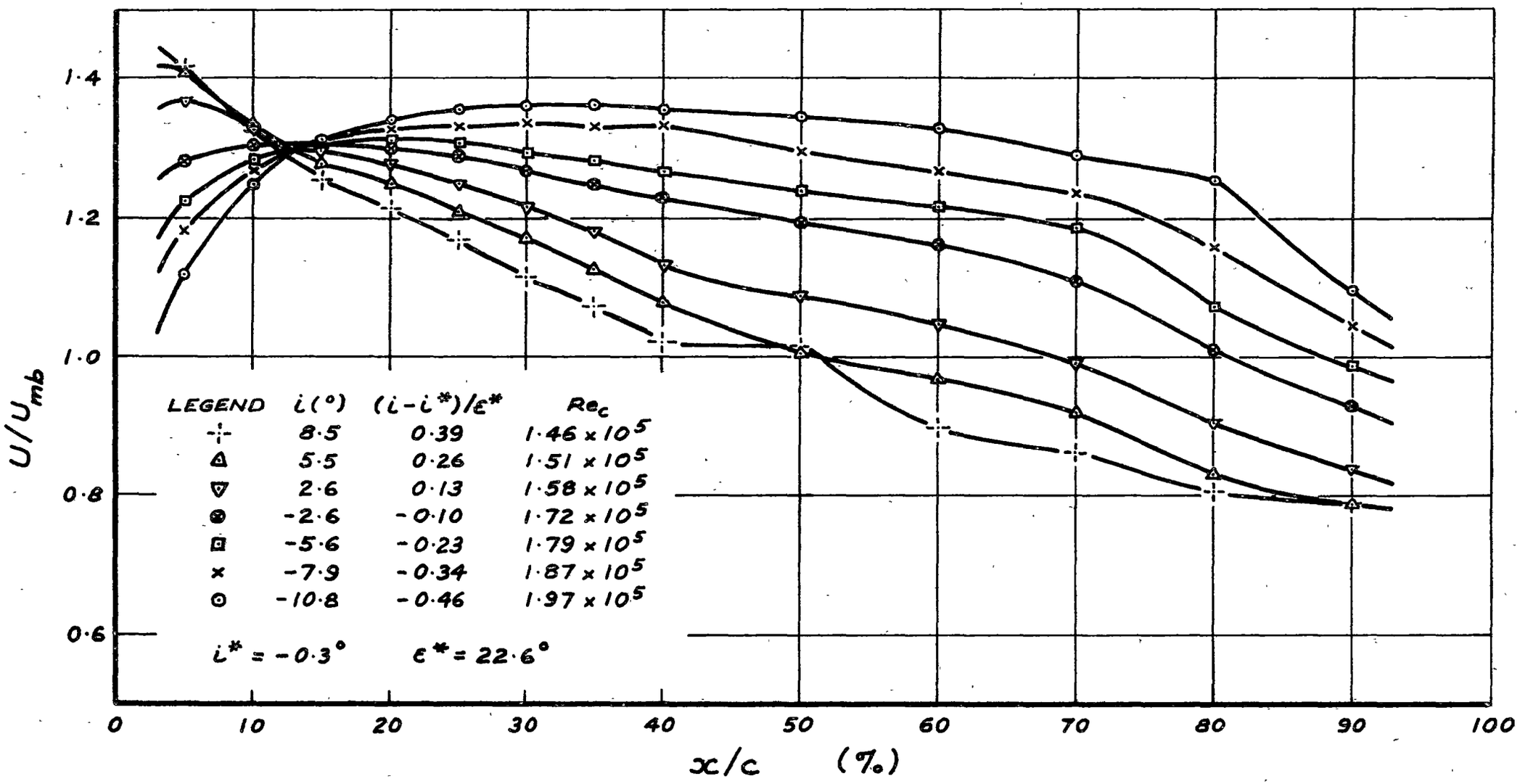


Fig. 4.1(a) Rotor Blade Suction Surface Velocity Distributions at Mid-Blade Height
(Compressor Speed 750 rpm)

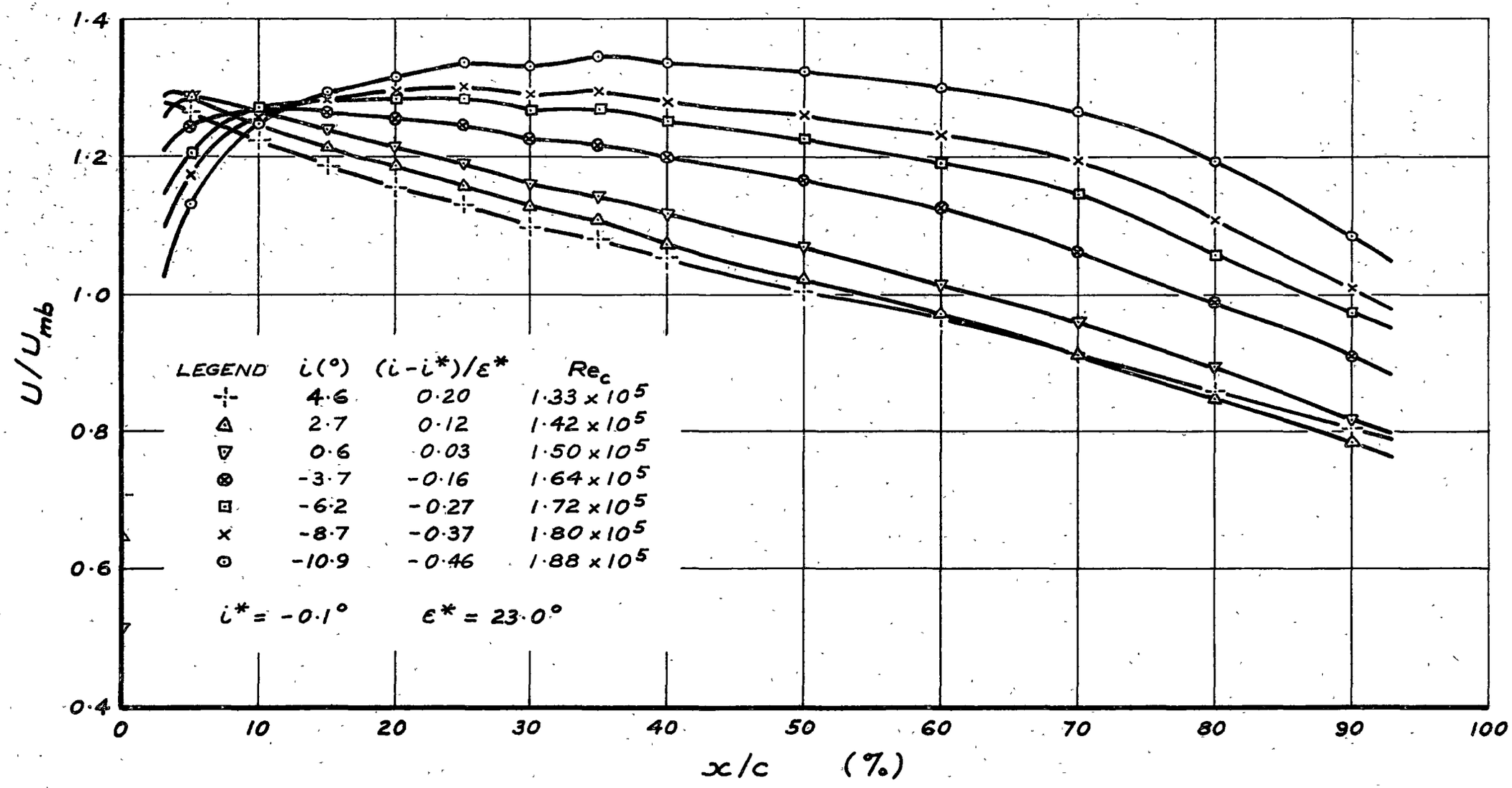


Fig. 4.1(b) Stator Blade Suction Surface Velocity Distributions at Mid-Blade Height
(Compressor Speed 750 rpm)

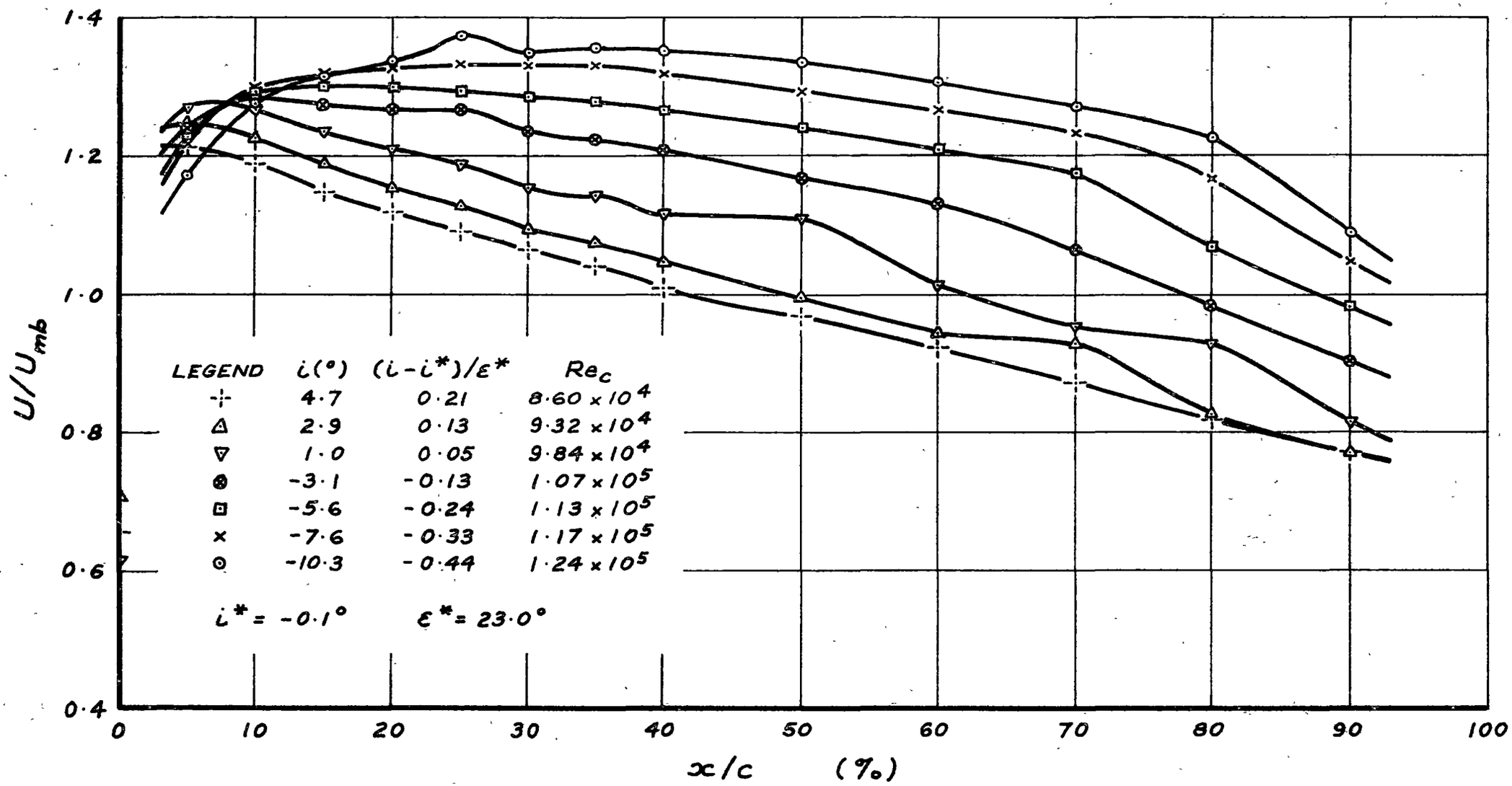


Fig. 4.1(c) Stator Blade Suction Surface Velocity Distributions at Mid-Blade Height

(Compressor Speed 500 rpm)

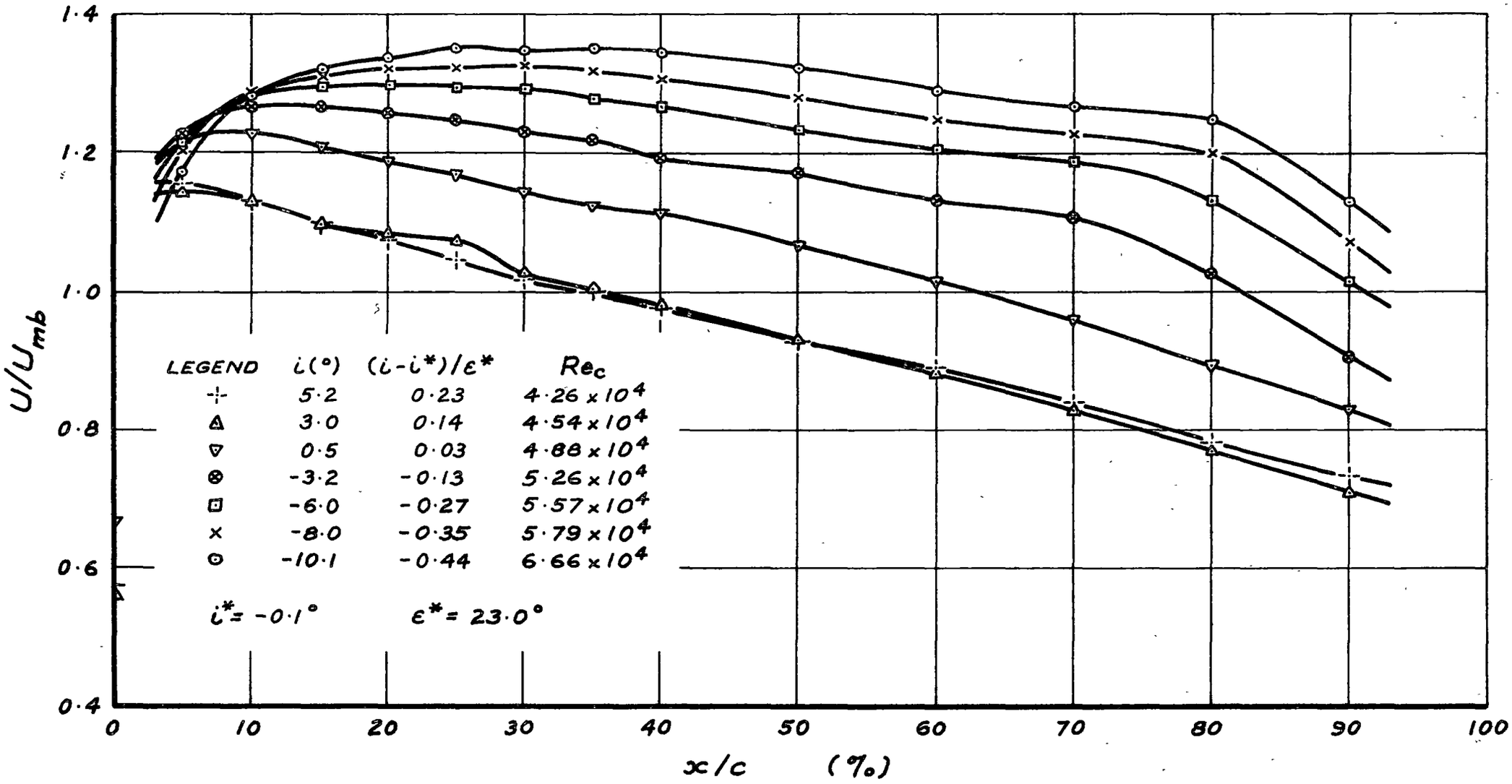


Fig. 4.1(d) Stator Blade Suction Surface Velocity Distributions at Mid-Blade Height
(Compressor Speed 250 rpm)

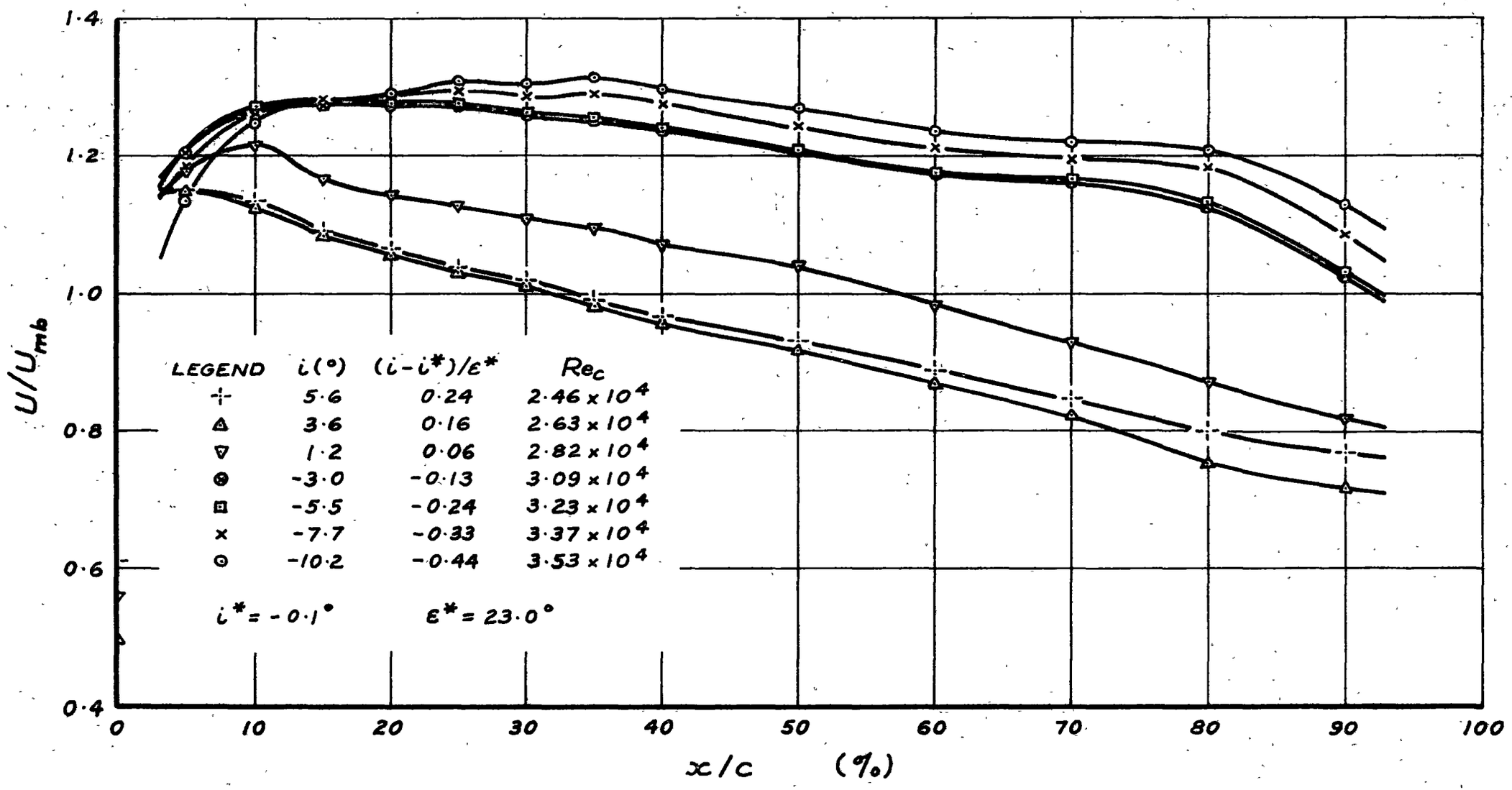


Fig. 4.1(e) Stator Blade Suction Surface Velocity Distributions at Mid-Blade Height
(Compressor Speed 150 rpm)

position in this case (see Appendix C). Near the stator hub and tip, however, the reattachment line curves sharply forward. This effect is most pronounced at the hub, where the secondary flows in the annulus wall boundary layer produce a large streamwise vortex in the corner between the stator suction surface and the hub wall of the compressor. The regions of strong secondary flow on the suction surface occupy 10 - 15% of the blade height at the stator hub, and 5 - 10% of the blade height at the stator tip; they vary in extent with the blade incidence, being largest near positive stall. There appears to be a rough correlation between the extent of the secondary flow regions and the magnitude of the axial velocity ratios, which are given in Table 3.1.

Fig. 4.2 clearly shows a number of white lines of more intense drying, trailing from small isolated roughness elements near the leading edge of the blade. These lines give a rough indication of the direction of the limiting streamlines at the blade surface, and their small radial movement implies that the boundary layer flow near the leading edge is closely two-dimensional over the central 80% of the blade height.

Fig. 4.3 shows a drying pattern from the rotor suction surface at a similar negative incidence ($i = -5.6^{\circ}$ at mid-blade) to that of the stator in Fig. 4.2. Comparison of these two patterns shows only minor differences between the flow behaviour on the rotor and stator blades at this incidence. The turbulent reattachment line on the rotor does not curve forward as markedly near the compressor hub, because less secondary flow is generated in the thinner hub wall boundary layer passing through the rotor. At the rotor tip, there is a fine drying line which is produced by secondary flows through the tip clearance. No radial movement can be observed in the accelerating flow over the forward part of the rotor suction surface, but some crossflow does become discernible over the rearward part of the laminar separation region, as shown by the path of the thick white traces trailing from some rather large roughness elements. However, the maximum deviation of these surface drying lines from the axial direction does not appear to exceed 2 or $3^{\circ}$.

At small positive incidence, the drying region near the leading edge of the suction surface is much shorter, as would be expected from the reduced length of accelerating flow there. An extensive region of low shear stress is still present, but it is further forward on the blade than at negative incidence, and the line of turbulent reattachment is rather ill-defined. These features can be seen in Fig. 4.4, which shows the drying pattern on the stator blade suction surface with $i = 4.6^{\circ}$ at mid-blade height. The reduced colour contrast of the drying pattern indicates that the drying rate over the low shear stress region is relatively faster than at negative incidence; this suggests that laminar separation may be suppressed at low incidences. The drying pattern on the rotor suction surface at small

TIP

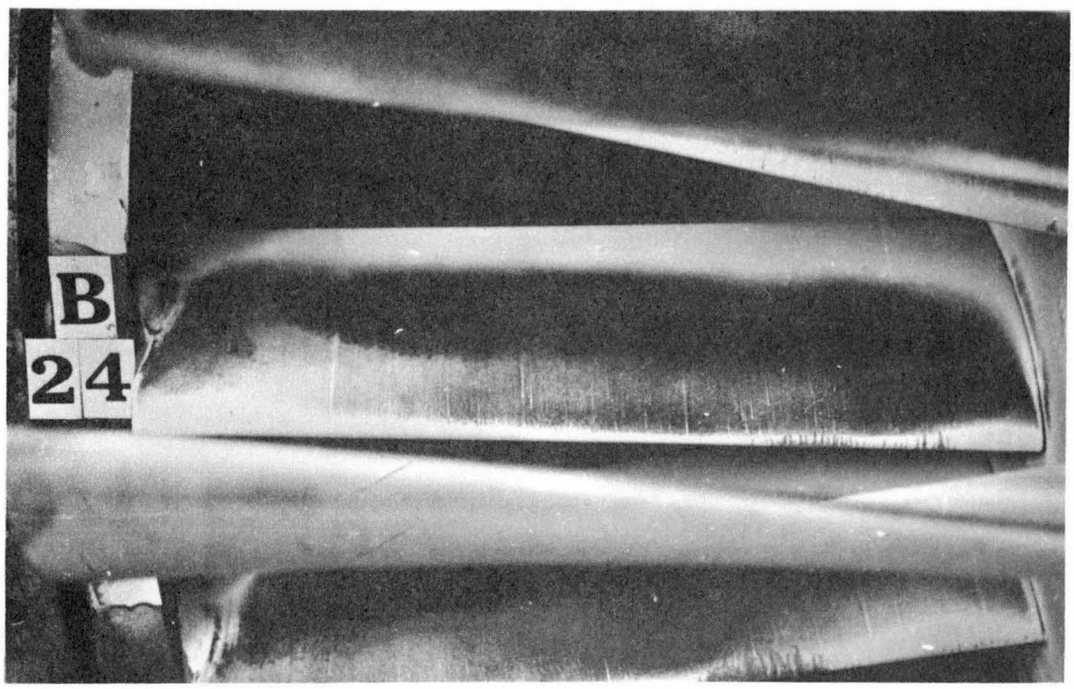


HUB

Fig. 4.2 China Clay Test - Stator Suction Surface
$i = -6.2^{\circ}$, $(i - i^*)/\varepsilon^* = -0.27$, $Re_c = 1.72 \times 10^5$ at mid-blade height
Compressor Speed 750 rpm
(Viewed through rotor)

HUB

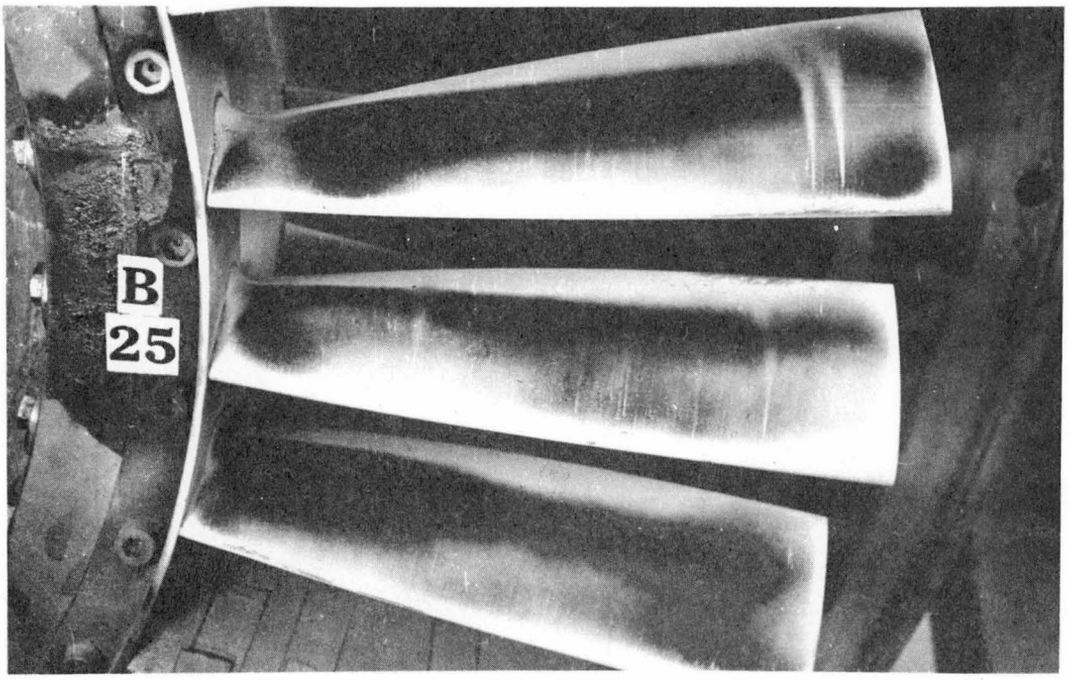


TIP

Fig. 4.3 China Clay Test - Rotor Suction Surface
$i = -5.6^{\circ}$, $(i - i^*)/\varepsilon^* = -0.23$, $Re_c = 1.79 \times 10^5$ at mid-blade height
Compressor Speed 750 rpm

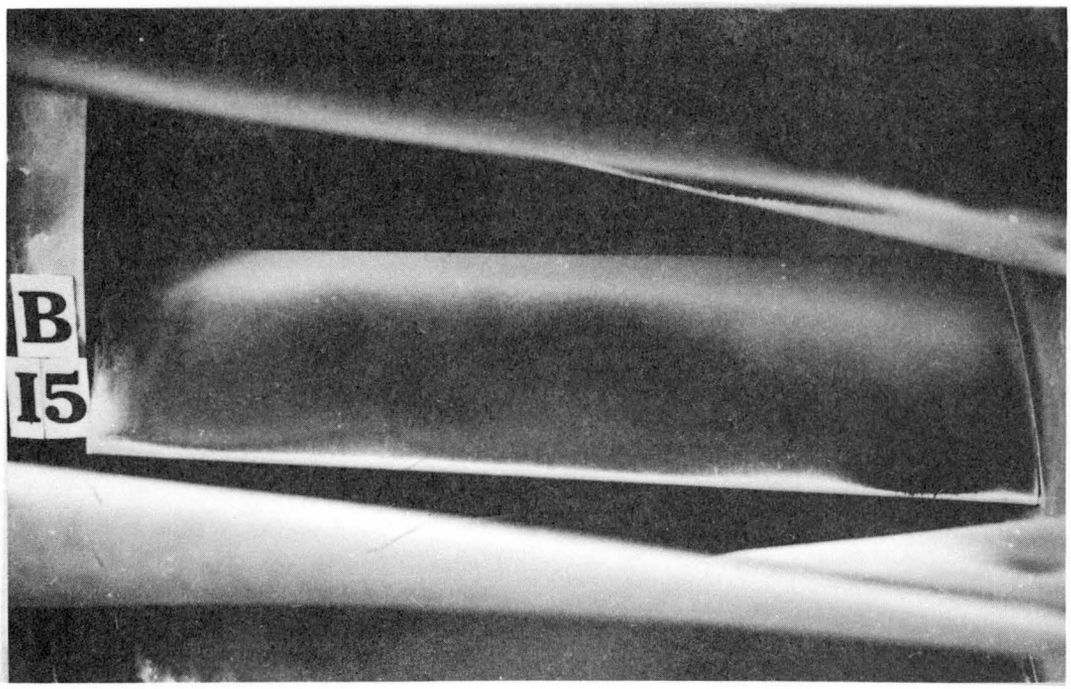


Fig. 4.4 China Clay Test - Stator Suction Surface
$i = 4.6^{\circ}$, $(i - i^*)/\varepsilon^* = 0.20$, $Re_c = 1.33 \times 10^5$ at mid-blade height
Compressor Speed 750 rpm
(Viewed through rotor)

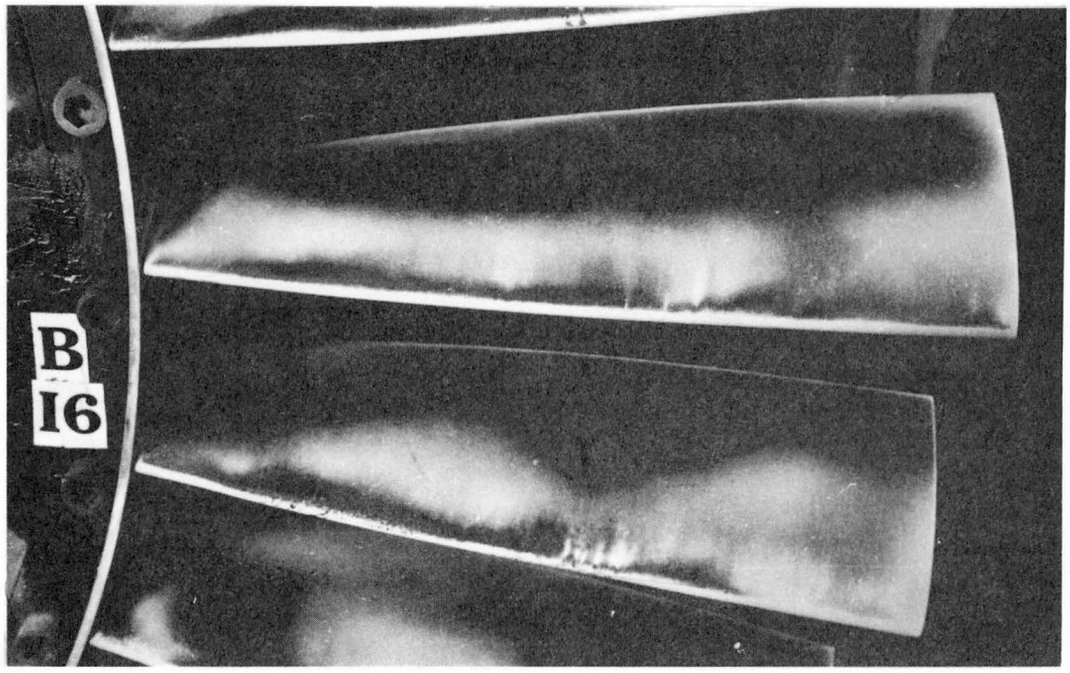


Fig. 4.5 China Clay Test - Rotor Suction Surface
$i = 8.5^{\circ}$, $(i - i^*)/\varepsilon^* = 0.39$, $Re_c = 1.46 \times 10^5$ at mid-blade height
Compressor Speed 750 rpm

positive incidence showed a similar behaviour.

At positive incidences greater than $5^{\circ}$, approximately (corresponding to $(i-i^*)/\epsilon^* \simeq 0.25$), the drying region at the leading edge of the rotor suction surface contracts to about 5% of chord, and is followed by a short low shear stress region of about the same length; a second low shear stress region, much longer in extent, appears over the rearward part of the blade. This behaviour is shown in Fig. 4.5, which was obtained from a test on the rotor suction surface with $i = 8.5^{\circ}$ and $(i-i^*)/\epsilon^* = 0.39$ at mid-blade height. (This is quite close to stall as defined by Howell (1).) The drying pattern indicates the formation of a short region of laminar separation in the strongly decelerating flow downstream of the suction peak, which is located less than 5% of chord from the leading edge in this particular case. Transition occurs very rapidly under these conditions, and the turbulent shear layer reattaches at about 10% chord with an initially high wall shear stress which causes the second drying zone over the central part of the blade; but the wall shear stress falls once again as the turbulent boundary layer approaches separation near the trailing edge, and this results in the appearance of another region of incomplete drying over the rearward 50% of chord. This type of pattern was not observed on the stator suction surface, as the maximum incidence achieved on the stator blades during the experimental investigation was about $5^{\circ}$ only.

## 4.3 Stethoscope Observations of Boundary Layer Transition

Fig. 4.6 shows the results of stethoscope observations on the stator blade suction surface at mid-blade height with a compressor speed of 750 rpm, which gives values of $Re_c$ in the range $1.3 - 1.9 \times 10^5$. The region between the point at which turbulent flow first appears and the point where the flow becomes continuously turbulent (i.e. the "transition region") occupies about 15% of the blade chord on the average, and its length does not vary greatly with incidence; it is situated well rearward on the suction surface at negative incidence, but moves steadily forward as the blade incidence becomes positive.

The calculated point of neutral stability to small two-dimensional disturbances in the laminar boundary layer (see Section 6.3.2) has also been plotted in Fig. 4.6 to indicate the length of the "instability region", where such disturbances receive amplification prior to the first appearance of turbulent spots. The maximum length of the instability region, about 45% of chord, occurs at a moderate negative incidence, $i = -6^{\circ}$. For $i < -6^{\circ}$, the instability length gradually decreases as a region of separated laminar flow forms over the rearward part of the suction surface. As the incidence becomes positive, the neutral stability point moves closer to the leading edge and the instability region becomes much shorter; at $i = +4^{\circ}$, the instability length has fallen to about 20% of chord.

The stethoscope observations agree moderately well with the china clay

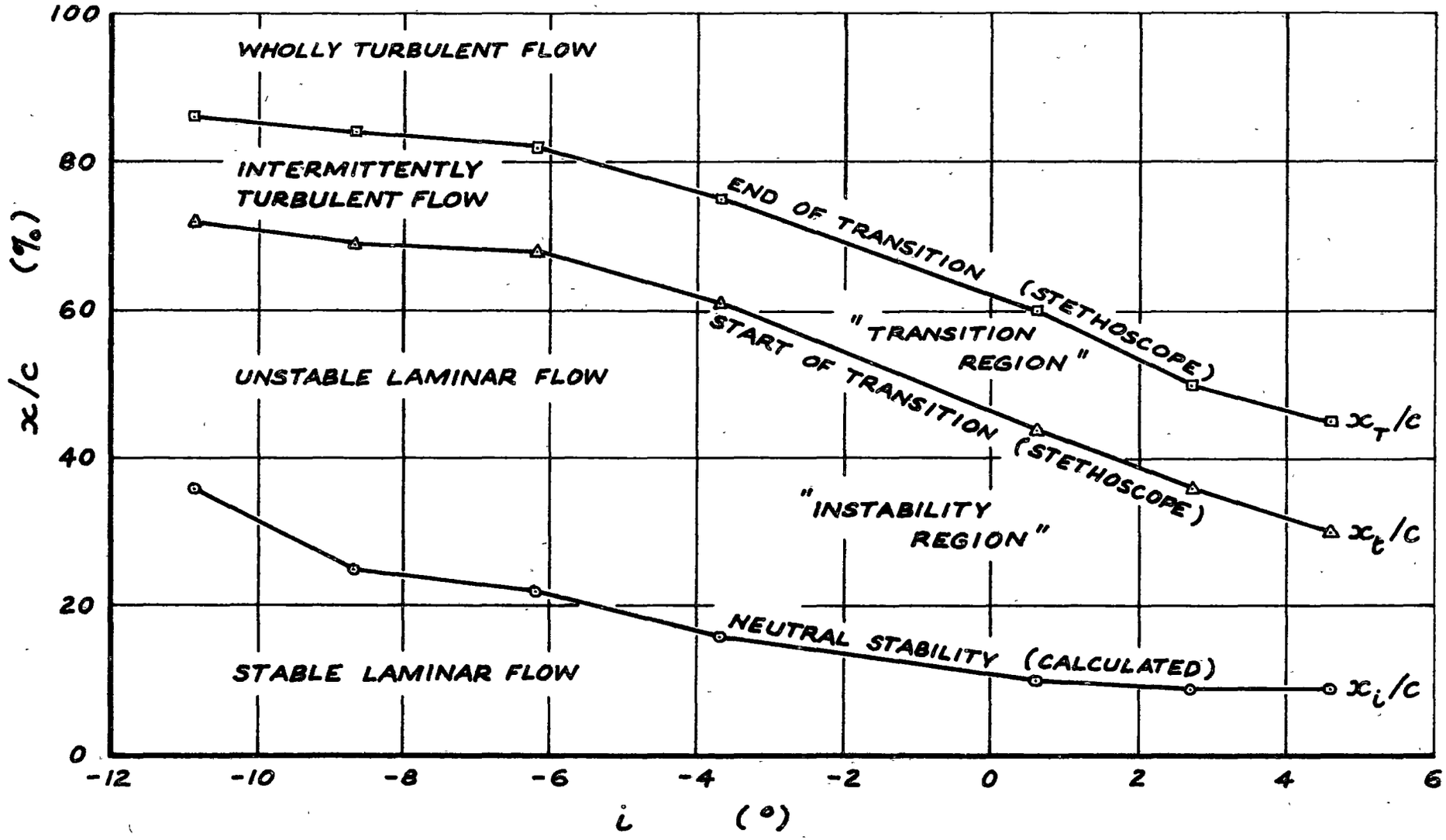


Fig. 4.6 Transition Behaviour on Stator Blade Suction Surface at Mid-Blade Height
(Compressor Speed 750 rpm, $Re_c$ = 1.3 - 1.9 x $10^5$)

drying patterns, and fully confirm that extensive regions of laminar flow are present on the stator suction surface at negative incidence.

4.4 Hot Wire Measurements of Boundary Layer Thickness

The variation in momentum thickness, $\theta$, and boundary layer shape factor, $H = \delta^*/\theta$, obtained from the hot wire measurements between 40% and 90% chord on the stator blade suction surface at mid-blade height are shown in Figs. 4.7 (a - d). The momentum thickness values indicate the contribution of the suction surface boundary layer to the blade profile drag, and the values of shape factor give a rough idea of the boundary layer flow regime. (The most convincing evidence of the extent of laminar flow is, of course, provided by the boundary layer velocity profiles. but these will be discussed later in Section 5.2.)

At positive incidence, the measured values of H are in the range 1.8 - 2.5, and generally fall slowly towards the trailing edge. This suggests that the boundary layer is turbulent over most of the region downstream of 40% chord, as the adverse pressure gradient there would give values of H greater than 2.6 if the boundary layer were still laminar. It is interesting to note that there are several cases in which the flow is continuously turbulent while the boundary layer Reynolds number, $Re_\theta$, is significantly less than the value of 320 suggested by Preston (75) as being the minimum required to achieve fully-developed turbulent flow. (See also Section 6.5.5.) For $i > +2^\circ$, the value of H increases from about 80% chord onwards, heralding the approach of positive blade stall through separation of the turbulent boundary layer at the trailing edge.

At negative incidence, the value of H on the stator suction surface increases with streamwise distance, x, up to 60 - 80% chord; over the remainder of the suction surface, where the pressure gradient is becoming increasingly adverse, the value of H falls steadily. This behaviour can only be explained by the presence of laminar flow up to about 70% chord, with the flow becoming turbulent rearward of this position. A region of laminar separation (indicated by $H > 3.70$, approximately) is nearly always present on the stator suction surface at negative incidence for $Re_c < 2 \times 10^5$; it moves towards the trailing edge of the blade and becomes more extensive as the incidence, i, is decreased.

Where laminar separation occurs, the shape factor continues to increase downstream of the separation point until transition occurs in the separated shear layer; the point at which H reaches its maximum value usually lies a little rearward of the location where turbulent flow is first detected with the stethoscope. The turbulent mixing then enables the shear layer to reattach as a turbulent boundary layer with a characteristically lower value of H. It takes about 20% of chord, on the average, for H to drop from its maximum value to a stable lower value following reattachment;

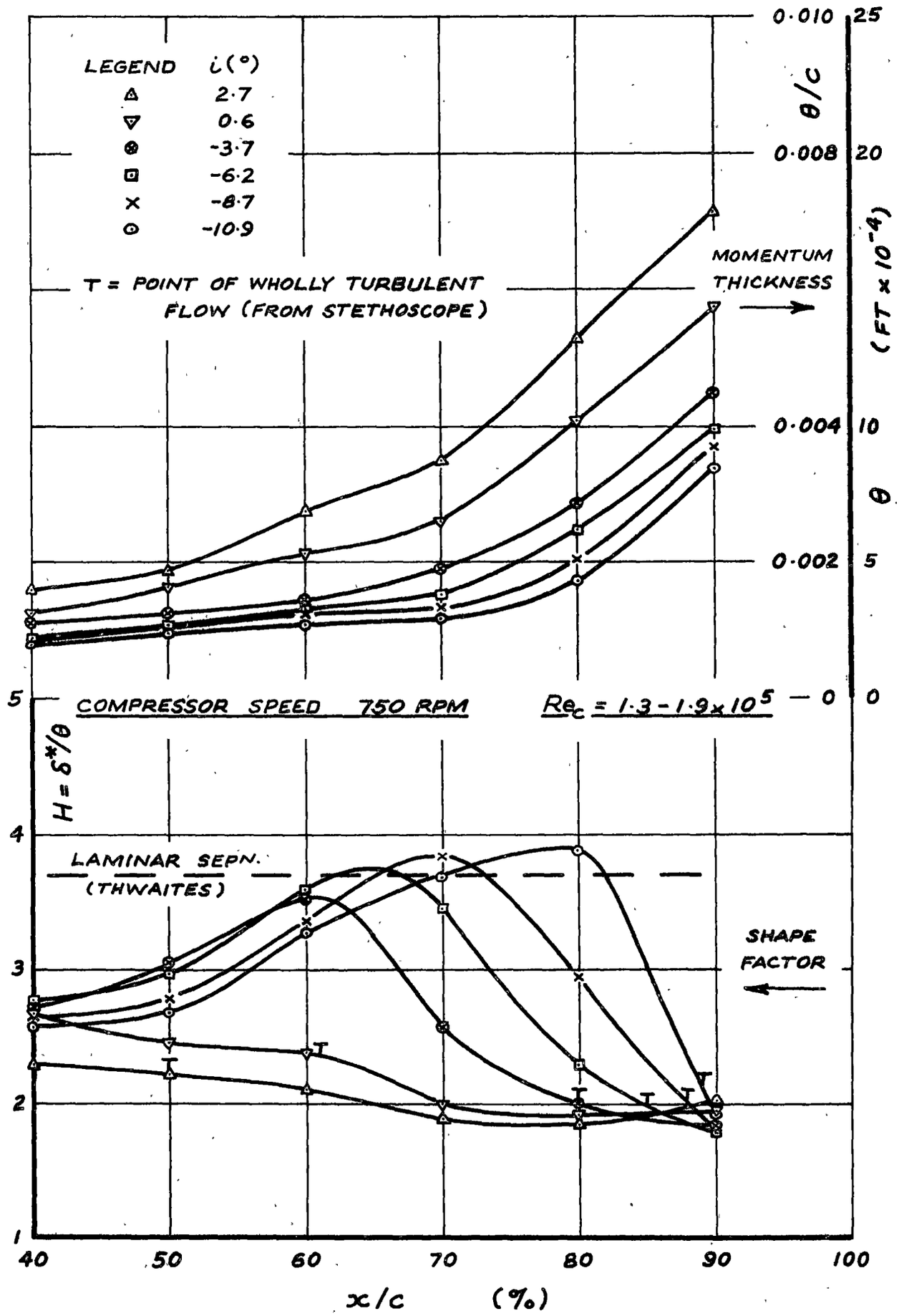


Fig. 4.7(a) Hot Wire Measurements of Stator Blade Suction Surface Boundary Layer at Mid-Blade Height (Compressor Speed 750 rpm)

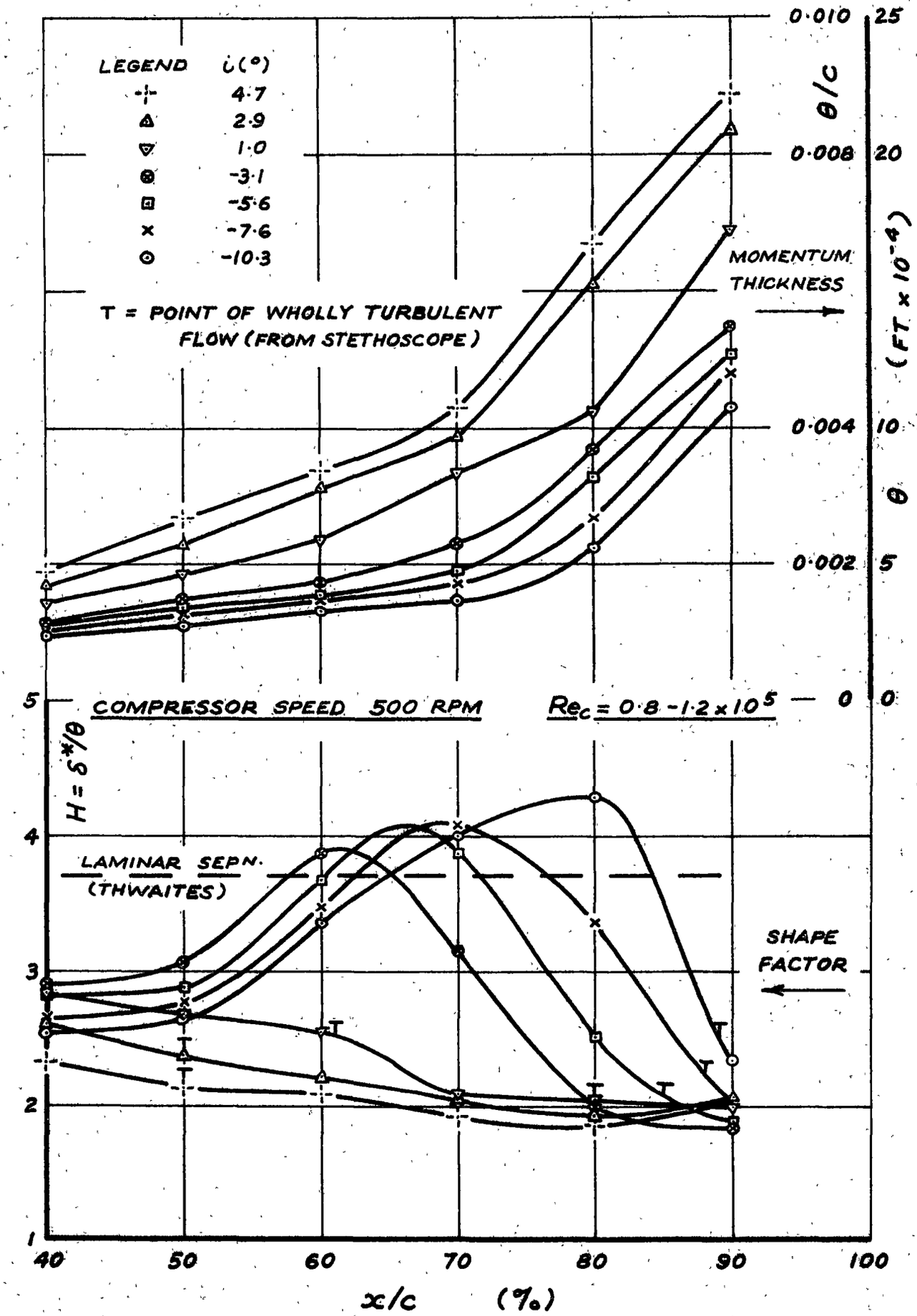


Fig. 4.7(b) Hot Wire Measurements of Stator Blade Suction Surface Boundary Layer at Mid-Blade Height (Compressor Speed 500 rpm)

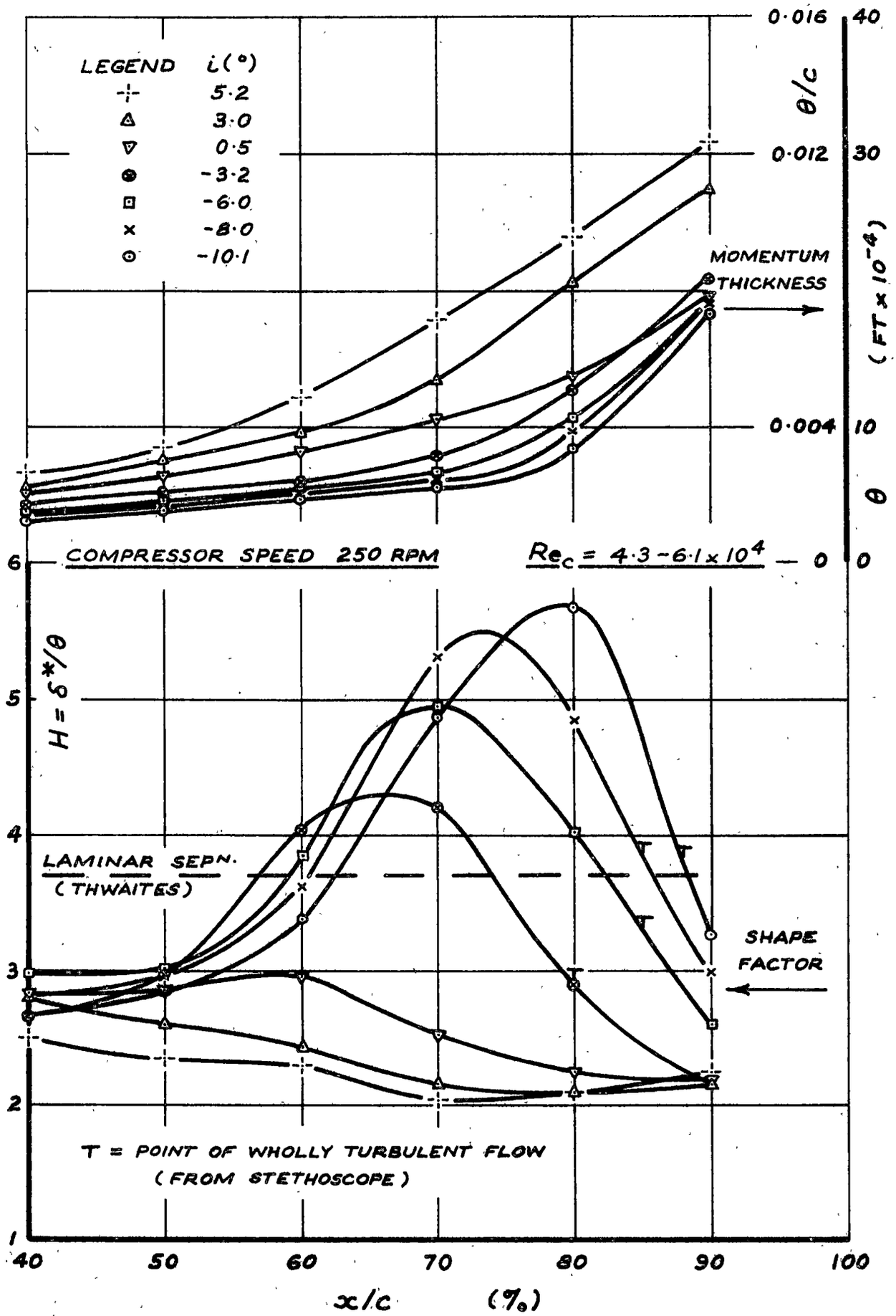


Fig. 4.7(c) Hot Wire Measurements of Stator Blade Suction Surface Boundary Layer at Mid-Blade Height (Compressor Speed 250 rpm)

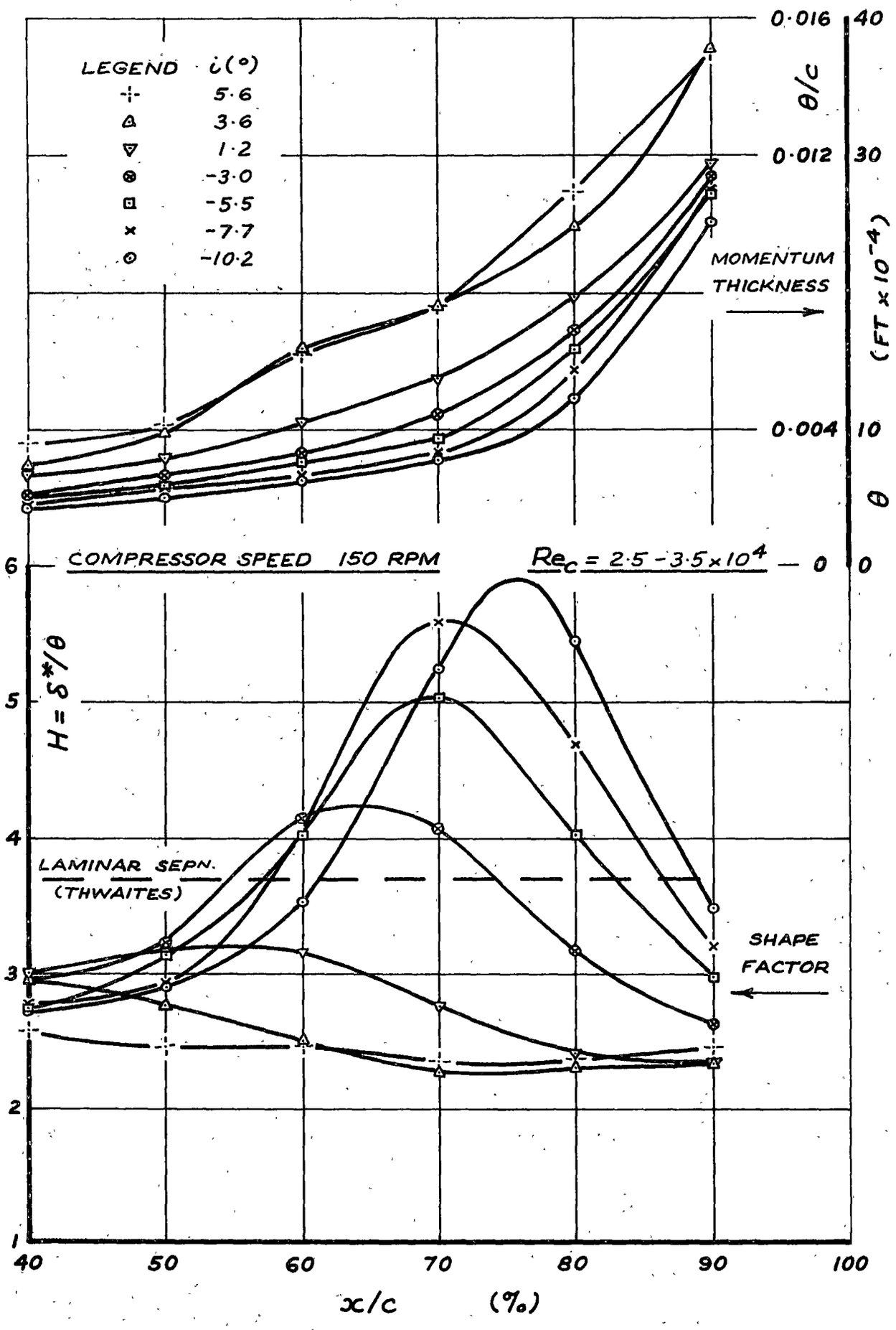


Fig. 4.7(d) Hot Wire Measurements of Stator Blade Suction Surface Boundary Layer at Mid-Blade Height (Compressor Speed 150 rpm)

this distance agrees fairly well with the length of the transition region observed with the stethoscope.

As the chord Reynolds number is increased by raising the compressor speed, the maximum value of H achieved over the laminar separation region steadily decreases. At a compressor speed of 150 rpm ($Re_c \simeq 3 \times 10^4$), H attains peak values of 5 or 6 at moderate negative incidence, and the separation of the shear layer is becoming quite well developed; at 750 rpm ($Re_c \simeq 1.5 \times 10^5$), however, the peak value of H is less than 4, and separation has been almost entirely suppressed. At a slightly higher Reynolds number, the separated flow regions would probably disappear altogether.

As expected, the measured values of momentum thickness on the stator suction surface are highest at positive incidence, due to the relatively greater length of turbulent flow and the larger positive pressure gradients to which the boundary layer is subjected. At negative incidence, there is a notable increase in the rate of growth of momentum thickness in the region where the turbulent shear layer is reattaching; this becomes more pronounced as the compressor speed is reduced and the laminar separation regions become more highly developed.

## 4.5 Deviations from Two-Dimensional Flow

The two-dimensional boundary layer momentum integral equation, neglecting second-order terms, is given by

$$(d\theta/dx)_{2-D} = -(H + 2)(\theta/U)(dU/dx) + C_f/2 \qquad (4.1)$$

Equation (4.1) applies to laminar boundary layers, and to turbulent boundary layers far enough from separation for the forces generated by the Reynolds normal stresses to be negligible.

The flow over an axial turbomachine blade is unlikely to be exactly two-dimensional, however, because of annulus wall boundary layer growth, secondary circulations in the bulk flow, and the radial pressure gradients which are inevitably present; a rough measure of the first two effects is provided by the axial velocity ratio (see Section 3.1). Where any departures from two-dimensional flow occur, the value of $d\theta/dx$ will be greater or less than that given by Equation (4.1) depending on whether the boundary layer flow is converging or diverging, respectively. A measure of the total amount of convergence or divergence is given by the quantity

$$(\theta_{EXP} - \theta_{2-D}) = \theta_{EXP} - \int_o^x (d\theta/dx)_{2-D} dx \qquad (4.2)$$

where $\theta_{EXP}$ is the experimentally measured momentum thickness at a given streamwise station, x, and $\int_o^x (d\theta/dx)_{2-D} dx$ is evaluated from Equation (4.1) by using the measured values of $\theta$, H, $C_f$, and U(x) at various positions over the range of integration.

Fig. 4.8 shows a plot of $(\theta_{EXP} - \theta_{2-D})$ against chordwise position for the boundary layers measured on the stator blade suction surface at a

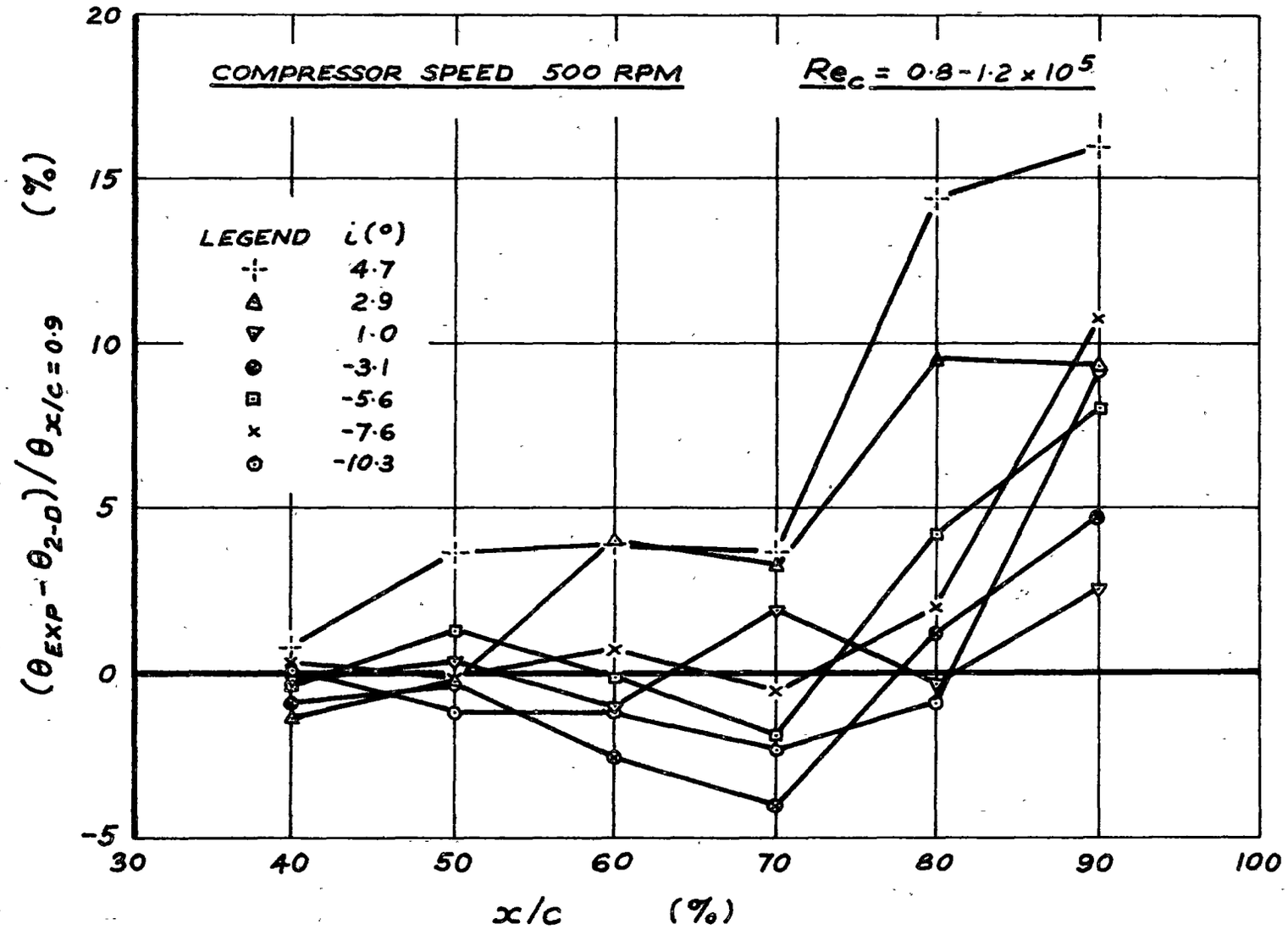


Fig. 4.8 Deviations from Two-Dimensional Flow in Stator Blade Suction Surface Boundary Layer at Mid-Blade Height (Compressor Speed 500 rpm , $Re_c$ = 0.8 - 1.2 x $10^5$)

compressor speed of 500 rpm; the difference in momentum thickness values has been made non-dimensional with respect to the measured value of $\theta$ at 90% chord. As no hot wire measurements were obtained forward of 40% chord, the value of $\theta_{2-D}$ at x/c = 40% was taken as that predicted by Thwaites's method (10) from the measured surface pressure distribution; the results of Section 5.4.2 indicate that this should have introduced little error. For $40\% \leq x/c \leq 90\%$, $(d\theta/dx)_{2-D}$ was evaluated from Equation (4.1) by using values of $\theta$, H and $C_f$ obtained from the hot wire traverses, and values of U and dU/dx obtained from the surface pressure tapping measurements.

It is seen from Fig. 4.8 that the worst deviations from two-dimensional flow (increasing $\theta$ at 90% chord by some 10 - 15%) occur at $2.9^\circ$ and $4.7^\circ$ incidence, where separation of the compressor hub wall boundary layer just downstream of the stator row produces an appreciable amount of convergence in the bulk flow. In both these cases, the approach of turbulent separation on the suction surface itself, particularly near the hub, would aid the development of cross flows over the rearward part of the blade.

There are also significant (but smaller) departures from two-dimensional flow at incidences of $-5.6^\circ$, $-7.6^\circ$, and $-10.3^\circ$, where the laminar boundary layer separates from the stator suction surface at about 60% chord. The greatest rates of flow convergence occur over the rearward parts of the laminar separation regions, i.e. about 70 - 80% chord, presumably because of the very low streamwise velocity near the blade surface allowing larger radial flow movements to develop in response to the radial pressure gradients.

At $1.0^\circ$ and $-3.1^\circ$ incidence, which are obtained close to the best efficiency and design points of the machine, respectively, the two-dimensional momentum integral equation (4.1) predicts $\theta$ at 90% chord to within 5%; this difference would be approximately halved by including the normal turbulent stress term in the momentum equation. It is thought that this good agreement is mainly due to the absence of well-developed separation regions on the stator blade surface and the annulus walls minimising the crossflow components induced by radial pressure gradients. In these cases, the departures from two-dimensional flow in the blade boundary layers would be expected to resemble those in the bulk flow, and this is confirmed by the experimental results; the streamlines in the suction surface boundary layer show a net convergence (since $\theta_{EXP} > \theta_{2-D}$ at 90% chord), and the values of A.V.R. = 1.04 - 1.05 (from Table 3.1) indicate that the bulk flow through the stator row converges by a similar amount at mid-blade height.

# CHAPTER 5

## LAMINAR BOUNDARY LAYER REGIONS AND LAMINAR SEPARATION BUBBLES

### 5.1 Introduction

The literature contains very little information concerning the state of boundary layer flow on axial turbomachine blading. Although areas of laminar flow have often been observed on aerofoils tested in two-dimensional cascades under conditions of low free-stream turbulence, it has been widely supposed (e.g. by Hawthorne (7) and Carter (25)) that the much higher level of free-stream turbulence generally obtained in a turbomachine would cause the machine blade boundary layers to be predominantly turbulent. A number of theoretical loss analyses for aerofoils in cascade have therefore assumed laminar flow regions to be entirely absent, and taken the leading edge of the blade as the origin of the turbulent boundary layer.

The results of the present investigation, on the other hand, indicate that the boundary layer flow on the suction surface of blades in the research compressor remains laminar up to 70% chord at negative incidence. But these laminar regions decrease rapidly in extent as the blade incidence becomes positive, until they occupy less than 10% chord around $i = +8^{\circ}$. It is quite possible, therefore, that much of the apparent conflict between the present observations and the assumptions of other workers concerning the extent of laminar flow on machine blades is simply due to incidence change effects (see also Section 6.7). At the design flow in the research compressor, the rotor and stator blades achieve only 85% of nominal deflection (as defined by Howell (1)), and therefore operate at negative incidence over 60-70% of the working range of the machine; most practical compressors operate at rather higher values of deflection and blade incidence, however, so that the limited extent of laminar flow assumed by other workers could well have been based on observations of machine blades operating at positive incidence.

### 5.2 Identification of Laminar Flow Regions

Because of the conflict of opinion described above, a more detailed examination of the hot wire measurements on the stator blade was undertaken so that the presence and extent of laminar flow could be established beyond reasonable doubt. The procedure adopted was to compare the measured velocity and vorticity profiles with appropriate theoretical solutions for the laminar boundary layer, and the measurements obtained on the stator suction surface with $i = -10.1^{\circ}$ and $Re_c = 7.2 \times 10^4$ will now be considered by way of example; the stethoscope observations and china clay tests suggest that laminar flow extends to about 75% of chord in this particular case (as shown by Table 6.2 and Appendix E, respectively).

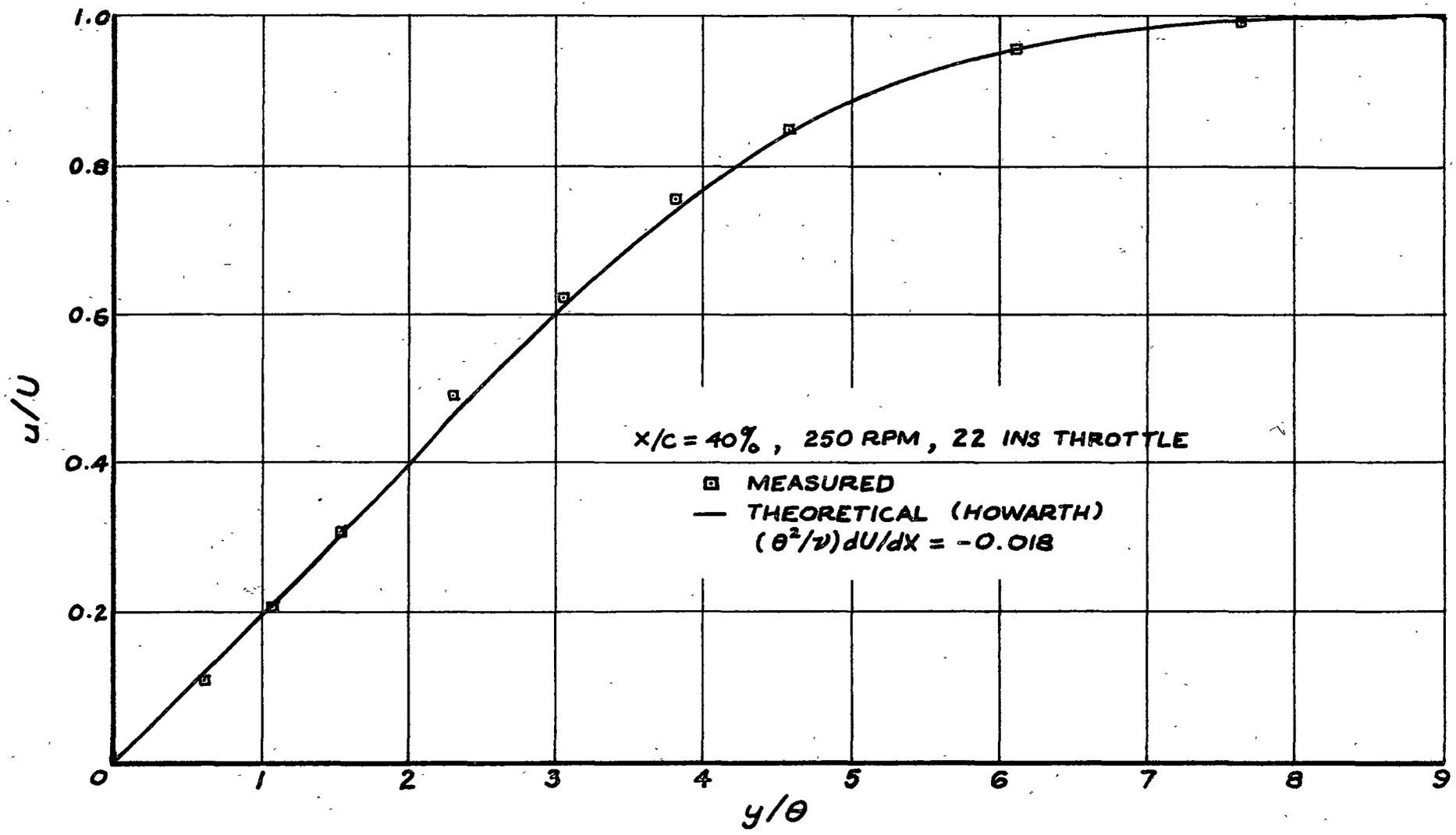


Fig. 5.1 Comparison of Measured and Theoretical Velocity Profiles in Laminar Boundary Layer on Stator Suction Surface
($i = -10.1^{\circ}$, $Re_c = 7.2 \times 10^4$, Compressor Speed 250 rpm)

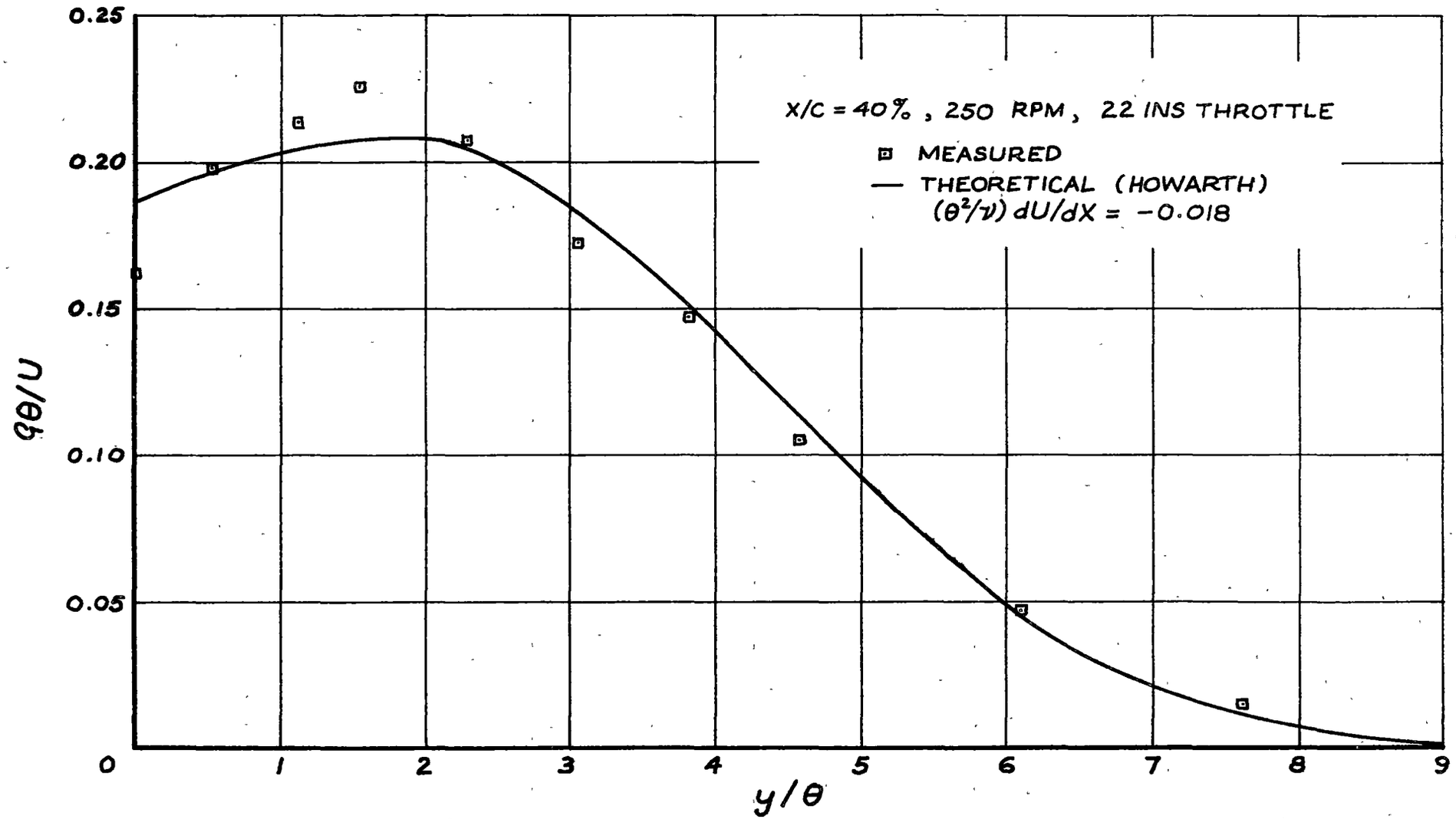


Fig. 5.2 Comparison of Measured and Theoretical Vorticity Profiles in Laminar Boundary Layer on Stator Suction Surface
($i = -10.1^{\circ}$, $Re_c = 7.2 \times 10^4$, Compressor Speed 250 rpm)

Figs. 5.1 and 5.2 show a comparison of the measured velocity and vorticity profiles at 40% chord with the theoretical solutions of Howarth (26) for a laminar boundary layer subjected to the measured value of streamwise pressure gradient parameter, $k = (\theta^2/\nu)(dU/dx)$. The good agreement in both cases clearly indicates the presence of an attached laminar boundary layer at this position. The difference between the measured and theoretical velocity profiles is only 0.01U on the average, which is surprisingly low considering the small dimensions involved and the possible sources of error in measurement; at $x/c = 0.40$ this boundary layer has a momentum thickness of only 0.0037 in. and a total thickness of 0.035 in. The small differences between the experimental and theoretical velocity profiles, although hardly greater than the possible errors in velocity measurement, appear to be systematic to a large extent, and characteristic of all the unsteady laminar boundary layers measured. Much of the distortion in the measured velocity profiles could be due to the effects of non-linear probe response to the unsteady flow in the compressor; but it is equally possible that there is a genuine distortion of the mean velocity profiles arising from the additional shear stresses produced by the laminar instability process and the passage of rotor wakes over the stator blade.

The state of the shear layer in the separated flow regions over the rearward part of the suction surface is most readily inferred from an examination of the measured vorticity profiles. The theoretical vorticity profiles for incompressible laminar boundary layers are markedly similar in the outer part, regardless of the streamwise pressure gradient, and there is little variation between different profiles in the maximum value of non-dimensional vorticity over the boundary layer height, $(\varsigma\theta/U)_{max}$; this results from the outer part of the vorticity profile being largely controlled by the rate at which vorticity is diffused outwards under the action of molecular viscosity, which is a property of the fluid and is not related to the local velocity distribution. The vorticity profiles for turbulent boundary layers are characteristically different from those for laminar flow because the turbulent mixing diffuses vorticity at a much faster rate; this leads to relatively smaller values of vorticity (and hence a flatter velocity profile) in the outer part of a turbulent boundary layer, and a relatively higher vorticity peak at the wall.

The measured vorticity profiles in the range $0.40 \leq x/c \leq 0.90$ for the boundary layer under consideration are shown in Fig. 5.3. Up to 70% of chord, the maximum values of vorticity, and the shape of the vorticity profiles in the outer part of the shear layer, are very similar to the respective properties of the theoretical laminar boundary layer profile shown in Fig. 5.2. At 80% chord, however, the measured vorticity profile shows a marked distortion near the vorticity peak, and the outer part is much steeper, indicating the presence of turbulent flow in the separated shear layer. The vorticity profile at 90% chord is typical of a turbulent boundary layer

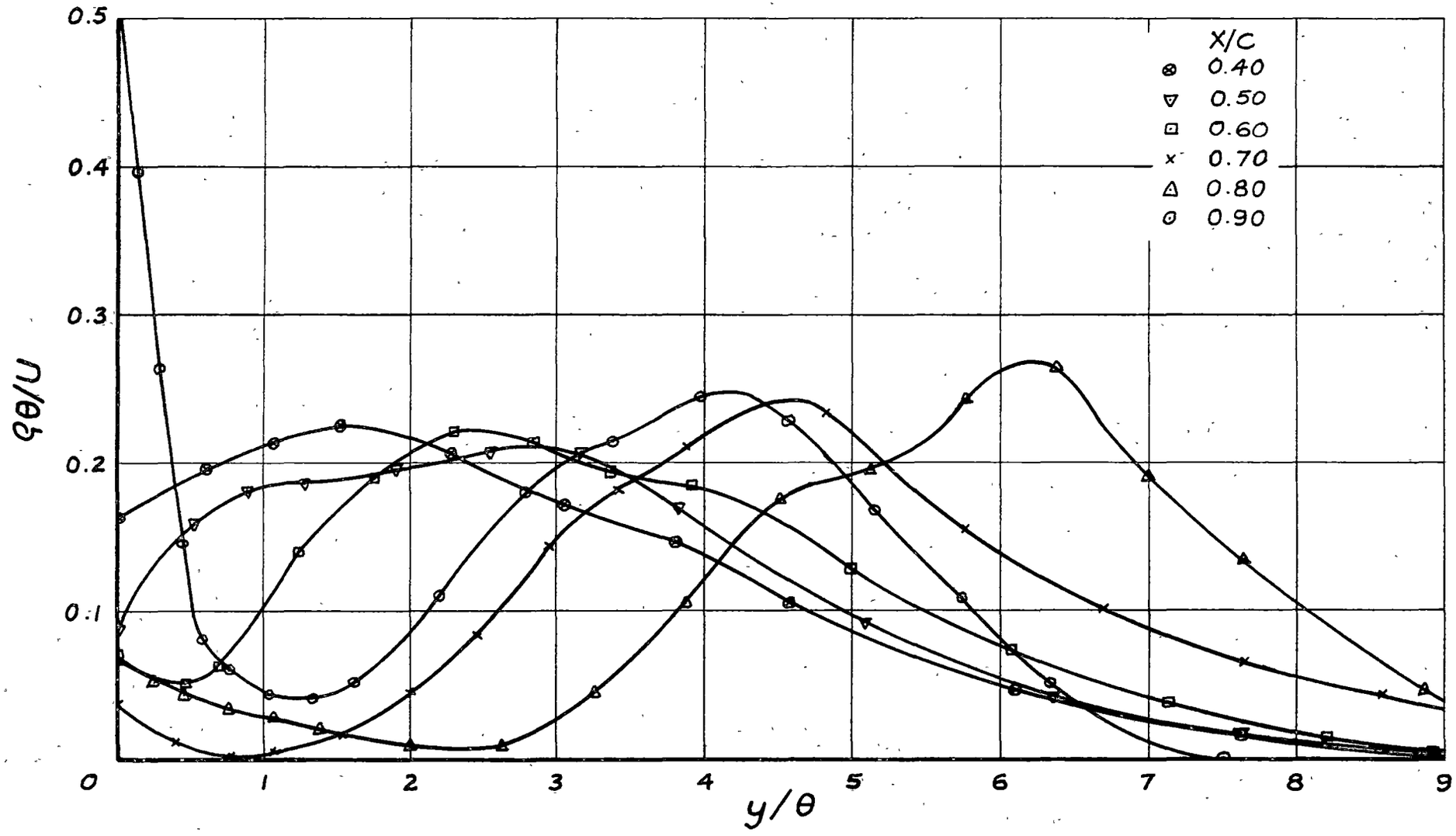


Fig. 5.3 Measured Vorticity Profiles for Boundary Layer on Stator Suction Surface
($i = -10.1^{\circ}$, $Re_c = 7.2 \times 10^4$, Compressor Speed 250 rpm)

immediately downstream of a reattachment point; the vorticity peak in the outer part has started to decay and move back towards the wall under the action of turbulent mixing, while a new and much higher vorticity peak has been generated at the wall. The behaviour of these vorticity profiles is consistent with the presence of laminar flow in the boundary layer and separated shear layer up to about 70% chord, with transition to turbulent flow occurring between 70% and 80% chord.

Hence a detailed examination of the measured velocity profiles fully confirms the initial inferences about the presence of laminar flow made from the stethoscope and china clay observations, and the values of boundary layer shape parameter, H, which were discussed earlier in Chapter 4. It is concluded that in this particular machine, the acceleration of flow on the suction surface of the compressor blades at negative incidence enables the boundary layer there to remain laminar despite the large disturbances arising from the wakes of other blade rows.

## 5.3 Implications of the Observation of Laminar Flow on Machine Blades

It would not be wise to imply from the results of the present investigation that the boundary layer on a turbomachine blade can always be kept laminar by maintaining an acceleration of the mean flow along the blade surface. In fact, it appears that turbulent flow can always be promoted by making the free stream disturbances sufficiently large (see Ref. 44 and Section 6.8.1). Nevertheless, the presence of laminar flow on compressor blades has been demonstrated in at least one situation of practical interest, and this result carries the following important implications for both the design and performance analysis of axial-flow turbomachine blading:

(i) first, it reopens the question of whether more efficient operation might be obtained by designing blade profiles which produce longer regions of laminar flow on the blade surface. This approach had previously been considered futile, as it was thought that the destabilising effect of free stream disturbances would always nullify any stabilisation gained by accelerating the flow near the leading edge;

(ii) secondly, it questions the validity of predictions of blade performance obtained by assuming the boundary layers to be completely turbulent. Such assumptions might not lead to very great errors at the design incidence, where the suction surface boundary layers on most compressor blade sections in current use will probably be predominantly turbulent. But at off-design incidences, the performance predictions of a completely turbulent flow model would become increasingly worse if appreciable lengths of laminar flow were actually present on the blade surface.

Given that extensive regions of laminar flow may exist on turbomachine blades under certain circumstances, it becomes essential to have reliable means of predicting the laminar boundary layer development and the origin of the turbulent boundary layer in order to achieve a reasonable estimate

of blade performance. The remainder of the present chapter and the whole of Chapter 6 will be devoted to a detailed discussion of these problems.

## 5.4 Prediction of the Laminar Boundary Layer

### 5.4.1 Thwaites's Method

The approximate calculation method of Thwaites (10) provides a simple, yet reasonably accurate means of calculating the development of the two-dimensional, incompressible laminar boundary layer. It is assumed that the boundary layer velocity profiles may be represented by a single-parameter family depending on the pressure gradient parameter $k = (\theta^2/\nu)(dU/dx)$, in which case the boundary layer momentum integral equation reduces to the form

$$Ud(\theta^2/\nu)/dx = F(k) \qquad (5.1)$$

The function $F(k)$ is approximated by the linear relation

$$F(k) = 0.45 - 6.0k \qquad (5.2)$$

which Thwaites found to fit closely all known exact solutions and accurate computations of the laminar boundary layer. This leads to an explicit relation for the boundary layer momentum thickness in terms of the surface velocity distribution,

$$(\theta^2/\nu)_x = (0.45/U_x^6)\int_0^x U^5 dx \qquad (5.3)$$

and the pressure gradient parameter, k, is given by

$$k_x = (0.45/U_x^6)(dU/dx)_x \int_0^x U^5 dx \qquad (5.4)$$

The displacement thickness and wall shear stress can then be obtained from the appropriate values of the functions $H = \delta^*/\theta$, and $T = \tau_w\theta/\mu U$, which Thwaites specified as functions of k.

But the values of H and T obtained from exact solutions of the laminar boundary layer are by no means functions of k alone; they also depend strongly on the curvature of the external velocity distribution, $d^2U/dx^2$. (The two-parameter method of Curle (29), for example, allows for this effect by introducing the additional parameter $k^2U(d^2U/dx^2)/(dU/dx)^2$.) Thus the greatest source of error in Thwaites's method (and any other single-parameter approximate method) arises from the necessity of choosing some suitable average of the exact solutions in order to specify the approximate functions H(k) and T(k). It is, however, possible to choose the values of these functions so that the approximate solution will coincide with one particular exact solution: the average values of H and T chosen by Thwaites are fairly close to the exact solution derived by Howarth (26) for the laminar boundary layer in linearly decelerating flow, i.e. with an external velocity distribution of the form

$$U(x) = a - bx \qquad (5.5)$$

This means that significant errors in the values of wall shear stress and displacement thickness predicted by Thwaites's method can be expected to occur whenever the external velocity distribution U(x) is markedly curved.

The errors in these quantities are likely to be greater when the boundary layer is subjected to an adverse pressure gradient, since the exact solutions for H and T diverge most widely at separation.

Fortunately, the accuracy of momentum thickness values predicted by Thwaites's method is not nearly as sensitive to the shape of the external velocity distribution, U(x), since the exact solutions for F all lie quite close to the approximating function given by Equation (5.2). Values of $\theta$ accurate to about 2% can therefore be expected in most cases.

5.4.2 Comparison of Predicted and Measured Boundary Layer Development on the Stator Blade

Predicted values of momentum thickness, shape factor H, and skin friction coefficient, $C_f = \tau_w/\frac{1}{2}\rho U^2$, for the laminar boundary layer regions on the stator blade suction surface have been tabulated in Appendix G; these were calculated by Thwaites's method from the measured surface velocity distributions specified in Appendix D. They may be compared with the corresponding values obtained from the hot wire measurements, which have been tabulated in Appendix F; the method of calculating the experimental values from the hot wire data is given in Section 3.3.12.1.

A comparison of the calculated and measured values of momentum thickness and shape factor obtained at a compressor speed of 500 rpm (with $Re_c \simeq 0.8 - 1.2 \times 10^5$) is shown in Figs. 5.4 and 5.5 respectively. The curves for the two highest values of blade incidence have been omitted because there were no laminar boundary layer regions within the range of the hot wire measurements in either of these cases.

It is seen from Fig. 5.4 that the values of momentum thickness predicted by Thwaites's method are in quite good agreement with experiment. The differences between the calculated and measured values of $\theta$ are about 4%, on the average, and seem to be fairly randomly distributed. Some of these deviations could have arisen from errors in measuring the boundary layer thicknesses and surface velocity distributions; the remainder would have been due to the approximations involved in Thwaites's method, and to departures from the physical model such as three-dimensional and unsteady flow effects. It is interesting to note that the relative differences between the calculated and measured momentum thickness values do not vary significantly with Reynolds number, i.e. they remain approximately the same over the whole range of compressor speeds investigated.

Fig. 5.5 shows that values of boundary layer shape factor H, (which are used to calculate the displacement thickness from $\delta^* = H\theta$) are predicted to about the same accuracy as the momentum thickness. The differences between the measured and predicted values of H show no significant variation with Reynolds number. However, there is a definite tendency for the measured values of H to fall below the theoretical values immediately

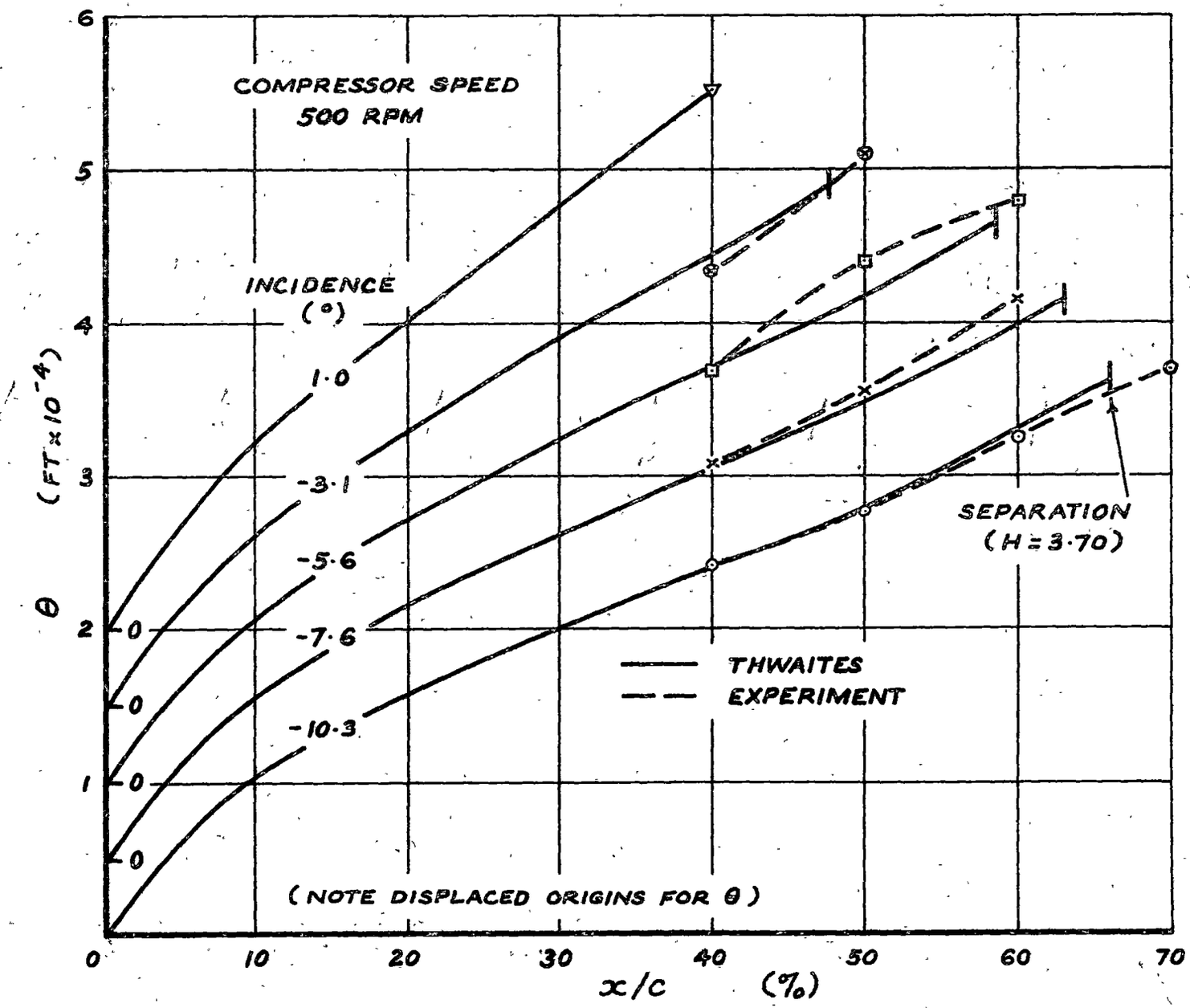


Fig. 5.4 Comparison of Predicted and Experimental Values of Momentum Thickness for Laminar Boundary Layer Regions on Stator Blade Suction Surface ($Re_c = 0.8 - 1.2 \times 10^5$)

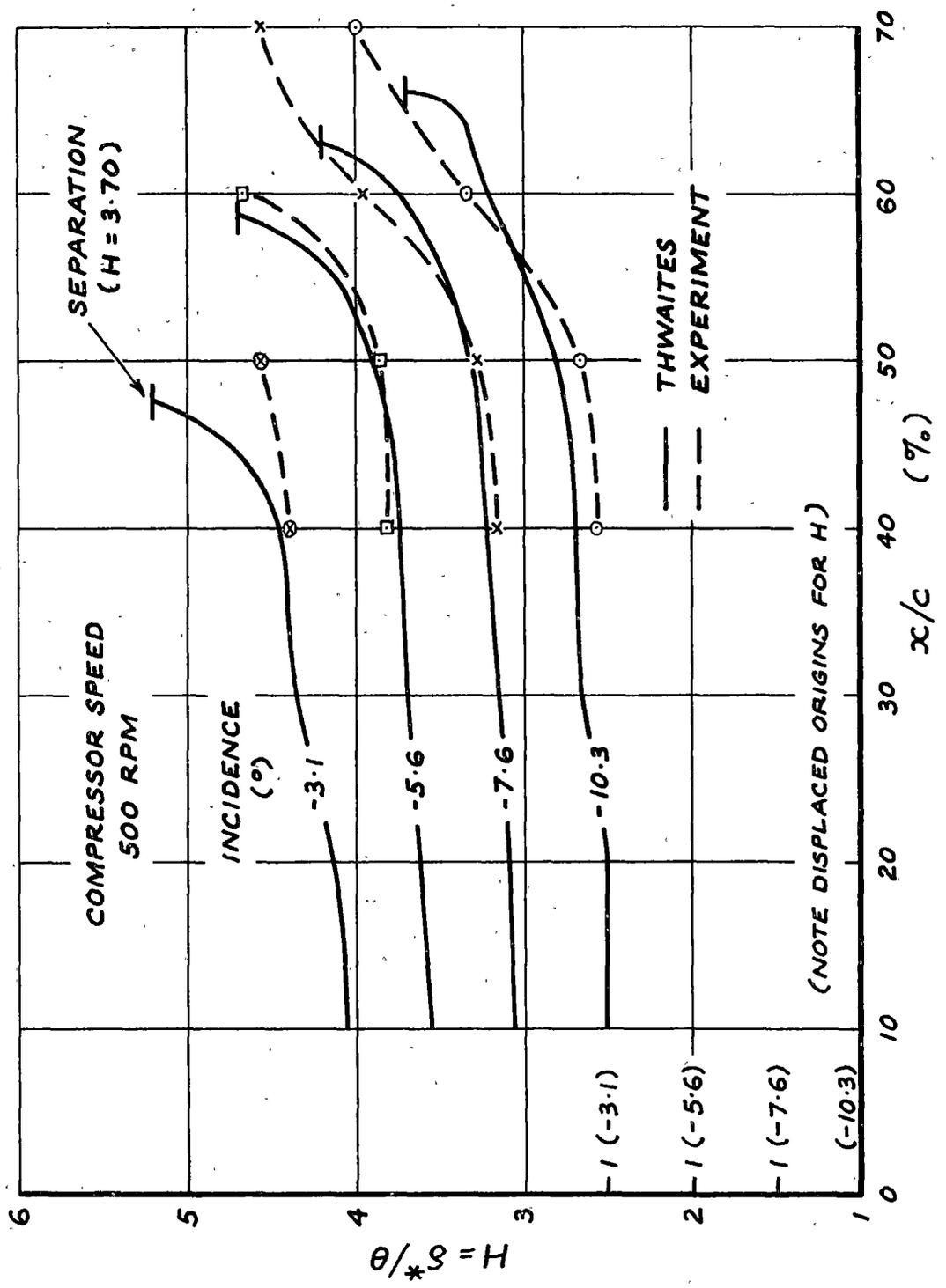


Fig. 5.5 Comparison of Predicted and Experimental Values of Shape Factor H for Laminar Boundary Layer Regions on Stator Blade Suction Surface ($Re_c$ = 0.8 - 1.2 x $10^5$)

upstream of the transition point as defined in Section 6.3.3. This effect, which can be seen in the behaviour of the boundary layer measured at $-3.1^{\circ}$ incidence, is probably due to a reduction in displacement thickness generated by the mixing from occasional bursts of turbulence which are starting to appear in the boundary layer.

It is seen from Appendices F and G that the values of skin friction coefficient calculated by Thwaites's method agree much less favourably with experiment than the momentum thickness predictions. At the three highest compressor speeds, the calculated and experimental values of $C_f$ differ by about 15% on the average, except near separation where the differences between them increase markedly. This is probably the best agreement that could be expected, however, in view of the possible errors of at least 10% in the experimental skin friction values, and the wide divergence of the exact solutions for the laminar boundary layer from which Thwaites's wall shear stress function, T(k), is averaged. At the lowest compressor speed investigated, i.e. 150 rpm, the difference between the measured and predicted values of $C_f$ is generally closer to 30%; but much of this discrepancy could simply be due to the poorer accuracy of the measured wall shear stress values at low velocities, which arises from errors in extrapolating the hot wire calibration and from the relatively larger effects of wall proximity and non-linear probe response to the unsteady flow.

### 5.4.3 Concluding Remarks

The good agreement between the measured and predicted values of the various boundary layer parameters provides a further indication that the flow on the stator blade suction surface is essentially two-dimensional. However, it should be borne in mind that the unsteady flow and three-dimensional flow effects could have been opposite in sign in this particular case: other situations might be found in which these secondary effects would add, and a two-dimensional flow model would then give less accurate results (see Chapter 8).

It appears that Thwaites's method will predict the development of laminar boundary layers on turbomachine blades with sufficient accuracy for engineering purposes, provided that the flow is closely two-dimensional. A refinement of the laminar flow model to take into account the effects of surface curvature and unsteady flows does not appear necessary at present, but these factors could become more important in machines having blade row spacing or blade leading edge radii much smaller than those of the compressor used in the present investigation. However, the only unsteady flow effect which could now be calculated with any confidence would be the potential flow interaction between blade rows; the unsteady flows due to blade wakes and wake-boundary layer interactions are rather complex, and not yet fully understood.

## 5.5 Prediction of Laminar Separation

### 5.5.1 Calculation by Thwaites's Method

With single-parameter approximate methods of calculating the laminar boundary layer, separation is predicted to occur when the pressure gradient parameter k or shape parameter H reach certain critical values corresponding to a zero value of the non-dimensional wall shear stress function, $T = \tau_w \theta/\mu U$. The approximate functions chosen by Thwaites indicate separation to occur when $k = -0.082$ and $H = 3.70$.

Thwaites's method should give a reasonably accurate prediction of the laminar separation point in linearly decelerating flow (Eqn. 5.5), as it uses values of the functions H and T which closely approximate the exact solutions of Howarth (26) for this particular case. However, because of the wide variation of the exact solutions for T(k) in adverse pressure gradients, the prediction of separation is likely to be much poorer whenever the external velocity distribution U(x) is markedly curved.

Curle and Skan (27) have suggested slight modifications of Thwaites's functions to give better agreement with the exact solutions of Görtler (28); the modified functions give $k = -0.090$ and $H = 3.55$ at separation. But this only represents a different means of choosing average values of H and T; it is not a fundamentally different calculation method, and is unlikely to give more accurate results than Thwaites's method in the general case.

### 5.5.2 Calculated Separation Points

The calculated positions of laminar separation on the suction surfaces of both rotor and stator blades in the research compressor are presented in Table 5.1. These points were obtained by Thwaites's method, using the blade surface velocity distributions, U(x), tabulated in Appendix D. Values of dU/dx required for calculating the pressure gradient parameter $k = (\theta^2/\nu)(dU/dx)$ were generally determined by fitting a parabolic curve through successive sets of three neighbouring points of the measured velocity distribution; the slope of the parabola at the middle point was taken as the streamwise velocity gradient at that point.

The parabolic fit to U(x) was employed in all cases except for the boundary layers on the stator blade at negative incidence (corresponding to 8 - 22 in. throttle opening) with compressor speeds of 250 and 150 rpm; here, it led to calculated separation positions which were obviously 10-15% of chord too far downstream. These errors occurred because the presence of a well developed laminar separation region caused the parabola approximating U(x) to become concave (i.e. $d^2U/dx^2 > 0$) so that the values of dU/dx and k just upstream of the true separation point were underestimated. In this type of situation it was found that much better agreement with experiment could be obtained by using a linear fit to the measured surface velocity distribution, and assuming a discontinuity in dU/dx to occur at separation,

as shown in Fig. 5.6. This procedure was therefore adopted in calculating the separation positions for the particular cases mentioned above.

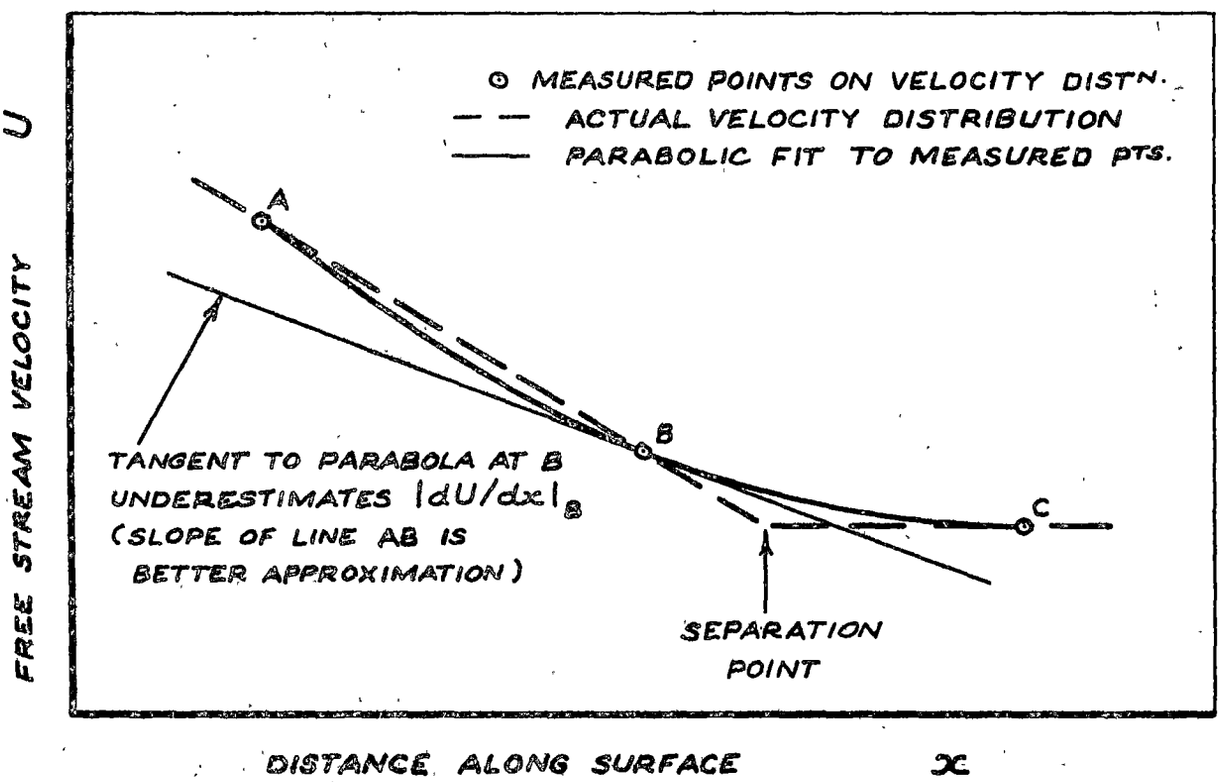


Fig. 5.6 Determination of dU/dx near Separation

5.5.3 Experimental Separation Points

The experimental positions of laminar separation obtained from the hot wire measurements on the stator blade suction surface are given in Table 5.2; these were taken as the points where the measured value of boundary layer shape factor H reached 3.70, the critical value adopted by Thwaites. It was not practicable to define the experimental separation point as the position where the measured wall shear stress, $\tau_w = \mu(\partial u/\partial y)_{y=o}$, fell to zero, because the hot wire readings always indicated non-zero values of $\partial u/\partial y$ at the blade surface in the unsteady flow over the compressor blade. (A single hot wire probe senses only the speed of flow normal to the wire, so that an intermittently reversing flow with zero mean velocity gives a non-zero mean speed reading.)

Admittedly, the value of H at separation can vary significantly from 3.70, depending on the shape of the surface velocity distribution, U(x). The work of Curle (29) indicates that H should be less than 3.70 when U(x) is convex (i.e. $d^2U/dx^2 < 0$), and greater than 3.70 when U(x) is concave (i.e. $d^2U/dx^2 > 0$), with the minimum possible value of H at separation being about 3.5. However, a variation of $\pm$ 0.2 in the critical value of H would have changed the experimental separation points on the stator blade by less than $\pm$ 3% chord in all cases except the measurements obtained at 750 rpm (see Figs. 4.7 (a - d)).

Table 5.1

Points of Laminar Separation Calculated from Thwaites's Method

MID BLADE HEIGHT

Values of x/c (%)

| Location | Compressor Speed (rpm) | Throttle Opening (ins) 4.8 | 5.2 | 6.0 | 8.0 | 10.0 | 13.0 | 22.0 |
|---|---|---|---|---|---|---|---|---|
| ROTOR SUCTION SURFACE | 750 | 8.5 | 22 | 26.5 | 50 | 61 | 63 | 66 |
| STATOR SUCTION SURFACE | 750 | 29 | 27 | 34 | 47 | 54 | 60 | 63 |
| | 500 | 28 | 27.5 | 42 | 47 | 59 | 61.5 | 63.5 |
| | 250 | 29.5 | 26 | 44 | 60.5 | 60.5 | 61.5 | 66 |
| | 150 | 31 | 29 | 39 | 56 | 58.5 | 59.5 | 62.5 |

(Note: Separation points calculated from Thwaites's method, i.e. $H = 3.70$, $(\theta^2/\nu)(dU/dx) = -0.082$ at separation.)

Table 5.2

Points of Laminar Separation from Hot Wire Measurements

MID BLADE HEIGHT

Values of x/c (%)

| Location | Compressor Speed (rpm) | Throttle Opening (ins) 4.8 | 5.2 | 6.0 | 8.0 | 10.0 | 13.0 | 22.0 |
|---|---|---|---|---|---|---|---|---|
| STATOR SUCTION SURFACE | 750 | T | T | T | T | 62 | 65 | 70 |
| | 500 | T | T | T | 57.5 | 60.5 | 62.5 | 65 |
| | 250 | T | T | T | 57 | 59 | 60.5 | 62 |
| | 150 | T | T | T | 54.5 | 57 | 58 | 61 |

(Note: Separation assumed to occur when $H = 3.70$.
T = Imminent transition suppresses laminar separation)

5.5.4 Comparison of Calculated and Measured Separation Points

The hot wire measurements indicate that there is no laminar separation from the stator blade suction surface at small positive incidence (corresponding to 4.8 - 6 in. throttle opening), even though the calculated separation point precedes the observed transition point by a few per cent of chord. In these cases separation is apparently suppressed by the mixing from three-dimensional disturbances in the rearward part of the laminar instability region (see Section 6.2) or from occasional bursts of turbulence which are starting to appear in the boundary layer. Thus a comparison of the measured and calculated separation points is only possible for the boundary layers obtained at negative incidence, where the separation regions become fairly well developed.

At the highest Reynolds numbers investigated (corresponding to a compressor speed of 750 rpm) the separation regions on the stator blade are generally less than 10% chord in length; the peak values of H only slightly exceed the critical value of 3.70, and the measured separation points lie downstream of those calculated from Thwaites's method by 5 - 8% of chord. This difference could be partly due to occasional turbulent mixing delaying separation, and partly due to errors from applying Thwaites's method in a situation where the surface velocity distribution is slightly convex.

At the lower compressor speeds of 500, 250, and 150 rpm, where separation from the stator blade is much more highly developed, the experimental and calculated separation points agree to within 2% of chord in most cases. This is rather better than might have been expected, considering the possible errors involved in determining both of these positions. The good agreement is possibly the fortuitous result of the surface velocity distributions on the stator suction surface at negative incidence being approximately linear in the neighbourhood of the separation point. The velocity distributions vary from slightly convex ($d^2U/dx^2 < 0$) at 750 rpm, to slightly concave ($d^2U/dx^2 > 0$) at 150 rpm, so that conditions favour Thwaites's method, on the average.

The laminar separation points were also calculated from the modification of Thwaites's method suggested by Curle and Skan (27), and compared with the experimental separation points obtained by using a critical value of $H = 3.55$. However, the agreement was significantly poorer, in most cases, than that obtained by using a critical value of $H = 3.70$.

5.5.5 Conclusions

It appears that Thwaites's method should give a reasonably accurate estimate of the laminar separation point on turbomachine blades in two-dimensional flow situations where the surface velocity distribution, $U(x)$, is approximately linear. But in cases where $U(x)$ is markedly curved and an accurate prediction of separation is required, it would probably

be desirable to use a two-parameter calculation method, such as that suggested by Curle (29).

## 5.6 Separated Laminar Flow Regions

### 5.6.1 Introduction

The separated laminar shear layer is so unstable that transition to turbulent flow usually occurs at a short distance downstream of the laminar separation point. Under certain circumstances it is possible for the turbulent shear layer thus formed to reattach to the bounding surface and so produce a closed region of separated flow known as a "laminar separation bubble". The appearance and growth of laminar separation bubbles on axial-flow compressor blades is generally considered to be responsible for the sudden increase in drag which occurs as the blade Reynolds number is decreased through the so-called "critical region" around $Re_c = 10^5$.

This section discusses the measurements of separated laminar flow regions on the blades of the research compressor : as mentioned previously (Sections 4.2 and 4.4) it appears that separation bubbles are present on the suction surfaces of both rotor and stator blades at negative incidence over most of the Reynolds number range investigated ($3 \times 10^4 < Re_c < 2 \times 10^5$). To put these observations in perspective, however, it will first be necessary to discuss briefly the bubble flow mechanism, classification of bubble types, and the results of previous experimental and theoretical work on this subject. The behaviour of the separated laminar flow regions on the compressor blades will then be examined in detail and compared with the empirical results and theoretical predictions of other workers. Finally, some modifications to an existing semi-empirical model of the laminar separation bubble will be suggested in order to obtain a reasonable description of the bubbles on the compressor blades.

### 5.6.2 Flow Mechanism in a Laminar Separation Bubble

A diagram of the flow mechanism in a two-dimensional laminar separation bubble is given in Fig. 5.7. Over the forward part of the bubble, where the flow remains laminar, there is very little entrainment of fluid by the separated shear layer, and the velocity of reverse flow underneath it is correspondingly small. This gives rise to an almost stagnant, or "dead air" region, which causes the surface pressure to remain almost constant, nearly equal to the pressure at separation.

Theoretical models of flow in separation bubbles usually assume instantaneous transition in the laminar shear layer, but it is more realistic to assume that transition to turbulent flow occurs over a finite distance, as shown in Fig. 5.7 (see also Section 6.9). When transition commences, the rate of entrainment by the shear layer rapidly increases, and the mean flow streamlines curve back towards the bounding surface.

The dividing streamline returns to the surface at the reattachment point to close the bubble. Continuity requires a much higher reverse flow velocity under the separated turbulent shear layer because of the faster rate at which fluid is entrained by the turbulent flow.

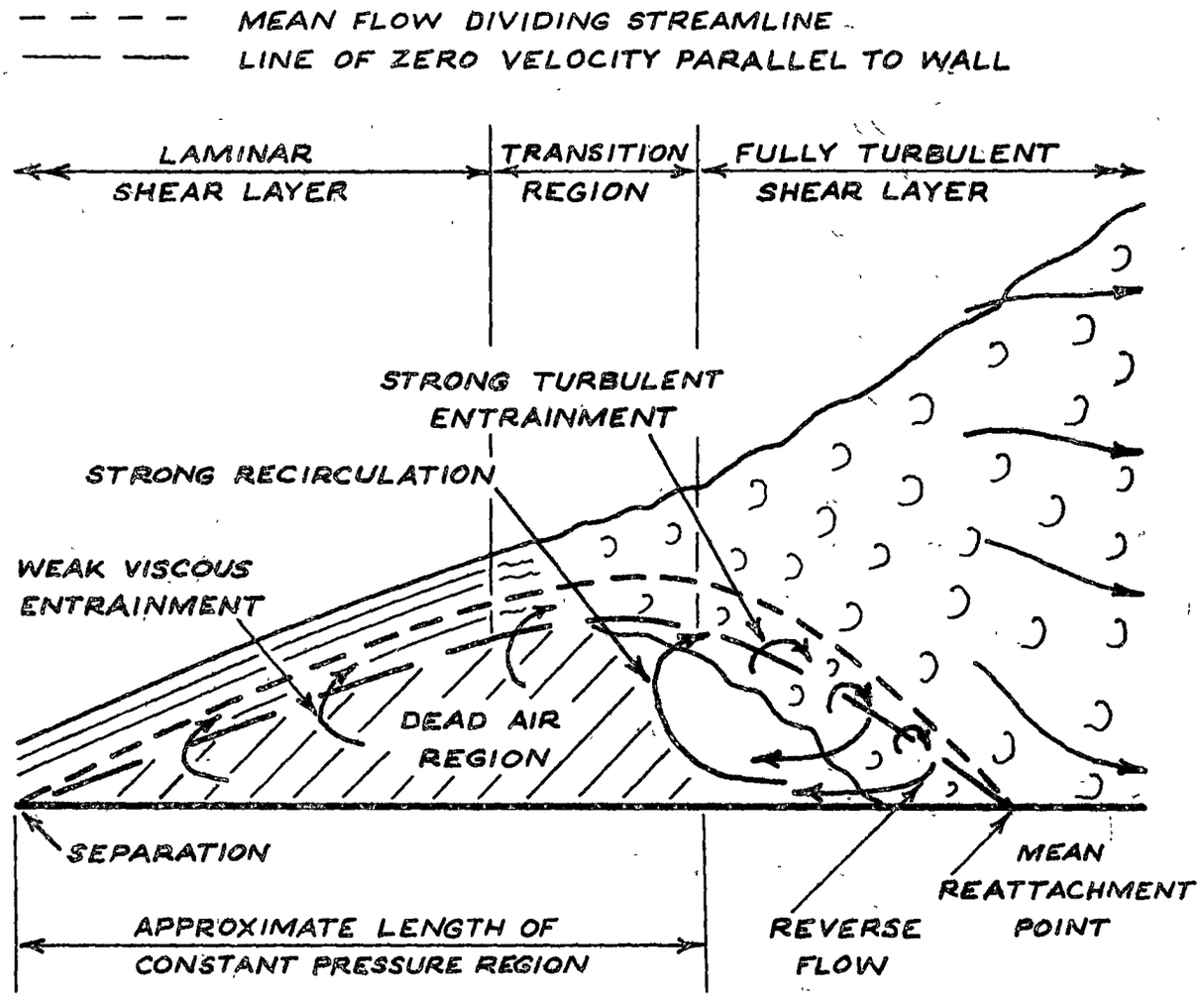


Fig. 5.7 Flow Mechanism in a Two-Dimensional Laminar Separation Bubble

In the rearward part of the bubble the flow is very unsteady because of the eddies reaching out from the spreading turbulent shear layer, and there is a zone of vigorous recirculation which limits the downstream extent of the dead air region. A strong rise in surface pressure is required to balance the inertia forces generated by the curvature of the mean streamlines in the reversing flow immediately upstream of the reattachment point. The pressure continues to rise rapidly for a short distance after reattachment due to the boundary layer displacement thickness initially tending to decrease.

5.6.3 Types of Laminar Separation Bubbles

On isolated aerofoils operating at high Reynolds number, laminar separation bubbles appear to fall into two broad classes:

(i) "short" bubbles, which occupy only 1% of chord or so, and have little

effect on the pressure distribution around the aerofoil;

(ii) "long" bubbles, which are one or two orders of magnitude larger in extent, and have a marked effect on the aerofoil pressure distribution, tending to collapse the suction peak near the leading edge.

With both types of bubble the surface pressure usually remains almost constant over the dead air region under the separated laminar shear layer, giving a characteristic "flat" in the aerofoil pressure distribution. Typical forms of pressure distribution on isolated aerofoils with short and long bubbles near the leading edge are shown in Fig. 5.8.

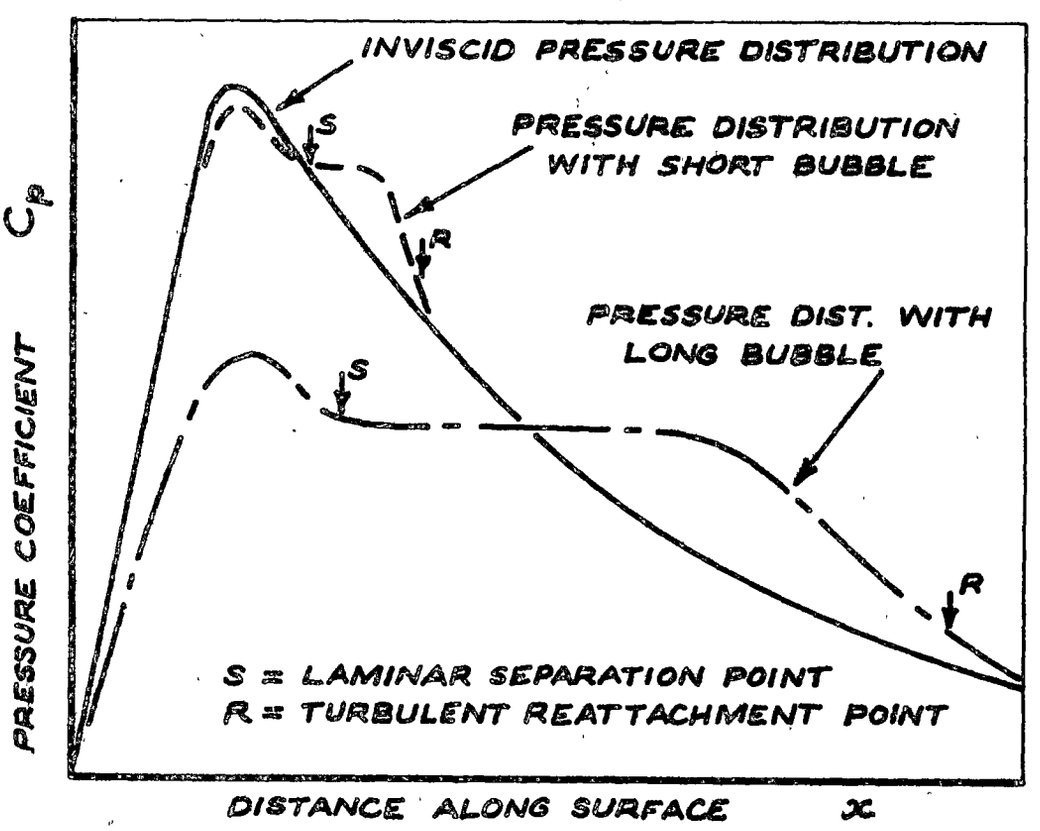


Fig. 5.8 Effect of a Separation Bubble Near the Leading Edge on the Pressure Distribution around an Isolated Aerofoil

5.6.4 Previous Work on Laminar Separation Bubbles

The earliest investigations of separated laminar flow regions were mostly associated with studies of the leading edge type of stall on isolated aerofoils. This phenomenon is caused by a short bubble formed near the leading edge at a moderate incidence suddenly expanding in length at a higher incidence to form either a long bubble or a completely separated shear layer. The sudden change in flow regime, which is usually called "short bubble bursting", causes a very sharp drop in lift, together with a marked drag rise and an undesirable change in pitching moment.

Various workers have attempted to correlate the bubble behaviour with

the properties of the laminar boundary layer at separation. Owen and Klanfer (30) analysed the results of tests on NACA 63-009 and 64-006 aerofoils, and suggested that bubbles would either be short, with a non-dimensional length $l/\delta^*_S = O[10^2]$, or long, with $l/\delta^*_S = O[10^3 - 10^4]$, depending on whether the boundary layer Reynolds number at separation, $Re_{\delta_S^*}$, was greater or less than about 450. Crabtree (31) correlated a large amount of data from various sources which mostly tended to confirm Owen and Klanfer's critical value of $Re_{\delta_S^*} \simeq 450$, but he noted that bursting appeared to occur at higher Reynolds numbers in some isolated cases observed by McGregor (32). This led Crabtree to introduce an additional parameter,

$$\sigma = (p_R - p_S)/\tfrac{1}{2}\rho U_S^2 = 1 - (U_R/U_S)^2 \qquad (5.6)$$

based on the pressure rise over the bubble; he suggested that bursting would occur either through $Re_{\delta_S^*}$ falling to 450, or by $\sigma$ rising to a critical value of about 0.35, but obtained only moderate agreement with experiment from this model.

To obtain more data about the bursting problem, Gaster (33, 34) carried out a series of detailed measurements on laminar separation bubbles formed on a flat plate under carefully controlled conditions. From the results obtained he formulated a two-parameter bursting criterion based on the separation Reynolds number, $Re_{\theta_S}$, and the non-dimensional pressure gradient over the bubble,

$$P = (\theta_S^2/\nu)(\Delta U/\Delta x) \qquad (5.7)$$

Here, $\Delta U = (U_R - U_S)$ is the change in free-stream velocity over the length of the bubble, $\Delta x = x_R - x_S$. Gaster was able to demonstrate a unique relationship between the parameters $Re_{\theta_S}$ and P at bursting, which is reproduced in Fig. 5.9. It appeared from this result that Owen and Klanfer's single-parameter bursting criterion was a special case of the more general two-parameter criterion. Another notable feature of Gaster's measurements was that the separated flow regions on the flat plate underwent a gradual transition from the short to the long bubble regime, rather than the sudden bursting process observed on isolated aerofoils.

Wallis (35) followed a completely different approach by suggesting that bubble bursting occurred through separation of the reattached turbulent boundary layer downstream of the bubble, but this model did not enjoy universal acceptance by other workers. In particular, Gaster (34) expressed the opinion that the turbulent separation mechanism was not the usual cause of bubble bursting on conventional aerofoils. However, the present author (36) noted that Gaster's bursting criterion, shown in Fig. 5.9, can be roughly approximated by the linear relation

$$P_b = C_1 \, Re_{\theta_S} \qquad (5.8)$$

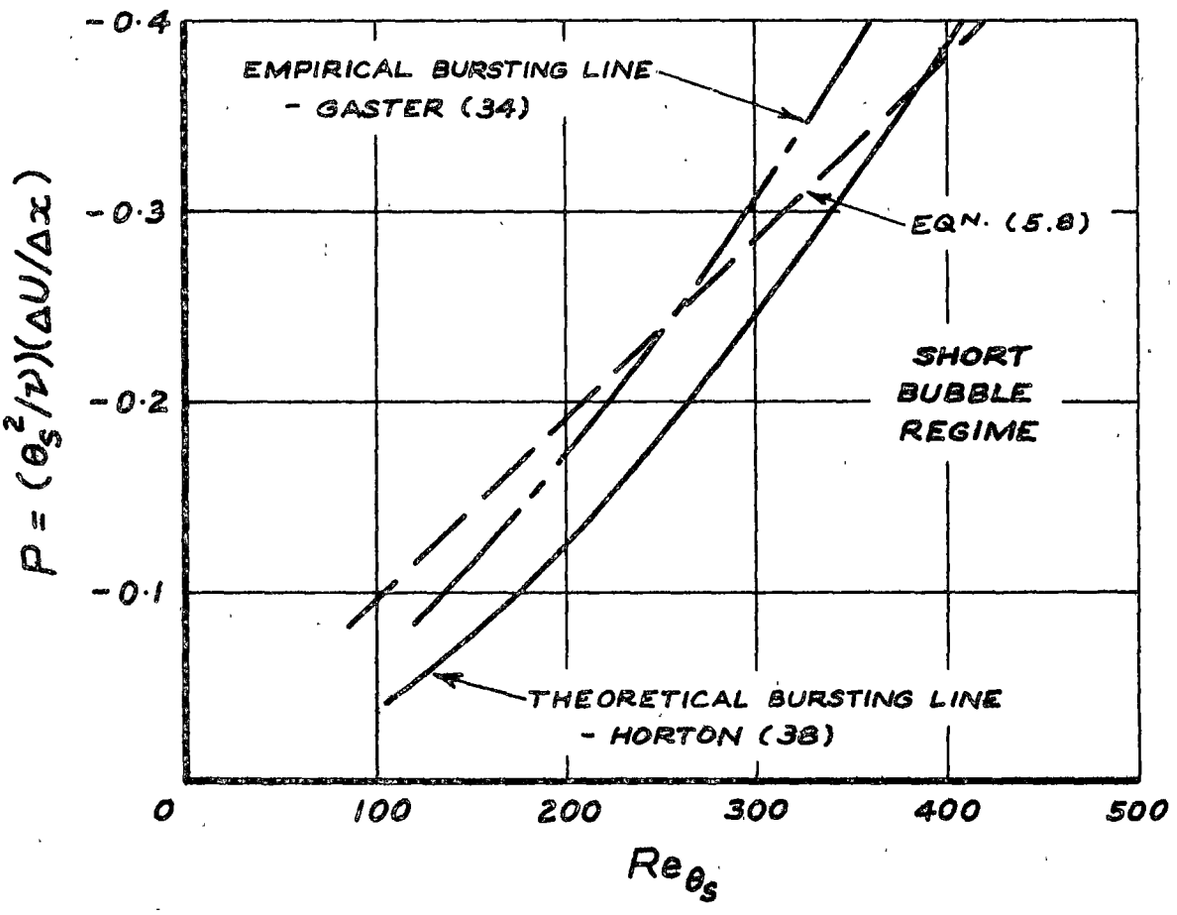


Fig. 5.9 Relationship between $Re_{\theta_s}$ and P at Bursting

which can alternatively be expressed as

$$\left\{(\theta_s/U_s)(\Delta U/\Delta x)\right\}_b = -C_1 = \text{constant} \qquad (5.9)$$

As Equation (5.9) does not involve the molecular viscosity, which is an essential parameter for describing the laminar shear layer behaviour, and the value of the pressure gradient parameter $(\theta/U)(dU/dx)$ provides an approximate separation criterion for the turbulent boundary layer (see Section 8.3.2.3), Walker (36) suggested that Gaster's empirical bursting criterion was in fact consistent with some mechanism of turbulent separation being the cause of bubble bursting.

A similar view of the bursting problem was taken by Woodward (37), who observed transition to occur at very nearly the same position in a laminar separation bubble just before and just after bursting; he therefore concluded that bursting was not due to a fundamental change in the stability of the separated laminar shear layer occurring at a critical value of $Re_{\theta_s}$. This led Woodward to postulate that bursting of a laminar separation bubble was caused by the sudden failure of the turbulent shear layer to reattach to the surface.

### 5.6.5 Horton's Semi-empirical Model for the Laminar Separation Bubble

Following Woodward's suggestion that bubble bursting was associated with the behaviour of the turbulent shear layer, Horton (38) developed a criterion for turbulent reattachment obtained from the boundary layer kinetic energy integral equation. The appropriate parameter was found to be $(\theta/U)(dU/dx)$, which took a value at the reattachment point of

$$\{(\theta/U)(dU/dx)\}_R = -0.0059 \qquad (5.10\ (a))$$

when the velocity profile shape factor for the reattaching turbulent shear layer was given the empirically determined value of

$$H_R = 3.50 \qquad (5.10\ (b))$$

and the eddy viscosity $\mu_t$, which was assumed to be constant across the layer, was defined by

$$\mu_t = 0.020\ \rho U \delta^* \qquad (5.10\ (c))$$

However, the experimental data analysed by Horton gave a slightly different result from Equation 5.10 (a), indicating an average value of

$$\{(\theta/U)/(dU/dx)\}_R = -0.0082 \qquad (5.11)$$

with a standard deviation of 0.0016. Horton suggested that this could be explained by the rate of entrainment and the dissipation coefficient for a reattaching turbulent shear layer being rather higher than that for a corresponding attached layer.

Horton (38) then formulated a simple model for the growth and bursting of short laminar separation bubbles in two-dimensional flow, based on the following assumptions:

(i) an external velocity distribution in the neighbourhood of the bubble as shown in Fig. 5.10;

(ii) a length of constant pressure region, $l_1 = x_T - x_S$, given by the empirical correlation

$$l_1/\theta_S = 4 \times 10^4/Re_{\theta_S} \qquad (5.12)$$

obtained from the experimental results of Refs. 32, 33 and 36;

(iii) a value of $(\theta/U)(dU/dx) = -0.0082$ at the point of turbulent reattachment.

The predictions of this model were in good qualitative and fair quantitative agreement with experiment, and thus confirmed that bubble bursting was caused by a fundamental breakdown of the turbulent reattachment process.

### 5.6.6 Observations of Separated Flow Regions on the Compressor Blades

#### 5.6.6.1 Introduction

During the early stages of the present investigation it was thought that the presence of a short laminar separation bubble on

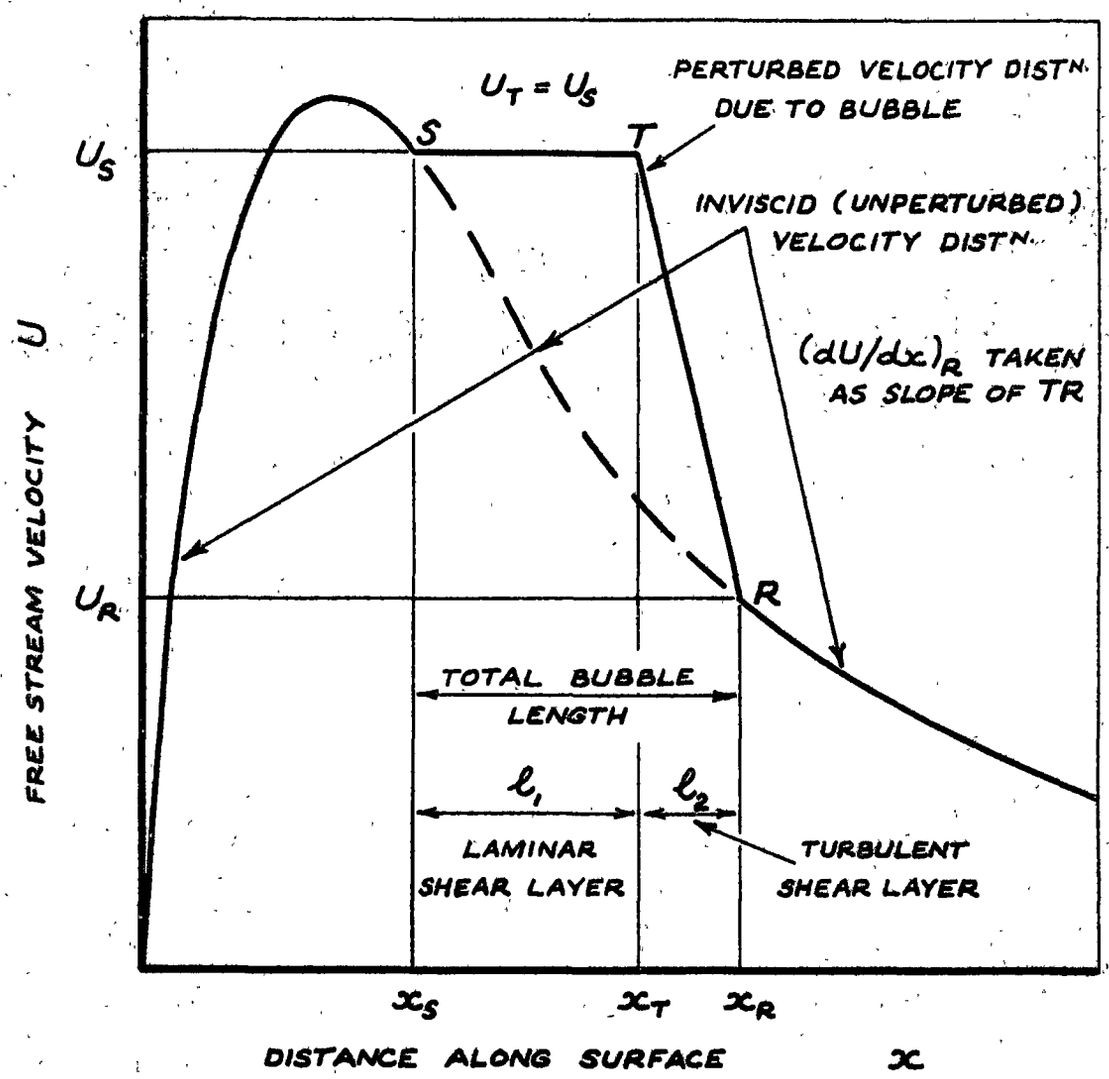


Fig. 5.10 Simplified Model of the External Velocity Distribution near a Short Laminar Separation Bubble - from Horton (38)

turbomachine blades operating at very low Reynolds numbers might have had the desirable effect of accelerating the transition process, and so preventing the occurrence of more extensive laminar flow separation. But it is now considered that a laminar separation bubble would only be of minimal use in promoting transition, and would be more likely to increase, rather than decrease, the blade losses. Nevertheless, the observations of separated laminar flow regions on the blades of the research compressor will still be discussed in some detail, as they are very interesting in themselves, and are also relevant to the problems of predicting the stalling behaviour and low Reynolds number performance of machine blades.

5.6.6.2 Length of the dead air region

Fig. 5.11 shows the non-dimensional lengths of the dead air region, $l_1/\theta_S$, plotted against the boundary layer Reynolds number at separation, $Re_{\theta_S}$, for laminar separation bubbles on the suction surfaces of both rotor and stator blades. The experimentally determined separation points specified in Table 5.2 were taken to define the upstream limit of the dead air region on the stator blade; for the bubbles on the rotor blade, the

calculated separation points specified in Table 5.1 were used. The point of apparent turbulent flow reattachment obtained from the china clay tests was taken as the downstream limit of the dead air region in all cases.

The china clay drying pattern is related to the evaporation rate of the surface oil-film, which is expected to depend more on the magnitude of the wall shear stress than on its direction. Hence the vigorous fluctuations in velocity which occur at a mean reattachment point should cause the drying rate there to be quite appreciable, even though the time mean value of the wall shear stress is zero. If, as appears likely, there is also a significant surface drying rate underneath the turbulent flow region in the rear of a separation bubble, the apparent point of reattachment obtained from the china clay tests should indicate the downstream limit of the dead air region under the separated shear layer, rather than the true mean reattachment point. This view is confirmed by measurements in separation bubbles on the stator blade suction surface at negative incidence, where the reattachment point indicated by the china clay tests generally lies close to the point at which pressure recovery commences, but well upstream of the reattachment point defined by $H_R = 3.50$.

Taking $\delta_S^* \simeq 4\theta_S$, it is seen from Fig. 5.11 that all the separation bubbles on the compressor blades had lengths of $O[10\,\delta_S^*]$. This at first suggests that they fall in the short bubble regime, although it is usually supposed in the literature that short bubbles have lengths of $O[10^2\,\delta_S^*]$, which is an order of magnitude greater. But whereas short bubbles on isolated aerofoils operating at high Reynolds number usually occupy only 1% of chord or so, the separation bubbles on the compressor blade suction surfaces occupy up to 30% of chord, which is more typical of the long bubble regime. It is obviously very difficult, if not impossible, to infer the bubble flow regime from the values of such relative length scales, and further attempts to classify the bubble regime are left until Section 5.6.4.6.

The values of $l_1/\theta_S$ for bubbles on the compressor blades do not exhibit any definite variation with $Re_{\theta_S}$, and certainly do not follow Equation 5.12, used by Horton (38) to correlate the measurements of Gaster (34) and other workers. Equation 5.12 can alternatively be written as

$$Re_{l_1} = U_S l_1/\nu = 4 \times 10^4 \qquad (5.13)$$

which indicates that the dead air region should occupy an increasingly large proportion of the surface of an aerofoil as the chord Reynolds number, $Re_c$, is reduced. In the separation bubbles on the compressor blades, however, the length of the dead air region at a given blade incidence remains essentially constant as the compressor speed is changed by a factor of 5; and whereas Equation 5.13 indicates that the bubbles should be longer than the blade chord at a compressor speed of 150 rpm, where $Re_c \simeq 3 \times 10^4$, the measured bubble lengths are only 10 - 30% chord.

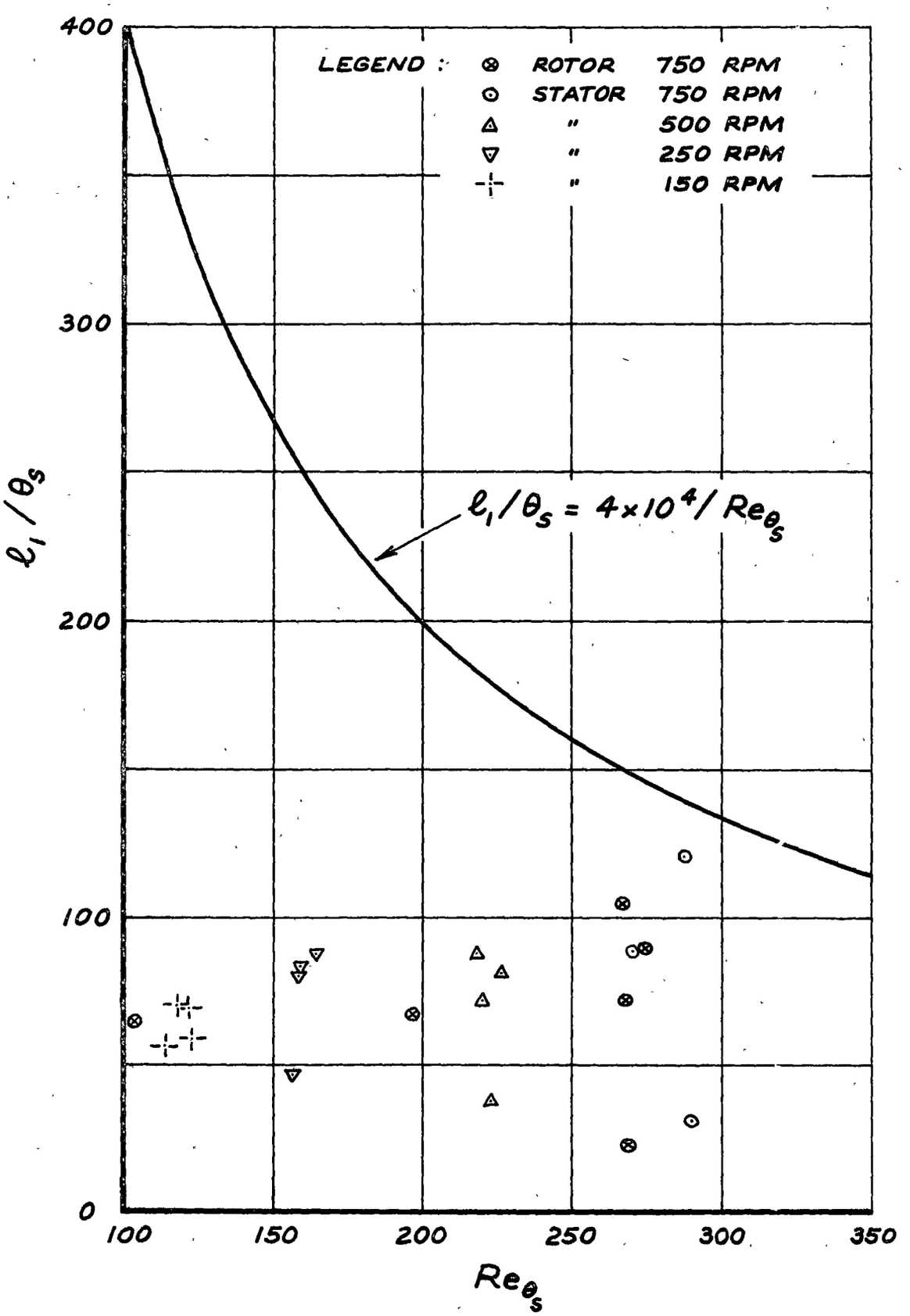


Fig. 5.11 Non-Dimensional Length of the Dead Air Region in Laminar Separation Bubbles Observed on the Rotor and Stator Blade Suction Surfaces

Finally, it is interesting to note that although there is a considerable scatter in the measured values of $l_1/\theta_s$ shown in Fig. 5.11, there does not appear to be any major difference between the flow behaviour on the rotating and stationary blade surfaces.

5.6.6.3 Velocity profiles in separated laminar flow regions

Because of the large velocity fluctuations and the intermittent flow reversals which occur in the rearward part of a separation bubble, where the turbulent shear layer is reattaching, the values of mean flow velocity indicated by a hot wire anemometer probe will always be too high. This gives rise to an apparently non-zero wall shear stress at a mean reattachment point, where the time mean value of the wall shear stress is actually zero. It is therefore necessary to exercise considerable care when interpreting hot wire measurements obtained in a separation bubble.

The measured mean velocity profiles in a typical separated laminar flow region on the stator blade suction surface at negative incidence are shown in Fig. 5.12. They are very similar to the velocity profiles measured by Gaster (34) in separation bubbles generated on a flat plate.

No points of zero velocity away from the surface were indicated by the measurements on the stator blade, but this was to be expected because of the probe response to the large velocity fluctuations present in the separation zone. Nevertheless, it was quite common to obtain velocity readings of only 1-2% of free stream velocity in the area beneath the separated laminar shear layer, as can be seen from the profile at x/c = 70% in Fig. 5.12. It is not possible to deduce from the hot wire readings whether continuous reversed flow was present underneath the separated shear layer in separated flow regions obtained on the compressor blades; but in view of the small mean velocities observed and the large disturbances present, it does seem likely that intermittent forward flow could have existed close to the blade surface in the bubbles obtained at the higher compressor speeds, where laminar separation was not so highly developed. The variations in streamwise pressure gradient impressed by blade wakes passing in the free stream would undoubtedly generate significant changes in the velocity of low inertia fluid in a separation bubble on a machine blade.

One of the most notable features of the velocity profile measurements on the stator blade is the large streamwise distance (relative to the blade chord) required to establish the normal turbulent boundary layer velocity profile downstream of a laminar separation bubble. For the case shown in Fig. 5.12, transition occurs in the separated laminar shear layer at x/c = 70%, with reattachment following at x/c = 83%; at the 90% chord position there is still a large amount of distortion in the central region of the turbulent boundary layer, and the wall similarity region has only just started to develop. In this particular boundary layer, it is unlikely that a fully developed velocity profile would be achieved before reaching the blade trailing edge.

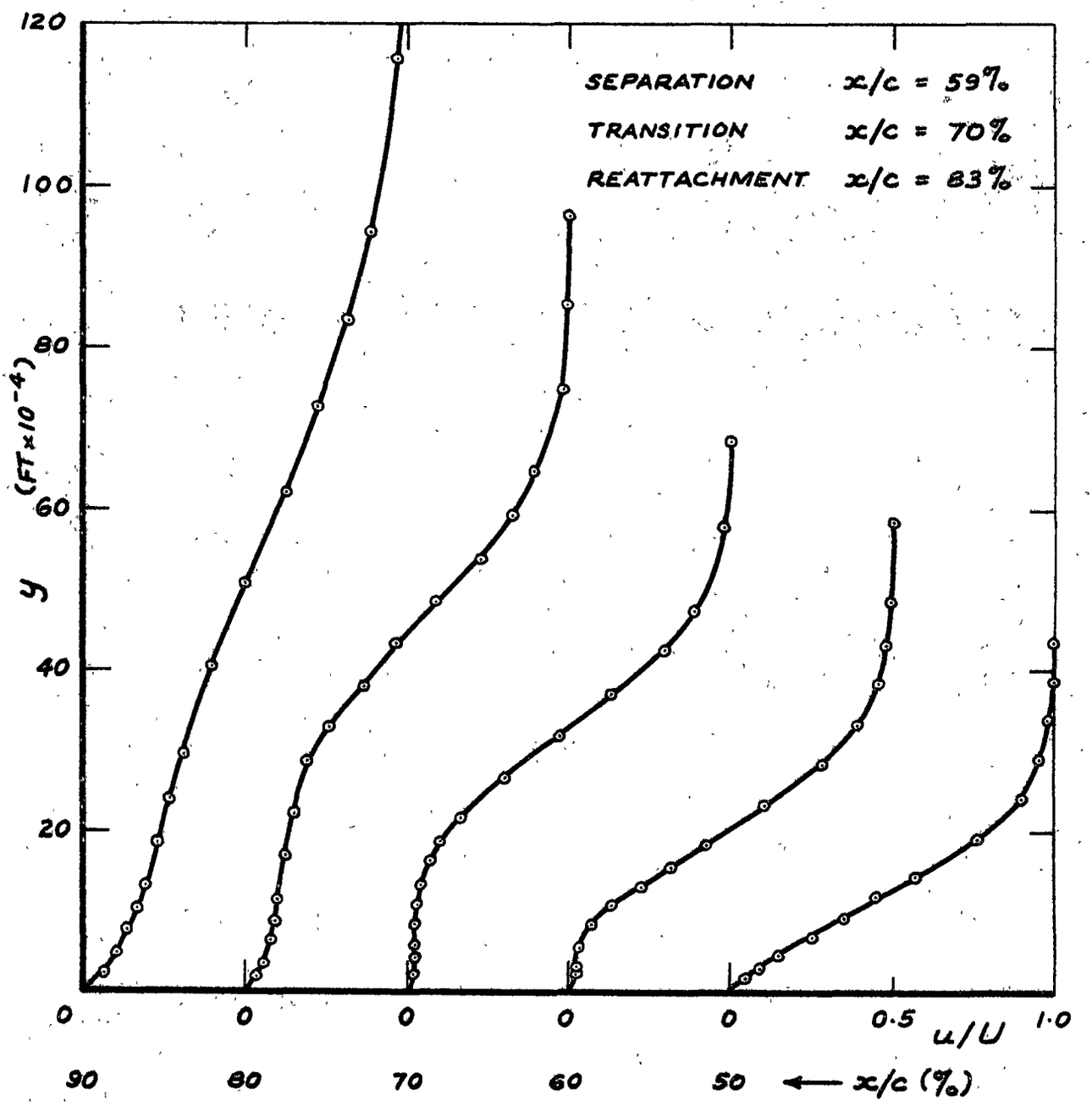


Fig. 5.12 Hot Wire Anemometer Measurements of Mean Velocity Profiles in a Separated Laminar Flow Region.
Stator Suction Surface, i = $-6.0^{\circ}$, $Re_c = 5.57 \times 10^4$

5.6.6.4 Effect of separation bubbles on the surface pressure distribution

The shape of the surface pressure distribution on blades in turbomachines or in two-dimensional cascades is often used, when no more detailed information is available, to infer the presence or absence of regions of flow separation from the blade surface. Following Fig. 5.8, it is usually supposed that a separation bubble causes the appearance of a "flat", or region of zero pressure gradient ($dp/dx = 0$). It is therefore of interest to examine the effects of separated laminar flow regions on the pressure distribution over a stator blade in the research compressor.

Fig. 5.13 shows the streamwise velocity distributions on the stator

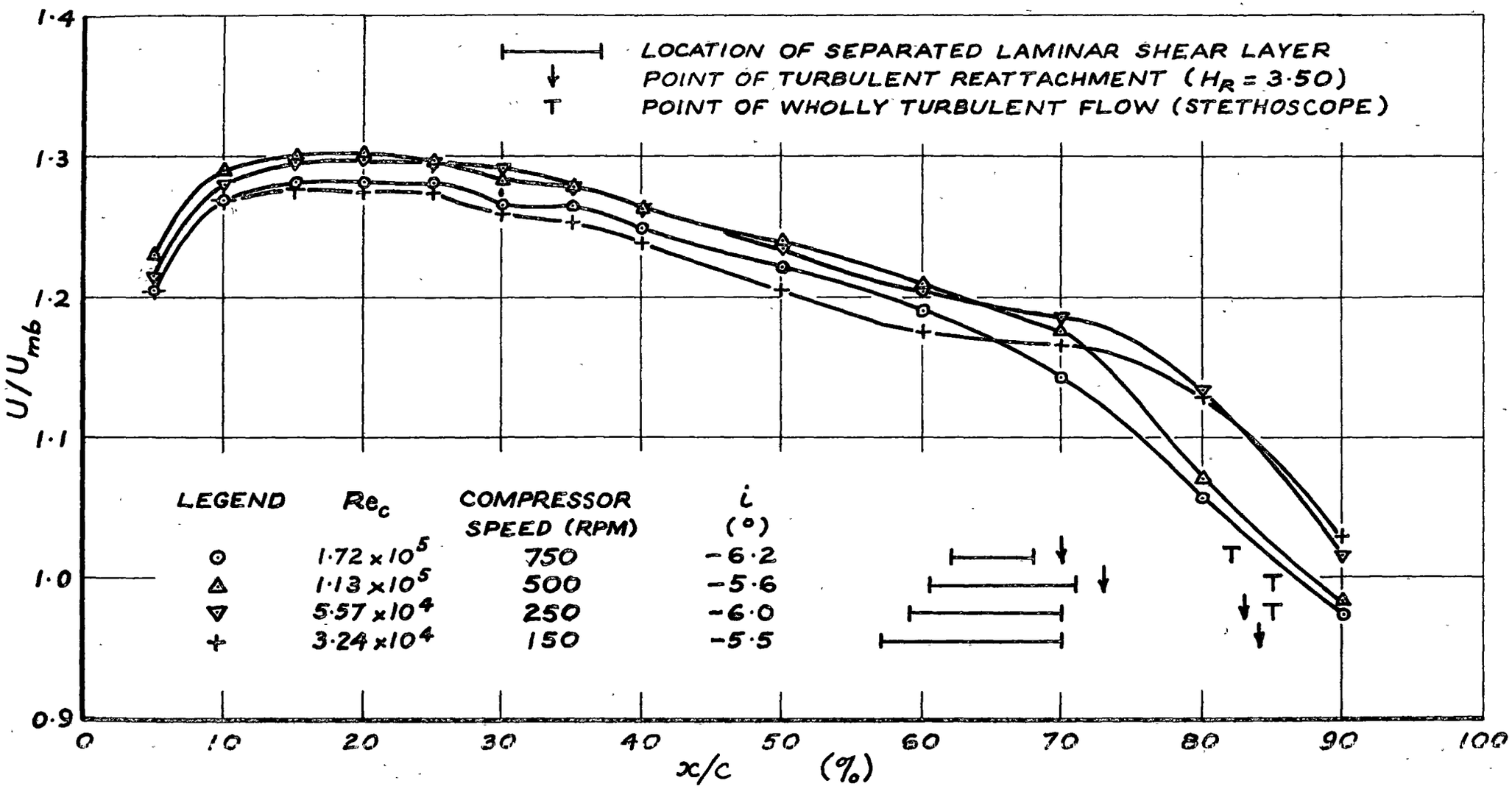


Fig. 5.13 Variation of Blade Surface Pressure Distribution with Reynolds Number
- Showing Effect of Developing Separated Laminar Flow Region
(Stator Suction Surface, Mid-Blade Height, 10 in. Throttle Opening)

suction surface at about $-6^{\circ}$ incidence for the four different compressor speeds investigated. There is a laminar separation bubble starting at about 60% chord which increases in length from 8 to 27% of chord as the compressor speed is decreased from 750 to 150 rpm, giving a corresponding reduction in $Re_c$ from $1.72 \times 10^5$ to $3.24 \times 10^4$. The resulting perturbations to the surface velocity distribution are confined mainly to the neighbourhood of the separation bubble, and there is little change in the shape of the velocity distribution near the leading edge of the blade as the speed is altered.

At $Re_c = 1.72 \times 10^5$, there is certainly no flat in the surface velocity distribution in the neighbourhood of the separation bubble; only a slight change in dU/dx is discernible near the transition point at the downstream end of the bubble where there is a discontinuity in the rate of growth of the boundary layer displacement thickness. As the blade Reynolds number is reduced, the length of the separation bubble gradually increases and the separated shear layer is able to move further from the blade surface, as indicated by the higher peak values of $H = \delta^*/\theta$ obtained from the hot wire measurements shown in Figs. 4.7 (a - d); this is accompanied by a gradual flattening of the velocity distribution in the neighbourhood of the bubble, but even at the lowest Reynolds number of $3.24 \times 10^4$ obtained at 150 rpm a small positive pressure gradient still appears to exist over the separated flow region.

To summarise, it seems probable that peak values of H = 5 or 6 are required before a true "flat" in the surface pressure distribution will be observed in the neighbourhood of a laminar separation bubble. With less well-developed separation, the streamwise pressure gradient over the forward part of a separation bubble should certainly be reduced, but would be unlikely to fall to zero. A separated flow region which is only just commencing to develop (say $H_{max} = 4$) would have such a minor effect on the surface pressure distribution that its presence might not be detected at all if the surface pressure tappings were widely spaced.

5.6.6.5 Length of wholly turbulent flow in the bubble

The position where the stethoscope observations indicate the flow on the stator blade to become wholly turbulent has been indicated in Fig. 5.13, together with the reattachment position obtained by applying Horton's (38) criterion of $H_R = 3.50$ (Eqn. 5.10 (b)). The distance between these points gives the length of wholly turbulent shear layer within the separation bubble.

At a compressor speed of 750 rpm, where the laminar separation bubbles on the stator suction surface at negative incidence are not very well developed, the point of wholly turbulent flow occurs well downstream of the separated flow region; in this case the separated shear layer is able to reattach while only intermittently turbulent. As the compressor speed is reduced, the value of H at the point of wholly turbulent flow gradually

increases until it eventually exceeds 3.50, indicating that transition has been completed before reattachment occurs. At a speed of 250 rpm transition occurs entirely within the separated shear layer in at least two cases ($i = -8.0^{\circ}$ and $-10.1^{\circ}$); here it seems that continuous turbulent mixing is required to enable the separated shear layer to reattach.

A very similar behaviour was observed by Gaster (34), who noted that the turbulent mixing region occupied an increasingly large proportion of a laminar separation bubble on a flat plate as the tunnel speed was reduced.

5.6.6.6 Bubble regime

In an attempt to resolve whether the separated flow regions on the compressor blades should be classified as long or short bubbles, trajectories of Gaster's parameter P against separation Reynolds number $Re_{\theta_s}$ were plotted for the bubbles formed on the stator suction surface at negative incidence; the results are shown in Fig. 5.14. Values of P were calculated by using the points of turbulent reattachment defined by Horton's criterion, Equation 5.10 (b).

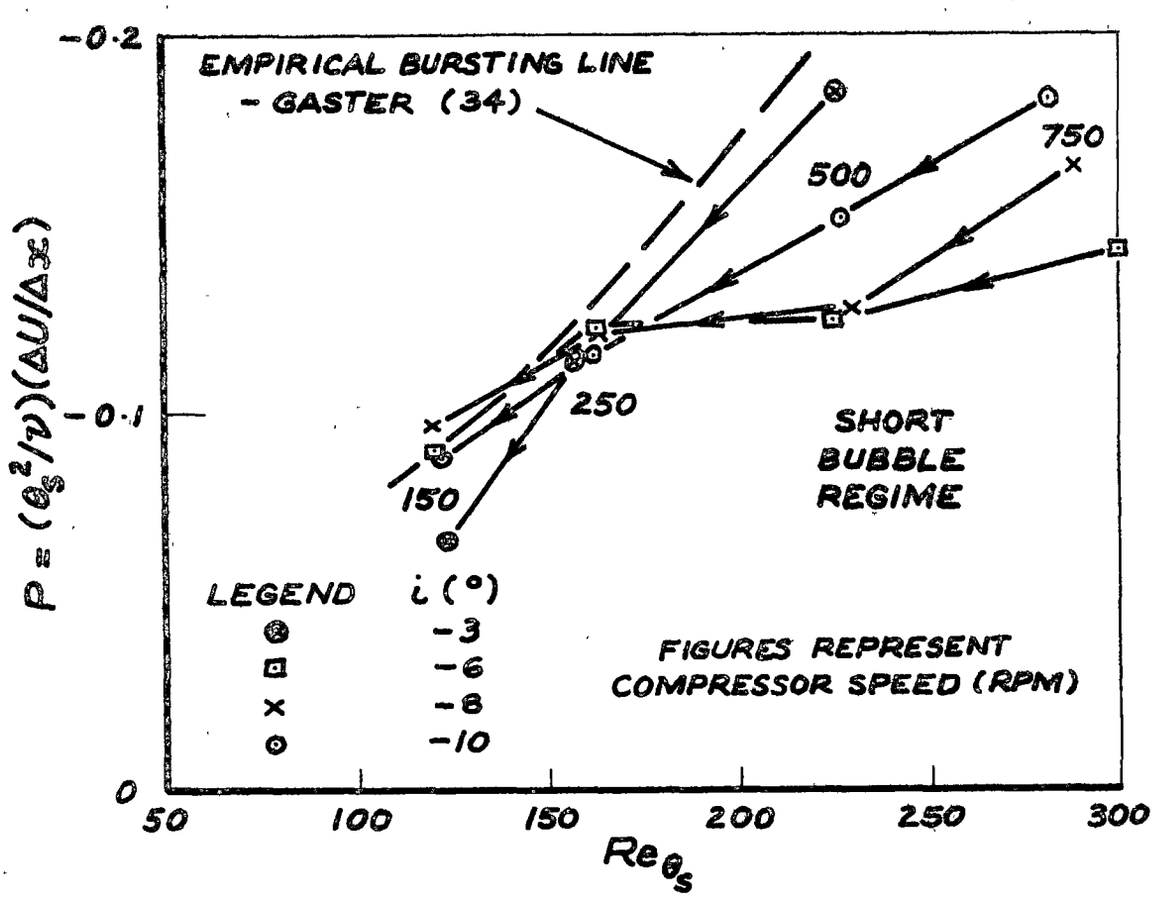


Fig. 5.14 Trajectories of $P \sim Re_{\theta_s}$ for Laminar Separation Bubbles on the Stator Suction Surface at Negative Incidence

At the highest compressor speed of 750 rpm, all the points in the $P \sim Re_{\theta_s}$ plane lie in the short bubble regime to the right of Gaster's empirical bursting line. As the compressor speed falls, the bubble

trajectories approach the bursting line, and appear to meet it when the speed is a little above 250 rpm; they then turn and follow the bursting line quite closely as the speed drops from 250 to 150 rpm. This behaviour is very similar to that observed by Gaster (34) in his Series II tests, and suggests that the bubbles occurring at 750 and 500 rpm are "short" bubbles, while those at 250 and 150 rpm should be classified as "long" bubbles.

It is seen from Fig. 5.13 that turbulent reattachment occurs within 2% of chord from the transition point in the short bubbles obtained at 750 and 500 rpm. With a fall in compressor speed to 250 rpm, the distance from transition to reattachment suddenly increases by about 10% of chord, but there is little further change in this distance as the speed is reduced to 150 rpm. The sudden change in reattachment behaviour between 500 and 250 rpm seems to confirm that bubble bursting occurs somewhere within this speed range.

Fig. 5.13 also shows that the transition point in the separated shear layer remains almost stationary as bursting of the separation bubble occurs. This is in agreement with the observation of Woodward (37), and reinforces the view that bubble bursting is related to the turbulent reattachment process rather than to the stability of the laminar shear layer.

Accepting that the bubbles formed at 250 and 150 rpm are in fact long bubbles, it is noteworthy that their non-dimensional lengths, $l/\delta_s^*$, are two or three orders of magnitude smaller than the values suggested by Owen and Klanfer (30). Another interesting feature is that the appearance of a long bubble on the rearward part of the stator suction surface does not cause the marked collapse in the suction peak which is observed when a long bubble is formed close to the leading edge of an isolated aerofoil (see Fig. 5.8). Although the non-dimensional velocity distributions shown in Fig. 5.13 differ significantly over the forward 60% of the stator suction surface, these variations are very largely explained by small changes in the axial velocity and blade incidence. (Note that the velocities in Fig. 5.13 are made non-dimensional with respect to the rotor velocity, $U_{mb}$, and that the flow coefficient, $V_a/U_{mb}$, changes slowly with compressor speed.) Thus in this particular case, the perturbation of the surface pressure distribution caused by the long bubble formation is mostly a displacement effect which is confined to the neighbourhood of the bubble.

The formation of a long bubble on the rearward part of an aerofoil must, of course, affect the pressure distribution near the leading edge to some extent, as the change in boundary layer thickness accompanying its appearance will shift the rear stagnation point and so alter the circulation around the aerofoil. However, it is suggested that such circulation changes will not be very large unless the location of the bubble does not permit the full pressure rise during reattachment to be achieved before the trailing edge is reached.

5.6.6.7 Effect of separation bubbles on blade losses

To give some idea of the effects of flow separation on the

profile drag of a compressor blade, the loss coefficient based on the measured boundary layer momentum thickness at 90% chord on the stator blade suction surface has been plotted against chord Reynolds number in Fig. 5.15. For the particular incidence chosen ($i \simeq -6^{\circ}$) the suction surface boundary layer probably contributes 50 - 60% of the total blade profile drag.

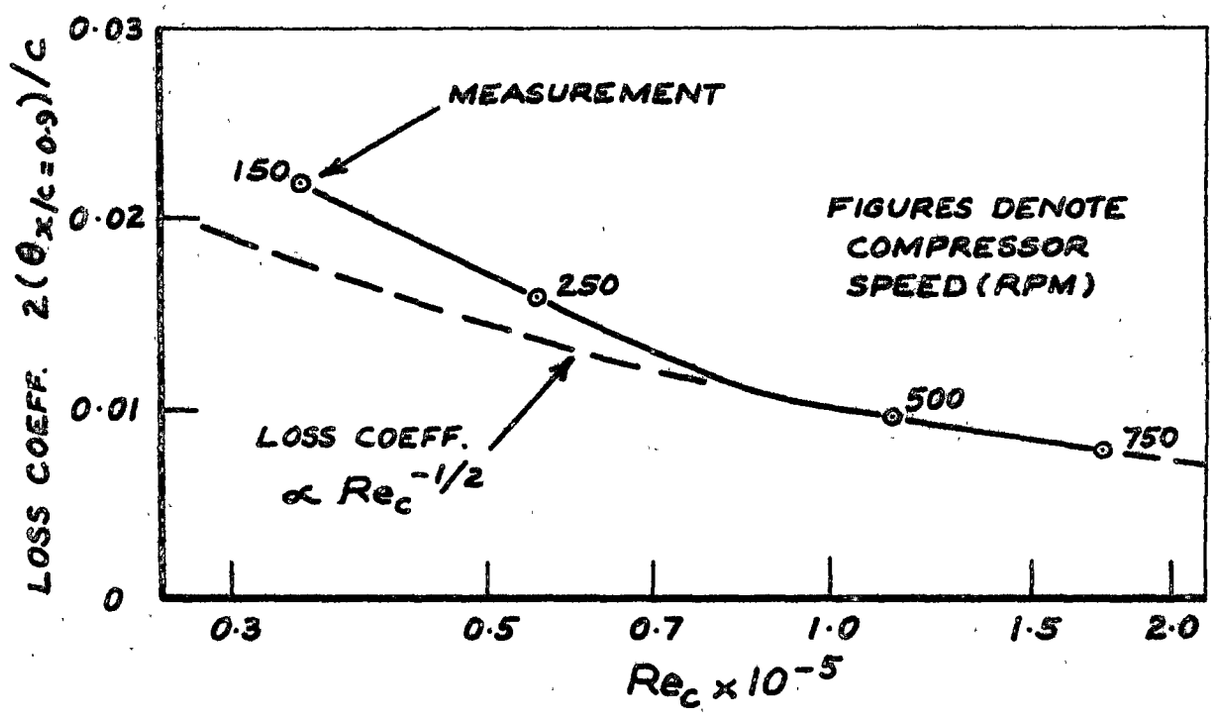


Fig. 5.15 Variation of Stator Blade Suction Surface Losses with Reynolds Number for $i \simeq -6^{\circ}$

For compressor speeds between 750 and 500 rpm, where the separation bubble occurs in the short regime, the loss coefficient is closely proportional to $Re_c^{-\frac{1}{2}}$, as would be expected with a predominantly laminar boundary layer growing in an essentially similar pressure distribution. As the compressor speed falls to 250 rpm and the bubble changes to the long regime, the loss coefficient commences to increase at a rate significantly greater than $Re_c^{-\frac{1}{2}}$, and this trend is continued down to the lowest compressor speed of 150 rpm.

The sudden change in rate of increase of blade losses with decrease in Reynolds number probably constitutes the upper limit of the so-called "critical region" of Reynolds number over which the profile drag of an aerofoil cascade rapidly increases. In this particular case, the critical drag rise commences not at the Reynolds number where separated laminar flow regions first appear in short bubble form, but rather at the somewhat lower Reynolds number where bubble bursting occurs.

5.6.6.8 Pressure rise over the turbulent part of the bubble

Horton's (38) model for calculating the pressure rise during reattachment of the turbulent shear layer assumes that the parameter $(\theta/U)(dU/dx)$ has a value of -0.0082 at the reattachment point. In order to see how adequately this model describes the flow behaviour on the compressor blades, the measured variation of $(\theta/U)(dU/dx)$ along the stator suction surface at about $-6^{\circ}$ incidence has been presented in Fig. 5.16; curves have been plotted for each of the four different compressor speeds investigated.

At the point of reattachment behind the short bubbles obtained at speeds of 750 and 500 rpm, $(\theta/U)(dU/dx)$ attains values of only -0.001 to -0.002, which are significantly smaller than the values suggested by Horton. The values observed on the compressor blades are not necessarily inconsistent with Horton's model, however, as the reattaching shear layer is only intermittently turbulent in these particular cases, and would therefore be expected to have a lower time mean value of the dissipation coefficient than a fully turbulent layer; according to Horton's theory, this should lead in turn to a smaller value of $(\theta/U)(dU/dx)$ at the reattachment point.

In the long separation bubbles obtained at 250 and 150 rpm, the flow is essentially fully turbulent at the point of reattachment for $i = -6^{\circ}$. Here $(\theta/U)(dU/dx)$ takes values in the range -0.009 to -0.010 which agrees reasonably well with the value of -0.0082 suggested by Horton. Very similar values of $(\theta/U)(dU/dx)$ are obtained behind long bubbles on the stator suction surface at other negative values of blade incidence. The agreement with Horton's model is within the range of experimental error, considering that dU/dx, which varies rapidly with x near reattachment, was determined from values of U measured at 10% intervals of chord. However, it is noteworthy that the values of $(\theta/U)(dU/dx)$ behind long bubbles on the compressor blades tend to lie around -0.010 on the average, and the long bubble data analysed by Horton shows a similar trend.

Provided that the shear layer is fully turbulent over the length, $l_2$, of the pressure recovery region at the rear of a separation bubble, the assumption of a linear surface velocity distribution during reattachment, together with a value of $(\theta/U)(dU/dx) = -0.0082$ at the reattachment point, leads to a unique relationship between the non-dimensional pressure rise over the bubble, $\sigma$, and the non-dimensional length $l_2/\theta_s$. This relation, which forms the basis of Horton's bubble bursting theory, is reproduced in Fig. 5.17, together with the measured values of pressure rise in separation bubbles on the stator blade suction surface. In calculating values of $l_2$ for the bubbles on the compressor blade, the pressure recovery was assumed to commence at the point of apparent turbulent reattachment obtained from the china clay tests, as this approximates the downstream limit of the dead air region in which the surface pressure remains nearly constant. (Inspection of the blade surface velocity distributions in Fig. 4.1 shows that at negative incidence there is usually a sudden increase in pressure gradient within 3 or 4% chord

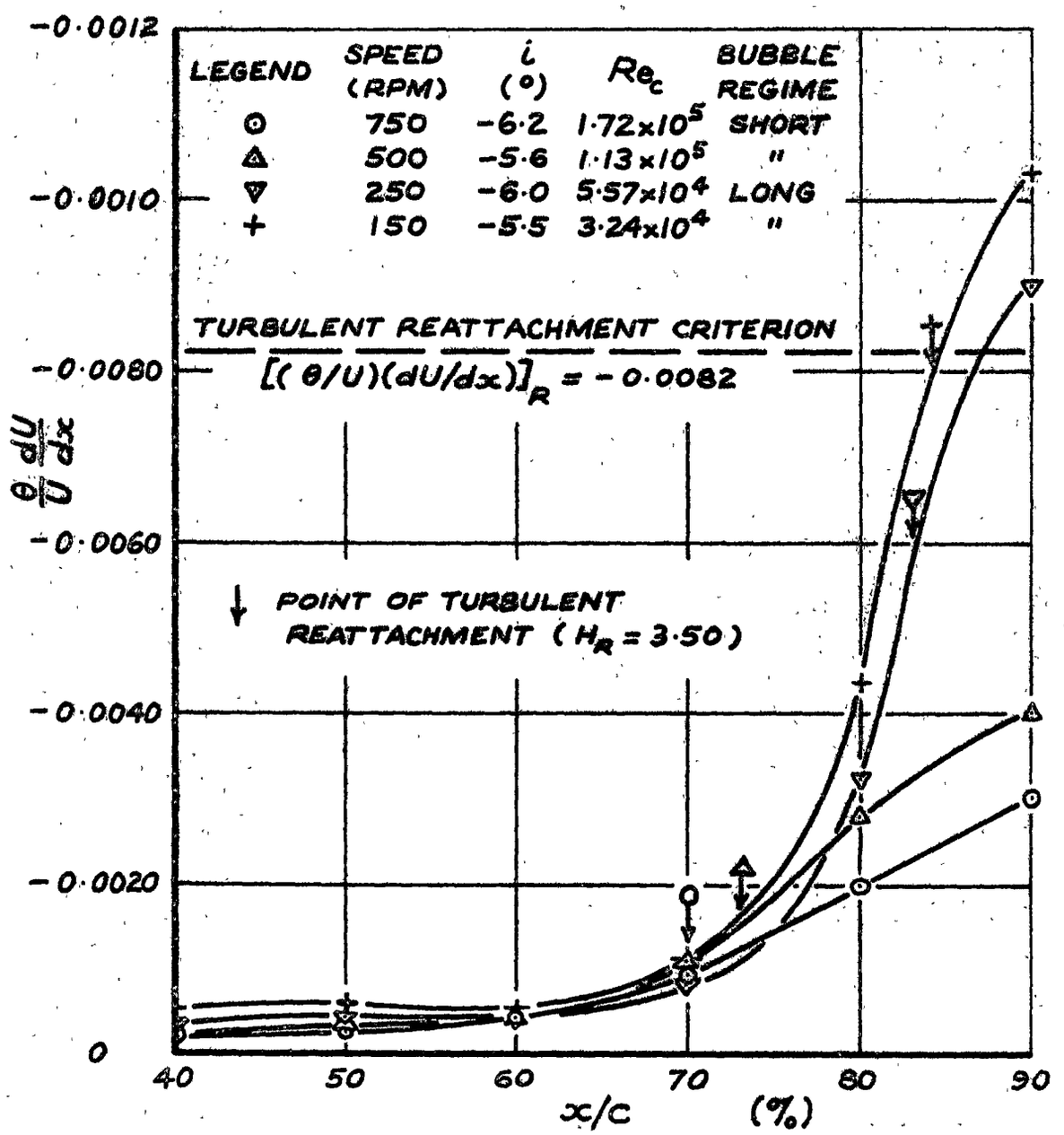


Fig. 5.16 Variation of Pressure Gradient Parameter (θ/U)(dU/dx) on Stator Blade Suction Surface at Mid-Blade Height

downstream of the china clay reattachment point.) The downstream end of the pressure recovery region was defined as the point where the measured value of H fell to 3.50.

It is seen from Fig. 5.17 that although the measurements show a similar trend to the theory, the streamwise distance required to achieve a given pressure rise on the compressor blade is at least double that predicted by Horton. This difference is considered significant in spite of the possible errors of at least 50% in determining $l_2$. The present observations do not completely invalidate Horton's theory, however, as the reattaching shear layers on the compressor blade are only intermittently turbulent, while the theoretical model assumes the flow to be fully turbulent. A reduction in

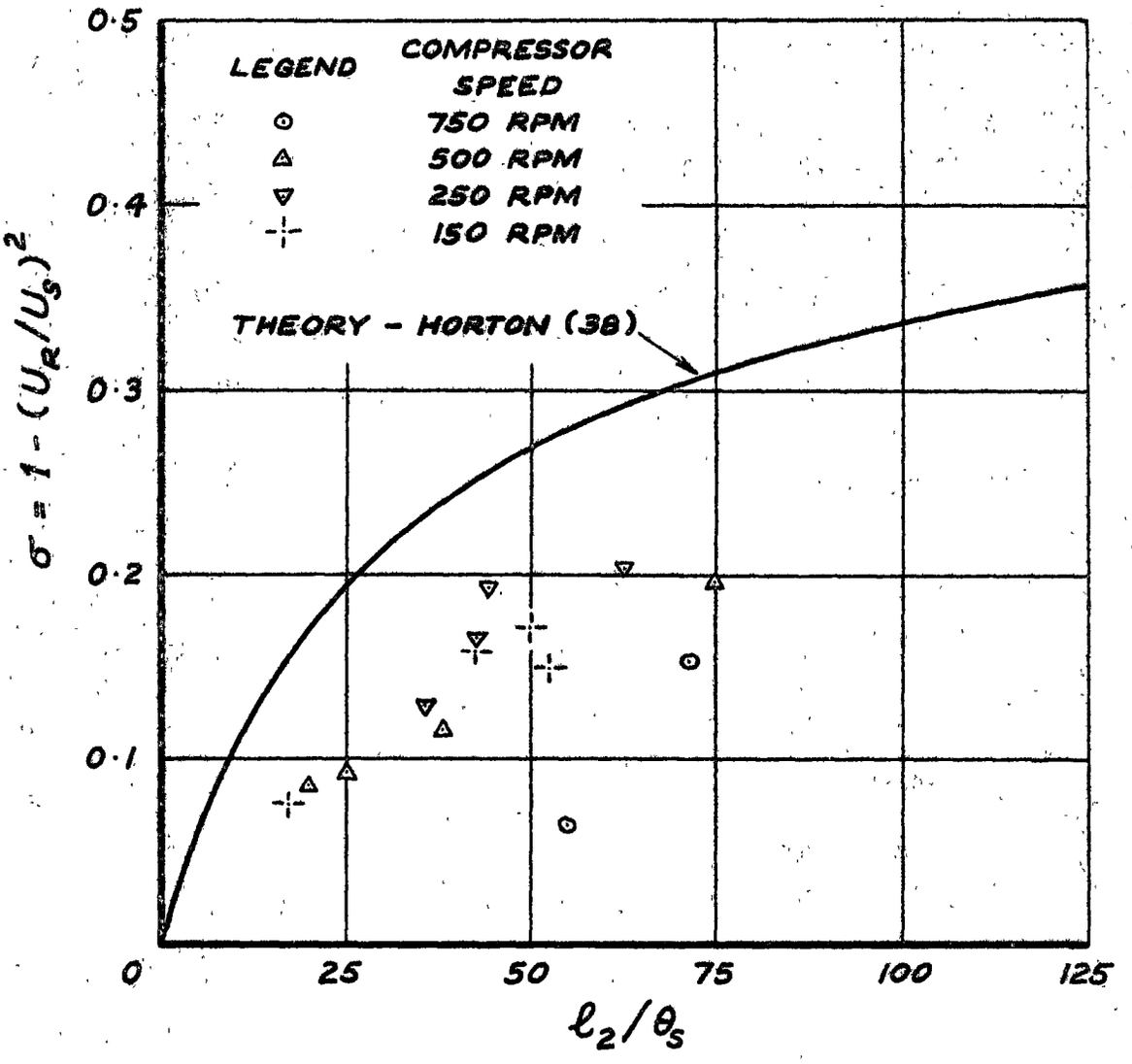


Fig. 5.17 Variation of Pressure Recovery Parameter with Length of Turbulent Flow in Separation Bubbles on Stator Blade Suction Surface

the mean rate of entrainment by the shear layer would be expected to increase the distance to reattachment, and there is, in fact, a notable tendency for the measured length of the pressure recovery region to be greater at the higher compressor speeds, where the intermittency of turbulence and the magnitude of $(\theta/U)(dU/dx)$ at the reattachment point are both much lower.

It is interesting to note that in the short separation bubbles obtained on the stator suction surface at compressor speeds of 750 and 500 rpm, the point of reattachment indicated by the china clay tests is, on the average, almost identical with the point at which turbulent flow is first observed with the stethoscope; this agrees fairly well with Horton's model of the flow in a short separation bubble (Fig. 5.10), which assumes that the length of the constant pressure region is approximately equal to the length of the separated laminar shear layer, and that pressure recovery commences at the transition point. In the long bubbles obtained at 250 and 150 rpm, however, the transition points consistently lie 4 - 5% of chord upstream of the china clay reattachment points, and the length of the

(approximately) constant pressure region is at least 50% greater than the length of the separated laminar shear layer; it is clearly invalid to assume that pressure recovery commences at the transition point in such cases, as this would lead to a serious underestimation of the total bubble length.

### 5.6.7 A New Model for Predicting Bubble Length

#### 5.6.7.1 Introduction

Although the measurements of the present investigation tend to support the theoretical aspects of Horton's (38) flow model for the laminar separation bubble, they indicate that the empirical correlations used by Horton are not sufficiently general to describe the bubble behaviour on the compressor blades. In particular, Equation 5.12 overestimates the length of the constant pressure region at low Reynolds numbers, and Equation 5.11 underestimates the length of the pressure recovery region when the reattaching shear layer is not fully turbulent. This section discusses the development of alternative empirical correlations which, it is believed, should overcome these difficulties to a large extent.

#### 5.6.7.2 Length of the constant pressure region

The length of the constant pressure region in a laminar separation bubble is basically dependent on the location of the transition point in the separated laminar shear layer. The transition point, in turn, is determined by the rate at which disturbances receive amplification in both the attached laminar boundary layer and the separated shear layer. Thus, if the surface pressure distribution upstream of the laminar separation point is arbitrary, the length of the constant pressure region cannot, in general, depend entirely on the local conditions at separation, as implied by Equation 5.12. It therefore appears physically more realistic to base a model of flow in the laminar separation bubble on some sort of transition correlation which takes due account of the history of flow upstream of the separation point; an estimate of the transition point is required in any case, to determine whether separation will occur at all.

The transition correlation shown in Fig. 6.19, which will be developed in detail in Chapter 6, expresses the instability length (i.e. the distance between the points of neutral stability and transition in the laminar shear layer) as a function of the mean values of momentum thickness, $\theta$, Reynolds number, $Re_\theta$, and shape factor, H, over this region. It successfully describes the transition behaviour in flows with both short and long separation bubbles on the compressor blades, and is also a reasonable fit to the data from Gaster's (33, 34) Series II measurements of separation bubbles generated on a flat plate. The values of instability length show an average deviation of some 10% from the mean curve given by Eqn. 6.19, so that if (as in Gaster's tests) the laminar separation point lies

roughly midway between the points of neutral stability and transition, the use of this correlation should predict the length of the separated laminar shear layer to within 20% in most cases; this should at least provide a good qualitative description of the flow, and may often lead to a quantitative description accurate enough for engineering purposes. It is not suggested that the transition correlation of Eqn. 6.19 should be applied to any flow case involving separation, as it was initially derived largely from boundary layer transition data, and might therefore be valid only in cases where there is a significant length of unstable laminar boundary layer upstream of the separation point; however, it is believed to be rather more widely applicable than Equation 5.12, which it replaces.

In a short separation bubble it should be sufficiently accurate to take the length of the constant pressure region equal to the length of the separated laminar shear layer, although this will normally prove to be a slight underestimate. This model cannot be applied in the case of a long bubble, however, as the constant pressure region is then significantly longer than the separated laminar shear layer (see Section 5.6.6.8).

5.6.7.3 Length of the pressure recovery region

It appears that Horton's model of the reattachment process should provide an adequate estimate of the distance between the end of the constant pressure region and the reattachment point when the separation bubble is sufficiently well-developed for the shear layer to be fully turbulent over most of the pressure recovery region. If the shear layer is only intermittently turbulent at the reattachment point, however, the distance to reattachment will be seriously underestimated; in this case some modification of Horton's method is required to take into account the lower dissipation coefficient of the partly turbulent flow, which leads to a smaller value of $(\theta/U)(dU/dx)$ at reattachment. It is suggested that even a crude model, such as the assumption of a linear variation of eddy viscosity over the length of the transition region, would lead to greatly improved agreement with experiment.

## 5.7 Summary

This chapter has established that regions of laminar flow were undoubtedly present on the blades of the research compressor. The measured development of the laminar boundary layer on a stator blade has been shown to agree remarkably well with the predictions of Thwaites's (10) method, based on the measured surface pressure distribution. Thwaites's method was also found to give a reasonable estimate of the point of laminar separation on the stator blade, but this could possibly have been the fortuitous result of the blade surface velocity distribution being roughly linear near separation in most cases.

The appearance of separated laminar flow regions on the compressor blades does not produce the local flattening of the surface pressure distribution usually considered to be characteristic of this flow regime until the separation bubbles become quite well developed. The measured lengths of the separated laminar shear layer in bubbles on the compressor blades do not fit correlations developed by other workers (30, 38) to describe the bubble behaviour on isolated aerofoils operating at higher Reynolds numbers. However, the use of a transition correlation developed by this author has been shown to provide an alternative means of predicting the length of separated laminar flow which is consistent with both the present measurements and the data of other workers.

Gaster's (34) bursting criterion indicates that the separation bubbles on the compressor blades change from the short to the long regime at about the middle of the Reynolds number range investigated. Bursting appears to be caused by a failure of the turbulent shear layer to reattach, rather than a sudden change in the stability of the laminar shear layer. The present observations have suggested that the "critical" Reynolds number at which the profile drag of axial-flow compressor blades increases markedly is probably associated with the bursting of short separation bubbles, rather than the first appearance of separated laminar flow.

The measurements on the stator blade support the basic assumptions of Horton's (38) theoretical model of the turbulent reattachment process in a laminar separation bubble. But the pressure rise during reattachment in bubbles on the compressor blade is seriously over-estimated by Horton's analysis because the reattaching shear layer is only intermittently turbulent in most cases.

# CHAPTER 6

# BOUNDARY LAYER TRANSITION BEHAVIOUR

## 6.1 Introduction

This chapter commences by reviewing previous work on the physical nature of the boundary layer transition process. The method of locating the transition region on the compressor blades is then explained, and the observations of velocity fluctuations during transition on the stator suction surface are discussed. Several existing techniques for predicting transition are examined, and a new empirical correlation is proposed which describes both the present results and a wide range of other transition data. Next, the effects of surface pressure distribution and free stream turbulence on transition are evaluated; particular reference is made to flat plate transition data and to performance comparisons of similar blade sections tested in axial-flow compressors and in two-dimensional cascades. The final section deals with the problem of predicting boundary layer development through the transition region.

## 6.2 The Physical Nature of the Transition Process

### 6.2.1 General Discussion

Although it is not yet possible to model mathematically the complete process of transition from laminar to turbulent flow, the experimental investigations of a large number of workers have given considerable insight into the basic physical features involved. In a comprehensive survey article reviewing both theoretical and experimental work on hydrodynamic stability, Stuart (39) suggests that the following sequence of events occurs as an initially stable laminar boundary layer on a flat plate becomes unstable and finally goes turbulent:

(i) a region of instability to small wavy disturbances, sometimes called Tollmien-Schlichting waves. Both two- and three-dimensional instability waves may occur;

(ii) a region of three-dimensional wave amplification in which minor irregularities in the flow can cause the wave growth rate to vary with spanwise position, thus leading an initially two-dimensional wave into a three-dimensional form. In many cases the flow is nearly periodic in the spanwise direction;

(iii) a region of peak-valley development with a streamwise vortex system. Here, the three-dimensional wave develops a much more pronounced structure as it progresses downstream, and an associated streamwise vortex system is produced. The longitudinal velocity fluctuations develop more rapidly at spanwise locations in the vicinity of the maximum wave distortions, which are therefore called "peaks"; neighbouring spanwise positions where the velocity fluctuations develop

more slowly are called "valleys". Where the three-dimensional wave develops naturally due to spanwise irregularities of the stream, the velocity component induced by the streamwise vortex system may be either towards or away from the wall at a peak. But if the three-dimensionality is induced artificially (e.g. by a vibrating ribbon), only the streamwise vortex pattern giving outflow at a peak is possible; Fig. 6.1 shows the induced velocities in this type of flow;

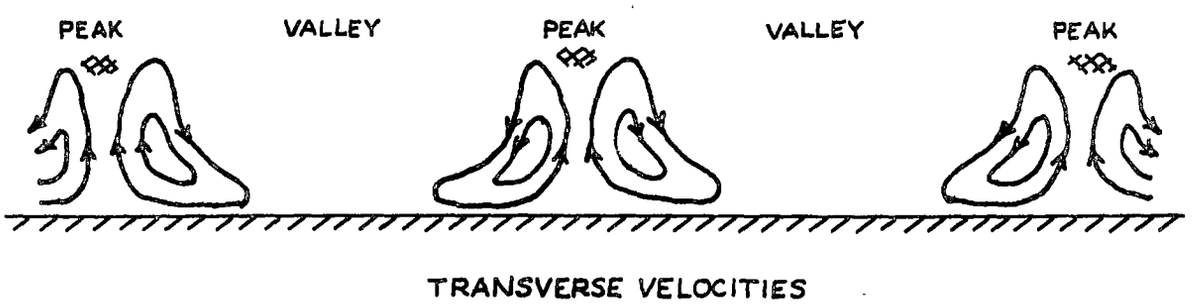


Fig. 6.1 Induced Velocities in a Streamwise Vortex System Giving Outflow at a Peak (Type A Disturbance)

(iv) a region of vorticity concentration and shear-layer development. With increase in distance downstream, the instantaneous streamwise velocity profile develops a region of large shear in the outer part of the boundary layer at spanwise stations corresponding to a peak; these regions have been indicated by hatching in Fig. 6.1. The form of the instantaneous velocity profile, which appears and disappears once each cycle of the primary wave, is shown in Fig. 6.2; as this profile has an associated point of inflexion (at which the vorticity has a maximum), it is expected to be very unstable. A weaker, but definite shear is also developed in the mean flow;

(v) a region of breakdown. When the instantaneous velocity profile produces a sufficiently strong shear in the outer part of the boundary layer, which will occur at a sufficiently large distance downstream, a velocity fluctuation at a frequency much higher than that of the basic wave suddenly appears in the vicinity of both the high shear region and the streamwise vortices. This phenomenon is called breakdown;

(vi) a region of turbulent spot development. Following breakdown, the high frequency fluctuations (which move downstream at a speed greater than the wave speed of the primary wave) spread spanwise and towards the wall to form "turbulent spots". At some greater distance downstream, the turbulent spots agglomerate to produce wholly turbulent flow.

(Knapp and Roache (42) include the additional region:

(vii) a laminar region following breakdown. During natural transition a

short calming period of laminar flow is usually observed after a turbulent spot has passed. This laminar region may be terminated by the appearance of either laminar instability waves or further turbulent spots.)

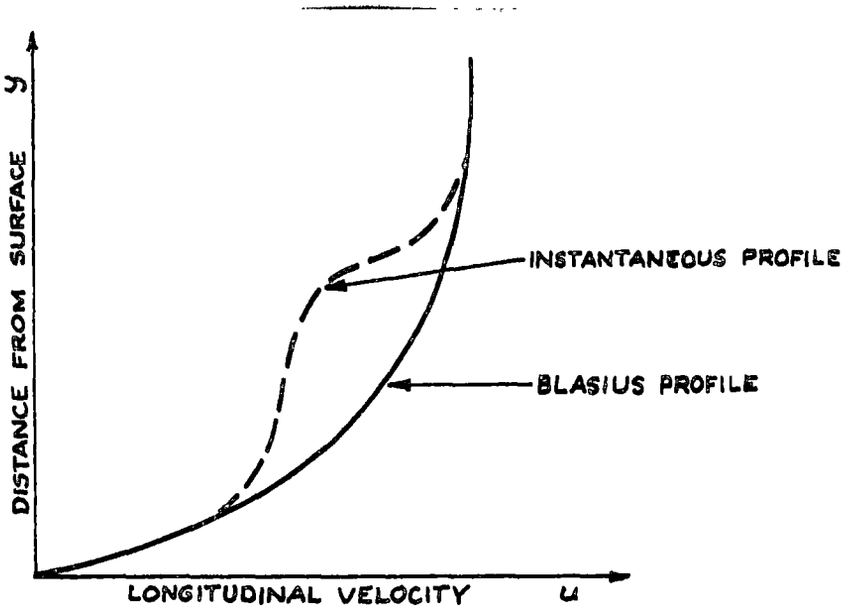


Fig. 6.2 Mean and Instantaneous (Inflexional) Velocity Profiles near a Peak for Transition in Zero Pressure Gradient (Type A Disturbance)

The measured behaviour of the primary (Tollmien-Schlichting) wave oscillations has been found to follow very closely the predictions of linearised stability theory as regards the wave numbers, frequencies, and growth rates, and the distribution of the velocity fluctuation amplitude across the boundary layer (see, for example, Schubauer and Skramstad (40)); this work is by now well known, and will not be reviewed in detail. The following discussion will concentrate on some more recent studies of the mechanics of breakdown and turbulent spot development, which will be found useful in interpreting the transition behaviour observed in the present investigation.

### 6.2.2 Detailed Nature of the Breakdown Process

#### 6.2.2.1 Thomson's model of breakdown

Thomson (41) has discussed the development of the streamwise vortex system in the unstable laminar boundary layer, and has suggested that the final breakdown phenomenon (region (v) as defined above) could be due to streamwise vortex bursting. Thomson envisages two possible forms of three-dimensional disturbance called types A and B, as shown below in Fig. 6.3. In the type A disturbance, a local acceleration of the flow perturbs the

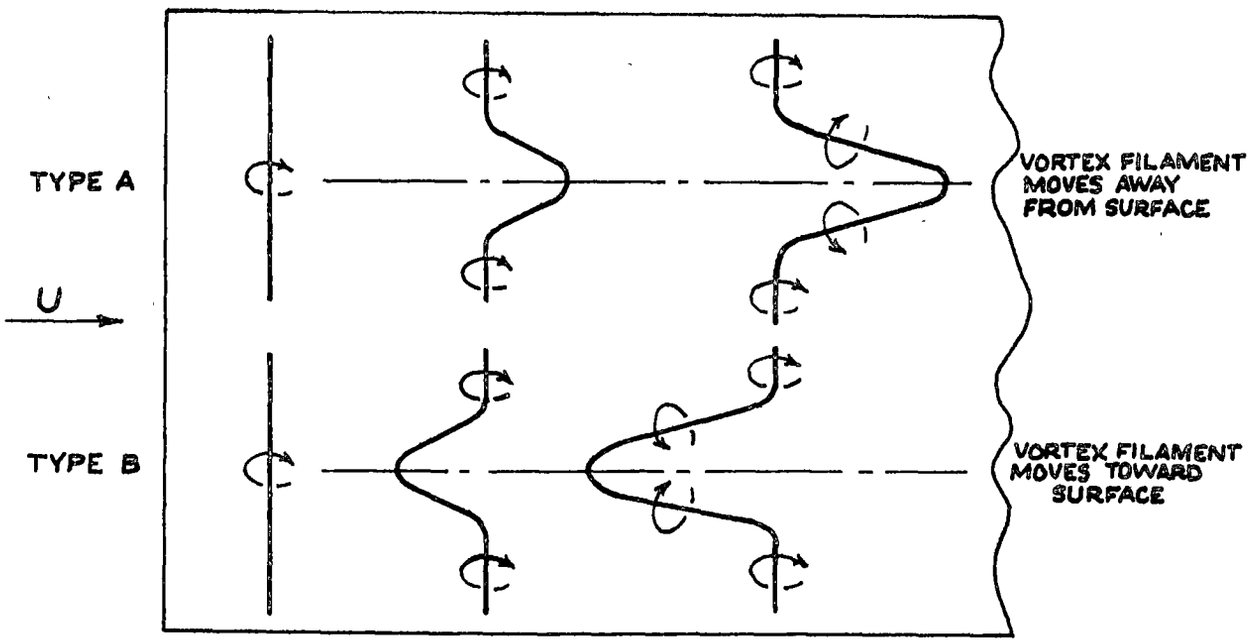


Fig. 6.3 Distortion of Vortex Filament by Two Types of Disturbance - after Thomson (41)

spanwise vortex lines in the downstream direction; this generates streamwise components of vorticity with an associated transverse velocity field as shown in Fig. 6.1, which convects the vortex filaments away from the surface into the faster flowing fluid. The resulting acceleration of these filaments causes an increasing amount of looping of the vortex line, until it finally appears as two streamwise vortex lines joined by a small spanwise section. Large velocity fluctuations are likely to occur in the neighbourhood of the streamwise vortices, due to the rolling up of bundles of vortex filaments. For a type B disturbance, a local retardation of the flow produces vortex loops which are stretched in the upstream direction as they are convected towards the surface; in this case the induced velocities are opposite to those shown in Fig. 6.1.

The spanwise vortex filaments are concentrated in the critical layer, where, according to linearised stability theory, the amplification rate is a maximum. On being convected away from this layer by the three-dimensional effects, their rate of amplification is reduced, so that a vorticity strength gradient exists along the streamwise legs of the vortex loops. In a type A disturbance, the vortex filaments at the downstream end of the vortex loop have originated further upstream, and so have undergone less amplification, than filaments near the upstream end of the loop; in this case there is therefore a weakening of vortex strength along the vortex loop in the streamwise direction. For a type B disturbance the behaviour is opposite to this, and the streamwise vortices have their greatest strength at their downstream extremities.

The bursting of a streamwise vortex has been shown to depend on at least two factors, namely vortex stretching and vortex strength gradient. Evidently bursting is encouraged by vortex compression and decreasing vortex strength in the streamwise direction, whilst it is inhibited by vortex stretching and increasing vortex strength in the streamwise direction. In the case of a type A disturbance, the vortex strength gradient encourages bursting and the vortex stretching inhibits it. However, Thomson concluded that the amplification of the Tollmien-Schlichting waves could be sufficiently large for the vortex strength gradient to overcome the vortex stretching effects and so cause a vortex burst to occur. For a type B disturbance, he was unable to predict from the available information whether or not vortex bursting would occur.

The effects of streamwise pressure gradient on the breakdown process are not discussed by Thomson. However, it would appear that an adverse pressure gradient should encourage vortex bursting in a type A disturbance because of the smaller amount of vortex stretching which would occur; this results from the higher velocity in the critical layer, and from the deceleration of flow in the streamwise direction in this case. On the other hand, a favourable pressure gradient should delay bursting of a type A disturbance by causing increased vortex stretching. The predictions of Thomson's vortex bursting model of breakdown are therefore qualitatively consistent with the observed behaviour of transition in a pressure gradient (see Section 6.7.1).

#### 6.2.2.2 Experimental observations of breakdown

##### (a) Breakdown in steady flow

Investigations by Knapp and Roache (42) of natural transition on ogive-nosed cylinders aligned parallel to the flow showed that the waves generated by the laminar instability process always broke down in sets. The breakdown of a wave set was followed by a short calming period of stable laminar flow (region (vii)), after which the instability waves reappeared and the breakdown process was repeated; this recurring cycle of breakdown implied that the various instability regions were not fixed on the body during natural transition. In zero pressure gradient, about 90% of the sets of vortex loops (or "trusses") from which breakdown occurred were arranged in a staggered (or "thatched") pattern, as shown in Fig. 6.4(a); but in a test where an adverse pressure gradient was applied, 40% of the sets became arrayed in streamwise rows, as shown in Fig. 6.4(b), while 45% stayed in the thatched pattern and the remaining sets were mixed.

Knapp and Roache found that although each set of two-dimensional waves in region (i) formed at a single frequency, successive sets observed during natural transition did not form at the same single frequency; the rate at which the breakdown cycle recurred was also rather irregular. This explains

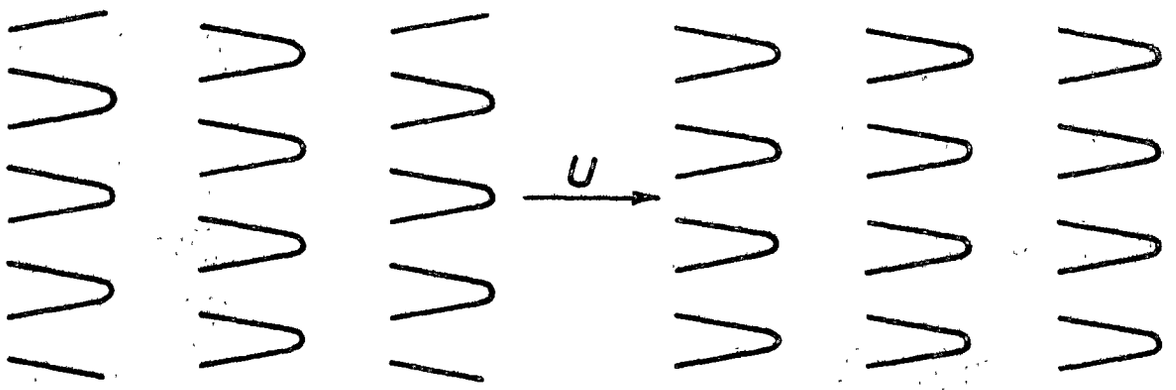


(a) Thatched pattern (b) Streamwise rows

Fig. 6.4 Possible Arrangements of Vortex Loops Prior to Breakdown - from Knapp and Roache (42)

why the picture of natural transition over a period of time is one of breakdown occurring at random positions in both the spanwise and streamwise directions, despite the considerable amount of order which exists at any particular instant.

The transition process becomes appreciably more regular in the presence of periodic disturbances in the external flow. Knapp and Roache observed that the introduction of sound at a frequency close to that of the natural instability waves caused all the transition regions to be more clearly visible and to move upstream. The calming periods disappeared under these conditions, implying that the various transition regions had assumed a fixed streamwise position on the body; furthermore, the frequency of all the wave regions (i) - (v) became locked into the sound frequency, and the waves broke down to turbulence individually rather than in sets. But when sound was introduced at a low frequency (near the frequency at which the breakdown cycle recurred in natural transition), the calming periods became controlled and were locked into the acoustic frequency rather than eliminated.

(b) Breakdown in oscillating flow

The transition behaviour on a flat plate in a non-steady boundary layer flow induced by sinusoidal oscillations in the free-stream velocity has been examined experimentally by Miller and Fejer (43) and Obremski and Fejer (44). These workers found that the manner in which transition occurred depended on the value of the "non-steady Reynolds number", $(Re)_{NS} = L\Delta U/2\pi\nu$, in which the characteristic length, $L = U/\omega$, is the distance travelled by a fluid particle in the free stream during one cycle of the imposed oscillation (frequency $\omega$ c/s), and the characteristic velocity, $\Delta U$, is the amplitude of the oscillation.

When $(Re)_{NS}$ exceeded a certain critical value (about 26,000 for zero pressure gradient), transition began with turbulent bursts* appearing periodically at the frequency of the free stream oscillation, as suggested by the theoretical analysis of Greenspan and Benney (45). In this case, the transition Reynolds number depended only on the amplitude of the free stream oscillations, to a first order, and not on their frequency, a result which confirmed the earlier prediction of Liepmann (46). Breakdown to turbulence was preceded in space and time by a packet of disturbance waves having the appearance of a Tollmien-Schlichting instability. For values of the frequency parameter $x\omega/U$ ( $\omega$ here is in rad/sec) between 0.6 and 1.3, the disturbance waves appeared first in the trough of the boundary layer velocity trace, as shown in Fig. 6.5(a); these instability waves subsequently increased in amplitude and moved into the accelerating part of the velocity trace, as shown in Fig. 6.5(b). (See also Fig. 6.7)

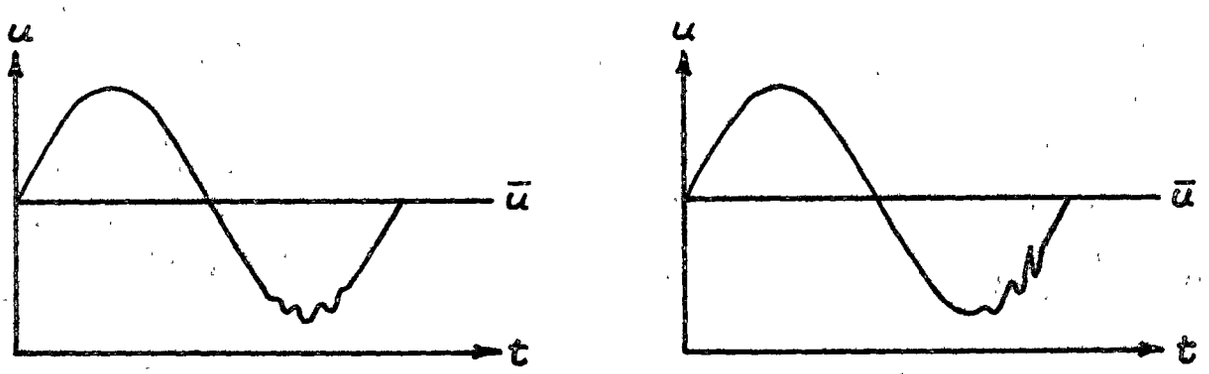


(a) Initial appearance

(b) Subsequent development at higher $Re_\delta$

Fig. 6.5 Schematic Diagram of Wave Packet Development during Transition in Oscillating Flow

In oscillating flow with $(Re)_{NS}$ less than the critical value described above, transition was still preceded by the appearance of wave packets in the trough of the velocity trace, but the transition Reynolds number became independent of both the amplitude and frequency of the oscillation in the range tested. The turbulent bursts then lacked the periodicity of those in the higher $(Re)_{NS}$ range, although the upper portions of the waveform closer to the crest were preferred for turbulent outbreak and development, as if tending to occur at the higher local Reynolds numbers; because of this

---

* In Ref. 44 the term "turbulent burst" refers to the duration in time of the turbulence at a fixed value of x. This is directly measurable from an oscilloscope trace.

preference, the turbulent bursts could not be characterised as occurring randomly in time and so were called "aperiodic" by Obremski and Fejer.

### 6.2.3 Detailed Nature of Turbulent Spot Development

#### 6.2.3.1 Development in steady flow

The tendency of the instability waves to break down in sets during natural transition in steady flow results in the periodic formation of sets of turbulent spots. Within an individual set, the turbulent spots are arranged in a similar manner to the vortex loops which precede transition (see Figs. 6.4 (a, b)); thus the streamwise spacing of the spots is largely determined by the frequency and velocity of propagation of the primary (two-dimensional) instability wave from region (i), while their spanwise spacing is equal to the wavelength of the secondary (three-dimensional) instability wave which appears in region (ii). The spacing of successive sets depends on the frequency at which the breakdown cycle recurs.

The agglomeration of turbulent spots within the individual sets leads initially to the formation of larger, but still separate, turbulent flow patches; the latter turbulent flow regions subsequently merge with similar patches developing from the breakdown of neighbouring wave sets to produce the final continuously turbulent flow state. In general, therefore, the intermittency of turbulence is governed by both the frequency of the primary wave and the rate at which the breakdown cycle recurs; but in cases where the primary wave frequency is much higher than that of the breakdown cycle, the agglomeration of turbulent spots within an individual set could effectively be treated as instantaneous.

The development of the individual three-dimensional turbulent spots that occur during natural transition in steady flow has been investigated by several workers, notably Emmons (47) and Schubauer and Klebanoff (48). The latter study indicated that an isolated turbulent spot was roughly wedge-shaped in plan, with the vertex pointing downstream as shown in Fig. 6.6. (This shape results from the turbulence initally appearing along the streamwise legs of the vortex loops.) It was found that the leading edge of the spot moved almost as fast as the free stream (0.88U), while the trailing edge moved at half the free stream velocity (0.50U); as the spot travelled downstream, it spread in the transverse direction at an angle of about $11^{\circ}$ to the longitudinal direction.

#### 6.2.3.2 Development in oscillating flow

During transition in an oscillating flow, the time-space distribution of turbulent spots becomes quite regular, provided that $(Re)_{NS}$ exceeds its critical value (see Section 6.2.2.2). This is due to the time distribution of shear which leads to breakdown being rigorously influenced by the oscillating component of the free stream velocity. If

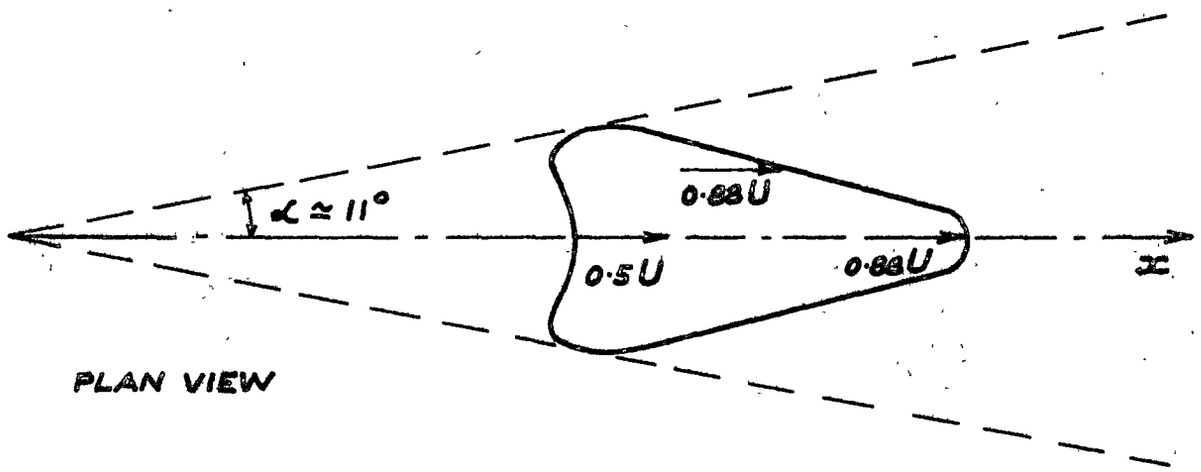


Fig. 6.6 Development of an Isolated Turbulent Spot
- after Schubauer and Klebanoff (48)

the imposed oscillations are two-dimensional, the longitudinal position of a turbulent spot at any particular instant does not vary with spanwise position, i.e. the turbulent spots essentially appear as two-dimensional ribbons and the random spanwise variation of the intermittency factor observed in steady flow transition is therefore absent.

Fig. 6.7 shows a typical time-space distribution of events during periodic transition on a flat plate in zero pressure gradient, as measured by Obremski and Fejer (44). Points on a horizontal line in this figure indicate conditions along the plate at a given instant, while points on a vertical line show the changes with time at a fixed value of streamwise position, x. $\tau^*$ represents the non-dimensional time (with respect to the period of the imposed oscillation) following the occurrence of a velocity minimum (or "trough") in the free stream.

Obremski and Fejer classified the development of turbulent spots during periodic transition into the following stages, which can all be seen from Fig. 6.7:

(a) the initial appearance of a turbulent spot from a point within the disturbance wave packet at a time slightly later than the occurrence of the minimum in the free stream velocity;

(b) a "creative mode" of development, during which large amplitude instability waves were still present at the spot boundary and the growth rate of the turbulent spot varied with time. This occurred immediately after the formation of a turbulent spot, and was characterised by a rapid spreading of the spot boundary in both the upstream and downstream directions. (Obremski and Morkovin (49) later suggested that the upstream spreading, represented by the section A - B of the turbulent spot boundary in Fig. 6.7, could have been due to the breakdown process moving sequentially along an incoming train of instability waves after the initial breakdown had occurred near the more highly

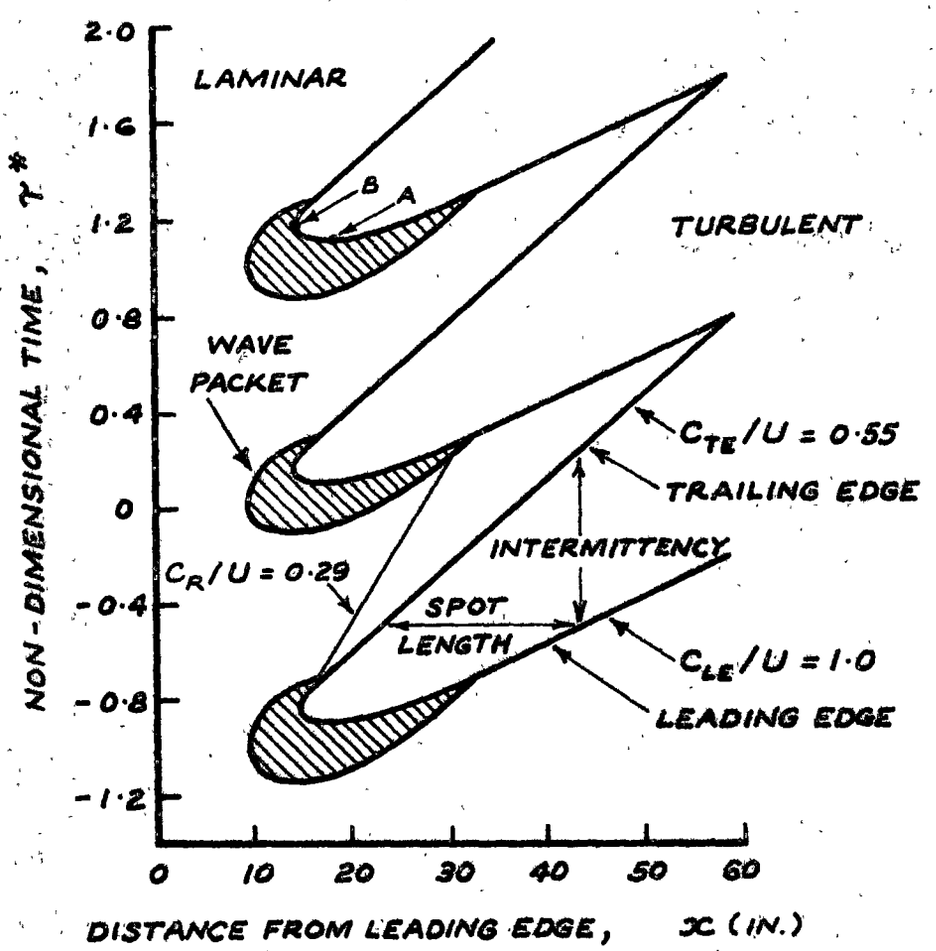


Fig. 6.7 Time-Space Distribution of Turbulent Spots during Periodic Transition in Zero Pressure Gradient. Run 15 from Obremski and Fejer (44)

amplified downstream end of the train.);

(c) a "convective mode" of development, during which laminar instability waves were absent from the spot boundary. Here, the growth rate of the turbulent spot became constant due to its leading and trailing edges moving downstream at constant, but different, velocities. For the zero pressure gradient case, Obremski and Fejer measured a leading edge velocity of 0.88U (with a standard deviation of 0.12U) and a trailing edge velocity of 0.58U (with a standard deviation of 0.06U); these agreed well with the corresponding values for a three-dimensional turbulent spot in steady-flow transition as measured by Schubauer and Klebanoff (see Fig. 6.6);

(d) a region of continuously turbulent flow formed by the merging of turbulent spots created during successive oscillations of the free stream.

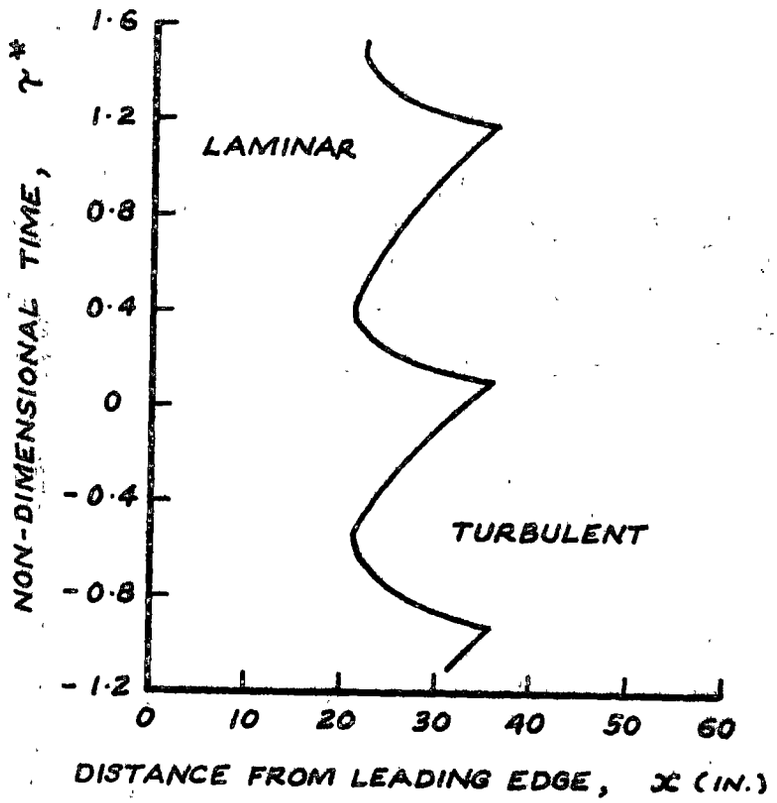


Fig. 6.8 Time-Space Distribution of Turbulent Spots during Periodic Transition in an Adverse Pressure Gradient. Run D-6 from Obremski and Fejer (44)

During periodic transition in an adverse pressure gradient, Obremski and Fejer found that a considerably larger proportion of the turbulent spot development occurred in the creative mode, as indicated by the greater curvature of the turbulent spot boundary in Fig. 6.8; this shortened the laminar tongues in the $x - \tau^*$ plane, and so reduced the length of the transition region. But the relative proportions of the creative and convective mode of development evidently depended on the properties of the free stream oscillation as well, and some cases were still obtained in which the convective mode predominated in spite of the adverse pressure gradient in the mean flow.

### 6.2.4 Calming Period Following Breakdown

The laminar calming period following the appearance of a turbulent spot has been reported by a number of workers (e.g. Refs. 40, 42, 44, 47, 48, 50).

Schubauer and Klebanoff (48) suggested that this calming resulted from the difference between the trailing edge velocity of the turbulent spot (0.50U) and the propagation velocity, $C_R$, of the disturbance waves following it (measured to be 0.23 - 0.29U in their experiments). Brown (50) proposed an alternative model which envisaged the initial breakdown of the three-dimensional instability waves setting up a local favourable pressure gradient

which delayed amplification of oncoming waves; after a turbulent spot had moved downstream, this favourable pressure gradient was expected to diminish and allow wave amplification to recommence. However, it seems quite possible that both of these effects could act simultaneously.

Obremski and Fejer (44) have suggested that the calming effect might play a role in terminating the creative mode of turbulent spot development during periodic transition in an oscillating flow. This was based on their observation that the point in the $x - \Upsilon^*$ plane at which the wave packet region terminated (see Fig. 6.7) lay close to a path which passed through the upstream end of a turbulent flow wedge and corresponded to a propagation velocity of 0.29U (the value observed in the steady flow transition experiments of Ref. 48). The present author agrees with this hypothesis, and notes that this model would predict the higher proportion of the creative mode observed during turbulent spot development in an adverse pressure gradient as a natural consequence of the higher values of $C_R/U$ under these conditions; conversely, a favourable pressure gradient (which gives a lower value of $C_R/U$) would be expected to reduce the proportion of creative mode development, thus producing a more marked laminar tongue and extending the length of the transition region.

In periodic transition there is another possible source of calming effect arising from changes in the frequency parameter, $\omega x/U$, with streamwise distance, x. The value of this parameter determines the instantaneous velocity profile shape throughout the oscillation cycle (see, for example, Farn and Arpaci (51)), and so must have a significant influence on the boundary layer stability characteristics.

## 6.3 Definition of the Instability and Transition Regions on the Compressor Blades

### 6.3.1 Introduction

As no detailed measurements of flow structure were obtained in the present investigation of boundary layers on the compressor blades, it was impossible to identify separately the several different steps occurring in the transition process, as described in Section 6.2.1. For the purpose of correlating the experimental data, the transition process was therefore divided into two stages only:

(a) a region (comprising steps (i) - (v)) which stretches from the point where the laminar flow first becomes unstable to small disturbances, to the point where turbulent spots first appear. This will be called the instability region;

(b) the region of turbulent spot development (step (vi)), which will be called the transition region.

This procedure follows broadly the method and notation of Miller and Fejer (43), who investigated transition in an oscillating flow.

The upstream limit of the instability region, which is the point of neutral stability to small two-dimensional disturbances in the laminar boundary layer, will be called the instability point.

The boundary between the instability and transition regions will be called the transition point.

The downstream limit of the transition region will be called the point of wholly turbulent flow.

A more detailed discussion of these limits, together with the method of determining them from the boundary layer measurements on the compressor blades, will now be presented.

### 6.3.2 Laminar Instability Point ($x = x_i$)

In natural transition of the two-dimensional laminar boundary layer, the two-dimensional type of Tollmien-Schlichting wave is usually the first to become unstable. The lowest value of boundary layer Reynolds number for which these disturbances can receive amplification (i.e. the "critical Reynolds number") is strongly influenced by the streamwise pressure gradient to which the boundary layer is subjected, since this determines the shape of the mean velocity profile. The pressure gradient is usually specified in terms of the parameter $k = (\theta^2/\nu)(dU/dx)$, or the velocity profile shape factor $H = \delta^*/\theta$.

In the present investigation, the points of neutral stability to small two-dimensional disturbances in the laminar boundary layers on the compressor blades were determined by using the curve of critical Reynolds number, $Re_{\theta_{crit}}$, against pressure gradient parameter, k, given by Stuart (52) as the mean of calculations by a number of workers. Some representative points scaled from this curve are presented in Table 6.1.

Table 6.1

Values of Critical Reynolds Number as a Function of Pressure Gradient Parameter - from Stuart (52)

| k | $Re_{\theta_{crit}}$ | k | $Re_{\theta_{crit}}$ | k | $Re_{\theta_{crit}}$ |
|---|---|---|---|---|---|
| -0.06 | 24 | -0.015 | 84 | 0.02 | 525 |
| -0.05 | 29 | -0.01 | 105 | 0.04 | 1360 |
| -0.04 | 36 | -0.005 | 131 | 0.06 | 2820 |
| -0.03 | 49 | 0.00 | 164 | 0.08 | 4680 |
| -0.02 | 70 | 0.01 | 291 | 0.10 | 6020 |

Because no hot wire measurements were obtained over the forward part of the stator blade, the boundary layer thicknesses calculated by Thwaites's

(10) method from the measured surface pressure distributions were used in the instability calculations. This procedure is thought to have introduced little error, in general, as the calculated and measured values of momentum thickness at the 40% chord position differed by only 4%, on the average (see Section 5.4.2). The greatest errors would have occurred at positive incidence, where the shape and location of the suction peak at the leading edge could not be very accurately specified due to the pressure measurements being obtained at 5% intervals of chord. Nevertheless, it is thought that the instability point was located to within 2% of chord from its correct position in most cases. The calculated positions of neutral stability on the stator blade suction surface at mid blade height are presented in Table 6.2.

There is admittedly some uncertainty in using the instability point calculated from the time-mean surface pressure distribution (as averaged by the manometer) in a situation where there is a high level of disturbance in the stream outside the boundary layer. As discussed in Section 6.4.2.4, the passage of rotor wakes over the stator blade undoubtedly causes the instantaneous position of the instability point to fluctuate about the "mean" location specified in Table 6.2. In the present investigation, however, the use of this "mean" instability point was found to yield useful results.

### 6.3.3 Transition Point ($x = x_t$)

The transition point is characterised by a decrease in boundary layer shape factor, $H = \delta^*/\theta$, and an increase in skin friction and rate of growth of momentum thickness, all arising from the increased mixing produced by the turbulent spots starting to appear in the boundary layer. There is also a significant rise in the level of velocity fluctuations within the shear layer, with an accompanying increase in pressure fluctuations and radiated noise.

The transition point in the stator blade boundary layer was assessed from the results of the stethoscope observations, the hot wire mean velocity measurements, and the china clay tests. The stethoscope observations are considered to have provided the most accurate and reliable information, and the transition locations determined by this means (see Section 3.5) are presented in Table 6.2. The possible error in locating transition with the stethoscope is thought to have been about 2%c on the average. However, as the variation in boundary layer noise level was much more distinct in separating flows than in attached flows, it is likely that slightly greater errors could have occurred in the latter cases. No measurements could be obtained with the stethoscope at very low velocities due to the boundary layer noise becoming inaudible; the transition point was then inferred, where possible, from the other observations.

It was generally impossible to locate the transition point to the required accuracy from the hot wire measurements alone, as these were obtained at the rather widely spaced intervals of 10% chord. At positive incidence, the transition point on the stator suction surface fell outside the range of the hot wire measurements altogether. Nevertheless, the hot wire traverses provided a useful check on the accuracy of the stethoscope observations, being consistent with the latter in all cases where a comparison could be made; it was found that the transition point determined with the stethoscope always lay at or slightly forward of the position at which the measured value of the boundary layer shape factor H reached a maximum.

The china clay observations indicate the point at which a sudden increase in wall shear stress occurs following transition. However, this provides only a downstream limit to the location of the transition point, as the turbulent flow originates at localised regions within the boundary layer near the layer of maximum shear, and can only spread to the bounding surface and cause an increase in wall shear stress after the flow has progressed some distance further downstream; this distance is expected to be greater in an adverse pressure gradient, since the layer of maximum shear is further from the surface in this case.

At negative incidence, the jump in wall shear stress indicated by the china clay tests on the stator blade suction surface occurs within a few percent of chord, on the average, behind the transition point measured with the stethoscope; at positive incidence, however, the difference between these points increases to 20 or 30% of chord (see Appendix E and Table 6.2). The large discrepancy observed at positive incidence is resolved by the hot wire measurements, which indicate the transition point measured with the stethoscope to be correct; in these cases it appears that the turbulent boundary layer remains close to separation (as indicated by a high value of H) for a considerable distance following transition, until a rather marked decrease in H occurs near the position where the china clay tests indicate the jump in wall shear stress. The fact that sudden changes in skin friction can be caused by factors other than boundary layer transition means that considerable caution must be exercised in attempting to locate transition from the results of surface visualisation tests alone.

### 6.3.4 Point of Wholly Turbulent Flow ($x = x_T$)

At the point of wholly turbulent flow, the intermittency of turbulence reaches unity over the inner 50% or so of the boundary layer. It should not be assumed, however, that the turbulence is "fully developed" at $x = x_T$, as its structure and spectrum will continue to change for some further distance downstream while the large disturbances produced in the transition process are still decaying.

Table 6.2

Calculated Points of Neutral Stability in the Laminar Boundary Layer and Location of the Transition Region Obtained from Stethoscope Observations

STATOR SUCTION SURFACE - MID BLADE HEIGHT

| Compressor Speed (rpm) | Throttle Opening (ins) | Incidence i (°) | Calculated $x_i/c$ (%) | Observed $x_t/c$ (%) | Observed $x_T/c$ (%) |
|---|---|---|---|---|---|
| 750 | 4.8 | 4.6 | 9 | 30 | 45 |
| | 5.2 | .2.7 | 9 | 36 | 50 |
| | 6.0 | 0.6 | 10 | 44 | 60 |
| | 8.0 | -3.7 | 16 | 61 | 75 |
| | 10.0 | -6.2 | 22 | 68 | 82 |
| | 13.0 | -8.7 | 25 | 69 | 84 |
| | 22.0 | -10.9 | 36 | 72 | 86 |
| 500 | 4.8 | 4.7 | 10 | 30 | 50 |
| | 5.2 | 2.9 | 10 | 32 | 50 |
| | 6.0 | 1.0 | 12 | 45 | 61 |
| | 8.0 | -3.1 | 21 | 65 | 80 |
| | 10.0 | -5.6 | 22 | 71 | 85 |
| | 13.0 | -7.6 | 30 | 74 | 88 |
| | 22.0 | -10.3 | 33 | 75 | 89 |
| 250 | 4.8 | 5.2 | 12 | N | N |
| | 5.2 | 3.0 | 14 | N | N |
| | 6.0 | 0.5 | 16 | N | N |
| | 8.0 | -3.2 | 22 | 65 | 80 |
| | 10.0 | -6.0 | 29 | 70 | 85 |
| | 13.0 | -8.0 | 32 | 70 | 85 |
| | 22.0 | -10.1 | 37 | 72 | 88 |
| 150 | 4.8 | 5.6 | 13 | N | N |
| | 5.2 | 3.6 | 13 | N | N |
| | 6.0 | 1.2 | 19 | N | N |
| | 8.0 | -3.0 | 29 | N | N |
| | 10.0 | -5.5 | 29 | N | N |
| | 13.0 | -7.7 | 36 | N | N |
| | 22.0 | -10.2 | 39 | N | N |

(N = Noise levels too low to obtain reliable measurements)

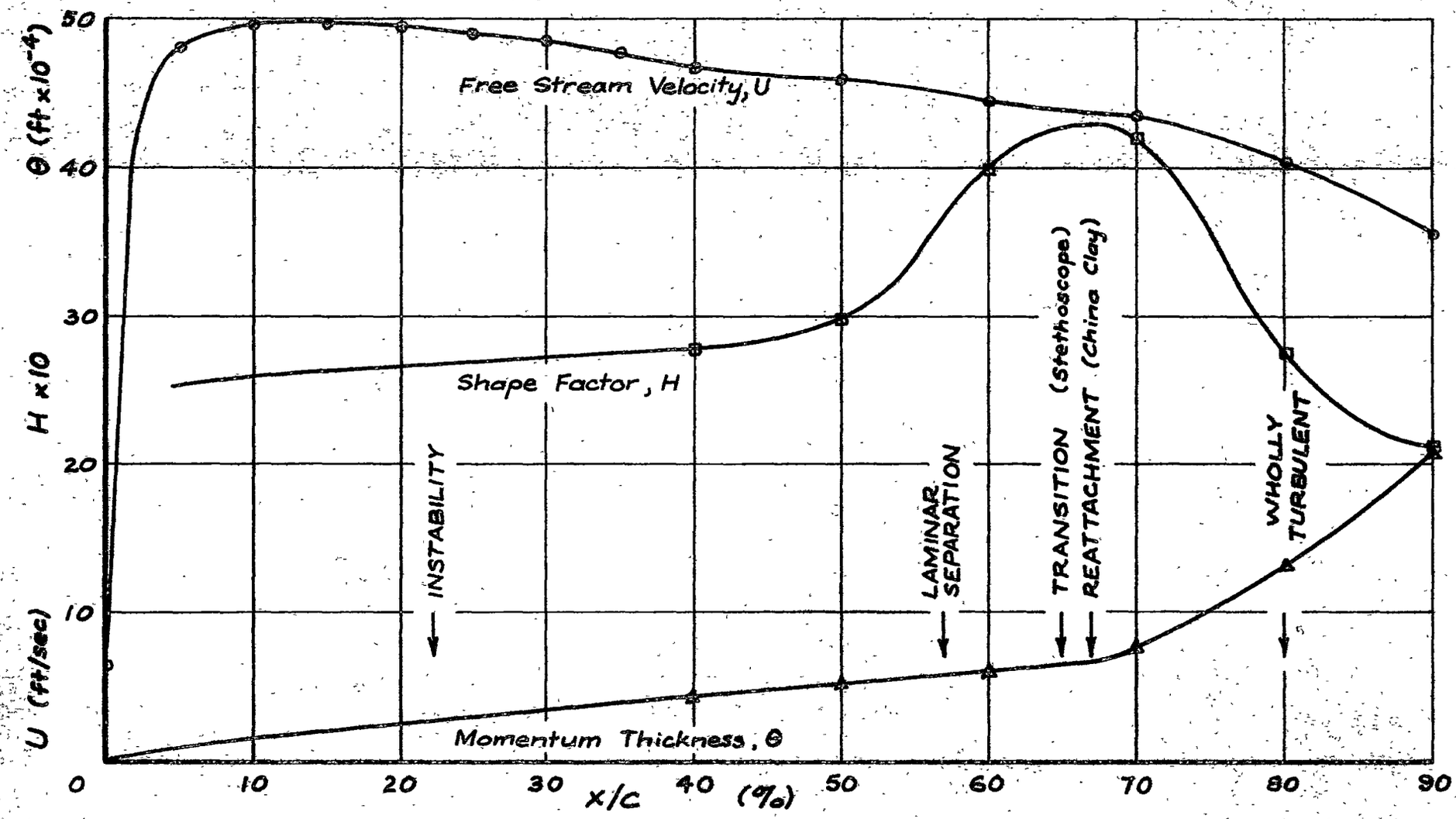


Fig. 6.9 Boundary Layer Development on Stator Suction Surface - Showing Location of Instability and Transition Regions ($i = -3.2^{\circ}$, $Re_c = 5.3 \times 10^4$, Compressor Speed 250 rpm)

The point of wholly turbulent flow on the stator blade suction surface was determined entirely from stethoscope observations with the total head tube, as discussed in Section 3.5. In all cases this point lay slightly upstream of the position at which the boundary layer shape factor, H, ceased to decrease and reached a roughly stable value characteristic of turbulent flow (see Figs. 4.7 (a - c)).

Fig. 6.9 shows the measured boundary layer development on the stator blade suction surface at small negative incidence, together with the estimated points of instability, transition, and wholly turbulent flow.

## 6.4 Physical Nature of Transition on the Compressor Blades

### 6.4.1 Inferences from Mean Velocity Measurements

Although no detailed measurements of unsteady flow structure were undertaken during the present investigation, some inferences about the nature of disturbances preceding transition in the stator blade boundary layer can still be drawn from the mean velocity measurements obtained. The most useful quantity to examine is the mean spanwise vorticity, $\zeta = \partial u/\partial y$, and Fig. 5.3 shows the mean vorticity profiles in the stator suction surface boundary layer at mid-blade height for $i = -10.1^{\circ}$ and $Re_c = 7.2 \times 10^4$. The profile measured at 40% chord (about 10% chord downstream of the instability point) has been compared with the corresponding theoretical vorticity distribution in Fig. 5.2; it is seen that there is a definite distortion of the experimental vorticity profile near the peak of the undisturbed vorticity distribution. The amount of distortion increases with distance downstream until it reaches a maximum in the profile measured at 80% chord, which is just rearward of the transition point. Here, the vorticity is increased on the outer side of the position of maximum vorticity for an undisturbed laminar flow, and decreased on the inner side, which is consistent with the presence of type A streamwise vortices as defined in Fig. 6.3. This behaviour is very similar to that observed during transition in zero pressure gradient, as discussed in Section 6.2; it agrees with the observations of other workers (e.g. Ref. 42) that an adverse pressure gradient does not greatly alter the basic physical nature of the transition process.

### 6.4.2 Velocity Fluctuations during Transition on the Stator Blade

#### 6.4.2.1 Introduction

This section discusses the records of velocity fluctuations obtained with a constant temperature hot wire anemometer at the 50% chord station in the stator blade suction surface boundary layer. The experimental detail has been given previously in Section 3.3.11; however, it is recalled that the boundary layer transition region on the compressor blade was moved relative to the hot wire probe by changing the compressor throttle setting and so altering the stator incidence.

6.4.2.2 Description of some typical observations

Figs. 6.10 (a - d) show a series of multiple trace records of anemometer bridge voltage fluctuations obtained in the outer part of the boundary layer. It is noted that the voltage fluctuations have not been linearised, and that the vertical scale for the last two photographs is half that of the first two; increases in velocity are upwards in all cases. The following sequence of events is observed as the blade incidence is increased:
(a) for $i = -10.1^{\circ}$, the hot wire probe is well forward in the instability region; $(x - \overline{x}_i)/(x_t - \overline{x}_i) = 0.37$, where x denotes the probe location. There is some vertical scatter of the individual traces; these are displaced roughly parallel to one another, indicating the presence of low frequency unsteadiness in the external flow. No velocity fluctuations characteristic of turbulence are apparent, except for those impressed on the stator blade boundary layer by disturbances in the rotor wakes; the rotor wake passage is marked by the large velocity defects (about 0.1U) occurring at 6.5 msec intervals. However, there is some evidence of regular oscillations with a small amplitude and a high frequency, around 3,250 c/s; although these are barely discernible in Fig. 6.10 (a) they are clearly visible in other records obtained nearer the blade surface. A plot of the non-dimensional disturbance frequency against boundary layer Reynolds number gives a point lying between the locus of maximum amplification rate and the upper branch of the neutral stability curve of Ref. 53 for small two-dimensional disturbances receiving spatial amplification; it seems reasonable to assume, therefore, that these high frequency disturbances are Tollmien-Schlichting waves;
(b) at $i = -3.2^{\circ}$, the probe is situated further rearward in the instability region, with $(x - \overline{x}_i)/(x_t - \overline{x}_i) = 0.65$. The boundary layer flow has become much more unsteady, particularly around the accelerating part of the velocity fluctuation imposed by the rotor wake passage; the traces show more of an oscillatory behaviour at a low frequency, and are no longer displaced parallel to each other in the vertical direction as in Fig. 6.10 (a). Other records at this incidence still show evidence of the high frequency Tollmien-Schlichting waves, and there is a definite tendency for the amplitude of these disturbances to increase during the accelerating phase of the wake "oscillation"; very occasionally, early breakdown is observed at this part of the cycle;
(c) at $i = 0.5^{\circ}$, the probe lies just inside the transition region, with $(x - x_t)/(x_T - x_t) \simeq 0.2$. Sharp downward spikes characteristic of breakdown can be seen during the accelerating phase of the wake oscillation, and the instant at which the maximum velocity is reached immediately following the wake passage appears greatly favoured for the outbreak of turbulent flow in this particular case. During the decelerating phase of the wake oscillation, breakdown rarely if ever occurs. It is quite obvious that the oscillation in velocity caused by the rotor wake passage imposes a considerable amount of uniformity on the time-space distribution of turbulent flow during transition on the stator blade;

(d) at $i = 5.2^{\circ}$, the probe is situated towards the rear of the transition region, with $(x - x_t)/(x_T - x_t) \simeq 0.8$. The intermittency of turbulence has increased considerably, and there appears to be a reduction in mean velocity at the phase of the wake passage where breakdown was first noted in Fig. 6.10 (c). There is now evidence of turbulent flow appearing a little before the passage of the velocity minimum of the wake oscillation.

Figs. 6.11 (b - d) show some single trace records obtained at different positions within the boundary layer for a fixed incidence, $i = 0.5^{\circ}$, which places the probe just inside the transition region. It is noted that these records are unlinearised, and were not obtained simultaneously. The multiple trace record in Fig. 6.11 (a) has been included to indicate more clearly the times at which wakes pass in the free stream. The regularity with which breakdown occurs is still apparent, even in the single trace records, and the turbulent mixing is seen to produce a sharp decrease in velocity in the outer part of the boundary layer and a sharp increase in velocity near the wall. The small, wavy disturbances characteristic of Tollmien-Schlichting waves are always visible next to the sharp spikes indicative of breakdown; thus there does not appear to be any calming period following breakdown during which stable laminar flow persists. However, there is clear evidence of the small wave amplitude varying with the phase of the free steam oscillation: in this case the amplitude reaches a minimum shortly after a wake has passed in the free stream, and then increases steadily as the next wake approaches and the flow starts to decelerate.

Fig. 6.12 shows another set of single trace records for $i = 5.2^{\circ}$, which places the probe near the rear of the transition region. These photographs are markedly similar to those in Fig. 6.11, except for the relatively greater proportion of time over which turbulent flow occurs.

6.4.2.3 Discussion of observations

The phase of the velocity fluctuations induced by the rotor wakes varies with both x and t due to the convection of these wakes by the free stream. Nevertheless, a fluid particle travelling within the stator blade boundary layer will "see" fluctuations in the free stream velocity at fairly regular intervals as the faster moving rotor wakes overtake it, and there is still a degree of similarity with the problem of transition in an oscillating flow which was studied in Refs. 43, 44 and 49. The results of work on periodic transition (discussed in Sections 6.2.2.2, 6.2.3.2) are therefore of some assistance in interpreting the present observations; but it should be remembered that the investigations of Refs. 43, 44 and 49 were restricted to cases in which the phase of the free stream oscillations varied only with time.

The time-space distribution of turbulent flow on the stator blade closely resembles that observed by Obremski and Fejer in oscillating flow

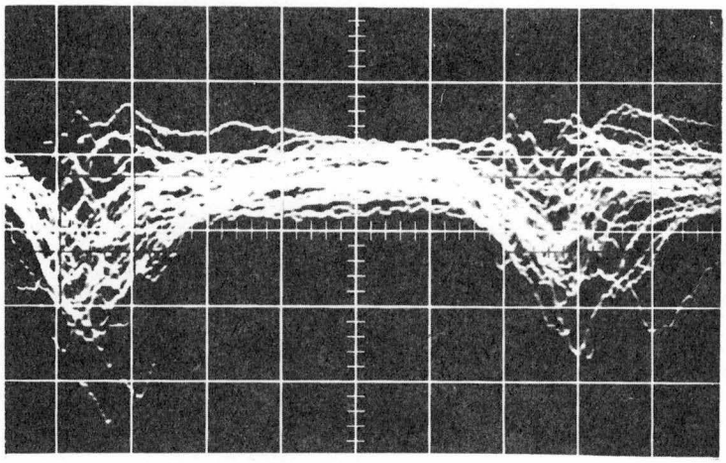

(a)

$i = -10.1^{\circ}$

$(x-\bar{x}_i)/(x_t-\bar{x}_i) = 0.37$

$y/\delta = 0.62$

0.1 volt/cm Vert.

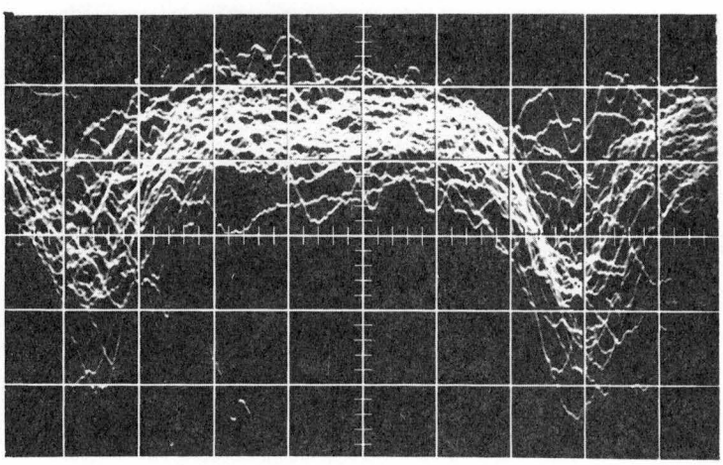

(b)

$i = -3.2^{\circ}$

$(x-\bar{x}_i)/(x_t-\bar{x}_i) = 0.65$

$y/\delta = 0.74$

0.1 volt/cm Vert.

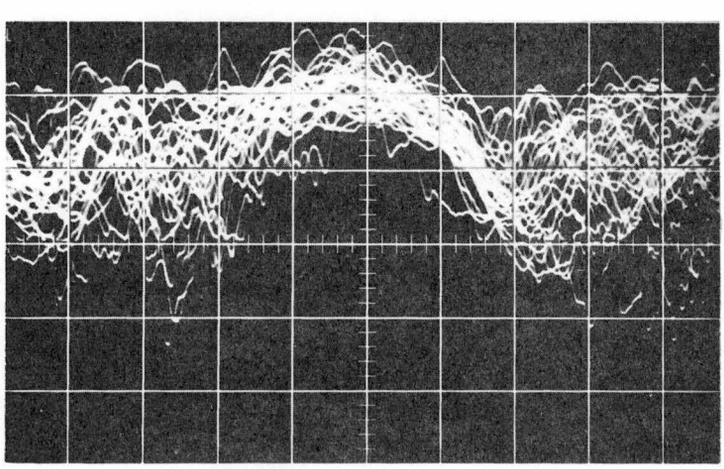

(c)

$i = 0.5^{\circ}$

$(x-x_t)/(x_T-x_t) \approx 0.2$

$y/\delta = 0.72$

0.2 volt/cm Vert.

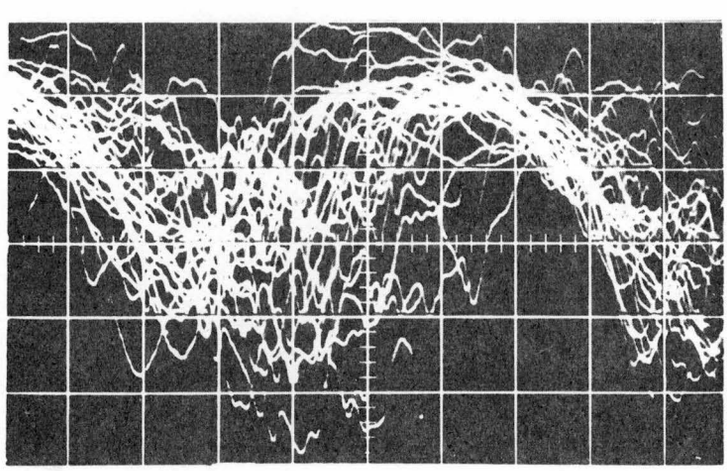

(d)

$i = 5.2^{\circ}$

$(x-x_t)/(x_T-x_t) \approx 0.8$

$y/\delta = 0.55$

0.2 volt/cm Vert.

Sweep 1 msec/cm Horiz.

Fig. 6.10 Multiple-Trace Records of Velocity Fluctuations during Boundary Layer Transition
Stator Suction Surface, Mid-Blade Height, x/c = 0.50. Compressor Speed 250 rpm.

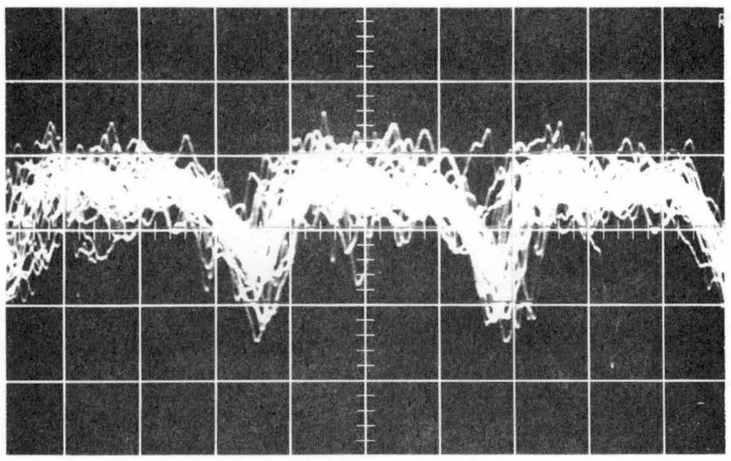

(a)

Multiple Trace
$y/\delta$ = 1.23

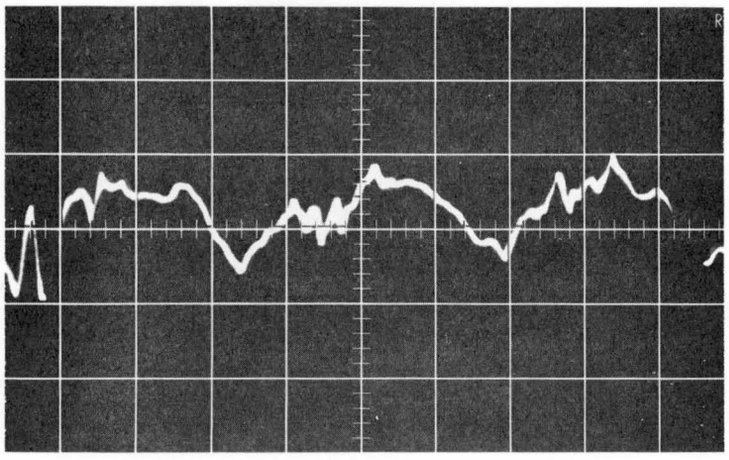

(b)

Single Trace
$y/\delta$ = 1.23

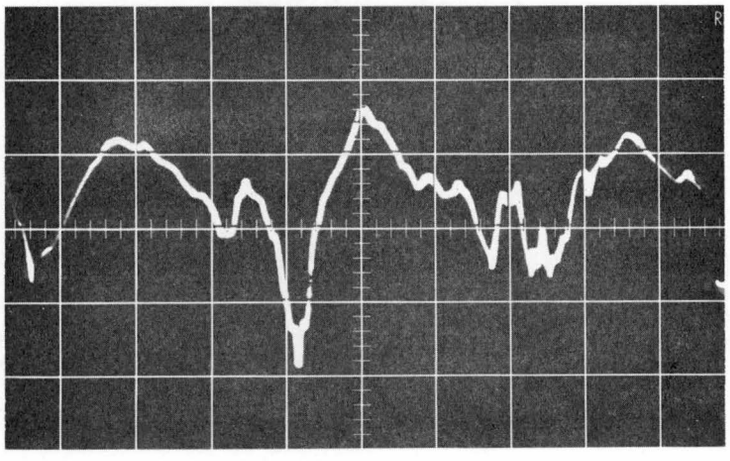

(c)

Single Trace
$y/\delta$ = 0.72

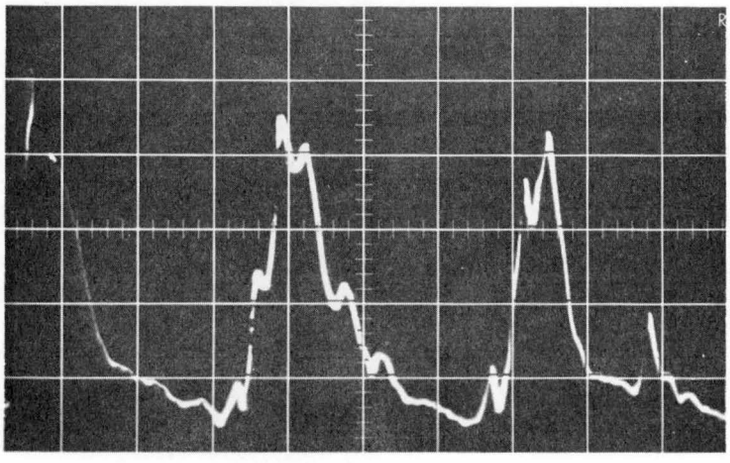

(d)

Single Trace
$y/\delta$ = 0.03

Sweep 2 msec/cm Horiz., 0.2 volt/cm Vert.

Fig. 6.11 Velocity Fluctuations in Stator Suction Surface Boundary Layer - Forward Part of Transition Region
Mid-Blade Height, x/c = 0.50. i = 0.5°, Compressor Speed 250 rpm.

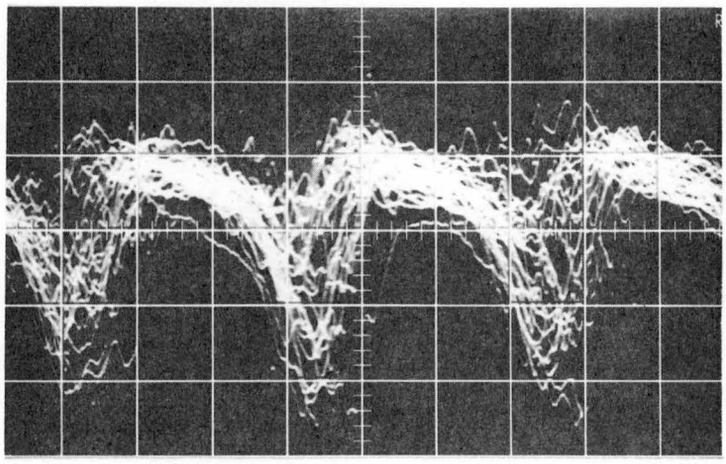

(a)

Multiple Trace
$y/\delta$ = 1.43

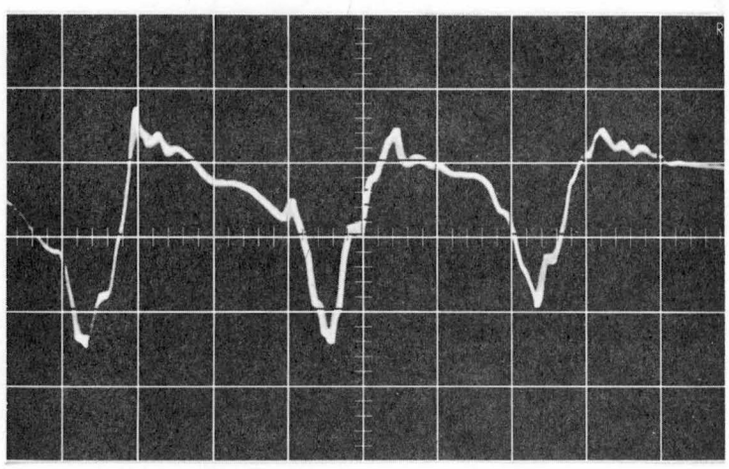

(b)

Single Trace
$y/\delta$ = 1.43

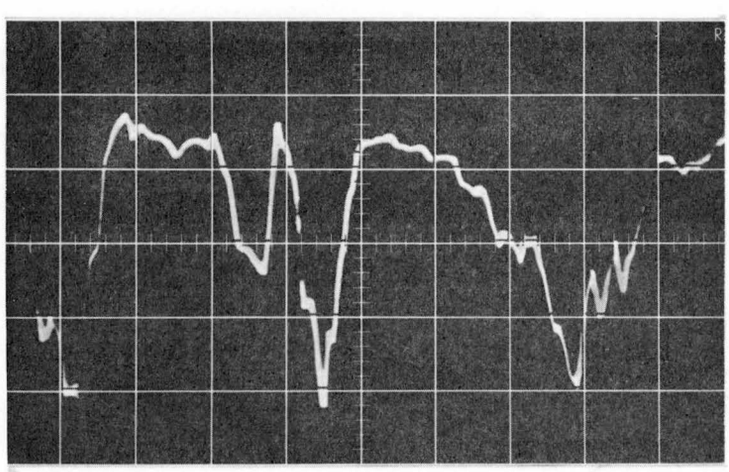

(c)

Single Trace
$y/\delta$ = 0.61

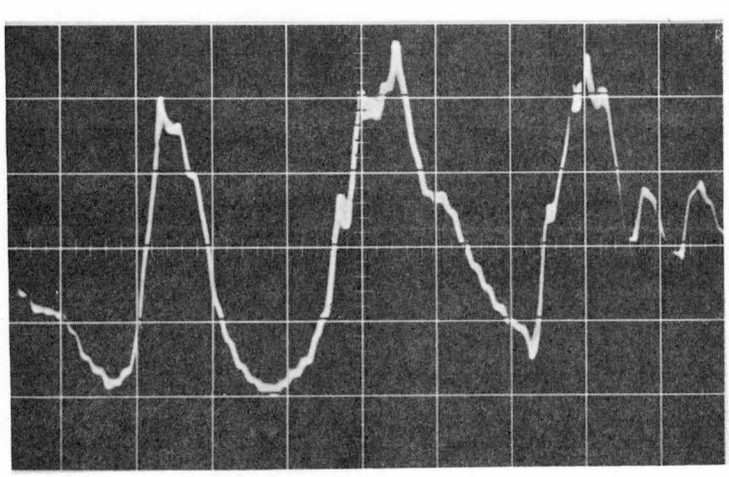

(d)

Single Trace
$y/\delta$ = 0.02

Sweep 2 msec/cm Horiz., 0.2 volt/cm Vert.

Fig. 6.12 Velocity Fluctuations in Stator Suction Surface Boundary Layer - Rearward Part of Transition Region
Mid-Blade Height, x/c = 0.50. $i = 5.2^{\circ}$; Compressor Speed 250 rpm.

over a flat plate (see Figs. 6.7, 8, 13). In both situations there is a considerable regularity about the appearance of turbulent bursts because of the time distribution of shear within the boundary layer being influenced by the periodic fluctuations in free stream velocity. There is clear evidence of the interface between the laminar and turbulent flow regions on the stator blade moving upstream during some phases of the rotor wake passage (see Fig. 6.13), indicating that the turbulent spots are developing in the "creative mode" defined in Section 6.2.3.2; this observation is consistent with the continuous presence of laminar instability waves contiguous to the turbulent bursts which was noted from the photographs in Figs. 6.11 and 6.12.

The earliest appearance of turbulent flow in the stator blade boundary layer occurs at the end of the accelerating segment of the velocity fluctuation induced by the rotor wake passage. Although it could be merely coincidental for the few cases examined, this behaviour is very similar to that of the "aperiodic" mode of transition described by Obremski and Fejer. It is recalled from Section 6.2.2.2 that in zero pressure gradient flow over a flat plate, the aperiodic mode occurred when the non-steady Reynolds number $(Re)_{NS}$ fell below about 25,000; in tests with an adverse pressure gradient of $dC_p/dx = 0.045/ft.$, $(Re)_{NS}$ was reduced to 6,000 without aperiodic transition occurring, so the critical value of $(Re)_{NS}$, if it existed, would have been lower than this. For the case of transition on the compressor blade shown in Fig. 6.10 (d), where $dC_p/dx$ varied between 0 and 4/ft. over the instability region, the effective value of $(Re)_{NS}$ for the disturbance created by the rotor wake passage was about 1,000 only; for most of the other flow cases investigated, $(Re)_{NS}$ was even smaller. Thus the possibility remains open that transition on the stator blade could be occurring in the aperiodic mode, and that the non-steady Reynolds number $(Re)_{NS}$ could be used to predict the effects of isolated free stream disturbances on the transition process. No more positive conclusion can be reached at present because of the unknown manner in which the critical value of $(Re)_{NS}$ might vary with the mean streamwise pressure gradient; in this respect it is pertinent to note that the significant pressure gradient parameter is likely to be the time mean value of boundary layer shape factor, rather than the dimensional quantity $dC_p/dx$.

In the zero pressure gradient experiments of Obremski and Fejer, the transition Reynolds number $Re_{x_t}$ remained almost constant for free stream oscillations in the lower $(Re)_{NS}$ range ( $< 25,000$); the value of $Re_{x_t}$ was then about 24% less than that observed in steady flow with the same free stream turbulence level. In an adverse pressure gradient, where the mean amplification rate of disturbances leading to transition will be much higher, the relative change in amplification rate caused by a given free stream disturbance is likely to be smaller than in zero pressure gradient; thus the difference between the values of $Re_{x_t}$ for steady and oscillating flow in the lower $(Re)_{NS}$ range could well be less than 24% during transition in an adverse pressure gradient. This is suggested as a possible explanation

for the relatively small scatter (mostly less than ± 10%) in the transition data correlated by Eqns. 6.11 and 6.26 despite the large range of free stream disturbance levels involved. It might also explain the observation of Shaw (54) that the presence of wakes from uncambered inlet guide vanes inserted upstream of an isolated rotor had little effect on the compressor performance.

6.4.2.4 A tentative model for transition on the stator blade

A tentative attempt to model the transition behaviour on the compressor blades has been made in Fig. 6.13, which shows the estimated time-space distribution of turbulent and unstable laminar flow on the stator suction surface at $i = 5.2^{\circ}$ with a compressor speed of 250 rpm. In constructing this diagram it was assumed that the flow behaviour remained similar for a given value of $(x - \bar{x}_i)/(x_t - \bar{x}_i)$ or $(x - x_t)/(x_T - x_t)$ so that the data from observations at other blade incidences could be utilised; this procedure was necessary because records of velocity fluctuations were obtained at only one streamwise location, x/c = 0.50.

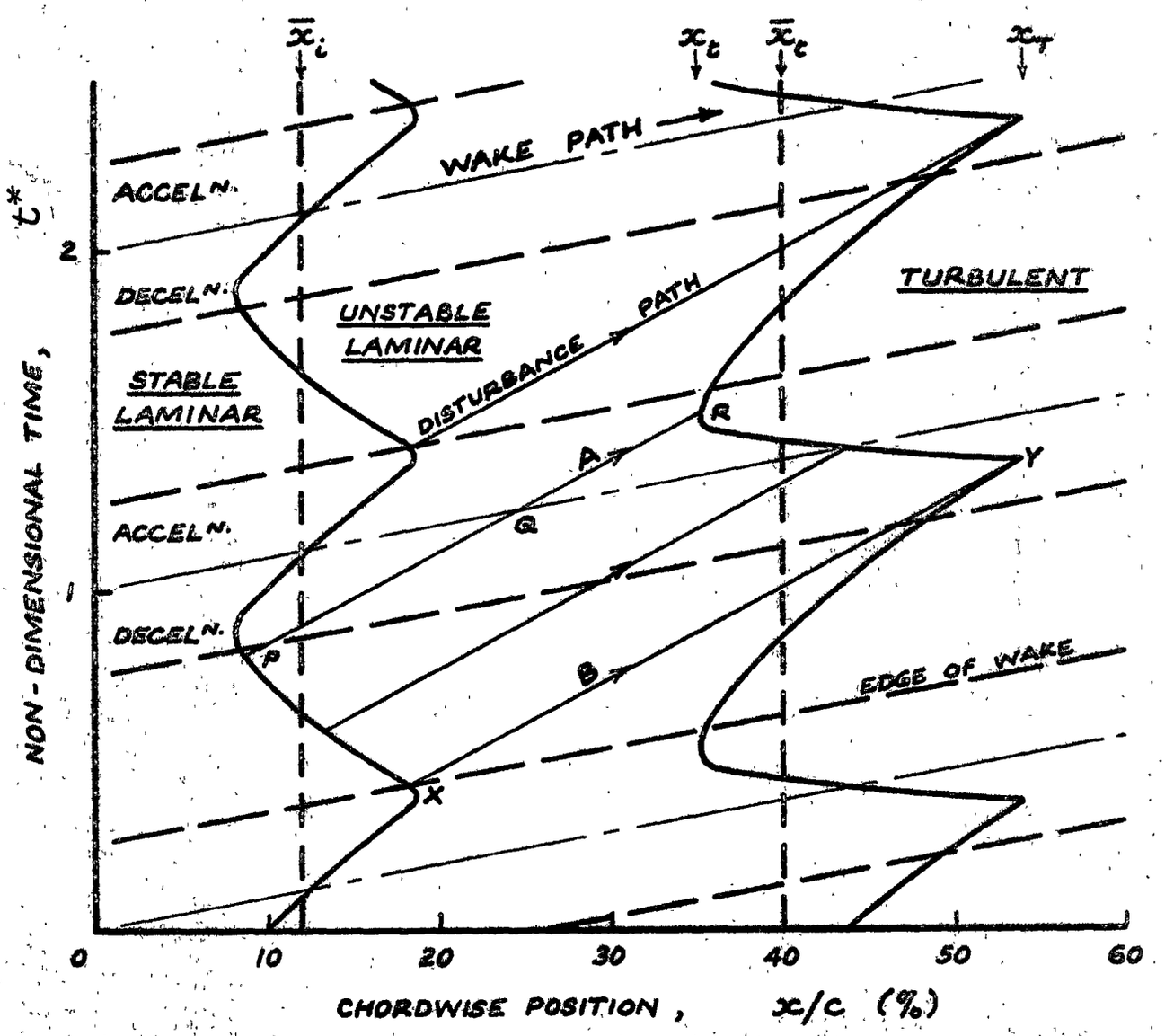


Fig. 6.13 Hypothetical Time-Space Distribution of Turbulent and Unstable Laminar Flow during Transition.
Stator Suction Surface, $i = 5.2^{\circ}$, Compressor Speed 250 rpm.

Values of time in Fig. 6.13 have been made non-dimensional with respect to the period of the rotor blade passage. For simplicity, the rotor wakes have been assumed to travel along the stator blade surface at a constant velocity, equal to an average value of the free stream velocity over the instability and transition regions; the disturbances leading to transition in the boundary layer have been assumed to travel at 35% of this average free stream velocity. Fig. 6.13 shows a hypothetical variation of the instantaneous neutral stability point, $x_i$, with time; it is expected that $x_i$ would be decreased during the decelerating phase of the rotor wake disturbance, and increased during the accelerating phase. Also indicated are the "steady flow" instability point $\bar{x}_i$, calculated from the time-mean surface velocity distribution, together with a hypothetical "steady flow" transition point, $\bar{x}_t$, defined similarly to $\bar{x}_i$.

Consider now the amplification histories of disturbances travelling along paths A and B in the $x \sim t^*$ plane, which pass respectively through the upstream and downstream limits of the points at which breakdown is observed:
(i) along path A, the additional deceleration caused by the passage of a rotor wake in the free stream causes amplification of disturbances in the laminar boundary layer to commence at a point P, which lies some distance upstream of the steady flow instability point, $\bar{x}_i$. Amplification of disturbances will continue to be enhanced along PQ, but on reaching Q the wake centre overtakes the slower-moving disturbances in the critical layer and the amplification rate is subsequently reduced during the accelerating phase of the rotor wake disturbance. Breakdown eventually occurs at point R, which should lie upstream of the steady flow transition point, $\bar{x}_t$; but $(\bar{x}_t - x_R)$ is not expected to be very large because the disturbances arriving at R have experienced a reduction in amplification rate during the latter stages of their development which partially offsets the increased amplification during the early stages;
(ii) along path B, amplification is delayed by the accelerating phase of the rotor wake disturbance until the point X, which lies downstream of the steady flow instability point, $\bar{x}_i$. Amplification of disturbances then proceeds under the almost steady free stream conditions between the wakes until the deceleration induced by the next wake in the stream enhances amplification just prior to breakdown at Y, which lies downstream of $\bar{x}_t$. Since the transition process along path B occurs at higher Reynolds numbers, $(x_Y - x_X)$ is expected to be rather greater than $(x_R - x_P)$ (see Eqn. 6.19) and so $(x_Y - \bar{x}_t)$ should exceed $(\bar{x}_t - x_R)$.
The position at which breakdown occurs is expected to fluctuate between the limits $x_R$ and $x_Y$ at other stages of the rotor wake passage.

The above flow model provides quite a plausible explanation for the observed transition behaviour on the stator blade in this particular case; but its qualitative and intuitive aspects need checking by more detailed quantitative measurements over a wider range of conditions before it can

finally be accepted. Bearing these limitations in mind, however, it is interesting to use the model to make some predictions about the possible effects of passing wakes on transition under different local flow conditions.

If, for example, the pressure gradient over the instability region was reduced so that the instability length $(\bar{x}_t - \bar{x}_i)$ became greater than that shown in Fig. 6.13, the initial breakdown would possibly occur at some point outside the wake path in the $x \sim t^*$ plane. Thus the first appearance of turbulent flow during the accelerating phase of the rotor wake disturbance, which was noted from Fig. 6.10, could well have resulted from a fortuitous combination of external flow variables and therefore might not be general.

Alternatively, if the local pressure gradient was increased so that $(\bar{x}_t - \bar{x}_i)$ became less than $(x_Q - x_P)$, say, the earliest breakdown would occur before $x_Q$, i.e. in the decelerating phase of the rotor wake disturbance. In this case, the forward movement of the transition point in the unsteady flow would be relatively greater than that shown in Fig. 6.13 because there would be no decrease in amplification rate over the latter part of the instability length to offset the increased amplification during the initial stages.

Thus the present model indicates that free stream disturbances should reduce the transition Reynolds number by a greater amount as the scale of the free stream disturbances becomes larger relative to the instability length (or, alternatively, as the scale of the instability length becomes smaller relative to that of the free stream disturbances). The transition data from the stator blade suction surface does appear to show this trend, as the non-dimensional instability lengths at incidences between 0 and $+5^\circ$ (where $\bar{x}_t - \bar{x}_i < 30\%$ chord, approximately) tend to lie a little below the mean curve in Fig. 6.19; relatively greater effects could be expected to occur at higher positive incidences, where the instability length becomes even shorter.

## 6.5 Existing Methods for Predicting the Transition Point

### 6.5.1 Introduction

This section deals with the problem of estimating the streamwise position at which breakdown to turbulence first occurs within the boundary layer. Because of the present incomplete understanding of the transition process, existing methods of predicting transition are either empirical, or at best semi-empirical. The more widely used of these techniques will now be reviewed and their success in describing the flow behaviour on the compressor blades will be evaluated.

### 6.5.2 Michel's Method

Michel (55) obtained a very simple empirical method of predicting the transition point, $x_t$, by correlating the boundary layer Reynolds number at

transition, $Re_{\theta_t}$, against the x-Reynolds number at transition, $Re_{x_t}$. This method does not require a separate calculation of the laminar instability point, as the conditions at transition are correlated directly. The original curve of $Re_{\theta_t} \sim Re_{x_t}$ given by Michel was derived from observations of transition on a range of NACA aerofoil sections tested in low-turbulence wind tunnels at moderately high Reynolds numbers. Smith (56) later examined a wider range of experimental data, including tests of aerofoils in flight, and found that the transition behaviour could be correlated by the relation

$$Re_{\theta_t} = 1.174\, Re_{x_t}^{0.46} \quad (0.3 \times 10^6 < Re_{x_t} < 20 \times 10^6) \qquad (6.1)$$

which was also a good fit to Michel's original data. In the 34 cases of transition on two-dimensional bodies examined by Smith, Equation 6.1 was found to predict $Re_{x_t}$ with a standard deviation of 18.7%.

Michel's method of predicting transition was initially received with some reserve because it was strictly empirical and no physical reason had been advanced to explain its success. But Smith (56) was later able to provide an explanation in terms of laminar stability theory (see Section 6.5.3).

Fig. 6.14 shows a comparison of Equation 6.1 with the experimental data from the present investigation of boundary layer transition on the compressor blades. (It should be noted that it was necessary to extrapolate Equation 6.1 below the Reynolds number range for which it was originally derived because of the low Reynolds numbers at which the compressor blades operated.) The correlation of $Re_{\theta_t} \sim Re_{x_t}$ for transition on the stator blade suction surface is only fair, with the measured values of $Re_{\theta_t}$ tending to lie above those predicted by Equation 6.1. Fig. 6.14 also shows curves of $Re_\theta \sim Re_x$ for Blasius flow and separating laminar flow. Considering that the trajectories of $Re_\theta \sim Re_x$ for laminar boundary layers on the stator suction surface will mostly lie between these rather narrow limits, the scatter of the experimental points is seen to be relatively large.

The deviations of the experimental points from the critical curve (Equation 6.1) cannot be explained by the possible effects of higher turbulence level in the compressor, as Michel observed that an increase in turbulence level up to 0.4% (corresponding to a change in the critical Reynolds number of a sphere from 380,000 to 295,000) caused a slight reduction in the value of $Re_{\theta_t}$ for a given value of $Re_{x_t}$. The most likely explanation for the failure of Equation 6.1 to describe the present data very closely is that the pressure distributions and Reynolds numbers corresponding to the compressor blade operation were not very similar to those for which Michel's correlation was originally obtained.

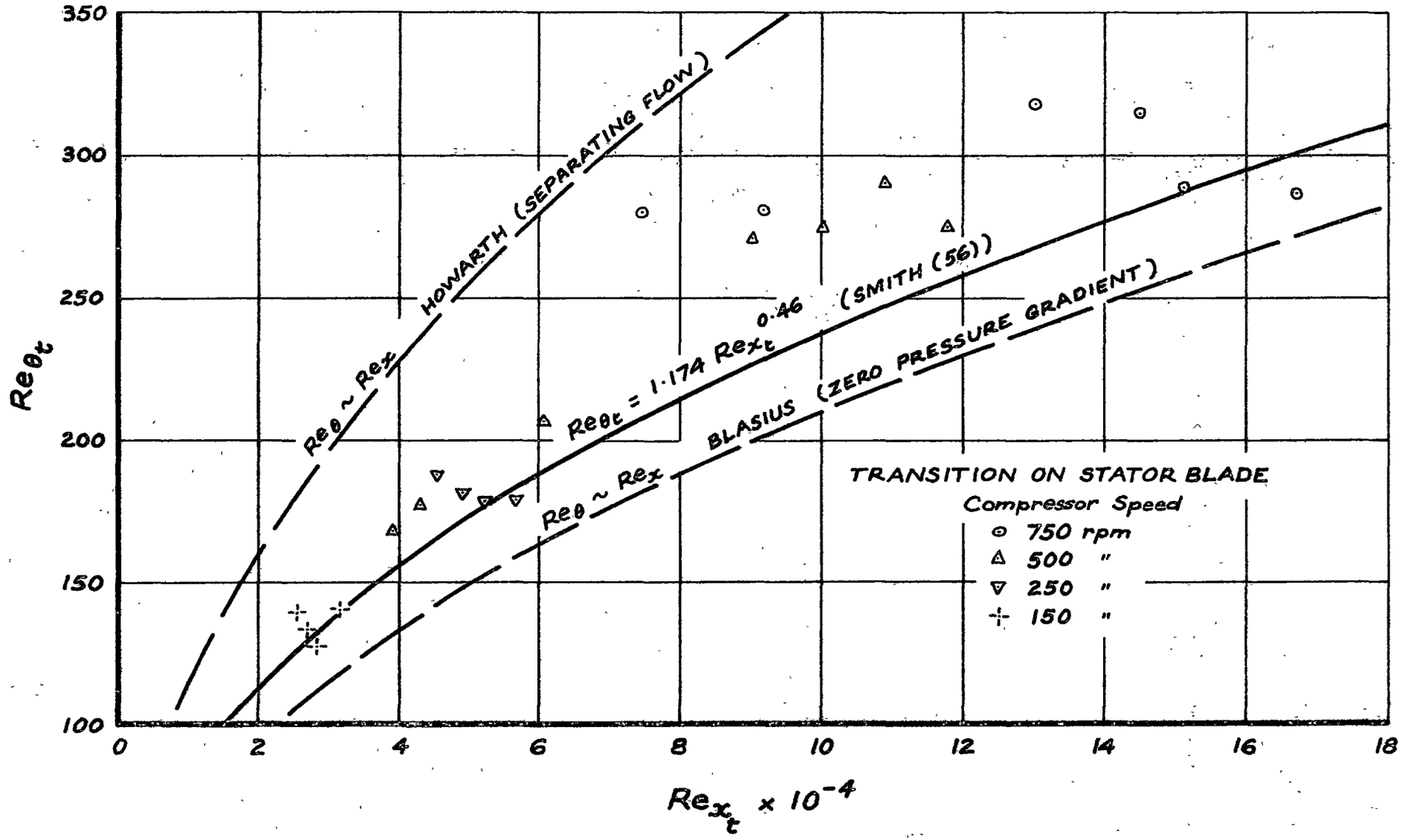


Fig. 6.14 Michel's Transition Correlation

6.5.3 The Method of Smith et al.

6.5.3.1 Introduction

This is a semi-empirical method of predicting transition which is based on laminar stability theory. It was developed from the suggestion of Liepmann (46) that transition should occur at the streamwise position where the Reynolds shear stress, $\tau_t = -\rho\overline{u'v'}$, due to the amplified boundary layer oscillations at any point in the boundary layer becomes equal to the laminar shear stress, $\tau_l = \mu \partial u/\partial y$, in the boundary layer. This criterion is given approximately by

$$\left\{(\tau_t)_{max}/\tau_l\right\} \simeq -(2/C_{f_l})\left\{kb(u'/U)_i^2\, a^2\right\} \simeq 1 \qquad (6.2)$$

where $b = v'/u'$ (the ratio of the y-velocity fluctuation component to the x-velocity fluctuation component), $C_{f_l}$ is the local laminar shear stress coefficient, and $k = \overline{u'v'}/u'v'$ is a correlation coefficient. Equation 6.2 also contains the product (squared) of the terms $(u'/U)_i$, representing the disturbance level at the instability point, and "a", which is the amplification ratio of the disturbances over the interval from instability to transition.

To be entirely consistent with Liepmann's theory it is really the value of $(\tau_t)_{max}/\tau_l$ at transition which should be correlated, i.e. the product of terms on the right hand side of Eqn. 6.2. But Smith et al.(56, 57, 61) simply correlated the amplification ratio, a; the stated reason for doing this was that "a" was of order $10^4$, and that the variation of $C_{f_l}$ and $(u'/U)_i$ were so small by comparison that they could be neglected in any first order analysis. The present author does not entirely agree with this view, as $C_{f_l}$ and $(u'/U)_i$ must each vary by one or perhaps two orders of magnitude over the range of conditions encountered in practice. Nevertheless, there is really no alternative to correlating "a" alone because of the lack of available information about the initial disturbance level $(u'/U)_i$ for most of the transition data given in the literature. (Note that a separate value of $(u'/U)_i$ is required for each frequency receiving amplification.)

6.5.3.2 Application of Smith's method to transition in steady flow

Smith and Gamberoni (57) used Pretsch's (58) charts for the stability characteristics of Falkner-Skan profiles having temporal disturbances to evaluate the "apparent" amplification ratio of Tollmien-Schlichting waves at the transition point, i.e.

$$a(t) = \exp \int_{t_i}^{t_t} \beta_i dt \qquad (6.3)$$

where $\beta_i$ is the temporal amplification rate, and the integration is carried out over the time interval required for the disturbance waves to travel from the neutral stability point to the transition point. (The term "apparent" is

used as a reminder that the linearised stability theory is strictly applicable only to the forward 80% or so of the instability region, where the disturbances remain small and two-dimensional.) As $\beta_i$ is a function of the disturbance frequency as well as the boundary layer Reynolds number, it is necessary to calculate a(t) for all frequencies in the range which receive amplification before the maximum value of a(t) at the transition point can be determined.

The wide range of experimental data examined in Ref. 57 gave maximum values of a(t) at the transition point in the range of $e^{4.2}$ to $e^{20.9}$. But for cases in which the level of free stream turbulence was reasonably low, the values of a(t) at transition appeared to lie around $e^{9}$, and the relation

$$a(t)_{max} = \left\{\exp \int_{t_i}^{t_t} \beta_i dt\right\}_{max} = e^{9} \qquad (6.4)$$

was therefore suggested by Smith and Gamberoni as an appropriate transition criterion under these conditions. In 31 cases of transition on two-dimensional bodies in flight and in low-turbulence wind tunnel tests examined by Smith (56), Equation 6.4 was found to predict the transition Reynolds number $Re_{x_t}$ with a standard deviation of 18.5%.

Smith (56) also applied the criterion $\int \beta_i dt = 9$ to several cases of similar flows (corresponding to constant values of Hartree's (59) pressure gradient parameter $\beta$) and found that the calculated values of $Re_{\theta_t}$ and $Re_{x_t}$ lay very close to the empirical curve of Michel (55) described previously in Section 6.5.2. This result demonstrated that Michel's correlation could be explained on the basis of stability theory. However, Smith cautioned that the use of Michel's method for predicting transition should be limited to cases where the surface pressure distribution resembled those used in obtaining the original correlation.

The original analysis of Smith (56, 57) which has been described above assumed the boundary layer disturbances were growing with respect to time. However, it was later demonstrated by Gaster (60) that the observed disturbances in the experiments of Schubauer and Skramstad (40) indicated transition arising from the growth of spatial disturbances. This led Jaffe, Okamura and Smith (61) to attempt a transition correlation based on the apparent amplification ratio

$$a(x) = \exp\left\{-\int_{x_i}^{x_t} \alpha_i dx\right\} \qquad (6.5)$$

where $\alpha_i$ is the spatial amplification rate, which, like $\beta_i$, depends on both the disturbance frequency and the boundary layer Reynolds number. Jaffe et al. applied the stability calculations of Wazzan, Okamura and Smith (62, 53) for Falkner-Skan profiles subject to spatial disturbances, and evaluated the values of a(x) at the observed transition locations from a limited number of low turbulence tests. The maximum value of a(x) (corresponding to the disturbance frequency receiving the most amplification) was found to range between

8.3 and 12.1 in the two-dimensional flow cases examined. This suggested the use of the relation

$$a(x)_{max} = \left[\exp\left\{-\int_{x_i}^{x_t} \alpha_i \, dx\right\}\right]_{max} = e^{10} \qquad (6.6)$$

as a transition criterion, with the reservation that free stream turbulence and surface roughness effects would be expected to reduce $a(x)_{max}$ below $e^{10}$. In 13 cases of transition on two-dimensional bodies under conditions of low free stream turbulence, Jaffe et al. found that Eqn. 6.6 predicted the transition Reynolds number $Re_{x_t}$ with a standard deviation of 8.3%.

6.5.3.3 Application of Smith's method to transition in oscillating flow

Obremski and Morkovin (49) used a generalised version of Smith's method to investigate the stability of an unsteady, periodic boundary layer on a flat plate, which had earlier been examined experimentally by Obremski and Fejer (44) (see Sections 6.2.2.2 and 6.2.3.2). This flow was generated by imposing sinusoidal oscillations on the mainstream velocity, so that the external flow was given by

$$U = U_o(1 + N_A \sin\omega t) \qquad (6.7)$$

After constructing the instantaneous boundary layer velocity profiles at various times $\omega t$ during the oscillation cycle for selected values of the parameters $N_A$ and $\omega x/U_o$, Obremski and Morkovin used the computer program of Landahl (63) to derive the stability characteristics of these profiles; the results are tabulated in Ref. 53. A quasi-steady analysis was then applied to calculate the spatial amplification histories of disturbances originating at different points in the oscillation cycle; it was assumed that the instantaneous amplification rate of disturbances within the unsteady boundary layer was identical to that obtained in a steady boundary layer having the same velocity profile (i.e. that the amplification rate was determined only by the local instantaneous vorticity distribution). Calculations were performed for free stream oscillations in both the high and low ranges of non-steady Reynolds number $(Re)_{NS}$ defined in Section 6.2.2.2.

The values of amplification ratio at the transition point $x_t$ observed in Ref. 44 were computed for neighbouring frequencies in the range of interest, and the dominant disturbance frequency (i.e. that having the maximum value of $a(x)$) was determined; this was always within 10% of the observed disturbance frequency given in Ref. 44. The variation of the calculated amplification ratio with the phase of the free stream oscillation correctly predicted the formation of a disturbance wave packet in the trough and the phase advance of its maximum at higher Reynolds numbers (as shown in Fig. 6.5). The calculated values of amplification ratio were also consistent with the apparent

upstream movement of the leading edge of a nascent turbulent burst during the creative mode of turbulent spot development which was discussed in Section 6.2.3.2.

For the two cases of periodic transition ($(Re)_{NS} > 27,000$) which were analysed in Ref. 49, the theoretical amplification ratio for the dominant disturbance frequency at the experimentally determined transition Reynolds number was $e^{4.9}$ and $e^{6.8}$; in this regime, amplification and breakdown occurred within half the oscillation period, approximately. Besides differing between each other, the calculated amplification ratios for the periodic transition cases are much smaller than the value of $e^{10}$ suggested by Jaffe et al.(61) as a criterion for transition in steady flow under conditions of low free stream turbulence. Obremski and Morkovin suggested that the difference between the calculated amplification ratios could have been partly attributable to the difference in the transition Reynolds number for these two runs; this, in turn, could have arisen from dissimilarities in the disturbance environment under different tunnel operating conditions (see also Ref. 64). The following possible explanations were proposed for the lower values of amplification ratio observed during periodic transition:

(a) errors in the quasi-steady theoretical flow model;

(b) unknown destabilising agents in the experimental environment;

(c) the unknown conditions for the initiation of turbulence becoming more permissive for the vorticity distributions associated with the velocity profiles in the supercritical $(Re)_{NS}$ range (see also Section 6.8.1).

In the lower non-steady Reynolds number regime ($(Re)_{NS} < 25,000$) the calculated amplification ratio of the dominant frequency appeared insufficient to cause transition within a single cycle of the free stream oscillation, and the disturbance was subsequently attenuated during the accelerating segment of the cycle. This caused the dominant disturbance frequency to shift to lower values and permitted the disturbance to endure additional cycles of the free stream oscillation before the critical amplification ratio was reached further downstream at a rather higher Reynolds number (which probably explains why the transition Reynolds number becomes independent of $N_A$ in this case). The maximum amplification ratio was calculated to occur near $\omega t = 0, \pi/2$, which was consistent with the observed trend for turbulent breakdown to occur near the crest of the free stream oscillation in the low $(Re)_{NS}$ regime.

6.5.3.4 Concluding remarks

Many features of the transition behaviour in both steady and non-steady flows can now be qualitatively described from the results of linearised stability theory as used by Smith's method or its generalisations; however, the appropriate value of apparent amplification ratio at the transition point remains unknown in the general case. A constant value of $e^{10}$ might suffice for conditions of low free stream turbulence, but the critical amplification ratio will in general vary with the transition Reynolds number,

pressure gradient, initial disturbance spectrum, and the behaviour of the non-linear disturbances which finally lead to breakdown. In addition to this uncertainty, Smith's method requires a considerable amount of computation, especially in the non-steady flow case.

Because of these difficulties, and in view of the success achieved with simpler empirical methods of predicting transition on the compressor blades, no comparison of Smith's method with experiment was made in the present investigation. The purpose in reviewing the method here has been to demonstrate the theoretical basis underlying empirical transition criteria, and to give further insight into the transition process in unsteady flow, which has an important influence on the boundary layer development over turbomachine blades.

### 6.5.4 Granville's Method

#### 6.5.4.1 Introduction

Granville (65) proposed a method of predicting transition which uses a purely empirical correlation to determine the instability length, $(x_t - x_i)$. The correlation expresses the difference in momentum thickness Reynolds number between the instability and transition points, $(Re_{\theta_t} - Re_{\theta_i})$, as a function of the mean pressure gradient parameter over this interval, $k_m$, which is defined by

$$k_m = \left\{(\theta^2/\nu)(dU/dx)\right\}_m = \left\{\int_{x_i}^{x_t} k\, dx\right\}/(x_t - x_i) \qquad (6.8)$$

Granville found that the data from transition measurements in two-dimensional flow on smooth walls both in flight (66, 67) and in low-turbulence wind tunnel tests (40, 68, 69) gave a single curve of $(Re_{\theta_t} - Re_{\theta_i})$ against $k_m$ which has been reproduced in Fig. 6.15.

In flows with a low free stream turbulence level, the prediction of transition by Granville's method involves first the calculation of the instability point $x_i$ to give $Re_{\theta_i}$; the laminar boundary layer calculation is then continued until $(Re_\theta - Re_{\theta_i})$ attains the critical value specified by Fig. 6.15, indicating that the transition point $x_t$ has been reached. To the present author, this method is more satisfying than Michel's (55) in that the instability point is calculated directly from laminar stability theory, so that the use of empirical data is restricted to the instability region. As Michel's method predicts $Re_{x_t}$ directly, it must contain implicit correlations for both the instability point and the instability length.

Granville also suggested a method of allowing for the effects of free stream turbulence on transition, based on the observed influence of turbulence for a boundary layer on a flat plate in nominally zero pressure gradient. The data of various workers (40, 70, 71) was correlated by plotting $(Re_{\theta_t} - Re_{\theta_i})$

against turbulence level, as shown in Fig. 6.16; this gave a single curve which showed the transition point to approach the steady flow instability point as the turbulence level increased. (It is noted that Granville used Schlichting's (72) value of $Re_{\theta_i} \simeq 250$ rather than Tollmien's (73) value of 163 which is in much better agreement with the experiments of Ref. 40, so that the values of $(Re_{\theta_t} - Re_{\theta_i})$ in Fig. 6.16 could be rather low.) For transition in a boundary layer with a pressure gradient, Granville assumed that $(Re_{\theta_t} - Re_{\theta_i})$ would vary with turbulence level in a similar manner to that observed in the zero pressure gradient case.

6.5.4.2 Comparison with the compressor blade measurements

It is seen from Fig. 6.15 that the transition data from the present investigation falls outside the range of Granville's original correlation because of the high adverse pressure gradients obtained on the stator blade suction surface. The measured values of $(Re_{\theta_t} - Re_{\theta_i})$ are very small, and appear to fall well below an extrapolation of Granville's transition data. Thus the use of Granville's low turbulence transition correlation would seriously overestimate the transition Reynolds number on the compressor blades.

The individual data points from the compressor blade measurements have been replotted on an expanded scale in Fig. 6.17. Although they do not all fall on a single curve, the following general trends can be noted:
(i) $(Re_{\theta_t} - Re_{\theta_i})$ becomes smaller as the blade chord Reynolds number, $Re_c$, is reduced;
(ii) there is a rough correlation of $(Re_{\theta_t} - Re_{\theta_i})$ against $k_m$ for the data obtained at any particular compressor speed, which corresponds to a narrow range of $Re_c$;
(iii) the correlation noted in (ii) above indicates that $(Re_{\theta_t} - Re_{\theta_i})$ increases as the pressure gradient becomes more adverse, a trend which is opposite to that of the single curve obtained by Granville.

For a fixed value of incidence, the pressure distribution and the instability point on the stator suction surface did not vary greatly with compressor speed; thus the instability length $(x_t - x_i)$ should have increased as $Re_c$ was reduced if $(Re_{\theta_t} - Re_{\theta_i})$ depended on the pressure gradient parameter $k_m$ alone. However, the instability length remained approximately constant as $Re_c$ varied by a factor of five. It is tempting at first to ascribe this behaviour, together with the low values of $(Re_{\theta_t} - Re_{\theta_i})$ observed on the stator blade, to the effects of free stream turbulence, which varied from around 2% at a compressor speed of 750 rpm to 6% at 150 rpm. But Granville's method of allowing for free stream turbulence effects (based on Fig. 6.16) indicates that the transition point on the stator blade should always lie within a few percent of chord from the instability point for turbulence levels greater than 2%; Table 6.2 shows that this prediction grossly underestimates the observed instability lengths.

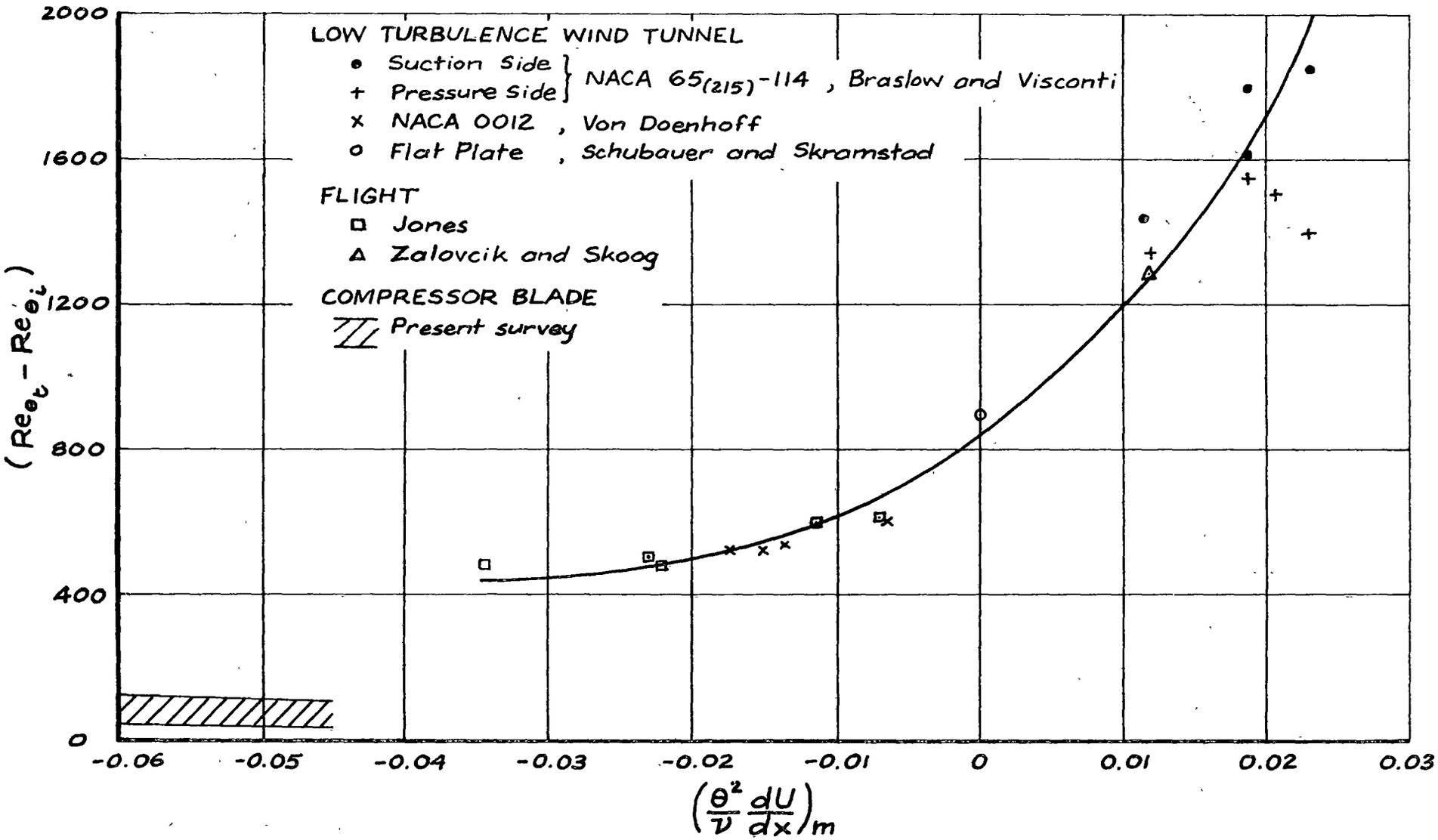


Fig. 6.15 Granville's Transition Correlation

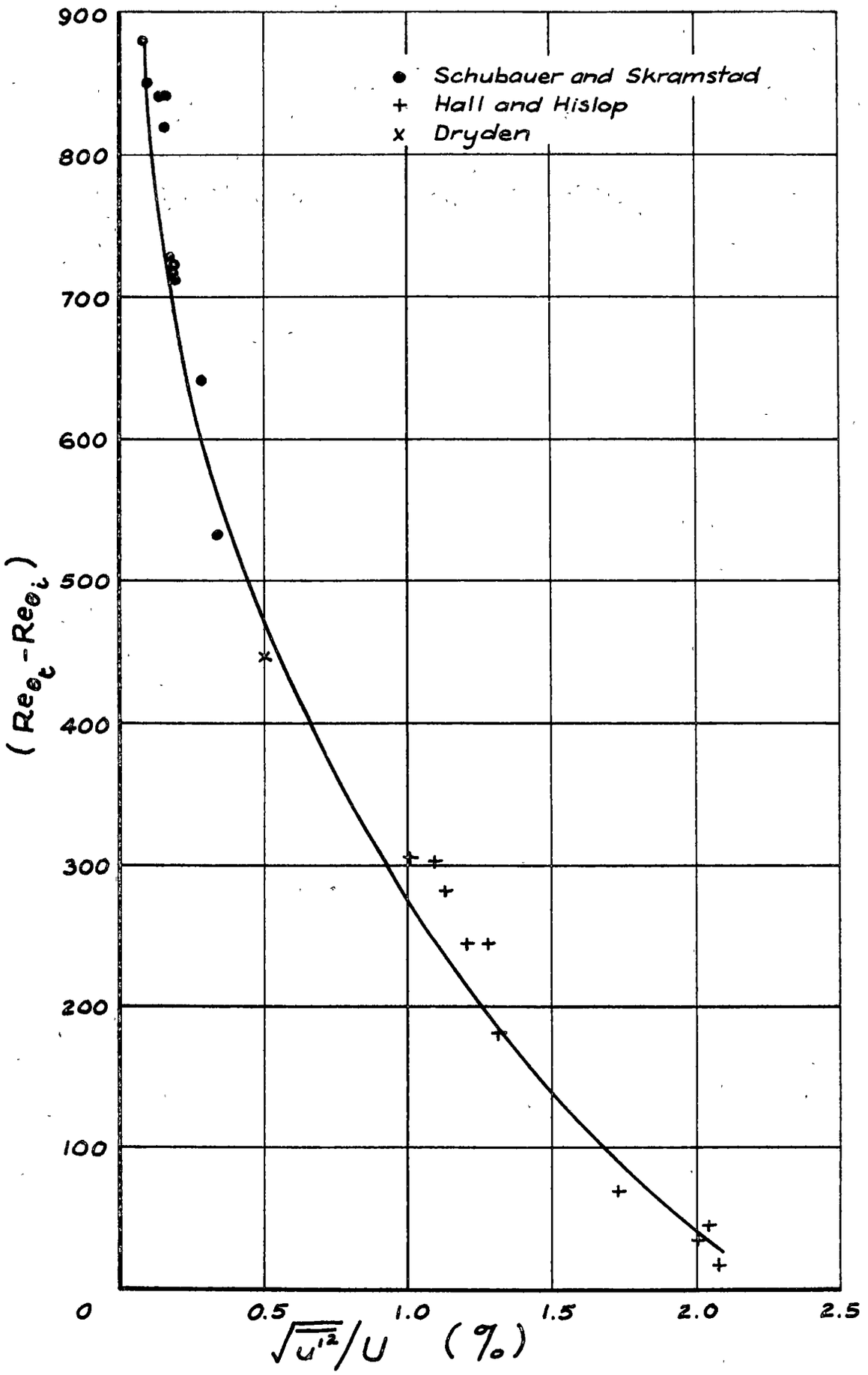


Fig. 6.16 Effect of Free Stream Turbulence Level on Transition on a Flat Plate. From Granville (65)

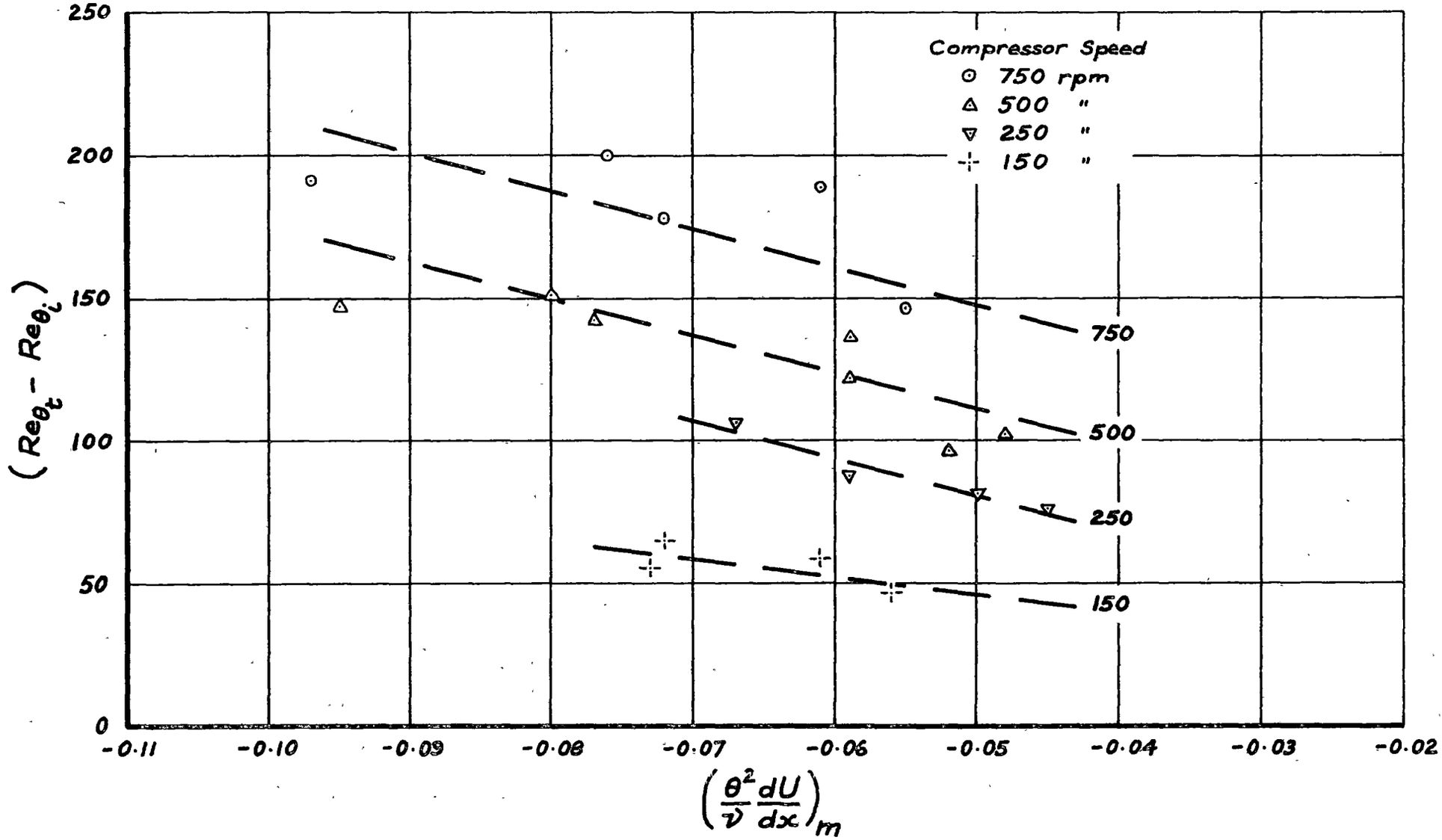


Fig. 6.17 Transition on Stator Blade Suction Surface : Granville's Correlation

The above results could be explained by:
(a) free stream turbulence affecting the transition process on the compressor blade in a dissimilar manner to that observed on a flat plate; or
(b) the transition process being dependent on some factor other than pressure gradient and free stream turbulence level; or
(c) a combination of factors (a) and (b).
Whichever alternative is selected, it must be concluded that Granville's method does not adequately describe the transition behaviour on the blades of the research compressor.

6.5.5 Constant Transition Reynolds Number Method

Some workers have used a constant value of boundary layer Reynolds number as a transition criterion. Gostelow et al.(74), for example, assumed $Re_{\theta_t} = 500$ following the suggestion of Preston (75) that the minimum value of $Re_\theta$ for fully developed turbulent flow on a flat plate (in zero pressure gradient) should be about 320. However, Smith (56) has pointed out that a constant Reynolds number assumption does not allow for variations in pressure distribution changing the value of $Re_{\theta_t}$, and this observation is fully confirmed by the results of the present investigation; the criterion $Re_{\theta_t}$ = constant completely fails to describe the movements of the transition point on the stator blade with changes in blade incidence.

It is noted that the minimum value of $Re_\theta$ for fully developed turbulent flow defined by Preston lies close to the Reynolds number at which the inner and outer similarity regions of the boundary layer overlap to produce a logarithmic velocity distribution near the wall. But the transition point in the present investigation is taken as the streamwise position where turbulent flow first appears, and this necessarily precedes the establishment of a logarithmic wall layer (see Section 7.3.2 for a more detailed discussion); the minimum value of $Re_{\theta_t}$ observed on the stator blade suction surface was about 130.

6.5.6 Other Methods

Various other approximate methods of predicting the transition point have been proposed, such as assuming that transition occurs close to the instability point or laminar separation point. Once again, it can be remarked that such methods are unlikely to be general, and do not describe the transition behaviour on the stator blade at all well (see Tables 5.1, 5.2, and 6.2). The instability, separation, and transition points will only lie close together in a limited range of flow situations, e.g. at very high incidences when they will all be located near the leading edge of a body on the suction surface.

## 6.6 A New Empirical Correlation of the Instability Length

### 6.6.1 Correlation of $(Re_{\theta_t} - Re_{\theta_i})/Re_{\theta_m}$

It has already been remarked in Section 6.5.4.2 that Granville's (65) scheme of correlating $(Re_{\theta_t} - Re_{\theta_i})$ against $k_m$ led to a different curve for each compressor speed in the case of the transition measurements on the stator blade. A closer study of these results indicated that the values of $(Re_{\theta_t} - Re_{\theta_i})$ for a given blade incidence varied approximately as the square root of the blade chord Reynolds number; this was a natural consequence of the instability and transition points both remaining almost fixed, and the value of $Re_\theta$ for the laminar boundary layer in the (nearly) similar pressure distributions varying as $Re_c^{\frac{1}{2}}$.

The above observation suggested that the curves of $(Re_{\theta_t} - Re_{\theta_i})$ for different speeds could be brought together through division by some quantity varying as $Re_c^{\frac{1}{2}}$. An obvious parameter to choose was the boundary layer Reynolds number at some point over the instability length, as this was known to influence the rate at which disturbances were amplified within the laminar boundary layer. The best results were obtained by using the mean value of $Re_\theta$ over the instability length, defined by

$$Re_{\theta_m} = \left\{ \int_{x_i}^{x_t} Re_\theta dx \right\} / (x_t - x_i) \qquad (6.9)$$

Instead of using $k_m$, as in Granville's correlation, the mean value of shape factor H over the instability length, defined by

$$H_m = \left\{ \int_{x_i}^{x_t} H \, dx \right\} / (x_t - x_i) \qquad (6.10)$$

was chosen as a pressure gradient parameter. The main reason for doing this was that H, being an integral quantity, could be determined experimentally to a greater accuracy than $k = (\theta^2/\nu)(dU/dx)$, whose calculation involved differentiating the measured values of U.

A plot of $(Re_{\theta_t} - Re_{\theta_i})/Re_{\theta_m}$ against $H_m$ for the transition data from the compressor blade measurements gave a single curve, with a standard deviation of about 10%. This good agreement encouraged a re-examination of the data used by Granville, and a similar correlation was again obtained*, there being no apparent difference between the correlation for free flight and low turbulence wind tunnel tests and the compressor blade studies (with the single exception of the flat plate measurements of Schubauer and Skramstad (40)). The new correlation is shown in Fig. 6.18, and a least squares linear fit to the 37 data points gives

$$(Re_{\theta_t} - Re_{\theta_i})/Re_{\theta_m} = 1.70 - 0.32 \, H_m \qquad (6.11)$$

---

* Values of $Re_\theta$ and H were calculated by Thwaites's (10) method from the surface pressure distributions given by the various authors.

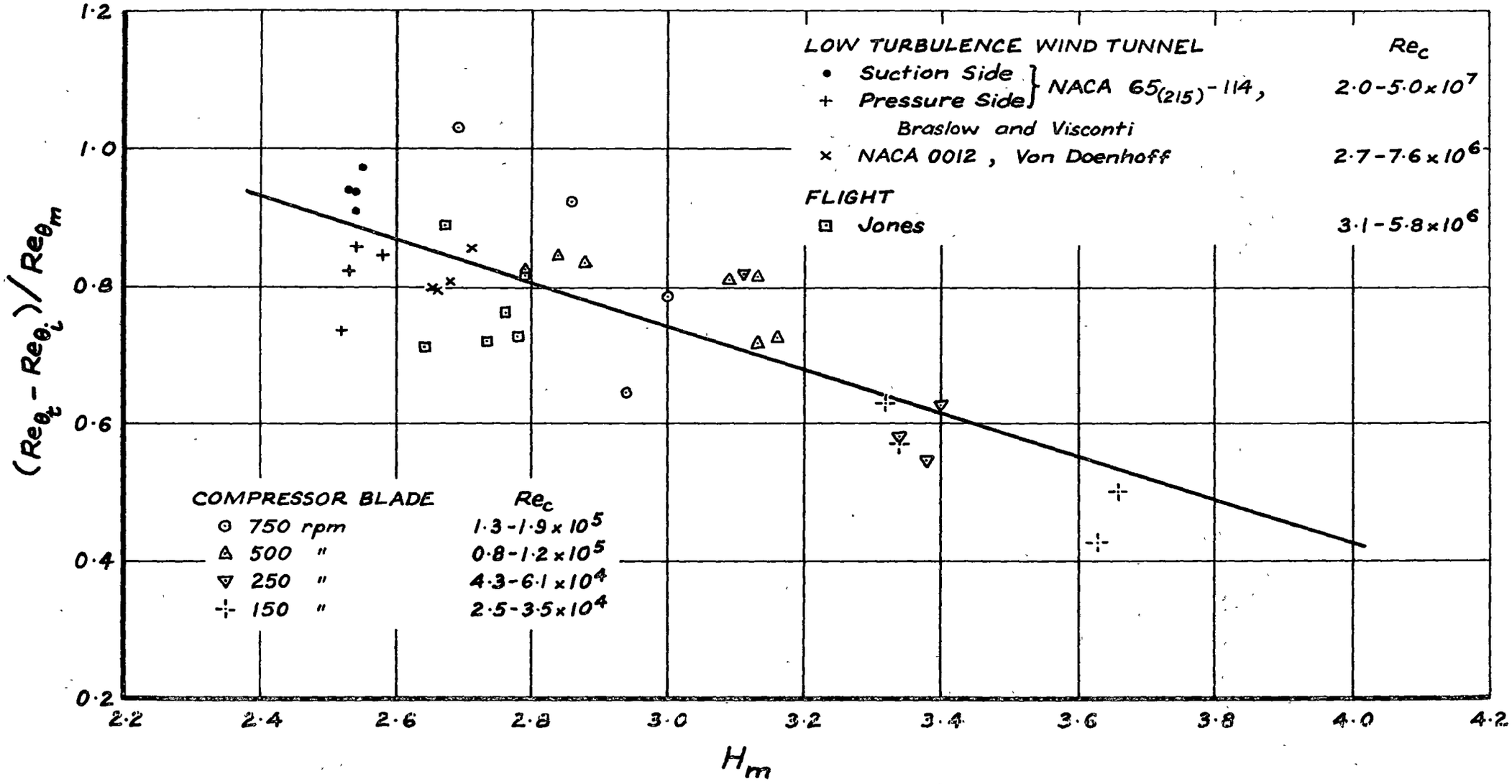


Fig. 6.18 Correlation of Instability Length : $(Re_{\theta_t} - Re_{\theta_i})/Re_{\theta_m} \sim H_m$

with a standard deviation of 0.09 in $(Re_{\theta_t} - Re_{\theta_i})/Re_{\theta_m}$. For the compressor blade measurements, this deviation is little greater than the possible experimental error. The correlation shown in Fig. 6.18 covers a remarkably wide range of external flow variables, with chord Reynolds numbers between $3 \times 10^4$ and $5 \times 10^7$, apparent turbulence levels up to 6%, and both favourable and adverse pressure gradients. The transition data from the compressor blade measurements contains a number of points involving separated laminar flow over part of the instability length, with local values of shape factor H reaching 6.

Schubauer and Skramstad (40) found that the transition Reynolds number, $Re_{x_t}$, for flow on a flat plate in nominally zero pressure gradient could be increased to $2.8 \times 10^6$ when the free stream turbulence level was reduced to 0.1%; even higher values of $Re_{x_t}$, up to $5 \times 10^6$, were achieved by Spangler and Wells (64) when acoustic disturbances were suppressed as well. The value of $Re_{x_t} = 2.8 \times 10^6$ corresponds to $(Re_{\theta_t} - Re_{\theta_i})/Re_{\theta_m} \simeq 1.10 - 1.25$, there being some uncertainty about the appropriate value of $Re_{\theta_i}$ due to the streamwise pressure gradient not being exactly zero (see also Section 6.7.3); this is significantly higher than the value of $(Re_{\theta_t} - Re_{\theta_i})/Re_{\theta_m} = 0.87$ obtained from Equation 6.11 after substituting the appropriate value of $H_m = 2.6$ for the zero pressure gradient case. Thus it appears that a reduction of the initial disturbance level can lead to an instability length markedly greater than that indicated by Equation 6.11.

In view of this observation it is most surprising that the data correlated in Fig. 6.18 shows a standard deviation of only 10% or so when the free stream turbulence level ranged from very small values for the wind tunnel and flight tests to over 6% for some of the transition measurements on the stator blade. As the amplitude of disturbances at the transition point depends on the initial disturbance level and the amplification ratio over the instability length (which is a function of both Reynolds number and pressure gradient), the following explanations for the success of the correlation are possible:
(i) for all cases considered in Fig. 6.18 the effective initial disturbance level was approximately the same, and the free stream turbulence had little net effect on the amplification ratio, or
(ii) the effects of increasing turbulence level as the compressor speed was reduced were compensated by the effects of changing Reynolds number ( or some other factor) so that the values of $(Re_{\theta_t} - Re_{\theta_i})/Re_{\theta_m}$ on the stator blade were fortuitously similar to those obtained by other workers in low turbulence tests.
In the author's opinion, the overall weight of evidence considered in the present study tends to favour the first explanation. This conclusion implies that the unsteady effect of the rotor wakes, which formed the major component of the free stream turbulence level in the compressor, did not greatly influence the location of the transition point on the stator blade. This is a most unexpected result, but as shown previously in Section 6.4.2.3 it can be very largely reconciled with other recent experimental and theoretical work on transition in unsteady flow (Refs. 43, 44, and 49). Further discussion

of the effects of free stream turbulence on transition is left until Section 6.8.

### 6.6.2 Correlation of $(x_t - x_i)/\theta_m$

#### 6.6.2.1 Introduction

A rather more useful version of the transition correlation described by Equation 6.11 will now be developed. This involves correlating the instability length $(x_t - x_i)$ itself, rather than the change in $Re_\theta$ over this interval. The derivation commences by writing

$$d(Re_\theta)/dx = (U/\nu)(d\theta/dx) + (\theta/\nu)(dU/dx) \qquad (6.12)$$

and substituting for $d\theta/dx$ from the two-dimensional boundary layer momentum integral equation (Eqn. 4.1), which leads to the general relation

$$d(Re_\theta)/dx = \left\{(H + 3)k + \tau_w\theta/\mu U\right\}/\theta \qquad (6.13)$$

Following Thwaites's (10) single-parameter method of calculating the laminar boundary layer, both k and $(\tau_w\theta/\mu U)$ are expressed as functions of H, giving

$$d(Re_\theta)/dx = \left\{(H + 3)f_1(H) + f_2(H)\right\}/\theta = f_3(H)/\theta \qquad (6.14)$$

To a first approximation, therefore, it is possible to write

$$\Delta Re_\theta \simeq (\Delta x/\theta_m)\, f_3(H_m) \qquad (6.15)$$

where $\theta_m$ and $H_m$ are mean values of the respective quantities over the interval $\Delta x$.

Finally, rewriting Equation 6.11 as

$$(Re_{\theta_t} - Re_{\theta_i})/Re_{\theta_m} = f_4(H_m) \qquad (6.16)$$

and substituting for $(Re_{\theta_t} - Re_{\theta_i})$ from Equation 6.15 gives

$$\left\{(x_t - x_i)/\theta_m\right\} f_3(H_m)/Re_{\theta_m} = f_4(H_m) \qquad (6.17)$$

$$\text{i.e. } (l_i/\theta_m)/Re_{\theta_m} = f_5(H_m) \qquad (6.18)$$

where $l_i = (x_t - x_i)$ is the instability length.

Equation 6.18 suggests that a plot of the parameter $(l_i/\theta_m)Re_{\theta_m}^{-1}$ against the pressure gradient parameter $H_m$ should provide an alternative means of correlating the instability length, and this is confirmed by Fig. 6.19; a

good fit to the data is obtained from the hyperbolic curve

$$(l_i/\theta_m)/Re_{\theta_m} = (0.606H_m - 0.414)/(H_m - 2.29) \qquad (6.19)$$

The new correlation indicates that the non-dimensional instability length, $l_i/\theta_m$, is a function of the mean boundary layer Reynolds number, $Re_{\theta_m}$, and the mean shape factor, $H_m$, over this interval. This is physically quite reasonable, as the pressure gradient (which is related to $H_m$) and the Reynolds number are known to be the most significant factors determining the rate of amplification of small disturbances within the laminar boundary layer. The sharp increase in $(l_i/\theta_m)/Re_{\theta_m}$ as the pressure gradient becomes negative is consistent with the lower amplification rate obtained in accelerating flow. For large positive pressure gradients, $(l_i/\theta_m)/Re_{\theta_m}$ appears to approach a roughly constant value, suggesting that the amplification rate does not vary greatly after separation.

6.6.2.2 Application to flows involving separation bubbles

Horton's (38) model of the laminar separation bubble, described previously in Section 5.6.5, assumes the surface pressure to remain constant after separation, and this leads to constant values of $\theta$ and $Re_\theta$ in the separated laminar shear layer. If the transition correlation of Equation 6.11 (which indicates the change in $Re_\theta$ over the instability length) was used in conjunction with Horton's flow model, there would be no solution for the transition point unless it preceded separation (1); this is obviously unrealistic. But with the modified correlation of Equation 6.19 (which indicates the instability length itself) it becomes theoretically possible to solve for the transition point even when this occurs downstream of the laminar separation point. It was therefore decided to plot some values of $(l_i/\theta_m)/Re_{\theta_m}$ from Gaster's (34) separation bubble measurements to see whether any useful extension of the correlation given by Equation 6.19 could be gained. There was admittedly little theoretical reason for doing this, since Equation 6.14 used in deriving the new correlation is valid only for attached boundary layer flow; but there was some experimental justification, as many of the data points from the compressor blade measurements corresponded to flows in which separation was present. The values (2) of $(l_i/\theta_m)/Re_{\theta_m}$ from Gaster's Series II measurements (in which $H_m$ varied between 4.5 and 8.2) were found to be essentially constant,

---

(1) This restriction does not apply when calculating the transition point from a measured surface pressure distribution, as both p and $Re_\theta$ can continue to increase downstream of separation in a real flow.

(2) Values of $\theta$ and $Re_\theta$ were calculated by Thwaites's (10) method from the surface pressure distributions given in Ref. 34. For the thinnest boundary layers there were some discrepancies between the calculated values of $\theta$ and the experimental values given by Gaster; as it appeared that these could have been due mainly to wall proximity effects on the hot wire readings, the calculated values were used in all cases.

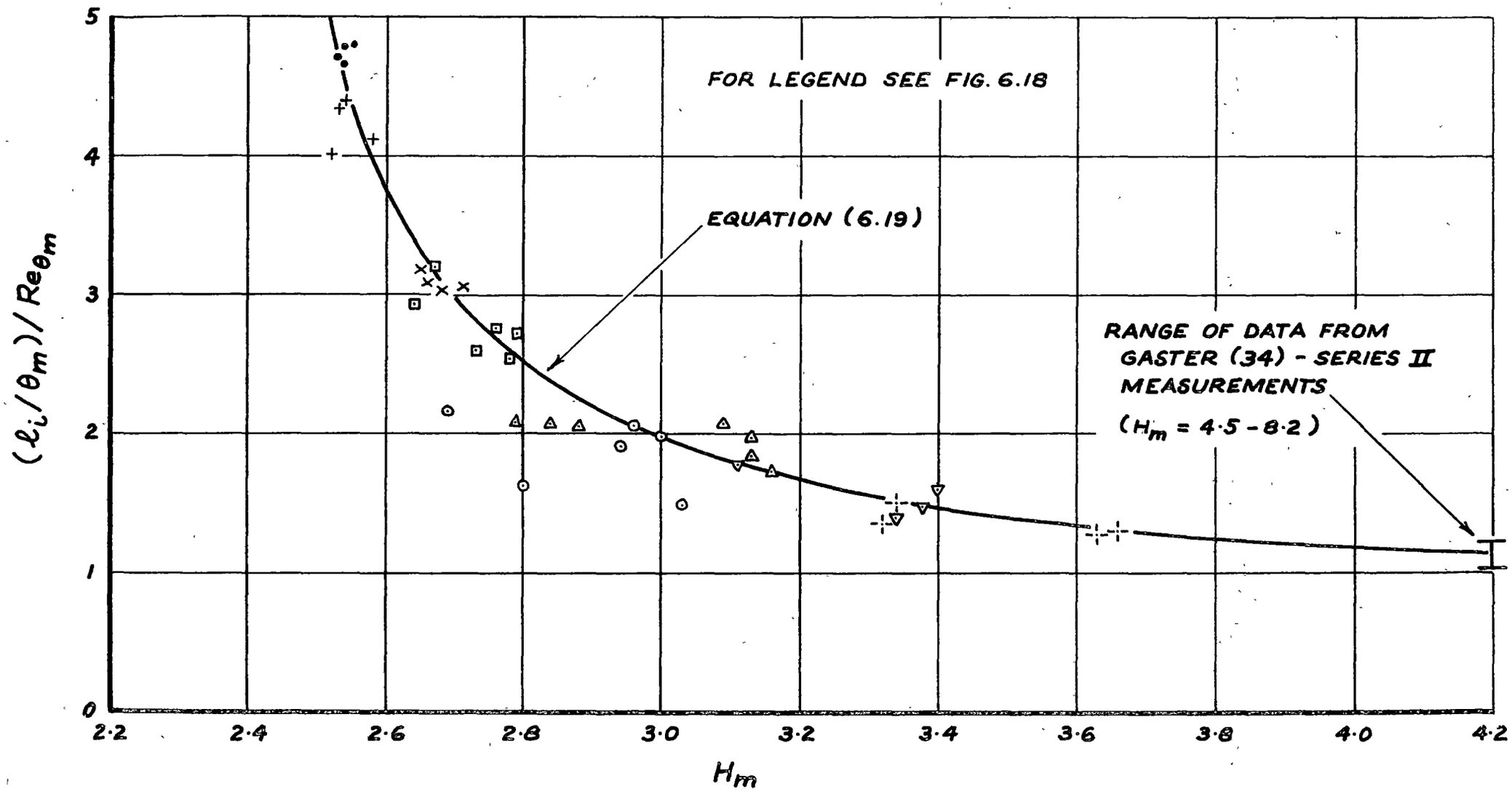


Fig. 6.19 Correlation of Instability Length : $(l_i/\theta_m)/Re_{\theta_m} \sim H_m$

with an average value of 1.12 (which is the value given by Equation 6.19 for $H_m = 4.20$); the scatter of about ± 10% in these points was no greater than that of the other data correlated by Equation 6.19. It therefore seems reasonable to extend the use of this correlation to predicting transition in flows involving separation bubbles by means of the additional relation

$$(l_i/\theta_m)/Re_{\theta_m} = 1.12 \qquad (H_m > 4.20) \qquad (6.20)$$

Equation 6.19 is employed for values of $H_m \leq 4.20$.

It is noted in conclusion that a significant length of unstable laminar boundary layer existed upstream of the separation point for all of the data correlated by Equations 6.19 and 6.20; the frequency of disturbances leading to transition was quite probably selected in this attached flow region. It might therefore be inadvisable to apply the above correlation to separated flow cases in which the instability and separation points are nearly identical, as the boundary layer stability characteristics would then play a less important role in determining the instability length.

6.6.3 Comparison with Other Empirical Transition Correlations

Multiplying Equation 6.18 by $U_t/\nu$, and making the substitutions

$$l_i = C_1 x_t \quad ; \quad U_t = C_2 U_m \quad ; \quad Re_{\theta_t} = C_3 Re_{\theta_m} \qquad (6.21)$$

leads after a little manipulation to the expression

$$Re_{\theta_t} = C_3 \left\{ C_1/(C_2 f_5(H_m)) \right\}^{\frac{1}{2}} Re_{x_t}^{\frac{1}{2}} \qquad (6.22)$$

in which the parameters $C_1$, $C_2$, and $C_3$ are expected to depend on the form of the surface pressure distribution. Taking the case of zero pressure gradient as some sort of mean of the conditions encountered in practice gives $C_2 = 1$ and $f_5 = 3.8$ (from Eqn. 6.19 with $H_m = 2.59$); an analysis of the data correlated in the present survey indicates suitable rough average values for $C_1$ and $C_3$ of 0.8 and 1.4, respectively. Finally, making all these substitutions in Equation 6.22 gives

$$Re_{\theta_t} = 0.643\, Re_{x_t}^{\frac{1}{2}} \qquad (6.23)$$

It is seen from Fig. 6.20 that Equation 6.23 lies quite close to the empirical curve obtained by Michel (55). Thus Michel's transition correlation could be construed as a particular case of the correlation shown in Fig. 6.19, corresponding to a narrow range of pressure gradient; this leads to the conclusion that the experimental points shown in Fig. 6.14 lay above the curve proposed by Smith (56) because of the high adverse pressure gradients

on the compressor blade (which give lower values of $f_5$ in Eqn. 6.22). The link with Michel's correlation which has just been demonstrated strengthens the opinion expressed in Section 6.6.1 that the variation with compressor speed in the values of $(Re_{\theta_t} - Re_{\theta_i})$ measured on the stator blade (see Fig. 6.17) was due to Reynolds number effects, rather than to changes in the free stream turbulence level.

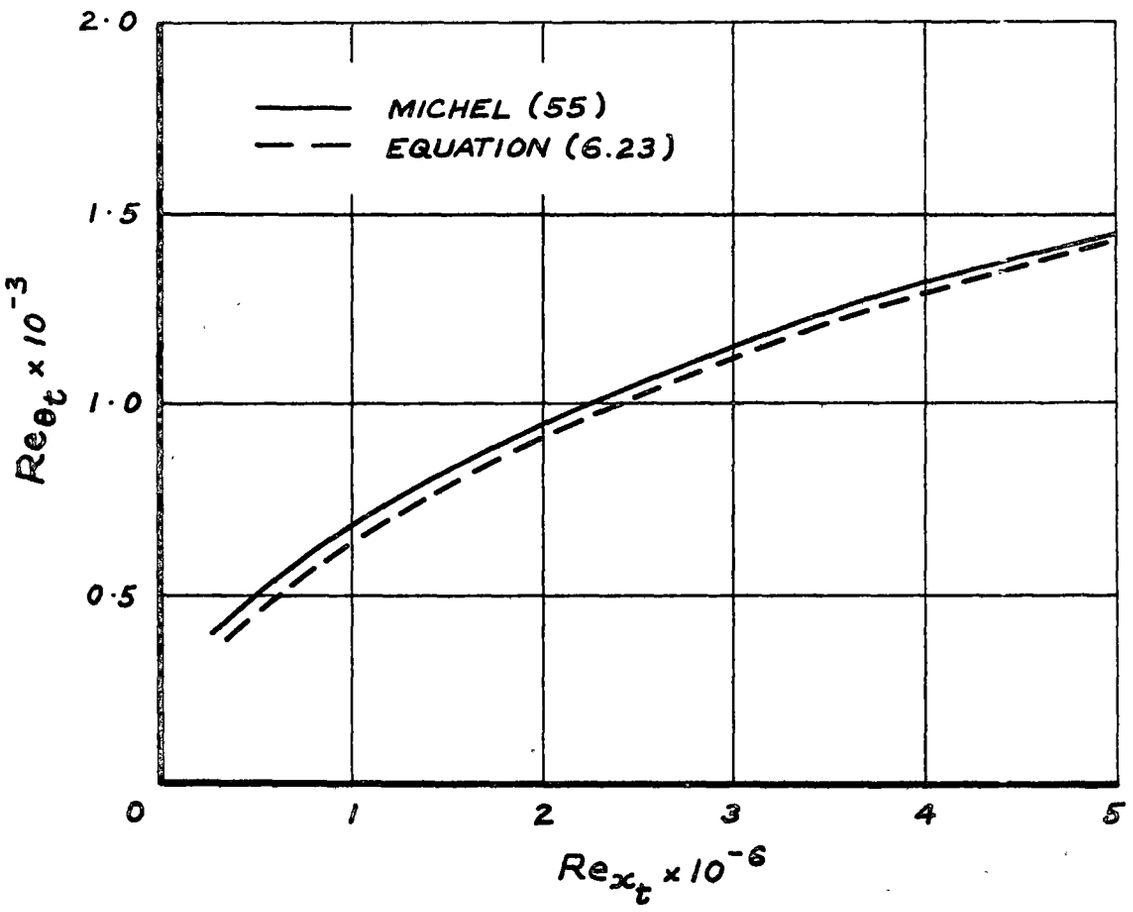


Fig. 6.20 Comparison of Equation 6.23 with Michel's Transition Correlation

Substituting for $H_m$ in terms of $k_m$ in Equation 6.11, and putting $Re_{\theta_m}$ constant leads to the expression

$$(Re_{\theta_t} - Re_{\theta_i}) = f(k_m) \qquad (6.24)$$

which is of the same form as the empirical correlation proposed by Granville (65). Thus the latter could be thought of as a particular case of the correlation shown in Fig. 6.19, corresponding to a limited range of boundary layer Reynolds number.

To sum up, it seems that the correlation for the instability length which has been developed from the present investigation of transition on a compressor blade is a generalised version of the earlier empirical correlations proposed by Michel and Granville. The new correlation appears to

take greater account of the effects of Reynolds number and pressure gradient on the transition process.

6.6.4 Application of the New Correlation

The following steps are required to determine the transition point, $x_t$, from the correlations for the instability length given by Equations 6.11 and 6.19:

(i) compute the development of the laminar boundary layer to locate the instability point, $x_i$, at which the local value of $Re_\theta$ becomes equal to the critical value obtained from Table 6.1. It is important to use these particular values of $Re_{\theta_{crit}}$ as they were the ones used in initially deriving the correlations for the instability length;

(ii) continue the computation of the laminar boundary layer (progressively calculating the mean values of $\theta$, $Re_\theta$, and H over the interval from the instability point) up to the streamwise position at which $(Re_\theta - Re_{\theta_i})/Re_{\theta_m}$ equals the value of $(Re_{\theta_t} - Re_{\theta_i})/Re_{\theta_m}$ from Equation 6.11 for the calculated value of $H_m$, or $\{(x - x_i)/\theta_m\}/Re_{\theta_m}$ equals the corresponding value of $(l_i/\theta_m)/Re_{\theta_m}$ from Equation 6.19; this is taken as the transition point, $x_t$.

In cases where laminar separation is predicted to precede transition and the surface pressure distribution is known from experimental results, the momentum integral equation could be used with $C_f = 0$ and a guessed distribution of H (e.g. taking H constant, or dH/dx constant equal to its value just upstream of separation) to estimate values of $\theta$ and $Re_\theta$ for the separated laminar shear layer. The fact that H is not known accurately is not greatly important, since neither of the quantities correlated by Equations 6.11 and 6.19 vary rapidly for values of $H_m$ near separation. Where the surface pressure distribution is not known, the simplest model is to assume $\theta$ and $Re_\theta$ remain constant after separation (see Section 5.6.5); Equation 6.11 then fails to give a solution for the transition point, and Equation 6.19, only, can be used.

The use of Equations 6.11 and 6.19 is restricted to two-dimensional flow situations in which the boundary layer is continuously unstable between the limits $x_i$ and $x_t$. (If amplification of disturbances was interrupted by a region of damping, so that there was more than one neutral stability point on the surface, it might be possible to recommence the transition calculation from the neutral stability point furthest downstream; however, there would be considerable doubt concerning the possible effects of disturbances amplified in the upstream instability region and not entirely eliminated in the intervening region of damping.) A detailed discussion of the influence of free stream disturbances on the validity of Equations 6.11 and 6.19 is rather too lengthy to give here, and will be left until Section 6.8.2.

To indicate the accuracy of the new correlations (Equations 6.11 and 6.19), the standard deviation of the calculated transition points from the positions measured experimentally has been given in Table 6.3 for some typical sets of data. The errors in the calculated transition points have been expressed both as a percentage of the measured value of $x_t$ (to enable a comparison with the results of Smith), and as a percentage of the aerofoil chord, c (to give a clearer indication of the likely accuracy of the overall boundary layer calculation).

Table 6.3

Differences between Calculated and Measured Transition Points

(Values of standard deviation)

| Data | No. of cases | Correlation Used | | | |
|---|---|---|---|---|---|
| | | Eqn. 6.11 | | Eqn. 6.19 | |
| | | (%c) | ($\%x_t$) | (%c) | ($\%x_t$) |
| NACA $65_{215}$-114 aerofoil Braslow & Visconti (68) | 8 | 6.1 | 17.4 | 6.1 | 21.5 |
| Present survey - stator blade Compressor speed 500 rpm | 7 | 3.9 | 8.5 | 6.1 | 13.1 |
| NACA 0012 aerofoil Von Doenhoff (69) | 4 | 3.5 | 10.0 | 3.2 | 8.8 |

The figures in Table 6.3 show that the present empirical methods of predicting transition are quite comparable in accuracy with the semi-empirical methods of Smith et al.(56, 57, 61) which were discussed in Section 6.5.3. There is a slight trend for the accuracy to decrease when transition occurs in accelerating flow, which is reflected in the wider scatter of the data in Figs. 6.18 and 6.19 at the lower values of $H_m$; this could be partly due to greater errors in determining $x_i$, as the critical value of $Re_\theta$ is much more sensitive to the local pressure gradient in accelerating flow.

The accuracy of the transition points obtained from Equation 6.19 is significantly poorer for the compressor blade data, but this reflects failures in the boundary layer calculation rather than errors in the transition correlation itself. In about half of these cases the laminar boundary layer is predicted to separate shortly before transition occurs, while the measurements show that separation is never actually reached; thus the calculated values of H and $H_m$ are too large, and the predicted transition point lies too far upstream. For flow cases not involving separation, the author feels that there will be little difference, on the average, between the transition points calculated from Equations 6.11 and 6.19.

## 6.7 Effects of the Surface Pressure Distribution on Transition

### 6.7.1 General Discussion

The streamwise pressure distribution over a body strongly influences both the location of the instability point and the length of unstable laminar flow required before transition occurs. Fig. 6.19 shows that the instability length increases markedly when the flow is accelerating ($H_m < 2.6$), and there will also be a greater length of stable laminar flow under these conditions because of the higher values of $Re_{\theta_{crit}}$ (see Table 6.1); conversely, both the stable and unstable laminar regions will become smaller in decelerating flow. These observations are in complete agreement with the comment of Stuart (39) that large positive pressure gradients accelerate transition, whilst negative gradients extend the region of laminar flow and cause the transition to turbulent flow to be more gradual when it eventually does take place.

The shape of the surface pressure distribution can influence the instability length in a rather more subtle manner by changing the mean values of momentum thickness and boundary layer Reynolds number over the unstable laminar flow region. A suction peak near the leading edge of a body will position the unstable laminar flow region well forward, so that the values of $\theta_m$ and $Re_{\theta_m}$ will be relatively small and the instability length, $l_i$, correspondingly short (according to Eqn. 6.19). As the suction peak is moved rearward, the transition process will occur at relatively higher values of $\theta_m$ and $Re_{\theta_m}$, and the instability length will increase, thus causing the transition point to move aft more rapidly than the instability point. This is illustrated by the transition measurements on the stator blade suction surface obtained in the present investigation (see Fig. 4.6), where incidence changes moved the transition point from 30 to 75% chord while the instability point shifted by a much smaller amount from 10 to 33% chord.

The new correlation for the instability length (Equation 6.11) was initially derived largely from measurements of transition on the stator blade suction surface at negative incidence, where extensive regions of laminar flow were maintained by the favourable pressure gradients near the leading edge. It is therefore interesting to note that this correlation correctly predicts the markedly reduced length of laminar flow observed at positive incidence, when the pressure gradient on the suction surface becomes more adverse as the suction peak shifts forward. This is illustrated in Fig. 6.21, which shows the location of the instability region on a compressor rotor blade as calculated from the experimental surface pressure distributions given by Shaw and Doyle (76). It is seen that the length of laminar flow on the suction surface is predicted by Equation 6.11 to fall from 44% chord at $i = 2.3^\circ$ to only 9% chord at $i = 9.7^\circ$. The latter figure is in excellent qualitative agreement with the flow behaviour observed on the rotor blades of the research compressor used in the present investigation; here, china clay tests indicated the flow on the rotor suction surface to become turbulent at 10% chord for $i = 8.5^\circ$ (see Fig. 4.5).

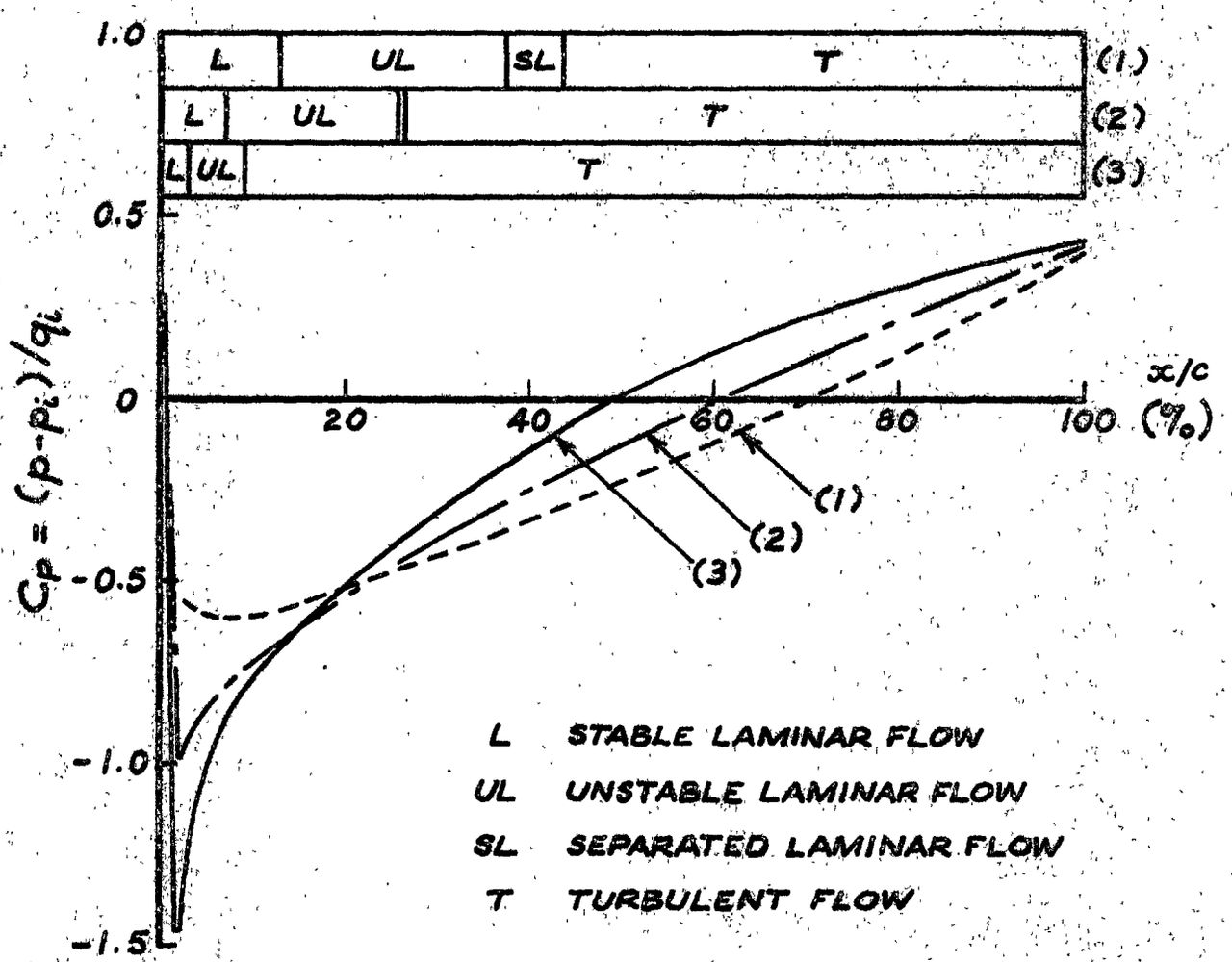


Fig. 6.21 Effects of Incidence Change on Transition as Predicted by Equation 6.11 for Compressor Rotor Blade Suction Surface Pressure Distributions given by Shaw & Doyle (76)

(1) $i = 2.3^\circ$; A.V.R. = 1.040; $Re_1 = 1.230 \times 10^5$

(2) $i = 5.5^\circ$; A.V.R. = 1.040; $Re_1 = 1.220 \times 10^5$

(3) $i = 9.7^\circ$; A.V.R. $\simeq$ 1.130; $Re_1 = 1.219 \times 10^5$

Blade Section: 10 C4/30 C50; $\xi = 36^\circ$; s/c = 0.875

6.7.2 Interpretation of Compressor - Cascade Performance Comparisons

The extreme sensitivity of the transition process to changes in the surface pressure distribution should be kept in mind when attempting to evaluate the effects of other external factors on the performance of an aerofoil. It is very difficult to vary such quantities as surface roughness or free stream turbulence level without altering the surface pressure distribution as well, and the effects of other flow variables on the boundary layer behaviour can only be properly identified after the influence of any accompanying pressure changes has been isolated.

A case in point is the comparison of flow over the blades of an axial flow compressor, in which the free stream turbulence level is high, with the flow over identical blade sections tested under low turbulence conditions in a two-dimensional cascade tunnel. One such comparison was carried out by Shaw and Doyle (76), and some of the blade surface pressure distributions they obtained have been reproduced in Figs. 6.22 and 6.23; in these particular cases it appears that separated laminar flow regions are present on the suction surface of the cascade blades, but absent from the compressor blades, even though both sections are operating at almost the same incidence and Reynolds number. At first, it is tempting to conclude that the absence of flow separation in the compressor is entirely due to the higher turbulence level (4 - 5%) promoting earlier transition in the compressor blade boundary layer. However, a closer inspection of the data reveals that in all cases there are small (but important) differences between the cascade and compressor blade pressure distributions, particularly as regards the location of the suction peak and the magnitude of the blade circulation. Only part of these differences can be explained by changes in axial velocity ratio, and it is not clear how the remainder arises; perhaps the free stream turbulence in the compressor could alter the mean blade incidence, or affect the blade circulation by shifting the rear stagnation point (either directly, or indirectly as a result of changes in boundary layer behaviour); alternatively, the measured incidence in the compressor might be slightly in error due to unsteady flow effects.

Fig. 6.22 shows a comparison of pressure distributions on the suction surfaces of the compressor rotor and cascade blades for $i \simeq 2^{\circ}$ and $Re_1 \simeq 1.3 \times 10^5$; it seems (from the shape of these pressure distributions near the leading edge) that the rotor incidence is effectively lower than that of the cascade blade, even though the measured incidence values are nearly identical. The point of laminar separation predicted by Thwaites's method, and the transition point calculated from Equation 6.11 have been indicated for each of these pressure distributions. The calculated transition points are seen to agree fairly well with the start of pressure recovery behind the separation bubbles on the cascade blade.

The separation point predicted for distribution (3) on the cascade blade is obviously too far downstream, probably for the reasons given in Section 5.5.2; the correct position would appear to lie near the discontinuity in pressure gradient around 32% chord (which has been indicated by a dashed line). Accepting the latter position as correct, the calculated length of separated laminar flow on the cascade blade is about 12% of chord for distribution (2) and 14% chord for distribution (3). For the rotor blade, however, the predicted length of separated flow is only 6% chord, due to the separation point being further rearward as a result of the lower pressure gradient near the leading edge; thus a shift of some 5% chord in either the separation or transition point would completely

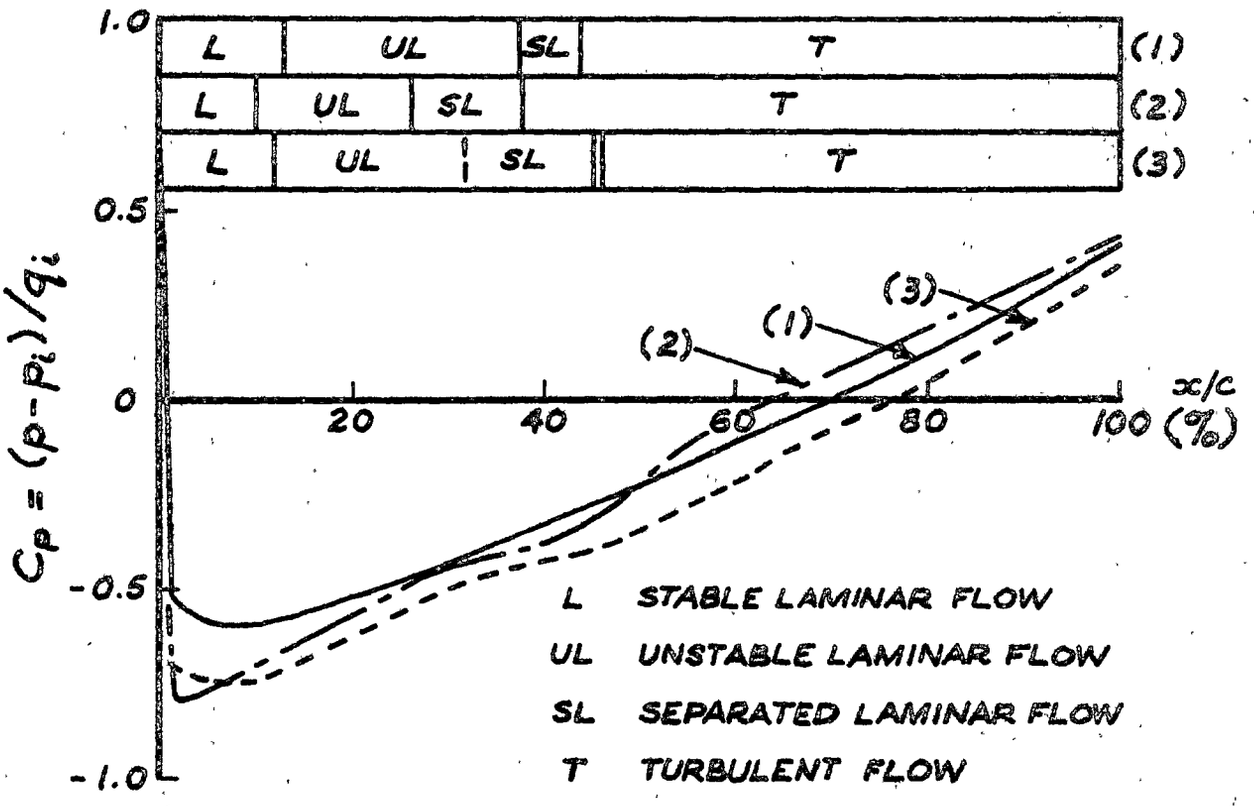


Fig. 6.22 Predicted Transition Behaviour on the Suction Surfaces of Similar Compressor Rotor and Cascade Blade Sections using Surface Pressure Distributions given by Shaw & Doyle (76)

(1) Rotor $i = 2.3^\circ$; A.V.R. = 1.040; $Re_1 = 1.230 \times 10^5$

(2) Cascade $i = 2.1^\circ$; A.V.R. = 0.932; $Re_1 = 1.320 \times 10^5$

(3) Cascade $i = 2.2^\circ$; A.V.R. = 1.153; $Re_1 = 1.320 \times 10^5$

Blade Section: 10 C4/30 C50; $\xi = 36^\circ$; s/c = 0.875

account for the absence of separation observed in the compressor. This could occur through separation being delayed by the effects of radial flows in the rotor blade boundary layer, as noted by Deverson, Marsh, and Oxford (77), or from earlier transition being promoted by the higher free stream turbulence level in the compressor. It is also possible that separation might be suppressed by the mixing from three-dimensional disturbances in the rearward part of the instability region: in the present investigation, for example, separation was absent from the stator suction surface at 750 rpm for $i = -3.7^\circ$ even though the calculated separation point preceded the measured transition point by 14% of chord; there was no detectable distortion of the surface velocity distribution in this case, despite the occurrence of incipient separation (see Figs. 4.1 (b), 4.7 (a)).

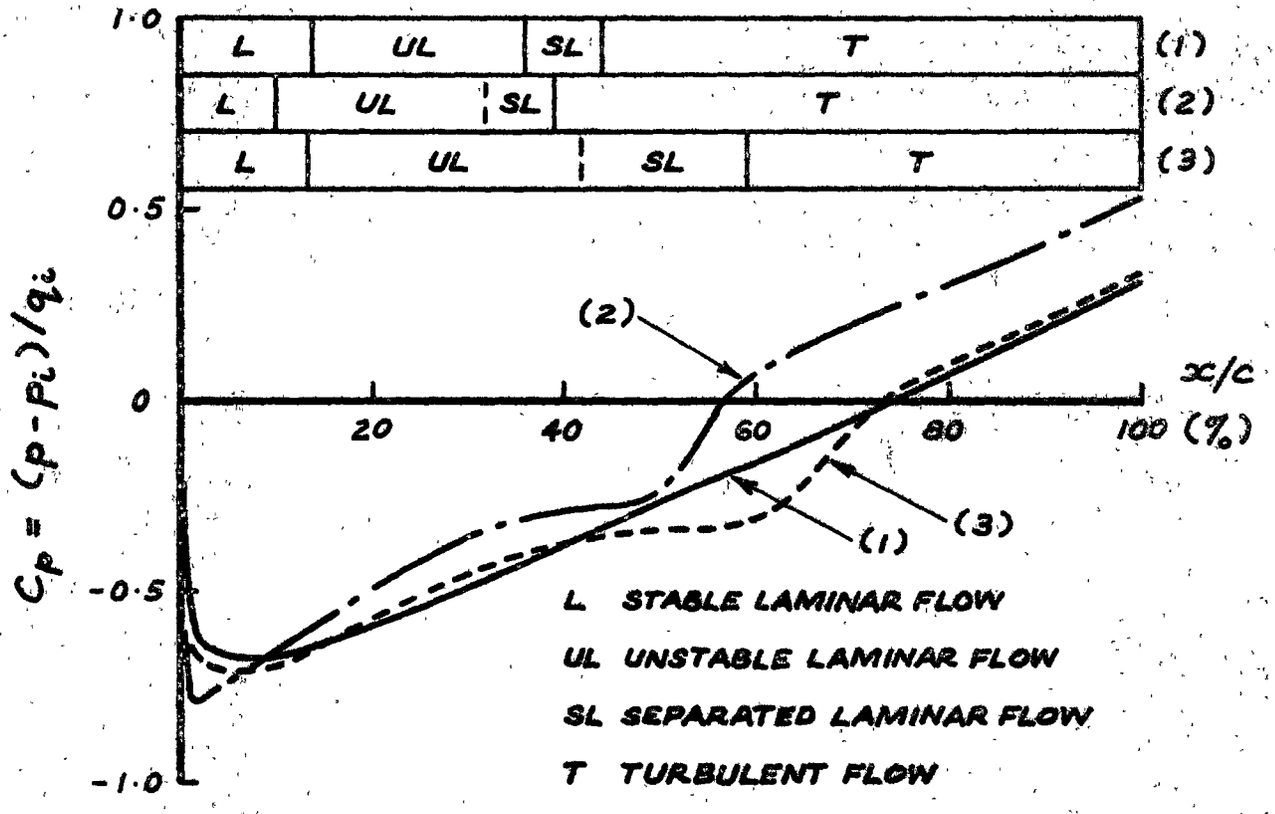


Fig. 6.23 Predicted Transition Behaviour on the Suction Surfaces of Similar Compressor Rotor and Cascade Blade Sections using Surface Pressure Distributions given by Shaw & Doyle (76)

(1) Rotor $i = 2.0^\circ$; A.V.R. = 1.060; $Re_1 = 7.70 \times 10^4$

(2) Cascade $i = 1.5^\circ$; A.V.R. = 0.993; $Re_1 = 6.95 \times 10^4$

(3) Cascade $i = 1.8^\circ$; A.V.R. = 1.138; $Re_1 = 6.95 \times 10^4$

Blade Section: 10 C4/30 C50; $\xi = 36^\circ$; s/c = 0.875

Fig. 6.23 shows another comparison of compressor rotor and cascade blade pressure distributions, this time for $i \simeq 2^\circ$ and $Re_1 \simeq 7 \times 10^4$. The separation points indicated for the cascade blade are estimated positions only, as Thwaites's method again failed to give a reasonable prediction, but they are probably accurate to better than 5% chord. A plot of $(\theta_s^2/\nu)(\Delta U/\Delta x)$ against $Re_{\theta_s}$ for the three cases shown in Fig. 6.23 indicates that separation from the rotor blade, if it occurred, would be in the short bubble form, while the separation regions on the cascade blade should both fall into the long bubble regime (see Fig. 5.9). The lower adverse pressure gradient near the leading edge of the rotor blade suggests that it operates at a lower effective incidence than the cascade blade; this leads to a smaller momentum thickness value at the separation point, which causes the long bubble formation on the rotor to be suppressed. The calculated separation point on the rotor suction surface precedes the transition point predicted from Equation

6.11 by 8% chord, so that only small movements of the separation and transition points would be required to eliminate separation from the rotor blade entirely. Once again, therefore, it appears possible to describe most of the observed differences between the cascade and compressor blade performance in terms of small changes in the surface pressure distribution.

### 6.7.3 Influence of the Surface Pressure Distribution on Flat Plate Transition Data

The term "flat plate flow" is often used as a synonym for the more specific expression "flow in zero pressure gradient". However, a close inspection of the data obtained by workers investigating the flow over flat plates set parallel to the oncoming stream reveals that zero pressure gradient is never exactly achieved. This is especially true near the leading edge, where the plate is usually sharpened to a wedge shape, and some steps are taken to ensure that the front stagnation point remains on one side of this wedge (to prevent premature transition being caused by movements of the stagnation point around the sharp leading edge, as noted experimentally in Ref. 44). The measures described above usually produce an acceleration of flow near the plate leading edge, which, if sufficiently prolonged, can maintain stable laminar flow up to values of boundary layer Reynolds number greater than the critical value of $Re_\theta$ obtained in the zero pressure gradient case; according to Equation 6.11 or 6.19, this should increase the instability length and so lead to larger values of the transition Reynolds number, $Re_{x_t}$.

The author knows of only one investigation of transition on a flat plate in which the value of $Re_{\theta_i}$ was calculated after making due allowance for pressure gradient effects: Miller and Fejer (43) gave a value of $Re_{\theta_i} \simeq 290$ ($Re_{x_i} \simeq 1.9 \times 10^5$) calculated from the results of Schlichting (72), and this is rather higher than Schlichting's value of $Re_{\theta_i} \simeq 250$ for the zero pressure gradient case. The data given by Schubauer and Skramstad (40) is not sufficient to determine the exact values of $Re_{\theta_i}$ in their experiments, but it appears that stable laminar flow could easily have been maintained up to $Re_\theta \simeq 200$ or even 250 in some cases (using the stability data from Table 6.1, in which $Re_{\theta_{crit}} = 164$ for $dp/dx = 0$); thus it seems that the effects of accelerating flow near the leading edge could have made a significant contribution to the higher values of $Re_{x_t}$ obtained by these workers.

## 6.8 Effect of Free Stream Turbulence on Transition

### 6.8.1 General Discussion

The use of the single parameter, percentage turbulence, to describe the effects of free stream turbulence on boundary layer transition is undoubtedly a gross oversimplification. The scale, amplitude, and frequency of the individual disturbances making up the complete turbulence spectrum are all

likely to be significant factors; so too are the location and length of the unstable laminar flow region, the mean streamwise pressure gradient over it, and the frequency of the disturbances which receive amplification in the boundary layer instability process. The overall effect of free stream turbulence will depend critically on the relative magnitudes of many of these quantities, as well as on their absolute values.

It is suggested that the most important ways in which predominantly two-dimensional disturbances in the free stream may influence the transition process in two-dimensional boundary layer flow are:
(i) by shifting the point of neutral stability to small two-dimensional disturbances;
(ii) by changing the initial amplitude of disturbances at the neutral stability point;
(iii) by altering the amplification rate of two-dimensional disturbances;
(iv) by accelerating or delaying the final breakdown of three-dimensional disturbances into turbulence.
These four major regions of influence will now be discussed separately:
(i) movement of the instability point

Variations in the instantaneous position of the instability point on an aerofoil will depend on the aerofoil shape and surface pressure distribution, the mean location of the instability region, and the relative scale and amplitude of the free stream turbulence.

Where the turbulence scale is large compared with the aerofoil chord, the incidence is temporarily altered as a disturbance passes, and significant changes in the surface pressure distribution are produced. The resulting movements of the instability point on the aerofoil surface will be greatest when the position of peak suction is most altered, and this will occur around the incidence where a suction peak is about to form near the leading edge. The changes in surface pressure coefficient accompanying a change in incidence are greatest at the leading edge, and decay rapidly in amplitude towards the trailing edge; thus movements of the instability point in response to incidence changes will probably be less marked when the instability point is normally well rearward on an aerofoil (as, for example, when there is a long region of accelerating flow near the leading edge).

When the turbulence scale is small compared with the aerofoil chord, any incidence change effects will become fairly negligible. Disturbances of small scale may still influence the location of the instability point by impressing local changes in streamwise pressure gradient on the boundary layer fluid; but unless the product of disturbance scale and amplitude is sufficiently large (as defined in paragraph (iii)) the resulting movements of the transition point are not likely to be very great.

(ii) variation of the initial disturbance amplitude

There is ample experimental evidence showing that the transition process is accelerated when the free stream turbulence contains regular disturbances (such as sound waves) whose frequency is close to that of the two-dimensional instability waves receiving amplification within the boundary layer. This is presumably due to the wave amplitude at the neutral stability point being increased by energy transfer from the external to the internal disturbances; according to Liepmann's (46) hypothesis (see Section 6.5.3.1) this would reduce the wave amplification to be supplied by the boundary layer prior to transition, and so shorten the instability length.

However, the boundary layer is highly selective as regards the frequency and type of external disturbances which may influence transition in this manner. Spangler and Wells (64) observed that any slight change from a frequency which influenced transition resulted in a very great loss of effectiveness. Another interesting result obtained by these workers was that travelling sound waves influenced transition, while standing waves did not (in their particular test facility).

In the present investigation, the primary frequency of instability waves in the stator blade suction surface boundary layer was over ten times the rotor blade passing frequency, making it unlikely that the initial disturbance amplitude was greatly affected by the rotor blade wakes. Any regular disturbances influencing transition (if they were in fact present) would necessarily have been part of the background free stream turbulence, and therefore much smaller in amplitude than the previously quoted values of 2 - 6% turbulence which include the rotor wake disturbances.

Where the initial disturbance amplitude is reduced to very low levels, the instability length should be increased and the transition point should move further downstream. Unfortunately, most observations of transition under conditions of very low free stream turbulence have been obtained from experiments on flat plates; it is not clear how this data should be applied to predicting transition on bodies of different shape.

(iii) changes in amplification rate

All free stream disturbances will have some effect on the boundary layer velocity profile, either by varying the streamwise pressure gradient or by applying a shear stress at the outer edge of the boundary layer. This, in turn, will alter the boundary layer stability characteristics and so change the amplification rate of disturbances growing within the boundary layer. The transition point should move upstream when amplification is enhanced, and downstream when amplification is diminished.

The scale of the free stream turbulence should again be an important parameter, as it determines the length of time for which the instability waves in the boundary layer "see" the faster moving disturbances in the free stream. If, for example, a free stream disturbance consists of a deceleration

followed by an acceleration, it will only cause a significant reduction of the instability length if the disturbance scale and amplitude are sufficiently large to cause breakdown through enhanced amplification of disturbances during the decelerating phase; otherwise the boundary layer disturbances will subsequently experience a decreased amplification rate during the accelerating phase of the external disturbance, and the net effect on the instability length will only be small (analagous to the aperiodic mode of transition in an oscillating flow).

It was noted previously in Section 6.4.2.3 that a critical value of the non-steady Reynolds number $(Re)_{NS}$ defined by Obremski and Fejer (44) for oscillating flow might prove a useful aid for predicting the effects of isolated (two-dimensional) free stream disturbances on transition; this parameter involves the product of the disturbance amplitude and the disturbance scale.

(iv) changes in the final breakdown process

Thomson's (41) model of the breakdown process (discussed in Section 6.2.2.1) suggests that turbulent flow is initiated by bursting of the streamwise legs of vortex loops formed by the three-dimensional disturbances in the rearward part of the instability region. As bursting is enhanced by vortex compression, it seems probable that a free stream disturbance which decelerates the flow could promote earlier breakdown and cause the transition point to move upstream; conversely, a disturbance which accelerates the flow might cause vortex stretching and so delay transition. However, the three-dimensional disturbances which lead to transition are highly developed over only a small proportion of the instability length (probably no more than 20%), and it seems unlikely that any effect of free stream turbulence on the breakdown process would shift the transition point by more than this amount.

Besides the unsteady flow effects noted in (i) - (iv) above, it appears that variations in the level of free stream turbulence will also change the time-mean surface pressure distribution on a body. It has already been demonstrated in Section 6.7.2 that perhaps 50% or more of the differences in boundary layer behaviour on aerofoils operating at the same nominal incidence and Reynolds number, but subjected to different turbulence levels, could be explained in terms of accompanying small changes in the aerofoil pressure distribution. The mechanism by which such changes occur is by no means clear: perhaps the mean incidence or the location of the rear stagnation point is effectively altered as a direct effect of the turbulent stream; alternatively, some differences in surface pressure distribution might be produced indirectly through changes in boundary layer behaviour induced by the free stream disturbances. (Heilmann (78), for example, observed that free stream turbulence altered the position of the turbulent separation point near the trailing edge of an aerofoil.) Whatever the cause, it is

probable that changes in the mean pressure distribution will considerably complicate attempts to predict the performance of an aerofoil in a turbulent stream.

The previous discussion is strictly applicable only to free stream disturbances of an essentially two-dimensional nature, i.e. those which do not vary rapidly in the spanwise direction (the ratio of the spanwise disturbance scale to the boundary layer thickness would appear to be the significant parameter here). It is, of course, quite possible to have free stream disturbances which do not satisfy this requirement, and these will influence transition in a rather different manner: for example, external disturbances which are roughly periodic in the spanwise direction might promote the secondary instability which leads the initially two-dimensional waves within the boundary layer into a three-dimensional form; an isolated ("three-dimensional") free stream disturbance might promote transition by distorting the spanwise vortex lines within the boundary layer in a manner analagous to that of an isolated roughness element placed on the surface. It is noted here that the disturbances arising from the wakes of upstream blade rows in an axial-flow turbomachine will in most cases be effectively two-dimensional.

### 6.8.2 Range of Validity of Equations 6.11 and 6.19

Having dealt with the effects of free stream turbulence on the transition process, it is now possible to make some statements about the limits of application of the correlations for the instability length (Eqns. 6.11 and 6.19) which were developed from the results of the present investigation. It is suggested that these correlations will be valid except in the following circumstances:

(i) where the disturbance scale and/or body shape are such that incidence changes due to the free stream turbulence cause large movements of the instability point;

(ii) where the external disturbance spectrum contains a significant level of energy at frequencies close to those of the disturbances receiving amplification within the boundary layer;

(iii) where the (two-dimensional) external disturbance scale and amplitude exceed some critical value (as yet unknown) which might be specified in terms of a non-steady Reynolds number similar to the parameter $(Re)_{NS}$ defined in Ref. 44.

In all three cases specified above, the instability length is expected to be lower than that predicted by Equations 6.11 and 6.19.

According to the flat plate transition data of Refs. 40 and 64, the instability length should exceed that predicted by Equations 6.11 and 6.19 when the free stream turbulence level is decreased to extremely low values, although there is some uncertainty regarding the extent to which pressure

gradient effects contributed to the high transition Reynolds number obtained in these experiments (see Section 6.7.3). However, because of the success achieved in correlating data from several low turbulence and free flight tests on aerofoils, the author feels that the instability lengths predicted by Equations 6.11 and 6.19 might provide an upper limit to the transition Reynolds number in cases of practical interest: there will always be a certain level of disturbance present in engineering situations, arising from surface waviness or vibration, aerodynamic or engine noise, etc.

Provided that none of the above restrictions apply and the flow is two-dimensional, the results of Table 6.3 indicate that Equations 6.11 and 6.19 should predict the instability length to better than 20% in most cases, and the transition point to within 5% chord, on the average. In these circumstances, it is suggested that no specific allowance be made for free stream turbulence effects when calculating the transition point by either of these methods.

### 6.8.3 Granville's Correlation for the Effects of Free Stream Turbulence

Granville's (65) correlation for the effects of free stream turbulence on boundary layer transition (see Fig. 6.16 in Section 6.5.4) indicates that the transition point should approach the instability point calculated from the time-mean surface pressure distribution as the level of free stream turbulence is raised. But this disagrees completely with the results of the present investigation, which suggest that free stream disturbances do not greatly influence the transition location on the blades of the research compressor. The most probable explanation for this difference in behaviour lies in Granville's correlation being derived almost entirely from observations of transition on a flat plate, where the surface pressure distribution and instantaneous position of the instability point are both extremely sensitive to small incidence changes; the compressor blades are much less sensitive in this regard because of their well rounded leading edge shape (nose radius 1.2% c ).

For the following reasons, the author feels that Granville's correlation of $(Re_{\theta_t} - Re_{\theta_i})$ against free stream turbulence level (Fig. 6.16) will not be generally applicable to any body shape or type of external disturbance:
(i) the frequency and scale of the free stream disturbances must also be important parameters, and these do not appear at all;
(ii) on many bodies it should be possible for transition to precede the steady flow instability point if the external disturbances become large enough;
(iii) the low values of $(Re_{\theta_t} - Re_{\theta_i})$ observed on a flat plate at high levels of free stream turbulence could be largely due to the external disturbances changing the plate incidence and moving the instability point forward. This being the case, the correlation would probably be invalid for transition on bodies having a shape markedly different from a flat plate.

Nevertheless, it is likely that Granville's correlation will achieve some success when applied to bodies whose geometry and surface pressure distribution closely resemble those of the flat plate for which the correlation was originally derived. This has been demonstrated in cascade tests carried out by Heilmann (78) on the NACA $T_1$ - $(18A_6I_{4b})08$ aerofoil, which has its maximum thickness at about 60% chord and a very sharp leading edge (nose radius 0.22% c). These measurements showed that significant changes in the transition behaviour occurred in response to variations in the free stream turbulence level, and the movements of the transition point were predicted moderately well by Granville's method; however, there was a definite tendency for the measured transition points to lie rearward of the calculated points.

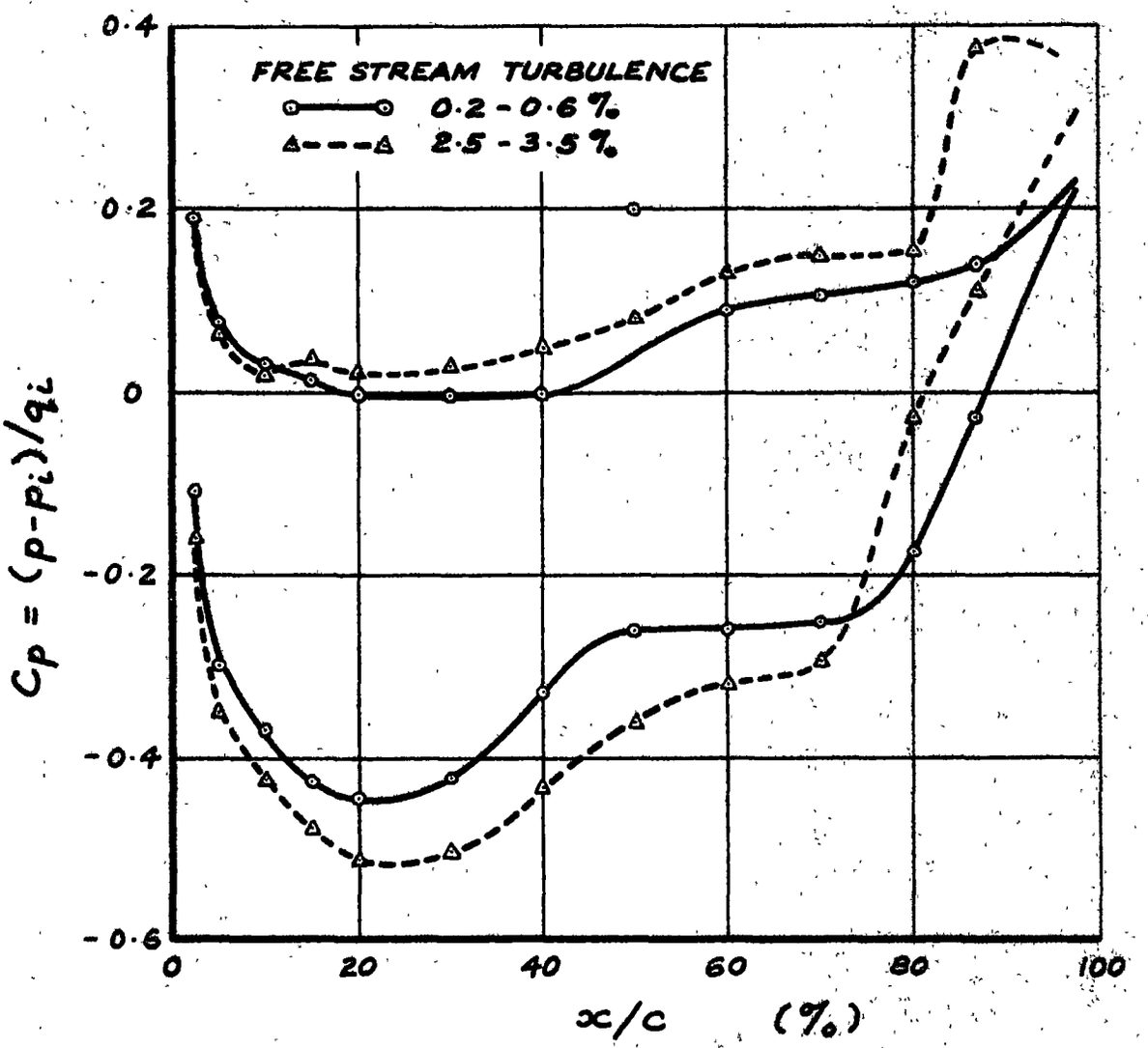


Fig. 6.24 Influence of Different Levels of Free Stream Turbulence on the Pressure Distribution of a Cascade of NACA 65 - 612 Aerofoils ($\xi = 40^\circ$, $\alpha_1 = 50^\circ$, s/c = 1.0, $Re_1 = 1 \times 10^5$, $Ma_1 = 0.5$)
From Hebbel (79)

On the other hand, the tests of Hebbel (79) on cascades of NACA 65 - 608 and 65 - 612 aerofoils appear quite inconsistent with Granville's correlation (Fig. 6.16): they are in substantial agreement with the results of the present investigation, and lend further weight to the opinion that free stream turbulence does not greatly alter the instability length in many cases. This inference is drawn from the published aerofoil surface pressure distributions, of which a typical pair have been reproduced in Fig. 6.24; both distributions show clear evidence of a laminar separation region being present around 50 - 70% chord on the suction surface, probably in the long bubble form. Taking the commencement of pressure recovery behind the bubble to indicate transition (see Section 5.6.2), it is seen that the transition point is moved upstream by only 5% chord (or about 10% of the instability length) by increasing the free stream turbulence level from around 0.4% to 3%. But according to Granville's correlation (Fig. 6.16), an increase in turbulence level of this magnitude should move the transition point upstream by 50% chord (to coincide with the mean instability point, which lies close to the point of minimum pressure around 25% chord in this particular case).

### 6.8.4 Influence of Free Stream Turbulence on Cascade Performance

The effect of free stream turbulence on the performance of aerofoils in cascade has been the subject of several experimental investigations in recent years. This work has largely been aimed at improving the performance of turbojet engines at high altitudes, where the low Reynolds numbers at which the blades operate normally lead to a marked drop in overall efficiency. Some studies of the influence of turbulence on compressor cascades have been reported by Shaw (54), Deverson et al.(77), Heilmann (78), Hebbel (79), and Schlichting and Das (80).

Hebbel (79) showed that an increase in free stream turbulence level from about 0.4% to 3% produced significant improvements in the low Reynolds number performance of compressor cascades of NACA 65 - series aerofoils; these included reductions of up to 50% in profile drag, and increases of a similar magnitude in flow deflection and pressure rise. The effects of turbulence were greatest at the lowest Reynolds number investigated ($Re_1 = 5 \times 10^4$), and decreased steadily as the Reynolds number was increased until they became rather insignificant around $Re_1 = 4 \times 10^5$. An inspection of these results indicates that separated flow regions were initially present in all cases where an increase in turbulence was observed to have a beneficial effect on the cascade performance; furthermore, there appears to be a rough correlation between the initial extent of flow separation and the improvement in performance which was gained. Hebbel noted that the free stream disturbances improved the performance by promoting earlier transition in the aerofoil boundary layer, and so reducing the extent of these separated flow regions.

The present author agrees with this assessment, but wishes to make the additional point that the movements of the transition point relative to the instability length are not necessarily of the same order of magnitude as the relative changes in overall performance of an aerofoil. This is illustrated by the example shown in Fig. 6.24, where an increase in turbulence level from about 0.4% to 3% reduces the profile drag coefficient by about 50%, while the transition point moves by only 5% chord, approximately. Evidently the flow around the aerofoil is extremely sensitive to the location of the transition point in this particular case because of the presence on the suction surface of a laminar separation region in the long bubble form. It is seen from Fig. 6.24 that the increase in turbulence has the following effects on the aerofoil surface pressure distribution:

(i) the pressure gradient over the separation bubble becomes slightly positive;

(ii) the transition point (at which pressure recovery commences behind the bubble) moves forward by about 5% chord, thus increasing the distance over which pressure recovery can occur before the trailing edge is reached;

(iii) there is a higher pressure gradient during pressure recovery behind the bubble (presumably because the changes in surface pressure distribution lead to a lower initial value of momentum thickness for the reattaching turbulent shear layer).

The net result of the above-mentioned changes is to give a greater pressure rise on the suction surface, and so increase the blade circulation; this, in turn, produces the observed improvement in pressure rise and flow deflection through the cascade. A secondary effect of the changes in shape of the surface pressure distribution is to shift the instability point and so cause further movements of the transition point; this feedback mechanism will either accentuate or diminish the influence of turbulence on the blade performance according to whether the secondary motion of the transition point reinforces or opposes the primary movement caused by the external disturbances.

A detailed examination of Hebbel's results suggests that in practically all cases the movement of the transition point was no greater than that of the example considered above. This behaviour is by no means universal, however, since it appears equally possible to find cases in which a large change in aerofoil performance caused by increasing the free stream turbulence is accompanied by a correspondingly large movement of the transition point on the aerofoil. For example, in the tests by Heilmann (78) on a cascade of NACA $T_1$ - $(18A_6I_{4b})08$ aerofoils, a change in turbulence level from 1.2% to 2.2% moved the transition point on both suction and pressure surfaces by 30% chord, and increased the total pressure loss coefficient by about 60%. The foregoing discussion clearly indicates how difficult it is to make accurate statements about the transition behaviour on cascade blades from measurements of overall performance parameters alone: this should emphasise the desirability of carrying out further detailed studies of boundary layers in

turbomachinery over as wide a range of flow situations as possible.

The effect of free stream turbulence on the stalling behaviour of a stationary cascade was investigated by Deverson, Marsh and Oxford (77), who found that the stalling angle increased and the stall became more gradual as the turbulence level was increased from 0.25% to 3.3% at a Reynolds number of $1.03 \times 10^5$. They suggested that these changes were due to the turbulence causing a reduction in the rate of growth of a long separation bubble which formed near the leading edge on the suction surface at high incidence; at low incidence, where separation was absent from the blade surface or occurred only in the short bubble form, the turbulence level had very little effect on the lift curve of the cascade. The broad similarity of these results to those obtained by Hebbel (79) suggests to the present author that the high sensitivity of flows with long separation bubbles to small movements of the transition point could well be the most common mechanism by which free stream turbulence influences cascade performance over the critical Reynolds number range around $Re_c = 10^5$.

## 6.9 The Transition Region

### 6.9.1 Introduction

On isolated aerofoils operating at high Reynolds numbers ($Re_c = 10^6 - 10^7$) the transition region as defined in Section 6.3.1 usually occupies 5 - 10% of chord only, and the assumption that transition is instantaneous leads to little overall error in the aerofoil boundary layer calculation. Roudebush and Lieblein (81) suggested that this model would also prove satisfactory for predicting the boundary layer development at lower Reynolds numbers on aerofoils in cascade. However, the present investigation has clearly shown this to be incorrect, in general, since the transition region was observed to occupy 15 - 20% of chord on the suction surface of stator blades in the research compressor (see Fig. 4.6). Thus some improvement on the point transition model appears necessary in order to achieve an accurate estimate of the profile losses for blades operating in an axial-flow turbomachine.

### 6.9.2 Length of the Transition Region

The author earlier suggested (82) that the length of the transition region would probably be a slowly varying function of Reynolds number, and might therefore be guessed to a sufficient accuracy from a knowledge of the chord Reynolds number at which an aerofoil was to operate. But the later study of the unsteady nature of transition on the blades of the research compressor (reported in Section 6.4.2) has indicated that the transition process on a turbomachine blade will also be influenced to a large extent by the relative passage of wakes from upstream blade rows. This considerably complicates the problem, and with the present state of knowledge it appears

possible to establish only rough limits for the transition length in this particular case.

A lower bound to the transition length on a turbomachine blade can be obtained by following McCormick's (83) procedure of assuming the turbulent spots to appear at the primary (Tollmien-Schlichting) instability wave frequency from a fixed position on the aerofoil. Using Schubauer and Klebanoff's (48) data for the growth rate of isolated turbulent spots gives the streamwise distance, $dx_1$, required for the leading and trailing edges of successive spots to merge as

$$dx_1 \simeq (x_T - x_t)_{min} = 1.16\ T_p\ U_{av} \qquad (6.25)$$

where $T_p$ is the period of the primary wave, and $U_{av}$ is the mean value of surface velocity over the interval $dx_1$. Using the primary wave frequencies obtained from the hot wire observations in the research compressor (see Section 6.4.2) leads to values of only 7 - 9% chord for the minimum transition length on the stator blade suction surface at a speed of 250 rpm. The observed transition length is 2 or 3 times greater than this, due almost certainly to the stabilisation of flow which occurs during the accelerating phase of the velocity fluctuation caused by the rotor wake passage.

An upper bound to the transition length on a turbomachine blade is obtained by assuming that turbulent spots are initiated from a fixed position at the frequency with which upstream blade wakes pass in the free stream (provided that the frequency of passing wakes controlling intermittency is lower than that of the primary instability wave); after initiation, these spots are assumed to develop entirely in the convective mode defined in Section 6.2.3.2. The streamwise distance, $dx_2$, required for successive spots to merge is then calculated from the leading and trailing edge velocities of 0.88U and 0.58U, respectively, measured by Obremski and Fejer (44) in oscillating flow; this gives

$$dx_2 \simeq (x_T - x_t)_{max} = 1.70\ T_w\ U_{av} \qquad (6.26)$$

where $T_w$ is the period between the passage of successive wakes, and $U_{av}$ is the mean value of surface velocity over the interval $dx_2$. Equation 6.26 gives the upper limit to the transition length on the stator suction surface as 180 - 220% chord; this is about 10 times the observed transition length, and unfortunately too high to be of much practical use. The reason for the actual transition length being so much smaller than predicted is that the turbulent spot development occurs almost entirely in the creative mode in this particular case. The ratio of the transition length predicted by Equation 6.26 to the actual transition length is expected to vary considerably, depending on the local pressure gradient and the shape of the wake

disturbance; the factor of 10 : 1 obtained above should therefore be used, if at all, as a very rough guide only.

In conclusion, it is noted that the upper bound to the transition length given by Equation 6.26 will not vary with compressor speed, provided that the location of the transition region and the shape of the surface pressure distribution remain unaltered. This could provide a partial explanation for the relatively constant values of $(x_T - x_t)$ observed on the stator blade during the present investigation (see Table 6.2). The lower bound to the transition length given by Equation 6.25 will change slowly with compressor speed due to the frequency of the primary instability wave varying with Reynolds number.

### 6.9.3 Calculation of Boundary Layer Growth in the Transition Region

In cases where the transition length $(x_T - x_t)$ is not small compared with the aerofoil chord, the author uses the boundary layer momentum integral equation (Eqn. 4.1) to calculate the boundary layer development through the transition region; the boundary layer shape factor, H, and skin friction coefficient, $C_f$, are assumed to vary linearly between the transition point, $x_t$, and the point of wholly turbulent flow, $x_T$ (as defined in Section 6.3). The initial values of H and $C_f$ are obtained directly from the laminar boundary layer calculation, provided that no laminar separation occurs, while the final values are those chosen as the starting conditions for the turbulent boundary layer calculation (see Section 7.6.7). The transition length $(x_T - x_t)$ must either be obtained from empirical data, or guessed after taking into consideration the effects of Reynolds number and regular free stream disturbances (as discussed in Section 6.9.2 above).

Alternatively, it might be possible to use a turbulent boundary layer calculation method suitably modified to allow for the intermittency of turbulence in the transition region; for example, the eddy viscosity or entrainment rate could be assumed to vary linearly between $x_t$ and $x_T$. But this procedure is likely to give unsatisfactory results when transition occurs in a laminar separation bubble, as is quite often the case on compressor blades operating at low Reynolds numbers.

## 6.10 Summary

The periodic disturbances arising from rotor blade wakes passing in the free stream imposed a considerable regularity on the time-space distribution of turbulent flow during boundary layer transition on the stator blades of the research compressor. However, the boundary layer Reynolds number at which turbulent flow first appeared did not seem to be greatly influenced by these disturbances, despite the apparently high level of free stream turbulence they created. This behaviour is very similar to the "aperiodic" mode of transition observed in oscillating boundary layer flow when the non-steady

Reynolds number $(Re)_{NS}$ defining the magnitude of the oscillations falls below a certain critical value.

A new empirical method of predicting transition, developed from the measurements obtained in the present investigation, was found to describe the transition behaviour in a wide range of other flow situations as well (including laminar separation bubbles). For the data considered, the new correlation (Eqns. 6.11 and 6.19) gave results of similar accuracy to the semi-empirical methods of Smith et al.(56, 57, 61) which are based on laminar stability theory. The empirical transition correlations of Michel (55) and Granville (65), which may be considered as particular cases of Eqns. 6.11 and 6.19, did not give useful predictions of the transition point on the stator blades of the research compressor.

The influence of free stream turbulence on the boundary layer behaviour on an aerofoil has been shown to depend very largely on accompanying changes in the aerofoil surface pressure distribution. These changes may be produced directly, by the free stream turbulence varying the aerofoil incidence or position of the rear stagnation point, or indirectly, by the turbulence effects moving the transition point and so changing the boundary layer displacement thickness distribution.

It is suggested that free stream turbulence will only have a major influence on the location of the transition point when one or more of the following conditions apply:

(i) the body shape, and the turbulence scale or amplitude, are such that incidence changes due to the free stream disturbances cause large movements of the boundary layer instability point;

(ii) the free stream turbulence spectrum contains a significant level of energy at frequencies close to those of the disturbances receiving amplification within the boundary layer;

(iii) the scale and amplitude of the free stream turbulence are large enough to promote breakdown within the "wavelength" of a single disturbance. It might be possible to specify the critical size of an essentially two-dimensional disturbance in terms of the non-steady Reynolds number $(Re)_{NS}$ mentioned above.

Provided that none of the above conditions apply, the present study indicates that free stream turbulence effects will not move the transition point by more than 10 - 20% of the instability length, $x_t - x_i$.

Small movements of the transition point can produce large variations in performance when the long bubble type of laminar separation is present on the surface of an aerofoil. It is therefore incorrect, in general, to assume that the relative movements of the transition point are similar in magnitude to the relative changes in overall performance parameters such as profile drag or pressure rise for a cascade.

Transition data from flat plate experiments should be treated with some reserve, for the following reasons:
(i) in some cases, the effects of flow acceleration near the plate leading edge could have stabilised the boundary layer beyond the critical Reynolds number for zero pressure gradient;
(ii) the reduction in transition Reynolds number obtained at high turbulence levels could stem largely from movements of the instability point in response to incidence changes. As this effect is strongly dependent on the body geometry, it is unlikely that Granville's (65) correlation of ($Re_{\theta_t} - Re_{\theta_i}$) against turbulence level for a flat plate will apply to bodies of arbitrary shape.

The transition region occupied 15 - 20% of chord on the stator blades of the research compressor, due mainly to the influence of the rotor blade wakes passing in the free stream. Accordingly, it seems unlikely that a point transition model will lead to very accurate predictions of the boundary layer development on turbomachine blades.

# CHAPTER 7

# TURBULENT BOUNDARY LAYER REGIONS

## 7.1 Introduction

This chapter commences by discussing the wall proximity correction used for hot wire readings obtained in turbulent boundary layer regions on the stator blade. The measured mean velocity profiles are then examined, and the logarithmic wall similarity region usually found in turbulent boundary layers is shown to be notably lacking. Next follow some comments on skin friction laws and the minimum Reynolds number required to sustain fully turbulent flow. In conclusion, the predictions of various existing methods of calculating the turbulent boundary layer development are compared with the experimental results.

## 7.2 Wall Proximity Corrections for Hot Wire Readings in Turbulent Flow Regions

It is recalled from Section 3.3.8 that the problem of correcting hot wire readings for the additional heat loss caused by wall proximity effects was examined experimentally by Wills (13): on the basis of measurements in a two-dimensional channel he suggested that the correction to be applied in turbulent flow should be of the same sign as that required in laminar flow, but smaller by a factor of $0.5 \pm 0.1$. Accordingly, the hot wire readings obtained in turbulent boundary layer regions on the stator blade were initially corrected by applying one-half of the laminar flow correction; the resulting velocity profiles were then examined to see whether they appeared physically reasonable.

Very close to the wall, where the inertia terms can be neglected, the two-dimensional boundary layer momentum equation reduces to

$$dp/dx = \partial\tau/\partial y \qquad (7.1)$$

provided that the Reynolds normal stress terms are also unimportant. In the viscous sublayer, the turbulent shear stress is negligible and Equation 7.1 becomes

$$\partial\tau/\partial y = \mu(\partial^2 u/\partial y^2) = \mu(\partial\zeta/\partial y) = dp/dx \qquad (7.2)$$

After writing the pressure gradient in kinematic form, Equation 7.2 can be expressed non-dimensionally as

$$\frac{\partial(\zeta\theta/U)}{\partial(y/\theta)} = -\frac{\theta^2}{\nu}\frac{dU}{dx} = -k \qquad (7.3)$$

Equation 7.3 (which is also valid for a laminar boundary layer) indicates that the slope of the mean vorticity profile at the wall is directly proportional to the streamwise pressure gradient; in a positive pressure gradient, therefore, $\zeta$ is expected to increase monotonically with y through the inner

part of the viscous sublayer. In the outer part of the sublayer, where the turbulent shear stress increases very rapidly, $\varsigma$ should decrease monotonically with y. The foregoing considerations require that $\varsigma$ reaches a maximum somewhere within the viscosity-dependent region of the wall layer : using the flow model proposed by McDonald (84) (see Section 7.3.3), this maximum is predicted to occur close to $y^+ = 4$ for pressure gradients of the order of those occurring on the stator blade suction surface.

Some typical measurements of the vorticity variation through the viscous sublayer are shown in Fig. 7.1. These profiles were obtained in turbulent flow regions on the stator suction surface at the 90% chord position; they have been plotted non-dimensionally as $(\varsigma\theta/U) \sim (y/\theta)$. It is seen that using one-half of the laminar flow wall proximity correction as suggested by Wills results in the vorticity decreasing monotonically throughout the wall layer ; in this case, $\varsigma$ has no maximum away from the wall, and $\partial\varsigma/\partial y$ is of the wrong sign at the wall. One possible explanation for these results is that the wall shear stress was too high due to the applied wall proximity correction being too small in magnitude ; it was therefore decided to reprocess the data using the full laminar flow wall correction to see whether the results obtained were physically more realistic, and this produced vorticity profiles much closer to those expected. Fig. 7.1 shows that the vorticity profiles obtained by using the full laminar flow correction all have a positive slope at the wall, and they reach a maximum quite close to $y^+ = 4$ before decreasing monotonically at greater values of y. The values of $(\partial\varsigma/\partial y)_{y = 0}$ are smaller than those predicted from Equation 7.2 by a factor of 2 or 3 : this suggests that perhaps the Reynolds normal stresses are not insignificant in the outer part of the sublayer, or the turbulent shear stress increases more rapidly with y than in a constant pressure layer; not too much weight should be given to this conclusion, however, since $(\partial\varsigma/\partial y)_{y = 0}$ is obtained from the second derivative of a limited number of experimental points which are themselves of doubtful accuracy.

Because of the more satisfactory results obtained, the full laminar flow wall proximity correction was applied to all of the hot wire readings from turbulent flow regions on the compressor blade. The velocity profiles described in the remainder of this chapter were all determined by this means.

## 7.3 Mean Velocity Profiles

### 7.3.1 Introduction

Two-dimensional turbulent flow past a smooth wall in the presence of streamwise pressure gradients that are not excessively large is characterised by two main types of similarity :

(a) an "inner" or "wall similarity" region in which the mean velocity profile is described by

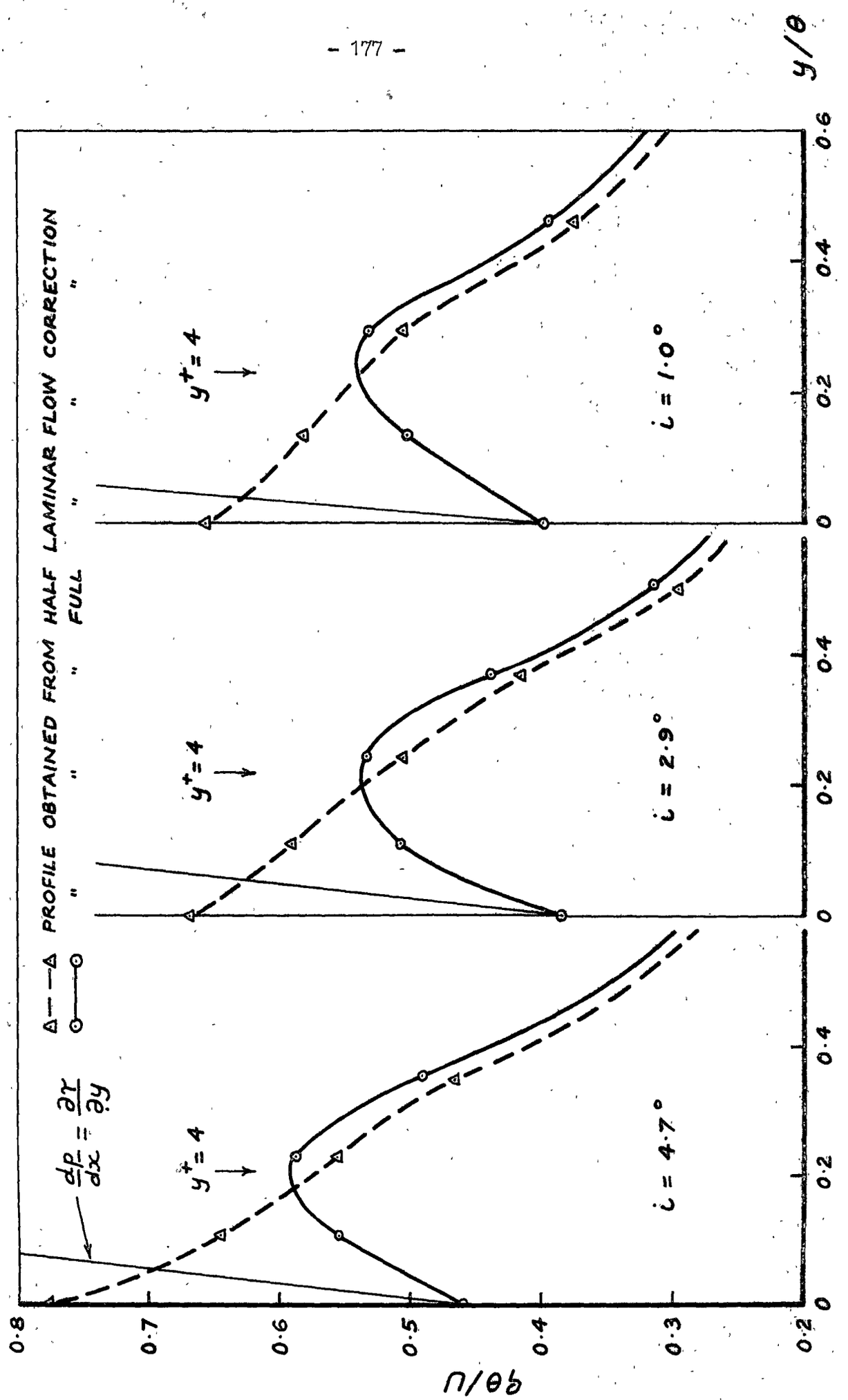


Fig. 7.1 Vorticity Profiles in Wall Region of Turbulent Boundary Layers on Stator Suction Surface : x/c = 0.90, Compressor Speed 500 rpm

- Showing Effect of Wall Proximity Correction to Hot Wire Readings.

$$u/u_\tau = f(yu_\tau/\nu) \qquad (u_\tau = \sqrt{\tau_w/\rho}) \tag{7.4}$$

(b) an "outer similarity" region in which the velocity defect is given by

$$(U - u)/u_\tau = \phi(y/\delta) \tag{7.5}$$

Where these two regions overlap, the flow must be described by both types of similarity, and this requirement leads to the familiar logarithmic form for the velocity distribution in the turbulent wall layer,

$$u/u_\tau = (1/K)\ln(yu_\tau/\nu) + C \tag{7.6}$$

where K and C are empirical constants.

Coles (85) has suggested that the departure of the mean velocity profile from the logarithmic curve in the outer part of the boundary layer can be expressed in terms of the apparently universal function $w(y/\delta_c)$, called the "law of the wake" because of its similarity to a half-wake profile. According to Cole's hypothesis, the mean velocity profile outside the viscous sublayer is given by

$$u/u_\tau = (1/K)\ln(yu_\tau/\nu) + C + (u_\beta/2u_\tau)\{w(y/\delta_c)\} \tag{7.7}$$

where $u_\beta$ is a parameter which depends on the streamwise pressure gradient. The wake function is approximated quite closely by the closed form expression

$$w(y/\delta_c) = 1 - \cos(\pi y/\delta_c) \qquad (0 \leq y \leq \delta_c) \tag{7.8}$$

The quantity $\delta_c$ occurring in Eqns. 7.7 and 7.8 is the distance from the wall at which w = 2.0, rather than the outer edge of the boundary layer ($y = \delta$) where u = U. Coles assumes, in effect, that the velocities at $y = \delta$ and $y = \delta_c$ are experimentally indistinguishable: this is not a bad approximation in an adverse pressure gradient, but Bull (86) has pointed out that it becomes unacceptable in strong favourable pressure gradients.

The validity of the law of the wall, Eqn. 7.6, and the law of the wake, Eqn. 7.8, is supported by a large body of experimental evidence obtained under conditions of high Reynolds number and moderate streamwise pressure gradients : in a recent comprehensive survey of available turbulent boundary layer measurements, Coles (87) claimed to be convinced of only three flow cases in which these similarity laws failed.

### 7.3.2 Logarithmic Wall Similarity Region

#### 7.3.2.1 General remarks

The existence of a logarithmic wall layer requires:

(a) the velocity near the wall to be given by

$$u = u_\tau f(y^+) \tag{7.9}$$

(b) a Reynolds number high enough for there to be a region sufficiently far from the surface that the direct effect of viscosity is negligible, but

sufficiently near the surface that the outer flow conditions do not matter. Equation 7.9 is obtained by dimensional analysis following the assumption that the flow at distance y from the wall depends only on the density, viscosity and wall shear stress, i.e.

$$u = f(\tau_w, \rho, \nu, y) \qquad (7.10)$$

The use of the wall shear stress is only valid when the stress gradient $\partial\tau/\partial y$ is small enough for the change in total shear stress, $\tau$, across the wall layer to be negligible. This will not be so where the boundary layer is subjected to very large streamwise pressure gradients, or to rapidly changing boundary conditions : in fact, it was in precisely these situations that Coles (87) found departures from logarithmic wall similarity to occur. Similar conclusions may be drawn from consideration of the turbulent kinetic energy equation (see for instance Bradshaw (94)).

In zero pressure gradient flow, condition (a) above is known to hold quite well when there are no sudden changes in boundary conditions ; here, the logarithmic wall layer will only be absent if the Reynolds number is so low that there is no viscosity independent region in which the inner and outer similarity regions overlap. This situation was examined by Preston (75): taking the outer edge of the logarithmic layer at $y/\delta = 0.2$ and the outer limit of the viscous sublayer at $yu_\tau/\nu = 30$, he obtained $Re_\theta = 389$ as the Reynolds number at which the logarithmic similarity region was expected to shrink to zero thickness; this was not much greater than the value of $Re_\theta = 320$ which appeared to be the lowest Reynolds number at which fully developed turbulent flow was observed experimentally on a flat plate. Thus Preston's analysis indicates that there will be, at best, only a very narrow range of Reynolds number over which the logarithmic wall layer will be absent in a zero pressure gradient flow.

In strong favourable pressure gradients, it appears that departure from the logarithmic inner law velocity profile does not occur until reverse transition commences; Patel & Head (88) have taken this to occur at a critical value of $(\nu/\rho u_\tau^3)(\partial\tau/\partial y) \simeq -0.009$. Bradshaw (89) has more recently shown that Patel & Head's criterion, together with that proposed by Preston as the minimum Reynolds number for turbulent flow in zero pressure gradient, are special cases of a more general eddy Reynolds number criterion for reverse transition : the latter result was deduced from the requirement that no part of the flow should be free from viscous effects on the shear-producing eddies.

The above discussion indicates that the existence of logarithmic wall similarity will be very nearly universal in conditions of zero or favourable pressure gradient, provided that the flow is fully turbulent. This only leaves the cases of large positive pressure gradients, rapid changes in boundary conditions, and low Reynolds numbers as possible situations in which

this similarity law might break down; however, these are precisely the circumstances which apply on the suction surface of an axial compressor blade (quite often in combination). The data obtained in the present investigation therefore affords an interesting opportunity to examine the validity of the logarithmic similarity law under these rather severe conditions : this question is also of considerable practical importance since the universal velocity profile proposed by Coles (Eqn. 7.7) is employed in several different methods of calculating the turbulent boundary layer.

7.3.2.2 Experimental results

A semi-logarithmic plot of the mean velocity profiles in a turbulent boundary layer developing on the stator suction surface at a compressor speed of 500 rpm is shown in Fig. 7.2 : these measurements were obtained at $2.9^{\circ}$ incidence where significant departures from two-dimensionality occur due to flow convergence near the trailing edge (see Fig. 4.8); however, it is necessary to tolerate this in order to consider a case in which the extent of turbulent flow is reasonably large. There is obviously a complete failure of logarithmic similarity in all of the profiles shown in Fig. 7.2 : the curves all lie well above the logarithmic law at $y^+ = 30$, where they would normally be expected to become asymptotic to it. The points where $y/\delta \simeq 0.2$, which is roughly the outer limit of the logarithmic layer in zero pressure gradient, lie variously between $y^+ = 20$ and 35 ; thus the logarithmic layer could perhaps have been absent because the Reynolds number was so low that the inner and outer similarity regions failed to overlap. However, the effects of streamwise pressure gradient appear even more significant : the measured velocity profile tends to move towards the logarithmic law as the boundary layer Reynolds number increases, but away from it as the pressure gradient (defined by the parameter $\alpha_o = (\nu/\rho u_\tau^3)(dp/dx)$) becomes more positive ; in the regions x/c = 0.50 - 0.60, and 0.80 - 0.90, the effect of increasing pressure gradient outweighs the effect of increasing Reynolds number.

The curves of $u/u_\tau \sim yu_\tau/\nu$ are of questionable accuracy because of uncertainties about the wall proximity correction required for hot wire readings obtained in turbulent flow : for the velocity profiles shown in Fig. 7.2, 50% of the laminar flow wall correction alters the measured value of $u_\tau$ by some 20 - 30%. But a close inspection of the measured profiles reveals that there is no knee in any of the curves around $y^+ = 20 - 30$, so that they cannot possibly be made to lie along the usual law of the wall by altering the value of $u_\tau$ (as was the case for the flat plate profile shown in Fig. 3.13) : in fact, not one of the 80 - odd velocity profiles measured in turbulent boundary layer regions showed any hint of logarithmic similarity.

Fig. 7.3 gives some indication of the influence of Reynolds number changes on the velocity profile in the wall layer. The measurements shown were obtained at the same chordwise position, x/c = 0.90, but at different

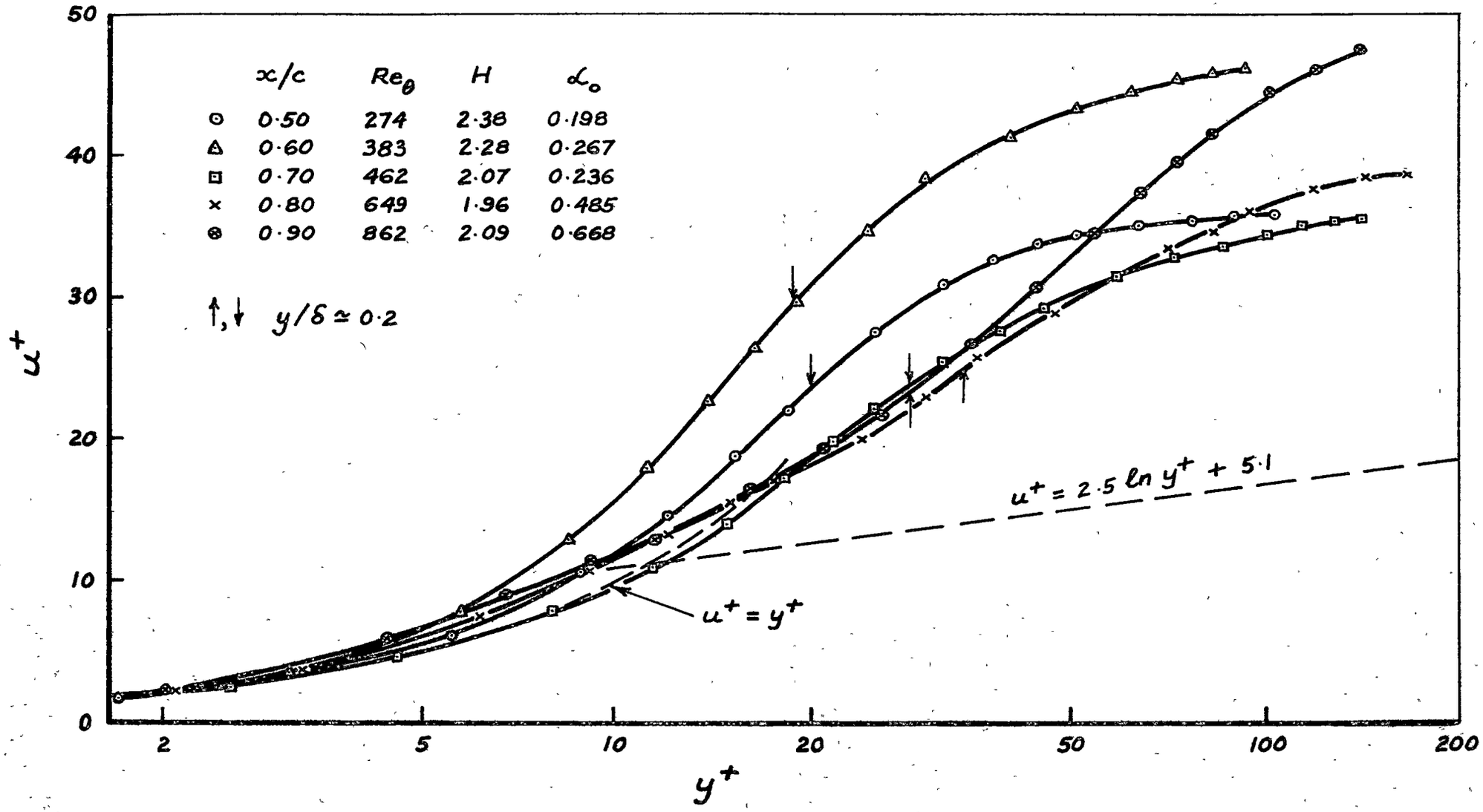


Fig. 7.2 Semi-Logarithmic Plot Showing Development of Mean Velocity Profile on Stator Suction Surface

( $i = 2.9^{\circ}$ ; Compressor Speed 500 rpm )

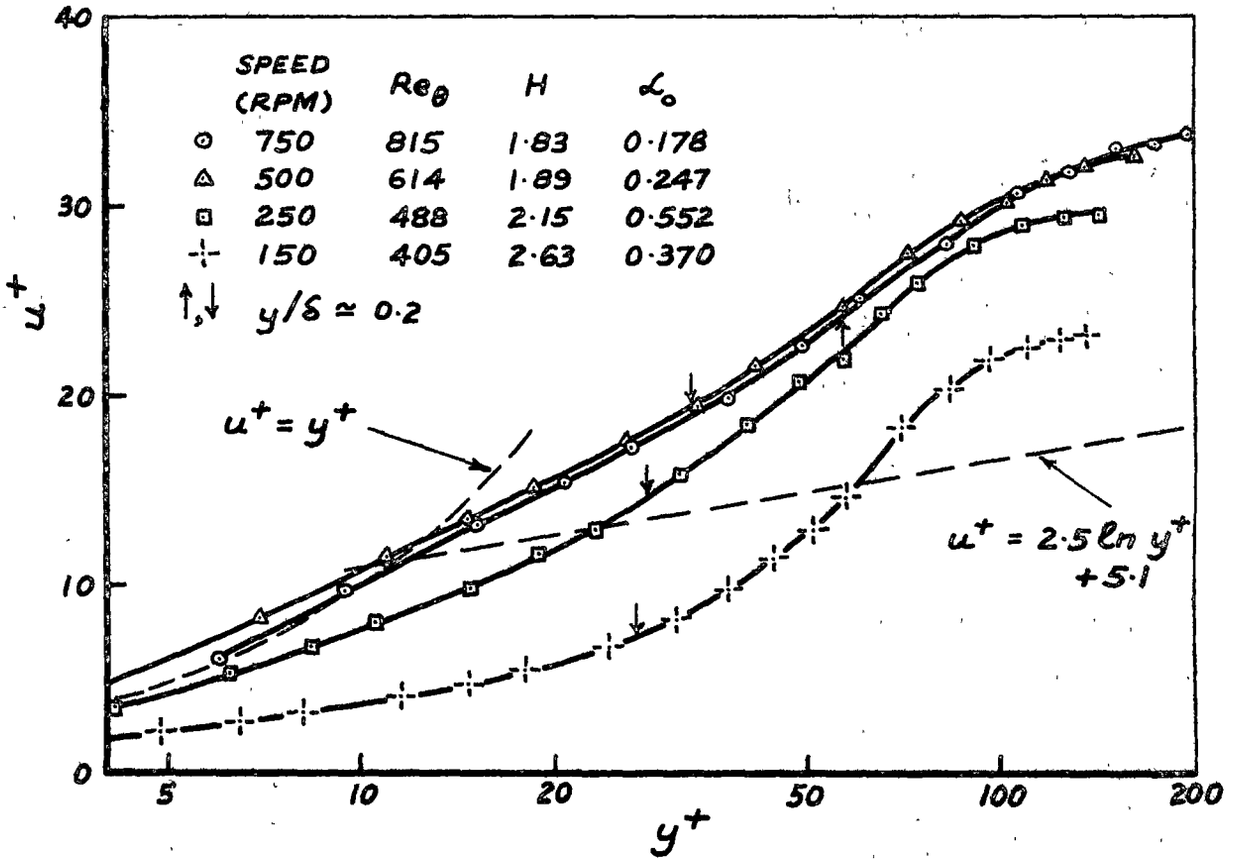


Fig. 7.3 Semi-Logarithmic Plot of Mean Velocity Profiles on Stator Suction Surface at x/c = 0.90 : 8 in. Throttle Opening ; $i \simeq -3^\circ$ - Showing Effect of Changing Compressor Speed

compressor speeds ; it should be noted that some significant changes in the pressure gradient parameter $\alpha_o$ also occurred. The general trend shown in Fig. 7.3 is for the velocity profiles to undershoot the law of the wall as the Reynolds number is reduced (using the smaller wall proximity correction for turbulent flow suggested by Wills would increase this effect); the undershoot first becomes apparent for the profile measured at 250 rpm, and is very marked indeed for the profile measured at 150 rpm, where $Re_\theta = 405$. It is interesting to note that this behaviour is opposite to that observed in reverse transition (or "relaminarisation"), which is characterised by an overshoot of velocity above the logarithmic profile (see Ref. 88). Although the measurements obtained at 150 rpm are admittedly the least accurate, they all show the same behaviour and it is considered that the undershooting effect is very largely genuine : this view is strenghened by the results of plotting the law of the wall in an alternative form which will be considered in Section 7.3.3.

The undershooting of the velocity profiles from the law of the wall also appears to be characteristic of the flow behaviour during reattachment of the

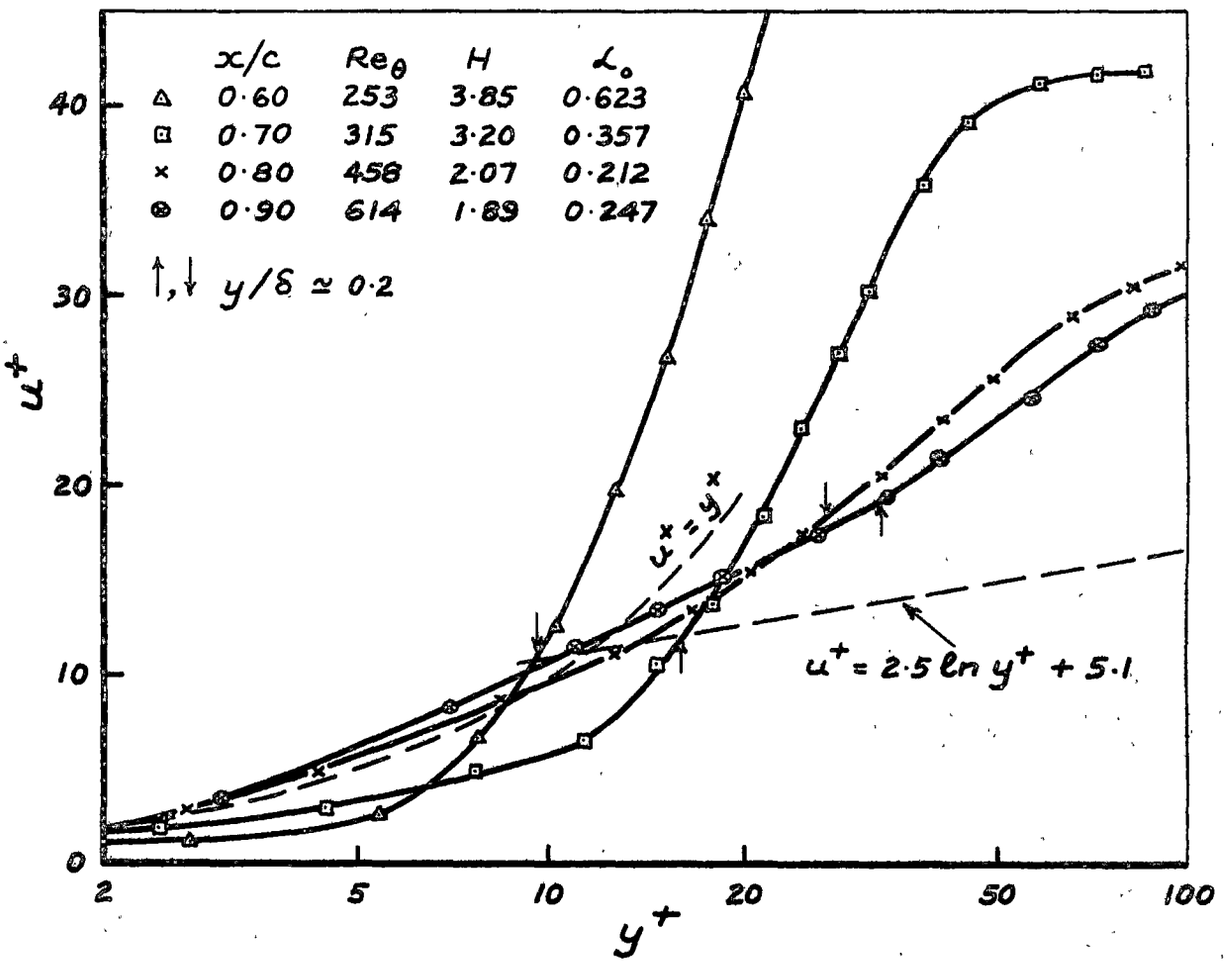


Fig. 7.4 Semi-Logarithmic Plot of Mean Velocity Profiles During Transition and Reattachment Behind Laminar Separation Bubble on Stator Suction Surface : Compressor Speed 500 rpm, i = $-3.1^{\circ}$

turbulent shear layer downstream of a laminar separation bubble. This is illustrated in Fig. 7.4, which shows some measurements on the stator blade suction surface at a compressor speed of 500 rpm. At x/c = 0.70, which is only a few percent of chord downstream of the reattachment point, the value of $u^+$ in the inner part of the sublayer is quite low ; at x/c = 0.80, the value of $u^+$ in this region has become much larger ; the general trend with increasing distance downstream is for $u^+$ to increase within the sublayer and decrease outside it, so that the curve of $u^+ \sim y^+$ progressively recovers towards the normal law of the wall. It is thought that this effect partly accounts for the large undershoot of the profile measured at 150 rpm which is shown in Fig. 7.3.

It is concluded from the above results that the absence of logarithmic similarity on the compressor blade probably resulted from the combined effects of low Reynolds number, large positive pressure gradient, and rapidly changing boundary conditions.

### 7.3.3 Effect of Pressure Gradient on the Law of the Wall

#### 7.3.3.1 Introduction

The effect of streamwise pressure gradient on the law of the wall in turbulent flow has been studied by a number of workers in recent years: notably Stratford (90), Townsend (91), Perry et al.(92), Mellor (94) and McDonald (84). This thesis will be mainly concerned with the analysis of McDonald (84); a summary of previous work on the subject can be found in his paper.

In the presence of moderate streamwise pressure gradients it becomes necessary to incorporate additional variables in Eqn. 7.10 to allow for changes in shear stress across the wall layer. McDonald suggests that the velocity distribution near the wall in this case is functionally expressed as

$$u = f(y, \nu, \rho, \tau, \partial\tau/\partial y, \ldots) \tag{7.11}$$

where $\tau$, the total shear stress, is given by

$$\tau = \rho\{\nu(\partial u/\partial y) - \overline{u'v'}\} \tag{7.12}$$

The mixing length concept

$$-\overline{u'v'} = (l\,\partial u/\partial y)^2 = (Ky\,\partial u/\partial y)^2 \tag{7.13}$$

can be used to replace the turbulent shear stress in Eqn. 7.12; then, if the von Karman constant K is taken independent of y in the fully turbulent wall layer, and the stress gradient $\partial\tau/\partial y$ is either a constant or a function only of $y, \nu, \rho$ and $\tau$, Eqn. 7.11 can be simplified to

$$u = f(y, \nu, \rho, \partial u/\partial y) \tag{7.14}$$

Dimensional analysis of the variables in Eqn. 7.14 gives

$$u = u_s f\left\{y\left(\frac{1}{\nu}\frac{\partial u}{\partial y}\right)^{\frac{1}{2}}\right\} \tag{7.15}$$

where $u_s$ is a velocity scale. McDonald's similarity coordinate is therefore

$$Y = y\left(\frac{1}{\nu}\frac{\partial u}{\partial y}\right)^{\frac{1}{2}} \tag{7.16}$$

where $(KY)^2$ is identical to the similarity parameter used in the earlier analysis of Mellor (94).

The variation of turbulent shear stress through the viscous sublayer is allowed for by assuming K = K(Y) in this region: the function K(Y) is obtained from empirical data for the zero pressure gradient case, which gives

$$K\begin{cases} = 0.41\{0.00714Y + \exp[3(Y-9)]\}^{\frac{1}{2}} & (Y < 9) \\ = 0.41 & (Y \geq 9) \end{cases} \tag{7.17}$$

Using Eqns. 7.12, 7.13 and 7.16, the velocity gradient is written as

$$\frac{\partial u}{\partial y} = \frac{\tau/\rho\nu}{1 + K^2Y^2} \tag{7.18}$$

and this can be integrated to give the velocity distribution u(y) provided that the shear stress distribution is known.

Very close to the wall, the stress gradient $\partial\tau/\partial y$ is equal to the pressure gradient dp/dx ; as distance from the wall increases, the stress and pressure gradients rapidly become unequal ; at large distances from the wall, the stress gradient becomes nearly constant in many cases. These considerations led McDonald to suggest a stress distribution of the form

$$\partial\tau/\partial y = \sum_{n=0}^{n} a_n \tanh^n(bY) \qquad (7.19)$$

The $a_n$ are determined by the wall boundary conditions, assuming that the velocity distribution in the wall layer is of the logarithmic form $u^+ = f(y^+)$; the functional dependence of the parameter b on Y in the viscous sublayer is again obtained from empirical data for constant pressure flows. For values of the argument bY greater than about 2.0, the hyperbolic tangent has a value of almost unity, and the stress gradient becomes nearly constant, given by

$$\partial\tau/\partial y = a = a_o + a_1(=0) + a_2 + a_3 + \cdots\cdots$$

$$= \frac{dp}{dx} + 0 + \frac{1}{2b_w^2}\frac{d\tau_w}{dx} + \frac{1}{3b_w^3}\frac{\nu}{u_\tau}\frac{d^2p}{dx^2} + \cdots \qquad (7.20)$$

which integrates to give

$$\tau = ay + \tau_o \ . \qquad (7.21)$$

$\tau_o$, the intercept of the linear total stress distribution with the y = 0 axis, is not equal to the wall shear stress, $\tau_w$, since the stress gradient in the viscous sublayer differs from "a" ; however, $\tau_o$ and $\tau_w$ are not expected to be greatly different unless the stress and pressure gradients are large. The value of the parameter $b_w$ is 1/14 in a constant pressure flow, and McDonald suggests that this can be used with little loss of accuracy even when the pressure gradient is large.

The velocity distribution in the turbulent wall layer (bY>2) can be obtained by analytical integration of Eqn. 7.18 after substituting for the shear stress distribution from Eqn. 7.21 : this gives

$$u = \frac{2}{\rho^{\frac{1}{2}}K}(ay + \tau_o)^{\frac{1}{2}} + \left(\frac{\tau_o}{\rho K^2}\right)^{\frac{1}{2}} \ln\left|\frac{(ay + \tau_o)^{\frac{1}{2}} - \tau_o^{\frac{1}{2}}}{(ay + \tau_o)^{\frac{1}{2}} + \tau_o^{\frac{1}{2}}}\right| + B$$

$$(\tau_o > 0,\ ay + \tau_o > 0) \qquad (7.22)$$

The velocity distribution in the viscous sublayer is obtained by numerical integration of Eqn. 7.18, together with Eqns. 7.17 and 7.20: at Y = 10, the stress distribution becomes linear and can be extrapolated back to y = 0 to give $\tau_o$ ; using this value of $\tau_o$ and the calculated values of u and y at some point where bY > 2, Eqn. 7.22 can be used to evaluate the constant, B.

The non-dimensional form of the law of the wall, using conventional coordinates, is

$$u^+ = \frac{A^{\frac{1}{2}}}{K} \ln \left| \frac{4A}{\alpha} \left\{ \frac{(\alpha y^+ + A)^{\frac{1}{2}} - A^{\frac{1}{2}}}{(\alpha y^+ + A)^{\frac{1}{2}} + A^{\frac{1}{2}}} \right\} \right| + \frac{2}{K} \left\{ (\alpha y^+ + A)^{\frac{1}{2}} - A^{\frac{1}{2}} \right\} + B^+$$

$$(\alpha y^+ A > 0,\ A > 0) \qquad (7.23)$$

where
$$\left.\begin{aligned} \alpha &= (a\nu/\rho u_\tau^3) = \alpha_0 + \alpha_2 + \alpha_3 + \ldots \\ A &= \tau_0/\tau_w \\ B^+ &= B/u_\tau - (A^{\frac{1}{2}}/K) \ln |4A/\alpha| + 2A^{\frac{1}{2}}/K \end{aligned}\right\} \qquad (7.24)$$

A more suitable form of the velocity profile in the case where the wall shear stress is small (or the pressure gradient is very large) is obtained by using the pressure velocity $u_p$ of Mellor (93): defining

$$u^* = u/u_p \quad ; \quad y^* = yu_p/\nu \qquad (7.25)$$

where
$$u_p = (\nu a_0/\rho)^{1/3} = \{(\nu/\rho)(dp/dx)\}^{1/3} \qquad (7.26)$$

leads to the alternative expressions

$$u^* = \frac{2}{K} \left\{ (Cy^* + A^*)^{\frac{1}{2}} - A^{*\frac{1}{2}} \right\} + \frac{A^{*\frac{1}{2}}}{K} \ln \left| \frac{4A}{\alpha} \left\{ \frac{(Cy^* + A^*)^{\frac{1}{2}} - A^{*\frac{1}{2}}}{(Cy^* + A^*)^{\frac{1}{2}} + A^{*\frac{1}{2}}} \right\} \right| + B^* \qquad (7.27)$$

where
$$\left.\begin{aligned} A^* &= A/\alpha_0^{2/3} \ ; \ B^* = B^+/\alpha_0^{1/3} \ ; \ C = a/a_0 = \alpha/\alpha_0 \\ \alpha_0 &= (u_p/u_\tau)^3 = (\nu a_0/\rho u_\tau^3) \end{aligned}\right\} \qquad (7.28)$$

Placing A = 1 in Eqn. 7.23 gives the law of the wall in the form suggested by Townsend (91) (who assumed $\tau = \tau_w + ay$) ; placing A = 1, C = 1 in Eqn. 7.27 gives the law of the wall in the second form suggested by Mellor (94) (who assumed $\tau = \tau_w + a_0 y$).

McDonald's law of the wall, Eqn. 7.23, is expected to be something of an improvement on Townsend's (91) law of the wall, since the additive constants A and $B^+$ are allowed to vary in response to pressure gradient and inertia effects. Nevertheless, McDonald's work is still subject to the same basic limitations which apply to Townsend's earlier analysis ; the most important of these are that:

(a) the adoption of a linear mixing length distribution in the turbulent wall layer (Eqn. 7.13) relies heavily on assumptions of energy equilibrium and structural similarity of the turbulence in this region;

(b) the use of a linear shear stress distribution in the turbulent wall layer (Eqn. 7.21) is based on a limited range of experimental observations which may not be generally valid (see, for instance, Perry et al.(92)).

A more subtle objection to McDonald's analysis is that the expressions for the parameters $a_2$ and $a_3$ which are used to relate the stress and pressure gradients in the turbulent wall layer (see Eqn. 7.20) are derived from the law of the wall for zero pressure gradient, Eqn. 7.6, which is assumed invariant with x : this will not be valid when the pressure gradient is large or the flow conditions change very rapidly in the streamwise direction. McDonald also neglects the effect of the turbulent normal stresses on the stress gradient in the wall layer, whereas it appears from the results of Ref. 19 that the normal stress terms can become comparable with the streamwise pressure gradient in a boundary layer close to separation.

7.3.3.2 Experimental results

The boundary layer mean velocity profiles shown previously in Fig. 7.2 in the conventional form $u^+ \sim y^+$ have been replotted in Fig. 7.5 in the alternative form $u^* \sim (y^*)^{\frac{1}{2}}$ ; they are compared with the theoretical wall layer profiles calculated by the theory of McDonald described above. The values of $u^* = u/u_p$ are likely to be much more accurate than the values of $u^+$ since the non-dimensionalising parameter $u_p$ is not influenced by possible large errors in the measured wall shear stress. There are still some uncertainties about the experimental mean velocity values close to the wall because of wall proximity effects and the extrapolation of the hot wire calibration to low velocities in some cases ; but these rapidly become smaller in magnitude as distance from the wall increases, and it is unlikely that the total error in the measured values of $u^*$ shown in Fig. 7.5 would exceed 5% in the fully turbulent part of the wall layer. In this form of plotting the law of the wall, the wall friction velocity appears only in the pressure gradient parameter $\alpha_o = (\nu/\rho u_\tau^3)(dp/dx)$, which is used in calculating the theoretical velocity profiles; but the possible error of 25% in $u_\tau$ would change the value of $\alpha_o$ by about 100%. This is not as serious as it first seems, however, since the theoretical velocity profiles change very slowly with $\alpha_o$ for $\alpha_o$ large : a change from $\alpha_o = 0.5$ to $\alpha_o = 1.0$, for example, alters $u^*$ by only 2.0 - 2.3 (i.e. between 10 and 3%) for $3 < (y^*)^{\frac{1}{2}} < 12$.

In deriving the theoretical profiles, the values of the inertia terms $a_2$ and $a_3$ (which determine the difference between the stress and pressure gradients in the turbulent wall layer) were calculated from the expressions given in Eqn. 7.20, using the measured values of p and $u_\tau$ and the constant pressure value of $b_w = 1/14$ suggested by McDonald. There is considerable uncertainty about the determination of $a_2$ and $a_3$, both in the analytical expressions used and in the graphical differentiation of experimental data required to evaluate them ; it was therefore decided to calculate the theoretical velocity profiles for the cases $a_3 = 0$ and $a_2 = a_3 = 0$ as well, in order to indicate the influence of possible errors in these parameters.

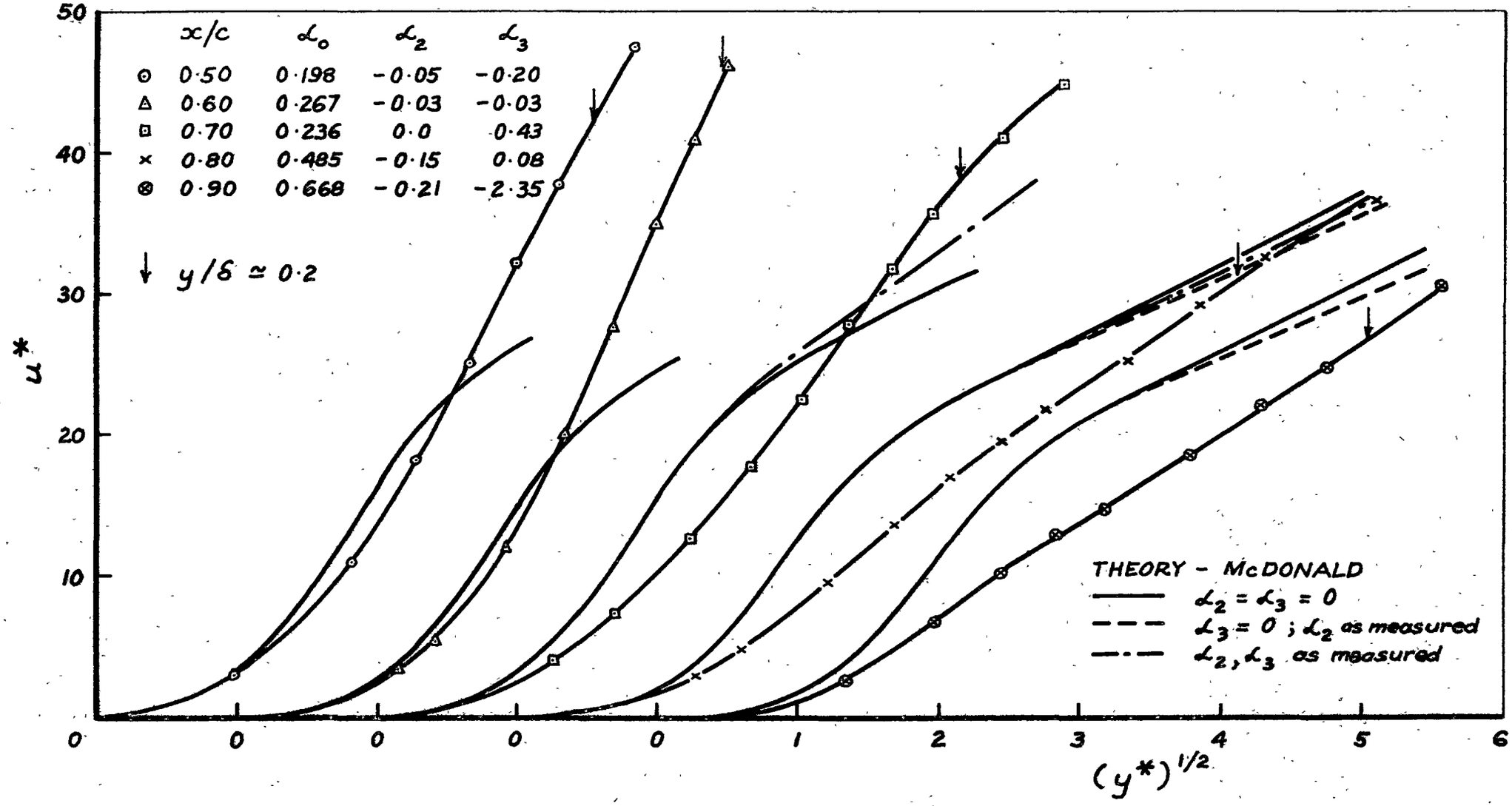


Fig. 7.5 Half-Power Plot Showing Development of Mean Velocity Profile on Stator Suction Surface
($i = 2.9^\circ$ , Compressor Speed 500 rpm)

The experimental velocity profiles in Fig. 7.5 show appreciable regions of "half-power similarity", where the curve of $u^* \sim (y^*)^{\frac{1}{2}}$ is approximately linear. As the boundary layer develops in the streamwise direction, the slope of the linear region falls progressively and the measured curves tend to wrap around the theoretical law of the wall predicted by McDonald's analysis. At x/c = 0.80, there is quite fair agreement between theory and experiment in the outer part of the wall layer (near $y/\delta = 0.2$ which is the approximate limit of validity of the mixing length assumption); but this agreement might be partly fortuitous, since the measured profile has fallen significantly below the theoretical one at x/c = 0.90. Inclusion of the inertia terms $\alpha_2$ and $\alpha_3$ produces a slightly more favourable agreement with experiment ; but as far as the velocity profiles in the wall layer are concerned, very little would be lost in most cases by placing $\alpha_2 = \alpha_3 = 0$ and so equating the stress and pressure gradients as in Mellor's (94) analysis.

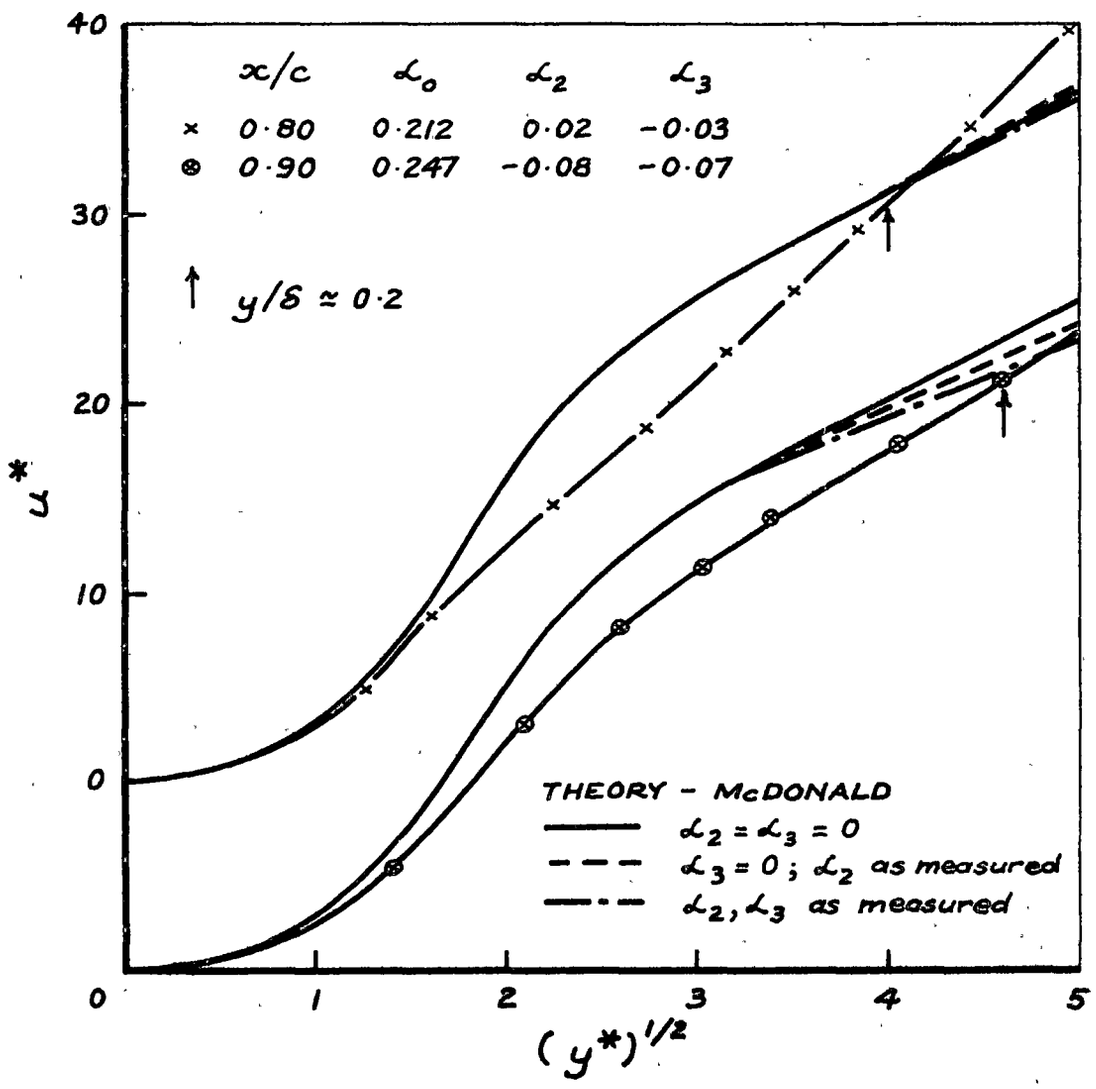


Fig. 7.6 Half-Power Plot Showing Development of Mean Velocity Profile on Stator Suction Surface : i =-3.1°, Compressor Speed 500 rpm

Some of the differences between the measured and theoretical profiles shown in Fig. 7.5 could possibly have arisen from the convergence of flow which occurred over the rearward part of the blade at $i = 2.9^{\circ}$. Fig. 7.6 shows the velocity profiles in this region at $i = -3.1^{\circ}$, where the departures from two-dimensional flow were not as great : here, the agreement is somewhat better, but still only fair. There is a general trend in these and most of the other measurements for the experimental velocity profiles to fall below the theoretical profiles in the outer part of the viscous sublayer ; this could perhaps reflect a change in the distribution of turbulent shear stress through the sublayer under conditions of very low Reynolds number and large positive pressure gradient.

Fig. 7.7 shows the effect of changes in compressor speed on the velocity profiles at $x/c = 0.90$ on the stator suction surface. These measurements were previously plotted in semi-logarithmic form in Fig. 7.4. At 750 rpm, the agreement between the experimental and theoretical profiles is quite reasonable, but it steadily worsens as the compressor speed falls and the boundary layer Reynolds number decreases. The sudden change occurring between 500 and 250 rpm probably arises from bursting of the laminar separation bubble situated further forward on the surface at this incidence : this causes the point of turbulent reattachment to jump rearwards and reduces the length of attached turbulent flow upstream of the point being considered ; at the lowest speed, therefore, conditions at $x/c = 0.90$ are still changing quite rapidly in the streamwise direction (see Fig. 4.7). The very large undershoot of the measured velocity below the theoretical law of the wall at 150 rpm cannot possibly be explained by likely errors in measuring the values of $\alpha_o$ or $u^*$ : the experimental curve even falls far below the theoretical curve for $\alpha_o = 10$, which is some 25 times as large as the measured value of $\alpha_o = 0.37$, while the uncertainty in $u^*$ due to wall proximity effects is less than 5% for $(y^*)^{\frac{1}{2}} > 2.5$.

In conclusion, it is suggested that the broad agreement between the theory of McDonald and the measurements at the higher compressor speeds indicates that pressure gradient effects played a significant role in producing the complete departures from the logarithmic law of the wall which were described in Section 7.3.2.

### 7.3.4 Outer Layer Velocity Profile

The wake function of Coles cannot be defined from the velocity profiles measured on the stator suction surface because of the complete absence of logarithmic similarity in the wall layer in all cases. Nevertheless, a somewhat indirect check on the validity of Coles's wake function can be made by comparing the experimental velocity profiles with Coles's "universal" velocity profile defined in Eqn. 7.7. Placing $\delta = \delta_c$ for convenience, and evaluating Eqn. 7.7 at the outer edge of the boundary layer gives, after subtraction of the original equation,

$$u = (u_\tau/K) \ln (y/\delta) + U - (u_\beta/2)\{1 + \cos(\pi y/\delta)\} \qquad (7.29)$$

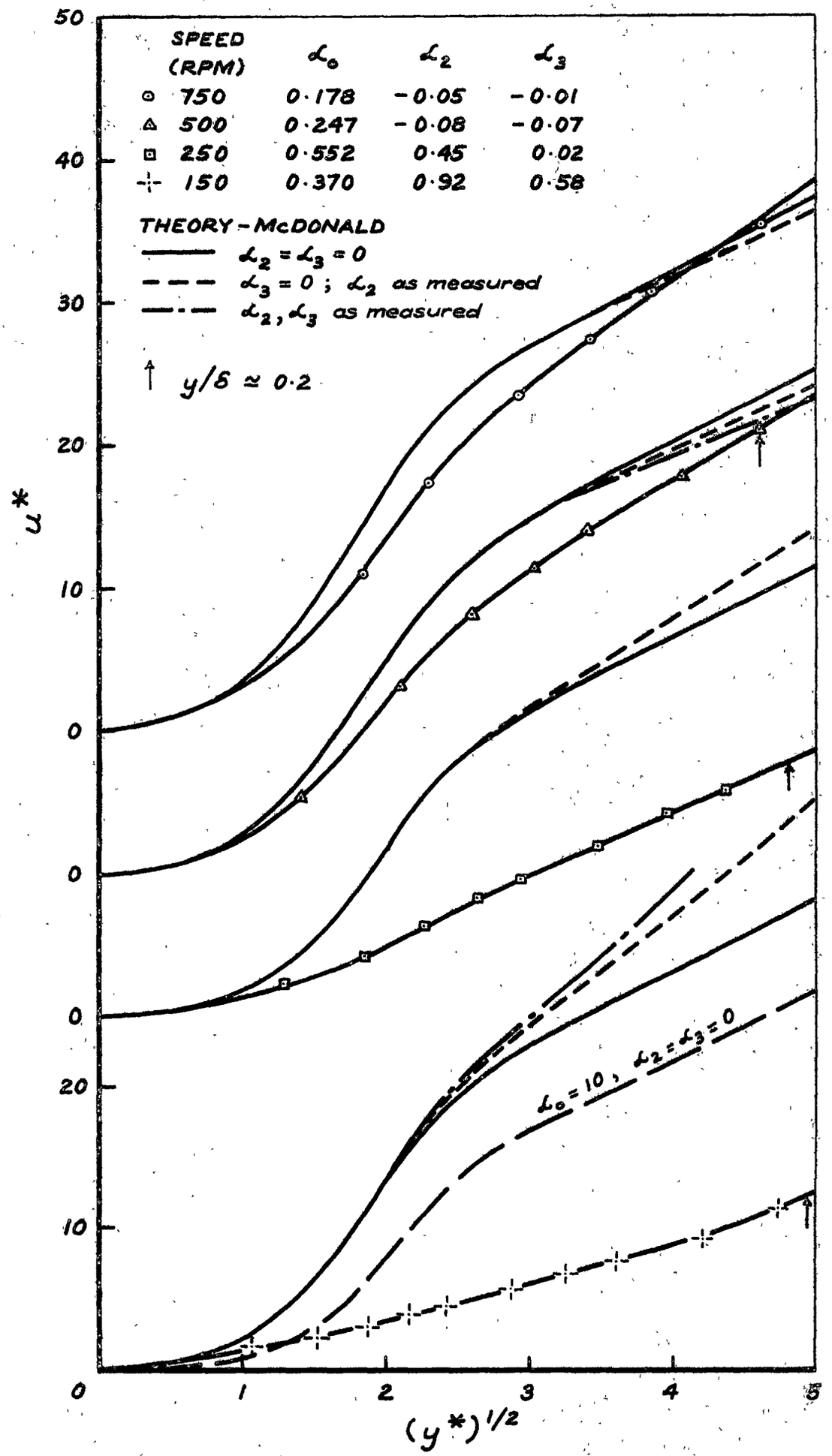


Fig. 7.7 Half-Power Plot of Mean Velocity Profiles on Stator Suction Surface at x/c = 0.90 - Showing Effect of Changing Compressor Speed (8 in. Throttle Opening ; i $\simeq -3^{\circ}$)

A convenient definition of the boundary layer thickness, $\delta$, is obtained from the two integral forms of Eqn. 7.29

$$\frac{\delta^*}{\delta} = \frac{1}{K}\frac{u_\gamma}{U} + \frac{u_\beta}{2U} \tag{7.30}$$

and

$$\frac{\theta}{\delta} = \frac{-2}{K^2}\left(\frac{u_\gamma}{U}\right)^2 + \frac{1}{K}\frac{u_\gamma}{U} - \frac{1.58949}{K}\frac{u_\gamma u_\beta}{U^2} + \frac{u_\beta}{2U} - 0.375\frac{u_\beta^2}{U^2} \tag{7.31}$$

Eliminating $\delta$ from Eqns. 7.30 and 7.31, and substituting the measured values of $\delta^*$, $\theta$, U and $u_\gamma$, together with K = 0.41, gives a quadratic equation which can be solved for $u_\beta$. The boundary layer thickness $\delta$ can then be evaluated from Eqn. 7.30, and the complete velocity profile is calculated from Eqn. 7.29 using the analytical form of the wake function specified by Eqn. 7.8.

A typical comparison between the velocity profile given by Eqn. 7.29 and experiment is shown in Fig. 7.8. It is seen that the value of $\delta$ calculated as described above is significantly smaller than the experimental value ; this, together with the use of Eqn. 7.8 for $y/\delta > 1$ where it is strictly not valid, is responsible for the low values of u/U predicted by Eqn. 7.29 in the outer part of the boundary layer. The agreement between the measurements and Coles's universal profile is only fair in the central region of the boundary layer, the experimental profile tending to be much more "full"; this effect would be heightened by using the experimental value of $\delta$ instead of the value calculated from the integral relations Eqns. 7.30 and 7.31. Near the wall, Coles's profile shows the expected deviation from the measurements through the viscous sublayer, which is relatively thick because of the low Reynolds number.

The power law profile

$$u/U = (y/\delta)^{(H - 1)/2} \tag{7.32}$$

has also been compared with the experimental velocity profile in Fig. 7.8. If $\delta$ is defined as the point on the measured velocity profile where u/U = 1.0, the power law is a much worse fit than Coles's profile. However, the power law could probably be made to fit a little better than Coles's profile by choosing a lower value of $\delta$.

## 7.4 Skin Friction Measurements

### 7.4.1 Comparison with Existing Skin Friction Laws

Integral methods of predicting the turbulent boundary layer development require the use of an auxiliary equation to estimate the local skin friction coefficient. Ludwieg and Tillmann (96) have suggested the skin

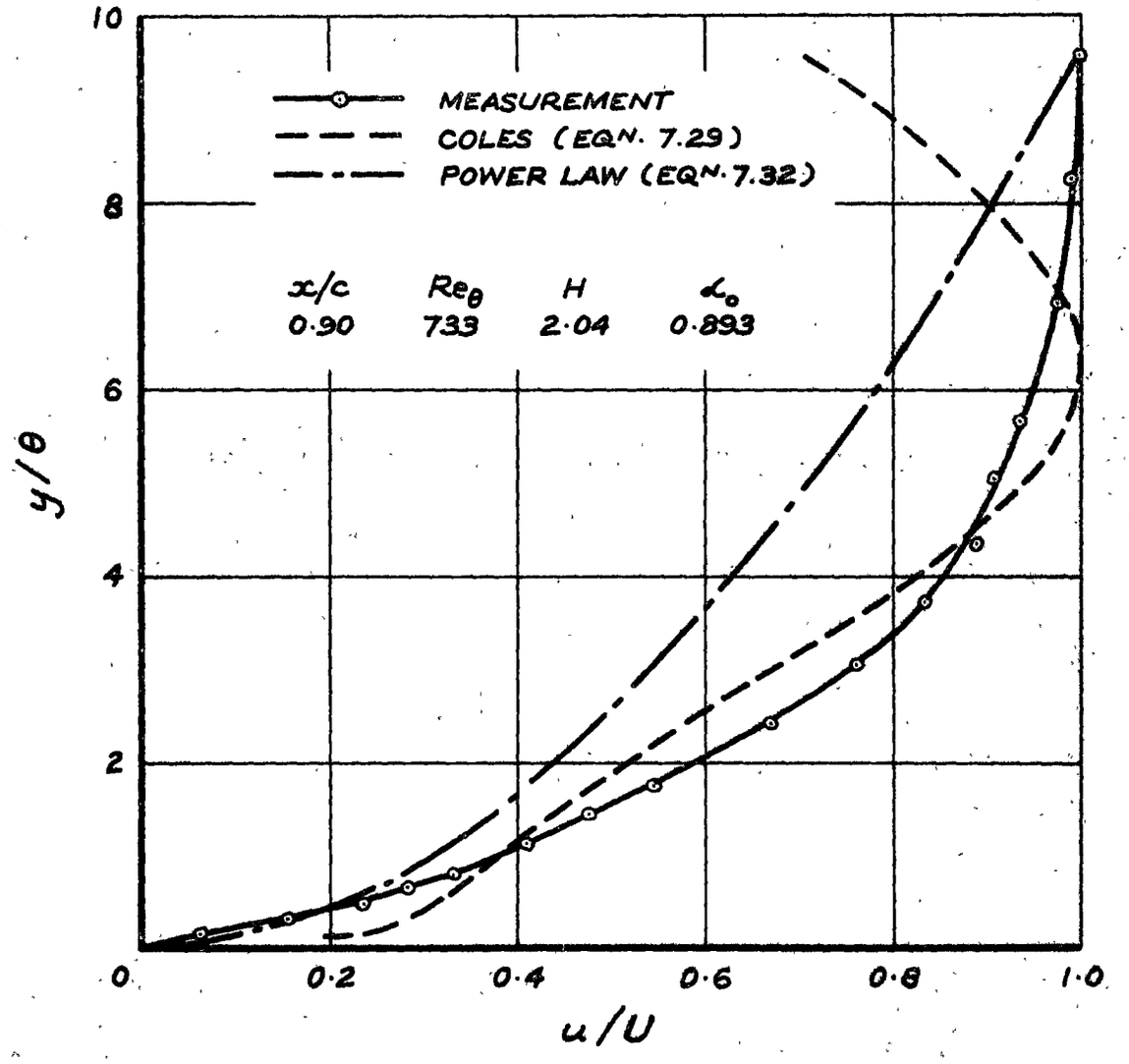


Fig. 7.8 Comparison of Measured and Theoretical Mean Velocity Profiles in Turbulent Boundary Layer on Stator Suction Surface
($i = 1.0^{\circ}$ , Compressor Speed 500 rpm)

friction law

$$C_f = 0.246\, Re_\theta^{-0.268} 10^{-0.678H} \qquad (7.33)$$

which is very convenient to use but is based on experiments covering only a limited range of Reynolds number. In Fig. 7.9, the skin friction values obtained from the hot wire measurements in turbulent boundary layer regions on the stator blade are compared with the values predicted by Eqn. 7.33 using the measured values of $Re_\theta$ and H : the agreement is quite poor, with the ratio of the two values varying by $\pm 40\%$ for the cases shown. The departures from the Ludwieg-Tillmann law tend to increase in magnitude as the pressure gradient parameter $\alpha_o$ increases, but they are clearly not functions of $\alpha_o$ alone. Data from boundary layers with values of shape factor H exceeding 2.3 has been excluded from Fig. 7.9 : in these cases the Ludwieg-Tillmann law breaks down quite hopelessly and predicts values of $C_f$ as low as 20% of those measured, but a significant proportion of these discrepancies could have arisen from measurement errors at very low speeds.

An alternative form of skin friction law can be derived from Coles's two-parameter family of velocity profiles for the turbulent boundary layer.

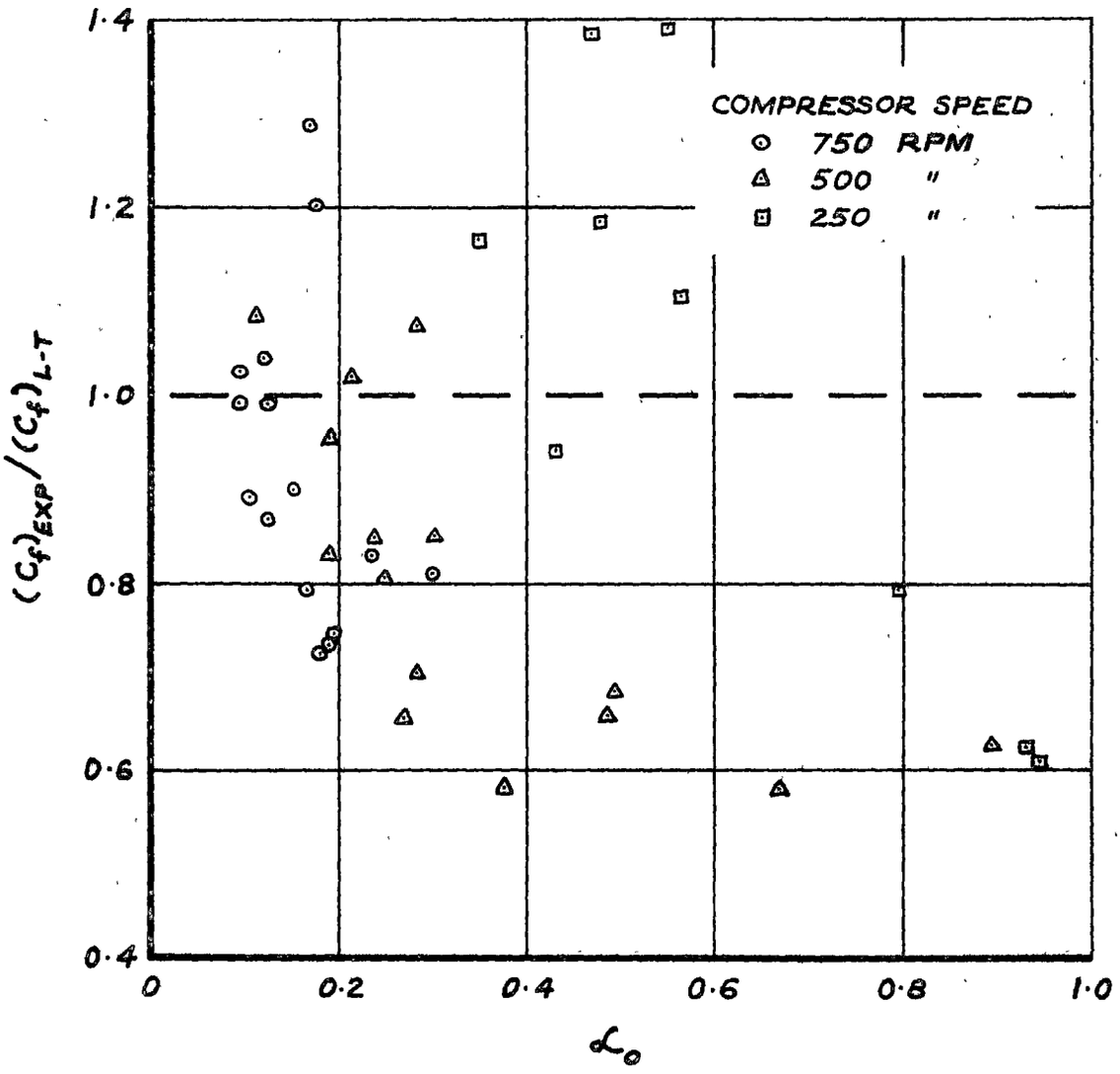


Fig. 7.9 Comparison of Skin Friction Values Measured in Turbulent Boundary Layer Regions on Stator Suction Surface with Values Predicted by Ludwieg-Tillmann Law (Eqn. 7.33)

- Showing Influence of Pressure Gradient Parameter $\alpha_o$

Placing $\delta = \delta_c$ and evaluating Eqn. 7.7 at $y = \delta$ gives

$$\sqrt{2/C_f} = U/u_\tau = (1/K)\ \ln(\delta u_\tau/\nu) + C + u_\beta/2u_\tau \qquad (7.34)$$

Substituting for $\delta$ in terms of $\theta$ from Eqn. 7.31, and writing $u_\beta$ in terms of Clauser's (97) velocity defect parameter

$$G = (u_\tau/U)\int_0^\infty \{(U - u)/u_\tau\}^2 d(y/\delta^*) = \sqrt{2/C_f}(1 - 1/H) \qquad (7.35)$$

leads to the more convenient form of expression

$$\sqrt{2/C_f} = (1/K)\ \ln(Re_\theta) + C + f(G) \qquad (7.36)$$

Nash and Macdonald (98) obtained empirical correlations for the quantities C and f(G) in Eqn. 7.36, and their skin friction law for the case of two-dimensional, incompressible flow past a smooth wall is

$$\sqrt{2/C_f} = 2.4711\ \ln(Re_\theta) + 1.5G + 1724/(G^2 + 200) - 12.12 \qquad (7.37)$$

In Fig. 7.10, the ratio of the experimental skin friction values to those predicted by Eqn. 7.37 (using the measured values of $Re_\theta$ and H) is plotted against the pressure gradient parameter $\alpha_o$ : it is seen that the Nash-Macdonald law also fails to give a good estimate of the skin friction values in turbulent boundary layers on the compressor blade, and that the errors increase with $\alpha_o$ as in Fig. 7.9.

For the cases considered in Figs. 7.9 and 7.10, the values of $C_f$ predicted by the Ludwieg-Tillmann and Nash-Macdonald laws mostly agree to within 10% of each other. Since this difference is small compared with the observed deviations from the experimental data, there is evidently little to choose between the two laws in this situation.

### 7.4.2 A Modified Skin Friction Law Allowing for Large Streamwise Pressure Gradients and Variations in Stress Gradient through the Viscous Sublayer

Mellor (93, 94) has proposed yet another skin friction law which is derived from a family of velocity distributions for the equilibrium turbulent boundary layer (i.e. a boundary layer in which the pressure gradient parameter $\Pi = (\delta^*/\tau_w)(dp/dx)$ is held constant in the streamwise direction). Mellor's velocity profile family, which is based on an effective viscosity hypothesis for the total shear stress within the boundary layer, consists of an inner and an outer (defect) law which overlap near the wall in a region where the eddy viscosity corresponds to that given by Prandtl's mixing length theory ; the effects of pressure gradient on the law of the wall are allowed for by assuming a shear stress distribution near y = 0 of the form

$$\tau = \tau_w + (dp/dx)y \qquad (7.38)$$

The skin friction law given in Ref. 94 is of the form

$$\sqrt{2/C_f} = (1/K)\ \ln(Re_{\delta^*}) + F(\Pi) + B^+(\alpha_o) \qquad (7.39)$$

Using the results of Refs. 93, 94 it is possible to express the function $F(\Pi)$ in terms of the defect parameter G, and to relate $\delta^*$ to $\theta$ : a possible alternative form of Eqn. 7.39 is, therefore

$$\sqrt{2/C_f} = (1/K)\ \ln(Re_\theta) + f(G) + B^+(\alpha_o) \qquad (7.40)$$

Assuming the Nash-Macdonald law to be the particular case of Eqn. 7.40 for which $\alpha_o$ is small, the function f(G) can be obtained from Eqn. 7.37. Nash and Macdonald's function f(G) was fitted to a reasonably wide range of experimental data which was not restricted to the case of "continuous" equilibrium ($\Pi$ = constant) for which Mellor and Gibson's function $F(\Pi)$ was derived: it appears that f(G) should at least be valid for the local equilibrium case (defined in Section 7.6.2 ), and will probably allow for some small departures from local equilibrium. Comparing Mellor's shear stress distribution, Eqn. 7.38, with that assumed by McDonald, Eqn. 7.21, it is

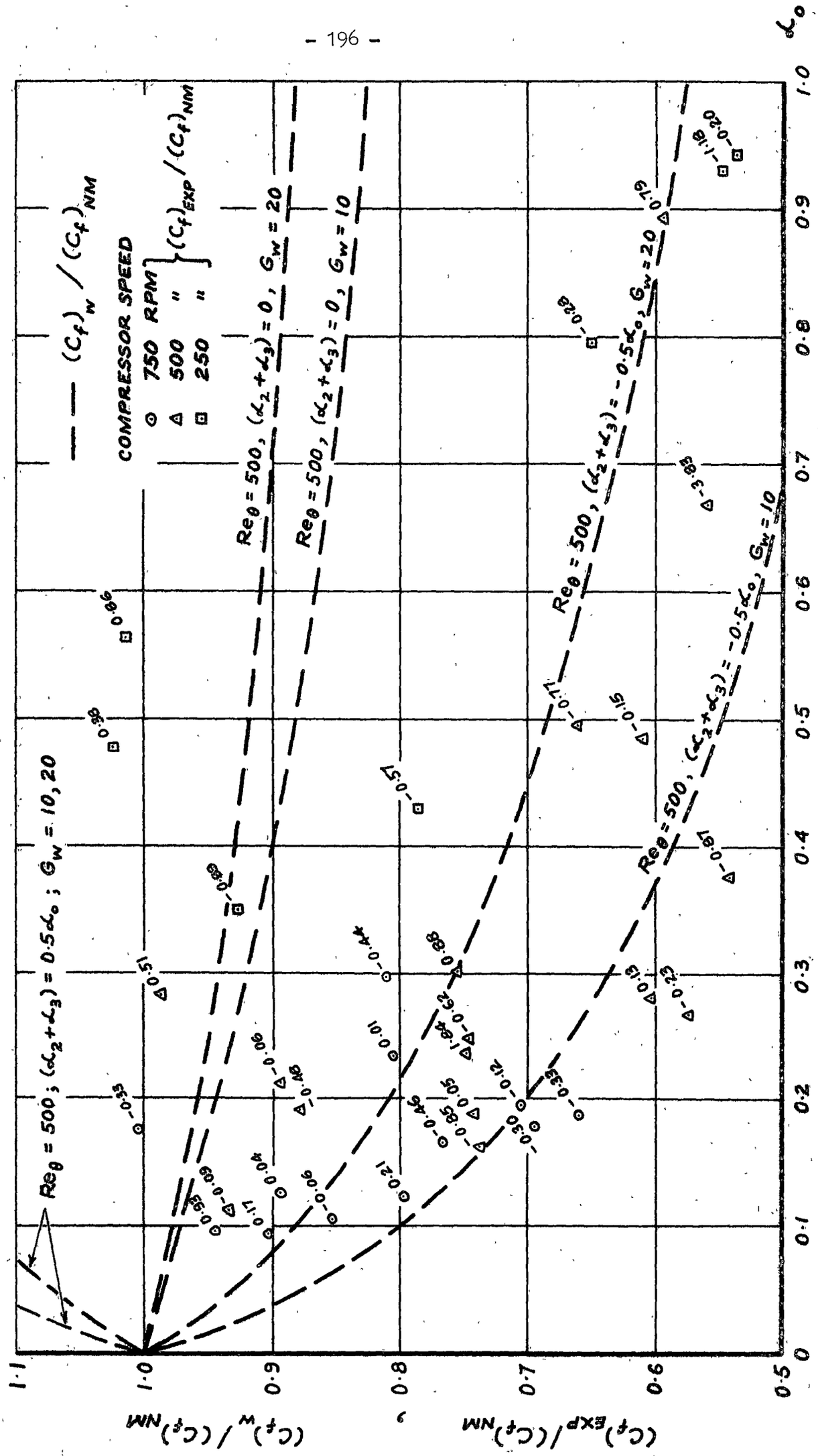


Fig. 7.10 Comparison of Experimental Skin Friction Values with Nash-Macdonald Skin Friction Law (Eqn. 7.37) and Modified Nash-Macdonald Law (Eqn. 7.47)

seen that the quantity $B^+(\alpha_o)$ in Eqn. 7.40 can be identified with the value of the function $B^+$ appearing in McDonald's law of the wall (Eqn. 7.23) for the particular case in which $\tau_o = \tau_w$ (i.e. A = 1) and $\partial\tau/\partial y = dp/dx$ (i.e. $\alpha_2 + \alpha_3 + .. = 0$).

In a boundary layer subjected to very large pressure gradients and rapid changes in the streamwise direction, the work of McDonald (Section 7.3.3) suggests that inertia effects will cause the stress gradient in the turbulent wall layer to depart from the pressure gradient, as indicated by Eqn. 7.20 ; furthermore, the expected changes in stress gradient through the viscous sublayer should cause the actual wall shear stress $\tau_w$ to differ appreciably from the value $\tau_o$ obtained by extrapolating the linear stress distribution in the wall layer to the point y = 0. In these cases, it is suggested that the Mellor/Nash-Macdonald skin friction law will still be valid, provided that the skin friction coefficient is based on the "apparent" (as far as the wall layer is concerned) wall shear stress $\tau_o$, and the stress gradient is substituted for the pressure gradient; this leads to the expression

$$\sqrt{2/C_{f_o}} = \sqrt{\rho U^2/\tau_o} = (1/K)\ \ln(Re_\theta) + f(G_o) + (B^+)' \qquad (7.41)$$

where
$$G_o = \sqrt{2/C_{f_o}}\,(1 - 1/H) \qquad (7.42)$$

$$\alpha' = \frac{\nu}{\rho u_{\tau_o}^3}\frac{\partial\tau}{\partial y} = \left(\frac{\nu}{\rho u_{\tau_w}^3}\frac{dp}{dx}\right)\left(\frac{u_{\tau_w}}{u_{\tau_o}}\right)^3\left(\frac{\partial\tau/\partial y}{dp/dx}\right)$$
$$= \alpha_o A^{-3/2}\left\{1 + (\alpha_2 + \alpha_3)/\alpha_o\right\}$$
$$(\alpha_4 = \alpha_5 = \ldots = 0) \qquad (7.43)$$

and $(B^+)'$ is the value of $B^+$ obtained from the theory of McDonald with $A = 1, \alpha_2 + \alpha_3 + .. = 0$, and $\alpha_o = \alpha'$. Relating $\tau_o$ to $\tau_w$ by means of Eqn. 7.24, and writing

$$G_w = \sqrt{2/C_{f_w}}\,(1 - 1/H) = G_o A^{\frac{1}{2}} \qquad (7.44)$$

the modified skin friction law becomes

$$\sqrt{2/C_{f_w}} = \sqrt{\rho U^2/\tau_w} = A^{\frac{1}{2}}\left\{(1/K)\ \ln(Re_\theta) + f(G_w/A^{\frac{1}{2}}) + (B^+)'\right\} \qquad (7.45)$$

The Nash-Macdonald law is now rewritten, for greater clarity, as

$$\sqrt{2/C_{f_{NM}}} = (1/K)\ \ln(Re_\theta) + f(G_w) + (B^+)^o \qquad (7.46)$$

where $(B^+)^o$ is the value of $(B^+)'$ in the case $\alpha_o = 0$, A = 1. Nash and Macdonald assume $(B^+)^o = 4.75$, which differs slightly from the value of 4.90 obtained by Mellor and McDonald; it is therefore more convenient to write

$$\sqrt{2/C_{f_w}} = A^{\frac{1}{2}}\left\{(1/K)\ \ln(Re_\theta) + f_1(G_w/A^{\frac{1}{2}})\right.$$
$$\left. + [(B^+)' - 4.75]\right\} \qquad (7.47)$$

and $$\sqrt{2/C_{f_{NM}}} = (1/K)\ \ln(Re_\theta) + f_1(G_w) \qquad (7.48)$$

where $f_1(G)$, obtained from Eqn. 7.37, is given by

$$f_1(G) = 1.5G + 1724/(G^2 + 200) - 12.12 \qquad (7.49)$$

Finally, the ratio of the shear stress predicted by the new law, Eqn. 7.47, to that predicted by the Nash-Macdonald law can be expressed as

$$\frac{C_{f_w}}{C_{f_{NM}}} = \frac{1}{A}\left\{\frac{(1/K)\ \ln(Re_\theta) + f_1(G_w)}{(1/K)\ \ln(Re_\theta) + f_1(G_w/A^{\frac{1}{2}}) + [(B^+)' - 4.75]}\right\}^2 \qquad (7.50)$$

Curves of $C_{f_w}/C_{f_{NM}} \sim \alpha_o$ calculated from Eqn. 7.50 for representative values of the various parameters involved have been plotted in Fig. 7.10 to enable the predictions of the new skin friction law to be compared with the experimental values from the stator blade measurements. It has been assumed for convenience that $\alpha_4 = \alpha_5 = \ldots = 0$ in Eqn. 7.24, so that $\alpha_2$ and $\alpha_3$ are the only inertia terms involved. Curves are drawn for $Re_\theta = 500$; $G_w = 10,\ 20$ ; $(\alpha_2 + \alpha_3)/\alpha_o = -0.5,\ 0,\ 0.5$. (The curve for $\alpha_2 + \alpha_3 = 0$, in which case $A = 1$, corresponds to the skin friction law proposed by Mellor (94) which allows for pressure gradient effects on the shear stress distribution in the wall layer, but does not take into account changes in stress gradient through the viscous sublayer.) The actual value of the stress gradient in the turbulent wall region of the stator blade boundary layer is unknown, as no direct shear stress measurements were obtained : but judging from the observations of other workers (Refs. 84, 88) it seems reasonable to assume that it should lie between 50 and 70% of the streamwise pressure gradient provided that conditions do not change too rapidly in the streamwise direction; this corresponds to values of $(\alpha_2 + \alpha_3)/\alpha_o$ in the range $-0.3$ to $-0.5$. The stress gradient can, of course, be estimated from the theory of McDonald using Eqn. 7.20, and the values of $(\alpha_2 + \alpha_3)/\alpha_o$ thus obtained have been indicated next to the experimental points in Fig. 7.10 ; however, it should be remembered that the validity of Eqn. 7.20 is suspect in the circumstances existing on the compressor blades, and that $\alpha_2$ and $\alpha_3$ cannot be evaluated from the experimental data with any great accuracy.

It is seen from Fig. 7.10 that the experimental skin friction values mostly lie within the expected range around the curves for $(\alpha_2 + \alpha_3)/\alpha_o = -0.5$. (The points in this large group arise almost entirely from situations where the streamwise changes are slow, i.e. dH/dx small.) There is another group of points (several out of range of Fig. 7.10) for which $C_{f_w}/C_{f_{NM}} > 1$ : these correspond to situations following transition, where $dH/dx < 0$, and have positive values of $(\alpha_2 + \alpha_3)/\alpha_o$ as required by Eqn. 7.50. Where H is very large and dH/dx is very large and negative, Eqn. 7.50 breaks down completely, as do all the other skin friction laws considered here.

The new skin friction law appears to give quite a reasonable prediction of the large departures from the Nash-Macdonald law which are observed for high values of the pressure gradient parameter $\alpha_0$. There is a considerable scatter in the calculated values of $(\alpha_2 + \alpha_3)/\alpha_0$ for the various experimental points, but the average for a number of different points is often of the right order. There are a number of points for which the calculated values of $(\alpha_2 + \alpha_3)/\alpha_0$ are in very marked disagreement with the curves obtained from Eqn. 7.50 ; but almost without exception these are found to be cases in which the calculated values are extremely doubtful due to the necessity of differentiating experimental data at points where sudden changes in slope occur.

The agreement obtained above appears sufficiently encouraging to warrant further investigation of the modified skin friction law given by Eqns. 7.47 and 7.49. But this would require direct measurements of the turbulent shear stress in the wall region, which would be very difficult, if not impossible, to obtain in the very thin boundary layers existing on compressor blades.

## 7.5 The Minimum Reynolds Number for a Turbulent Boundary Layer Under a Pressure Gradient

### 7.5.1 Preston's Model

In the case of pipe flow there is a lower experimental limit to the Reynolds number for fully developed turbulent flow. From the similarity and close agreement between the curves of $C_f \sim Re_\theta$ for the flat plate and circular pipe, Preston (75) anticipated that there would be a lower limit to the Reynolds number $Re_\theta$ for fully developed turbulent boundary layer flow on a plate (in zero pressure gradient) : rather limited experimental evidence confirmed this and placed the lower limit at $Re_\theta = 320$.

There is also a lower limit to the Reynolds number range for which the inner and outer similarity laws overlap to give a logarithmic velocity distribution near the wall. Following Landweber (102), this is expected to occur when the effects of viscosity become significant over the whole wall layer. Taking the outer limit of the viscous sublayer at $yu_\tau/\nu = 30$, and the outer edge of the logarithmic layer at $y/\delta = 0.2$, Preston obtained

$$\delta u_\tau/\nu = 150 \qquad (7.51)$$

as the condition for the logarithmic overlap region to be of zero thickness : this corresponded to $Re_\theta = 389$, which agreed fairly closely with the experimentally observed minimum value of $Re_\theta = 320$ for fully developed turbulent flow in the case of the flat plate.

On the assumption that this agreement would be generally true, Preston was able to use the "no overlap" condition to make some predictions about the minimum Reynolds number for a turbulent boundary layer under a pressure

gradient. In considering this problem it is convenient to write

$$(Re_\theta)_{min} = \left(\frac{\delta u_\tau}{\nu}\right)_{min}\left(\frac{\theta}{\delta}\right)\left(\frac{U}{u_\tau}\right) \qquad (7.52)$$

Preston expected that $(\delta u_\tau/\nu)_{min}$ should exceed 150 in an adverse pressure gradient (due to the value of $y/\delta$ at the outer edge of the logarithmic layer becoming smaller than 0.2); the values of both $\theta/\delta$ and $U/u_\tau$ were also expected to be greater in this case. Thus it seemed to Preston that the lower limit of $Re_\theta$ for fully developed turbulent flow should increase in adverse pressure gradients and decrease in favourable pressure gradients; however, there was no available experimental evidence against which this hypothesis could be tested at the time when it was proposed.

The present investigation has revealed values of $Re_\theta$ as low as 200 in turbulent boundary layers subjected to very large adverse pressure gradients on the stator blade suction surface. This trend is opposite to that predicted by Preston's hypothesis and therefore requires some explanation. It is believed that the differences between theory and experiment do not reflect a breakdown of the basic physical model adopted by Preston, but are rather due to a lack of generality in the empirical data used to determine the no overlap condition given by Eqn. 7.51. The value of $(\delta u_\tau/\nu)_{min} = 150$ obtained by Preston was based on a value of $yu_\tau/\nu = 30$ at the outer edge of the viscous sublayer, and this is strictly applicable only to the zero pressure gradient case : in conditions of adverse pressure gradient, the later work of Refs. 84, 94 indicates that the value of $yu_\tau/\nu$ at the outer edge of the viscous sublayer should fall progressively as the pressure gradient becomes more positive. In the case where $\alpha_o = 1$, for example, the outer edge of the viscous sublayer is predicted to occur at $yu_\tau/\nu \simeq 10$, which is smaller by a factor of 3 than the value assumed by Preston : it is suggested that this difference could be great enough to offset the expected increases in $\theta/\delta$ and $U/u_\tau$ in an adverse pressure gradient, and so result in a value of $(Re_\theta)_{min} < 320$ in this case. Accepting that a lower minimum value of $Re_\theta$ is in fact possible, it is seen (for instance from Eqn. 7.33) that the increase in $U/u_\tau$ caused by the positive pressure gradient will be somewhat offset by the decrease in $U/u_\tau$ occurring at the lower value of $Re_\theta$.

### 7.5.2 An Alternative Model Using Mellor's Effective Viscosity Hypothesis

The existence of a lower minimum Reynolds number for turbulent flow in an adverse pressure gradient is also supported by the eddy viscosity hypothesis of Mellor (94). In this analysis, the effective viscosity distribution for the turbulent boundary layer (see Fig. 7.11) is expressed as

$$\left.\begin{aligned} \nu_e/\nu &= \phi\{(K^2y^2/\nu)\,|\partial u/\partial y|\} \quad \text{for y small} \\ \nu_e/U\delta^* &= \Phi\{(K^2y^2/U\delta^*)\,|\partial u/\partial y|\} \quad \text{for y large} \end{aligned}\right\} \qquad (7.53)$$

Both functions apply in a region of overlap near the wall, where

$\nu_e \simeq \varepsilon = K^2y^2|\partial u/\partial y|$ in accordance with Prandtl's mixing length theory. The outer edge of the viscous sublayer is placed at

$$(K^2y^2/\nu)\,|\partial u/\partial y| = 11 \tag{7.54}$$

and for very large y outside the overlap region a constant value of

$$\nu_e/U\delta^* = 0.016 \tag{7.55}$$

is chosen.

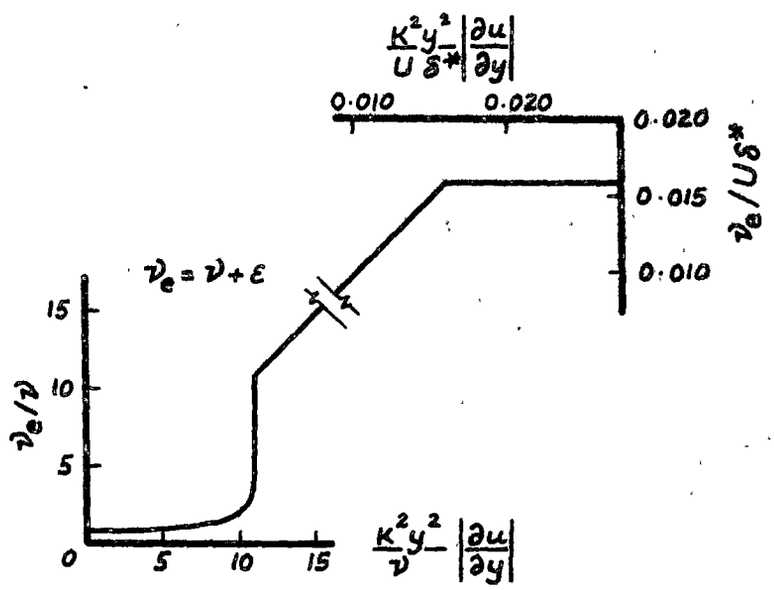


Fig. 7.11 Effective Viscosity Function of Mellor (94)

As the Reynolds number is reduced, the thickness of the overlap region decreases, and it finally reaches zero when

$$\nu_e = 11\nu = 0.016\ U\delta^* \tag{7.56}$$

Following Preston's hypothesis and assuming this to be the minimum Reynolds number at which fully developed turbulent flow may exist gives

$$(Re_{\delta^*})_{min} = (U\delta^*/\nu)_{min} = 11/0.016 = 688 \tag{7.57}$$

The minimum value of $Re_\theta$ is therefore

$$(Re_\theta)_{min} = (Re_{\delta^*})_{min}/H = 688/H \tag{7.58}$$

Since the shape factor H has a larger value in an adverse pressure gradient, Eqn. 7.58 indicates that the minimum Reynolds number for turbulent flow should decrease in an adverse pressure gradient and increase in a favourable pressure gradient. The lowest possible value of $Re_\theta$ at which any fully developed turbulent boundary layer may exist corresponds to the case where H is largest : this will occur at separation where H = 2.3 (say) compared with H = 1.4 (say) for zero pressure gradient. Accepting the experimental minimum value of $Re_\theta$ = 320 proposed by Preston for the zero pressure gradient case, the lowest attainable value of $(Re_\theta)_{min}$ should be

$$\left\{(Re_\theta)_{min}\right\}_{lowest} = 320\ (1.4/2.3) = 195 \tag{7.59}$$

which is not inconsistent with the results of the compressor blade measurements.

The crucial assumption underlying this result is that the effective viscosity in the outer part of the boundary layer is given by $\nu_e/U\delta^* = 0.016$ (Eqn. 7.55). This is based on Clauser's (97) constant eddy viscosity hypothesis for the outer region of equilibrium boundary layers, which is well supported by experiment. Eqn. 7.57 cannot possibly be generally valid, however, since the value of the non-dimensional eddy viscosity $\varepsilon/U\delta^*$ may differ very widely from 0.016 in non-equilibrium boundary layers. All that can fairly be claimed from this analysis, therefore, is that Eqn. 7.58 should indicate the probable trend in $(Re_\theta)_{min}$ with changes in pressure gradient.

### 7.5.3 A Model Using the Eddy Reynolds Number Concept of Bradshaw

Bradshaw (89) showed that both Preston's (75) criterion for the minimum Reynolds number for a turbulent boundary layer in zero pressure gradient, and Patel & Head's (88) criterion for the start of reverse transition in a strong favourable pressure gradient, agreed well with an eddy Reynolds number criterion

$$\left\{(\tau/\rho)^{\frac{1}{2}}L/\nu\right\}_{max} = 30K \qquad (7.60)$$

Here, $K \simeq 0.4$ is the von Karman constant, and L is a dissipation length parameter (which becomes equal to the mixing length in the particular case of energy equilibrium where the advection and diffusion terms in the turbulent energy equation are zero and production equals dissipation). The quantity $(\tau/\rho)^{\frac{1}{2}}L/\nu$ is an approximate measure of the degree of overlap of the energy-containing and dissipating ranges of eddy size : in the limiting case specified by Eqn. 7.60, these ranges overlap at every point within the boundary layer, so that no part of the turbulent flow is free from viscous effects on the shear-producing eddies.

In the two cases considered by Bradshaw, the maximum value of $(\tau/\rho)^{\frac{1}{2}}L/\nu$ occurred either in, or at the edge of, the inner layer, so that L was (to a good first approximation) a unique length scale of the energy-containing eddies. The analysis was not expected to be valid in the outer layer where there would be no unique length scale, and this strictly excluded its application to cases of flow in adverse pressure gradients. Bradshaw did suggest, however, that his eddy Reynolds number would be a useful quantity for correlating experimental data : in this spirit, the present author decided to apply Bradshaw's analysis to the problem of predicting the minimum Reynolds number for the turbulent boundary layer in an adverse pressure gradient despite the objections noted above.

In a strong positive pressure gradient, the maximum value of $(\tau/\rho)^{\frac{1}{2}}L/\nu$ should occur near $y/\delta = 0.5$, where both $\tau$ and L attain their highest values. Following Bradshaw, Ferriss & Atwell (99), the maximum value of L is assumed to be $0.095\delta$. The maximum value of the shear stress is obtained from the

expression

$$C_\tau/C_f = 0.01473G^2 - 0.0423 \qquad (7.61)$$

suggested by Nash & Macdonald (100) for equilibrium boundary layers, and the empirical correlation

$$C_\tau = 0.58\ \tau_{max}/\tfrac{1}{2}\rho U^2 + 0.42\ \phi_m C_f \qquad (7.62)$$

proposed by McDonald and Stoddart (101) : here, $\phi_m$ is the value of $y/\delta$ at which the maximum shear stress $\tau_{max}$ occurs, and $C_\tau$ is the integral of the shear stress distribution over the boundary layer height. Near separation, the second term on the right hand side of both Eqns. 7.61 and 7.62 may be neglected, and substituting for G from Eqn. 7.35 gives

$$(\tau_{max}/\rho)^{\frac{1}{2}} = 0.16\ U(1 - 1/H) \qquad (7.63)$$

Substituting the maximum values of $\tau$ and L into Eqn. 7.60, which is assumed to remain valid in this case, gives the minimum Reynolds number for fully developed turbulent flow as

$$(U\delta/\nu)_{min} = 791\ H/(H - 1) \qquad (7.64)$$

Finally, taking the case (chosen previously in Section 7.5.2) where H = 2.3 and $\delta/\theta = 7$, say, gives the minimum value of momentum thickness Reynolds number as

$$(Re_\theta)_{min} = 200 \qquad (7.65)$$

This is in reasonable agreement with the results of Section 7.5.2 above, and is once again not inconsistent with the results of the compressor blade measurements: it suggests that the eddy Reynolds number criterion proposed by Bradshaw is perhaps more general than might have been expected.

### 7.5.4 Concluding Remarks

Although values of $Re_\theta$ as low as 200 were observed in apparently fully turbulent boundary layer regions on the compressor blade, there was no evidence to suggest that this represented an absolute minimum value. Thus the results of the present investigation can only be regarded as indicating a trend for the minimum value of $Re_\theta$ for fully developed turbulent flow in a strong adverse pressure gradient to be lower than that in zero pressure gradient.

It is important to note that the initial breakdown to turbulent flow may occur at even lower values of $Re_\theta$ than the limiting value of 200 suggested above for the fully turbulent flow case : the minimum value of $Re_{\theta_t}$ observed during the present investigation was nearer to 100. In conditions of strong adverse pressure gradient, $Re_\theta$ is increasing rapidly with x, and a turbulent spot initiated at this lower Reynolds number has only to survive for a short period before the minimum Reynolds number needed to sustain fully developed turbulent flow is reached. Bradshaw's (89) observatio

that a well-organised spot of turbulence can maintain itself at a lower Reynolds number than a large body of turbulence suggests that this is by no means impossible.

## 7.6 Prediction of the Turbulent Boundary Layer

### 7.6.1 Introduction

The major difficulty in predicting the development of turbulent boundary layers is that the total shear stress is strongly dependent on the upstream history of the flow, and is not determined solely by the local mean velocity profile as in the laminar flow case. Changes in the local boundary conditions such as pressure gradient or wall shear stress are not immediately impressed on the whole boundary layer but diffuse slowly through it as the turbulent shear stress distribution gradually assumes its altered shape: since a length in the streamwise direction of some 10-50 boundary layer thicknesses is required for this process to near completion, no method of predicting the turbulent boundary layer can be expected to give realistic results unless the "memory" of the turbulent shear stress for the upstream history of the flow is taken into account.

The tendency of the turbulent boundary layer mean velocity profile to "lag" behind changes in external conditions assumes even greater importance at the low Reynolds numbers typical of turbomachine blade operation. The case of the machine blade provides an extremely severe test of any method of predicting turbulent boundary layer development, since the turbulence lag is very large compared with the blade chord : in the compressor blade boundary layers studied in the present investigation, for instance, the total length of turbulent boundary layer was often as low as 10 times the trailing edge boundary layer thickness. Calculations for aerofoils operating at higher Reynolds numbers, such as aircraft wings, are rather less critical in this respect, since the boundary layer thickness and turbulence lag are much smaller relative to the aerofoil chord.

As all methods of calculating the turbulent boundary layer rely to some extent on empirical data, there is a risk of considerable errors occurring if they are used too far outside the range of conditions for which this data was obtained. Unfortunately for the machine designer, most of the existing data has come from laboratory boundary layers and isolated aerofoil boundary layers formed at moderately high Reynolds numbers with low levels of external disturbance : turbomachine boundary layers have low Reynolds numbers and are subjected to much higher curvature of flow and free-stream turbulence. It follows that existing methods of predicting turbulent flow must be thoroughly checked by experiment on actual machine blades before they can be applied with confidence in this new situation.

The input data for a two-dimensional turbulent boundary layer calculation consists of initial values of the flow variables at some particular streamwise location (most frequently the transition point), together with a specification of the surface pressure distribution. The output from the calculation should provide at the very least an estimate of the variation in momentum thickness, wall shear stress, and boundary layer shape factor along the surface; a reliable prediction of separation is also very desirable. The mean velocity and shear stress profiles, and the behaviour of various other turbulence properties, may or may not be determined according to the type of calculation method used. Boundary layer calculation methods can be divided into two general classes :
(i) "integral" methods, which only predict the variation in integral properties of the mean velocity and shear stress profiles, such as $\theta$, H, $C_\tau$;
(ii) "non-integral" methods, which solve for the complete velocity profiles, and sometimes for the complete distribution of shear stress as well.

The initial values required for starting a turbulent boundary layer calculation vary from the value of $\theta$ alone for the simplest integral methods, to the complete mean velocity and shear stress profiles for the more complicated non-integral methods. Where calculation methods are tested against laboratory boundary layers, the starting conditions are at least partly known from the experimental measurements. In the problem of predicting the boundary layer development on an aerofoil, however, the starting conditions for the turbulent boundary layer calculation are usually completely unknown, and must be estimated from the laminar boundary layer and transition predictions : any errors in estimating the starting conditions will carry through into the turbulent boundary layer calculation and make it less reliable.

As the behaviour of turbulent flow is still not completely understood, all available prediction methods are necessarily based on approximate physical models of the real flow. The many prediction methods at present available may conveniently be divided into three sub-groups according to the type of physical model used to describe the effects of flow history:
(i) "local equilibrium" or "zero-order" methods, which entirely neglect the effect of upstream history, and assume both the mean velocity and shear stress profiles to depend only on the local conditions;
(ii) "first-order" methods, which assume the rate of change of mean velocity (or some integral parameter of the mean velocity profile) to depend on the local mean flow variables, but still neglect the effect of history on the turbulent shear stress distribution. It is assumed either explicitly or implicitly that the shear stress is determined by the local conditions alone;
(iii) "second-order" methods, which assume the rate of change of shear stress (or some integral shear stress parameter) to depend on the local

values of shear stress and mean velocity. These give the closest approximation to the behaviour of real turbulent flow.

Extensive reviews of existing methods of predicting turbulent boundary layer development have been given by Thompson (103), Rotta (104), Bradshaw (95), and Kline et al.(105). A few examples of the various types of calculation methods will be discussed in detail in the following sections, and their success in predicting the boundary layer development on the blades of the research compressor will be evaluated.

### 7.6.2 Local Equilibrium Methods

If the pressure gradient parameter $\Pi = (\delta^*/\tau_w)(dp/dx)$ defined by Clauser (106) is held constant in the streamwise direction, the velocity defect parameter G for the turbulent boundary layer settles to an almost constant value and the boundary layer is then said to be "in equilibrium" or "self-preserving". There is a functional relationship between G and $\Pi$ for equilibrium boundary layers which has been given by Nash (107) as

$$\hat{G} = 6.1\sqrt{\Pi + 1.81} - 1.7 \qquad (7.66)$$

on the basis of both experimental and theoretical results; this relation has been plotted in Fig. 7.12.

The momentum integral equation for the turbulent boundary layer can be integrated with respect to x by using the auxiliary equation

$$G = \hat{G} \qquad (7.67)$$

together with a suitable skin friction law (for example, the Ludwieg-Tillmann law specified by Eqn. 7.33). This is called a local equilibrium method, since it is assumed that the value of G depends only on the local value of the pressure gradient parameter $\Pi$ : it is analagous to Pohlhausen's (108) method for predicting the laminar boundary layer, which assumes the shape factor H to be determined by the pressure gradient parameter $(\theta^2/\nu)(dU/dx)$.

Local equilibrium methods can only be expected to give acceptable results in cases where the external velocity distribution U(x) is such that the value of G always remains close to the local equilibrium state defined by Eqn. 7.66 : turbulent boundary layers developing in arbitrary pressure distributions may exhibit considerable departures from local equilibrium, particularly when there are any sudden changes in the streamwise pressure gradient. Some typical trajectories of $G \sim \Pi$ for boundary layers measured on the stator blade suction surface in the research compressor are shown in Fig. 7.12 : it is seen that shortly after transition is completed, the measured value of G exceeds the equilibrium value $\hat{G}$; as the boundary layer proceeds into regions of higher adverse pressure gradient, the ratio of G to $\hat{G}$ steadily falls ; over the rearward part of

the blade, G is less than the equilibrium value $\hat{G}$. This behaviour appears to be fairly typical of boundary layers developing under a "convex" pressure distribution, where $d^2p/dx^2 > 0$.

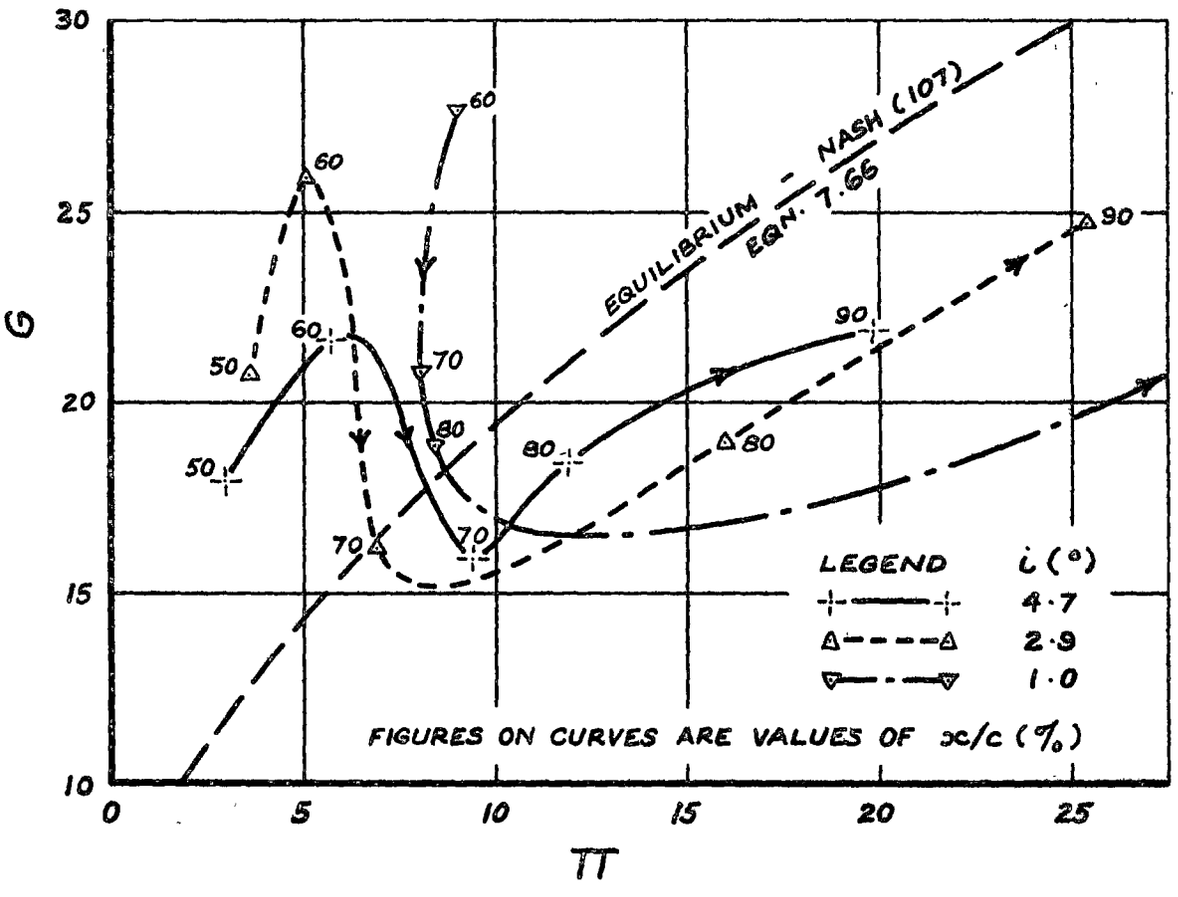


Fig. 7.12 Trajectories of $G \sim \Pi$ for Turbulent Boundary Layers on Stator Suction Surface : Compressor Speed 500 rpm

The shape factor development calculated from Eqns. 4.1, 7.33, and 7.67 for a pressure distribution measured on the stator blade suction surface is shown in Fig. 7.13. The local equilibrium value of H is less than the measured value in regions where $dH/dx < 0$, and exceeds the experimental value where $dH/dx > 0$. This behaviour is a natural consequence of assuming the turbulent boundary layer to follow any changes in pressure gradient immediately : in the real boundary layer it takes a finite streamwise distance for changes in the shear stress and mean velocity distributions to occur. It is clear from Fig. 7.13 that the local equilibrium method is of little use for turbomachine blades having a convex pressure distribution, since the measured values of H lag behind the local equilibrium values by up to 25% of the blade chord. The prediction of turbulent boundary layer separation is particularly bad in this case, since the real boundary layer will withstand a much greater pressure rise than is indicated by the local equilibrium solution.

Better results might be obtained for "concave" pressure distributions having $d^2p/dx^2 < 0$, as the deviations from the local equilibrium state are likely to be smaller in this case; but the author does not know of any detailed boundary layer measurements on compressor blades with this type of pressure distribution. It would be useful to undertake such a study in the future, since published data indicates that the behaviour of boundary layers experiencing augmentation of pressure gradient is rather different from those subject to alleviation of pressure gradient.

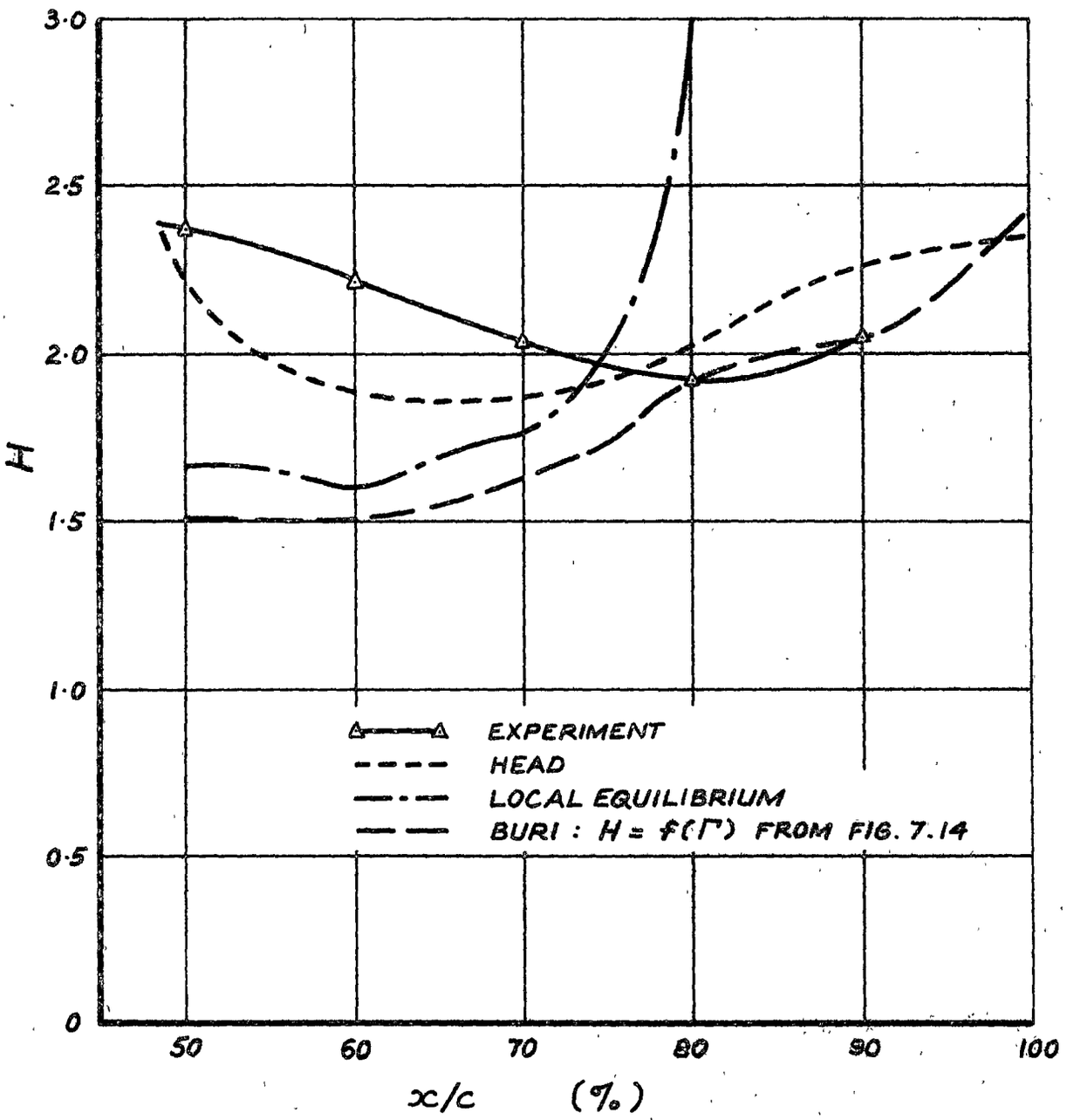


Fig. 7.13 Shape Factor Prediction for a Turbulent Boundary Layer Developing on the Stator Blade Suction Surface at a Compressor Speed of 500 rpm : $Re_c = 9.3 \times 10^4$, $i = 2.9^\circ$

7.6.3 Buri's Method

The inclusion of Buri's method perhaps requires some justification, since it is a local equilibrium type of solution now regarded as being superseded by more modern methods of predicting the turbulent boundary layer (see Thompson (103)). The method is of some historical interest, being the first attempt (in 1931) at calculating the turbulent boundary layer; however, its relevance in the present context arises mainly from the fact that it has previously been used in several theoretical models of compressor blade performance (see, for instance, Smith (109)).

Buri (110) used a similar approach to that already applied by Pohlhausen for the laminar boundary layer by assuming

$$C_f = f_1(\Gamma) \; / \; Re_\theta^{1/n} \tag{7.68}$$

and

$$H = f_2(\Gamma \text{ only}) \tag{7.69}$$

where

$$\Gamma = (\theta/U)(dU/dx)\, Re_\theta^{1/n} \tag{7.70}$$

with $n = 4$ an average value. These assumptions allow the momentum integral equation to be written as

$$d(\theta\, Re_\theta^{1/n}) \; / \; dx = F(\Gamma) \tag{7.71}$$

From a limited range of experimental data, Buri obtained a linear correlation of $F(\Gamma) \sim \Gamma$, and hence was able to integrate Eqn. 7.71 to give $\theta\, Re_\theta^{1/n}$ as a function of the external velocity distribution $U(x)$. Thompson (103) has noted that the use of an empirical correlation for $F(\Gamma)$ does not assume a unique dependency of boundary layer velocity profile shape on local pressure gradient as far as the momentum thickness prediction is concerned.

The prediction of displacement thickness and separation position is critically dependent on the assumption of a unique relation between H and $\Gamma$, but $\Gamma$ cannot in general be expressed as a function of H alone : approximating the skin friction law by

$$C_f = k_1(10^{\,k_2 H}) Re_\theta^{-\frac{1}{4}} \tag{7.72}$$

gives

$$\Gamma = \frac{\theta}{U}\frac{dU}{dx} Re_\theta^{\frac{1}{4}} = -\frac{\Pi}{2H}(k_1\, 10^{\,k_2 H}) = -\Pi f_3(H) \tag{7.73}$$

Since there is no unique relation between $\Pi$ and H, but rather $H = f_4(\Pi, Re_\theta, G/\hat{G})$, a correlation between H and $\Gamma$ can only be expected for boundary layers having similar values of $Re_\theta$ and similar deviations from equilibrium as indicated by $G/\hat{G}$.

A plot of H against $\Gamma$ from the boundary layer measurements on the stator blade suction surface is shown in Fig. 7.14. The large amount of scatter in the experimental points clearly indicates that there is no universal correlation between these two parameters. The dashed line

indicates a very rough correlation for boundary layers measured at 90% of chord which happen to deviate from the local equilibrium state by about the same amount ; the points lying above this line correspond to boundary layers nearer the leading edge which are further from equilibrium and have much smaller values of $Re_\theta$.

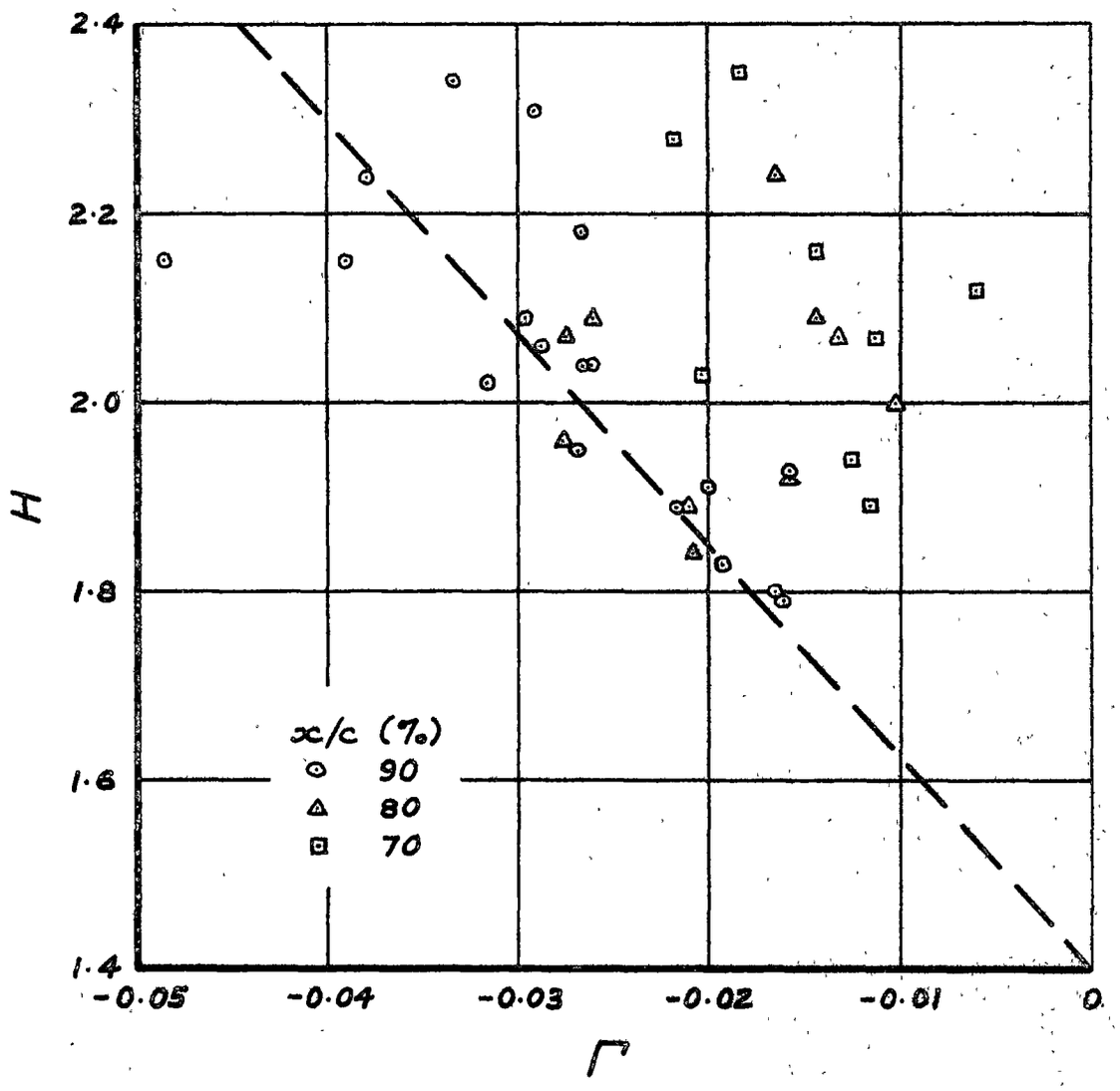


Fig. 7.14 Correlation of H and $\Gamma$ for Turbulent Boundary Layers Measured on Stator Blade Suction Surface

The shape factor development calculated from the assumed correlation of Fig. 7.14 has been indicated in Fig. 7.13. The predicted values of H agree roughly with the measured values near the blade trailing edge where the correlation was obtained, but further forward on the blade where the correlation did not apply the prediction of H is very poor. It is concluded that empirical methods such as Buri's are of little use for calculating the development of a turbulent boundary layer in an arbitrary pressure gradient : similar conclusions have been reached by other workers, notably Thompson (103).

7.6.4 Head's Entrainment Method

A survey by Thompson (103) of known methods of calculating the turbulent boundary layer showed that the method of Head (111) was generally the most satisfactory one available at that time. Head assumes the rate of fluid entrainment per unit width of the boundary layer to be a function of the shape parameter $H_1 = (\delta - \delta^*)/\theta$,

i.e. $$dQ/dx = d\{U(\delta - \delta^*)\} / dx = U\, F(H_1) \qquad (7.74)$$

where $Q = \int_0^\infty u\, dy$ is the volume flux in the boundary layer. This hypothesis may be justified by crude physical arguments about the turbulent flow. The rate of entrainment of irrotational fluid by the turbulent boundary layer depends on the intensity of the velocity fluctuations near its outer edge; the turbulent shear stress, which controls the mean velocity profile, is also a function of the fluctuation intensity. Hence it is plausible to expect the rate of entrainment to depend on the shape of the mean velocity profile. It is noted that the implicit assumption of a relation between the turbulent shear stress and the local velocity profile classifies Head's method as a first-order type of calculation.

The entrainment function $F(H_1)$ is determined from experimental measurements, and Thompson (103) gives

$$F(H_1) = 0.0299\ (H_1 - 3.0)^{-0.6169} \qquad (7.75)$$

The relation between $H_1$ and H is also found empirically, but there is some scatter in the data for $H > 2.0$. The equation

$$H_1 = 2H/(H - 1) \qquad (7.76)$$

was found to give a better prediction of the compressor blade boundary layers than the relation suggested by Thompson. This is perhaps surprising since the power law profiles from which Eqn. 7.76 is derived are not a very good fit to the boundary layer velocity profiles on the stator blade (see Section 7.3.4).

The shape factor development is calculated from the auxiliary equation

$$\theta \frac{dH}{dx} = -\frac{\theta}{U}\frac{dU}{dx}(H^2 - 1)\,H + \tfrac{1}{2} C_f H(H - 1) - \tfrac{1}{2}(H - 1)^2 F(H_1) \qquad (7.77)$$

where the skin friction coefficient $C_f$ is obtained from the Ludwieg-Tillmann formula, Eqn. 7.33, and the value of $F(H_1)$ for a given value of H is found from Eqns. 7.75 and 7.76. The momentum integral equation (4.1) can then be integrated with respect to x, using Eqns. 7.33 and 7.77, to give the boundary layer momentum thickness and shape factor distributions.

The results of a typical shape factor calculation have been compared with experiment in Fig. 7.13. In this case, the initial value of H was chosen to match the experimentally measured value immediately following transition. It is seen that Head's method predicts H to within about 10% of its correct value. Changes in H are of the correct sign, but it is

evident that the influence of the shear stress distribution is still not accurately modelled : H falls too rapidly for the reattaching turbulent shear layer following boundary layer transition, whilst it rises too rapidly in the region of increasing pressure gradient near the blade trailing edge. These results suggest that the shear stress distribution implicit in Head's boundary layer model changes more rapidly than the shear stress distribution of the real boundary layer. Nevertheless, the predictions of Head's method are far better than those of the local equilibrium solution, which assumes the shear stress distribution to change instantaneously.

Bradshaw (95) has pointed out that it is $d^2H/dx^2$ rather than $dH/dx$ that is determined by the mean flow parameters. Hence first-order integral methods (such as Head's), which use equations for $dH/dx$, are bound to be inaccurate if the boundary layer is changing fairly rapidly.

### 7.6.5 Second-Order Integral Calculation Methods

Some more recent attempts to predict the turbulent boundary layer in an arbitrary pressure gradient have assumed that the turbulent shear stress profiles may be represented by a single-parameter family of curves. In this case, there are two auxiliary equations of the form (see Ref. 95)

$$dC_\tau/dx = f_1(C_\tau, H) \quad ; \quad dH/dx = f_2(C_\tau, H) \qquad (7.78)$$

where $C_\tau$ is some integral shear stress parameter. Eqn. 7.78 classifies this type of approach as a second-order integral method. This model still fails to represent the turbulence properties exactly, since the real shear stress profiles change much more rapidly near the wall than in the outer regions, and cannot always be accurately represented by a one-parameter family.

The introduction of the additional parameter $C_\tau$ means that some property of the initial shear stress profile must also be specified before the turbulent boundary layer calculation can proceed. Some calculation methods are unduly sensitive to the initial values chosen : the predicted boundary layer development may agree well with experiment if measured values of $C_\tau$ and H are used for starting the calculation, but small variations in the initial conditions may lead to much larger deviations in the predicted development than would be exhibited by a real boundary layer given a similar small perturbation. These comments apply particularly to the calculation methods of McDonald & Stoddart (101), which uses the quantity $\phi_m$ as shear stress parameter, and of McDonald (112), which employs the maximum shear stress value $\tau_m$ : the application of these methods to predicting the boundary layer development on the stator blade was considered likely to be unfruitful because of the lack of information about the initial shear stress profile.

The calculation method of Nash & Macdonald (100), on the other hand, shows quite a low sensitivity to changes in the initial conditions : the

shear stress parameter used in this case is $\int_0^\infty \tau \, dy$. Some attempts were made to apply this method to predicting the boundary layer development on the stator blade, but only moderate success was achieved. Provided that suitable starting values were chosen, the Nash-Macdonald method was able to predict quite accurately many features of the measured shape factor distribution H(x) ; however, there were a significant number of cases in which the calculation method became very unstable. In addition, the choice of the initial shear stress value proved extremely difficult : the use of the local equilibrium value of $C_\tau$, as suggested by McDonald (112), was found to be particularly inappropriate (which is hardly surprising considering that the boundary layers were not very close to the local equilibrium state at the end of transition (see Fig. 7.12)).

A possible source of error in all the calculation methods (100, 101, 112) mentioned above is the approximation of the boundary layer mean velocity profile by the Coles two-parameter family of distributions, which assumes the existence of a logarithmic flow similarity region near the wall : the results of Section 7.3 have shown the logarithmic wall similarity region to be completely absent in boundary layers subjected to large positive pressure gradients at very low Reynolds numbers. It must therefore be expected that these calculation methods will prove less successful under such conditions.

### 7.6.6 Non-Integral Calculation Methods

First-order non-integral methods use an empirical assumption about the relation between the shear stress and mean velocity at each point in the flow (such as a "universal" mixing length or eddy viscosity distribution) to obtain a partial differential equation for the local mean velocity. Integral versions would lead to first-order differential equations for H (cf Head's method). Bradshaw (95) has noted that this type of method seriously overestimates the rate at which the turbulent shear stress responds to changes in mean flow conditions, and should therefore be avoided in rapidly changing boundary layers, especially if separation is imminent. This effectively precludes their application to the boundary layer on the suction surface of an axial compressor blade.

Second-order non-integral methods use a system of partial differential equations to solve for the local shear stress as well as the local mean velocity components. This type of calculation gives a much more realistic physical representation of the turbulent flow than either first-order non-integral or second-order integral methods : not only are the local velocity and shear stress profiles allowed to be independent of each other, but $\partial\tau/\partial x$ is allowed to vary with y as it must do in practice. Such methods are clearly to be preferred in difficult flow situations.

Perhaps the most successful means yet devised for predicting the turbulent boundary layer development is the method of Bradshaw, Ferriss & Atwell (99): this is a second-order non-integral calculation method based on the turbulent energy equation, and it uses the method of characteristics to solve the partial differential equations for $u(x,y)$, $v(x,y)$ and $\tau(x,y)$. In order to start the calculation, it is necessary to specify completely the initial velocity and shear stress profiles: Bradshaw generates the starting velocity profiles from Coles's wall-plus-wake family for given values of $C_f$ and $Re_\theta$ (or H and $Re_\theta$); shear stress profiles are then generated from a "universal" mixing length distribution. Unfortunately, this procedure gives adequate results in mild pressure gradients only, and must be expected to fail completely in the severe conditions immediately after transition that were observed in the present investigation. The application of Bradshaw's method to compressor blade boundary layers (at least on the suction surface), therefore seems quite impracticable at present.

### 7.6.7 Choice of Starting Values for the Turbulent Boundary Layer Calculation

Because of the need for accurate specification of the starting values, the turbulent boundary layer calculation becomes much more difficult when the initial conditions are not completely known from experimental measurements. Since a detailed prediction of the flow behaviour during transition is as yet unavailable, it is necessary in this case to use an informed, but crude, guess of the appropriate starting values: this must be based on the predicted state of the laminar boundary layer at the start of transition, the pressure gradient over the transition region, and both empirical and theoretical knowledge of the turbulent flow behaviour.

With local equilibrium methods of predicting the turbulent boundary layer, the only information required for starting is the initial value of momentum thickness, which is readily available from the laminar boundary layer calculation. The need to specify the initial velocity or shear stress profiles is obviated because they are assumed to depend on the local conditions alone. This makes local equilibrium methods much simpler to apply, but they are not to be preferred on this account since their results are of very doubtful accuracy in rapidly changing boundary layers.

First-order integral methods require the specification of shape factor H as well as the initial momentum thickness before the turbulent boundary layer calculation can proceed. An initial value of shear stress is not required because it is assumed that the shear stress is related to the local mean flow quantities : in Head's method, for example, this relation is determined by the empirical function for the entrainment rate. The initial value of H is expected to depend mainly on the pressure gradient

over the transition region and the value of H in the laminar boundary layer immediately prior to transition. The boundary layer measurements on the stator blade suction surface at $Re_c \simeq 1 \times 10^5$ suggested H = 2.3 as a suitable starting value for the turbulent boundary layer following actual or incipient laminar separation ; the initial value of H showed a slight Reynolds number dependence as well, tending to increase gradually as $Re_c$ was reduced. These results clearly indicate that the zero pressure gradient value of $H \simeq 1.4$, which has sometimes been assumed as a starting value in theoretical studies of cascade performance, is quite an unrealistic choice for conditions of arbitrary pressure gradient. The local equilibrium value of H is similarly inappropriate ; however, the results of Fig. 7.13 suggest that it could perhaps be used as a lower limit to the likely range of initial values. Fortunately, Head's calculation method exhibits neutral stability to errors in choosing the initial value of H, and it should be possible to guess the starting conditions accurately enough to obtain useful results in most cases.

Second-order integral methods require the specification of some integral parameter concerning the initial turbulent shear stress distribution, in addition to the initial values of momentum thickness and velocity profile shape factor. At present, there appears to be little available information about shear stress behaviour following transition at low Reynolds numbers in high adverse pressure gradients ; under these conditions, guessed values of shear stress parameters will probably be much more inaccurate than guessed values of shape factor. It is noted that a second-order calculation method with incorrect starting values could well give a less accurate prediction of boundary layer development than a physically cruder first-order method in which the starting conditions were better specified : it would therefore seem prudent to avoid using second-order integral methods for calculating compressor blade boundary layers until the initial shear stress behaviour can be more confidently estimated.

Non-integral methods of predicting the turbulent boundary layer development require a complete specification of the initial velocity profile, in the case of first-order methods, or the velocity and shear stress profiles in the case of second-order methods. As pointed out in Section 7.6.6, the specification of the initial shear stress profile for a boundary layer developing on the suction surface of an axial compressor blade does not yet appear feasible.

### 7.6.8 Prediction of Turbulent Boundary Layer Separation

Separation of the two-dimensional turbulent boundary layer is defined to occur at the point where the time-mean value of wall shear stress falls to zero. With integral calculation methods, it is necessary to assume that separation corresponds to some integral parameter reaching a critical value. It is, of course, physically unrealistic to attempt a

correlation of separation with any integral parameter such as $H = \delta^*/\theta$ unless the external conditions are only very slowly changing, since the local shear stress changes at different rates over the boundary layer height in the real flow. Until the boundary layer development can be predicted in more detail, however, it appears that a critical value of H will have to suffice for predicting separation on a turbomachine blade.

Experimental data available in the literature indicates that H most frequently lies in the range 2.2 to 2.6 at separation on smooth walls. In the present investigation, values of H up to 2.5 were observed in unseparated turbulent boundary layers on the stator blade suction surface, so a critical value of H = 2.2 would probably be quite conservative. The question arises as to whether the critical value might be altered to allow for the fact that first-order calculation methods usually overestimate the rate at which the turbulent shear stress distribution changes ; but an inspection of published boundary layer calculations does not suggest any "universal" rule for doing this. Prediction of separation by integral methods is likely to be very poor when separation is approached slowly, as occurs in a concave pressure distribution ; a more accurate prediction is likely when separation is approached rapidly and dH/dx is large.

With non-integral calculation methods, the separation point is obtained directly, as the streamwise position where the wall shear stress falls to zero. Second-order methods of this type, such as Bradshaw's (99), should predict separation with reasonable accuracy provided that the normal boundary layer approximations can be applied right up to the separation point; but Küchemann (113) has noted that this is only likely to be so where the resulting separated flow region is very thin. If the flow is turned through a large angle at separation, the self-induced velocity field generated by the vorticity in the shear layer may produce an appreciable velocity component normal to the surface; the downstream conditions will then have a significant influence on the location of the separation point. Küchemann has examined the effect of downstream conditions on the separation point near the trailing edge of a thick symmetrical aerofoil by means of a conformal mapping approach; an alternative method of modelling the behaviour of the separating shear layer has been proposed by Oliver (114), who envisages a potential flow solution in which the shear layer is replaced by two vortex sheets; Fairlie (115) has also investigated this problem by means of an electrical analogue.

### 7.6.9 Effect of Wall Curvature on the Turbulent Flow

Bradshaw (116) has suggested that pronounced differences between the behaviour of boundary layers on curved and on plane surfaces (as represented by a change of more than 10% in the apparent mixing length) first appear at distances from the surface of roughly 1/300 of the radius

of curvature, R: it appears that the effects of curvature on the turbulence structure are far more important than the direct effects of pressure gradients normal to the surface on the mean flow. For the boundary layers measured on the stator blade suction surface during the present investigation, the value of $\delta/R$ at 90% chord varied roughly between 1/20 and 1/50 depending on the compressor speed, so that curvature effects would always have been very significant in the outer layer ; however, the influence of curvature on the flow in the wall layer ($y < 0.1 - 0.2\delta$) would not have been large in the majority of cases.

The above figures clearly indicate the desirability of allowing for curvature effects in calculating the development of turbulent boundary layers on highly cambered aerofoils such as turbomachine blades. The extension to curved flows of calculation methods using integral parameters is rather difficult because the effects of curvature vary across the flow, but Thompson (117) has suggested a modified entrainment function for use with Head's method; the treatment of non-integral methods has been discussed by Bradshaw (116). It is interesting to note that the inclusion of curvature effects in the shape factor calculation by Head's method shown in Fig. 7.13 would probably result in a poorer agreement with experiment over the rearward part of the blade: evidently the errors arising from rapid changes in the streamwise direction are much greater than those produced by neglecting curvature effects in this particular case.

## 7.7 Summary

The mean velocity profiles measured in turbulent flow regions on the stator blade suction surface showed no evidence of the usual logarithmic wall similarity. Most of the observed deviations from the logarithmic law probably resulted from the presence of large positive pressure gradients on the compressor blade, since fair agreement was obtained between experiment at the higher Reynolds numbers and the theory of McDonald (84) which allows for the influence of pressure gradient on the law of the wall. As the Reynolds number was decreased, however, some very significant departures from McDonald's law of the wall appeared. The mean velocity profile for the whole boundary layer was not described very well by either Coles's wall-plus-wake profile or a power law profile.

The Ludwieg-Tillmann and Nash-Macdonald skin friction laws overestimated the wall shear stress on the stator blade in most cases : it appeared that this was again due to pressure gradient effects. A new skin friction law based on McDonald's law of the wall was found to agree with experiment to within the precision of the measurements (which was only fair due to uncertainties regarding the heat loss correction required to allow for wall proximity effects on the hot wire readings).

The minimum value of boundary layer Reynolds number $Re_\theta$ observed in turbulent flow regions on the stator blade was around 200 ; this conflicted with the suggestion of Preston (75) that the minimum value of $Re_\theta$ for a fully developed turbulent boundary layer in an adverse pressure gradient should exceed 320. It appeared that the value proposed by Preston followed from the assumption, current in the literature at that time, that the outer edge of the viscous sublayer should occur at a constant value of $yu_\tau/\nu$: later work has indicated that the thickness of the viscous sublayer should vary with pressure gradient, and on substituting this result into the physical model used by Preston, values of minimum Reynolds number consistent with the measurements of the present investigation were obtained. Similar results were derived from the eddy Reynolds number concept of Bradshaw (89).

Of the several methods for calculating the turbulent boundary layer which were examined, Head's entrainment method was found to give the most reliable overall prediction of the flow behaviour on the stator blade; however, the predicted shape factor development was still only in fair agreement with experiment. It appeared that second-order calculation methods were capable of much more accurate predictions than Head's method, but attempts to use these were abandoned because of troubles with stability of the calculations and difficulties in specifying the initial shear stress profiles.

The effects of flow curvature on the turbulent flow in the stator blade suction surface boundary layer were undoubtedly significant. However, it appeared that making an allowance for these effects would generally have worsened the agreement between experiment and the predictions of Head's calculation method.

# CHAPTER 8

# APPLICATION OF EXPERIMENTAL RESULTS

## 8.1 Introduction

This chapter discusses the application of the preceding experimental results to the design and performance analysis of axial-flow turbomachine blading. First, the problem of predicting the boundary layer development from a specified surface pressure distribution is examined, and the accuracy likely to be achieved with present calculation methods is assessed ; the influence of various real flow phenomena on the surface pressure distribution is also mentioned. Next, a family of surface velocity distributions giving unseparated flow over the suction surface of an axial compressor blade is derived, and their computed performance is analysed. In conclusion, some problem areas requiring further research are outlined.

## 8.2 Theoretical Performance Analysis of Axial-Flow Turbomachine Blading

### 8.2.1 General Remarks

In reviewing a decade of progress in the aerodynamic design of axial-flow compressors in the United States, Serovy (118) suggested that in 1955 the whole area of off-design performance of cascades of blade elements in compressors was practically untouched from the designer's viewpoint, and that the estimation of the effects of low Reynolds number operation was difficult. He was able to claim only limited improvements in this situation over the period 1955-65, and concluded from a review of the open literature that methods used for selection of blade profiles had not changed appreciably during that period.

The continued reliance on cascade data is clearly unsatisfactory, as the designer is restricted very largely to the limited range of conventional blade sections and cascade geometries for which reasonably accurate empirical correlations of performance are available. Even then,it is only the performance near the design point that can be predicted with much certainty.

The broad aim of the present research has been to discover ways of computing turbomachine blade performance with a reduced reliance on empirical data: once reliable means of predicting the viscous flows become available, the need for two-dimensional cascade tests should be almost entirely obviated. Use of the high speed digital computer should make it quite feasible to carry out a complete theoretical performance analysis for any given blading configuration : this will hopefully result in a better understanding of the behaviour of real machines, especially those with non-standard blade geometry, and lead to improved predictions of off-design performance and stall boundaries. It should also become possible, within

certain limits, to design special blade profiles for particular applications such as low Reynolds number operation ; ultimately, the development of blade sections capable of better performance than those in current use can be contemplated.

### 8.2.2 Prediction of Boundary Layer Development from a Specified Surface Pressure Distribution

The key step in the problems of blade element design and performance analysis is the prediction of the viscous flow behaviour from a calculated or measured blade surface pressure distribution. It will be assumed here that the surface pressure distribution is already specified : the problem of estimating the surface pressure distribution is mentioned in Section 8.2.3.

This section discusses the accuracy to be expected from using a two-dimensional flow model to calculate the boundary layer development on a machine blade. Although some significant departures from two-dimensional flow will occur in certain situations, it appears that the design performance of high aspect ratio blading in regions away from the annulus walls can be estimated with reasonable accuracy without taking crossflows into account. Even when crossflows become significant, it should often be possible to use the two-dimensional flow model as a first approximation and treat the three-dimensional effects as small perturbations in subsequent iterations; however, a three-dimensional analysis will certainly be necessary for regions of the blade immersed in the annulus wall boundary layer or associated secondary flow regions, and it is taken for granted in the following discussion that such regions are excluded.

The results of the present investigation suggest that all aspects of the laminar boundary layer development on a real machine blade should be predicted quite well by Thwaites's (10) method provided that the surface velocity distribution $U(x)$ is roughly linear. On high aspect ratio blading (say $AR \geq 3$) it appears that values of $\theta$ and $\delta^*$ accurate to 5% and separation positions correct to within 5% of chord can be expected, even including errors due to three-dimensional effects. When the surface velocity distribution is markedly curved, the prediction of separation by Thwaites's method will be rather poor, and the use of a two-parameter calculation method such as Curle's (29) would be justified if the effects of laminar separation seemed likely to be important. The empirical transition correlations (Eqns. 6.11 and 6.19) proposed in Chapter 6 will probably predict the transition point to within about 5% of chord, on the average, provided that the free stream turbulence does not exceed a certain critical level which is expected to depend in part on the blade geometry (see Section 8.2.5). Estimates of the length of the transition region, in which the flow is intermittently

turbulent, and the values of the various boundary layer parameters at the end of transition will still have to be based largely on experience; however, some rough limits for these quantities can be established from the results of Sections 6.9 and 7.6.7. The turbulent boundary layer should be predicted with fair accuracy by Head's (111) method, although errors of 10% or more in H and $\delta^*$ must be expected to occur on the suction surface of a compressor blade at low Reynolds numbers ; slightly better results will probably be obtained under conditions of higher Reynolds numbers or lower pressure gradients.

Prediction of the viscous flow in the near wake, while very desirable, lies outside the scope of the present investigation. Errors from disregarding the losses due to mixing of flow in the wake will probably be acceptably small at the design incidence, but are likely to become appreciable near stall as the turbulent separation point moves forward from the trailing edge and the wake becomes markedly curved.

For the stator blade suction surface boundary layer which was studied experimentally, a two-dimensional calculation based on the measured surface pressure distribution predicted the trailing edge momentum thickness at mid-blade height to better than 10% over the incidence range $-4^\circ < i < 1^\circ$, where the crossflows were minimal due to the almost complete absence of flow separation from the blade surface and annulus walls. Differences between theory and experiment became steadily larger with increasing incidence, and reached a maximum of around 30% at the upper and lower operating limits of the machine : the predicted values of $\theta$ were too low in all cases, and it appeared that most of the errors arose from neglecting the effects of flow convergence on the suction surface (see Fig. 4.8). The absence of the turbulent normal stress terms in the momentum integral equation would have accounted for a significant proportion of the total errors observed in the low incidence range.

The above results indicate that with the present state of the art it should be possible to compute the profile losses of an axial turbomachine blade to within 10% in the reasonably favourable conditions which can be expected near the design point (provided of course that the surface pressure distribution is correctly specified). The greatest errors are likely to arise from the use of an incorrect transition position, inaccuracies in the starting values used for the turbulent boundary layer calculation, and from imperfections in the turbulent boundary layer calculation method itself. Whilst there is obviously room for further improvement, the achievable accuracy is nevertheless good enough to allow the direct design of blade profiles to proceed. Calculations of off-design performance obtained from a two-dimensional flow model should be treated with some reserve at high values of blade incidence; however, they should give useful qualitative indications of performance trends for high aspect ratio machine blades.

8.2.3 Viscous-Potential Flow Interactions : Prediction of Blade Surface Pressure Distribution

It is clearly impossible for any boundary layer calculation method to give an accurate estimate of the losses of a machine blade unless a reasonable estimate of the blade surface pressure distribution is first obtained. In the general design problem, the surface pressure distribution is not known from experimental measurements, and must therefore be calculated from potential flow theory. As a first approximation, viscous flow regions are assumed to be entirely absent and the rear stagnation point is usually located at the centre of the blade trailing edge; the resulting pressure distribution is used to provide a first estimate of the viscous flow behaviour, and the potential flow solution is then modified to allow for the presence of the viscous flow regions ; further iterations may be carried out, if desired, to obtain greater accuracy. Detailed discussion of the potential flow solution has deliberately been avoided in this thesis, since it is believed that currently available numerical methods of calculating the potential flow itself are quite adequate, and that differences at present obtained between the calculated and measured surface pressure distributions over a body are almost entirely due to errors in correcting for viscous flow effects : it follows that any improvement in the prediction of viscous flows which may be gained from applying the results of the present investigation should automatically lead to improved agreement between theory and experiment as far as the surface pressure distribution is concerned.

Modification of the initial potential flow solution to allow for viscous effects is normally accomplished by insertion of a single vortex sheet, of strength equal to the local free stream velocity, at the displacement thickness of the boundary layer or half-wake : this produces a potential flow having the same volume flux but a higher momentum flux than the real flow. Oliver (114) has suggested a refined model which replaces a shear layer by two vortex sheets chosen so as to give a potential flow having the same momentum and volume flux as the real flow. The location of the viscous flow displacement surface on the blade itself is obtained from the boundary layer calculation, provided of course that no significant flow separation occurs; the initial displacement thickness of the wake may be taken as the sum of the trailing edge thickness of the blade and the upper and lower surface boundary layer displacement thicknesses, provided that the latter are strictly defined ; the displacement thickness of the wake downstream of the trailing edge must at present be obtained by applying some empirical wake decay rule. Oliver (114) has pointed out that the normal definition of displacement thickness (in which the potential flow velocity is assumed constant with y) cannot be applied in the near wake, since there is an appreciable velocity deficiency in this region even in an entirely potential flow : calculation of the flow around a stationary compressor blade

showed the potential flow velocity deficiency near the stagnation streamline at a point 0.3 chord lengths downstream of the trailing edge to be as large as 5% of the measured maximum velocity deficiency at this point. The latter observation could account in part for the results of Gostelow et al. (74), who found that a rather worse estimate of the surface pressure distribution in a compressor cascade was obtained when attempts were made to allow for the displacement effects of the blade wakes.

Perhaps the greatest problem area in allowing for the viscous effects is the choice of the upper and lower surface velocities at the trailing edge of the blade : these effectively define the blade circulation, location of the rear stagnation point, and the potential flow deviation angle. At small incidence, the assumption that these velocities are equal will probably give adequate results (see, for instance, Ref. 74) ; but this model clearly becomes inadequate at high blade loadings, where the flow curvature near the trailing edge is not negligible and there is an appreciable amount of circulation in the blade wake. Accurate predictions of the blade surface pressure distribution at large positive or negative incidence are unlikely to be obtained until the effects of wake curvature and trailing edge separation can be properly allowed for : it is hoped that the two vortex sheet model of Oliver (114) will ultimately lead to better predictions in this regard than are at present available from the method of Spence (119).

Quite poor estimates of the surface pressure distribution must be expected when the long type of laminar separation bubble is present on the blade surface, as the viscous flows cannot be predicted with much precision in this case.

### 8.2.4 Three-Dimensional Flow Effects

In calculating the performance of low aspect ratio blading, or high aspect ratio blading operating at high incidence, it is unlikely that any great accuracy will be achieved unless the effects of radial flows within the blade boundary layers are taken into account. The inclusion of cross flows induced by radial pressure gradients in the bulk flow could certainly be contemplated using currently available methods, but it is doubtful whether the extra labour involved would produce very useful improvements in the performance estimate : the major source of radial flow on a machine blade is considered to be the convergence produced by the large streamwise secondary flow vortex situated in the corner between the suction surface of the blade and the annulus wall, and no accurate model of this phenomenon is yet available.

8.2.5 Reynolds Number Effects

Some fairly comprehensive summaries of previous experimental work on Reynolds number effects in cascades and axial-flow turbomachines have been given in Refs. 120, 121 and 122. It appears that the efficiency of a compressor cascade can be correlated by the relation

$$(1 - \eta) = k \, Re_c^{-n} \qquad (8.1)$$

where k and n are functions of blade geometry and Reynolds number, n usually lying between 2 and 5. Below a certain critical Reynolds number, normally in the range $0.5 \times 10^5$ to $1.0 \times 10^5$, compressor cascades of high aspect ratio (AR $\geq$ 3) show a sudden increase in losses and flow deviation; this phenomenon is not as marked in cascades of low aspect ratio (AR $\simeq$ 2), due in the present author's opinion to the extension of secondary flows over the whole blade height.

The two-dimensional boundary layer calculation method discussed in Section 8.2.2 should give quite useful quantitative predictions of the variations in losses at Reynolds numbers above critical, provided that the radial flows are not too large (i.e. for high aspect ratio blades operating at moderately small incidence); it is noted that since the exponent n in Eqn. 8.1 depends very largely on the relative proportions of laminar and turbulent flow on the blade surface, the accuracy with which Reynolds number effects can be predicted is determined mainly by the reliability of the transition criterion used.

The present study has shown the drag rise at the critical Reynolds number to be caused by bursting of a short laminar separation bubble formed at a Reynolds number somewhat higher than critical ; it seems that a reasonable estimate of the critical Reynolds number itself should be obtained by use of Gaster's (34) bursting criterion for the laminar separation bubble (see Section 5.6). Present predictions of blade performance at subcritical Reynolds numbers will undoubtedly be poor, since the influence of a long separation bubble on the blade surface pressure distribution cannot be predicted with confidence, and the development of large radial flows will render the two-dimensional approximation invalid.

It is important to note that "short" regions of laminar flow separation may exist on a machine blade at supercritical Reynolds numbers without having much effect on either the surface pressure distribution or the blade losses: the drag rise occurring at the critical Reynolds number, being produced by separation bubble bursting, is rather more closely associated with separation of the turbulent boundary layer than of the laminar boundary layer. It is certainly possible that complete laminar separation could occur through the Reynolds number of the separated shear layer falling below the minimum value needed to sustain fully developed turbulent flow; however, the author considers that this is not the normal explanation for the critical drag rise on conventional turbomachine blades.

8.2.6 Free Stream Turbulence Effects

The author believes that transition on axial turbomachine blades will usually be initiated by the normal two-dimensional laminar instability process. Free stream turbulence should mostly influence transition by altering the amplification rate of small disturbances within the boundary layer, rather than by changing the basic physical nature of the transition process : the major sources of external disturbance for a machine blade boundary layer are the wakes and pressure fields of neighbouring blade rows, and these are essentially two-dimensional in character.

The effect of free stream turbulence on transition, and hence on the blade performance, is expected to depend on a number of factors including the longitudinal fluctuation intensity, $\sqrt{\overline{u'^2}}/U_\infty$, the non-steady Reynolds number $(Re)_{NS}$ for individual disturbances, the shape of the blade surface pressure distribution, and the length of the instability region relative to the disturbance scale. However, it appears from the present study that there may be a considerable range of operating conditions over which the free stream disturbances have only a minor effect on the location of transition ; within this range, it is suggested that the boundary layer calculation method of Section 8.2.2 should be used without modification. Above a certain turbulence level, which will probably be determined by a critical value of $(Re)_{NS}$ or $u'/U_\infty$ for individual disturbances, the movements of the transition point in response to free stream turbulence will probably increase significantly, and transition predictions (such as Eqns. 6.11 and 6.19) which are based on the time-mean surface pressure distribution will then break down. The critical disturbance level cannot be predicted at present, but it should depend to a large extent on the blade geometry and operating incidence : on the C4 blades studied in the present investigation, the free stream turbulence level reached over 6% without causing any significant departures from the transition correlation of Eqns. 6.11 and 6.19; but as noted in Section 6.8.4, profiles having sharp leading edges and little flow acceleration over the forward part of the blade will probably be much more sensitive in this regard. It is stressed once again that correlations of transition Reynolds number against free stream turbulence level for a flat plate cannot possibly be expected to apply to transition on aerofoils of arbitrary shape : the ultimate means of allowing for the effects of free stream disturbances is thought more likely to lie in a quasi-steady stability analysis of the type suggested by Obremski and Morkovin (49).

Experimental evidence reported in the literature suggests that free stream disturbances may change the critical Reynolds number at which a sudden increase in compressor blade losses is observed. At subcritical Reynolds numbers, increases in free stream disturbances usually cause a significant reduction in blade losses, but as noted in Section 6.8.4 this phenomenon does not necessarily imply a change of similar magnitude in the location of the transition point : evidently small movements of the

transition region can produce quite large variations in blade performance when the long bubble type of flow separation is present on the blade surface, and this provides yet another reason for expecting the accuracy of performance estimates at subcritical Reynolds numbers to be very poor.

## 8.3 Model Suction Surface Velocity Distribution for a Compressor Blade

### 8.3.1 Introduction

As a first step towards the development of compressor blade sections having improved performance characteristics, the experimental results obtained in the present investigation have been used to generate a family of surface velocity distributions expected to give unseparated flow over the suction surface of a compressor blade. An approximate estimate of the blade lift was obtained by assuming the velocity on the pressure surface to remain constant, equal to the velocity on the suction surface at the trailing edge; an estimate of the two-dimensional blade profile drag was obtained by calculating the boundary layer growth on the suction surface. These figures should give a fairly useful indication of the performance capabilities of a complete blade having the design suction surface velocity distribution, since tests of conventional compressor blade sections show that the suction surface contributes some 90% of the total lift and 75% of the total profile drag when operating near the design incidence.

The model suction surface velocity distribution commences with a region of acceleration near the leading edge to maintain stable laminar flow. This is followed by a region of mildly decelerating flow which allows transition to occur without separation of the laminar boundary layer. Finally, there is a region of strong flow deceleration near the trailing edge where the boundary layer is fully turbulent. A typical velocity distribution is shown in Fig. 8.2. A similar approach was used successfully by Wortmann (123) in designing isolated aerofoil profiles for high Reynolds number operation.

The derivation of this model distribution will now be discussed in detail.

### 8.3.2 Derivation of Model Suction Surface Velocity Distribution

#### 8.3.2.1 Region 1 : stable laminar flow

A length of linearly accelerating flow extending from the leading edge to the point $x_M$, where the surface velocity reaches its peak value $U_M$,

i.e. $$U = U_M - a\,(x_M - x) \qquad (8.2)$$

is used to stabilise the laminar boundary layer for $x < x_M$. The required value of the constant, a, depends on the chord Reynolds number, $Re_c$.

The provision of a region of accelerating flow near the leading edge should decrease the sensitivity of the boundary layer to effects of free stream turbulence, and should also minimise the boundary layer thickness at $x = x_M$.

8.3.2.2 Region 2 : unstable laminar flow and transition

This is a length of mildly decelerating flow with the velocity distribution chosen so as to maintain a constant value of pressure gradient parameter k for the laminar boundary layer. Laminar separation will be avoided by keeping $k > -0.08$, approximately. Using Thwaites's approximate solution for the laminar boundary layer, the required velocity distribution is found to be

$$U = U_M \left\{ 1 - \frac{k(5 - 0.45/k)}{\theta_M \, Re_{\theta_M}} (x - x_M) \right\}^{-1/(5 - 0.45/k)} \qquad (8.3)$$

This distribution is maintained until a point 15% of chord downstream of the transition point calculated from the correlation of Eqn. 6.11, to allow for the completion of transition and the establishment of a turbulent boundary layer with sufficiently large shear stress near the wall to withstand a high adverse pressure gradient without separation. The transition length of 15% of chord is based on the measurements of the present investigation, which were obtained on compressor blades operating at chord Reynolds numbers of about $10^5$ : for aerofoils working at higher Reynolds numbers, a somewhat smaller distance would possibly suffice, but it should be remembered that the transition length may be increased in some cases by the effects of wakes from upstream blade rows passing in the free stream (see Section 6.9).

8.3.2.3 Region 3 : turbulent flow continuously close to separation

In this final region, which extends to the trailing edge of the aerofoil, a length of strongly decelerating flow is used to maintain the turbulent boundary layer continuously close to separation. This gives the greatest possible amount of diffusion and minimises the energy loss for a given pressure rise and initial boundary layer thickness. The turbulent boundary layer should not be held too close to separation, however, as this might allow the development of large cross-flows on a machine blade, which would lead to an undesirable increase in losses.

Stratford (90, 124) has made a theoretical and experimental study of the turbulent boundary layer on the point of separation, and gives the pressure distribution required to produce a flow with continuously zero skin friction as

$$C_p = 1 - \left(\frac{U}{U_o}\right)^2 = 0.645 \left\{ 0.435 \, R_o^{1/5} \left[ \left(\frac{x}{x_o}\right)^{1/5} - 1 \right] \right\}^{2/n}$$

$$\text{for } C_p \leq \frac{n-2}{n+1} \tag{8.4}$$

where $R_o = U_o x_o/\nu$, and $x_o$ (the length of flat plate necessary for a continuously turbulent boundary layer to grow to the same initial momentum thickness, $\theta_o$) is given approximately by

$$\theta_o = 0.036\, x_o\, R_o^{-1/5} \tag{8.5}$$

At the point $x = x_o$, where $U = U_o$, the initial boundary layer velocity profile is assumed to be represented by a power law

$$u/U_o = (y/\delta_o)^{1/n} \tag{8.6}$$

where

$$n \simeq \log_{10} R_o \tag{8.7}$$

Stratford's experimental investigation was carried out with $R_o = 1.0 \times 10^6$.

Since Stratford's work was restricted to boundary layers at high Reynolds numbers which had developed initially in zero pressure gradient, there is considerable doubt whether the values of $x_o$ and n obtained by his analysis are applicable to the case of a boundary layer which has developed in an arbitrary adverse pressure gradient at much lower Reynolds numbers. Because of this uncertainty, an alternative approach to specifying the pressure distribution required to maintain the turbulent boundary layer near separation was sought by assuming the developing flow to pass through a succession of local equilibrium states as defined by Eqn. 7.66. This assumption is based on the results of various workers, such as Bradshaw (125) and Spangenberg et al.(19), who found that turbulent boundary layers at high Reynolds numbers remained quite close to local equilibrium when subjected to a "concave" external velocity distribution of the form $U = U_o\,(x - x_o)^{-n}$. While no direct experimental evidence is yet available, it seems reasonable to assume that the lower Reynolds number boundary layers on a compressor blade would behave similarly: the Reynolds number certainly has little effect on the form of departures from local equilibrium for boundary layers experiencing augmentation of pressure gradient (see Section 7.6.2 and Fig. 7.12).

The derivation of the appropriate form for Region 3 of the model velocity distribution is commenced by expressing the parameter $(\theta/U)(dU/dx)$ in terms of $\Pi$, G and H by the general relation

$$(\theta/U)(dU/dx) = -\Pi/G^2(1/H - 2/H^2 + 1/H^3) \tag{8.8}$$

For the particular case of a boundary layer in local equilibrium, where $G = \hat{G}$, substitution for $\hat{G}$ in terms of $\Pi$ from Eqn. 7.66 gives

$$(\theta/U)(dU/dx) = f(\Pi)\ (1/H - 2/H^2 + 1/H^3) \tag{8.9}$$

If the force parameter $\Pi$ is large, as will be the case with boundary layers close to separation, the function $f(\Pi)$ becomes almost constant :

for example, $f(\Pi) = -0.0270$ for $\Pi = 10$, and varies by no more than a few percent for larger values of $\Pi$. Setting $f(\Pi) = -0.027$ = constant leads to

$$(\theta/U)(dU/dx) = -0.027\ (1/H - 2/H^2 + 1/H^3) \tag{8.10}$$

which indicates that for equilibrium boundary layers near separation, the shape factor H will be a function of $(\theta/U)(dU/dx)$, only. Choosing $H = 2.1$ a suitable value not too close to separation requires

$$(\theta/U)(dU/dx) = -0.0035 \tag{8.11}$$

The two-dimensional boundary layer momentum integral equation for a strong adverse pressure gradient, in which case the skin friction coefficient $C_f$ is negligible, becomes

$$d\theta/dx = -(H + 2)(\theta/U)(dU/dx) \tag{8.12}$$

and substituting the chosen values of H and $(\theta/U)(dU/dx)$ gives

$$d\theta/dx = 0.0144 \tag{8.13}$$

which results in a linear growth in momentum thickness,

$$\theta = 0.0144\ (x - x_o) \tag{8.14}$$

Substituting Eqn. 8.14 into Eqn. 8.11 gives

$$(1/U)(dU/dx) = -0.0035 / \theta = -0.244\ (x - x_o)^{-1} \tag{8.15}$$

which may be integrated to give the required free stream velocity distribution as

$$U = U_o(x - x_o)^{-0.244} \tag{8.16}$$

If the conditions at the point $x_T$, where the adverse pressure gradient is initially applied, are $\theta_T$ and $U_T$, then the constants in Eqns. 8.14 and 8.16 are given by

$$\left.\begin{aligned} x_o &= x_T - \theta_T / 0.0144 \\ \text{and} \qquad U_o &= U_T(x_T - x_o)^{0.244} \end{aligned}\right\} \tag{8.17}$$

The main assumptions made in developing the velocity distribution specified by Eqns. 8.16 and 8.17 are that the boundary layer remains close to local equilibrium with high values of $\Pi$ and H. Due to the restriction of both $\Pi$ and H being large, there is some doubt about the applicability of the newly derived surface velocity distribution for a boundary layer which has developed initially in zero pressure gradient with $\Pi = 0$. It is therefore of interest to compare the experimental pressure distribution for flows of this type with the predictions of Eqns. 8.16 and 8.17. Fig. 8.1 shows the surface velocity distribution "A" from Spangenberg et al.(19) which gave the maximum obtainable pressure rise for a turbulent boundary layer initially developed in zero pressure gradient on a duct wall. The velocity distribution from Eqns. 8.16 and 8.17 is closely similar to the

experimental curve of Spangenberg, but it yields a slightly lower pressure rise (7% less at x = 20 ft); a similar comparison is obtained with the experimental results of Stratford (124). The probable reason for the theoretical velocity distribution in Fig. 8.1 being slightly conservative is that $\theta$ initially grows more slowly than assumed in Eqn. 8.14, since it takes a finite length for the shape factor H to rise toits separation value after the pressure gradient has been applied.

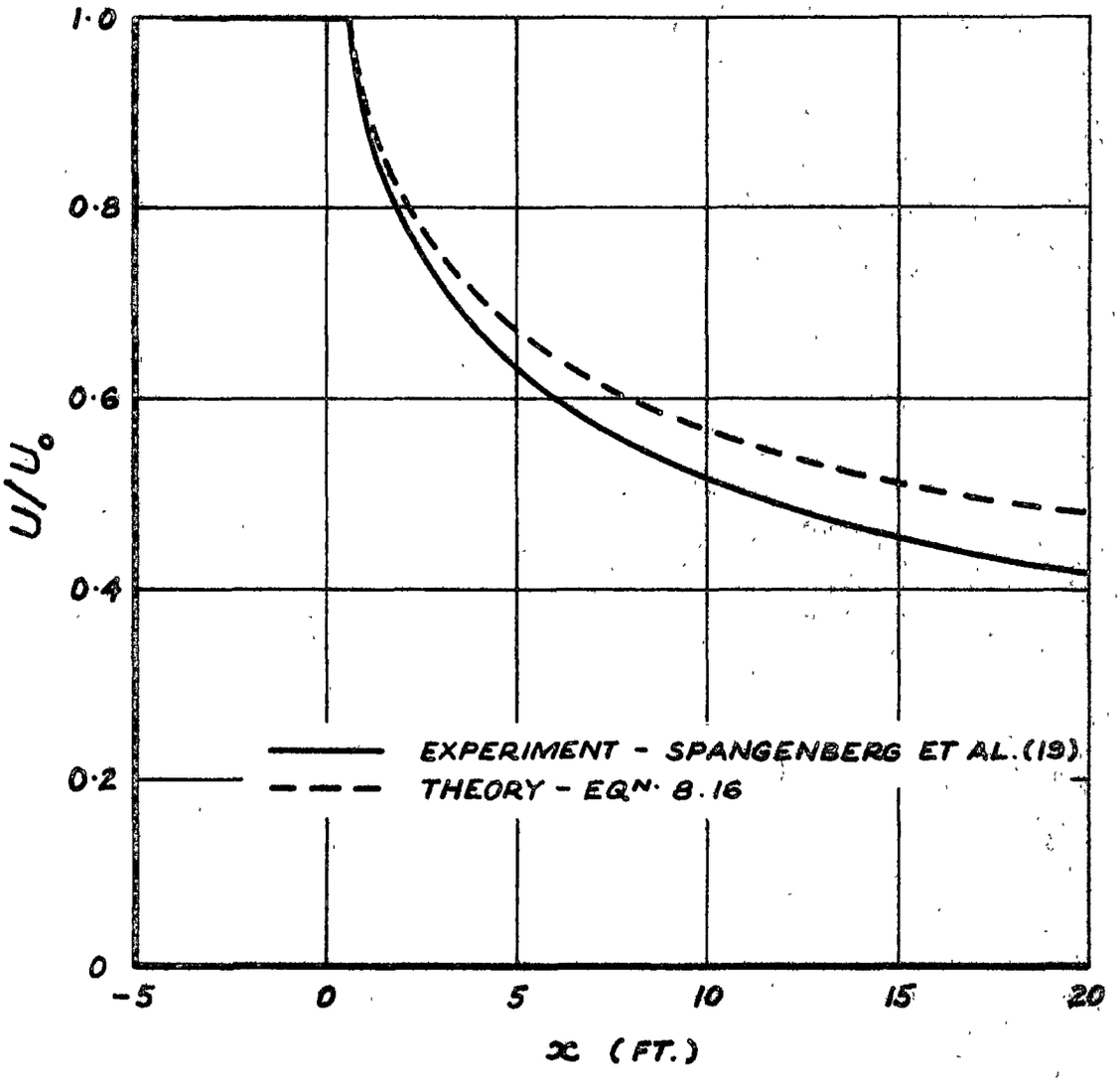


Fig. 8.1 Surface Velocity Distribution Required to Maintain a Turbulent Boundary Layer in a Nearly Separating Condition

As there was little difference between Stratford's pressure distribution and that given by $U = U_o(x - x_o)^{-0.244}$, the latter was chosen because of its greater ease of manipulation, and because of the smaller degree of uncertainty in choosing the parameters $U_o$ and $x_o$. But to be a little more conservative, an exponent of 0.23 instead of 0.244 was used in the model velocity distributions.

It is noted that whereas Eqn. 8.10 predicts separation of the equilibrium turbulent boundary layer for $(\theta/U)(dU/dx) \simeq -0.0040$, some of the measurements on the stator blade suction surface obtained during the present investigation showed values of $(\theta/U)(dU/dx) < -0.0060$ near the trailing edge without separation occurring. The greater resistance to separation in this case, where the surface velocity distribution was convex, most probably resulted from the finite time required for the turbulent shear stress distribution to adjust to changes in pressure gradient: the measured boundary layers had a higher wall shear stress than an equilibrium layer and were therefore capable of withstanding a higher pressure gradient until the shear stress near the wall had dropped. It may not be possible to achieve pressure gradients as high as these with a concave velocity distribution of the form $U = U_o(x - x_o)^{-n}$, since the boundary layer should then remain closer to equilibrium and have a lower wall shear stress; nevertheless, it still seems very likely that the pressure rise given by the surface velocity distribution $U = U_o(x - x_o)^{-0.244}$ may not be the maximum attainable at low Reynolds numbers where the turbulence lag becomes comparable with the aerofoil chord. It is concluded that an optimum design for a compressor blade cannot be expected until the turbulent shear stress distribution can be predicted with some degree of accuracy from the start of transition onwards.

8.3.2.4 Summary

The model velocity distribution designed to give unseparated flow on the suction surface of a compressor blade is divided into three regions:

1. Stable laminar flow

$$U = U_M - a(x_M - x) \qquad (0 < x < x_M) \tag{8.2}$$

2. Unstable laminar flow and transition

$$U = U_M\left\{1 - \frac{k(5 - 0.45/k)}{\theta_M \, Re_{\theta_M}}(x - x_M)\right\}^{-1/(5 - 0.45/k)} \qquad (x_M < x < x_T) \tag{8.3}$$

3. Turbulent flow continuously near separation

$$U = U_o(x - x_o)^{-0.23} \qquad (x_T < x < c) \tag{8.18}$$

where

$$\left.\begin{aligned} x_o &= x_T - \theta_T / 0.0144 \\ U_o &= U_T\,(x_T - x_o)^{0.23} \end{aligned}\right\} \tag{8.19}$$

In the above relations, x is the arc length from the leading edge stagnation point; the total suction surface arc length is assumed equal to the aerofoil chord, c. The quantities c, $\nu$, $U_M$ and $x_M$ are free parameters; k must be chosen greater than -0.08, approximately, to prevent laminar separation from occurring; the value of a must be chosen large enough to maintain stable laminar flow up to the point of peak velocity, $x = x_M$. A typical example of the model suction surface velocity distribution is shown in Fig. 8.2.

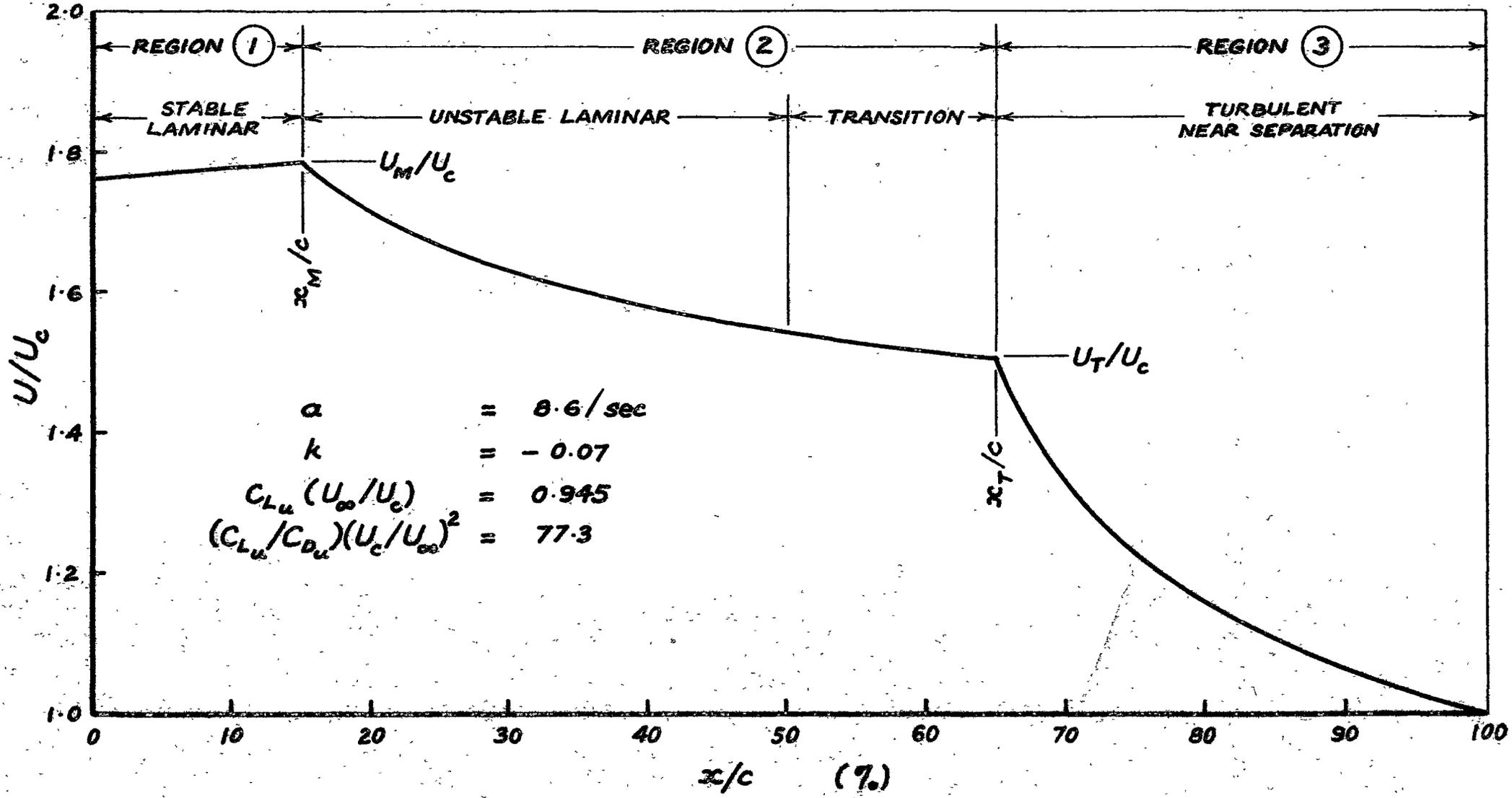


Fig. 8.2 A Typical Example of the Model Suction Surface Velocity Distribution for a Compressor Blade

$Re_2 = Re_c(U_c/U_\infty) = 3.0 \times 10^5$

8.3.3 Estimation of Blade Performance

Once the parameters of the model suction surface velocity distribution have been specified, the trailing edge velocity on the suction surface, $U_c = (U)_{x=c}$, can be calculated. This determines the Reynolds number based on the trailing edge velocity and surface arc length,

$$Re_2 = U_c\, c/\nu = Re_c\, (U_c/U_\infty) \tag{8.20}$$

Assuming the velocity on the pressure surface to be constant equal to $U_c$, the lift coefficient $C_{L_u}$ obtained from the model suction surface velocity distribution is given by

$$C_{L_u}\, (U_\infty/U_c) = 2 \int_0^1 (U/U_c - 1)\, d\,(x/c) \tag{8.21}$$

The drag coefficient for an aerofoil in a two-dimensional cascade is related to the total pressure loss coefficient far downstream of the blade row by the expression

$$C_D = (\bar{\omega}/\tfrac{1}{2}\rho V_a^2)\ (s/c)\ \cos^3\alpha_\infty \tag{8.22}$$

Lieblein and Roudebush (126) give an approximate relation between the total pressure loss coefficient and the wake momentum thickness at the blade trailing edge as

$$\left(\frac{\bar{\omega}}{\frac{1}{2}\rho V_a^2}\right)_c \cos^2\alpha_c = 2\,\hat{\theta}_c \left\{\frac{2H_W/(3H_W - 1)}{(1 - \hat{\theta}\, H_W)^3}\right\}_c \tag{8.23}$$

where $\hat{\theta} = (\theta_W/c)(c/s\cos\alpha)$, $H_W$ is the form factor for the wake velocity profile, and the subscript c denotes evaluation at the blade trailing edge. In the present analysis, the right hand side of Eqn. 8.23 will be set equal to $2\,\hat{\theta}_c$, which is a fair approximation for $\hat{\theta}_c < 0.04$. Substituting this into Eqn. 8.22 gives

$$C_{D_c} = 2\left(\frac{\theta_W}{c}\right)_c \frac{\cos^3\alpha_\infty}{\cos^3\alpha_c} \simeq 2\left(\frac{\theta_W}{c}\right)_c \left(\frac{U_c}{U_\infty}\right)^3 \tag{8.24}$$

where $C_{D_c}$ is a drag coefficient based on the pressure loss coefficient at the trailing edge, and neglects subsequent mixing losses in the blade wake.

Since only the boundary layer development on the suction surface of the blade is considered in the present model, the drag coefficient must be based solely on the upper surface boundary layer momentum thickness at the trailing edge, $\theta_{u_c}$, giving

$$C_{D_u}\, (U_\infty/U_c)^3 = 2\,\theta_{u_c}/c \tag{8.25}$$

The ratio of lift to upper surface drag is then found from

$$(C_{L_u}/C_{D_u})(U_c/U_\infty)^2 = (c/\theta_{u_c}) \int_0^1 (U/U_c - 1)\, d(x/c) \tag{8.26}$$

It is impossible to obtain the lift and drag coefficients explicitly at this

stage because the ratio of the trailing edge velocity to the vector mean velocity is not yet known. In an actual design problem, however, this ratio would be approximately specified by the inlet and outlet angles required.

As mentioned previously, the lower surface velocity distribution obtained in a practical blade design should make little difference to the lift coefficient given by Eqn. 8.21, and near the design incidence the upper surface should produce the major part of the total blade profile drag.

### 8.3.4 Predicted Performance for Compressor Blades Having the Model Suction Surface Velocity Distribution

The theoretical suction surface velocity distribution and its associated boundary layer development were calculated for a wide range of values of peak velocity, $U_M$, location of peak velocity, $x_M$, and pressure gradient parameter for the unstable laminar flow region, k. The values of lift coefficient, lift/drag ratio, and diffusion ratio, $U_M/U_c$, obtained for a fixed value of $x_M/c$ were then plotted against Reynolds number $Re_2$, different curves being obtained for each different value of k. A typical result is shown in Fig. 8.3, which emphasises the strong dependence of aerofoil performance on Reynolds number for a compressor blade: as Reynolds number is reduced, the laminar boundary layer thickness increases, giving a greater initial thickness for the turbulent boundary layer; this reduces the maximum pressure gradient that the turbulent flow can withstand without separation, and leads to a lower lift coefficient. Thus the maximum lift coefficient is decreased, and the minimum drag is increased, as Reynolds number is reduced: Fig. 8.3 shows a fall in lift of up to 15% as $Re_2$ drops from $2 \times 10^5$ to $1 \times 10^5$. These results are of obvious significance in model testing of fans or compressors, since too large a Reynolds number difference between the model and prototype could cause regions of blade stall in the model which would not occur in the prototype.

For greater ease in selecting the best velocity distribution for a particular application, the results were cross plotted to give performance at a constant Reynolds number as shown in Fig. 8.4. Contours of constant lift coefficient, lift/drag ratio and diffusion ratio, $U_M/U_c$, were obtained on a plot of pressure gradient parameter, k, for the unstable laminar boundary layer against the location of the peak velocity, $x_M/c$. The most striking feature of Fig. 8.4 is that the three sets of contours are all roughly parallel to each other; this indicates that for a given Reynolds number, a reasonable correlation should be obtained between the wake momentum thickness ratio, $\theta_W/c$, and the diffusion ratio, $U_M/U_c$ (or the local diffusion factor, $D_{loc} = (U_M - U_c)/U_M$). A similar observation was made by Lieblein (127) from the results of cascade tests on NACA 65-($A_{10}$) - series blade sections (see Fig. 8.5). It is interesting to note that while the present model indicates

an almost unique relationship between the local diffusion factor and the blade losses, there is apparently no single-valued relation between the local diffusion factor and the blade lift; it is not known to what extent the assumption of a constant velocity on the lower surface contributed to the latter result.

The contours of maximum lift coefficient and maximum lift/drag ratio in Fig. 8.4 are seen to be fairly well separated, thus allowing a wide range of possible designs for different applications. If minimum size and weight of a compressor are the most important considerations, then the maximum lift design is appropriate ; where the efficiency is of prime importance, the best lift/drag ratio design should be used. Practical designs will probably fall between these two limits, since the present model indicates that large increases in efficiency are possible if a relatively small reduction in lift coefficient can be tolerated.

The position of the velocity peak for a given lift coefficient varies with the pressure gradient parameter, k. However, there is no optimum value of k at $Re_2 = 3 \times 10^5$ since the same maximum values of lift coefficient and lift/drag ratio are obtained for any adverse pressure gradient which does not produce separation. Assuming it is valid to extrapolate this result to values of k slightly less than -0.08, it can be inferred that there is no advantage in using regions of separated laminar flow to promote transition on a compressor blade. In practice, the use of a value of k too close to the separation value of about -0.08 would probably detract from the performance through allowing larger cross flows to develop on the blade surface. Nevertheless, it would be best to keep the laminar layer reasonably close to separation as this gives a longer region of accelerating flow near the blade leading edge, and should therefore result in decreased sensitivity to free stream disturbances.

Taking k = -0.07 gives the velocity peak at 10% of chord for the maximum lift design and 22% of chord for the best lift/drag ratio design for $Re_2 = 3 \times 10^5$. Whichever one is chosen, the velocity peak and the maximum thickness should obviously be fairly well forward on a compressor blade operating at low Reynolds numbers : as low drag isolated aerofoil sections designed for high Reynolds number operation frequently have their maximum thickness at about 50% of chord, their application in turbomachinery appears somewhat dubious. Even a relatively small change in $Re_2$ from $2 \times 10^5$ to $3 \times 10^5$ requires $x_M/c$ to be increased by $1\frac{1}{2}$ - 2% for the maximum lift design ; this clearly indicates that a compressor blade should be specifically designed for the Reynolds number range in which it is required to operate in order to achieve the optimum performance.

Fig. 8.5 shows a plot of wake momentum thickness ratio, $\theta_W/c$, against local diffusion factor, $D_{loc} = (U_M - U_c)/U_M$, from Lieblein's results for the

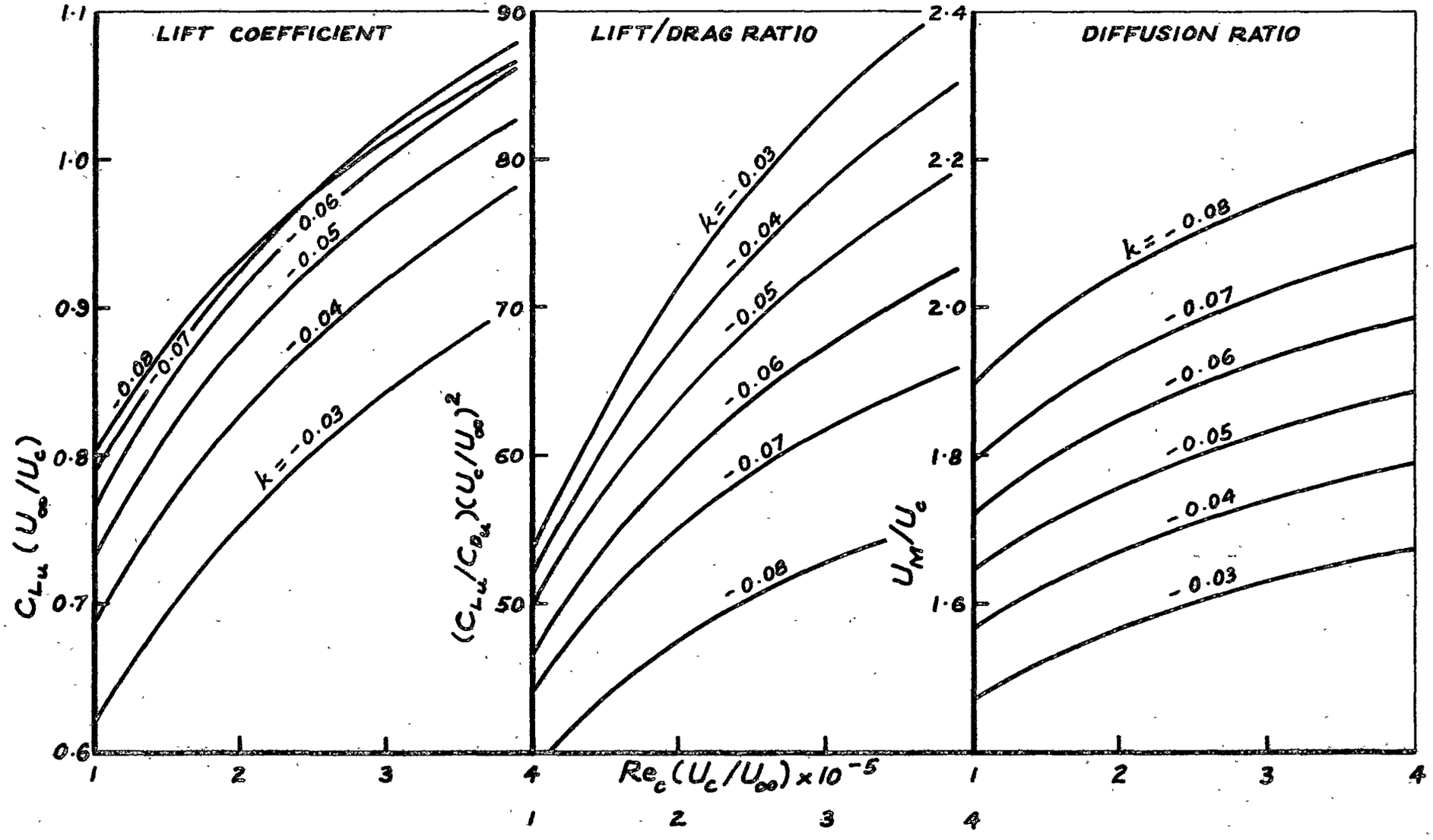


Fig. 8.3 Compressor Blade Performance Calculated from Model Suction Surface Velocity Distribution

$x_M/c = 0.10$

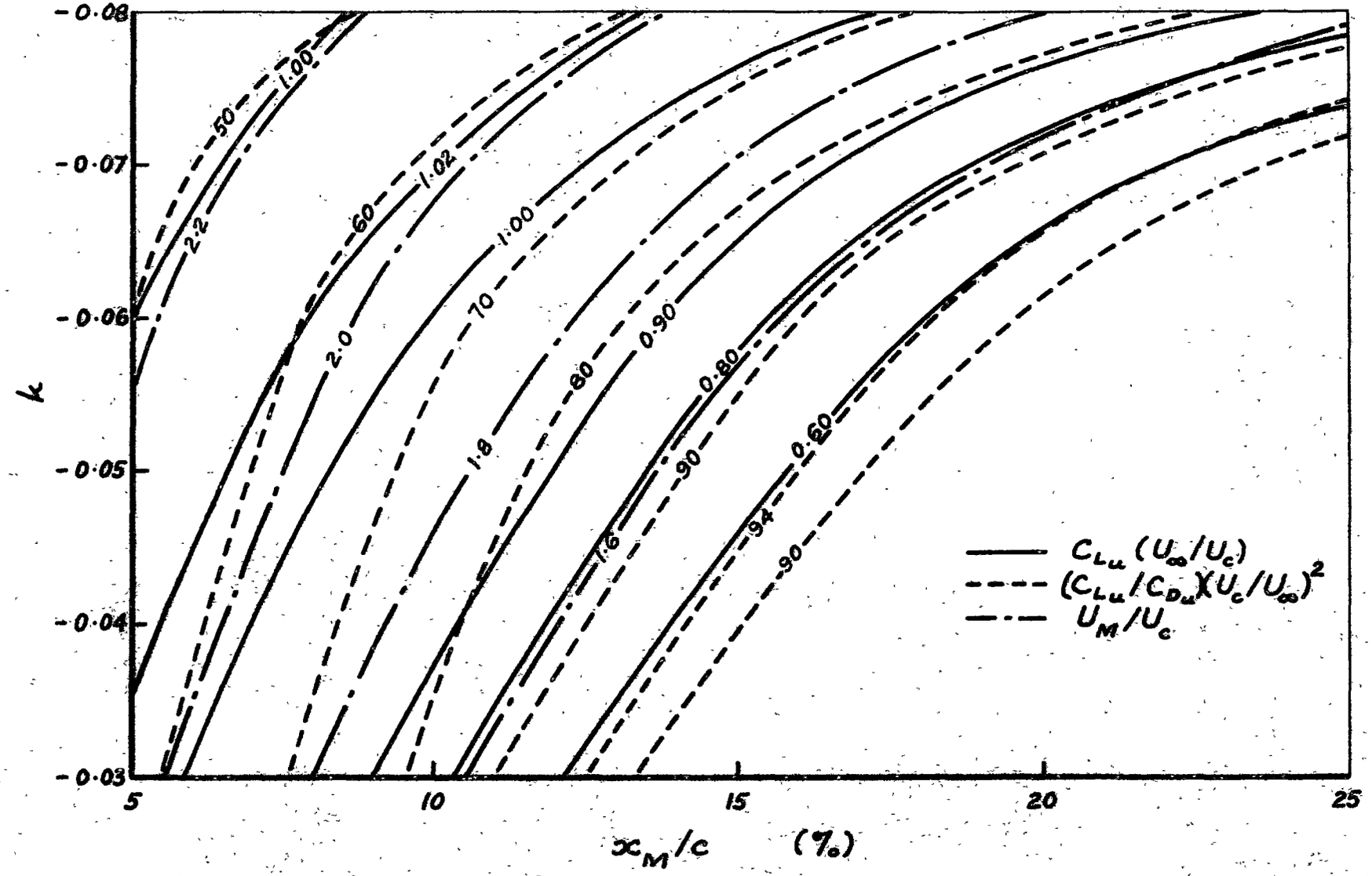


Fig. 8.4 Compressor Blade Performance Calculated from Model Suction Surface Velocity Distribution

$Re_2 = Re_c\ (U_c/U_\infty) = 3.0 \times 10^5$

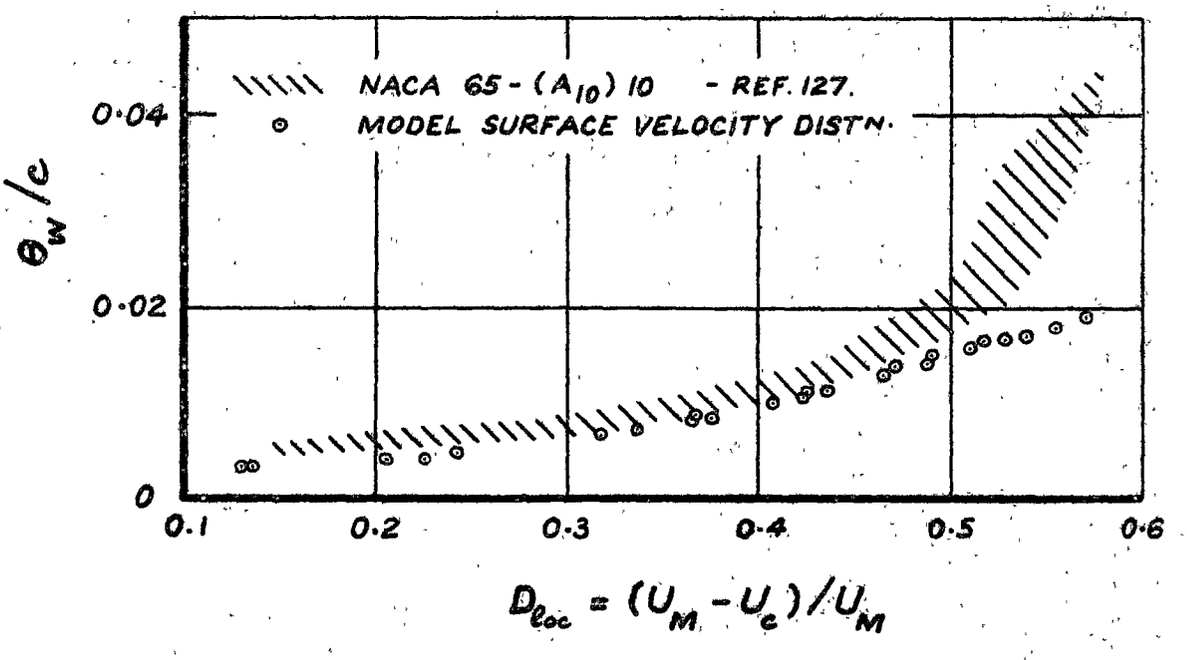


Fig. 8.5 Variation of Wake Momentum Thickness Ratio with Local Diffusion Factor at Reference Incidence Angle for NACA Low Speed Cascade Data, and Comparison with Predicted Performance of Model Surface Velocity Distribution : $Re_c \simeq 2.5 \times 10^5$

NACA 65 - $(A_{10})$ 10 blade section operating at $Re_c \simeq 2.5 \times 10^5$. In order to compare the predicted performance of the present model with Lieblein's data, it is first necessary to make some assumptions about the pressure surface and wake mixing losses, and the value of $U_\infty/U_c$ : it will be assumed that the lower surface losses amount to 33% of the upper surface losses, that the wake mixing losses are 10% of the total blade losses, and that $U_\infty/U_c = 1.15$. The foregoing values are believed to be fairly realistic estimates for conventional blade sections operating near design.

In Fig. 8.5, the points corresponding to the theoretical performance calculated from the model surface velocity distribution tend to fall slightly below the range of Lieblein's experimental data : this trend becomes particularly marked for values of $D_{loc} > 0.5$, where it appears that separation from the suction surface causes the losses of the NACA blades to rise rapidly. These results indicate that the model velocity distribution is achieving rather more efficient diffusion than is obtained on the NACA 65 - $(A_{10})$ 10 section, i.e. that the new model allows more diffusion for the same blade losses ; however, the maximum obtainable values of $D_{loc}$ for the model velocity distribution and the NACA blades are very nearly the same. Values of $\theta_w/c$ from the model velocity distribution for $D_{loc} < 0.3$ are thought to be erroneously low : in these case the lift

coefficient is quite small, and the pressure surface losses will be relatively higher than was initially assumed.

The performance predicted by the present model is also comparable with that achieved by C4 blades : the theoretical lift/drag ratios are a little better, but the maximum lift coefficients of the model are slightly less than those used in current practice. The lower lift coefficients most probably result from the conservative values of pressure gradient applied to the transition and turbulent boundary layer regions, and from neglecting the small contribution of the pressure surface to the total lift. Ultimately, it should be possible to obtain slightly higher lift coefficients by increasing the pressure gradient over the transition and turbulent flow regions, but before this can be done with any confidence it will first be necessary to carry out detailed studies of the boundary layer behaviour on blades with concave pressure distributions similar to those of the model.

It appears possible even now to obtain small reductions in drag over that of existing blades, but this can only be confirmed by experiment. Drag reductions of some 20% over those of the best empirical isolated aerofoil sections have been achieved by Wortmann (123), and it does not seem unreasonable to contemplate similar improvements in turbomachine blade performance in the long run. The more immediate benefit of the present work, however, is to offer the possibility of designing a turbomachine blade profile for a specific application, and of obtaining a more realistic prediction of its performance.

## 8.4 Problems Requiring Further Research

### 8.4.1 General Remarks

There is still a great deal to be learnt about the design and performance analysis of axial flow turbomachine blading. The most pressing need is for a better understanding of the region of developing turbulent flow following transition, so that a reasonable estimate of the initial shear stress profile in the fully turbulent flow region can be obtained : without such knowledge, no great improvement in the accuracy of predicting the turbulent boundary layer development on a machine blade can be expected. A better prediction of the annulus wall boundary layer behaviour in a machine, particularly as regards the development of the streamwise secondary flow vortex located in the corner between the hub wall and the suction surface of each blade, is needed in order to calculate the magnitude of cross flows within the blade boundary layers : accurate theoretical performance estimates over the whole operating range of blade incidence are unlikely to be achieved until these three-dimensional flow effects are properly taken into account. A detailed study of turbulent flow separation at the blade trailing edge, and of the associated flow development in the

near wake, should be a fruitful field for further research : such work could be expected to lead to better estimates of blade circulation, blade surface pressure distribution, wake decay and associated mixing losses, and deviation angle.

The experimental measurements of the present investigation were carried out entirely at low speed, where compressibility effects were negligible. It is believed that the transition correlation developed from these results, being based on the boundary layer shape factor H, should lend itself to application in high speed subsonic flow situations with little or no modification provided that an appropriate calculation method is used for the laminar boundary layer development ; however, it would be desirable to check this assumption by experiment in a high speed test facility.

8.4.2 Unsteady Flow Phenomena

The whole area of unsteady flow phenomena in axial flow turbomachines is in need of much more detailed examination. The influence of unsteady flows on the development of a machine blade boundary layer has already been mentioned as regards the manner in which passing blade wakes controlled the time-space distribution of laminar and turbulent flow in the transition region : this particular phenomenon resulted from shear stresses imposed by oscillations in the free stream velocity, and from fluctuations in streamwise pressure gradient being impressed on the boundary layer. Another effect which has not previously been dealt with is the direct mixing of fluid from the passing wakes with fluid from the blade boundary layers : due to the relative flow in the wakes, there will be a tendency for fluid to be removed from one surface of the blade and accumulated in the passing wake, whilst on the other side of the blade a discharge of fluid from the wake into the blade boundary layer will occur. Fig. 8.6 shows a schematic diagram of these wake-boundary layer interactions. It is noted that the detailed measurements of the present investigation were carried out only on the stator suction surface, where the relative flow into the passing rotor wakes would have had a thinning effect on the boundary layer (see Fig. 8.6) ; the pressure surface boundary layer might well be thickened by the discharge of fluid from the rotor wakes, and this could result in a less favourable agreement between the calculated and actual boundary layer development.

Fulford (128) observed that the passage of a rotor wake caused a local thickening of the stator suction surface boundary layer, which was manifest by a marked local acceleration in the irrotational flow immediately outside the boundary layer: this probably resulted from pressure gradients induced by the passing wake causing a deceleration of the fluid within the boundary layer. It is possible that this thickening effect increased the rate of

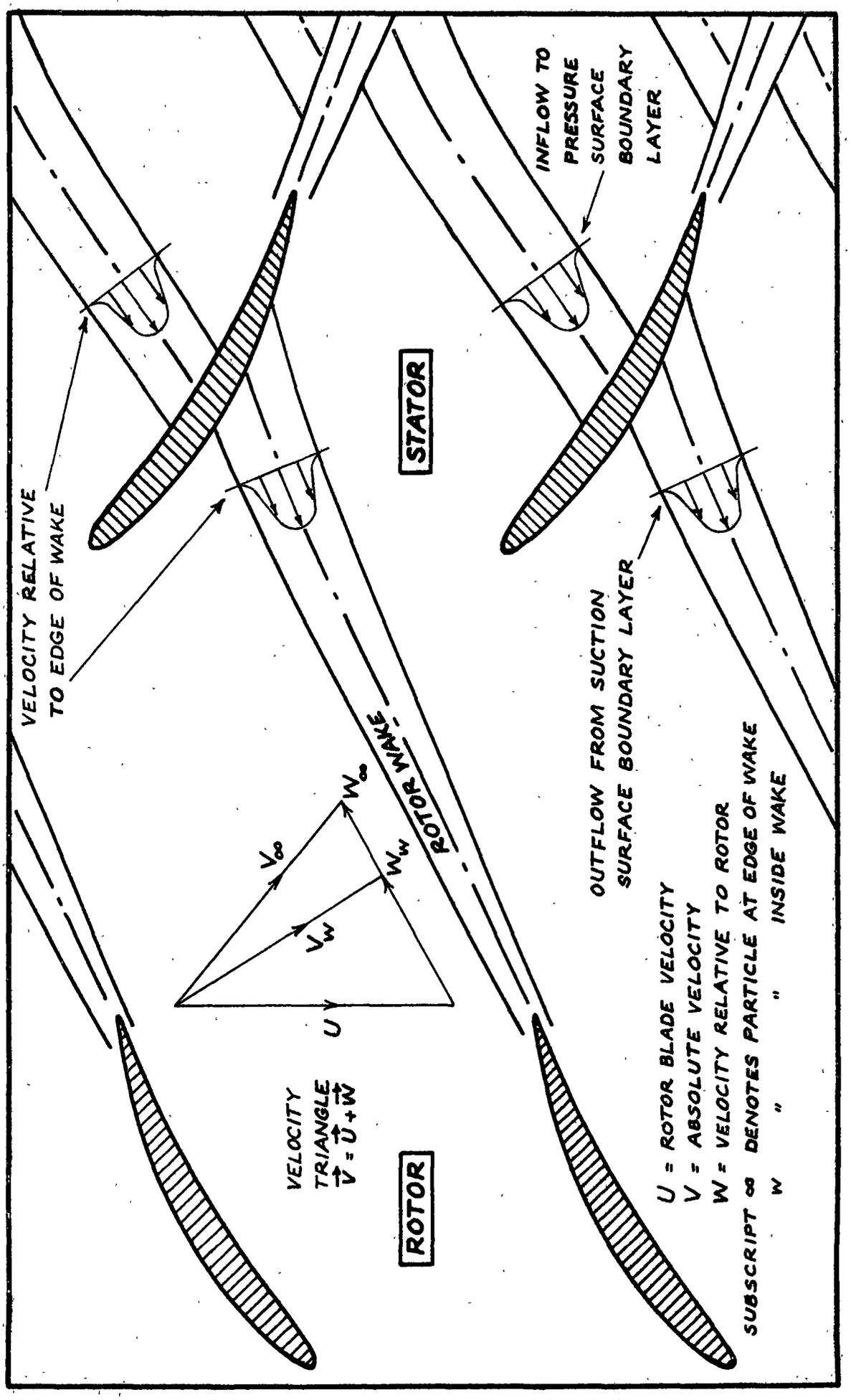


Fig. 8.6 Relative Flow in Blade Wakes of the Research Compressor
(Inlet Guide Vane Wakes Not Shown)

- Figure Indicates Instantaneous Position of Fluid Particles

fluid entrainment from the potential flow into the boundary layer, and so offset the thinning effect due to the flow from the boundary layer into the passing rotor wake ; however, some much more detailed measurements would be required before this point could be definitely established.

Fluctuations in pressure gradient caused by the passage of wakes and other disturbances in the free stream will undoubtedly influence the instantaneous location of the laminar and turbulent separation points, and the rear stagnation point on a turbomachine blade ; the mean positions of these points may also be altered, thus changing the time-mean surface pressure distribution over the whole blade. These problems are in urgent need of further study, since the latter effect is expected to have an important bearing on the influence of free stream turbulence on the blade performance : it is, unfortunately, impossible to dismiss such changes as being of second order, since the present study has shown the boundary layer behaviour under these circumstances to be very largely explainable in terms of accompanying small changes in the time-mean surface pressure distribution.

# CHAPTER 9

## GENERAL CONCLUSIONS

The present investigation has led to a considerable improvement in understanding of the boundary layer behaviour on the blades of the research compressor, and, it is believed, in axial flow turbomachines generally. One of the most important results of this study has been to demonstrate that extensive regions of laminar flow may exist on the surface of a machine blade despite the high level of free stream turbulence which is always present due to the effects of neighbouring blade rows.

Observations of flow on the suction surfaces of both rotor and stator blades in the research compressor showed the extent of the laminar boundary layer to be strongly dependent on the blade incidence. The length of laminar flow was less than 10% of chord at large positive incidence, but increased to 80% of chord at large negative incidence where there was an appreciable region of flow acceleration near the leading edge of the blade. It was therefore concluded that accurate theoretical predictions of turbomachine blade performance were unlikely to be obtained unless the laminar boundary layer development and the location of transition to turbulent flow could be estimated with reasonable precision.

Hot wire measurements at mid-blade height on the stator suction surface showed that all aspects of the laminar boundary layer development, including the laminar separation point, were predicted remarkably well by Thwaites's (10) method when the calculation was based on the measured surface pressure distribution. It is possible, however, that the reasonable estimate of separation was the fortuitous result of the blade surface velocity distribution being roughly linear upstream of the separation point in most cases.

Regions of separated laminar flow were present on the stator blade suction surface at negative incidence over the whole speed range tested. However, the flattening of the surface pressure distribution usually considered characteristic of this phenomenon only became apparent at the lower compressor speeds, where the separation bubbles were quite well developed.

The measured lengths of separated laminar shear layer in bubbles on the compressor blades did not agree with correlations proposed by other workers to describe the behaviour of separation bubbles on isolated aerofoils operating at high Reynolds numbers. An alternative means of predicting separation bubble length, based on a new empirical transition correlation proposed by the author, was found to describe all of the available data reasonably well.

Gaster's (34) bursting criterion indicated that the separation bubbles on the stator suction surface changed from the short to the long regime at about the middle of the Reynolds number range investigated: bursting appeared to result from a failure of the turbulent shear layer to reattach, rather than from a sudden change in the stability of the separated laminar shear layer. The present study has suggested that the critical Reynolds number below which the profile drag of an axial flow compressor blade increases markedly is associated with the separation bubble bursting phenomenon, rather than the first appearance of separated laminar flow : it is evidently possible for the short type of separation bubble to occur at Reynolds numbers above critical without causing any great deterioration of the blade performance.

The detailed measurements on the stator blade tended to support the basic physical assumptions involved in Horton's (38) model for the turbulent reattachment process in a laminar separation bubble. However, the pressure rise during reattachment in bubbles on the compressor blade was in most cases seriously overestimated by Horton's analysis, apparently because the reattaching shear layer was not fully turbulent : it seemed likely that a suitable allowance for the intermittency of turbulence would have significantly improved the agreement with experiment.

The periodic disturbances arising from the passage of rotor wakes in the free stream imposed a considerable degree of regularity on the time-space distribution of laminar and turbulent flow during transition on the stator blades of the research compressor. However, the boundary layer Reynolds number at which turbulent flow first appeared did not seem to be greatly influenced by these disturbances despite the apparently high level of free stream turbulence they created. This behaviour was very similar to the "aperiodic" mode of transition observed by Fejer et al.(43, 44) in oscillating flow past a flat plate when the non-steady Reynolds number $(Re)_{NS}$, based on the amplitude of the oscillations, fell below a certain critical value.

The stabilisation of flow which occurred during the accelerating phase of the rotor wake disturbance appeared to cause a significant lengthening of the transition region on the stator blade. As the measured transition lengths varied from 15 to 20% of chord on the stator suction surface, it was concluded that a point transition model would not lead to very accurate predictions of the boundary layer development on turbomachine blades.

A new empirical method of predicting transition, developed from the results of the present investigation, was found to describe the transition behaviour in a wide range of other flow situations as well. The commonly used transition correlations of Granville (65) and Michel (55) were shown to be particular cases of the new correlation for limited ranges of Reynolds number or streamwise pressure gradient. For the transition data considered,

the new correlation gave results of similar accuracy to the semi-empirical methods of Smith et al.(56, 57, 61) which are based on laminar stability theory. No other empirical method known to the author gave any useful prediction of the transition point on the blades of the research compressor.

The author believes that free stream turbulence will only have a major influence on the location of the transition point when :

(a) individual disturbances cause large movements of the neutral stability point on a body ; or

(b) the free stream disturbance spectrum contains a significant level of energy at frequencies close to those of the disturbances receiving amplification within the boundary layer ; or

(c) the individual free stream disturbances are large enough to promote breakdown within the wavelength of the disturbance. (The critical size of an essentially two-dimensional disturbance, such as a blade wake in a turbomachine, could possibly be specified in terms of the non-steady Reynolds number $(Re)_{NS}$, or calculated from the quasi-steady stability analysis of Obremski and Morkovin (49).)

Unless one or more of the above conditions apply, the present study has indicated that free stream turbulence effects should not move the transition point by more than 10-20% of the instability length, even when the amplitude of individual disturbances is quite large (say 5-10% of the mean free stream velocity). Data concerning the influence of free stream turbulence on transition on a flat plate is not expected to be generally applicable, since movements of the instability point in response to individual free stream disturbances will depend strongly on the body geometry.

Using the results of the present investigation relating to laminar separation, separation bubble bursting, and transition, it was found that the boundary layer behaviour on cascade blades observed by other workers could usually be predicted quite well from the measured surface pressure distribution, regardless of the free stream turbulence level. This implied that the influence of free stream turbulence on the blade performance arose mainly from accompanying small changes in the time-mean surface pressure distribution, rather than from some basic change in the physical nature of the transition process. The mechanism by which the free stream turbulence altered the time-mean surface pressure distribution was not entirely clear : it could possibly have resulted from a direct influence of free stream disturbances on the mean location of the rear stagnation point, or from small movements of the transition point altering the boundary layer displacement thickness distribution. A survey of available data suggested that small movements of the transition point were able to produce large variations in blade performance when the long bubble type of laminar flow separation was present on the blade surface ; thus it is incorrect, in general, to assume that relative movements of the transition point are similar in magnitude to relative changes in the overall performance of a cascade.

Measurements in turbulent flow regions on a stator blade of the research compressor showed no evidence of the usual logarithmic wall similarity in the boundary layer mean velocity profiles : most of the observed departures from the logarithmic law probably resulted from the large positive pressure gradients on the suction surface of the compressor blade. Fair agreement between experiment and McDonald's (84) law of the wall was obtained at the higher Reynolds numbers investigated, but the agreement progressively deteriorated as the compressor speed was reduced. The outer regions of the measured boundary layer velocity profiles were not described very well by either the Coles (85) wall-plus-wake or the power law families.

The Ludwieg-Tillmann (96) and Nash-Macdonald (98) skin friction laws seriously overestimated the measured wall shear stress on the stator blade in most cases. A new skin friction law developed by the author from McDonald's (84) law of the wall gave much better agreement with experiment; however, the measured skin friction values could not be regarded as very accurate because of doubts concerning the correction required for wall proximity effects on the hot wire readings.

The minimum value of boundary layer Reynolds number $Re_\theta$ observed in fully turbulent flow regions on the compressor blades was about 200; this conflicted with Preston's (75) earlier suggestion of a minimum value exceeding 320 in a positive pressure gradient. However, on using the results of more recent theories of the turbulent wall layer, together with Preston's original physical assumptions, it was found that theoretical values of minimum Reynolds number consistent with the present measurements could be obtained. Similar results were derived from the effective viscosity hypothesis of Mellor (94) and the eddy Reynolds number concept of Bradshaw (89).

Head's (111) entrainment method was found to give the most reliable overall prediction of the boundary layer development on the stator blade suction surface, although it consistently overestimated the rate at which the boundary layer responded to changes in external conditions, and the agreement between the measured and predicted values of shape factor was only fair. Attempts to use calculation methods based on more accurate physical models of the turbulent flow were abandoned because of troubles with the stability of the calculations and difficulties in specifying the initial turbulent shear stress profiles. The influence of flow curvature on the turbulent flow in the stator suction surface boundary layer was undoubtedly significant, but it appeared that any allowance for this effect would generally have worsened the agreement between experiment and the boundary layer development predicted by Head's method.

A two-dimensional boundary layer calculation based on the measured surface pressure distribution and using the methods of Thwaites and Head together with the author's transition correlation was found to predict the

stator blade suction surface losses at mid-blade height to within 10% in the incidence range $-4^{\circ} < i < 1^{\circ}$. Outside this range, the errors steadily increased until they reached about 30% at the maximum positive and negative incidence investigated; the predicted losses were too low in all cases. While errors arising from the approximate nature of the boundary layer calculation methods used were not insignificant, the major source of differences between experiment and the predictions of the above model appeared to be the neglecting of three-dimensional (i.e. radial) flow effects: departures from two-dimensional flow were mainly associated with the development of separated flow regions on the blade surface and the annulus walls, and the displacement effect of the secondary flow vortex located in the corner between the suction surface of the blade and the hub wall of the compressor.

The two-dimensional calculation method proposed above should give reasonably accurate performance estimates for high aspect ratio machine blading operating near the design incidence at Reynolds numbers above critical ; a useful indication of the critical Reynolds number itself should be given by Gaster's (34) bursting criterion for the laminar separation bubble. Slightly greater errors in performance estimates must be expected where the surface pressure distribution is not known and has to be calculated from potential flow theory suitably modified to allow for viscous flow effects. Accurate predictions of off-design performance over the whole range of operating incidence are unlikely to be obtained until the effects of radial flows can be properly accounted for.

The results of the present investigation were used to derive a family of surface velocity distributions considered likely to give unseparated flow over the suction surface of an axial flow compressor blade, and the approximate performance of blades having the model distribution was calculated. There appeared to be no particular advantage in using laminar separation to promote transition at low Reynolds numbers. For chord Reynolds numbers of about $3 \times 10^5$, which are typical of turbomachine blade operation, the location of the velocity peak ranged from 10% of chord for the maximum lift design to 22% of chord for the best efficiency design; this contrasted markedly with the values of about 50% chord typical of conventional high-performance isolated aerofoils. The optimum chordwise location of the velocity peak in the model distribution moved steadily rearwards as the chord Reynolds number was increased.

The performance calculated from the model surface velocity distribution family was roughly comparable with that of conventional compressor blade sections : the theoretical lift/drag ratios were a little better, but the maximum lift coefficients of the model were slightly less than those obtained in current practice. The lower lift coefficients most probably resulted from the conservative values of pressure gradients applied to the transition and turbulent boundary layer regions, and from neglecting the small contribution of the pressure surface to the total

blade lift. An almost unique relation was obtained between the calculated wake momentum thickness ratio, $\theta_w/c$, and the local diffusion factor, $D_{loc}$, for the model suction surface velocity distribution family; there was, however, no single-valued relation between the estimated lift coefficient and the local diffusion factor.

The present study has identified a number of problems which must be overcome before further improvements in the theoretical performance analysis of axial flow turbomachine blading can be obtained. The main areas in need of additional research are:

(i) the flow behaviour during transition, and the calculation of the initial shear stress profile for the turbulent boundary layer;

(ii) the prediction of turbulent separation and the development of flow in the near wake of a turbomachine blade;

(iii) the calculation of radial flows on the blade surface produced by the annulus wall boundary layer growth and its associated secondary flows;

(iv) the whole area of unsteady flow phenomena in turbomachines, particularly the problem of wake-boundary layer interactions.

# APPENDIX A

## Correction of Hot Wire Readings for Variation in Atmospheric Conditions

In deriving suitable corrections to allow for changes in wire resistance or anemometer bridge voltage due to ambient pressure and temperature variations, it is convenient to express the rate of heat loss from cylindrical wires in the power law form given by Hilpert (17)

$$Nu = C\,[Re_w(T_m/T_a)^{\frac{1}{4}}]^n \qquad (A.1)$$

When the fluid properties are all evaluated at the mean film temperature, $T_m = \frac{1}{2}(T_w+T_a)$, the values of C and n specified in Table A.1 are obtained.

Table A.1

Values of Parameters in Equation A.1

| $Re_w$ | C | n |
|---|---|---|
| 1 - 4 | 0.891 | 0.330 |
| 4 - 40 | 0.821 | 0.385 |
| 40 - 4000 | 0.615 | 0.466 |

For small changes in ambient conditions the temperature loading factor may be treated as constant, in which case Equation (A.1) simplifies to

$$Nu = C_1 Re_w^{\,n} \qquad (A.2)$$

where $C_1$ is constant. Equation (A.2) can be written in terms of dimensional variables as

$$(hd/k) = C_1\,(ud/\nu)^n \qquad (A.3)$$

where h is the heat transfer coefficient, d the wire diameter, u the fluid velocity, and k and $\nu$ are the fluid thermal conductivity and kinematic viscosity respectively. Hence the heat transfer coefficient is given by

$$h = C_1\,(k/d)(ud/\nu)^n \qquad (A.4)$$

The fluid properties for air are now expressed in the approximate analytical forms given by Pinkel (18) as

$$k = k_o\,(T_m/T_o)^{0.85}; \qquad \nu = \nu_o\,(T_m/T_o)^{0.68}(P_o/P) \qquad (A.5)$$

where $k_o$ and $\nu_o$ are the values of the respective properties at air temperature $T_o$ and pressure $P_o$. Equation (A.4) then becomes

$$h = C_2\,T_m^{(0.85-0.68n)}\,P^n \qquad (A.6)$$

where $C_2$ is a constant.

The partial differentials of the heat transfer coefficient with respect to changes in mean film temperature $T_m$ or ambient pressure P are then obtained from Equation (A.6) as

$$\frac{\partial h}{\partial T_m} = (0.85-0.68n)\frac{h}{T_m} \qquad (A.7)$$

and

$$\frac{\partial h}{\partial P} = \frac{nh}{P} \qquad (A.8)$$

(a) Correction for constant temperature operation

The rate of heat loss from the hot wire probe is given by

$$Q = V^2/R_w = hA\theta \qquad (A.9)$$

where V is the voltage applied across the wire, $R_w$ is the (constant) wire resistance, A is the surface area of the wire, and $\theta = (T_w - T_a)$ is the temperature difference between the wire and the ambient air.

Differentiating Equation (A.9) and rearranging gives the relative change in voltage corresponding to changes in pressure and temperature difference of dP and dθ, respectively, as

$$\frac{dV}{V} = \tfrac{1}{2}\left(1 + \frac{\theta}{h}\frac{\partial h}{\partial \theta}\right)\frac{d\theta}{\theta} + \frac{1}{2h}\frac{\partial h}{\partial P}\,dP \qquad (A.10)$$

For constant temperature operation, $T_w$ = constant, so that

$$d\theta = -dT_a; \qquad dT_m = \tfrac{1}{2}dT_a = -\tfrac{1}{2}d\theta \qquad (A.11)$$

and

$$\frac{\partial h}{\partial \theta} = \frac{\partial h}{\partial T_m}\frac{dT_m}{d\theta} = -\tfrac{1}{2}\frac{\partial h}{\partial T_m} \qquad (A.12)$$

Substituting Equations (A.7), (A.8) and (A.12) into Equation (A.10) gives

$$\frac{dV}{V} = \tfrac{1}{2}\left\{1 + (0.34n-0.425)\frac{\theta}{T_m}\right\}\frac{d\theta}{\theta} + \frac{n\,dP}{P} \qquad (A.13)$$

Finally, using n = 0.36 as an average value for the range $1 < Re_w < 40$, and writing the temperature difference, θ, as

$$\theta = (T_w - T_a) = (R_w - R_a)/R_o\alpha \qquad (A.14)$$

where $R_a$ is the wire resistance at ambient temperature $T_a$, and $R_o$ and $\alpha$ respectively are the wire resistance and temperature coefficient of resistance at ambient temperature $T_o$, gives

$$\frac{dV}{V} = -\left\{1-0.303\frac{\theta}{T_m}\right\}\frac{R_o\alpha\,dT_a}{2(R_w - R_a)} + \frac{0.18\,dP}{P} \qquad (A.15)$$

(b) Correction for constant current operation

In this case the rate of heat loss from the hot wire probe is

$$Q = I^2R_w = hA\theta \tag{A.16}$$

where the heating current, I, is constant. Hence

$$\theta = (T_w - T_a) = I^2R_w/hA \tag{A.17}$$

and

$$\frac{\partial\theta}{\partial T_a} = \frac{\partial T_w}{\partial T_a} - 1 = \frac{I^2}{hA}\frac{\partial R_w}{\partial T_a} - \frac{I^2R_w}{Ah^2}\frac{\partial h}{\partial T_a} \tag{A.18}$$

Substituting

$$\frac{\partial T_w}{\partial T_a} = \frac{1}{R_o\alpha}\frac{\partial R_w}{\partial T_a} \tag{A.19}$$

into Equation (A.18) and simplifying gives

$$\frac{\partial R_w}{\partial T_a}\left(\frac{1}{R_o\alpha} - \frac{I^2}{hA}\right) = 1 - \frac{I^2R_w}{Ah^2}\frac{\partial h}{\partial T_a} \tag{A.20}$$

For small values of $\theta$ and small changes in ambient temperature it can be assumed that $dT_w \simeq dT_a$, so that

$$\frac{\partial h}{\partial T_a} \simeq \frac{\partial h}{\partial T_m} = (0.85-0.68n)\frac{h}{T_m} \tag{A.21}$$

Substituting Equation (A.21) into Equation (A.20), and simplifying by means of Equations (A.14) and (A.17) leads to

$$\frac{\partial R_w}{\partial T_a} = \frac{R_o\alpha R_w}{R_a}\left\{1 - (0.85-0.68n)\frac{\theta}{T_m}\right\} \tag{A.22}$$

To obtain the resistance changes due to ambient pressure variations, Equation (A.17) is differentiated with respect to P, giving

$$\frac{\partial\theta}{\partial P} = \frac{\partial T_w}{\partial P} = \frac{1}{R_o\alpha}\frac{\partial R_w}{\partial P} = \frac{I^2}{hA}\frac{\partial R_w}{\partial P} - \frac{I^2R_w}{Ah^2}\frac{\partial h}{\partial P} \tag{A.23}$$

Substituting for $\frac{\partial h}{\partial P}$ from Equation (A.8) and simplifying gives

$$\frac{\partial R_w}{\partial P} = \frac{nR_w}{P}\left(1 - \frac{R_w}{R_a}\right) \tag{A.24}$$

The total change in resistance, $dR_w$, corresponding to an ambient temperature variation of $dT_a$, and an ambient pressure change of dP, is given by

$$\frac{dR_w}{R_w} = \frac{1}{R_w}\frac{\partial R_w}{\partial T_a} dT_a + \frac{1}{R_w}\frac{\partial R_w}{\partial P} dP \qquad (A.25)$$

Substituting Equations (A.22) and (A.24) into Equation (A.25), and again using $n = 0.36$ an average value for $1 < Re_w < 40$, gives finally

$$\frac{dR_w}{R_w} = \left(1 - 0.606\,\frac{\theta}{T_m}\right)\frac{R_o \alpha\, dT_a}{R_a} + 0.36\left(1 - \frac{R_w}{R_a}\right)\frac{dP}{P} \qquad (A.26)$$

It should be noted that the above correction formulae do not take into account any changes in the amount of heat conducted to the supporting prongs, which might become significant for wires of low l/d ratio. For constant current operation the temperature distribution along the wire remains nearly the same for small ambient temperature changes, since $dT_w \simeq dT_a$, and there should be little variation in the amount of heat lost to the supports. For constant temperature operation, however, the temperature distribution along the wire must change with $T_a$, assuming that the supports remain at ambient temperature; variations in the amount of heat lost to the supports could therefore be more significant in this case.

## APPENDIX B

### Mean Flow Coefficients and Mid-Blade Incidence

| Compressor Speed (rpm) | Throttle Opening (ins) | Mean Flow Coefficient $\phi = V_a/U_{mb}$ | Stator Incidence at Mid-Blade (°) | Rotor Incidence at Mid-Blade (°) |
|---|---|---|---|---|
| 750* | 4.8 | 0.56 | 4.6 | 8.5 |
| | 5.2 | 0.61 | 2.7 | 5.5 |
| | 6.0 | 0.66 | 0.6 | 2.6 |
| | 8.0 | 0.75 | -3.7 | -2.6 |
| | 10.0 | 0.80 | -6.2 | -5.6 |
| | 13.0 | 0.85 | -8.7 | -7.9 |
| | 22.0 | 0.90 | -10.9 | -10.8 |
| 500 | 4.8 | 0.555 | 4.7 | - |
| | 5.2 | 0.60 | 2.9 | - |
| | 6.0 | 0.65 | 1.0 | - |
| | 8.0 | 0.735 | -3.1 | - |
| | 10.0 | 0.785 | -5.6 | - |
| | 13.0 | 0.83 | -7.6 | - |
| | 22.0 | 0.885 | -10.3 | - |
| 250 | 4.8 | 0.54 | 5.2 | - |
| | 5.2 | 0.585 | 3.0 | - |
| | 6.0 | 0.645 | 0.5 | - |
| | 8.0 | 0.72 | -3.2 | - |
| | 10.0 | 0.775 | -6.0 | - |
| | 13.0 | 0.82 | -8.0 | - |
| | 22.0 | 0.87 | -10.1 | - |
| 150 | 4.8 | 0.52 | 5.6 | - |
| | 5.2 | 0.565 | 3.6 | - |
| | 6.0 | 0.62 | 1.2 | - |
| | 8.0 | 0.705 | -3.0 | - |
| | 10.0 | 0.75 | -5.5 | - |
| | 13.0 | 0.795 | -7.7 | - |
| | 22.0 | 0.845 | -10.2 | - |

*Values for rotor from measurements of Salter (9)

## APPENDIX C

### Radial Variation of Air Angle and Axial Velocity - Rotor*

COMPRESSOR SPEED 750 RPM

| Throttle Opening (ins) | Quantity | $R/R_T$ 0.65 | 0.70 | 0.80 | 0.90 | 0.95 |
|---|---|---|---|---|---|---|
| 4.8 | $V_a/U_{mb}$ | 0.55 | 0.56 | 0.57 | 0.58 | 0.59 |
| | $\alpha_1$(°) | 44.9 | 47.9 | 53.5 | 58.5 | 61.0 |
| | i(°) | 11.8 | 9.0 | 8.5 | 8.8 | 8.9 |
| 5.2 | $V_a/U_{mb}$ | 0.60 | 0.61 | 0.62 | 0.62 | 0.61 |
| | $\alpha_1$(°) | 41.4 | 44.5 | 50.5 | 56.2 | 59.0 |
| | i(°) | 8.3 | 5.6 | 5.5 | 6.5 | 6.9 |
| 6.0 | $V_a/U_{mb}$ | 0.65 | 0.66 | 0.67 | 0.68 | 0.67 |
| | $\alpha_1$(°) | 37.7 | 41.2 | 47.6 | 53.3 | 56.4 |
| | i(°) | 4.6 | 2.3 | 2.6 | 3.6 | 4.3 |
| 8.0 | $V_a/U_{mb}$ | 0.75 | 0.75 | 0.77 | 0.77 | 0.75 |
| | $\alpha_1$(°) | 31.7 | 35.5 | 42.4 | 48.6 | 52.6 |
| | i(°) | -1.4 | -3.4 | -2.6 | -1.1 | 0.5 |
| 10.0 | $V_a/U_{mb}$ | 0.80 | 0.81 | 0.82 | 0.81 | 0.79 |
| | $\alpha_1$(°) | 28.6 | 32.3 | 39.4 | 46.6 | 50.6 |
| | i(°) | -4.5 | -6.6 | -5.6 | -3.1 | -1.5 |
| 13.0 | $V_a/U_{mb}$ | 0.85 | 0.85 | 0.87 | 0.86 | 0.84 |
| | $\alpha_1$(°) | 25.9 | 29.7 | 37.1 | 44.1 | 48.6 |
| | i(°) | -7.2 | -9.2 | -7.9 | -5.6 | -3.5 |
| 22.0 | $V_a/U_{mb}$ | 0.91 | 0.92 | 0.93 | 0.92 | 0.91 |
| | $\alpha_1$(°) | 22.9 | 26.5 | 34.2 | 41.6 | 46.3 |
| | i(°) | -10.2 | -12.4 | -10.8 | -8.1 | -5.8 |

* From measurements of Salter (9)

APPENDIX C (cont.)

Radial Variation of Air Angle and Axial Velocity - Stator*

COMPRESSOR SPEED 750 RPM

| Throttle Opening (ins) | Quantity | $R/R_T$ 0.65 | 0.70 | 0.80 | 0.90 | 0.95 |
|---|---|---|---|---|---|---|
| 4.8 | $V_a/U_{mb}$ | 0.41 | 0.52 | 0.59 | 0.63 | 0.64 |
| | $\alpha_3(^o)$ | 59.0 | 53.8 | 48.6 | 44.1 | 40.2 |
| | $i(^o)$ | 7.8 | 4.7 | 3.6 | 2.6 | 0.3 |
| 5.2 | $V_a/U_{mb}$ | 0.56 | 0.58 | 0.63 | 0.65 | 0.66 |
| | $\alpha_3(^o)$ | 53.5 | 50.9 | 47.3 | 43.7 | 40.2 |
| | $i(^o)$ | 2.3 | 1.8 | 2.3 | 2.2 | 0.3 |
| 6.0 | $V_a/U_{mb}$ | 0.61 | 0.64 | 0.66 | 0.68 | 0.69 |
| | $\alpha_3(^o)$ | 51.1 | 48.8 | 45.5 | 41.1 | 37.5 |
| | $i(^o)$ | -0.1 | -0.3 | 0.5 | -0.4 | -2.4 |
| 8.0 | $V_a/U_{mb}$ | 0.70 | 0.74 | 0.75 | 0.75 | 0.75 |
| | $\alpha_3(^o)$ | 47.0 | 44.8 | 40.7 | 36.2 | 32.6 |
| | $i(^o)$ | -4.2 | -4.3 | -4.3 | -5.3 | -7.3 |
| 10.0 | $V_a/U_{mb}$ | 0.76 | 0.79 | 0.81 | 0.81 | 0.80 |
| | $\alpha_3(^o)$ | 44.9 | 42.5 | 38.2 | 33.1 | 30.1 |
| | $i(^o)$ | -6.3 | -6.6 | -6.8 | -8.4 | -9.8 |
| 13.0 | $V_a/U_{mb}$ | 0.83 | 0.85 | 0.85 | 0.85 | 0.85 |
| | $\alpha_3(^o)$ | 42.4 | 40.8 | 36.1 | 31.0 | 27.8 |
| | $i(^o)$ | -8.8 | -8.3 | -8.9 | -10.5 | -12.1 |
| 22.0 | $V_a/U_{mb}$ | 0.90 | 0.92 | 0.92 | 0.92 | 0.90 |
| | $\alpha_3(^o)$ | 40.4 | 38.3 | 32.9 | 28.2 | 25.0 |
| | $i(^o)$ | -10.8 | -10.8 | -12.1 | -13.3 | -14.9 |

* From measurements of Salter (9)

## Values of $U/U_{mb}$ Measured from Blade Surface Pressure Tappings

| Location | Compressor Speed (rpm) | Throttle Opening (ins) | Chordwise Position x/c (%) | | | | | | | | | | | | |
|---|---|---|---|---|---|---|---|---|---|---|---|---|---|---|---|
| | | | 0 | 5 | 10 | 15 | 20 | 25 | 30 | 35 | 40 | 50 | 60 | 70 | 80 | 90 |
| ROTOR* | 750 | 4.8 | 0.282 | 1.416 | 1.326 | 1.255 | 1.215 | 1.168 | 1.115 | 1.074 | 1.022 | 1.014 | 0.898 | 0.863 | 0.806 | 0.790 |
| SUCTION | | 5.2 | 0.228 | 1.405 | 1.336 | 1.279 | 1.250 | 1.210 | 1.172 | 1.125 | 1.079 | 1.005 | 0.968 | 0.920 | 0.832 | 0.788 |
| SURFACE | | 6.0 | 0.164 | 1.367 | 1.331 | 1.298 | 1.279 | 1.252 | 1.215 | 1.182 | 1.134 | 1.090 | 1.046 | 0.994 | 0.905 | 0.838 |
| | | 8.0 | 0.114 | 1.281 | 1.304 | 1.303 | 1.301 | 1.290 | 1.266 | 1.247 | 1.227 | 1.194 | 1.161 | 1.110 | 1.011 | 0.932 |
| MID | ($U_{mb}$= | 10.0 | 0 | 1.223 | 1.281 | 1.300 | 1.311 | 1.306 | 1.294 | 1.282 | 1.265 | 1.240 | 1.217 | 1.186 | 1.074 | 0.986 |
| BLADE | 117.8fps) | 13.0 | 0 | 1.181 | 1.271 | 1.310 | 1.328 | 1.331 | 1.327 | 1.321 | 1.314 | 1.296 | 1.266 | 1.236 | 1.159 | 1.094 |
| HEIGHT | | 22.0 | 0 | 1.120 | 1.251 | 1.309 | 1.340 | 1.355 | 1.359 | 1.362 | 1.354 | 1.343 | 1.331 | 1.290 | 1.254 | 1.095 |
| STATOR* | 750 | 4.8 | 0.706 | 1.264 | 1.223 | 1.186 | 1.156 | 1.130 | 1.098 | 1.080 | 1.052 | 1.003 | 0.961 | 0.912 | 0.858 | 0.803 |
| SUCTION | | 5.2 | 0.645 | 1.285 | 1.250 | 1.214 | 1.185 | 1.158 | 1.126 | 1.105 | 1.173 | 1.020 | 0.971 | 0.912 | 0.850 | 0.784 |
| SURFACE | | 6.0 | 0.516 | 1.286 | 1.267 | 1.230 | 1.215 | 1.190 | 1.160 | 1.142 | 1.115 | 1.066 | 1.016 | 0.960 | 0.896 | 0.818 |
| | | 8.0 | 0.127 | 1.243 | 1.271 | 1.264 | 1.257 | 1.245 | 1.225 | 1.218 | 1.198 | 1.165 | 1.124 | 1.062 | 0.991 | 0.910 |
| MID | ($U_{mb}$= | 10.0 | 0 | 1.206 | 1.270 | 1.282 | 1.282 | 1.282 | 1.266 | 1.266 | 1.250 | 1.223 | 1.192 | 1.144 | 1.057 | 0.974 |
| BLADE | 117.8fps) | 13.0 | 0 | 1.176 | 1.259 | 1.283 | 1.293 | 1.300 | 1.288 | 1.294 | 1.279 | 1.259 | 1.230 | 1.194 | 1.106 | 1.011 |
| HEIGHT | | 22.0 | 0 | 1.132 | 1.249 | 1.292 | 1.315 | 1.335 | 1.331 | 1.345 | 1.335 | 1.322 | 1.298 | 1.264 | 1.194 | 1.085 |

* from measurements of Salter (9)

## Values of $U/U_{mb}$ Measured from Blade Surface Presure Tappings

| Location | Compressor Speed (rpm) | Throttle Opening (ins) | Chordwise Position x/c (%) 0 | 5 | 10 | 15 | 20 | 25 | 30 | 35 | 40 | 50 | 60 | 70 | 80 | 90 |
|---|---|---|---|---|---|---|---|---|---|---|---|---|---|---|---|---|
| STATOR | 500 | 4.8 | 0.658 | 1.213 | 1.190 | 1.151 | 1.121 | 1.093 | 1.063 | 1.043 | 1.011 | 0.968 | 0.924 | 0.874 | 0.818 | 0.770 |
| SUCTION | | 5.2 | 0.708 | 1.248 | 1.227 | 1.191 | 1.157 | 1.128 | 1.096 | 1.076 | 1.048 | 0.998 | 0.944 | 0.930 | 0.826 | 0.769 |
| SURFACE | | 6.0 | 0.614 | 1.271 | 1.267 | 1.237 | 1.213 | 1.190 | 1.157 | 1.143 | 1.118 | 1.112 | 1.014 | 0.955 | 0.932 | 0.816 |
| | | 8.0 | 0.250 | 1.241 | 1.284 | 1.276 | 1.267 | 1.268 | 1.236 | 1.225 | 1.207 | 1.171 | 1.132 | 1.065 | 0.984 | 0.904 |
| MID | ($U_{mb}$= | 10.0 | 0 | 1.231 | 1.291 | 1.301 | 1.301 | 1.297 | 1.284 | 1.279 | 1.265 | 1.241 | 1.211 | 1.177 | 1.071 | 0.984 |
| BLADE | 78.6fps) | 13.0 | 0 | 1.219 | 1.299 | 1.320 | 1.328 | 1.333 | 1.329 | 1.329 | 1.318 | 1.293 | 1.263 | 1.234 | 1.168 | 1.046 |
| HEIGHT | | 22.0 | 0 | 1.173 | 1.277 | 1.318 | 1.338 | 1.375 | 1.352 | 1.359 | 1.351 | 1.335 | 1.304 | 1.273 | 1.226 | 1.091 |
| STATOR | 250 | 4.8 | 0.574 | 1.155 | 1.133 | 1.097 | 1.073 | 1.045 | 1.017 | 0.998 | 0.973 | 0.926 | 0.886 | 0.838 | 0.782 | 0.734 |
| SUCTION | | 5.2 | 0.562 | 1.143 | 1.132 | 1.096 | 1.084 | 1.074 | 1.024 | 1.002 | 0.979 | 0.929 | 0.882 | 0.829 | 0.770 | 0.708 |
| SURFACE | | 6.0 | 0.670 | 1.220 | 1.229 | 1.209 | 1.189 | 1.168 | 1.143 | 1.124 | 1.114 | 1.065 | 1.016 | 0.960 | 0.895 | 0.830 |
| | | 8.0 | 0.167 | 1.225 | 1.266 | 1.266 | 1.259 | 1.248 | 1.231 | 1.218 | 1.193 | 1.171 | 1.133 | 1.110 | 1.027 | 0.906 |
| MID | ($U_{mb}$= | 10.0 | 0 | 1.215 | 1.281 | 1.295 | 1.298 | 1.295 | 1.293 | 1.277 | 1.264 | 1.234 | 1.205 | 1.188 | 1.135 | 1.015 |
| BLADE | 39.3fps) | 13.0 | 0 | 1.203 | 1.285 | 1.310 | 1.320 | 1.323 | 1.325 | 1.316 | 1.304 | 1.278 | 1.246 | 1.225 | 1.200 | 1.074 |
| HEIGHT | | 22.0 | 0 | 1.173 | 1.278 | 1.320 | 1.338 | 1.350 | 1.346 | 1.351 | 1.344 | 1.321 | 1.291 | 1.265 | 1.246 | 1.129 |

## Values of $U/U_{mb}$ Measured from Blade Surface Pressure Tappings

| Location | Compressor Speed (rpm) | Throttle Opening (ins) | Chordwise Position x/c (%) | | | | | | | | | | | | | |
|---|---|---|---|---|---|---|---|---|---|---|---|---|---|---|---|---|
| | | | 0 | 5 | 10 | 15 | 20 | 25 | 30 | 35 | 40 | 50 | 60 | 70 | 80 | 90 |
| STATOR | 150 | 4.8 | 0.611 | 1.151 | 1.134 | 1.091 | 1.065 | 1.036 | 1.020 | 0.992 | 0.965 | 0.933 | 0.890 | 0.848 | 0.800 | 0.769 |
| SUCTION | | 5.2 | 0.500 | 1.146 | 1.123 | 1.083 | 1.056 | 1.031 | 1.010 | 0.980 | 0.955 | 0.916 | 0.868 | 0.812 | 0.754 | 0.716 |
| SURFACE | | 6.0 | 0.558 | 1.180 | 1.217 | 1.166 | 1.145 | 1.130 | 1.108 | 1.096 | 1.072 | 1.040 | 0.984 | 0.928 | 0.873 | 0.820 |
| | | 8.0 | 0.078 | 1.203 | 1.266 | 1.274 | 1.271 | 1.271 | 1.256 | 1.250 | 1.234 | 1.203 | 1.171 | 1.161 | 1.124 | 1.023 |
| MID | ($U_{mb}$= | 10.0 | 0 | 1.206 | 1.271 | 1.278 | 1.275 | 1.275 | 1.261 | 1.254 | 1.239 | 1.206 | 1.176 | 1.167 | 1.129 | 1.029 |
| BLADE | 23.6fps) | 13.0 | 0 | 1.185 | 1.265 | 1.283 | 1.286 | 1.295 | 1.285 | 1.289 | 1.274 | 1.242 | 1.210 | 1.197 | 1.181 | 1.088 |
| HEIGHT | | 22.0 | 0 | 1.136 | 1.248 | 1.281 | 1.289 | 1.309 | 1.303 | 1.315 | 1.298 | 1.268 | 1.236 | 1.221 | 1.209 | 1.131 |

APPENDIX E

Points of Apparent Turbulent Reattachment from China Clay Tests

Values of x/c (%)

| Location | Compressor Speed (rpm) | Throttle Opening (ins) | $R/R_T$ 0.65 | 0.70 | 0.80 | 0.90 | 0.95 |
|---|---|---|---|---|---|---|---|
| ROTOR SUCTION SURFACE | 750 | 4.8 | 7 | 7 | 10 | 8 | 8 |
| | | 5.2 | 15 | 18 | 12 | 27 | 25 |
| | | 6.0 | 53 | 57 | 67 | 63 | 63 |
| | | 8.0 | 47 | 57 | 58 | 70 | 70 |
| | | 10.0 | 67 | 67 | 70 | 70 | 77 |
| | | 13.0 | 68 | 73 | 75 | 77 | 77 |
| | | 22.0 | 72 | 75 | 78 | 80 | 83 |
| STATOR SUCTION SURFACE | 750 | 4.8* | 33 | 43 | 60 | 57 | 50 |
| | | 5.2* | 57 | 70 | 72 | 77 | 70 |
| | | 6.0 | 57 | 60 | 62 | 65 | 63 |
| | | 8.0 | 60 | 62 | 67 | 73 | 72 |
| | | 10.0 | 50 | 58 | 63 | 63 | 60 |
| | | 13.0 | 58 | 70 | 77 | 78 | 77 |
| | | 22.0 | 55 | 62 | 75 | 78 | 78 |
| STATOR SUCTION SURFACE | 500 | 4.8* | 52 | 55 | 57 | 60 | 59 |
| | | 5.2* | 33 | 30 | 43 | 47 | 50 |
| | | 6.0 | 57 | 57 | 60 | 67 | 57 |
| | | 8.0 | 60 | 62 | 63 | 63 | 63 |
| | | 10.0 | 58 | 67 | 70 | 70 | 70 |
| | | 13.0 | 60 | 67 | 73 | 77 | 77 |
| | | 22.0 | 68 | 73 | 75 | 75 | 72 |
| STATOR SUCTION SURFACE | 250 | 4.8 | 53 | 73 | 73 | 73 | 73 |
| | | 5.2 | 50 | 67 | 70 | 73 | 77 |
| | | 6.0 | 43 | 58 | 60 | 67 | 58 |
| | | 8.0 | 52 | 65 | 67 | 70 | 70 |
| | | 10.0 | 62 | 73 | 74 | 74 | 73 |
| | | 13.0 | 68 | 77 | 78 | 78 | 77 |
| | | 22.0 | 72 | 75 | 77 | 75 | 73 |
| STATOR SUCTION SURFACE | 150 | 4.8 | 52 | 57 | 60 | 65 | 62 |
| | | 5.2 | 43 | 49 | 54 | 59 | 56 |
| | | 6.0 | 46 | 52 | 62 | 62 | 56 |
| | | 8.0 | 52 | 65 | 71 | 71 | 65 |
| | | 10.0 | 62 | 68 | 70 | 71 | 60 |
| | | 13.0 | 65 | 71 | 75 | 78 | 71 |
| | | 22.0 | 78 | 81 | 79 | 78 | 78 |

* Points ill defined

## APPENDIX F

### Measured Values of Boundary Layer Parameters

STATOR SUCTION SURFACE - MID BLADE HEIGHT

COMPRESSOR SPEED 750 RPM

| Throttle Opening (ins) | Quantity | Chordwise Position x/c (%) | | | | | |
|---|---|---|---|---|---|---|---|
| | | 40 | 50 | 60 | 70 | 80 | 90 |
| 4.8 | $\theta x10^4$(ft) | Not measured due to blade vibration | | | | | |
| | H | | | | | | |
| | $C_f x10^3$ | | | | | | |
| 5.2 | $\theta x10^4$(ft) | 3.95 | 4.69 | 6.89 | 8.78 | 13.22 | 17.87 |
| | H | 2.30 | 2.22 | 2.11 | 1.89 | 1.84 | 2.02 |
| | $C_f x10^3$ | 1.82 | 1.93 | 1.27 | 2.04 | 1.81 | 1.29 |
| 6.0 | $\theta x10^4$(ft) | 3.11 | 4.07 | 5.29 | 6.55 | 10.22 | 14.35 |
| | H | 2.66 | 2.46 | 2.38 | 2.00 | 1.92 | 1.95 |
| | $C_f x10^3$ | 1.65 | 1.44 | 0.94 | 2.13 | 1.57 | 1.56 |
| 8.0 | $\theta x10^4$(ft) | 2.74 | 3.09 | 3.62 | 4.82 | 7.18 | 11.29 |
| | H | 2.71 | 3.05 | 3.52 | 2.57 | 2.00 | 1.83 |
| | $C_f x10^3$ | 1.50 | 0.79 | 0.32 | 1.64 | 1.99 | 1.70 |
| 10.0 | $\theta x10^4$(ft) | 2.26 | 2.70 | 3.26 | 3.80 | 6.21 | 9.93 |
| | H | 2.78 | 2.97 | 3.59 | 3.46 | 2.30 | 1.79 |
| | $C_f x10^3$ | 1.66 | 1.20 | 0.28 | 0.45 | 1.66 | 2.26 |
| 13.0 | $\theta x10^4$(ft) | 2.13 | 2.61 | 3.10 | 3.32 | 5.10 | 9.29 |
| | H | 2.64 | 2.79 | 3.37 | 3.83 | 2.95 | 1.80 |
| | $C_f x10^3$ | 2.08 | 1.39 | 0.24 | 0.29 | 0.95 | 2.50 |
| 22.0 | $\theta x10^4$(ft) | 1.98 | 2.41 | 2.73 | 2.96 | 4.33 | 8.51 |
| | H | 2.57 | 2.69 | 3.28 | 3.69 | 3.88 | 1.93 |
| | $C_f x10^3$ | 2.34 | 1.60 | 0.33 | 0.40 | 0.55 | 2.13 |

APPENDIX F (cont.)

Measured Values of Boundary Layer Parameters

STATOR SUCTION SURFACE - MID BLADE HEIGHT

COMPRESSOR SPEED 500 RPM

| Throttle Opening (ins) | Quantity | Chordwise Position x/c (%) | | | | | |
|---|---|---|---|---|---|---|---|
| | | 40 | 50 | 60 | 70 | 80 | 90 |
| 4.8 | $\theta x10^4$(ft) | 4.73 | 6.83 | 8.36 | 11.22 | 16.39 | 21.92 |
| | H | 2.31 | 2.12 | 2.15 | 1.94 | 1.89 | 2.06 |
| | $C_f x10^3$ | 2.00 | 1.74 | 1.23 | 1.89 | 1.31 | 1.11 |
| 5.2 | $\theta x10^4$(ft) | 4.15 | 5.70 | 7.81 | 9.93 | 15.06 | 20.68 |
| | H | 2.60 | 2.38 | 2.28 | 2.07 | 1.96 | 2.09 |
| | $C_f x10^3$ | 1.32 | 1.56 | 0.94 | 1.59 | 1.34 | 0.89 |
| 6.0 | $\theta x10^4$(ft) | 3.52 | 4.59 | 5.97 | 8.33 | 10.50 | 16.59 |
| | H | 2.83 | 2.68 | 2.61 | 2.12 | 2.09 | 2.04 |
| | $C_f x10^3$ | 1.21 | 1.33 | 1.00 | 1.94 | 1.52 | 1.09 |
| 8.0 | $\theta x10^4$(ft) | 2.85 | 3.64 | 4.36 | 5.81 | 9.15 | 13.23 |
| | H | 2.91 | 3.10 | 3.85 | 3.20 | 2.07 | 1.89 |
| | $C_f x10^3$ | 1.46 | 0.95 | 0.57 | 1.14 | 1.91 | 1.87 |
| 10.0 | $\theta x10^4$(ft) | 2.73 | 3.43 | 3.88 | 4.72 | 8.09 | 12.07 |
| | H | 2.80 | 2.90 | 3.68 | 3.96 | 2.58 | 1.91 |
| | $C_f x10^3$ | 2.02 | 0.87 | 0.44 | 0.67 | 1.45 | 2.14 |
| 13.0 | $\theta x10^4$(ft) | 2.62 | 3.04 | 3.67 | 4.29 | 6.53 | 11.59 |
| | H | 2.63 | 2.81 | 3.50 | 4.09 | 3.48 | 2.04 |
| | $C_f x10^3$ | 2.39 | 1.22 | 0.50 | 0.48 | 1.00 | 1.98 |
| 22.0 | $\theta x10^4$(ft) | 2.42 | 2.77 | 3.26 | 3.67 | 5.41 | 10.61 |
| | H | 2.56 | 2.70 | 3.37 | 4.02 | 4.43 | 2.35 |
| | $C_f x10^3$ | 2.83 | 1.64 | 0.53 | 0.41 | 0.62 | 1.65 |

APPENDIX F (cont.)

Measured Values of Boundary Layer Parameters

STATOR SUCTION SURFACE - MID BLADE HEIGHT

COMPRESSOR SPEED 250 RPM

| Throttle Opening (ins) | Quantity | Chordwise Position x/c (%) | | | | | |
|---|---|---|---|---|---|---|---|
| | | 40 | 50 | 60 | 70 | 80 | 90 |
| 4.8 | $\theta x10^4$(ft) | 6.52 | 8.28 | 12.15 | 17.86 | 22.94 | 30.67 |
| | H | 2.49 | 2.34 | 2.29 | 2.03 | 2.07 | 2.24 |
| | $C_f x10^3$ | 1.87 | 2.83 | 2.52 | 2.04 | 1.17 | 1.90 |
| 5.2 | $\theta x10^4$(ft) | 5.48 | 7.43 | 9.61 | 13.44 | 20.73 | 27.36 |
| | H | 2.81 | 2.60 | 2.44 | 2.16 | 2.09 | 2.15 |
| | $C_f x10^3$ | 1.51 | 2.18 | 2.49 | 2.19 | 1.12 | 1.74 |
| 6.0 | $\theta x10^4$(ft) | 5.16 | 6.31 | 8.18 | 10.57 | 13.70 | 19.71 |
| | H | 2.83 | 2.85 | 2.95 | 2.52 | 2.24 | 2.18 |
| | $C_f x10^3$ | 1.35 | 1.92 | 1.91 | 1.68 | 1.27 | 1.94 |
| 8.0 | $\theta x10^4$(ft) | 4.12 | 5.10 | 5.96 | 7.87 | 12.79 | 20.93 |
| | H | 2.80 | 2.97 | 4.03 | 4.20 | 2.89 | 2.15 |
| | $C_f x10^3$ | 2.04 | 1.59 | 1.25 | 1.33 | 1.14 | 2.28 |
| 10.0 | $\theta x10^4$(ft) | 3.67 | 4.57 | 5.52 | 6.67 | 10.63 | 19.74 |
| | H | 2.97 | 3.01 | 3.85 | 4.95 | 4.01 | 2.61 |
| | $C_f x10^3$ | 1.67 | 1.42 | 1.17 | 0.79 | 1.03 | 2.07 |
| 13.0 | $\theta x10^4$(ft) | 3.45 | 4.21 | 5.16 | 6.12 | 9.82 | 19.19 |
| | H | 2.67 | 2.95 | 3.61 | 5.30 | 4.84 | 2.99 |
| | $C_f x10^3$ | 2.96 | 1.39 | 0.98 | 0.69 | 0.74 | 2.21 |
| 22.0 | $\theta x10^4$(ft) | 3.10 | 3.89 | 4.68 | 5.60 | 8.44 | 18.23 |
| | H | 2.66 | 2.85 | 3.38 | 4.86 | 5.66 | 3.28 |
| | $C_f x10^3$ | 3.37 | 1.74 | 1.04 | 0.63 | 0.51 | 2.10 |

APPENDIX F (cont.)

Measured Values of Boundary Layer Parameters

STATOR SUCTION SURFACE - MID BLADE HEIGHT

COMPRESSOR SPEED 150 RPM

| Throttle Opening (ins) | Quantity | Chordwise Position x/c (%) | | | | | |
|---|---|---|---|---|---|---|---|
| | | 40 | 50 | 60 | 70 | 80 | 90 |
| 4.8 | $\theta x10^4$(ft) | 8.91 | 10.16 | 15.55 | 19.00 | 27.43 | 37.41 |
| | H | 2.58 | 2.46 | 2.46 | 2.35 | 2.37 | 2.45 |
| | $C_f x10^3$ | 3.08 | 6.04 | 8.04 | 5.60 | 2.29 | 5.53 |
| 5.2 | $\theta x10^4$(ft) | 7.32 | 9.84 | 15.88 | 19.01 | 24.78 | 37.91 |
| | H | 2.95 | 2.77 | 2.50 | 2.28 | 2.32 | 2.34 |
| | $C_f x10^3$ | 2.62 | 3.28 | 7.26 | 4.43 | 2.10 | 4.88 |
| 6.0 | $\theta x10^4$(ft) | 6.57 | 7.99 | 10.52 | 13.71 | 19.85 | 29.39 |
| | H | 3.00 | 3.17 | 3.15 | 2.76 | 2.40 | 2.33 |
| | $C_f x10^3$ | 1.78 | 2.86 | 5.22 | 3.54 | 1.62 | 3.32 |
| 8.0 | $\theta x10^4$(ft) | 5.16 | 6.85 | 8.25 | 11.07 | 17.44 | 28.63 |
| | H | 2.98 | 3.21 | 4.14 | 4.08 | 3.18 | 2.63 |
| | $C_f x10^3$ | 2.09 | 2.97 | 3.89 | 2.97 | 1.94 | 3.71 |
| 10.0 | $\theta x10^4$(ft) | 5.13 | 5.96 | 7.83 | 9.36 | 15.85 | 27.20 |
| | H | 2.73 | 3.13 | 4.01 | 5.03 | 4.02 | 2.98 |
| | $C_f x10^3$ | 2.39 | 3.15 | 3.51 | 2.82 | 1.49 | 3.42 |
| 13.0 | $\theta x10^4$(ft) | 4.57 | 5.91 | 6.69 | 8.39 | 14.28 | 27.69 |
| | H | 2.78 | 2.92 | 4.01 | 5.57 | 4.79 | 3.20 |
| | $C_f x10^3$ | 3.08 | 2.66 | 3.15 | 2.48 | 1.46 | 3.08 |
| 22.0 | $\theta x10^4$(ft) | 4.30 | 5.11 | 6.38 | 7.82 | 12.29 | 25.19 |
| | H | 2.70 | 2.91 | 3.53 | 5.23 | 5.44 | 3.49 |
| | $C_f x10^3$ | 3.35 | 2.84 | 3.07 | 2.36 | 1.21 | 2.98 |

## APPENDIX G

Laminar Boundary Layer Parameters
Calculated from Thwaites's Method
STATOR SUCTION SURFACE - MID BLADE HEIGHT
COMPRESSOR SPEED 750 RPM

| Throttle Opening (ins) | Quantity | Chordwise Position x/c (%) | | | | | |
|---|---|---|---|---|---|---|---|
| | | 10 | 20 | 30 | 40 | 50 | 60 |
| 4.8 | $\theta x10^4$(ft) | 1.08 | 1.79 | | | | |
| | H | 2.72 | 2.90 | | | | |
| | $C_f x10^3$ | 3.76 | 1.80 | | | | |
| 5.2 | $\theta x10^4$(ft) | 1.13 | 1.81 | | | | |
| | H | 2.70 | 2.91 | | | | |
| | $C_f x10^3$ | 3.60 | 1.71 | | | | |
| 6.0 | $\theta x10^4$(ft) | 1.07 | 1.71 | 2.32 | | | |
| | H | 2.66 | 2.82 | 3.28 | | | |
| | $C_f x10^3$ | 4.08 | 2.07 | 0.82 | | | |
| 8.0 | $\theta x10^4$(ft) | 0.97 | 1.51 | 2.02 | 2.46 | | |
| | H | 2.57 | 2.65 | 2.76 | 3.03 | | |
| | $C_f x10^3$ | 5.29 | 2.96 | 1.94 | 1.01 | | |
| 10.0 | $\theta x10^4$(ft) | 0.92 | 1.42 | 1.86 | 2.26 | 2.69 | |
| | H | 2.53 | 2.61 | 2.62 | 2.84 | 2.99 | |
| | $C_f x10^3$ | 5.95 | 3.41 | 2.45 | 1.47 | 0.96 | |
| 13.0 | $\theta x10^4$(ft) | 0.89 | 1.36 | 1.78 | 2.22 | 2.59 | 3.01 |
| | H | 2.51 | 2.57 | 2.58 | 2.77 | 2.85 | 3.70 |
| | $C_f x10^3$ | 6.42 | 3.73 | 2.81 | 1.62 | 1.23 | 0.00 |
| 22.0 | $\theta x10^4$(ft) | 0.84 | 1.27 | 1.64 | 1.96 | 2.30 | 2.68 |
| | H | 2.49 | 2.53 | 2.58 | 2.67 | 2.72 | 2.97 |
| | $C_f x10^3$ | 7.25 | 4.20 | 2.98 | 2.05 | 1.64 | 0.95 |

APPENDIX G (cont.)

Laminar Boundary Layer Parameters
Calculated from Thwaites's Method
STATOR SUCTION SURFACE - MID BLADE HEIGHT
COMPRESSOR SPEED 500 RPM

| Throttle Opening (ins) | Quantity | Chordwise Position x/c (%) | | | | | |
|---|---|---|---|---|---|---|---|
| | | 10 | 20 | 30 | 40 | 50 | 60 |
| 4.8 | $\theta x10^4$(ft) | 1.26 | 2.14 | | | | |
| | H | 2.67 | 2.90 | | | | |
| | $C_f x10^3$ | 5.29 | 2.30 | | | | |
| 5.2 | $\theta x10^4$(ft) | 1.24 | 2.14 | | | | |
| | H | 2.66 | 2.94 | | | | |
| | $C_f x10^3$ | 5.21 | 2.05 | | | | |
| 6.0 | $\theta x10^4$(ft) | 1.24 | 2.04 | 2.80 | 3.45 | | |
| | H | 2.63 | 2.80 | 3.12 | 3.06 | | |
| | $C_f x10^3$ | 5.39 | 2.66 | 1.13 | 1.08 | | |
| 8.0 | $\theta x10^4$(ft) | 1.11 | 1.80 | 2.41 | 2.96 | | |
| | H | 2.57 | 2.62 | 2.88 | 2.99 | | |
| | $C_f x10^3$ | 6.81 | 3.86 | 2.07 | 1.31 | | |
| 10.0 | $\theta x10^4$(ft) | 1.08 | 1.70 | 2.24 | 2.72 | 3.21 | |
| | H | 2.55 | 2.61 | 2.66 | 2.91 | 2.93 | |
| | $C_f x10^3$ | 7.29 | 4.06 | 2.79 | 1.62 | 1.33 | |
| 13.0 | $\theta x10^4$(ft) | 1.05 | 1.64 | 2.10 | 2.54 | 3.03 | 3.54 |
| | H | 2.53 | 2.58 | 2.65 | 2.74 | 2.88 | 3.18 |
| | $C_f x10^3$ | 7.74 | 4.44 | 3.15 | 2.14 | 1.46 | 0.82 |
| 22.0 | $\theta x10^4$(ft) | 1.03 | 1.55 | 2.02 | 2.41 | 2.84 | 3.34 |
| | H | 2.50 | 2.50 | 2.64 | 2.68 | 2.78 | 3.06 |
| | $C_f x10^3$ | 8.36 | 5.21 | 3.04 | 2.44 | 1.75 | 0.96 |

APPENDIX G (cont.)

Laminar Boundary Layer Parameters
Calculated from Thwaites's Method
STATOR SUCTION SURFACE - MID BLADE HEIGHT
COMPRESSOR SPEED 250 RPM

| Throttle Opening (ins) | Quantity | Chordwise Position x/c (%) | | | | | |
|---|---|---|---|---|---|---|---|
| | | 10 | 20 | 30 | 40 | 50 | 60 |
| 4.8 | $\theta x10^4$(ft) | 1.80 | 3.10 | | | | |
| | H | 2.67 | 2.88 | | | | |
| | $C_f x10^3$ | 7.75 | 3.43 | | | | |
| 5.2 | $\theta x10^4$(ft) | 1.80 | 2.97 | | | | |
| | H | 2.65 | 2.67 | | | | |
| | $C_f x10^3$ | 8.00 | 4.94 | | | | |
| 6.0 | $\theta x10^4$(ft) | 1.68 | 2.77 | 3.79 | 4.61 | | |
| | H | 2.62 | 2.74 | 3.00 | 3.13 | | |
| | $C_f x10^3$ | 8.77 | 4.30 | 2.16 | 1.52 | | |
| 8.0 | $\theta x10^4$(ft) | 1.57 | 2.52 | 3.37 | 4.23 | 4.92 | 5.50 |
| | H | 2.58 | 2.64 | 2.75 | 3.02 | 2.98 | 3.61 |
| | $C_f x10^3$ | 9.57 | 5.31 | 2.32 | 1.79 | 1.56 | 0.43 |
| 10.0 | $\theta x10^4$(ft) | 1.52 | 2.37 | 3.07 | 3.83 | 4.59 | 5.36 |
| | H | 2.54 | 2.61 | 2.67 | 2.84 | 3.00 | 3.60 |
| | $C_f x10^3$ | 10.55 | 5.95 | 4.04 | 2.53 | 1.63 | 0.42 |
| 13.0 | $\theta x10^4$(ft) | 1.49 | 2.29 | 2.93 | 3.63 | 4.33 | 5.10 |
| | H | 2.52 | 2.58 | 2.62 | 2.75 | 2.92 | 3.50 |
| | $C_f x10^3$ | 11.20 | 6.30 | 4.50 | 2.95 | 1.93 | 0.66 |
| 22.0 | $\theta x10^4$(ft) | 1.45 | 2.18 | 2.83 | 3.41 | 4.07 | 4.78 |
| | H | 2.50 | 2.56 | 2.60 | 2.68 | 2.83 | 3.10 |
| | $C_f x10^3$ | 11.72 | 6.88 | 4.78 | 3.34 | 2.30 | 1.32 |

APPENDIX G (cont.)

Laminar Boundary Layer Parameters
Calculated from Thwaites's Method
STATOR SUCTION SURFACE - MID BLADE HEIGHT
COMPRESSOR SPEED 150 RPM

| Throttle Opening (ins) | Quantity | Chordwise Position x/c (%) | | | | | |
|---|---|---|---|---|---|---|---|
| | | 10 | 20 | 30 | 40 | 50 | 60 |
| 4.8 | $\theta x10^4$(ft) | 2.34 | 3.93 | 5.52 | | | |
| | H | 2.67 | 2.88 | 3.40 | | | |
| | $C_f x10^3$ | 10.04 | 4.54 | 1.63 | | | |
| 5.2 | $\theta x10^4$(ft) | 2.38 | 4.09 | | | | |
| | H | 2.67 | 2.89 | | | | |
| | $C_f x10^3$ | 9.84 | 4.38 | | | | |
| 6.0 | $\theta x10^4$(ft) | 2.12 | 3.79 | 5.02 | | | |
| | H | 2.66 | 2.73 | 2.88 | | | |
| | $C_f x10^3$ | 11.35 | 5.58 | 3.47 | | | |
| 8.0 | $\theta x10^4$(ft) | 1.94 | 3.17 | 4.16 | 5.10 | 6.11 | |
| | H | 2.54 | 2.61 | 2.67 | 2.87 | 3.06 | |
| | $C_f x10^3$ | 13.90 | 7.49 | 4.96 | 3.16 | 1.90 | |
| 10.0 | $\theta x10^4$(ft) | 1.99 | 3.16 | 4.15 | 5.08 | 6.11 | |
| | H | 2.54 | 2.61 | 2.67 | 2.87 | 3.06 | |
| | $C_f x10^3$ | 13.60 | 7.49 | 4.95 | 3.16 | 1.90 | |
| 13.0 | $\theta x10^4$(ft) | 1.94 | 3.12 | 3.96 | 4.80 | 5.82 | |
| | H | 2.53 | 2.58 | 2.62 | 2.83 | 3.01 | |
| | $C_f x10^3$ | 14.48 | 8.07 | 5.80 | 3.47 | 2.22 | |
| 22.0 | $\theta x10^4$(ft) | 1.89 | 2.95 | 3.77 | 4.57 | 5.53 | 6.50 |
| | H | 2.49 | 2.56 | 2.58 | 2.67 | 2.93 | 3.37 |
| | $C_f x10^3$ | 15.50 | 8.93 | 6.68 | 4.47 | 2.50 | 1.18 |

APPENDIX G (cont.)

Laminar Boundary Layer Parameters
Calculated from Thwaites's Method
ROTOR SUCTION SURFACE - MID BLADE HEIGHT
COMPRESSOR SPEED 750 RPM

| Throttle Opening (ins) | Quantity | Chordwise Position x/c (%) | | | | | |
|---|---|---|---|---|---|---|---|
| | | 10 | 20 | 30 | 40 | 50 | 60 |
| 4.8 | $\theta x10^4$(ft) | | | | | | |
| | H | | | | | | |
| | $C_f x10^3$ | | | | | | |
| 5.2 | $\theta x10^4$(ft) | 1.17 | 1.85 | | | | |
| | H | 2.88 | 3.04 | | | | |
| | $C_f x10^3$ | 2.49 | 1.20 | | | | |
| 6.0 | $\theta x10^4$(ft) | 1.10 | 1.70 | | | | |
| | H | 2.69 | 2.77 | | | | |
| | $C_f x10^3$ | 3.52 | 1.41 | | | | |
| 8.0 | $\theta x10^4$(ft) | 1.00 | 1.52 | 2.02 | 2.52 | 2.96 | |
| | H | 2.57 | 2.63 | 2.89 | 3.05 | 3.70 | |
| | $C_f x10^3$ | 4.91 | 2.92 | 1.52 | 0.93 | 0.00 | |
| 10.0 | $\theta x10^4$(ft) | 0.91 | 1.39 | 1.83 | 2.28 | 2.68 | 3.06 |
| | H | 2.53 | 2.60 | 2.69 | 2.86 | 2.87 | 3.16 |
| | $C_f x10^3$ | 5.97 | 3.44 | 2.18 | 1.41 | 1.16 | 0.67 |
| 13.0 | $\theta x10^4$(ft) | 0.91 | 1.32 | 1.72 | 2.10 | 2.64 | 2.90 |
| | H | 2.49 | 2.57 | 2.62 | 2.67 | 2.87 | 3.21 |
| | $C_f x10^3$ | 6.50 | 3.83 | 2.55 | 1.92 | 1.20 | 0.64 |
| 22.0 | $\theta x10^4$(ft) | 0.82 | 1.22 | 1.58 | 1.93 | 2.27 | 2.58 |
| | H | 2.48 | 2.52 | 2.58 | 2.65 | 2.66 | 2.87 |
| | $C_f x10^3$ | 7.50 | 4.27 | 2.97 | 2.12 | 1.77 | 1.12 |

# APPENDIX H

## Boundary Layer Data from Hot Wire Measurements

### H.1 Introduction

The following results were obtained from hot wire measurements at mid-blade height in the stator blade suction surface boundary layer with a compressor speed of 500 rpm. The method of reducing the experimental data is discussed in Section 3.3.12. The hot wire readings were corrected for wall proximity effects by using Wills's laminar flow correction (Table 3.3) in all cases, even in turbulent boundary layer regions.

The measured velocity profiles have been tabulated in both dimensional and non-dimensional form, together with values of some commonly used boundary layer parameters. For convenience in tabulation, the values of velocity have all been given to two decimal places ; the actual measurements were not this accurate. The velocity profiles are also presented in graphical form in Figs. H.1 - 6.

### H.2 Notation

Because of the limited character set on the line-printer, it was necessary to use a slightly different notation for the tabulated results. The notation adopted in Appendices H and I is set out below:

| Symbol | Meaning |
|---|---|
| X/C | $x/c$ |
| UE | $U$ |
| UT | $u_\gamma$ |
| UP | $u_p$ |
| UB | $u_\beta$ |
| CFE | $C_f$ (experimental value) |
| CFLT | $C_f$ from Ludwieg-Tillmann law, Eqn. 7.33 |
| CFNM | $C_f$ from Nash-Macdonald law, Eqn. 7.37 |
| CDEL | $\Delta = \int_0^\infty (U - u)/u_\gamma dy = \delta^* \sqrt{2/C_f}$ (Clauser thickness) |
| DSTAR | $\delta^*$ |
| THETA | $\theta$ |
| DELTA** | $\delta^{**}$ |
| DUEDX | $dU/dx$ (from surface pressure tapping measurements, Appendix D) |
| CTEQ | Value of $C_\gamma$ for an equilibrium boundary layer, obtained from Eqn. 7.61 |
| DELTA | Value of $\delta$ for the Coles velocity profile, obtained from Eqns. 7.30 and 7.31 |
| REDSTAR | $Re_{\delta^*}$ |

APPENDIX H (cont.)

| Symbol | Meaning |
|---|---|
| RETHETA | $Re_\theta$ |
| H | H |
| H** | $H^{**}$ |
| PI | $\Pi$ |
| G | G |
| GEQ | $\hat{G}$ |
| GAMMA | $\Gamma$ |
| A | $(1/\rho)(dp/dx)$ |
| ALPHA 0 | $\alpha_o$ |
| TH/UE * DUEDX | $(\theta/U)(dU/dx)$ |
| K | k |
| NU | $\nu$ |
| Y | y |
| U | u |
| Z * TH/UE | $\varsigma\theta/U$ |
| YY | Y |
| Y+ | $y^+$ |
| U+ | $u^+$ |
| (Y*)↑0.5 | $(y^*)^{\frac{1}{2}}$ |
| U* | $u^*$ |
| UC/UE | u/U obtained from the Coles velocity profile, Eqn. 7.29, with value of $\delta$ defined by Eqns. 7.30 and 7.31. |
| * | Multiplication |
| ↑ | Exponentiation |
| 10-3, etc. | $10^{-3}$, etc. |

X/C = 0.40 4.8 INS THROTTLE 500.0 RPM

| | | | | | |
|---|---|---|---|---|---|
| UE | 82.35 FPS | DUEDX | -168.0 /SEC | H | 2.31 |
| UT | 2.60 FPS | UT/UE | 0.0316 | H** | 1.64 |
| UP | 1.32 FPS | | | PI | 2.23 |
| UB | 47.47 FPS | UB/UE | 0.577 | G | 17.95 |
| CFE | 1.995 *10-3 | CTEQ | 9.385 *10-3 | GEQ | 10.56 |
| CFLT | 1.549 *10-3 | CFE/CFLT | 1.288 | GAMMA | -0.377 *10-2 |
| CFNM | 2.024 *10-3 | CFE/CFNM | 0.986 | A | 1.383 *104 FT/SEC↑2 |
| CDEL | 345.51 *10-4 FT | DELTA | 29.87 *10-4 FT | ALPHA0 | 0.130 |
| DSTAR | 10.91 *10-4 FT | REDSTAR | 541.9 | TH/UE*DUEDX | -0.964 *10-3 |
| THETA | 4.73 *10-4 FT | RETHETA | 234.7 | K | -0.226 |
| DELTA** | 7.74 *10-4 FT | | | NU | 1.658 *10-4 FT↑2/SEC |

| Y*10 4 (FT) | U (FPS) | U/UE | Y/THETA | Z*TH/UE | YY | Y+ | U+ | (Y*)↑0.5 | U* | Y/CDEL | (UE-U)/UT | UC/UE |
|---|---|---|---|---|---|---|---|---|---|---|---|---|
| 0.0 | 0.00 | 0.000 | 0.000 | 0.234 | 0.00 | 0.00 | 0.00 | 0.00 | 0.00 | 0.0000 | 31.66 | 0.000 |
| 3.1 | 14.14 | 0.172 | 0.661 | 0.285 | 5.41 | 4.90 | 5.44 | 1.58 | 10.72 | 0.0090 | 26.22 | 0.265 |
| 5.5 | 26.71 | 0.324 | 1.162 | 0.283 | 9.46 | 8.61 | 10.27 | 2.09 | 20.25 | 0.0159 | 21.39 | 0.340 |
| 7.9 | 37.44 | 0.455 | 1.663 | 0.243 | 12.55 | 12.32 | 14.40 | 2.50 | 28.39 | 0.0227 | 17.26 | 0.414 |
| 10.2 | 46.74 | 0.568 | 2.163 | 0.218 | 15.48 | 16.04 | 17.97 | 2.85 | 35.44 | 0.0296 | 13.69 | 0.492 |
| 12.6 | 55.45 | 0.673 | 2.664 | 0.191 | 17.84 | 19.75 | 21.32 | 3.16 | 42.04 | 0.0364 | 10.34 | 0.575 |
| 17.3 | 67.92 | 0.825 | 3.666 | 0.111 | 18.71 | 27.17 | 26.11 | 3.71 | 51.50 | 0.0501 | 5.55 | 0.741 |
| 22.1 | 73.75 | 0.896 | 4.667 | 0.059 | 17.30 | 34.60 | 28.36 | 4.19 | 55.92 | 0.0638 | 3.30 | 0.885 |
| 26.8 | 77.57 | 0.942 | 5.669 | 0.035 | 16.27 | 42.02 | 29.83 | 4.62 | 58.82 | 0.0775 | 1.84 | 0.977 |
| 36.3 | 79.66 | 0.967 | 7.672 | 0.012 | 13.09 | 56.87 | 30.63 | 5.37 | 60.40 | 0.1049 | 1.03 | 0.952 |
| 45.7 | 81.66 | 0.992 | 9.675 | 0.008 | 13.37 | 71.72 | 31.40 | 6.03 | 61.92 | 0.1323 | 0.26 | 0.717 |
| 55.2 | 82.35 | 1.000 | 11.678 | 0.000 | 0.00 | 86.57 | 31.66 | 6.63 | 62.44 | 0.1597 | 0.00 | 0.503 |

X/C = 0.40 5.2 INS THROTTLE 500.0 RPM

| | | | | | | | |
|---|---|---|---|---|---|---|---|
| UE | 88.42 FPS | DUEDX | -166.0 /SEC | H | 2.60 | | |
| UT | 2.27 FPS | UT/UE | 0.0257 | H** | 1.60 | | |
| UP | 1.35 FPS | | | PI | 3.07 | | |
| UB | 59.76 FPS | UB/UE | 0.676 | G | 23.97 | | |
| CFE | 1.318 $*_{10}$-3 | CTEQ | 11.093 $*_{10}$-3 | GEQ | 11.77 | | |
| CFLT | 1.002 $*_{10}$-3 | CFE/CFLT | 1.315 | GAMMA | -0.300 | $*_{10}$-2 | |
| CFNM | 1.152 $*_{10}$-3 | CFE/CFNM | 1.144 | A | 1.468 | $*_{10}$4 FT/SEC↑2 | |
| CDEL | 419.63 $*_{10}$-4 FT | DELTA | 26.89 $*_{10}$-4 FT | ALPHA0 | 0.208 | | |
| DSTAR | 10.77 $*_{10}$-4 FT | REDSTAR | 574.0 | TH/UE*DUEDX | -0.778 | $*_{10}$-3 | |
| THETA | 4.15 $*_{10}$-4 FT | RETHETA | 220.9 | K | -0.172 | | |
| DELTA** | 6.62 $*_{10}$-4 FT | | | NU | 1.659 | $*_{10}$-4 FT↑2/SEC | |

| Y*$_{10}$4 (FT) | U (FPS) | U/UE | Y/THETA | Z*TH/UE | YY | Y+ | U+ | (Y*)↑0.5 | U* | Y/CDEL | (UE-U)/UT | UC/UE |
|---|---|---|---|---|---|---|---|---|---|---|---|---|
| 0.0 | 0.00 | 0.000 | 0.000 | 0.146 | 0.00 | 0.00 | 0.00 | 0.00 | 0.00 | 0.0000 | 38.96 | 0.000 |
| 3.0 | 11.79 | 0.133 | 0.719 | 0.225 | 5.08 | 4.08 | 5.20 | 1.56 | 8.77 | 0.0071 | 33.76 | 0.207 |
| 5.3 | 24.77 | 0.280 | 1.290 | 0.238 | 9.36 | 7.32 | 10.91 | 2.08 | 18.41 | 0.0127 | 28.04 | 0.287 |
| 7.7 | 35.82 | 0.405 | 1.861 | 0.218 | 12.91 | 10.55 | 15.78 | 2.50 | 26.63 | 0.0184 | 23.17 | 0.374 |
| 10.1 | 46.74 | 0.529 | 2.432 | 0.212 | 16.66 | 13.79 | 20.59 | 2.86 | 34.74 | 0.0240 | 18.36 | 0.471 |
| 12.4 | 57.27 | 0.648 | 3.003 | 0.193 | 19.60 | 17.03 | 25.23 | 3.18 | 42.57 | 0.0297 | 13.72 | 0.575 |
| 17.2 | 73.54 | 0.832 | 4.145 | 0.116 | 21.00 | 23.50 | 32.40 | 3.73 | 54.66 | 0.0409 | 6.55 | 0.777 |
| 21.9 | 80.72 | 0.913 | 5.287 | 0.058 | 18.91 | 29.98 | 35.57 | 4.22 | 60.00 | 0.0522 | 3.39 | 0.932 |
| 26.6 | 85.24 | 0.964 | 6.429 | 0.033 | 17.35 | 36.45 | 37.56 | 4.65 | 63.36 | 0.0635 | 1.40 | 0.999 |
| 36.1 | 87.16 | 0.986 | 8.712 | 0.008 | 11.49 | 49.40 | 38.40 | 5.41 | 64.78 | 0.0861 | 0.55 | 0.841 |
| 45.6 | 88.42 | 1.000 | 10.996 | 0.000 | 0.00 | 62.35 | 38.96 | 6.08 | 65.72 | 0.1086 | 0.00 | 0.501 |



APPENDIX H (cont.)

X/C = 0.40 6.0 INS THROTTLE 500.0 RPM

| | | | | | | | | |
|---|---|---|---|---|---|---|---|---|
| UE | 92.70 FPS | DUEDX | -90.0 /SEC | H | 2.83 | | | |
| UT | 2.28 FPS | UT/UE | 0.0246 | H** | 1.56 | | | |
| UP | 1.12 FPS | | | PI | 1.60 | | | |
| UB | 67.15 FPS | UB/UE | 0.724 | G | 26.31 | | | |
| CFE | 1.209 $*_{10}$-3 | CTEQ | 12.270 $*_{10}$-3 | GEQ | 9.57 | | | |
| CFLT | 0.720 $*_{10}$-3 | CFE/CFLT | 1.678 | GAMMA | -0.128 $*_{10}$-2 | | | |
| CFNM | 0.514 $*_{10}$-3 | CFE/CFNM | 2.351 | A | 0.834 $*_{10}$4 FT/SEC↑2 | | | |
| CDEL | 405.54 $*_{10}$-4 FT | DELTA | 23.62 $*_{10}$-4 FT | ALPHA0 | 0.117 | | | |
| DSTAR | 9.97 $*_{10}$-4 FT | REDSTAR | 555.5 | TH/UE*DUEDX | -0.342 $*_{10}$-3 | | | |
| THETA | 3.52 $*_{10}$-4 FT | RETHETA | 196.2 | K | -0.067 | | | |
| DELTA** | 5.49 $*_{10}$-4 FT | | | NU | 1.664 $*_{10}$-4 FT↑2/SEC | | | |

| Y*$_{10}$4 (FT) | U (FPS) | U/UE | Y/THETA | Z*TH/UE | YY | Y+ | U+ | (Y*)↑0.5 | U* | Y/CDEL | (UE-U)/UT | UC/UE |
|---|---|---|---|---|---|---|---|---|---|---|---|---|
| 0.0 | 0.00 | 0.000 | 0.000 | 0.119 | 0.00 | 0.00 | 0.00 | 0.00 | 0.00 | 0.0000 | 40.68 | 0.000 |
| 2.9 | 11.98 | 0.129 | 0.833 | 0.192 | 5.11 | 4.02 | 5.26 | 1.40 | 10.74 | 0.0072 | 35.42 | 0.178 |
| 5.3 | 25.74 | 0.278 | 1.505 | 0.205 | 9.54 | 7.26 | 11.30 | 1.89 | 23.08 | 0.0131 | 29.38 | 0.272 |
| 7.7 | 37.46 | 0.404 | 2.177 | 0.203 | 13.75 | 10.50 | 16.44 | 2.27 | 33.58 | 0.0189 | 24.24 | 0.381 |
| 10.0 | 51.06 | 0.551 | 2.849 | 0.197 | 17.71 | 13.74 | 22.40 | 2.59 | 45.77 | 0.0247 | 18.27 | 0.502 |
| 12.4 | 61.99 | 0.669 | 3.521 | 0.164 | 20.00 | 16.99 | 27.20 | 2.88 | 55.57 | 0.0306 | 13.48 | 0.628 |
| 17.1 | 79.71 | 0.860 | 4.865 | 0.103 | 21.88 | 23.47 | 34.98 | 3.39 | 71.46 | 0.0423 | 5.70 | 0.854 |
| 21.9 | 87.67 | 0.946 | 6.209 | 0.049 | 19.21 | 29.95 | 38.47 | 3.83 | 78.59 | 0.0539 | 2.21 | 0.986 |
| 26.6 | 91.86 | 0.991 | 7.553 | 0.024 | 16.25 | 36.44 | 40.31 | 4.22 | 82.35 | 0.0656 | 0.37 | 0.979 |
| 36.1 | 92.70 | 1.000 | 10.240 | 0.000 | 0.00 | 49.40 | 40.68 | 4.92 | 83.10 | 0.0889 | 0.00 | 0.632 |



APPENDIX H (cont.)

X/C = 0.40 8.0 INS THROTTLE 500.0 RPM

| | | | | | |
|---|---|---|---|---|---|
| UE | 98.35 FPS | DUEDX | -112.0 /SEC | H | 2.91 |
| UT | 2.66 FPS | UT/UE | 0.0270 | H** | 1.55 |
| UP | 1.22 FPS | | | PI | 1.29 |
| UB | 71.11 FPS | UB/UE | 0.723 | G | 24.28 |
| CFE | 1.461 *10-3 | CTEQ | 12.625 *10-3 | GEQ | 9.05 |
| CFLT | 0.664 *10-3 | CFE/CFLT | 2.200 | GAMMA | -0.117 *10-2 |
| CFNM | 0.347 *10-3 | CFE/CFNM | 4.208 | A | 1.102 *10↑4 FT/SEC↑2 |
| CDEL | 307.04 *10-4 FT | DELTA | 19.42 *10-4 FT | ALPHA0 | 0.098 |
| DSTAR | 8.30 *10-4 FT | REDSTAR | 490.1 | TH/UE*DUEDX | -0.325 *10-3 |
| THETA | 2.85 *10-4 FT | RETHETA | 168.5 | K | -0.055 |
| DELTA** | 4.41 *10-4 FT | | | NU | 1.665 *10-4 FT↑2/SEC |

| Y*10↑4 (FT) | U (FPS) | U/UE | Y/THETA | Z*TH/UE | YY | Y+ | U+ | (Y*)↑0.5 | U* | Y/CDEL | (UE-U)/UT | UC/UE |
|---|---|---|---|---|---|---|---|---|---|---|---|---|
| 0.0 | 0.00 | 0.000 | 0.000 | 0.123 | 0.00 | 0.00 | 0.00 | 0.00 | 0.00 | 0.0000 | 37.00 | 0.000 |
| 2.9 | 15.11 | 0.154 | 1.012 | 0.181 | 5.58 | 4.61 | 5.69 | 1.46 | 12.35 | 0.0094 | 31.31 | 0.190 |
| 5.3 | 31.77 | 0.323 | 1.842 | 0.200 | 10.70 | 8.39 | 11.95 | 1.97 | 25.95 | 0.0171 | 25.05 | 0.314 |
| 7.6 | 47.79 | 0.486 | 2.671 | 0.196 | 15.36 | 12.17 | 17.98 | 2.37 | 39.04 | 0.0248 | 19.02 | 0.457 |
| 10.0 | 63.80 | 0.649 | 3.501 | 0.175 | 18.99 | 15.94 | 24.00 | 2.71 | 52.12 | 0.0325 | 13.00 | 0.611 |
| 12.4 | 76.29 | 0.776 | 4.330 | 0.136 | 20.74 | 19.72 | 28.70 | 3.01 | 62.32 | 0.0402 | 8.30 | 0.759 |
| 17.1 | 92.96 | 0.945 | 5.989 | 0.067 | 20.06 | 27.28 | 34.97 | 3.54 | 75.94 | 0.0557 | 2.03 | 0.966 |
| 21.8 | 98.02 | 0.997 | 7.648 | 0.017 | 12.76 | 34.83 | 36.87 | 4.01 | 80.07 | 0.0711 | 0.13 | 0.981 |
| 26.6 | 98.35 | 1.000 | 9.308 | 0.000 | 0.00 | 42.39 | 37.00 | 4.42 | 80.34 | 0.0865 | 0.00 | 0.805 |



APPENDIX H (cont.)

X/C = 0.40 10.0 INS THROTTLE 500.0 RPM

| | | | | | |
|---|---|---|---|---|---|
| UE | 101.46 FPS | DUEDX | -82.0 /SEC | H | 2.80 |
| UT | 3.23 FPS | UT/UE | 0.0318 | H** | 1.55 |
| UP | 1.10 FPS | | | PI | 0.61 |
| UB | 68.67 FPS | UB/UE | 0.677 | G | 20.21 |
| CFE | 2.022 $*_{10}$-3 | CTEQ | 12.075 $*_{10}$-3 | GEQ | 7.79 |
| CFLT | 0.788 $*_{10}$-3 | CFE/CFLT | 2.567 | GAMMA | -0.080 $*_{10}$-2 |
| CFNM | 0.742 $*_{10}$-3 | CFE/CFNM | 2.724 | A | 0.832 $*_{10}$4 FT/SEC↑2 |
| CDEL | 240.42 $*_{10}$-4 FT | DELTA | 18.37 $*_{10}$-4 FT | ALPHA0 | 0.040 |
| DSTAR | 7.64 $*_{10}$-4 FT | REDSTAR | 478.3 | TH/UE*DUEDX | -0.221 $*_{10}$-3 |
| THETA | 2.73 $*_{10}$-4 FT | RETHETA | 171.0 | K | -0.038 |
| DELTA** | 4.25 $*_{10}$-4 FT | | | NU | 1.621 $*_{10}$-4 FT↑2/SEC |

| Y*$_{10}$4 (FT) | U (FPS) | U/UE | Y/THETA | Z*TH/UE | YY | Y+ | U+ | (Y*)↑0.5 | U* | Y/CDEL | (UE-U)/UT | UC/UE |
|---|---|---|---|---|---|---|---|---|---|---|---|---|
| 0.0 | 0.00 | 0.000 | 0.000 | 0.173 | 0.00 | 0.00 | 0.00 | 0.00 | 0.00 | 0.0000 | 31.45 | 0.000 |
| 2.9 | 19.23 | 0.190 | 1.057 | 0.186 | 5.96 | 5.74 | 5.96 | 1.40 | 17.41 | 0.0120 | 25.49 | 0.220 |
| 5.3 | 36.05 | 0.355 | 1.923 | 0.199 | 11.22 | 10.45 | 11.18 | 1.89 | 32.63 | 0.0219 | 20.28 | 0.354 |
| 7.6 | 54.21 | 0.534 | 2.789 | 0.197 | 16.20 | 15.16 | 16.81 | 2.28 | 49.06 | 0.0317 | 14.65 | 0.504 |
| 10.0 | 70.75 | 0.697 | 3.655 | 0.164 | 19.35 | 19.87 | 21.93 | 2.61 | 64.03 | 0.0415 | 9.52 | 0.660 |
| 12.4 | 83.03 | 0.818 | 4.521 | 0.121 | 20.56 | 24.58 | 25.74 | 2.90 | 75.15 | 0.0514 | 5.71 | 0.805 |
| 17.1 | 97.64 | 0.962 | 6.253 | 0.052 | 18.72 | 33.99 | 30.27 | 3.41 | 88.37 | 0.0711 | 1.18 | 0.986 |
| 21.8 | 101.46 | 1.000 | 7.985 | 0.000 | 0.00 | 43.41 | 31.45 | 3.86 | 91.82 | 0.0908 | 0.00 | 0.956 |



APPENDIX H (cont.)

X/C = 0.40 13.0 INS THROTTLE 500.0 RPM

| | | | | | | | |
|---|---|---|---|---|---|---|---|
| UE | 105.91 FPS | DUEDX | -74.0 /SEC | H | 2.63 | | |
| UT | 3.66 FPS | UT/UE | 0.0346 | H** | 1.58 | | |
| UP | 1.08 FPS | | | PI | 0.40 | | |
| UB | 66.82 FPS | UB/UE | 0.631 | G | 17.96 | | |
| CFE | 2.388 *10-3 | CTEQ | 11.239 *10-3 | GEQ | 7.38 | | |
| CFLT | 1.016 *10-3 | CFE/CFLT | 2.351 | GAMMA | -0.066 *10-2 | | |
| CFNM | 1.278 *10-3 | CFE/CFNM | 1.869 | A | 0.784 *10^4 | FT/SEC↑2 | |
| CDEL | 199.70 *10-4 FT | DELTA | 17.26 *10-4 FT | ALPHA0 | 0.026 | | |
| DSTAR | 6.90 *10-4 FT | REDSTAR | 449.7 | TH/UE*DUEDX | -0.183 *10-3 | | |
| THETA | 2.62 *10-4 FT | RETHETA | 170.7 | K | -0.031 | | |
| DELTA** | 4.13 *10-4 FT | | | NU | 1.625 *10^4 | FT↑2/SEC | |

| Y*10^4 (FT) | U (FPS) | U/UE | Y/THETA | Z*TH/UE | YY | Y+ | U+ | (Y*)↑0.5 | U* | Y/CDEL | (UE-U)/UT | UC/UE |
|---|---|---|---|---|---|---|---|---|---|---|---|---|
| 0.0 | 0.00 | 0.000 | 0.000 | 0.204 | 0.00 | 0.00 | 0.00 | 0.00 | 0.00 | 0.0000 | 28.94 | 0.000 |
| 2.9 | 24.18 | 0.228 | 1.102 | 0.210 | 6.61 | 6.50 | 6.61 | 1.39 | 22.30 | 0.0145 | 22.34 | 0.261 |
| 5.3 | 44.57 | 0.421 | 2.006 | 0.209 | 11.97 | 11.83 | 12.18 | 1.87 | 41.12 | 0.0263 | 16.76 | 0.402 |
| 7.6 | 64.13 | 0.606 | 2.910 | 0.187 | 16.43 | 17.16 | 17.53 | 2.25 | 59.16 | 0.0382 | 11.42 | 0.558 |
| 10.0 | 80.33 | 0.759 | 3.813 | 0.141 | 18.72 | 22.49 | 21.95 | 2.58 | 74.11 | 0.0500 | 6.99 | 0.716 |
| 12.4 | 91.17 | 0.861 | 4.717 | 0.095 | 19.03 | 27.82 | 24.92 | 2.87 | 84.11 | 0.0619 | 4.03 | 0.854 |
| 17.1 | 102.58 | 0.969 | 6.524 | 0.038 | 16.72 | 38.47 | 28.03 | 3.38 | 94.64 | 0.0856 | 0.91 | 0.999 |
| 21.8 | 105.91 | 1.000 | 8.331 | 0.000 | 0.00 | 49.13 | 28.94 | 3.82 | 97.70 | 0.1093 | 0.00 | 0.917 |

X/C = 0.40 22.0 INS THROTTLE 500.0 RPM

| | | | | | | | | |
|---|---|---|---|---|---|---|---|---|
| UE | 110.74 FPS | DUEDX | -51.0 /SEC | H | 2.56 | | | |
| UT | 4.17 FPS | UT/UE | 0.0376 | H** | 1.58 | | | |
| UP | 0.97 FPS | | | PI | 0.20 | | | |
| UB | 66.10 FPS | UB/UE | 0.597 | G | 16.18 | | | |
| CFE | 2.832 *10-3 | CTEQ | 10.797 *10-3 | GEQ | 6.95 | | | |
| CFLT | 1.160 *10-3 | CFE/CFLT | 2.441 | GAMMA | -0.040 *10-2 | | | |
| CFNM | 1.591 *10-3 | CFE/CFNM | 1.780 | A | 0.565 *104 FT/SEC↑2 | | | |
| CDEL | 164.09 *10-4 FT | DELTA | 15.82 *10-4 FT | ALPHA0 | 0.013 | | | |
| DSTAR | 6.17 *10-4 FT | REDSTAR | 419.8 | TH/UE*DUEDX | -0.111 *10-3 | | | |
| THETA | 2.42 *10-4 FT | RETHETA | 164.3 | K | -0.018 | | | |
| DELTA** | 3.83 *10-4 FT | | | NU | 1.629 *10-4 FT↑2/SEC | | | |

| Y*10⁴ (FT) | U (FPS) | U/UE | Y/THETA | Z*TH/UE | YY | Y+ | U+ | (Y*)↑0.5 | U* | Y/CDEL | (UE-U)/UT | UC/UE |
|---|---|---|---|---|---|---|---|---|---|---|---|---|
| 0.0 | 0.00 | 0.000 | 0.000 | 0.233 | 0.00 | 0.00 | 0.00 | 0.00 | 0.00 | 0.0000 | 26.58 | 0.000 |
| 2.9 | 29.86 | 0.270 | 1.195 | 0.219 | 7.16 | 7.39 | 7.17 | 1.31 | 30.70 | 0.0176 | 19.41 | 0.295 |
| 5.3 | 52.96 | 0.478 | 2.175 | 0.205 | 12.61 | 13.44 | 12.71 | 1.77 | 54.46 | 0.0320 | 13.87 | 0.450 |
| 7.6 | 74.25 | 0.670 | 3.154 | 0.166 | 16.48 | 19.50 | 17.82 | 2.13 | 76.34 | 0.0464 | 8.76 | 0.617 |
| 10.0 | 89.03 | 0.804 | 4.134 | 0.117 | 18.13 | 25.55 | 21.37 | 2.44 | 91.54 | 0.0609 | 5.21 | 0.779 |
| 12.4 | 99.65 | 0.900 | 5.114 | 0.080 | 18.48 | 31.61 | 23.91 | 2.72 | 102.46 | 0.0753 | 2.66 | 0.909 |
| 17.1 | 108.93 | 0.984 | 7.073 | 0.026 | 14.49 | 43.71 | 26.14 | 3.19 | 112.00 | 0.1041 | 0.43 | 0.998 |
| 21.8 | 110.74 | 1.000 | 9.032 | 0.000 | 0.00 | 55.82 | 26.58 | 3.61 | 113.86 | 0.1330 | 0.00 | 0.842 |

X/C = 0.50 4.8 INS THROTTLE 500.0 RPM

| | | | | | | | | |
|---|---|---|---|---|---|---|---|---|
| UE | 76.26 FPS | DUEDX | -137.0 /SEC | | | H | 2.12 | |
| UT | 2.25 FPS | UT/UE | 0.0295 | | | H** | 1.68 | |
| UP | 1.20 FPS | | | | | PI | 2.99 | |
| UB | 40.89 FPS | UB/UE | 0.536 | | | G | 17.90 | |
| CFE | 1.739 *10-3 | CTEQ | 8.133 *10-3 | | | GEQ | 11.66 | |
| CFLT | 1.929 *10-3 | CFE/CFLT | 0.902 | | | GAMMA | -0.518 *10-2 | |
| CFNM | 2.359 *10-3 | CFE/CFNM | 0.737 | | | A | 1.045 *10^4 | FT/SEC↑2 |
| CDEL | 490.74 *10-4 FT | DELTA | 42.56 *10-4 FT | | | ALPHA0 | 0.151 | |
| DSTAR | 14.47 *10-4 FT | REDSTAR | 670.0 | | | TH/UE*DUEDX | -1.228 *10-3 | |
| THETA | 6.83 *10-4 FT | RETHETA | 316.4 | | | K | -0.388 | |
| DELTA** | 11.47 *10-4 FT | | | | | NU | 1.647 *10-4 | FT↑2/SEC |

| Y*10^4 (FT) | U (FPS) | U/UE | Y/THETA | Z*TH/UE | YY | Y+ | U+ | (Y*)↑0.5 | U* | Y/CDEL | (UE-U)/UT | UC/UE |
|---|---|---|---|---|---|---|---|---|---|---|---|---|
| 0.0 | 0.00 | 0.000 | 0.000 | 0.275 | 0.00 | 0.00 | 0.00 | 0.00 | 0.00 | 0.0000 | 33.91 | 0.000 |
| 1.4 | 4.51 | 0.059 | 0.206 | 0.299 | 2.00 | 1.92 | 2.00 | 1.01 | 3.76 | 0.0029 | 31.91 | 0.220 |
| 4.3 | 15.00 | 0.197 | 0.632 | 0.358 | 6.73 | 5.90 | 6.67 | 1.77 | 12.52 | 0.0088 | 27.24 | 0.313 |
| 6.7 | 25.49 | 0.334 | 0.987 | 0.352 | 10.43 | 9.21 | 11.33 | 2.22 | 21.27 | 0.0137 | 22.58 | 0.364 |
| 9.2 | 34.09 | 0.447 | 1.343 | 0.297 | 13.02 | 12.53 | 15.16 | 2.58 | 28.45 | 0.0187 | 18.75 | 0.413 |
| 11.6 | 41.60 | 0.545 | 1.698 | 0.260 | 15.40 | 15.84 | 18.50 | 2.91 | 34.71 | 0.0236 | 15.42 | 0.463 |
| 14.0 | 48.17 | 0.632 | 2.053 | 0.223 | 17.26 | 19.15 | 21.42 | 3.19 | 40.20 | 0.0286 | 12.49 | 0.515 |
| 18.9 | 58.17 | 0.763 | 2.763 | 0.144 | 18.67 | 25.78 | 25.87 | 3.71 | 48.54 | 0.0385 | 8.05 | 0.626 |
| 23.7 | 63.80 | 0.837 | 3.474 | 0.087 | 18.25 | 32.41 | 28.37 | 4.16 | 53.24 | 0.0484 | 5.54 | 0.738 |
| 28.6 | 67.63 | 0.887 | 4.184 | 0.052 | 17.01 | 39.04 | 30.07 | 4.56 | 56.43 | 0.0583 | 3.84 | 0.841 |
| 33.4 | 69.46 | 0.911 | 4.894 | 0.033 | 15.88 | 45.66 | 30.89 | 4.93 | 57.96 | 0.0682 | 3.02 | 0.924 |
| 38.3 | 71.23 | 0.934 | 5.605 | 0.027 | 16.39 | 52.29 | 31.67 | 5.28 | 59.44 | 0.0780 | 2.24 | 0.979 |
| 48.0 | 72.94 | 0.956 | 7.025 | 0.012 | 13.80 | 65.55 | 32.43 | 5.91 | 60.87 | 0.0978 | 1.48 | 0.987 |
| 57.7 | 73.88 | 0.969 | 8.446 | 0.011 | 15.40 | 78.80 | 32.85 | 6.48 | 61.65 | 0.1176 | 1.06 | 0.871 |
| 67.4 | 75.22 | 0.986 | 9.867 | 0.011 | 18.43 | 92.06 | 33.45 | 7.00 | 62.77 | 0.1374 | 0.47 | 0.695 |
| 77.1 | 76.26 | 1.000 | 11.288 | 0.000 | 0.00 | 105.31 | 33.91 | 7.49 | 63.64 | 0.1572 | 0.00 | 0.552 |



APPENDIX H (cont.)

X/C = 0.50 5.2 INS THROTTLE 500.0 RPM

| | | | | | |
|---|---|---|---|---|---|
| UE | 79.37 FPS | DUEDX | -164.0 /SEC | H | 2.38 |
| UT | 2.22 FPS | UT/UE | 0.0279 | H** | 1.64 |
| UP | 1.29 FPS | | | PI | 3.59 |
| UB | 48.76 FPS | UB/UE | 0.614 | G | 20.74 |
| CFE | 1.558 $*_{10}$-3 | CTEQ | 9.811 $*_{10}$-3 | GEQ | 12.47 |
| CFLT | 1.341 $*_{10}$-3 | CFE/CFLT | 1.162 | GAMMA | -0.479 $*_{10}$-2 |
| CFNM | 1.641 $*_{10}$-3 | CFE/CFNM | 0.950 | A | 1.302 $*_{10}$4 FT/SEC↑2 |
| CDEL | 484.66 $*_{10}$-4 FT | DELTA | 36.05 $*_{10}$-4 FT | ALPHA0 | 0.198 |
| DSTAR | 13.53 $*_{10}$-4 FT | REDSTAR | 650.5 | TH/UE*DUEDX | -1.177 $*_{10}$-3 |
| THETA | 5.70 $*_{10}$-4 FT | RETHETA | 273.8 | K | -0.322 |
| DELTA** | 9.33 $*_{10}$-4 FT | | | NU | 1.651 $*_{10}$-4 FT↑2/SEC |

| Y*$_{10}$4 (FT) | U (FPS) | U/UE | Y/THETA | Z*TH/UE | YY | Y+ | U+ | (Y*)↑0.5 | U* | Y/CDEL | (UE-U)/UT | UC/UE |
|---|---|---|---|---|---|---|---|---|---|---|---|---|
| 0.0 | 0.00 | 0.000 | 0.000 | 0.213 | 0.00 | 0.00 | 0.00 | 0.00 | 0.00 | 0.0000 | 35.82 | 0.000 |
| 1.3 | 3.85 | 0.049 | 0.222 | 0.224 | 1.74 | 1.69 | 1.74 | 0.99 | 2.98 | 0.0026 | 34.09 | 0.159 |
| 4.2 | 13.48 | 0.170 | 0.733 | 0.269 | 6.29 | 5.60 | 6.08 | 1.81 | 10.44 | 0.0086 | 29.74 | 0.259 |
| 6.6 | 23.46 | 0.296 | 1.159 | 0.280 | 10.16 | 8.86 | 10.59 | 2.27 | 18.18 | 0.0136 | 25.23 | 0.320 |
| 9.0 | 32.44 | 0.409 | 1.585 | 0.270 | 13.62 | 12.12 | 14.64 | 2.66 | 25.14 | 0.0186 | 21.18 | 0.382 |
| 11.5 | 41.70 | 0.525 | 2.011 | 0.243 | 16.39 | 15.38 | 18.82 | 2.99 | 32.32 | 0.0236 | 17.00 | 0.448 |
| 13.9 | 48.84 | 0.615 | 2.437 | 0.202 | 18.12 | 18.63 | 22.04 | 3.29 | 37.85 | 0.0286 | 13.78 | 0.519 |
| 18.7 | 61.22 | 0.771 | 3.290 | 0.146 | 20.81 | 25.15 | 27.63 | 3.83 | 47.44 | 0.0387 | 8.19 | 0.667 |
| 23.6 | 68.61 | 0.864 | 4.142 | 0.083 | 19.77 | 31.66 | 30.97 | 4.29 | 53.17 | 0.0487 | 4.86 | 0.807 |
| 28.4 | 72.48 | 0.913 | 4.994 | 0.046 | 17.69 | 38.18 | 32.71 | 4.72 | 56.17 | 0.0587 | 3.11 | 0.919 |
| 33.3 | 74.81 | 0.943 | 5.846 | 0.026 | 15.73 | 44.69 | 33.77 | 5.10 | 57.97 | 0.0687 | 2.06 | 0.986 |
| 38.2 | 76.06 | 0.958 | 6.699 | 0.017 | 14.32 | 51.21 | 34.33 | 5.46 | 58.94 | 0.0787 | 1.50 | 0.999 |
| 47.9 | 77.86 | 0.981 | 8.403 | 0.009 | 13.33 | 64.24 | 35.14 | 6.12 | 60.33 | 0.0988 | 0.68 | 0.871 |
| 57.6 | 78.54 | 0.990 | 10.108 | 0.005 | 11.63 | 77.27 | 35.45 | 6.71 | 60.86 | 0.1188 | 0.37 | 0.633 |
| 67.3 | 79.17 | 0.997 | 11.812 | 0.003 | 10.83 | 90.30 | 35.73 | 7.25 | 61.35 | 0.1388 | 0.09 | 0.455 |
| 77.0 | 79.37 | 1.000 | 13.517 | 0.000 | 0.00 | 103.33 | 35.82 | 7.76 | 61.51 | 0.1588 | 0.00 | 0.465 |

X/C = 0.50 6.0 INS THROTTLE 500.0 RPM

| | | | | | |
|---|---|---|---|---|---|
| UE | 84.69 FPS | DUEDX | -163.0 /SEC | H | 2.68 |
| UT | 2.18 FPS | UT/UE | 0.0258 | H** | 1.59 |
| UP | 1.32 FPS | | | PI | 3.57 |
| UB | 58.52 FPS | UB/UE | 0.691 | G | 24.33 |
| CFE | 1.327 *10-3 | CTEQ | 11.519 *10-3 | GEQ | 12.45 |
| CFLT | 0.869 *10-3 | CFE/CFLT | 1.527 | GAMMA | -0.346 *10-2 |
| CFNM | 0.851 *10-3 | CFE/CFNM | 1.560 | A | 1.381 *10↑4 FT/SEC↑2 |
| CDEL | 477.61 *10-4 FT | DELTA | 30.13 *10-4 FT | ALPHA0 | 0.220 |
| DSTAR | 12.30 *10-4 FT | REDSTAR | 628.3 | TH/UE*DUEDX | -0.884 *10-3 |
| THETA | 4.59 *10-4 FT | RETHETA | 234.5 | K | -0.207 |
| DELTA** | 7.30 *10-4 FT | | | NU | 1.659 *10-4 FT↑2/SEC |

| Y*10↑4 (FT) | U (FPS) | U/UE | Y/THETA | Z*TH/UE | YY | Y+ | U+ | (Y*)↑0.5 | U* | Y/CDEL | (UE-U)/UT | UC/UE |
|---|---|---|---|---|---|---|---|---|---|---|---|---|
| 0.0 | 0.00 | 0.000 | 0.000 | 0.156 | 0.00 | 0.00 | 0.00 | 0.00 | 0.00 | 0.0000 | 38.82 | 0.000 |
| 1.2 | 3.61 | 0.043 | 0.264 | 0.167 | 1.65 | 1.60 | 1.66 | 0.98 | 2.74 | 0.0025 | 37.16 | 0.110 |
| 4.1 | 13.33 | 0.157 | 0.899 | 0.213 | 6.35 | 5.43 | 6.11 | 1.81 | 10.12 | 0.0086 | 32.71 | 0.216 |
| 6.6 | 24.04 | 0.284 | 1.427 | 0.236 | 10.62 | 8.62 | 11.02 | 2.28 | 18.24 | 0.0137 | 27.80 | 0.291 |
| 9.0 | 34.50 | 0.407 | 1.956 | 0.225 | 14.21 | 11.81 | 15.81 | 2.67 | 26.17 | 0.0188 | 23.01 | 0.374 |
| 11.4 | 44.19 | 0.522 | 2.484 | 0.210 | 17.42 | 15.01 | 20.26 | 3.01 | 33.53 | 0.0239 | 18.56 | 0.465 |
| 13.8 | 53.26 | 0.629 | 3.013 | 0.191 | 20.18 | 18.20 | 24.41 | 3.32 | 40.41 | 0.0290 | 14.41 | 0.561 |
| 18.7 | 68.36 | 0.807 | 4.070 | 0.130 | 22.44 | 24.59 | 31.33 | 3.85 | 51.87 | 0.0391 | 7.48 | 0.752 |
| 23.5 | 76.47 | 0.903 | 5.127 | 0.064 | 19.94 | 30.97 | 35.05 | 4.33 | 58.02 | 0.0493 | 3.77 | 0.906 |
| 28.4 | 79.91 | 0.944 | 6.185 | 0.034 | 17.49 | 37.36 | 36.63 | 4.75 | 60.63 | 0.0595 | 2.19 | 0.991 |
| 33.3 | 82.58 | 0.975 | 7.242 | 0.022 | 16.61 | 43.74 | 37.85 | 5.14 | 62.66 | 0.0696 | 0.97 | 0.988 |
| 38.1 | 83.93 | 0.991 | 8.299 | 0.011 | 13.52 | 50.13 | 38.47 | 5.50 | 63.68 | 0.0798 | 0.35 | 0.902 |
| 47.8 | 84.61 | 0.999 | 10.413 | 0.002 | 7.36 | 62.90 | 38.78 | 6.16 | 64.20 | 0.1001 | 0.04 | 0.591 |
| 57.5 | 84.69 | 1.000 | 12.528 | 0.000 | 0.00 | 75.67 | 38.82 | 6.76 | 64.26 | 0.1204 | 0.00 | 0.364 |



APPENDIX H (cont.)

X/C = 0.50 8.0 INS THROTTLE 500.0 RPM

| | | | | | | | |
|---|---|---|---|---|---|---|---|
| UE | 85.92 FPS | DUEDX | -118.0 /SEC | H | 3.10 | | |
| UT | 1.87 FPS | UT/UE | 0.0218 | H** | 1.55 | | |
| UP | 1.19 FPS | | | PI | 3.26 | | |
| UB | 67.13 FPS | UB/UE | 0.781 | G | 31.05 | | |
| CFE | 0.952 *10-3 | CTEQ | 13.477 *10-3 | GEQ | 12.03 | | |
| CFLT | 0.479 *10-3 | CFE/CFLT | 1.986 | GAMMA | -0.185 *10-2 | | |
| CFNM | 0.010 *10-3 | CFE/CFNM | 95.172 | A | 1.014 *10^4 | FT/SEC^2 | |
| CDEL | 517.72 *10-4 FT | DELTA | 25.44 *10-4 FT | ALPHA0 | 0.257 | | |
| DSTAR | 11.29 *10-4 FT | REDSTAR | 581.4 | TH/UE*DUEDX | -0.500 *10-3 | | |
| THETA | 3.64 *10-4 FT | RETHETA | 187.6 | K | -0.094 | | |
| DELTA** | 5.66 *10-4 FT | | | NU | 1.669 *10-4 | FT^2/SEC | |

| Y*10^4 (FT) | U (FPS) | U/UE | Y/THETA | Z*TH/UE | YY | Y+ | U+ | (Y*)^0.5 | U* | Y/CDEL | (UE-U)/UT | UC/UE |
|---|---|---|---|---|---|---|---|---|---|---|---|---|
| 0.0 | 0.00 | 0.000 | 0.000 | 0.089 | 0.00 | 0.00 | 0.00 | 0.00 | 0.00 | 0.0000 | 45.84 | 0.000 |
| 1.2 | 2.65 | 0.031 | 0.320 | 0.104 | 1.41 | 1.31 | 1.41 | 0.91 | 2.22 | 0.0023 | 44.43 | 0.059 |
| 2.6 | 6.52 | 0.076 | 0.719 | 0.128 | 3.52 | 2.94 | 3.48 | 1.37 | 5.47 | 0.0051 | 42.36 | 0.118 |
| 4.1 | 11.41 | 0.133 | 1.119 | 0.159 | 6.10 | 4.58 | 6.09 | 1.71 | 9.57 | 0.0079 | 39.76 | 0.170 |
| 6.5 | 22.04 | 0.257 | 1.785 | 0.196 | 10.84 | 7.30 | 11.76 | 2.16 | 18.49 | 0.0126 | 34.08 | 0.265 |
| 8.9 | 33.89 | 0.394 | 2.451 | 0.219 | 15.72 | 10.03 | 18.08 | 2.53 | 28.44 | 0.0173 | 27.76 | 0.377 |
| 11.4 | 47.13 | 0.549 | 3.117 | 0.209 | 19.51 | 12.76 | 25.14 | 2.85 | 39.55 | 0.0219 | 20.70 | 0.501 |
| 13.8 | 57.78 | 0.673 | 3.783 | 0.173 | 21.54 | 15.48 | 30.83 | 3.14 | 48.49 | 0.0266 | 15.01 | 0.628 |
| 18.6 | 74.49 | 0.867 | 5.116 | 0.106 | 22.83 | 20.93 | 39.74 | 3.65 | 62.51 | 0.0360 | 6.10 | 0.854 |
| 23.5 | 82.09 | 0.955 | 6.448 | 0.046 | 19.02 | 26.38 | 43.80 | 4.10 | 68.89 | 0.0454 | 2.04 | 0.984 |
| 28.3 | 85.11 | 0.991 | 7.780 | 0.015 | 12.89 | 31.83 | 45.41 | 4.50 | 71.42 | 0.0548 | 0.43 | 0.981 |
| 33.2 | 85.44 | 0.994 | 9.112 | 0.004 | 7.42 | 37.28 | 45.59 | 4.87 | 71.70 | 0.0641 | 0.25 | 0.848 |
| 38.1 | 85.92 | 1.000 | 10.445 | 0.000 | 0.00 | 42.74 | 45.84 | 5.21 | 72.10 | 0.0735 | 0.00 | 0.636 |

X/C = 0.50 10.0 INS THROTTLE 500.0 RPM

| | | | | | | | |
|---|---|---|---|---|---|---|---|
| UE | 100.59 FPS | DUEDX | -85.0 /SEC | H | 2.90 | | |
| UT | 2.10 FPS | UT/UE | 0.0209 | H** | 1.57 | | |
| UP | 1.13 FPS | | | PI | 1.93 | | |
| UB | 76.14 FPS | UB/UE | 0.757 | G | 31.35 | | |
| CFE | 0.874 *10-3 | CTEQ | 12.612 *10-3 | GEQ | 10.09 | | |
| CFLT | 0.637 *10-3 | CFE/CFLT | 1.371 | GAMMA | -0.110 *10-2 | | |
| CFNM | 0.257 *10-3 | CFE/CFNM | 3.394 | A | 0.855 *104 FT/SEC↑2 | | |
| CDEL | 476.52 *10-4 FT | DELTA | 23.19 *10-4 FT | ALPHA0 | 0.154 | | |
| DSTAR | 9.96 *10-4 FT | REDSTAR | 597.8 | TH/UE*DUEDX | -0.290 *10-3 | | |
| THETA | 3.43 *10-4 FT | RETHETA | 206.1 | K | -0.060 | | |
| DELTA** | 5.38 *10-4 FT | | | NU | 1.676 *10-4 FT↑2/SEC | | |

| Y*10^4 (FT) | U (FPS) | U/UE | Y/THETA | Z*TH/UE | YY | Y+ | U+ | (Y*)↑0.5 | U* | Y/CDEL | (UE-U)/UT | UC/UE |
|---|---|---|---|---|---|---|---|---|---|---|---|---|
| 0.0 | 0.00 | 0.000 | 0.000 | 0.090 | 0.00 | 0.00 | 0.00 | 0.00 | 0.00 | 0.0000 | 47.84 | 0.000 |
| 1.2 | 3.82 | 0.038 | 0.339 | 0.134 | 1.78 | 1.46 | 1.82 | 0.89 | 3.39 | 0.0024 | 46.02 | 0.095 |
| 2.6 | 10.70 | 0.106 | 0.763 | 0.168 | 4.49 | 3.29 | 5.09 | 1.33 | 9.49 | 0.0055 | 42.75 | 0.156 |
| 4.1 | 18.15 | 0.180 | 1.187 | 0.190 | 7.44 | 5.12 | 8.63 | 1.66 | 16.10 | 0.0086 | 39.21 | 0.211 |
| 6.5 | 33.52 | 0.333 | 1.894 | 0.212 | 12.53 | 8.16 | 15.94 | 2.09 | 29.73 | 0.0137 | 31.90 | 0.316 |
| 8.9 | 48.35 | 0.481 | 2.601 | 0.210 | 17.10 | 11.20 | 22.99 | 2.45 | 42.88 | 0.0187 | 24.85 | 0.439 |
| 11.4 | 63.35 | 0.630 | 3.308 | 0.189 | 20.63 | 14.25 | 30.13 | 2.76 | 56.19 | 0.0238 | 17.71 | 0.573 |
| 13.8 | 75.18 | 0.747 | 4.015 | 0.155 | 22.66 | 17.29 | 35.75 | 3.05 | 66.68 | 0.0289 | 12.09 | 0.706 |
| 16.2 | 85.33 | 0.848 | 4.721 | 0.116 | 23.12 | 20.34 | 40.58 | 3.30 | 75.69 | 0.0340 | 7.26 | 0.825 |
| 18.6 | 91.73 | 0.912 | 5.428 | 0.074 | 21.14 | 23.38 | 43.63 | 3.54 | 81.36 | 0.0391 | 4.21 | 0.919 |
| 23.5 | 97.53 | 0.970 | 6.842 | 0.028 | 16.29 | 29.47 | 46.39 | 3.98 | 86.51 | 0.0493 | 1.45 | 1.000 |
| 28.3 | 99.55 | 0.990 | 8.255 | 0.011 | 12.29 | 35.56 | 47.35 | 4.37 | 88.30 | 0.0595 | 0.49 | 0.922 |
| 33.2 | 100.59 | 1.000 | 9.669 | 0.000 | 0.00 | 41.65 | 47.84 | 4.73 | 89.22 | 0.0697 | 0.00 | 0.721 |



APPENDIX H (cont.)

X/C = 0.50 13.0 INS THROTTLE 500.0 RPM

| | | | | | | | | |
|---|---|---|---|---|---|---|---|---|
| UE | 101.09 | FPS | DUEDX | -86.0 | /SEC | H | 2.81 | |
| UT | 2.50 | FPS | UT/UE | 0.0247 | | H** | 1.57 | |
| UP | 1.13 | FPS | | | | PI | 1.19 | |
| UB | 72.80 | FPS | UB/UE | 0.720 | | G | 26.04 | |
| CFE | 1.224 | $*_{10}$-3 | CTEQ | 12.173 | $*_{10}$-3 | GEQ | 8.86 | |
| CFLT | 0.757 | $*_{10}$-3 | CFE/CFLT | 1.616 | | GAMMA | -0.095 | $*_{10}$-2 |
| CFNM | 0.638 | $*_{10}$-3 | CFE/CFNM | 1.917 | | A | 0.869 | $*_{10}$4 FT/SEC↑2 |
| CDEL | 345.63 | $*_{10}$-4 FT | DELTA | 20.34 | $*_{10}$-4 FT | ALPHA0 | 0.093 | |
| DSTAR | 8.55 | $*_{10}$-4 FT | REDSTAR | 514.2 | | TH/UE*DUEDX | -0.259 | $*_{10}$-3 |
| THETA | 3.04 | $*_{10}$-4 FT | RETHETA | 183.0 | | K | -0.047 | |
| DELTA** | 4.77 | $*_{10}$-4 FT | | | | NU | 1.681 | $*_{10}$-4 FT↑2/SEC |

| Y$*_{10}$4 (FT) | U (FPS) | U/UE | Y/THETA | Z*TH/UE | YY | Y+ | U+ | (Y*)↑0.5 | U* | Y/CDEL | (UE-U)/UT | UC/UE |
|---|---|---|---|---|---|---|---|---|---|---|---|---|
| 0.0 | 0.00 | 0.000 | 0.000 | 0.112 | 0.00 | 0.00 | 0.00 | 0.00 | 0.00 | 0.0000 | 40.43 | 0.000 |
| 1.2 | 5.12 | 0.051 | 0.383 | 0.152 | 2.02 | 1.73 | 2.05 | 0.89 | 4.51 | 0.0034 | 38.38 | 0.113 |
| 2.6 | 13.72 | 0.136 | 0.862 | 0.201 | 5.22 | 3.90 | 5.49 | 1.33 | 12.09 | 0.0076 | 34.94 | 0.185 |
| 4.1 | 24.53 | 0.243 | 1.340 | 0.216 | 8.43 | 6.07 | 9.81 | 1.66 | 21.62 | 0.0118 | 30.62 | 0.252 |
| 6.5 | 41.02 | 0.406 | 2.138 | 0.206 | 13.13 | 9.68 | 16.40 | 2.10 | 36.15 | 0.0188 | 24.02 | 0.378 |
| 8.9 | 57.78 | 0.572 | 2.936 | 0.198 | 17.66 | 13.29 | 23.11 | 2.46 | 50.92 | 0.0258 | 17.32 | 0.522 |
| 11.4 | 72.91 | 0.721 | 3.734 | 0.163 | 20.36 | 16.90 | 29.16 | 2.77 | 64.25 | 0.0329 | 11.27 | 0.671 |
| 13.8 | 84.00 | 0.831 | 4.532 | 0.111 | 20.42 | 20.51 | 33.59 | 3.05 | 74.02 | 0.0399 | 6.84 | 0.807 |
| 16.2 | 90.82 | 0.898 | 5.330 | 0.076 | 19.84 | 24.12 | 36.32 | 3.31 | 80.03 | 0.0469 | 4.11 | 0.916 |
| 18.6 | 96.22 | 0.952 | 6.127 | 0.052 | 18.94 | 27.73 | 38.48 | 3.55 | 84.79 | 0.0539 | 1.95 | 0.982 |
| 23.5 | 99.89 | 0.988 | 7.723 | 0.015 | 12.84 | 34.95 | 39.95 | 3.98 | 88.03 | 0.0680 | 0.48 | 0.967 |
| 28.3 | 101.09 | 1.000 | 9.319 | 0.000 | 0.00 | 42.18 | 40.43 | 4.37 | 89.09 | 0.0820 | 0.00 | 0.778 |



APPENDIX H (cont.)

X/C = 0.50 22.0 INS THROTTLE 500.0 RPM

| | | | | | | | | |
|---|---|---|---|---|---|---|---|---|
| UE | 105.63 | FPS | DUEDX | -75.0 | /SEC | H | 2.70 | |
| UT | 3.02 | FPS | UT/UE | 0.0286 | | H** | 1.58 | |
| UP | 1.10 | FPS | | | | PI | 0.65 | |
| UB | 71.58 | FPS | UB/UE | 0.678 | | G | 21.98 | |
| CFE | 1.639 | *10-3 | CTEQ | 11.596 | *10-3 | GEQ | 7.86 | |
| CFLT | 0.916 | *10-3 | CFE/CFLT | 1.790 | | GAMMA | -0.072 | *10-2 |
| CFNM | 1.061 | *10-3 | CFE/CFNM | 1.545 | | A | 0.792 | *10 4 FT/SEC↑2 |
| CDEL | 261.35 | *10-4 FT | DELTA | 18.31 | *10-4 FT | ALPHA0 | 0.048 | |
| DSTAR | 7.48 | *10-4 FT | REDSTAR | 469.2 | | TH/UE*DUEDX | -0.197 | *10-3 |
| THETA | 2.77 | *10-4 FT | RETHETA | 173.9 | | K | -0.034 | |
| DELTA** | 4.37 | *10-4 FT | | | | NU | 1.685 | *10-4 FT↑2/SEC |

| Y*10 4 (FT) | U (FPS) | U/UE | Y/THETA | Z*TH/UE | YY | Y+ | U+ | (Y*)↑0.5 | U* | Y/CDEL | (UE-U)/UT | UC/UE |
|---|---|---|---|---|---|---|---|---|---|---|---|---|
| 0.0 | 0.00 | 0.000 | 0.000 | 0.143 | 0.00 | 0.00 | 0.00 | 0.00 | 0.00 | 0.0000 | 34.93 | 0.000 |
| 1.2 | 7.07 | 0.067 | 0.420 | 0.176 | 2.32 | 2.09 | 2.34 | 0.87 | 6.42 | 0.0045 | 32.59 | 0.137 |
| 2.6 | 17.99 | 0.170 | 0.945 | 0.222 | 5.87 | 4.71 | 5.95 | 1.31 | 16.34 | 0.0100 | 28.98 | 0.220 |
| 4.1 | 31.71 | 0.300 | 1.470 | 0.234 | 9.38 | 7.32 | 10.49 | 1.63 | 28.80 | 0.0156 | 24.45 | 0.297 |
| 6.5 | 51.32 | 0.486 | 2.345 | 0.203 | 13.94 | 11.68 | 16.97 | 2.06 | 46.61 | 0.0249 | 17.96 | 0.440 |
| 8.9 | 69.25 | 0.656 | 3.220 | 0.169 | 17.47 | 16.03 | 22.90 | 2.42 | 62.90 | 0.0342 | 12.03 | 0.598 |
| 11.4 | 82.59 | 0.782 | 4.095 | 0.131 | 19.51 | 20.39 | 27.31 | 2.72 | 75.01 | 0.0435 | 7.62 | 0.753 |
| 13.8 | 93.39 | 0.884 | 4.970 | 0.092 | 19.90 | 24.75 | 30.88 | 3.00 | 84.82 | 0.0527 | 4.05 | 0.883 |
| 16.2 | 99.63 | 0.943 | 5.845 | 0.047 | 16.78 | 29.10 | 32.94 | 3.26 | 90.49 | 0.0620 | 1.99 | 0.970 |
| 18.6 | 102.15 | 0.967 | 6.720 | 0.024 | 13.74 | 33.46 | 33.78 | 3.49 | 92.78 | 0.0713 | 1.15 | 1.001 |
| 23.5 | 105.40 | 0.998 | 8.470 | 0.009 | 10.85 | 42.17 | 34.85 | 3.92 | 95.73 | 0.0899 | 0.08 | 0.892 |
| 28.3 | 105.63 | 1.000 | 10.220 | 0.000 | 0.00 | 50.89 | 34.93 | 4.30 | 95.94 | 0.1085 | 0.00 | 0.641 |

X/C = 0.60 4.8 INS THROTTLE 500.0 RPM

| | | | | | |
|---|---|---|---|---|---|
| UE | 75.19 FPS | DUEDX | -148.0 /SEC | H | 2.15 |
| UT | 1.86 FPS | UT/UE | 0.0248 | H** | 1.67 |
| UP | 1.22 FPS | | | PI | 5.76 |
| UB | 43.12 FPS | UB/UE | 0.574 | G | 21.59 |
| CFE | 1.229 *10-3 | CTEQ | 8.382 *10-3 | GEQ | 15.09 |
| CFLT | 1.737 *10-3 | CFE/CFLT | 0.707 | GAMMA | -0.729 *10-2 |
| CFNM | 2.039 *10-3 | CFE/CFNM | 0.602 | A | 1.113 *10↑4 FT/SEC↑2 |
| CDEL | 725.85 *10-4 FT | DELTA | 51.81 *10-4 FT | ALPHA0 | 0.281 |
| DSTAR | 17.99 *10-4 FT | REDSTAR | 828.5 | TH/UE*DUEDX | -1.647 *10-3 |
| THETA | 8.36 *10-4 FT | RETHETA | 385.2 | K | -0.634 |
| DELTA** | 13.94 *10-4 FT | | | NU | 1.633 *10-4 FT↑2/SEC |

| Y*10↑4 (FT) | U (FPS) | U/UE | Y/THETA | Z*TH/UE | YY | Y+ | U+ | (Y*)↑0.5 | U* | Y/CDEL | (UE-U)/UT | UC/UE |
|---|---|---|---|---|---|---|---|---|---|---|---|---|
| 0.0 | 0.00 | 0.000 | 0.000 | 0.237 | 0.00 | 0.00 | 0.00 | 0.00 | 0.00 | 0.0000 | 40.35 | 0.000 |
| 2.0 | 4.68 | 0.062 | 0.241 | 0.281 | 2.50 | 2.30 | 2.51 | 1.23 | 3.84 | 0.0028 | 37.83 | 0.232 |
| 3.0 | 7.32 | 0.097 | 0.361 | 0.313 | 3.97 | 3.45 | 3.93 | 1.50 | 6.00 | 0.0042 | 36.42 | 0.259 |
| 5.5 | 15.63 | 0.208 | 0.662 | 0.371 | 7.91 | 6.32 | 8.39 | 2.03 | 12.81 | 0.0076 | 31.96 | 0.307 |
| 8.1 | 24.11 | 0.321 | 0.963 | 0.341 | 11.03 | 9.19 | 12.94 | 2.45 | 19.76 | 0.0111 | 27.41 | 0.347 |
| 10.6 | 31.05 | 0.413 | 1.264 | 0.305 | 13.70 | 12.06 | 16.66 | 2.81 | 25.45 | 0.0146 | 23.68 | 0.387 |
| 13.1 | 37.92 | 0.504 | 1.565 | 0.271 | 15.99 | 14.94 | 20.35 | 3.13 | 31.07 | 0.0180 | 20.00 | 0.429 |
| 15.6 | 43.32 | 0.576 | 1.865 | 0.240 | 17.95 | 17.81 | 23.24 | 3.41 | 35.50 | 0.0215 | 17.10 | 0.473 |
| 18.1 | 48.79 | 0.649 | 2.166 | 0.215 | 19.72 | 20.68 | 26.18 | 3.68 | 39.98 | 0.0250 | 14.17 | 0.519 |
| 23.2 | 56.11 | 0.746 | 2.768 | 0.134 | 19.92 | 26.43 | 30.11 | 4.16 | 45.98 | 0.0319 | 10.24 | 0.617 |
| 28.2 | 60.96 | 0.811 | 3.370 | 0.092 | 20.10 | 32.17 | 32.71 | 4.59 | 49.96 | 0.0388 | 7.64 | 0.716 |
| 38.3 | 66.62 | 0.886 | 4.573 | 0.046 | 19.34 | 43.66 | 35.75 | 5.35 | 54.60 | 0.0527 | 4.60 | 0.890 |
| 48.3 | 69.36 | 0.922 | 5.777 | 0.032 | 20.26 | 55.15 | 37.22 | 6.01 | 56.84 | 0.0666 | 3.13 | 0.989 |
| 58.4 | 72.39 | 0.963 | 6.980 | 0.024 | 21.40 | 66.64 | 38.85 | 6.61 | 59.33 | 0.0804 | 1.50 | 0.985 |
| 68.5 | 73.78 | 0.981 | 8.184 | 0.012 | 17.60 | 78.13 | 39.59 | 7.15 | 60.46 | 0.0943 | 0.76 | 0.883 |
| 78.5 | 74.57 | 0.992 | 9.387 | 0.008 | 16.26 | 89.62 | 40.01 | 7.66 | 61.11 | 0.1082 | 0.33 | 0.724 |
| 88.6 | 75.19 | 1.000 | 10.591 | 0.000 | 0.00 | 101.11 | 40.35 | 8.14 | 61.62 | 0.1220 | 0.00 | 0.570 |



APPENDIX H (cont.)

X/C = 0.60 5.2 INS THROTTLE 500.0 RPM

| | | | | | |
|---|---|---|---|---|---|
| UE | 80.06 FPS | DUEDX | -107.0 /SEC | H | 2.28 |
| UT | 1.74 FPS | UT/UE | 0.0217 | H** | 1.66 |
| UP | 1.12 FPS | | | PI | 5.05 |
| UB | 50.12 FPS | UB/UE | 0.626 | G | 25.86 |
| CFE | 0.941 *10-3 | CTEQ | 9.226 *10-3 | GEQ | 14.28 |
| CFLT | 1.429 *10-3 | CFE/CFLT | 0.658 | GAMMA | -0.462 *10-2 |
| CFNM | 1.643 *10-3 | CFE/CFNM | 0.573 | A | 0.857 *10↑4 FT/SEC↑2 |
| CDEL | 819.92 *10-4 FT | DELTA | 48.59 *10-4 FT | ALPHA0 | 0.267 |
| DSTAR | 17.78 *10-4 FT | REDSTAR | 872.0 | TH/UE*DUEDX | -1.044 *10-3 |
| THETA | 7.81 *10-4 FT | RETHETA | 383.0 | K | -0.400 |
| DELTA** | 12.98 *10-4 FT | | | NU | 1.633 *10-4 FT↑2/SEC |

| Y*10↑4 (FT) | U (FPS) | U/UE | Y/THETA | Z*TH/UE | YY | Y+ | U+ | (Y*)↑0.5 | U* | Y/CDEL | (UE-U)/UT | UC/UE |
|---|---|---|---|---|---|---|---|---|---|---|---|---|
| 0.0 | 0.00 | 0.000 | 0.000 | 0.180 | 0.00 | 0.00 | 0.00 | 0.00 | 0.00 | 0.0000 | 46.11 | 0.000 |
| 1.9 | 3.82 | 0.048 | 0.245 | 0.209 | 2.19 | 2.03 | 2.20 | 1.14 | 3.41 | 0.0023 | 43.91 | 0.205 |
| 2.9 | 6.06 | 0.076 | 0.374 | 0.237 | 3.56 | 3.10 | 3.49 | 1.41 | 5.42 | 0.0036 | 42.62 | 0.231 |
| 5.4 | 13.49 | 0.169 | 0.696 | 0.316 | 7.66 | 5.78 | 7.77 | 1.93 | 12.07 | 0.0066 | 38.34 | 0.277 |
| 8.0 | 22.38 | 0.280 | 1.018 | 0.341 | 11.63 | 8.46 | 12.89 | 2.33 | 20.01 | 0.0097 | 33.22 | 0.319 |
| 10.5 | 31.08 | 0.388 | 1.341 | 0.326 | 14.97 | 11.13 | 17.90 | 2.68 | 27.79 | 0.0128 | 28.21 | 0.362 |
| 13.0 | 39.19 | 0.490 | 1.663 | 0.285 | 17.36 | 13.81 | 22.57 | 2.98 | 35.05 | 0.0158 | 23.54 | 0.408 |
| 15.5 | 45.77 | 0.572 | 1.985 | 0.240 | 19.01 | 16.49 | 26.36 | 3.26 | 40.92 | 0.0189 | 19.75 | 0.458 |
| 18.0 | 51.55 | 0.644 | 2.307 | 0.206 | 20.47 | 19.16 | 29.69 | 3.51 | 46.10 | 0.0220 | 16.42 | 0.511 |
| 23.1 | 60.22 | 0.752 | 2.952 | 0.144 | 21.93 | 24.52 | 34.69 | 3.97 | 53.85 | 0.0281 | 11.42 | 0.622 |
| 28.1 | 66.43 | 0.830 | 3.596 | 0.097 | 21.93 | 29.87 | 38.26 | 4.39 | 59.40 | 0.0343 | 7.85 | 0.734 |
| 38.2 | 71.67 | 0.895 | 4.885 | 0.042 | 19.60 | 40.58 | 41.28 | 5.11 | 64.09 | 0.0465 | 4.83 | 0.919 |
| 48.2 | 75.11 | 0.938 | 6.174 | 0.027 | 19.83 | 51.28 | 43.26 | 5.75 | 67.16 | 0.0588 | 2.85 | 0.999 |
| 58.3 | 77.23 | 0.965 | 7.464 | 0.018 | 19.37 | 61.99 | 44.48 | 6.32 | 69.06 | 0.0711 | 1.63 | 0.950 |
| 68.4 | 78.74 | 0.983 | 8.753 | 0.012 | 18.41 | 72.69 | 45.35 | 6.84 | 70.41 | 0.0834 | 0.76 | 0.796 |
| 78.4 | 79.61 | 0.994 | 10.042 | 0.006 | 15.74 | 83.40 | 45.85 | 7.33 | 71.19 | 0.0956 | 0.26 | 0.603 |
| 88.5 | 80.06 | 1.000 | 11.331 | 0.000 | 0.00 | 94.10 | 46.11 | 7.79 | 71.59 | 0.1079 | 0.00 | 0.454 |

X/C = 0.60 6.0 INS THROTTLE 500.0 RPM

| | | | | | | | |
|---|---|---|---|---|---|---|---|
| UE | 84.92 FPS | DUEDX | -246.0 /SEC | H | 2.61 | | |
| UT | 1.90 FPS | UT/UE | 0.0223 | H** | 1.61 | | |
| UP | 1.51 FPS | | | PI | 9.04 | | |
| UB | 59.17 FPS | UB/UE | 0.697 | G | 27.60 | | |
| CFE | 0.997 $*_{10}$-3 | CTEQ | 11.152 $*_{10}$-3 | GEQ | 18.39 | | |
| CFLT | 0.903 $*_{10}$-3 | CFE/CFLT | 1.104 | GAMMA | -0.725 | $*_{10}$-2 | |
| CFNM | 0.860 $*_{10}$-3 | CFE/CFNM | 1.159 | A | 2.089 | $*_{10}$4 | FT/SEC↑2 |
| CDEL | 696.50 $*_{10}$-4 FT | DELTA | 38.61 $*_{10}$-4 FT | ALPHA0 | 0.500 | | |
| DSTAR | 15.55 $*_{10}$-4 FT | REDSTAR | 808.5 | TH/UE*DUEDX | -1.728 | $*_{10}$-3 | |
| THETA | 5.97 $*_{10}$-4 FT | RETHETA | 310.1 | K | -0.536 | | |
| DELTA** | 9.62 $*_{10}$-4 FT | | | NU | 1.634 | $*_{10}$-4 | FT↑2/SEC |

| Y*$_{10}$4 (FT) | U (FPS) | U/UE | Y/THETA | Z*TH/UE | YY | Y+ | U+ | (Y*)↑0.5 | U* | Y/CDEL | (UE-U)/UT | UC/UE |
|---|---|---|---|---|---|---|---|---|---|---|---|---|
| 0.0 | 0.00 | 0.000 | 0.000 | 0.155 | 0.00 | 0.00 | 0.00 | 0.00 | 0.00 | 0.0000 | 44.78 | 0.000 |
| 1.9 | 4.02 | 0.047 | 0.312 | 0.149 | 2.12 | 2.16 | 2.12 | 1.31 | 2.67 | 0.0027 | 42.66 | 0.142 |
| 2.9 | 6.14 | 0.072 | 0.481 | 0.164 | 3.43 | 3.33 | 3.24 | 1.63 | 4.08 | 0.0041 | 41.55 | 0.171 |
| 5.4 | 13.45 | 0.158 | 0.903 | 0.243 | 7.84 | 6.25 | 7.09 | 2.23 | 8.93 | 0.0077 | 37.69 | 0.229 |
| 7.9 | 23.58 | 0.278 | 1.325 | 0.263 | 11.97 | 9.17 | 12.43 | 2.70 | 15.66 | 0.0113 | 32.35 | 0.286 |
| 10.4 | 32.33 | 0.381 | 1.746 | 0.251 | 15.40 | 12.09 | 17.05 | 3.10 | 21.47 | 0.0150 | 27.73 | 0.350 |
| 12.9 | 41.54 | 0.489 | 2.168 | 0.234 | 18.48 | 15.02 | 21.90 | 3.45 | 27.59 | 0.0186 | 22.88 | 0.419 |
| 15.5 | 49.12 | 0.578 | 2.590 | 0.216 | 21.20 | 17.94 | 25.90 | 3.77 | 32.62 | 0.0222 | 18.88 | 0.494 |
| 18.0 | 57.01 | 0.671 | 3.012 | 0.198 | 23.62 | 20.86 | 30.06 | 4.07 | 37.87 | 0.0258 | 14.72 | 0.572 |
| 23.0 | 68.06 | 0.801 | 3.856 | 0.120 | 23.53 | 26.70 | 35.89 | 4.60 | 45.21 | 0.0330 | 8.89 | 0.727 |
| 28.0 | 74.21 | 0.874 | 4.699 | 0.067 | 21.42 | 32.55 | 39.14 | 5.08 | 49.29 | 0.0403 | 5.65 | 0.861 |
| 33.1 | 77.66 | 0.915 | 5.543 | 0.048 | 21.28 | 38.39 | 40.95 | 5.52 | 51.58 | 0.0475 | 3.83 | 0.957 |
| 38.1 | 81.03 | 0.954 | 6.387 | 0.037 | 21.61 | 44.23 | 42.73 | 5.93 | 53.82 | 0.0547 | 2.05 | 0.999 |
| 48.2 | 83.43 | 0.983 | 8.074 | 0.012 | 15.51 | 55.92 | 44.00 | 6.66 | 55.42 | 0.0692 | 0.78 | 0.912 |
| 58.2 | 84.44 | 0.994 | 9.762 | 0.005 | 12.38 | 67.60 | 44.53 | 7.33 | 56.08 | 0.0836 | 0.25 | 0.665 |
| 68.3 | 84.92 | 1.000 | 11.449 | 0.000 | 0.00 | 79.29 | 44.78 | 7.93 | 56.40 | 0.0981 | 0.00 | 0.422 |



APPENDIX H (cont.)

X/C = 0.60 8.0 INS THROTTLE 500.0 RPM

| | | | | | |
|---|---|---|---|---|---|
| UE | 94.86 FPS | DUEDX | -167.0 /SEC | H | 3.85 |
| UT | 1.61 FPS | UT/UE | 0.0169 | H** | 1.54 |
| UP | 1.37 FPS | | | PI | 10.30 |
| UB | 84.74 FPS | UB/UE | 0.893 | G | 43.70 |
| CFE | 0.574 *10-3 | CTEQ | 16.130 *10-3 | GEQ | 19.53 |
| CFLT | 0.136 *10-3 | CFE/CFLT | 4.216 | GAMMA | -0.306 *10-2 |
| CFNM | 0.010 *10-3 | CFE/CFNM | 57.432 | A | 1.584 *10↑4 FT/SEC↑2 |
| CDEL | 991.77 *10-4 FT | DELTA | 34.44 *10-4 FT | ALPHA0 | 0.623 |
| DSTAR | 16.81 *10-4 FT | REDSTAR | 976.2 | TH/UE*DUEDX | -0.768 *10-3 |
| THETA | 4.36 *10-4 FT | RETHETA | 253.3 | K | -0.195 |
| DELTA** | 6.70 *10-4 FT | | | NU | 1.633 *10-4 FT↑2/SEC |

| Y*10↑4 (FT) | U (FPS) | U/UE | Y/THETA | Z*TH/UE | YY | Y+ | U+ | (Y*)↑0.5 | U* | Y/CDEL | (UE-U)/UT | UC/UE |
|---|---|---|---|---|---|---|---|---|---|---|---|---|
| 0.0 | 0.00 | 0.000 | 0.000 | 0.073 | 0.00 | 0.00 | 0.00 | 0.00 | 0.00 | 0.0000 | 59.01 | 0.000 |
| 1.8 | 1.79 | 0.019 | 0.404 | 0.021 | 0.93 | 1.73 | 1.11 | 1.22 | 1.31 | 0.0018 | 57.90 | -0.010 |
| 2.8 | 1.92 | 0.020 | 0.635 | 0.017 | 1.31 | 2.72 | 1.20 | 1.53 | 1.40 | 0.0028 | 57.82 | 0.017 |
| 5.3 | 4.31 | 0.045 | 1.212 | 0.081 | 5.50 | 5.20 | 2.68 | 2.11 | 3.14 | 0.0053 | 56.33 | 0.080 |
| 7.8 | 10.82 | 0.114 | 1.789 | 0.147 | 10.90 | 7.68 | 6.73 | 2.56 | 7.88 | 0.0079 | 52.28 | 0.154 |
| 10.3 | 20.35 | 0.215 | 2.366 | 0.192 | 16.52 | 10.16 | 12.66 | 2.95 | 14.83 | 0.0104 | 46.35 | 0.241 |
| 12.8 | 31.89 | 0.336 | 2.943 | 0.208 | 21.38 | 12.63 | 19.84 | 3.28 | 23.23 | 0.0129 | 39.17 | 0.339 |
| 15.4 | 43.17 | 0.455 | 3.520 | 0.208 | 25.57 | 15.11 | 26.86 | 3.59 | 31.45 | 0.0155 | 32.16 | 0.444 |
| 17.9 | 54.69 | 0.577 | 4.097 | 0.203 | 29.40 | 17.59 | 34.02 | 3.88 | 39.84 | 0.0180 | 24.99 | 0.553 |
| 20.4 | 65.43 | 0.690 | 4.674 | 0.185 | 31.98 | 20.06 | 40.70 | 4.14 | 47.66 | 0.0206 | 18.31 | 0.659 |
| 22.9 | 74.93 | 0.790 | 5.251 | 0.152 | 32.57 | 22.54 | 46.61 | 4.39 | 54.58 | 0.0231 | 12.40 | 0.758 |
| 27.9 | 86.80 | 0.915 | 6.405 | 0.080 | 28.85 | 27.50 | 54.00 | 4.85 | 63.23 | 0.0282 | 5.01 | 0.915 |
| 33.0 | 92.46 | 0.975 | 7.559 | 0.032 | 21.68 | 32.45 | 57.52 | 5.26 | 67.35 | 0.0332 | 1.49 | 0.994 |
| 38.0 | 93.91 | 0.990 | 8.713 | 0.010 | 14.06 | 37.41 | 58.42 | 5.65 | 68.41 | 0.0383 | 0.59 | 0.981 |
| 48.1 | 94.86 | 1.000 | 11.022 | 0.000 | 0.00 | 47.31 | 59.01 | 6.36 | 69.10 | 0.0485 | 0.00 | 0.711 |

X/C = 0.60 10.0 INS THROTTLE 500.0 RPM

| | | | | | | | | |
|---|---|---|---|---|---|---|---|---|
| UE | 96.94 FPS | DUEDX | -100.0 /SEC | H | 3.68 | | | |
| UT | 1.44 FPS | UT/UE | 0.0148 | H** | 1.54 | | | |
| UP | 1.17 FPS | | | PI | 6.72 | | | |
| UB | 86.17 FPS | UB/UE | 0.889 | G | 49.18 | | | |
| CFE | 0.439 *10-3 | CIEQ | 15.605 *10-3 | GEQ | 16.11 | | | |
| CFLT | 0.183 *10-3 | CFE/CFLT | 2.393 | GAMMA | -0.156 *10-2 | | | |
| CFNM | 0.010 *10-3 | CFE/CFNM | 43.860 | A | 0.969 *10↑4 FT/SEC↑2 | | | |
| CDEL | 964.15 *10-4 FT | DELTA | 29.71 *10-4 FT | ALPHA0 | 0.535 | | | |
| DSTAR | 14.28 *10-4 FT | REDSTAR | 847.8 | TH/UE*DUEDX | -0.400 *10-3 | | | |
| THETA | 3.88 *10-4 FT | RETHETA | 230.4 | K | -0.092 | | | |
| DELTA** | 5.98 *10-4 FT | | | NU | 1.633 *10-4 FT↑2/SEC | | | |

| Y*10↑4 (FT) | U (FPS) | U/UE | Y/THETA | Z*TH/UE | YY | Y+ | U+ | (Y*)↑0.5 | U* | Y/CDEL | (UE-U)/UT | UC/UE |
|---|---|---|---|---|---|---|---|---|---|---|---|---|
| 0.0 | 0.00 | 0.000 | 0.000 | 0.051 | 0.00 | 0.00 | 0.00 | 0.00 | 0.00 | 0.0000 | 67.53 | 0.000 |
| 1.8 | 1.88 | 0.019 | 0.454 | 0.035 | 1.29 | 1.55 | 1.31 | 1.12 | 1.62 | 0.0018 | 66.22 | 0.017 |
| 2.8 | 2.65 | 0.027 | 0.713 | 0.046 | 2.32 | 2.43 | 1.85 | 1.41 | 2.28 | 0.0029 | 65.68 | 0.044 |
| 5.3 | 7.91 | 0.082 | 1.362 | 0.120 | 7.15 | 4.65 | 5.51 | 1.94 | 6.79 | 0.0055 | 62.01 | 0.116 |
| 7.8 | 17.71 | 0.183 | 2.011 | 0.177 | 12.84 | 6.86 | 12.34 | 2.36 | 15.20 | 0.0081 | 55.19 | 0.206 |
| 10.3 | 30.18 | 0.311 | 2.659 | 0.200 | 18.07 | 9.07 | 21.03 | 2.71 | 25.90 | 0.0107 | 46.50 | 0.312 |
| 12.8 | 42.91 | 0.443 | 3.308 | 0.217 | 23.41 | 11.29 | 29.89 | 3.03 | 36.82 | 0.0133 | 37.64 | 0.431 |
| 15.4 | 57.51 | 0.593 | 3.956 | 0.209 | 27.47 | 13.50 | 40.06 | 3.31 | 49.35 | 0.0159 | 27.46 | 0.555 |
| 17.9 | 69.22 | 0.714 | 4.605 | 0.171 | 28.91 | 15.71 | 48.22 | 3.57 | 59.40 | 0.0185 | 19.31 | 0.676 |
| 20.4 | 79.03 | 0.815 | 5.254 | 0.132 | 28.96 | 17.92 | 55.05 | 3.81 | 67.81 | 0.0211 | 12.48 | 0.787 |
| 22.9 | 85.81 | 0.885 | 5.902 | 0.092 | 27.24 | 20.14 | 59.78 | 4.04 | 73.64 | 0.0238 | 7.75 | 0.880 |
| 27.9 | 93.54 | 0.965 | 7.199 | 0.040 | 21.99 | 24.56 | 65.17 | 4.47 | 80.27 | 0.0290 | 2.36 | 0.990 |
| 33.0 | 95.99 | 0.990 | 8.497 | 0.013 | 14.97 | 28.99 | 66.87 | 4.85 | 82.37 | 0.0342 | 0.66 | 0.978 |
| 38.0 | 96.94 | 1.000 | 9.794 | 0.000 | 0.00 | 33.41 | 67.53 | 5.21 | 83.18 | 0.0394 | 0.00 | 0.849 |

X/C = 0.60 13.0 INS THROTTLE 500.0 RPM

| | | | | | | | | |
|---|---|---|---|---|---|---|---|---|
| UE | 102.00 FPS | DUEDX | -92.0 /SEC | H | 3.50 | | | |
| UT | 1.61 FPS | UT/UE | 0.0157 | H** | 1.55 | | | |
| UP | 1.15 FPS | | | PI | 4.68 | | | |
| UB | 88.29 FPS | UB/UE | 0.866 | G | 45.38 | | | |
| CFE | 0.496 $*_{10}$-3 | CTEQ | 15.026 $*_{10}$-3 | GEQ | 13.84 | | | |
| CFLT | 0.241 $*_{10}$-3 | CFE/CFLT | 2.055 | GAMMA | -0.129 $*_{10}$-2 | | | |
| CFNM | 0.010 $*_{10}$-3 | CFE/CFNM | 49.595 | A | 0.938 $*_{10}$4 FT/SEC↑2 | | | |
| CDEL | 817.02 $*_{10}$-4 FT | DELTA | 27.30 $*_{10}$-4 FT | ALPHA0 | 0.371 | | | |
| DSTAR | 12.87 $*_{10}$-4 FT | REDSTAR | 801.0 | TH/UE*DUEDX | -0.331 $*_{10}$-3 | | | |
| THETA | 3.67 $*_{10}$-4 FT | RETHETA | 228.5 | K | -0.076 | | | |
| DELTA** | 5.69 $*_{10}$-4 FT | | | NU | 1.638 $*_{10}$-4 FT↑2/SEC | | | |

| Y*$_{10}$4 (FT) | U (FPS) | U/UE | Y/THETA | Z*TH/UE | YY | Y+ | U+ | (Y*)↑0.5 | U* | Y/CDEL | (UE-U)/UT | UC/UE |
|---|---|---|---|---|---|---|---|---|---|---|---|---|
| 0.0 | 0.00 | 0.000 | 0.000 | 0.057 | 0.00 | 0.00 | 0.00 | 0.00 | 0.00 | 0.0000 | 63.50 | 0.000 |
| 1.8 | 2.73 | 0.027 | 0.494 | 0.052 | 1.70 | 1.78 | 1.70 | 1.13 | 2.36 | 0.0022 | 61.81 | 0.040 |
| 2.8 | 4.13 | 0.041 | 0.768 | 0.067 | 3.01 | 2.76 | 2.57 | 1.41 | 3.58 | 0.0034 | 60.93 | 0.070 |
| 5.3 | 11.79 | 0.116 | 1.453 | 0.141 | 8.26 | 5.23 | 7.34 | 1.94 | 10.22 | 0.0065 | 56.16 | 0.151 |
| 7.9 | 23.88 | 0.234 | 2.139 | 0.198 | 14.40 | 7.70 | 14.87 | 2.35 | 20.69 | 0.0096 | 48.63 | 0.251 |
| 10.4 | 39.52 | 0.387 | 2.825 | 0.225 | 20.25 | 10.16 | 24.60 | 2.70 | 34.24 | 0.0127 | 38.90 | 0.370 |
| 12.9 | 55.35 | 0.543 | 3.510 | 0.211 | 24.38 | 12.63 | 34.46 | 3.01 | 47.96 | 0.0158 | 29.04 | 0.500 |
| 15.4 | 69.03 | 0.677 | 4.196 | 0.178 | 26.76 | 15.10 | 42.98 | 3.29 | 59.81 | 0.0189 | 20.52 | 0.632 |
| 17.9 | 80.24 | 0.787 | 4.881 | 0.145 | 28.14 | 17.57 | 49.95 | 3.55 | 69.52 | 0.0219 | 13.55 | 0.755 |
| 20.4 | 89.37 | 0.876 | 5.567 | 0.100 | 26.64 | 20.03 | 55.64 | 3.79 | 77.43 | 0.0250 | 7.86 | 0.861 |
| 23.0 | 94.25 | 0.924 | 6.253 | 0.060 | 23.15 | 22.50 | 58.68 | 4.02 | 81.66 | 0.0281 | 4.83 | 0.940 |
| 28.0 | 99.91 | 0.980 | 7.624 | 0.025 | 18.30 | 27.44 | 62.20 | 4.44 | 86.56 | 0.0343 | 1.30 | 1.000 |
| 33.0 | 101.31 | 0.993 | 8.995 | 0.007 | 11.75 | 32.37 | 63.07 | 4.82 | 87.77 | 0.0404 | 0.43 | 0.917 |
| 38.1 | 102.00 | 1.000 | 10.366 | 0.000 | 0.00 | 37.30 | 63.50 | 5.18 | 88.38 | 0.0466 | 0.00 | 0.722 |

X/C = 0.60 22.0 INS THROTTLE 500.0 RPM

| | | | | | | | | |
|---|---|---|---|---|---|---|---|---|
| UE | 108.39 FPS | DUEDX | -97.0 /SEC | H | 3.37 | | | |
| UT | 1.77 FPS | UT/UE | 0.0163 | H** | 1.54 | | | |
| UP | 1.20 FPS | | | PI | 3.67 | | | |
| UB | 91.75 FPS | UB/UE | 0.847 | G | 43.01 | | | |
| CFE | 0.534 $*_{10}$-3 | CTEQ | 14.534 $*_{10}$-3 | GEQ | 12.58 | | | |
| CFLT | 0.305 $*_{10}$-3 | CFE/CFLT | 1.752 | GAMMA | -0.112 $*_{10}$-2 | | | |
| CFNM | 0.010 $*_{10}$-3 | CFE/CFNM | 53.419 | A | 1.051 $*_{10}$4 FT/SEC↑2 | | | |
| CDEL | 670.88 $*_{10}$-4 FT | DELTA | 23.67 $*_{10}$-4 FT | ALPHA0 | 0.311 | | | |
| DSTAR | 10.96 $*_{10}$-4 FT | REDSTAR | 721.7 | TH/UE*DUEDX | -0.291 $*_{10}$-3 | | | |
| THETA | 3.26 $*_{10}$-4 FT | RETHETA | 214.4 | K | -0.062 | | | |
| DELTA** | 5.03 $*_{10}$-4 FT | | | NU | 1.647 $*_{10}$-4 FT↑2/SEC | | | |

| Y*$_{10}$4 (FT) | U (FPS) | U/UE | Y/THETA | Z*TH/UE | YY | Y+ | U+ | (Y*)↑0.5 | U* | Y/CDEL | (UE-U)/UT | UC/UE |
|---|---|---|---|---|---|---|---|---|---|---|---|---|
| 0.0 | 0.00 | 0.000 | 0.000 | 0.057 | 0.00 | 0.00 | 0.00 | 0.00 | 0.00 | 0.0000 | 61.19 | 0.000 |
| 1.8 | 4.12 | 0.038 | 0.556 | 0.079 | 2.30 | 1.95 | 2.33 | 1.15 | 3.43 | 0.0027 | 58.86 | 0.063 |
| 2.8 | 6.99 | 0.064 | 0.865 | 0.101 | 4.03 | 3.03 | 3.95 | 1.43 | 5.82 | 0.0042 | 57.24 | 0.098 |
| 5.3 | 18.65 | 0.172 | 1.638 | 0.171 | 9.91 | 5.74 | 10.53 | 1.97 | 15.53 | 0.0080 | 50.66 | 0.196 |
| 7.9 | 35.60 | 0.328 | 2.411 | 0.209 | 16.14 | 8.45 | 20.10 | 2.39 | 29.65 | 0.0117 | 41.09 | 0.319 |
| 10.4 | 53.65 | 0.495 | 3.183 | 0.210 | 21.37 | 11.15 | 30.29 | 2.75 | 44.68 | 0.0155 | 30.90 | 0.462 |
| 12.9 | 70.80 | 0.653 | 3.956 | 0.184 | 24.82 | 13.86 | 39.97 | 3.07 | 58.96 | 0.0192 | 21.22 | 0.611 |
| 15.4 | 84.42 | 0.779 | 4.729 | 0.144 | 26.28 | 16.57 | 47.66 | 3.35 | 70.30 | 0.0230 | 13.53 | 0.752 |
| 17.9 | 94.92 | 0.876 | 5.502 | 0.095 | 24.88 | 19.28 | 53.59 | 3.61 | 79.05 | 0.0267 | 7.60 | 0.871 |
| 20.4 | 100.39 | 0.926 | 6.274 | 0.061 | 22.68 | 21.98 | 56.67 | 3.86 | 83.61 | 0.0305 | 4.51 | 0.956 |
| 23.0 | 105.13 | 0.970 | 7.047 | 0.044 | 21.60 | 24.69 | 59.35 | 4.09 | 87.55 | 0.0342 | 1.84 | 0.997 |
| 28.0 | 108.20 | 0.998 | 8.592 | 0.010 | 12.41 | 30.10 | 61.08 | 4.52 | 90.11 | 0.0417 | 0.11 | 0.939 |
| 33.0 | 108.39 | 1.000 | 10.138 | 0.000 | 0.00 | 35.52 | 61.19 | 4.91 | 90.27 | 0.0492 | 0.00 | 0.727 |

X/C = 0.70 4.8 INS THROTTLE 500.0 RPM

| | | | | | |
|---|---|---|---|---|---|
| UE | 70.56 FPS | DUEDX | -167.0 /SEC | H | 1.94 |
| UT | 2.17 FPS | UT/UE | 0.0307 | H** | 1.68 |
| UP | 1.24 FPS | | | PI | 5.46 |
| UB | 33.21 FPS | UB/UE | 0.471 | G | 15.78 |
| CFE | 1.867 $*_{10}$-3 | CFEQ | 6.837 $*_{10}$-3 | GEQ | 14.75 |
| CFLT | 2.266 $*_{10}$-3 | CFE/CFLT | 0.833 | GAMMA | -1.248 $*_{10}$-2 |
| CFNM | 2.545 $*_{10}$-3 | CFE/CFNM | 0.742 | A | 1.178 $*_{10}$4 FT/SEC↑2 |
| CDEL | 708.65 $*_{10}$-4 FT | DELTA | 70.16 $*_{10}$-4 FT | ALPHA0 | 0.188 |
| DSTAR | 21.77 $*_{10}$-4 FT | REDSTAR | 946.6 | TH/UE*DUEDX | -2.655 $*_{10}$-3 |
| THETA | 11.22 $*_{10}$-4 FT | RETHETA | 487.9 | K | -1.296 |
| DELTA** | 18.86 $*_{10}$-4 FT | | | NU | 1.623 $*_{10}$-4 FT↑2/SEC |

| Y*$_{10}$4 (FT) | U (FPS) | U/UE | Y/THETA | Z*TH/UE | YY | Y+ | U+ | (Y*)↑0.5 | U* | Y/CDEL | (UE-U)/UT | UC/UE |
|---|---|---|---|---|---|---|---|---|---|---|---|---|
| 0.0 | 0.00 | 0.000 | 0.000 | 0.460 | 0.00 | 0.00 | 0.00 | 0.00 | 0.00 | 0.0000 | 32.56 | 0.000 |
| 2.0 | 5.97 | 0.085 | 0.181 | 0.473 | 2.76 | 2.72 | 2.76 | 1.25 | 4.81 | 0.0029 | 29.80 | 0.265 |
| 3.6 | 10.68 | 0.151 | 0.321 | 0.463 | 4.82 | 4.81 | 4.93 | 1.66 | 8.61 | 0.0051 | 27.63 | 0.310 |
| 6.2 | 17.85 | 0.253 | 0.553 | 0.412 | 7.85 | 8.29 | 8.24 | 2.18 | 14.39 | 0.0088 | 24.32 | 0.357 |
| 8.8 | 24.21 | 0.343 | 0.786 | 0.352 | 10.30 | 11.78 | 11.17 | 2.60 | 19.51 | 0.0124 | 21.38 | 0.392 |
| 11.4 | 29.42 | 0.417 | 1.018 | 0.361 | 13.51 | 15.26 | 13.57 | 2.96 | 23.70 | 0.0161 | 18.98 | 0.424 |
| 14.0 | 36.04 | 0.511 | 1.251 | 0.349 | 16.33 | 18.74 | 16.63 | 3.28 | 29.04 | 0.0198 | 15.93 | 0.454 |
| 16.6 | 40.88 | 0.579 | 1.483 | 0.243 | 16.13 | 22.23 | 18.86 | 3.57 | 32.93 | 0.0235 | 13.70 | 0.484 |
| 19.2 | 44.00 | 0.624 | 1.716 | 0.186 | 16.34 | 25.71 | 20.30 | 3.84 | 35.45 | 0.0272 | 12.25 | 0.515 |
| 24.5 | 49.79 | 0.706 | 2.181 | 0.143 | 18.24 | 32.68 | 22.98 | 4.33 | 40.12 | 0.0345 | 9.58 | 0.578 |
| 29.7 | 53.41 | 0.757 | 2.646 | 0.088 | 17.35 | 39.65 | 24.64 | 4.77 | 43.03 | 0.0419 | 7.92 | 0.644 |
| 34.9 | 55.58 | 0.788 | 3.111 | 0.070 | 18.18 | 46.62 | 25.64 | 5.17 | 44.78 | 0.0492 | 6.91 | 0.710 |
| 45.3 | 60.68 | 0.860 | 4.041 | 0.059 | 21.76 | 60.55 | 28.00 | 5.89 | 48.89 | 0.0640 | 4.56 | 0.836 |
| 55.8 | 63.37 | 0.898 | 4.971 | 0.042 | 22.38 | 74.49 | 29.24 | 6.53 | 51.06 | 0.0787 | 3.32 | 0.936 |
| 66.2 | 66.13 | 0.937 | 5.900 | 0.031 | 23.07 | 88.42 | 30.51 | 7.12 | 53.28 | 0.0934 | 2.04 | 0.992 |
| 76.6 | 67.48 | 0.956 | 6.830 | 0.020 | 21.38 | 102.36 | 31.14 | 7.66 | 54.37 | 0.1081 | 1.42 | 0.997 |
| 87.1 | 68.76 | 0.975 | 7.760 | 0.022 | 25.17 | 116.30 | 31.73 | 8.16 | 55.40 | 0.1229 | 0.83 | 0.952 |
| 97.5 | 70.31 | 0.997 | 8.690 | 0.014 | 22.46 | 130.23 | 32.44 | 8.64 | 56.65 | 0.1376 | 0.11 | 0.869 |
| 107.9 | 70.56 | 1.000 | 9.620 | 0.000 | 0.00 | 144.17 | 32.56 | 9.09 | 56.85 | 0.1523 | 0.00 | 0.769 |

X/C = 0.70 5.2 INS THROTTLE 500.0 RPM

| | | | | | |
|---|---|---|---|---|---|
| UE | 75.81 FPS | DUEDX | -186.0 /SEC | H | 2.07 |
| UT | 2.14 FPS | UT/UE | 0.0282 | H** | 1.67 |
| UP | 1.32 FPS | | | PI | 6.37 |
| UB | 40.22 FPS | UB/UE | 0.531 | G | 18.38 |
| CFE | 1.587 *10-3 | CTEQ | 7.831 *10-3 | GEQ | 15.74 |
| CFLT | 1.866 *10-3 | CFE/CFLT | 0.850 | GAMMA | -1.130 *10-2 |
| CFNM | 2.123 *10-3 | CFE/CFNM | 0.747 | A | 1.410 *10↑4 FT/SEC↑2 |
| CDEL | 731.15 *10-4 FT | DELTA | 61.67 *10-4 FT | ALPHA0 | 0.236 |
| DSTAR | 20.60 *10-4 FT | REDSTAR | 958.2 | TH/UE*DUEDX | -2.437 *10-3 |
| THETA | 9.93 *10-4 FT | RETHETA | 462.1 | K | -1.126 |
| DELTA** | 16.58 *10-4 FT | | | NU | 1.630 *10-4 FT↑2/SEC |

| Y*10↑4 (FT) | U (FPS) | U/UE | Y/THETA | Z*TH/UE | YY | Y+ | U+ | (Y*)↑0.5 | U* | Y/CDEL | (UE-U)/UT | UC/UE |
|---|---|---|---|---|---|---|---|---|---|---|---|---|
| 0.0 | 0.00 | 0.000 | 0.000 | 0.367 | 0.00 | 0.00 | 0.00 | 0.00 | 0.00 | 0.0000 | 35.50 | 0.000 |
| 1.9 | 5.37 | 0.071 | 0.194 | 0.363 | 2.52 | 2.53 | 2.52 | 1.25 | 4.07 | 0.0026 | 32.98 | 0.233 |
| 3.5 | 9.69 | 0.128 | 0.352 | 0.360 | 4.54 | 4.58 | 4.54 | 1.68 | 7.35 | 0.0048 | 30.96 | 0.276 |
| 6.1 | 16.83 | 0.222 | 0.615 | 0.344 | 7.74 | 8.00 | 7.88 | 2.22 | 12.76 | 0.0083 | 27.62 | 0.323 |
| 8.7 | 23.38 | 0.308 | 0.877 | 0.323 | 10.71 | 11.42 | 10.95 | 2.66 | 17.72 | 0.0119 | 24.55 | 0.361 |
| 11.3 | 29.68 | 0.392 | 1.140 | 0.337 | 14.22 | 14.83 | 13.90 | 3.03 | 22.50 | 0.0155 | 21.60 | 0.396 |
| 13.9 | 36.80 | 0.485 | 1.402 | 0.314 | 16.89 | 18.25 | 17.23 | 3.36 | 27.89 | 0.0191 | 18.27 | 0.431 |
| 16.5 | 42.19 | 0.557 | 1.665 | 0.260 | 18.26 | 21.67 | 19.76 | 3.66 | 31.97 | 0.0226 | 15.74 | 0.468 |
| 19.1 | 47.16 | 0.622 | 1.928 | 0.225 | 19.67 | 25.09 | 22.08 | 3.94 | 35.74 | 0.0262 | 13.42 | 0.506 |
| 24.4 | 54.18 | 0.715 | 2.453 | 0.152 | 20.54 | 31.93 | 25.37 | 4.44 | 41.06 | 0.0333 | 10.13 | 0.585 |
| 29.6 | 59.24 | 0.781 | 2.978 | 0.104 | 20.65 | 38.76 | 27.74 | 4.89 | 44.89 | 0.0405 | 7.76 | 0.667 |
| 34.8 | 62.46 | 0.824 | 3.503 | 0.075 | 20.58 | 45.60 | 29.25 | 5.31 | 47.34 | 0.0476 | 6.25 | 0.749 |
| 45.2 | 67.41 | 0.889 | 4.554 | 0.050 | 21.80 | 59.27 | 31.57 | 6.05 | 51.09 | 0.0619 | 3.93 | 0.891 |
| 55.7 | 70.36 | 0.928 | 5.604 | 0.027 | 19.82 | 72.94 | 32.95 | 6.71 | 53.32 | 0.0761 | 2.55 | 0.981 |
| 66.1 | 71.72 | 0.946 | 6.655 | 0.022 | 21.31 | 86.62 | 33.59 | 7.32 | 54.35 | 0.0904 | 1.91 | 0.998 |
| 76.5 | 73.90 | 0.975 | 7.705 | 0.020 | 23.34 | 100.29 | 34.61 | 7.87 | 56.00 | 0.1047 | 0.89 | 0.942 |
| 87.0 | 74.89 | 0.988 | 8.756 | 0.010 | 19.07 | 113.96 | 35.07 | 8.39 | 56.75 | 0.1189 | 0.43 | 0.832 |
| 97.4 | 75.53 | 0.996 | 9.806 | 0.006 | 16.03 | 127.63 | 35.37 | 8.88 | 57.24 | 0.1332 | 0.13 | 0.701 |
| 107.8 | 75.81 | 1.000 | 10.857 | 0.000 | 0.00 | 141.31 | 35.50 | 9.34 | 57.45 | 0.1475 | 0.00 | 0.587 |

X/C = 0.70 6.0 INS THROTTLE 500.0 RPM

| | | | | | |
|---|---|---|---|---|---|
| UE | 79.86 FPS | DUEDX | -130.0 /SEC | H | 2.12 |
| UT | 2.49 FPS | UT/UE | 0.0312 | H** | 1.66 |
| UP | 1.19 FPS | | | PI | 2.97 |
| UB | 42.17 FPS | UB/UE | 0.528 | G | 16.98 |
| CFE | 1.941 *10-3 | CTEQ | 8.164 *10-3 | GEQ | 11.63 |
| CFLT | 1.788 *10-3 | CFE/CFLT | 1.086 | GAMMA | -0.608 *10-2 |
| CFNM | 2.081 *10-3 | CFE/CFNM | 0.933 | A | 1.038 *10^4 FT/SEC↑2 |
| CDEL | 567.74 *10-4 FT | DELTA | 52.02 *10-4 FT | ALPHA0 | 0.111 |
| DSTAR | 17.69 *10-4 FT | REDSTAR | 861.0 | TH/UE*DUEDX | -1.356 *10-3 |
| THETA | 8.33 *10-4 FT | RETHETA | 405.5 | K | -0.550 |
| DELTA** | 13.84 *10-4 FT | | | NU | 1.641 *10-4 FT↑2/SEC |

| Y*10^4 (FT) | U (FPS) | U/UE | Y/THETA | Z*TH/UE | YY | Y+ | U+ | (Y*)↑0.5 | U* | Y/CDEL | (UE-U)/UT | UC/UE |
|---|---|---|---|---|---|---|---|---|---|---|---|---|
| 0.0 | 0.00 | 0.000 | 0.000 | 0.394 | 0.00 | 0.00 | 0.00 | 0.00 | 0.00 | 0.0000 | 32.10 | 0.000 |
| 1.9 | 6.62 | 0.083 | 0.225 | 0.341 | 2.65 | 2.85 | 2.66 | 1.17 | 5.54 | 0.0033 | 29.44 | 0.221 |
| 3.4 | 11.41 | 0.143 | 0.413 | 0.326 | 4.75 | 5.22 | 4.59 | 1.58 | 9.56 | 0.0061 | 27.51 | 0.271 |
| 6.1 | 19.81 | 0.248 | 0.726 | 0.330 | 8.40 | 9.18 | 7.96 | 2.10 | 16.59 | 0.0107 | 24.13 | 0.326 |
| 8.7 | 27.90 | 0.349 | 1.040 | 0.267 | 10.82 | 13.13 | 11.21 | 2.51 | 23.36 | 0.0153 | 20.88 | 0.371 |
| 11.3 | 33.18 | 0.415 | 1.353 | 0.286 | 14.57 | 17.09 | 13.34 | 2.86 | 27.78 | 0.0198 | 18.76 | 0.415 |
| 13.9 | 42.21 | 0.529 | 1.666 | 0.289 | 18.02 | 21.04 | 16.96 | 3.18 | 35.34 | 0.0244 | 15.13 | 0.459 |
| 16.5 | 47.62 | 0.596 | 1.979 | 0.229 | 19.06 | 25.00 | 19.14 | 3.46 | 39.87 | 0.0290 | 12.96 | 0.505 |
| 19.1 | 53.65 | 0.672 | 2.292 | 0.209 | 21.12 | 28.96 | 21.56 | 3.73 | 44.92 | 0.0336 | 10.53 | 0.553 |
| 24.3 | 60.94 | 0.763 | 2.918 | 0.128 | 21.01 | 36.87 | 24.49 | 4.21 | 51.03 | 0.0428 | 7.61 | 0.651 |
| 29.5 | 66.44 | 0.832 | 3.545 | 0.094 | 21.87 | 44.78 | 26.70 | 4.64 | 55.63 | 0.0520 | 5.39 | 0.749 |
| 34.7 | 70.33 | 0.881 | 4.171 | 0.066 | 21.50 | 52.69 | 28.27 | 5.03 | 58.89 | 0.0612 | 3.83 | 0.838 |
| 45.2 | 74.42 | 0.932 | 5.423 | 0.030 | 18.88 | 68.51 | 29.91 | 5.73 | 62.32 | 0.0796 | 2.18 | 0.967 |
| 55.6 | 76.31 | 0.956 | 6.676 | 0.017 | 17.73 | 84.33 | 30.67 | 6.36 | 63.90 | 0.0979 | 1.43 | 0.999 |
| 66.0 | 77.90 | 0.976 | 7.928 | 0.010 | 15.79 | 100.16 | 31.31 | 6.93 | 65.23 | 0.1163 | 0.79 | 0.929 |
| 76.5 | 78.27 | 0.980 | 9.181 | 0.007 | 15.71 | 115.98 | 31.46 | 7.46 | 65.54 | 0.1347 | 0.64 | 0.790 |
| 86.9 | 79.35 | 0.994 | 10.433 | 0.008 | 18.75 | 131.80 | 31.89 | 7.95 | 66.44 | 0.1531 | 0.21 | 0.640 |
| 97.3 | 79.86 | 1.000 | 11.686 | 0.000 | 0.00 | 147.62 | 32.10 | 8.42 | 66.87 | 0.1715 | 0.00 | 0.541 |

X/C = 0.70 8.0 INS THROTTLE 500.0 RPM

| | | | | | | | | |
|---|---|---|---|---|---|---|---|---|
| UE | 88.43 | FPS | DUEDX | -233.0 | /SEC | H | 3.20 | |
| UT | 2.11 | FPS | UT/UE | 0.0239 | | H** | 1.54 | |
| UP | 1.50 | FPS | | | | PI | 8.60 | |
| UB | 69.29 | FPS | UB/UE | 0.784 | | G | 28.81 | |
| CFE | 1.140 | *10-3 | CTEQ | 13.892 | *10-3 | GEQ | 17.99 | |
| CFLT | 0.354 | *10-3 | CFE/CFLT | 3.220 | | GAMMA | -0.645 | *10-2 |
| CFNM | 0.010 | *10-3 | CFE/CFNM | 114.012 | | A | 2.060 | *10^4 FT/SEC^2 |
| CDEL | 779.63 | *10-4 FT | DELTA | 41.36 | *10-4 FT | ALPHA0 | 0.357 | |
| DSTAR | 18.61 | *10-4 FT | REDSTAR | 1010.7 | | TH/UE*DUEDX | -1.531 | *10-3 |
| THETA | 5.81 | *10-4 FT | RETHETA | 315.5 | | K | -0.483 | |
| DELTA** | 8.94 | *10-4 FT | | | | NU | 1.629 | *10-4 FT^2/SEC |

| Y*10^4 (FT) | U (FPS) | U/UE | Y/THETA | Z*TH/UE | YY | Y+ | U+ | (Y*)^0.5 | U* | Y/CDEL | (UE-U)/UT | UC/UE |
|---|---|---|---|---|---|---|---|---|---|---|---|---|
| 0.0 | 0.00 | 0.000 | 0.000 | 0.180 | 0.00 | 0.00 | 0.00 | 0.00 | 0.00 | 0.0000 | 41.88 | 0.000 |
| 1.9 | 4.31 | 0.049 | 0.323 | 0.121 | 2.00 | 2.43 | 2.04 | 1.31 | 2.88 | 0.0024 | 39.84 | 0.040 |
| 3.4 | 6.62 | 0.075 | 0.593 | 0.099 | 3.31 | 4.46 | 3.13 | 1.78 | 4.42 | 0.0044 | 38.75 | 0.085 |
| 6.1 | 10.64 | 0.120 | 1.042 | 0.092 | 5.62 | 7.85 | 5.04 | 2.36 | 7.10 | 0.0078 | 36.85 | 0.145 |
| 8.7 | 13.94 | 0.158 | 1.491 | 0.147 | 10.15 | 11.23 | 6.60 | 2.82 | 9.31 | 0.0111 | 35.28 | 0.207 |
| 11.3 | 22.30 | 0.252 | 1.940 | 0.191 | 15.07 | 14.61 | 10.56 | 3.22 | 14.90 | 0.0145 | 31.32 | 0.276 |
| 13.9 | 29.15 | 0.330 | 2.388 | 0.212 | 19.53 | 17.99 | 13.81 | 3.57 | 19.47 | 0.0178 | 28.08 | 0.351 |
| 16.5 | 39.13 | 0.442 | 2.837 | 0.250 | 25.22 | 21.37 | 18.53 | 3.89 | 26.13 | 0.0211 | 23.35 | 0.432 |
| 19.1 | 49.03 | 0.554 | 3.286 | 0.226 | 27.75 | 24.75 | 23.22 | 4.19 | 32.75 | 0.0245 | 18.66 | 0.516 |
| 21.7 | 57.07 | 0.645 | 3.735 | 0.190 | 28.91 | 28.13 | 27.03 | 4.47 | 38.12 | 0.0278 | 14.85 | 0.601 |
| 24.3 | 64.10 | 0.725 | 4.184 | 0.168 | 30.42 | 31.52 | 30.36 | 4.73 | 42.82 | 0.0312 | 11.52 | 0.684 |
| 29.5 | 75.90 | 0.858 | 5.082 | 0.119 | 31.08 | 38.28 | 35.95 | 5.21 | 50.70 | 0.0379 | 5.93 | 0.832 |
| 34.7 | 82.92 | 0.938 | 5.980 | 0.068 | 27.61 | 45.04 | 39.28 | 5.65 | 55.39 | 0.0446 | 2.61 | 0.941 |
| 45.2 | 87.03 | 0.984 | 7.776 | 0.016 | 17.49 | 58.57 | 41.22 | 6.44 | 58.13 | 0.0579 | 0.66 | 0.989 |
| 55.6 | 88.02 | 0.995 | 9.572 | 0.004 | 11.29 | 72.09 | 41.69 | 7.15 | 58.79 | 0.0713 | 0.19 | 0.809 |
| 66.0 | 88.43 | 1.000 | 11.368 | 0.000 | 0.00 | 85.62 | 41.88 | 7.79 | 59.07 | 0.0847 | 0.00 | 0.518 |



APPENDIX H (cont.)

X/C = 0.70 10.0 INS THROTTLE 5000 RPM

| | | | | | | | |
|---|---|---|---|---|---|---|---|
| UE | 94.30 FPS | DUEDX | -221.0 /SEC | H | 3.96 | | |
| UT | 1.72 FPS | UT/UE | 0.0183 | H** | 1.54 | | |
| UP | 1.50 FPS | | | PI | 13.10 | | |
| UB | 84.39 FPS | UB/UE | 0.895 | G | 40.88 | | |
| CFE | 0.668 *10-3 | CTEQ | 16.424 *10-3 | GEQ | 21.86 | | |
| CFLT | 0.113 *10-3 | CFE/CFLT | 5.894 | GAMMA | -0.450 | *10-2 | |
| CFNM | 0.010 *10-3 | CFE/CFNM | 66.835 | A | 2.084 | *10↑4 | FT/SEC↑2 |
| CDEL | 1022.04 *10-4 FT | DELTA | 37.97 *10-4 FT | ALPHA0 | 0.660 | | |
| DSTAR | 18.68 *10-4 FT | REDSTAR | 1085.6 | TH/UE*DUEDX | -1.106 | *10-3 | |
| THETA | 4.72 *10-4 FT | RETHETA | 274.3 | K | -0.303 | | |
| DELTA** | 7.26 *10-4 FT | | | NU | 1.623 | *10-4 | FT↑2/SEC |

| Y*10↑4 (FT) | U (FPS) | U/UE | Y/THETA | Z*TH/UE | YY | Y+ | U+ | (Y*)↑0.5 | U* | Y/CDEL | (UE-U)/UT | UC/UE |
|---|---|---|---|---|---|---|---|---|---|---|---|---|
| 0.0 | 0.00 | 0.000 | 0.000 | 0.092 | 0.00 | 0.00 | 0.00 | 0.00 | 0.00 | 0.0000 | 54.70 | 0.000 |
| 1.4 | 1.82 | 0.019 | 0.287 | 0.043 | 0.99 | 1.44 | 1.06 | 1.12 | 1.22 | 0.0013 | 53.65 | -0.041 |
| 2.4 | 2.33 | 0.025 | 0.508 | 0.024 | 1.30 | 2.55 | 1.35 | 1.49 | 1.55 | 0.0023 | 53.35 | -0.009 |
| 3.4 | 2.82 | 0.030 | 0.729 | 0.028 | 2.04 | 3.66 | 1.64 | 1.78 | 1.88 | 0.0034 | 53.07 | 0.016 |
| 6.1 | 4.94 | 0.052 | 1.282 | 0.065 | 5.42 | 6.43 | 2.87 | 2.37 | 3.29 | 0.0059 | 51.84 | 0.078 |
| 8.7 | 9.61 | 0.102 | 1.834 | 0.115 | 10.30 | 9.20 | 5.57 | 2.83 | 6.40 | 0.0085 | 49.13 | 0.149 |
| 11.3 | 16.93 | 0.180 | 2.387 | 0.167 | 16.17 | 11.97 | 9.82 | 3.23 | 11.28 | 0.0110 | 44.88 | 0.232 |
| 13.9 | 27.04 | 0.287 | 2.939 | 0.227 | 23.18 | 14.74 | 15.69 | 3.58 | 18.01 | 0.0136 | 39.02 | 0.324 |
| 16.5 | 40.55 | 0.430 | 3.492 | 0.243 | 28.52 | 17.51 | 23.52 | 3.90 | 27.01 | 0.0161 | 31.18 | 0.423 |
| 19.1 | 52.38 | 0.555 | 4.044 | 0.216 | 31.12 | 20.28 | 30.39 | 4.20 | 34.90 | 0.0187 | 24.32 | 0.526 |
| 21.7 | 63.04 | 0.668 | 4.597 | 0.192 | 33.38 | 23.05 | 36.57 | 4.48 | 41.99 | 0.0212 | 18.14 | 0.627 |
| 24.3 | 72.42 | 0.768 | 5.149 | 0.159 | 34.01 | 25.82 | 42.01 | 4.74 | 48.24 | 0.0238 | 12.70 | 0.723 |
| 29.5 | 84.61 | 0.897 | 6.254 | 0.082 | 29.61 | 31.36 | 49.08 | 5.23 | 56.37 | 0.0289 | 5.62 | 0.884 |
| 34.7 | 89.44 | 0.948 | 7.359 | 0.039 | 24.11 | 36.90 | 51.89 | 5.67 | 59.59 | 0.0340 | 2.82 | 0.980 |
| 40.0 | 92.77 | 0.984 | 8.464 | 0.023 | 21.18 | 42.44 | 53.81 | 6.08 | 61.80 | 0.0391 | 0.89 | 0.996 |
| 45.2 | 94.20 | 0.999 | 9.569 | 0.009 | 15.32 | 47.98 | 54.64 | 6.46 | 62.75 | 0.0442 | 0.06 | 0.931 |
| 55.6 | 94.30 | 1.000 | 11.779 | 0.000 | 0.00 | 59.07 | 54.70 | 7.17 | 62.82 | 0.0544 | 0.00 | 0.619 |



APPENDIX H (cont.)

X/C = 0.70 13.0 INS THROTTLE 500.0 RPM

| | | | | | | | | |
|---|---|---|---|---|---|---|---|---|
| UE | 96.68 | FPS | DUEDX | -149.0 | /SEC | H | 4.09 | |
| UT | 1.50 | FPS | UT/UE | 0.0155 | | H** | 1.54 | |
| UP | 1.32 | FPS | | | | PI | 11.26 | |
| UB | 89.10 | FPS | UB/UE | 0.922 | | G | 48.78 | |
| CFE | 0.480 | *10-3 | CTEQ | 16.795 | *10-3 | GEQ | 20.36 | |
| CFLT | 0.094 | *10-3 | CFE/CFLT | 5.114 | | GAMMA | -0.265 | *10-2 |
| CFNM | 0.010 | *10-3 | CFE/CFNM | 47.970 | | A | 1.441 | *10^4 FT/SEC^2 |
| CDEL | 1131.84 | *10-4 FT | DELTA | 35.16 | *10-4 FT | ALPHA0 | 0.691 | |
| DSTAR | 17.53 | *10-4 FT | REDSTAR | 1052.6 | | TH/UE*DUEDX | -0.660 | *10-3 |
| THETA | 4.29 | *10-4 FT | RETHETA | 257.4 | | K | -0.170 | |
| DELTA** | 6.61 | *10-4 FT | | | | NU | 1.610 | *10-4 FT^2/SEC |

| Y*10^4 (FT) | U (FPS) | U/UE | Y/THETA | Z*TH/UE | YY | Y+ | U+ | (Y*)^0.5 | U* | Y/CDEL | (UE-U)/UT | UC/UE |
|---|---|---|---|---|---|---|---|---|---|---|---|---|
| 0.0 | 0.00 | 0.000 | 0.000 | 0.062 | 0.00 | 0.00 | 0.00 | 0.00 | 0.00 | 0.0000 | 64.57 | 0.000 |
| 1.4 | 1.33 | 0.014 | 0.316 | 0.025 | 0.80 | 1.26 | 0.89 | 1.06 | 1.00 | 0.0012 | 63.68 | -0.041 |
| 2.4 | 1.59 | 0.016 | 0.560 | 0.017 | 1.16 | 2.23 | 1.06 | 1.40 | 1.20 | 0.0021 | 63.51 | -0.012 |
| 3.4 | 2.12 | 0.022 | 0.803 | 0.028 | 2.16 | 3.20 | 1.42 | 1.68 | 1.60 | 0.0030 | 63.15 | 0.012 |
| 6.1 | 4.57 | 0.047 | 1.412 | 0.070 | 5.99 | 5.63 | 3.05 | 2.23 | 3.45 | 0.0053 | 61.52 | 0.078 |
| 8.7 | 10.36 | 0.107 | 2.021 | 0.134 | 11.86 | 8.05 | 6.92 | 2.67 | 7.82 | 0.0077 | 57.65 | 0.157 |
| 11.3 | 20.31 | 0.210 | 2.629 | 0.180 | 17.87 | 10.48 | 13.57 | 3.04 | 15.35 | 0.0100 | 51.00 | 0.250 |
| 13.9 | 31.48 | 0.326 | 3.238 | 0.227 | 24.76 | 12.90 | 21.02 | 3.38 | 23.78 | 0.0123 | 43.55 | 0.354 |
| 16.5 | 47.06 | 0.487 | 3.846 | 0.239 | 30.17 | 15.33 | 31.43 | 3.68 | 35.55 | 0.0146 | 33.14 | 0.466 |
| 19.1 | 59.61 | 0.617 | 4.455 | 0.193 | 31.37 | 17.76 | 39.81 | 3.96 | 45.03 | 0.0169 | 24.76 | 0.578 |
| 21.7 | 69.73 | 0.721 | 5.064 | 0.173 | 33.79 | 20.18 | 46.57 | 4.22 | 52.68 | 0.0192 | 18.00 | 0.687 |
| 24.3 | 79.98 | 0.827 | 5.672 | 0.146 | 34.81 | 22.61 | 53.41 | 4.47 | 60.42 | 0.0215 | 11.16 | 0.786 |
| 29.5 | 90.65 | 0.938 | 6.889 | 0.061 | 27.38 | 27.46 | 60.54 | 4.93 | 68.48 | 0.0261 | 4.03 | 0.936 |
| 34.7 | 94.42 | 0.977 | 8.106 | 0.021 | 18.76 | 32.31 | 63.06 | 5.34 | 71.33 | 0.0307 | 1.51 | 0.999 |
| 40.0 | 95.54 | 0.988 | 9.324 | 0.007 | 12.67 | 37.16 | 63.81 | 5.73 | 72.18 | 0.0353 | 0.76 | 0.963 |
| 45.2 | 96.11 | 0.994 | 10.541 | 0.005 | 11.77 | 42.01 | 64.19 | 6.09 | 72.61 | 0.0399 | 0.38 | 0.837 |
| 50.4 | 96.68 | 1.000 | 11.758 | 0.000 | 0.00 | 46.86 | 64.57 | 6.44 | 73.04 | 0.0445 | 0.00 | 0.649 |



APPENDIX H (cont.)

X/C = 0.70 22.0 INS THROTTLE 500.0 RPM

| | | | | | | | | |
|---|---|---|---|---|---|---|---|---|
| UE | 102.94 | FPS | DUEDX | -123.0 | /SEC | H | 4.02 | |
| UT | 1.48 | FPS | UT/UE | 0.0144 | | H** | 1.51 | |
| UP | 1.27 | FPS | | | | PI | 8.53 | |
| UB | 94.92 | FPS | UB/UE | 0.922 | | G | 52.25 | |
| CFE | 0.413 | *10-3 | CTEQ | 16.609 | *10-3 | GEQ | 17.92 | |
| CFLT | 0.107 | *10-3 | CFE/CFLT | 3.852 | | GAMMA | -0.172 | *10-2 |
| CFNM | 0.010 | *10-3 | CFE/CFNM | 41.345 | | A | 1.266 | *10^4 FT/SEC^2 |
| CDEL | 1026.92 | *10-4 FT | DELTA | 29.76 | *10-4 FT | ALPHA0 | 0.632 | |
| DSTAR | 14.77 | *10-4 FT | REDSTAR | 939.4 | | TH/UE*DUEDX | -0.439 | *10-3 |
| THETA | 3.67 | *10-4 FT | RETHETA | 233.7 | | K | -0.103 | |
| DELTA** | 5.56 | *10-4 FT | | | | NU | 1.618 | *10-4 FT^2/SEC |

| Y*10^4 (FT) | U (FPS) | U/UE | Y/THETA | Z*TH/UE | YY | Y+ | U+ | (Y*)^0.5 | U* | Y/CDEL | (UE-U)/UT | UC/UE |
|---|---|---|---|---|---|---|---|---|---|---|---|---|
| 0.0 | 0.00 | 0.000 | 0.000 | 0.048 | 0.00 | 0.00 | 0.00 | 0.00 | 0.00 | 0.0000 | 69.55 | 0.000 |
| 1.4 | 1.73 | 0.017 | 0.369 | 0.043 | 1.17 | 1.24 | 1.17 | 1.03 | 1.37 | 0.0013 | 68.38 | -0.026 |
| 3.4 | 4.01 | 0.039 | 0.937 | 0.055 | 3.35 | 3.15 | 2.71 | 1.64 | 3.16 | 0.0034 | 66.84 | 0.032 |
| 6.1 | 9.44 | 0.092 | 1.648 | 0.094 | 7.73 | 5.54 | 6.38 | 2.18 | 7.43 | 0.0059 | 63.17 | 0.113 |
| 8.7 | 17.79 | 0.173 | 2.358 | 0.149 | 13.93 | 7.92 | 12.02 | 2.61 | 14.01 | 0.0084 | 57.53 | 0.214 |
| 11.3 | 31.28 | 0.304 | 3.068 | 0.200 | 20.98 | 10.31 | 21.14 | 2.97 | 24.63 | 0.0110 | 48.42 | 0.333 |
| 13.9 | 47.05 | 0.457 | 3.778 | 0.221 | 27.13 | 12.69 | 31.79 | 3.30 | 37.04 | 0.0135 | 37.76 | 0.463 |
| 16.5 | 63.56 | 0.617 | 4.488 | 0.201 | 30.76 | 15.08 | 42.94 | 3.60 | 50.04 | 0.0161 | 26.61 | 0.596 |
| 19.1 | 76.43 | 0.742 | 5.199 | 0.164 | 32.15 | 17.47 | 51.64 | 3.87 | 60.18 | 0.0186 | 17.91 | 0.722 |
| 21.7 | 87.49 | 0.850 | 5.909 | 0.130 | 32.56 | 19.85 | 59.11 | 4.13 | 68.89 | 0.0211 | 10.44 | 0.832 |
| 24.3 | 95.42 | 0.927 | 6.619 | 0.086 | 29.64 | 22.24 | 64.47 | 4.37 | 75.13 | 0.0237 | 5.08 | 0.919 |
| 29.5 | 101.32 | 0.984 | 8.039 | 0.026 | 19.70 | 27.01 | 68.46 | 4.81 | 79.78 | 0.0288 | 1.09 | 1.000 |
| 34.7 | 102.94 | 1.000 | 9.460 | 0.000 | 0.00 | 31.78 | 69.55 | 5.22 | 81.05 | 0.0338 | 0.00 | 0.943 |



APPENDIX H (cont.)

X/C = 0.80 4.8 INS THROTTLE 500.0 RPM

| | | | | | |
|---|---|---|---|---|---|
| UE | 64.76 FPS | DUEDX | -164.0 /SEC | H | 1.89 |
| UI | 1.66 FPS | UI/UE | 0.0256 | H** | 1.67 |
| UP | 1.20 FPS | | | PI | 11.97 |
| UB | 31.30 FPS | UB/UE | 0.483 | G | 18.41 |
| CFE | 1.312 $*_{10}$-3 | CTEQ | 6.495 $*_{10}$-3 | GEQ | 20.94 |
| CFLT | 2.253 $*_{10}$-3 | CFE/CFLT | 0.582 | GAMMA | -2.102 $*_{10}$-2 |
| CFNM | 2.420 $*_{10}$-3 | CFE/CFNM | 0.542 | A | 1.062 $*_{10}$4 FT/SEC↑2 |
| CDEL | 1210.50 $*_{10}$-4 FT | DELTA | 101.95 $*_{10}$-4 FT | ALPHA0 | 0.375 |
| DSTAR | 31.01 $*_{10}$-4 FT | REDSTAR | 1245.5 | TH/UE*DUEDX | -4.150 $*_{10}$-3 |
| THETA | 16.39 $*_{10}$-4 FT | RETHETA | 658.2 | K | -2.731 |
| DELTA** | 27.44 $*_{10}$-4 FT | | | NU | 1.612 $*_{10}$-4 FT↑2/SEC |

| Y*$_{10}$4 (FT) | U (FPS) | U/UE | Y/THETA | Z*IH/UE | YY | Y+ | U+ | (Y*)↑0.5 | U* | Y/CDEL | (UE-U)/UT | UC/UE |
|---|---|---|---|---|---|---|---|---|---|---|---|---|
| 0.0 | 0.00 | 0.000 | 0.000 | 0.432 | 0.00 | 0.00 | 0.00 | 0.00 | 0.00 | 0.0000 | 39.04 | 0.000 |
| 2.0 | 3.86 | 0.060 | 0.119 | 0.566 | 2.31 | 2.01 | 2.33 | 1.21 | 3.23 | 0.0016 | 36.71 | 0.270 |
| 3.0 | 6.38 | 0.098 | 0.184 | 0.614 | 3.70 | 3.10 | 3.84 | 1.50 | 5.33 | 0.0025 | 35.19 | 0.298 |
| 5.7 | 13.11 | 0.202 | 0.346 | 0.578 | 6.74 | 5.83 | 7.90 | 2.05 | 10.96 | 0.0047 | 31.14 | 0.340 |
| 8.3 | 18.47 | 0.285 | 0.507 | 0.449 | 8.71 | 8.55 | 11.13 | 2.48 | 15.44 | 0.0069 | 27.91 | 0.368 |
| 11.0 | 22.49 | 0.347 | 0.668 | 0.375 | 10.51 | 11.27 | 13.56 | 2.85 | 18.80 | 0.0090 | 25.48 | 0.391 |
| 13.6 | 26.32 | 0.406 | 0.830 | 0.339 | 12.40 | 13.99 | 15.87 | 3.18 | 22.00 | 0.0112 | 23.17 | 0.412 |
| 16.2 | 29.59 | 0.457 | 0.991 | 0.284 | 13.54 | 16.72 | 17.84 | 3.47 | 24.73 | 0.0134 | 21.20 | 0.432 |
| 21.5 | 34.31 | 0.530 | 1.314 | 0.227 | 16.06 | 22.16 | 20.68 | 4.00 | 28.67 | 0.0178 | 18.36 | 0.471 |
| 26.8 | 39.07 | 0.603 | 1.637 | 0.191 | 18.34 | 27.60 | 23.55 | 4.46 | 32.66 | 0.0222 | 15.49 | 0.511 |
| 32.1 | 42.28 | 0.653 | 1.960 | 0.142 | 18.94 | 33.05 | 25.48 | 4.88 | 35.34 | 0.0265 | 13.55 | 0.554 |
| 42.7 | 47.27 | 0.730 | 2.606 | 0.116 | 22.78 | 43.94 | 28.49 | 5.63 | 39.51 | 0.0353 | 10.55 | 0.643 |
| 53.3 | 51.99 | 0.803 | 3.252 | 0.092 | 25.32 | 54.83 | 31.34 | 6.29 | 43.45 | 0.0440 | 7.70 | 0.735 |
| 63.9 | 54.97 | 0.849 | 3.898 | 0.061 | 24.69 | 65.72 | 33.14 | 6.88 | 45.95 | 0.0528 | 5.90 | 0.823 |
| 74.5 | 57.09 | 0.882 | 4.543 | 0.060 | 28.51 | 76.61 | 34.41 | 7.43 | 47.72 | 0.0615 | 4.63 | 0.899 |
| 85.0 | 59.97 | 0.926 | 5.189 | 0.054 | 31.08 | 87.50 | 36.15 | 7.94 | 50.13 | 0.0702 | 2.89 | 0.957 |
| 106.2 | 62.10 | 0.959 | 6.481 | 0.020 | 23.61 | 109.28 | 37.43 | 8.88 | 51.91 | 0.0877 | 1.60 | 1.000 |
| 127.4 | 63.35 | 0.978 | 7.773 | 0.016 | 25.14 | 131.05 | 38.18 | 9.72 | 52.95 | 0.1052 | 0.85 | 0.943 |
| 148.5 | 64.76 | 1.000 | 9.064 | 0.000 | 0.00 | 152.83 | 39.04 | 10.50 | 54.13 | 0.1227 | 0.00 | 0.814 |

X/C = 0.80 5.2 INS THROTTLE 500.0 RPM

| | | | | | | | |
|---|---|---|---|---|---|---|---|
| UE | 69.68 FPS | DUEDX | -253.0 /SEC | H | 1.96 | | |
| UT | 1.80 FPS | UT/UE | 0.0259 | H** | 1.66 | | |
| UP | 1.42 FPS | | | PI | 15.98 | | |
| UB | 35.27 FPS | UB/UE | 0.506 | G | 18.91 | | |
| CFE | 1.341 *10-3 | CTEQ | 7.007 *10-3 | GEQ | 24.03 | | |
| CFLT | 2.036 *10-3 | CFE/CFLT | 0.659 | GAMMA | -2.761 *10-2 | | |
| CFNM | 2.197 *10-3 | CFE/CFNM | 0.610 | A | 1.763 *10↑4 FT/SEC↑2 | | |
| CDEL | 1139.93 *10-4 FT | DELTA | 93.35 *10-4 FT | ALPHA0 | 0.485 | | |
| DSTAR | 29.52 *10-4 FT | REDSTAR | 1272.1 | TH/UE*DUEDX | -5.469 *10-3 | | |
| THETA | 15.06 *10-4 FT | RETHETA | 649.2 | K | -3.551 | | |
| DELTA** | 25.01 *10-4 FT | | | NU | 1.617 *10-4 FT↑2/SEC | | |

| Y*10↑4 (FT) | U (FPS) | U/UE | Y/THETA | Z*TH/UE | YY | Y+ | U+ | (Y*)↑0.5 | U* | Y/CDEL | (UE-U)/UT | UC/UE |
|---|---|---|---|---|---|---|---|---|---|---|---|---|
| 0.0 | 0.00 | 0.000 | 0.000 | 0.435 | 0.00 | 0.00 | 0.00 | 0.00 | 0.00 | 0.0000 | 38.62 | 0.000 |
| 1.9 | 4.11 | 0.059 | 0.123 | 0.523 | 2.27 | 2.07 | 2.28 | 1.27 | 2.90 | 0.0016 | 36.34 | 0.247 |
| 2.9 | 6.79 | 0.097 | 0.193 | 0.547 | 3.64 | 3.25 | 3.76 | 1.60 | 4.79 | 0.0026 | 34.86 | 0.276 |
| 5.6 | 13.42 | 0.193 | 0.369 | 0.505 | 6.68 | 6.20 | 7.44 | 2.21 | 9.47 | 0.0049 | 31.18 | 0.320 |
| 8.2 | 19.16 | 0.275 | 0.544 | 0.429 | 9.09 | 9.15 | 10.62 | 2.68 | 13.51 | 0.0072 | 28.00 | 0.350 |
| 10.8 | 23.93 | 0.343 | 0.720 | 0.346 | 10.80 | 12.11 | 13.26 | 3.08 | 16.88 | 0.0095 | 25.36 | 0.375 |
| 13.5 | 27.63 | 0.397 | 0.896 | 0.283 | 12.14 | 15.06 | 15.31 | 3.44 | 19.49 | 0.0118 | 23.31 | 0.397 |
| 16.1 | 30.85 | 0.443 | 1.071 | 0.244 | 13.49 | 18.01 | 17.10 | 3.76 | 21.76 | 0.0142 | 21.52 | 0.419 |
| 21.4 | 35.91 | 0.515 | 1.423 | 0.216 | 16.86 | 23.92 | 19.90 | 4.34 | 25.33 | 0.0188 | 18.72 | 0.464 |
| 26.7 | 41.44 | 0.595 | 1.774 | 0.213 | 20.86 | 29.82 | 22.97 | 4.84 | 29.23 | 0.0234 | 15.65 | 0.511 |
| 32.0 | 46.33 | 0.665 | 2.125 | 0.173 | 22.53 | 35.73 | 25.68 | 5.30 | 32.68 | 0.0281 | 12.94 | 0.560 |
| 42.6 | 52.21 | 0.749 | 2.828 | 0.107 | 23.56 | 47.54 | 28.94 | 6.11 | 36.82 | 0.0374 | 9.68 | 0.663 |
| 53.2 | 56.80 | 0.815 | 3.530 | 0.083 | 25.86 | 59.35 | 31.48 | 6.83 | 40.06 | 0.0467 | 7.14 | 0.766 |
| 63.8 | 60.30 | 0.865 | 4.233 | 0.059 | 26.20 | 71.16 | 33.42 | 7.48 | 42.53 | 0.0559 | 5.20 | 0.861 |
| 74.3 | 62.58 | 0.898 | 4.936 | 0.049 | 27.84 | 82.97 | 34.68 | 8.07 | 44.13 | 0.0652 | 3.94 | 0.936 |
| 84.9 | 65.10 | 0.934 | 5.638 | 0.044 | 30.13 | 94.78 | 36.08 | 8.63 | 45.91 | 0.0745 | 2.54 | 0.984 |
| 106.1 | 67.93 | 0.975 | 7.043 | 0.022 | 26.43 | 118.40 | 37.65 | 9.65 | 47.91 | 0.0931 | 0.97 | 0.985 |
| 127.3 | 69.35 | 0.995 | 8.449 | 0.009 | 20.38 | 142.02 | 38.43 | 10.56 | 48.91 | 0.1116 | 0.19 | 0.872 |
| 148.4 | 69.68 | 1.000 | 9.854 | 0.000 | 0.00 | 165.64 | 38.62 | 11.41 | 49.15 | 0.1302 | 0.00 | 0.706 |



APPENDIX H (cont.)

X/C = 0.80 6.0 INS THROTTLE 500.0 RPM

| | | | | | |
|---|---|---|---|---|---|
| UE | 75.10 FPS | DUEDX | -219.0 /SEC | H | 2.09 |
| UT | 2.07 FPS | UT/UE | 0.0276 | H** | 1.64 |
| UP | 1.39 FPS | | | PI | 8.43 |
| UB | 40.56 FPS | UB/UE | 0.540 | G | 18.95 |
| CFE | 1.519 *10-3 | CTEQ | 7.970 *10-3 | GEO | 17.82 |
| CFLT | 1.787 *10-3 | CFE/CFLT | 0.850 | GAMMA | -1.437 *10-2 |
| CFNM | 2.015 *10-3 | CFE/CFNM | 0.754 | A | 1.645 *10↑4 FT/SEC↑2 |
| CDEL | 797.12 *10-4 FT | DELTA | 65.13 *10-4 FT | ALPHA0 | 0.301 |
| DSTAR | 21.97 *10-4 FT | REDSTAR | 1017.0 | TH/UE*DUEDX | -3.060 *10-3 |
| THETA | 10.50 *10-4 FT | RETHETA | 485.9 | K | -1.487 |
| DELTA** | 17.25 *10-4 FT | | | NU | 1.622 *10-4 FT↑2/SEC |

| Y*10↑4 (FT) | U (FPS) | U/UE | Y/THETA | Z*TH/UE | YY | Y+ | U+ | (Y*)↑0.5 | U* | Y/CDEL | (UE-U)/UT | UC/UE |
|---|---|---|---|---|---|---|---|---|---|---|---|---|
| 0.0 | 0.00 | 0.000 | 0.000 | 0.369 | 0.00 | 0.00 | 0.00 | 0.00 | 0.00 | 0.0000 | 36.29 | 0.000 |
| 1.8 | 5.04 | 0.067 | 0.171 | 0.415 | 2.43 | 2.30 | 2.44 | 1.24 | 3.64 | 0.0023 | 33.85 | 0.220 |
| 2.9 | 8.29 | 0.110 | 0.272 | 0.425 | 3.91 | 3.65 | 4.00 | 1.56 | 5.98 | 0.0036 | 32.28 | 0.252 |
| 5.5 | 16.16 | 0.215 | 0.524 | 0.373 | 7.06 | 7.02 | 7.81 | 2.17 | 11.65 | 0.0069 | 28.48 | 0.303 |
| 8.1 | 22.42 | 0.298 | 0.776 | 0.313 | 9.58 | 10.40 | 10.83 | 2.64 | 16.16 | 0.0102 | 25.46 | 0.341 |
| 10.8 | 28.03 | 0.373 | 1.029 | 0.277 | 11.93 | 13.77 | 13.54 | 3.04 | 20.21 | 0.0135 | 22.75 | 0.375 |
| 13.4 | 32.91 | 0.438 | 1.281 | 0.243 | 13.92 | 17.15 | 15.90 | 3.39 | 23.73 | 0.0169 | 20.39 | 0.409 |
| 16.1 | 37.23 | 0.496 | 1.533 | 0.219 | 15.82 | 20.52 | 17.99 | 3.71 | 26.84 | 0.0202 | 18.30 | 0.443 |
| 21.4 | 44.85 | 0.597 | 2.037 | 0.190 | 19.58 | 27.27 | 21.67 | 4.28 | 32.34 | 0.0268 | 14.62 | 0.516 |
| 26.7 | 51.64 | 0.688 | 2.541 | 0.169 | 23.05 | 34.03 | 24.95 | 4.78 | 37.23 | 0.0335 | 11.34 | 0.594 |
| 32.0 | 57.68 | 0.768 | 3.045 | 0.133 | 24.51 | 40.78 | 27.87 | 5.23 | 41.58 | 0.0401 | 8.42 | 0.674 |
| 42.5 | 63.82 | 0.850 | 4.054 | 0.067 | 23.17 | 54.28 | 30.83 | 6.03 | 46.01 | 0.0534 | 5.45 | 0.826 |
| 53.1 | 67.86 | 0.904 | 5.062 | 0.049 | 24.61 | 67.78 | 32.79 | 6.74 | 48.92 | 0.0667 | 3.50 | 0.942 |
| 63.7 | 71.18 | 0.948 | 6.071 | 0.036 | 25.52 | 81.28 | 34.39 | 7.38 | 51.32 | 0.0799 | 1.89 | 0.998 |
| 84.9 | 74.40 | 0.991 | 8.087 | 0.013 | 20.28 | 108.29 | 35.95 | 8.52 | 53.64 | 0.1065 | 0.34 | 0.904 |
| 106.0 | 75.10 | 1.000 | 10.104 | 0.000 | 0.00 | 135.29 | 36.29 | 9.52 | 54.15 | 0.1330 | 0.00 | 0.657 |



APPENDIX H (cont.)

X/C = 0.80 8.0 INS THROTTLE 500.0 RPM

| | | | | | |
|---|---|---|---|---|---|
| UE | 81.42 FPS | DUEDX | -254.0 /SEC | H | 2.07 |
| UT | 2.51 FPS | UI/UE | 0.0309 | H** | 1.63 |
| UP | 1.50 FPS | | | PI | 6.20 |
| UB | 41.86 FPS | UB/UE | 0.514 | G | 16.76 |
| CFE | 1.906 *10-3 | CTEQ | 7.810 *10-3 | GEQ | 15.57 |
| CFLT | 1.873 *10-3 | CFE/CFLT | 1.018 | GAMMA | -1.320 *10-2 |
| CFNM | 2.134 *10-3 | CFE/CFNM | 0.893 | A | 2.068 *10↑4 FT/SEC↑2 |
| CDEL | 614.01 *10-4 FT | DELTA | 57.03 *10-4 FT | ALPHA0 | 0.212 |
| DSTAR | 18.96 *10-4 FT | REDSTAR | 950.1 | TH/UE*DUEDX | -2.853 *10-3 |
| THETA | 9.15 *10-4 FT | RETHETA | 458.4 | K | -1.308 |
| DELTA** | 14.92 *10-4 FT | | | NU | 1.625 *10-4 FT↑2/SEC |

| Y*10↑4 (FT) | U (FPS) | U/UE | Y/THETA | Z*TH/UE | YY | Y+ | U+ | (Y*)↑0.5 | U* | Y/CDEL | (UE-U)/UT | UC/UE |
|---|---|---|---|---|---|---|---|---|---|---|---|---|
| 0.0 | 0.00 | 0.000 | 0.000 | 0.437 | 0.00 | 0.00 | 0.00 | 0.00 | 0.00 | 0.0000 | 32.39 | 0.000 |
| 1.7 | 7.42 | 0.091 | 0.191 | 0.517 | 2.94 | 2.70 | 2.95 | 1.27 | 4.95 | 0.0028 | 29.44 | 0.225 |
| 2.8 | 12.52 | 0.154 | 0.307 | 0.502 | 4.65 | 4.34 | 4.98 | 1.61 | 8.36 | 0.0046 | 27.41 | 0.262 |
| 5.5 | 22.04 | 0.271 | 0.596 | 0.330 | 7.33 | 8.43 | 8.77 | 2.24 | 14.71 | 0.0089 | 23.62 | 0.321 |
| 8.1 | 28.06 | 0.345 | 0.885 | 0.255 | 9.58 | 12.53 | 11.16 | 2.73 | 18.74 | 0.0132 | 21.23 | 0.364 |
| 10.7 | 34.07 | 0.418 | 1.174 | 0.229 | 12.04 | 16.62 | 13.55 | 3.15 | 22.75 | 0.0175 | 18.84 | 0.404 |
| 13.4 | 38.86 | 0.477 | 1.464 | 0.205 | 14.20 | 20.72 | 15.46 | 3.51 | 25.95 | 0.0218 | 16.93 | 0.444 |
| 16.0 | 43.75 | 0.537 | 1.753 | 0.196 | 16.60 | 24.81 | 17.40 | 3.84 | 29.21 | 0.0261 | 14.99 | 0.484 |
| 21.3 | 51.86 | 0.637 | 2.332 | 0.166 | 20.34 | 33.00 | 20.63 | 4.43 | 34.62 | 0.0347 | 11.76 | 0.570 |
| 26.6 | 59.39 | 0.729 | 2.910 | 0.136 | 22.99 | 41.19 | 23.63 | 4.95 | 39.65 | 0.0433 | 8.77 | 0.659 |
| 31.9 | 64.68 | 0.794 | 3.489 | 0.105 | 24.16 | 49.37 | 25.73 | 5.42 | 43.19 | 0.0520 | 6.66 | 0.747 |
| 42.5 | 73.08 | 0.898 | 4.646 | 0.065 | 25.28 | 65.75 | 29.07 | 6.26 | 48.79 | 0.0692 | 3.32 | 0.900 |
| 53.1 | 76.86 | 0.944 | 5.803 | 0.034 | 22.91 | 82.13 | 30.58 | 7.00 | 51.32 | 0.0864 | 1.82 | 0.989 |
| 63.7 | 79.48 | 0.976 | 6.960 | 0.022 | 22.11 | 98.50 | 31.62 | 7.66 | 53.07 | 0.1037 | 0.77 | 0.991 |
| 84.8 | 81.42 | 1.000 | 9.274 | 0.000 | 0.00 | 131.25 | 32.39 | 8.84 | 54.36 | 0.1382 | 0.00 | 0.783 |



APPENDIX H (cont.)

X/C = 0.80 10.0 INS THROTTLE 500.0 RPM

| | | | | | |
|---|---|---|---|---|---|
| UE | 87.31 FPS | DUEDX | -304.0 /SEC | H | 2.58 |
| UT | 2.35 FPS | UT/UE | 0.0269 | H** | 1.56 |
| UP | 1.62 FPS | | | PI | 10.02 |
| UB | 58.07 FPS | UB/UE | 0.665 | G | 22.75 |
| CFE | 1.451 *10-3 | CTEQ | 10.995 *10-3 | GEQ | 19.28 |
| CFLT | 0.857 *10-3 | CFE/CFLT | 1.692 | GAMMA | -1.288 *10-2 |
| CFNM | 0.719 *10-3 | CFE/CFNM | 2.016 | A | 2.654 *10↑4 FT/SEC↑2 |
| CDEL | 775.03 *10-4 FT | DELTA | 52.41 *10-4 FT | ALPHA0 | 0.329 |
| DSTAR | 20.87 *10-4 FT | REDSTAR | 1129.2 | TH/UE*DUEDX | -2.816 *10-3 |
| THETA | 8.09 *10-4 FT | RETHETA | 437.4 | K | -1.232 |
| DELTA** | 12.62 *10-4 FT | | | NU | 1.614 *10-4 FT↑2/SEC |

| Y*10↑4 (FT) | U (FPS) | U/UE | Y/THETA | Z*TH/UE | YY | Y+ | U+ | (Y*)↑0.5 | U* | Y/CDEL | (UE-U)/UT | UC/UE |
|---|---|---|---|---|---|---|---|---|---|---|---|---|
| 0.0 | 0.00 | 0.000 | 0.000 | 0.317 | 0.00 | 0.00 | 0.00 | 0.00 | 0.00 | 0.0000 | 37.13 | 0.000 |
| 1.7 | 5.84 | 0.067 | 0.216 | 0.302 | 2.48 | 2.54 | 2.48 | 1.33 | 3.60 | 0.0023 | 34.65 | 0.113 |
| 2.8 | 9.24 | 0.106 | 0.347 | 0.273 | 3.79 | 4.09 | 3.93 | 1.68 | 5.69 | 0.0036 | 33.20 | 0.147 |
| 5.5 | 15.28 | 0.175 | 0.674 | 0.196 | 6.24 | 7.94 | 6.50 | 2.34 | 9.41 | 0.0070 | 30.63 | 0.204 |
| 8.1 | 20.43 | 0.234 | 1.001 | 0.172 | 8.67 | 11.80 | 8.69 | 2.85 | 12.58 | 0.0104 | 28.44 | 0.251 |
| 10.7 | 25.08 | 0.287 | 1.328 | 0.152 | 10.83 | 15.65 | 10.67 | 3.29 | 15.44 | 0.0139 | 26.46 | 0.297 |
| 13.4 | 29.10 | 0.333 | 1.656 | 0.179 | 14.65 | 19.51 | 12.38 | 3.67 | 17.92 | 0.0173 | 24.75 | 0.347 |
| 16.0 | 35.31 | 0.404 | 1.983 | 0.209 | 18.96 | 23.36 | 15.02 | 4.02 | 21.74 | 0.0207 | 22.11 | 0.399 |
| 18.7 | 41.04 | 0.470 | 2.310 | 0.220 | 22.64 | 27.22 | 17.45 | 4.34 | 25.27 | 0.0241 | 19.68 | 0.455 |
| 21.3 | 47.86 | 0.548 | 2.637 | 0.225 | 26.14 | 31.07 | 20.35 | 4.63 | 29.47 | 0.0275 | 16.78 | 0.512 |
| 26.6 | 59.08 | 0.677 | 3.292 | 0.184 | 29.50 | 38.78 | 25.13 | 5.18 | 36.38 | 0.0343 | 12.00 | 0.631 |
| 31.9 | 68.85 | 0.789 | 3.946 | 0.142 | 31.08 | 46.49 | 29.28 | 5.67 | 42.39 | 0.0412 | 7.85 | 0.746 |
| 37.2 | 75.28 | 0.862 | 4.600 | 0.108 | 31.58 | 54.20 | 32.02 | 6.12 | 46.35 | 0.0480 | 5.11 | 0.849 |
| 42.5 | 81.15 | 0.929 | 5.255 | 0.077 | 30.51 | 61.91 | 34.51 | 6.54 | 49.97 | 0.0548 | 2.62 | 0.929 |
| 53.1 | 84.09 | 0.963 | 6.564 | 0.027 | 22.53 | 77.33 | 35.76 | 7.31 | 51.78 | 0.0685 | 1.37 | 1.001 |
| 63.7 | 87.31 | 1.000 | 7.873 | 0.000 | 0.00 | 92.75 | 37.13 | 8.00 | 53.76 | 0.0821 | 0.00 | 0.940 |



APPENDIX H (cont.)

X/C = 0.80 13.0 INS THROTTLE 500.0 RPM

| | | | | | | | |
|---|---|---|---|---|---|---|---|
| UE | 95.11 FPS | DUEDX | -296.0 /SEC | H | 3.48 | | |
| UI | 2.13 FPS | UT/UE | 0.0224 | H** | 1.50 | | |
| UP | 1.66 FPS | | | PI | 14.07 | | |
| UB | 78.44 FPS | UB/UE | 0.825 | G | 31.80 | | |
| CFE | 1.004 $*_{10}$-3 | CTEQ | 14.908 $*_{10}$-3 | GEQ | 22.61 | | |
| CFLT | 0.219 $*_{10}$-3 | CFE/CFLT | 4.575 | GAMMA | -0.899 | $*_{10}$-2 | |
| CFNM | 0.010 $*_{10}$-3 | CFE/CFNM | 100.391 | A | 2.815 | $*_{10}$4 | FT/SEC↑2 |
| CDEL | 1013.03 $*_{10}$-4 FT | DELTA | 48.60 $*_{10}$-4 FT | ALPHA0 | 0.471 | | |
| DSTAR | 22.70 $*_{10}$-4 FT | REDSTAR | 1334.6 | TH/UE*DUEDX | -2.032 | $*_{10}$-3 | |
| THETA | 6.53 $*_{10}$-4 FT | RETHETA | 383.9 | K | -0.780 | | |
| DELTA** | 9.76 $*_{10}$-4 FT | | | NU | 1.617 | $*_{10}$-4 | FT↑2/SEC |

| Y*$_{10}$4 (FT) | U (FPS) | U/UE | Y/THETA | Z*TH/UE | YY | Y+ | U+ | (Y*)↑0.5 | U* | Y/CDEL | (UE-U)/UT | UC/UE |
|---|---|---|---|---|---|---|---|---|---|---|---|---|
| 0.0 | 0.00 | 0.000 | 0.000 | 0.193 | 0.00 | 0.00 | 0.00 | 0.00 | 0.00 | 0.0000 | 44.63 | 0.000 |
| 1.8 | 4.58 | 0.048 | 0.276 | 0.157 | 2.14 | 2.37 | 2.15 | 1.36 | 2.77 | 0.0018 | 42.48 | -0.002 |
| 2.9 | 6.84 | 0.072 | 0.438 | 0.128 | 3.07 | 3.76 | 3.21 | 1.71 | 4.13 | 0.0028 | 41.42 | 0.027 |
| 5.5 | 10.00 | 0.105 | 0.843 | 0.068 | 4.30 | 7.25 | 4.69 | 2.37 | 6.04 | 0.0054 | 39.94 | 0.082 |
| 8.1 | 12.06 | 0.127 | 1.248 | 0.062 | 6.08 | 10.74 | 5.66 | 2.89 | 7.28 | 0.0080 | 38.98 | 0.134 |
| 10.8 | 14.77 | 0.155 | 1.654 | 0.089 | 9.67 | 14.22 | 6.93 | 3.33 | 8.91 | 0.0107 | 37.70 | 0.189 |
| 13.4 | 18.93 | 0.199 | 2.059 | 0.141 | 15.17 | 17.71 | 8.88 | 3.71 | 11.42 | 0.0133 | 35.75 | 0.251 |
| 16.1 | 25.67 | 0.270 | 2.464 | 0.186 | 20.85 | 21.19 | 12.05 | 4.06 | 15.49 | 0.0159 | 32.59 | 0.318 |
| 18.7 | 33.31 | 0.350 | 2.870 | 0.219 | 26.29 | 24.68 | 15.63 | 4.38 | 20.09 | 0.0185 | 29.00 | 0.390 |
| 21.4 | 42.53 | 0.447 | 3.275 | 0.226 | 30.50 | 28.17 | 19.96 | 4.68 | 25.66 | 0.0211 | 24.67 | 0.465 |
| 24.0 | 50.72 | 0.533 | 3.680 | 0.237 | 35.07 | 31.65 | 23.80 | 4.96 | 30.60 | 0.0237 | 20.83 | 0.542 |
| 26.7 | 60.77 | 0.639 | 4.086 | 0.235 | 38.83 | 35.14 | 28.52 | 5.23 | 36.67 | 0.0263 | 16.11 | 0.618 |
| 32.0 | 75.00 | 0.789 | 4.896 | 0.157 | 37.98 | 42.11 | 35.20 | 5.72 | 45.25 | 0.0316 | 9.43 | 0.761 |
| 37.3 | 84.94 | 0.893 | 5.707 | 0.103 | 35.97 | 49.08 | 39.86 | 6.18 | 51.25 | 0.0368 | 4.77 | 0.879 |
| 42.5 | 90.96 | 0.956 | 6.517 | 0.060 | 31.39 | 56.05 | 42.69 | 6.60 | 54.88 | 0.0420 | 1.95 | 0.962 |
| 53.1 | 94.83 | 0.997 | 8.139 | 0.013 | 18.49 | 70.00 | 44.51 | 7.38 | 57.22 | 0.0524 | 0.13 | 0.987 |
| 63.7 | 95.11 | 1.000 | 9.760 | 0.000 | 0.00 | 83.94 | 44.63 | 8.08 | 57.38 | 0.0629 | 0.00 | 0.833 |



APPENDIX H (cont.)

X/C = 0.80 22.0 INS THROTTLE 500.0 RPM

| | | | | | |
|---|---|---|---|---|---|
| UE | 101.11 FPS | DUEDX | -287.0 /SEC | H | 4.43 |
| UT | 1.78 FPS | UT/UE | 0.0176 | H** | 1.49 |
| UP | 1.67 FPS | | | PI | 22.03 |
| UB | 94.55 FPS | UB/UE | 0.935 | G | 44.04 |
| CFE | 0.619 *10-3 | CTEQ | 17.645 *10-3 | GEQ | 28.08 |
| CFLT | 0.051 *10-3 | CFE/CFLT | 12.157 | GAMMA | -0.659 *10-2 |
| CFNM | 0.010 *10-3 | CFE/CFNM | 61.867 | A | 2.902 *10↑4 FT/SEC↑2 |
| CDEL | 1364.82 *10-4 FT | DELTA | 47.03 *10-4 FT | ALPHA0 | 0.834 |
| DSTAR | 24.00 *10-4 FT | REDSTAR | 1501.5 | TH/UE*DUEDX | -1.536 *10-3 |
| THETA | 5.41 *10-4 FT | RETHETA | 338.6 | K | -0.520 |
| DELTA** | 8.08 *10-4 FT | | | NU | 1.616 *10-4 FT↑2/SEC |

| Y*10↑4 (FT) | U (FPS) | U/UE | Y/THETA | Z*TH/UE | YY | Y+ | U+ | (Y*)↑0.5 | U* | Y/CDEL | (UE-U)/UT | UC/UE |
|---|---|---|---|---|---|---|---|---|---|---|---|---|
| 0.0 | 0.00 | 0.000 | 0.000 | 0.105 | 0.00 | 0.00 | 0.00 | 0.00 | 0.00 | 0.0000 | 56.86 | 0.000 |
| 1.8 | 2.82 | 0.028 | 0.332 | 0.063 | 1.54 | 1.98 | 1.59 | 1.37 | 1.68 | 0.0013 | 55.27 | -0.072 |
| 2.9 | 3.83 | 0.038 | 0.528 | 0.044 | 2.05 | 3.14 | 2.15 | 1.72 | 2.29 | 0.0021 | 54.71 | -0.047 |
| 5.5 | 5.23 | 0.052 | 1.017 | 0.018 | 2.53 | 6.05 | 2.94 | 2.39 | 3.12 | 0.0040 | 53.92 | 0.004 |
| 8.1 | 5.64 | 0.056 | 1.505 | 0.021 | 3.97 | 8.97 | 3.17 | 2.91 | 3.37 | 0.0060 | 53.69 | 0.057 |
| 10.8 | 7.26 | 0.072 | 1.994 | 0.056 | 8.71 | 11.88 | 4.08 | 3.34 | 4.34 | 0.0079 | 52.78 | 0.118 |
| 13.4 | 11.21 | 0.111 | 2.483 | 0.126 | 16.20 | 14.79 | 6.30 | 3.73 | 6.70 | 0.0098 | 50.55 | 0.187 |
| 16.1 | 19.68 | 0.195 | 2.972 | 0.176 | 22.97 | 17.70 | 11.07 | 4.08 | 11.76 | 0.0118 | 45.79 | 0.264 |
| 18.7 | 28.65 | 0.283 | 3.461 | 0.199 | 28.44 | 20.61 | 16.11 | 4.40 | 17.11 | 0.0137 | 40.75 | 0.346 |
| 21.4 | 39.39 | 0.390 | 3.949 | 0.217 | 33.87 | 23.52 | 22.15 | 4.71 | 23.53 | 0.0157 | 34.71 | 0.432 |
| 24.0 | 50.12 | 0.496 | 4.438 | 0.229 | 39.05 | 26.43 | 28.18 | 4.99 | 29.94 | 0.0176 | 28.67 | 0.520 |
| 26.7 | 62.00 | 0.613 | 4.927 | 0.221 | 42.63 | 29.34 | 34.86 | 5.26 | 37.04 | 0.0195 | 22.00 | 0.606 |
| 32.0 | 80.06 | 0.792 | 5.905 | 0.154 | 42.59 | 35.16 | 45.02 | 5.75 | 47.82 | 0.0234 | 11.84 | 0.766 |
| 37.3 | 92.37 | 0.914 | 6.882 | 0.093 | 38.56 | 40.99 | 51.94 | 6.21 | 55.18 | 0.0273 | 4.91 | 0.894 |
| 42.5 | 98.38 | 0.973 | 7.860 | 0.045 | 30.72 | 46.81 | 55.32 | 6.64 | 58.77 | 0.0312 | 1.54 | 0.975 |
| 53.1 | 101.11 | 1.000 | 9.815 | 0.000 | 0.00 | 58.45 | 56.86 | 7.42 | 60.40 | 0.0389 | 0.00 | 0.967 |

X/C = 0.90 4.8 INS THROTTLE 500.0 RPM

| | | | | | |
|---|---|---|---|---|---|
| UE | 61.89 FPS | DUEDX | -151.0 /SEC | H | 2.06 |
| UT | 1.46 FPS | UT/UE | 0.0236 | H** | 1.62 |
| UP | 1.15 FPS | | | PI | 19.88 |
| UB | 34.30 FPS | UB/UE | 0.554 | G | 21.87 |
| CFE | 1.110 *10-3 | CTEQ | 7.778 *10-3 | GEQ | 26.71 |
| CFLT | 1.622 *10-3 | CFE/CFLT | 0.685 | GAMMA | -2.869 *10-2 |
| CFNM | 1.680 *10-3 | CFE/CFNM | 0.661 | A | 0.934 *104 FT/SEC↑2 |
| CDEL | 1919.68 *10-4 FT | DELTA | 135.16 *10-4 FT | ALPHA0 | 0.494 |
| DSTAR | 45.23 *10-4 FT | REDSTAR | 1708.4 | TH/UE*DUEDX | -5.348 *10-3 |
| THETA | 21.92 *10-4 FT | RETHETA | 827.9 | K | -4.428 |
| DELTA** | 35.50 *10-4 FT | | | NU | 1.638 *10-4 FT↑2/SEC |

| Y*10↑4 (FT) | U (FPS) | U/UE | Y/THETA | Z*TH/UE | YY | Y+ | U+ | (Y*)↑0.5 | U* | Y/CDEL | (UE-U)/UT | UC/UE |
|---|---|---|---|---|---|---|---|---|---|---|---|---|
| 0.0 | 0.00 | 0.000 | 0.000 | 0.460 | 0.00 | 0.00 | 0.00 | 0.00 | 0.00 | 0.0000 | 42.44 | 0.000 |
| 2.4 | 3.40 | 0.055 | 0.108 | 0.555 | 2.32 | 2.11 | 2.33 | 1.29 | 2.95 | 0.0012 | 40.11 | 0.214 |
| 5.1 | 8.05 | 0.130 | 0.231 | 0.589 | 5.11 | 4.51 | 5.52 | 1.89 | 6.98 | 0.0026 | 36.92 | 0.259 |
| 7.8 | 12.37 | 0.200 | 0.354 | 0.491 | 7.15 | 6.91 | 8.49 | 2.34 | 10.73 | 0.0040 | 33.96 | 0.286 |
| 13.2 | 17.52 | 0.283 | 0.601 | 0.289 | 9.29 | 11.72 | 12.01 | 3.04 | 15.20 | 0.0069 | 30.43 | 0.325 |
| 18.6 | 21.18 | 0.342 | 0.847 | 0.267 | 12.59 | 16.52 | 14.52 | 3.61 | 18.37 | 0.0097 | 27.92 | 0.357 |
| 24.0 | 25.65 | 0.414 | 1.093 | 0.248 | 15.67 | 21.32 | 17.59 | 4.11 | 22.26 | 0.0125 | 24.85 | 0.388 |
| 29.4 | 28.74 | 0.464 | 1.339 | 0.190 | 16.79 | 26.12 | 19.71 | 4.54 | 24.94 | 0.0153 | 22.73 | 0.420 |
| 40.1 | 33.73 | 0.545 | 1.832 | 0.171 | 21.78 | 35.73 | 23.13 | 5.31 | 29.27 | 0.0209 | 19.31 | 0.488 |
| 50.9 | 39.15 | 0.633 | 2.324 | 0.156 | 26.40 | 45.33 | 26.85 | 5.99 | 33.97 | 0.0265 | 15.59 | 0.562 |
| 61.7 | 43.23 | 0.699 | 2.816 | 0.126 | 28.80 | 54.93 | 29.65 | 6.59 | 37.51 | 0.0322 | 12.80 | 0.640 |
| 72.5 | 46.85 | 0.757 | 3.309 | 0.115 | 32.28 | 64.54 | 32.13 | 7.14 | 40.65 | 0.0378 | 10.31 | 0.719 |
| 83.3 | 50.23 | 0.812 | 3.801 | 0.105 | 35.37 | 74.14 | 34.45 | 7.66 | 43.58 | 0.0434 | 7.99 | 0.794 |
| 94.1 | 53.22 | 0.860 | 4.293 | 0.087 | 36.54 | 83.74 | 36.50 | 8.14 | 46.18 | 0.0490 | 5.94 | 0.862 |
| 115.7 | 57.26 | 0.925 | 5.278 | 0.058 | 36.52 | 102.95 | 39.27 | 9.02 | 49.68 | 0.0603 | 3.17 | 0.963 |
| 137.3 | 60.27 | 0.974 | 6.263 | 0.034 | 33.37 | 122.16 | 41.34 | 9.83 | 52.30 | 0.0715 | 1.11 | 1.001 |
| 158.9 | 61.44 | 0.993 | 7.247 | 0.013 | 23.98 | 141.37 | 42.13 | 10.57 | 53.30 | 0.0827 | 0.31 | 0.968 |
| 180.4 | 61.89 | 1.000 | 8.232 | 0.000 | 0.00 | 160.57 | 42.44 | 11.27 | 53.69 | 0.0940 | 0.00 | 0.877 |



APPENDIX H (cont.)

X/C = 0.90 5.2 INS THROTTLE 500.0 RPM

| | | | | | | | |
|---|---|---|---|---|---|---|---|
| UE | 68.38 FPS | DUEDX | -180.0 /SEC | H | 2.09 | | |
| UT | 1.45 FPS | UT/UE | 0.0211 | H** | 1.62 | | |
| UP | 1.26 FPS | | | PI | 25.48 | | |
| UB | 39.49 FPS | UB/UE | 0.577 | G | 24.69 | | |
| CFE | 0.894 *10-3 | CTEQ | 7.995 *10-3 | GEQ | 30.17 | | |
| CFLT | 1.533 *10-3 | CFE/CFLT | 0.584 | GAMMA | -2.950 *10-2 | | |
| CFNM | 1.569 *10-3 | CFE/CFNM | 0.570 | A | 1.231 *104 | FT/SEC↑2 | |
| CDEL | 2047.04 *10-4 FT | DELTA | 127.20 *10-4 FT | ALPHA0 | 0.668 | | |
| DSTAR | 43.29 *10-4 FT | REDSTAR | 1803.4 | TH/UE*DUEDX | -5.444 *10-3 | | |
| THETA | 20.68 *10-4 FT | RETHETA | 861.7 | K | -4.691 | | |
| DELTA** | 33.57 *10-4 FT | | | NU | 1.641 *10-4 | FT↑2/SEC | |

| Y*10↑4 (FT) | U (FPS) | U/UE | Y/THETA | Z*TH/UE | YY | Y+ | U+ | (Y*)↑0.5 | U* | Y/CDEL | (UE-U)/UT | UC/UE |
|---|---|---|---|---|---|---|---|---|---|---|---|---|
| 0.0 | 0.00 | 0.000 | 0.000 | 0.385 | 0.00 | 0.00 | 0.00 | 0.00 | 0.00 | 0.0000 | 47.29 | 0.000 |
| 2.3 | 3.43 | 0.050 | 0.112 | 0.508 | 2.35 | 2.04 | 2.37 | 1.34 | 2.71 | 0.0011 | 44.92 | 0.217 |
| 5.0 | 8.59 | 0.126 | 0.243 | 0.535 | 5.21 | 4.42 | 5.94 | 1.97 | 6.80 | 0.0025 | 41.35 | 0.258 |
| 7.7 | 12.96 | 0.190 | 0.373 | 0.439 | 7.25 | 6.80 | 8.96 | 2.44 | 10.25 | 0.0038 | 38.33 | 0.283 |
| 10.4 | 16.42 | 0.240 | 0.504 | 0.316 | 8.31 | 9.17 | 11.35 | 2.83 | 12.99 | 0.0051 | 35.94 | 0.303 |
| 13.1 | 18.60 | 0.272 | 0.634 | 0.257 | 9.44 | 11.55 | 12.86 | 3.18 | 14.71 | 0.0064 | 34.43 | 0.320 |
| 18.5 | 23.62 | 0.345 | 0.895 | 0.261 | 13.43 | 16.30 | 16.34 | 3.78 | 18.69 | 0.0090 | 30.95 | 0.353 |
| 23.9 | 27.93 | 0.408 | 1.156 | 0.219 | 15.86 | 21.06 | 19.32 | 4.29 | 22.09 | 0.0117 | 27.97 | 0.385 |
| 29.3 | 31.42 | 0.459 | 1.417 | 0.198 | 18.50 | 25.81 | 21.73 | 4.75 | 24.85 | 0.0143 | 25.56 | 0.419 |
| 40.1 | 38.64 | 0.565 | 1.938 | 0.183 | 24.36 | 35.32 | 26.72 | 5.56 | 30.56 | 0.0196 | 20.57 | 0.493 |
| 50.9 | 44.50 | 0.651 | 2.460 | 0.159 | 28.83 | 44.83 | 30.78 | 6.26 | 35.20 | 0.0249 | 16.51 | 0.575 |
| 61.7 | 50.01 | 0.731 | 2.982 | 0.132 | 31.86 | 54.33 | 34.58 | 6.89 | 39.56 | 0.0301 | 12.71 | 0.660 |
| 72.5 | 53.96 | 0.789 | 3.504 | 0.104 | 33.10 | 63.84 | 37.31 | 7.47 | 42.68 | 0.0354 | 9.98 | 0.745 |
| 83.3 | 57.40 | 0.839 | 4.025 | 0.085 | 34.42 | 73.35 | 39.70 | 8.01 | 45.41 | 0.0407 | 7.59 | 0.824 |
| 94.0 | 60.01 | 0.878 | 4.547 | 0.068 | 34.85 | 82.86 | 41.50 | 8.51 | 47.47 | 0.0459 | 5.79 | 0.893 |
| 115.6 | 64.16 | 0.938 | 5.591 | 0.046 | 35.13 | 101.87 | 44.37 | 9.44 | 50.75 | 0.0565 | 2.92 | 0.983 |
| 137.2 | 66.55 | 0.973 | 6.634 | 0.030 | 33.48 | 120.88 | 46.02 | 10.28 | 52.64 | 0.0670 | 1.27 | 0.995 |
| 158.8 | 68.38 | 1.000 | 7.678 | 0.000 | 0.00 | 139.90 | 47.29 | 11.06 | 54.09 | 0.0776 | 0.00 | 0.928 |

X/C = 0.90 6.0 INS THROTTLE 500.0 RPM

| | | | | | |
|---|---|---|---|---|---|
| UE | 72.52 FPS | DUEDX | -365.0 /SEC | H | 2.04 |
| UT | 1.69 FPS | UT/UE | 0.0234 | H** | 1.64 |
| UP | 1.63 FPS | | | PI | 31.22 |
| UB | 39.76 FPS | UB/UE | 0.548 | G | 21.83 |
| CFE | 1.092 *10-3 | CTEQ | 7.617 *10-3 | GEQ | 33.36 |
| CFLT | 1.735 *10-3 | CFE/CFLT | 0.629 | GAMMA | -4.345 *10-2 |
| CFNM | 1.835 *10-3 | CFE/CFNM | 0.595 | A | 2.647 *104 FT/SEC↑2 |
| CDEL | 1449.24 *10-4 FT | DELTA | 102.25 *10-4 FT | ALPHA0 | 0.893 |
| DSTAR | 33.86 *10-4 FT | REDSTAR | 1496.4 | TH/UE*DUEDX | -8.350 *10-3 |
| THETA | 16.59 *10-4 FT | RETHETA | 733.2 | K | -6.122 |
| DELTA** | 27.24 *10-4 FT | | | NU | 1.641 *10-4 FT↑2/SEC |

| Y*10↑4 (FT) | U (FPS) | U/UE | Y/THETA | Z*TH/UE | YY | Y+ | U+ | (Y*)↑0.5 | U* | Y/CDEL | (UE-U)/UT | UC/UE |
|---|---|---|---|---|---|---|---|---|---|---|---|---|
| 0.0 | 0.00 | 0.000 | 0.000 | 0.400 | 0.00 | 0.00 | 0.00 | 0.00 | 0.00 | 0.0000 | 42.80 | 0.000 |
| 2.3 | 4.48 | 0.062 | 0.137 | 0.504 | 2.63 | 2.34 | 2.64 | 1.50 | 2.74 | 0.0016 | 40.16 | 0.235 |
| 5.0 | 11.15 | 0.154 | 0.299 | 0.532 | 5.91 | 5.13 | 6.58 | 2.22 | 6.83 | 0.0034 | 36.22 | 0.283 |
| 7.7 | 17.02 | 0.235 | 0.462 | 0.396 | 7.87 | 7.91 | 10.04 | 2.76 | 10.43 | 0.0053 | 32.76 | 0.312 |
| 10.4 | 20.49 | 0.282 | 0.625 | 0.300 | 9.26 | 10.70 | 12.09 | 3.21 | 12.56 | 0.0071 | 30.71 | 0.335 |
| 13.1 | 24.09 | 0.332 | 0.787 | 0.284 | 11.36 | 13.48 | 14.22 | 3.60 | 14.77 | 0.0090 | 28.58 | 0.356 |
| 18.5 | 29.76 | 0.410 | 1.112 | 0.221 | 14.17 | 19.05 | 17.56 | 4.28 | 18.24 | 0.0127 | 25.24 | 0.397 |
| 23.8 | 34.53 | 0.476 | 1.438 | 0.208 | 17.73 | 24.63 | 20.38 | 4.87 | 21.16 | 0.0165 | 22.42 | 0.439 |
| 29.2 | 39.55 | 0.545 | 1.763 | 0.207 | 21.74 | 30.20 | 23.34 | 5.39 | 24.24 | 0.0202 | 19.46 | 0.484 |
| 40.0 | 48.82 | 0.673 | 2.413 | 0.165 | 26.55 | 41.34 | 28.81 | 6.31 | 29.92 | 0.0276 | 13.99 | 0.581 |
| 50.8 | 55.12 | 0.760 | 3.064 | 0.124 | 29.20 | 52.48 | 32.53 | 7.11 | 33.78 | 0.0351 | 10.27 | 0.684 |
| 61.6 | 60.50 | 0.834 | 3.714 | 0.098 | 31.49 | 63.62 | 35.71 | 7.83 | 37.08 | 0.0425 | 7.09 | 0.784 |
| 72.4 | 64.37 | 0.888 | 4.365 | 0.056 | 28.00 | 74.77 | 37.99 | 8.49 | 39.45 | 0.0500 | 4.81 | 0.873 |
| 83.2 | 65.80 | 0.907 | 5.016 | 0.038 | 26.36 | 85.91 | 38.84 | 9.10 | 40.33 | 0.0574 | 3.97 | 0.943 |
| 94.0 | 67.92 | 0.937 | 5.666 | 0.040 | 30.60 | 97.05 | 40.09 | 9.67 | 41.63 | 0.0649 | 2.71 | 0.986 |
| 115.6 | 70.68 | 0.975 | 6.967 | 0.020 | 26.94 | 119.34 | 41.72 | 10.72 | 43.32 | 0.0798 | 1.08 | 0.984 |
| 137.2 | 71.77 | 0.990 | 8.268 | 0.010 | 22.09 | 141.62 | 42.36 | 11.68 | 43.99 | 0.0946 | 0.44 | 0.874 |
| 158.7 | 72.52 | 1.000 | 9.569 | 0.000 | 0.00 | 163.91 | 42.80 | 12.56 | 44.45 | 0.1095 | 0.00 | 0.706 |



APPENDIX H (cont.)

X/C = 0.90 8.0 INS THROTTLE 500.0 RPM

| | | | | | |
|---|---|---|---|---|---|
| UE | 76.95 FPS | DUEDX | -252.0 /SEC | H | 1.89 |
| UT | 2.35 FPS | UT/UE | 0.0306 | H** | 1.66 |
| UP | 1.48 FPS | | | PI | 8.73 |
| UB | 34.73 FPS | UB/UE | 0.451 | G | 15.36 |
| CFE | 1.870 *10-3 | CTEQ | 6.420 *10-3 | GEQ | 18.11 |
| CFLT | 2.319 *10-3 | CFE/CFLT | 0.806 | GAMMA | -2.156 *10-2 |
| CFNM | 2.512 *10-3 | CFE/CFNM | 0.745 | A | 1.939 *10↑4 FT/SEC↑2 |
| CDEL | 815.58 *10-4 FT | DELTA | 83.06 *10-4 FT | ALPHA0 | 0.247 |
| DSTAR | 24.94 *10-4 FT | REDSTAR | 1157.2 | TH/UE*DUEDX | -4.331 *10-3 |
| THETA | 13.23 *10-4 FT | RETHETA | 613.7 | K | -2.658 |
| DELTA** | 21.92 *10-4 FT | | | NU | 1.658 *10-4 FT↑2/SEC |

| Y*10↑4 (FT) | U (FPS) | U/UE | Y/THETA | Z*TH/UE | YY | Y+ | U+ | (Y*)↑0.5 | U* | Y/CDEL | (UE-U)/UT | UC/UE |
|---|---|---|---|---|---|---|---|---|---|---|---|---|
| 0.0 | 0.00 | 0.000 | 0.000 | 0.574 | 0.00 | 0.00 | 0.00 | 0.00 | 0.00 | 0.0000 | 32.70 | 0.000 |
| 2.2 | 8.00 | 0.104 | 0.167 | 0.669 | 3.39 | 3.14 | 3.40 | 1.40 | 5.42 | 0.0027 | 29.30 | 0.279 |
| 4.9 | 19.42 | 0.252 | 0.371 | 0.605 | 7.15 | 6.97 | 8.25 | 2.09 | 13.15 | 0.0060 | 24.45 | 0.342 |
| 7.6 | 26.99 | 0.351 | 0.575 | 0.393 | 8.94 | 10.80 | 11.47 | 2.60 | 18.28 | 0.0093 | 21.23 | 0.380 |
| 10.3 | 31.76 | 0.413 | 0.779 | 0.276 | 10.14 | 14.62 | 13.50 | 3.03 | 21.52 | 0.0126 | 19.21 | 0.410 |
| 13.0 | 35.64 | 0.463 | 0.983 | 0.225 | 11.56 | 18.45 | 15.15 | 3.40 | 24.15 | 0.0159 | 17.56 | 0.437 |
| 18.4 | 41.31 | 0.537 | 1.391 | 0.165 | 14.00 | 26.11 | 17.56 | 4.05 | 27.99 | 0.0226 | 15.15 | 0.489 |
| 23.8 | 46.01 | 0.598 | 1.799 | 0.154 | 17.48 | 33.76 | 19.55 | 4.60 | 31.17 | 0.0292 | 13.15 | 0.541 |
| 29.2 | 50.97 | 0.662 | 2.207 | 0.145 | 20.80 | 41.42 | 21.66 | 5.10 | 34.53 | 0.0358 | 11.04 | 0.595 |
| 40.0 | 58.40 | 0.759 | 3.023 | 0.111 | 24.94 | 56.73 | 24.82 | 5.97 | 39.57 | 0.0490 | 7.88 | 0.707 |
| 50.8 | 64.90 | 0.843 | 3.839 | 0.085 | 27.67 | 72.04 | 27.58 | 6.72 | 43.97 | 0.0623 | 5.12 | 0.815 |
| 61.6 | 69.04 | 0.897 | 4.655 | 0.050 | 25.68 | 87.36 | 29.34 | 7.40 | 46.77 | 0.0755 | 3.37 | 0.907 |
| 72.4 | 71.16 | 0.924 | 5.471 | 0.038 | 26.53 | 102.67 | 30.23 | 8.03 | 48.19 | 0.0887 | 2.47 | 0.971 |
| 83.1 | 73.85 | 0.960 | 6.287 | 0.037 | 29.88 | 117.98 | 31.38 | 8.60 | 50.03 | 0.1020 | 1.32 | 1.000 |
| 93.9 | 75.75 | 0.984 | 7.103 | 0.023 | 26.92 | 133.29 | 32.19 | 9.14 | 51.32 | 0.1152 | 0.51 | 0.990 |
| 115.5 | 76.95 | 1.000 | 8.735 | 0.000 | 0.00 | 163.92 | 32.70 | 10.14 | 52.13 | 0.1416 | 0.00 | 0.875 |



APPENDIX H (cont.)

X/C = 0.90 10.0 INS THROTTLE 500.0 RPM

| | | | | | |
|---|---|---|---|---|---|
| UE | 81.72 FPS | DUEDX | -273.0 /SEC | H | 1.91 |
| UT | 2.67 FPS | UT/UE | 0.0327 | H** | 1.64 |
| UP | 1.54 FPS | | | PI | 7.20 |
| UB | 36.61 FPS | UB/UE | 0.448 | G | 14.57 |
| CFE | 2.141 $*_{10}$-3 | CTEQ | 6.605 $*_{10}$-3 | GEQ | 16.61 |
| CFLT | 2.240 $*_{10}$-3 | CFE/CFLT | 0.956 | GAMMA | -1.998 $*_{10}$-2 |
| CFNM | 2.436 $*_{10}$-3 | CFE/CFNM | 0.879 | A | 2.231 $*_{10}$4 FT/SEC↑2 |
| CDEL | 704.85 $*_{10}$-4 FT | DELTA | 75.91 $*_{10}$-4 FT | ALPHA0 | 0.191 |
| DSTAR | 23.06 $*_{10}$-4 FT | REDSTAR | 1152.4 | TH/UE*DUEDX | -4.031 $*_{10}$-3 |
| THETA | 12.07 $*_{10}$-4 FT | RETHETA | 603.0 | K | -2.431 |
| DELTA** | 19.84 $*_{10}$-4 FT | | | NU | 1.635 $*_{10}$-4 FT↑2/SEC |

| Y*$_{10}$4 (FT) | U (FPS) | U/UE | Y/THETA | Z*H/UE | YY | Y+ | U+ | (Y*)↑0.5 | U* | Y/CDEL | (UE-U)/UT | UC/UE |
|---|---|---|---|---|---|---|---|---|---|---|---|---|
| 0.0 | 0.00 | 0.000 | 0.000 | 0.646 | 0.00 | 0.00 | 0.00 | 0.00 | 0.00 | 0.0000 | 30.56 | 0.000 |
| 2.2 | 9.89 | 0.121 | 0.183 | 0.675 | 3.70 | 3.62 | 3.70 | 1.44 | 6.43 | 0.0031 | 26.86 | 0.271 |
| 4.9 | 22.55 | 0.276 | 0.407 | 0.560 | 7.47 | 8.03 | 8.43 | 2.15 | 14.65 | 0.0070 | 22.13 | 0.338 |
| 7.6 | 30.34 | 0.371 | 0.630 | 0.340 | 9.03 | 12.44 | 11.35 | 2.68 | 19.70 | 0.0108 | 19.22 | 0.379 |
| 10.3 | 34.98 | 0.428 | 0.854 | 0.217 | 9.76 | 16.85 | 13.08 | 3.11 | 22.72 | 0.0146 | 17.48 | 0.413 |
| 13.0 | 38.25 | 0.468 | 1.078 | 0.177 | 11.13 | 21.26 | 14.30 | 3.50 | 24.84 | 0.0184 | 16.26 | 0.443 |
| 18.4 | 44.57 | 0.545 | 1.525 | 0.167 | 15.30 | 30.08 | 16.67 | 4.16 | 28.95 | 0.0261 | 13.89 | 0.501 |
| 23.8 | 50.45 | 0.617 | 1.972 | 0.140 | 18.14 | 38.90 | 18.87 | 4.73 | 32.77 | 0.0338 | 11.69 | 0.560 |
| 29.2 | 54.83 | 0.671 | 2.419 | 0.118 | 20.43 | 47.73 | 20.51 | 5.24 | 35.61 | 0.0414 | 10.06 | 0.620 |
| 40.0 | 63.25 | 0.774 | 3.313 | 0.109 | 26.83 | 65.37 | 23.66 | 6.13 | 41.09 | 0.0567 | 6.91 | 0.744 |
| 50.8 | 70.72 | 0.865 | 4.207 | 0.080 | 29.28 | 83.01 | 26.45 | 6.91 | 45.94 | 0.0720 | 4.11 | 0.857 |
| 61.6 | 75.00 | 0.918 | 5.102 | 0.052 | 28.64 | 100.66 | 28.05 | 7.61 | 48.71 | 0.0873 | 2.52 | 0.945 |
| 72.4 | 78.36 | 0.959 | 5.996 | 0.037 | 28.41 | 118.30 | 29.31 | 8.25 | 50.90 | 0.1027 | 1.26 | 0.994 |
| 83.1 | 80.44 | 0.984 | 6.890 | 0.023 | 25.66 | 135.94 | 30.08 | 8.85 | 52.25 | 0.1180 | 0.48 | 0.997 |
| 93.9 | 81.72 | 1.000 | 7.785 | 0.000 | 0.00 | 153.59 | 30.56 | 9.40 | 53.08 | 0.1333 | 0.00 | 0.957 |



APPENDIX H (cont.)

X/C = 0.90 13.0 INS THROTTLE 500.0 RPM

| | | | | | | | |
|---|---|---|---|---|---|---|---|
| UE | 84.77 FPS | DUEDX | -385.0 /SEC | H | 2.04 | | |
| UT | 2.67 FPS | UT/UE | 0.0314 | H** | 1.62 | | |
| UP | 1.75 FPS | | | PI | 10.85 | | |
| UB | 42.38 FPS | UB/UE | 0.500 | G | 16.21 | | |
| CFE | 1.977 $*_{10}$-3 | CTEQ | 7.563 $*_{10}$-3 | GEQ | 20.01 | | |
| CFLT | 1.837 $*_{10}$-3 | CFE/CFLT | 1.076 | GAMMA | -2.605 $*_{10}$-2 | | |
| CFNM | 2.003 $*_{10}$-3 | CFE/CFNM | 0.987 | A | 3.264 $*_{10}$4 FT/SEC↑2 | | |
| CDEL | 751.28 $*_{10}$-4 FT | DELTA | 72.30 $*_{10}$-4 FT | ALPHA0 | 0.282 | | |
| DSTAR | 23.62 $*_{10}$-4 FT | REDSTAR | 1225.0 | TH/UE*DUEDX | -5.261 $*_{10}$-3 | | |
| THETA | 11.59 $*_{10}$-4 FT | RETHETA | 600.9 | K | -3.161 | | |
| DELTA** | 18.72 $*_{10}$-4 FT | | | NU | 1.634 $*_{10}$-4 FT↑2/SEC | | |

| Y*$_{10}$4 (FT) | U (FPS) | U/UE | Y/THETA | Z*TH/UE | YY | Y+ | U+ | (Y*)↑0.5 | U* | Y/CDEL | (UE-U)/UT | UC/UE |
|---|---|---|---|---|---|---|---|---|---|---|---|---|
| 0.0 | 0.00 | 0.000 | 0.000 | 0.594 | 0.00 | 0.00 | 0.00 | 0.00 | 0.00 | 0.0000 | 31.81 | 0.000 |
| 2.2 | 9.77 | 0.115 | 0.191 | 0.613 | 3.67 | 3.61 | 3.67 | 1.54 | 5.59 | 0.0029 | 28.14 | 0.234 |
| 3.3 | 14.65 | 0.173 | 0.284 | 0.575 | 5.28 | 5.37 | 5.50 | 1.88 | 8.39 | 0.0044 | 26.31 | 0.266 |
| 4.9 | 20.71 | 0.244 | 0.424 | 0.456 | 7.01 | 8.01 | 7.77 | 2.29 | 11.85 | 0.0065 | 24.04 | 0.299 |
| 7.6 | 27.88 | 0.329 | 0.657 | 0.296 | 8.76 | 12.41 | 10.46 | 2.85 | 15.96 | 0.0101 | 21.35 | 0.341 |
| 10.3 | 32.41 | 0.382 | 0.890 | 0.216 | 10.13 | 16.80 | 12.16 | 3.32 | 18.55 | 0.0137 | 19.65 | 0.375 |
| 13.0 | 36.40 | 0.429 | 1.122 | 0.190 | 11.98 | 21.20 | 13.66 | 3.73 | 20.83 | 0.0173 | 18.15 | 0.407 |
| 18.4 | 42.88 | 0.506 | 1.588 | 0.154 | 15.29 | 30.00 | 16.09 | 4.44 | 24.54 | 0.0245 | 15.72 | 0.471 |
| 23.8 | 48.58 | 0.573 | 2.054 | 0.157 | 19.98 | 38.80 | 18.23 | 5.04 | 27.80 | 0.0317 | 13.58 | 0.537 |
| 29.2 | 55.31 | 0.652 | 2.520 | 0.148 | 23.74 | 47.60 | 20.76 | 5.59 | 31.66 | 0.0389 | 11.05 | 0.606 |
| 34.6 | 60.25 | 0.711 | 2.986 | 0.130 | 26.37 | 56.39 | 22.61 | 6.08 | 34.48 | 0.0460 | 9.20 | 0.677 |
| 40.0 | 65.56 | 0.773 | 3.451 | 0.126 | 30.05 | 65.19 | 24.60 | 6.54 | 37.52 | 0.0532 | 7.21 | 0.746 |
| 50.8 | 74.17 | 0.875 | 4.383 | 0.089 | 31.98 | 82.79 | 27.83 | 7.37 | 42.45 | 0.0676 | 3.98 | 0.871 |
| 61.6 | 79.56 | 0.939 | 5.314 | 0.053 | 30.00 | 100.38 | 29.85 | 8.11 | 45.53 | 0.0819 | 1.96 | 0.961 |
| 72.4 | 82.55 | 0.974 | 6.246 | 0.027 | 25.33 | 117.98 | 30.98 | 8.80 | 47.25 | 0.0963 | 0.83 | 1.000 |
| 83.1 | 83.88 | 0.989 | 7.177 | 0.014 | 20.86 | 135.58 | 31.48 | 9.43 | 48.01 | 0.1107 | 0.33 | 0.983 |
| 93.9 | 84.77 | 1.000 | 8.109 | 0.000 | 0.00 | 153.17 | 31.81 | 10.02 | 48.52 | 0.1250 | 0.00 | 0.917 |



APPENDIX H (cont.)

X/C = 0.90 22.0 INS THROTTLE 500.0 RPM

| | | | | | |
|---|---|---|---|---|---|
| UE | 90.48 FPS | DUEDX | -426.0 /SEC | H | 2.35 |
| UT | 2.60 FPS | UT/UE | 0.0287 | H** | 1.57 |
| UP | 1.85 FPS | | | PI | 14.28 |
| UB | 54.73 FPS | UB/UE | 0.605 | G | 20.05 |
| CFE | 1.646 *10-3 | CTEQ | 9.682 *10-3 | GEQ | 22.77 |
| CFLT | 1.129 *10-3 | CFE/CFLT | 1.459 | GAMMA | -2.458 *10-2 |
| CFNM | 1.115 *10-3 | CFE/CFNM | 1.477 | A | 3.855 *10↑4 FT/SEC↑2 |
| CDEL | 870.43 *10-4 FT | DELTA | 67.06 *10-4 FT | ALPHA0 | 0.360 |
| DSTAR | 24.97 *10-4 FT | REDSTAR | 1382.1 | TH/UE*DUEDX | -4.993 *10-3 |
| THETA | 10.61 *10-4 FT | RETHETA | 587.0 | K | -2.931 |
| DELTA** | 16.62 *10-4 FT | | | NU | 1.635 *10-4 FT↑2/SEC |

| Y*10↑4 (FT) | U (FPS) | U/UE | Y/THETA | Z*TH/UE | YY | Y+ | U+ | (Y*)↑0.5 | U* | Y/CDEL | (UE-U)/UT | UC/UE |
|---|---|---|---|---|---|---|---|---|---|---|---|---|
| 0.0 | 0.00 | 0.000 | 0.000 | 0.483 | 0.00 | 0.00 | 0.00 | 0.00 | 0.00 | 0.0000 | 34.86 | 0.000 |
| 2.2 | 8.44 | 0.093 | 0.209 | 0.411 | 3.24 | 3.51 | 3.25 | 1.58 | 4.57 | 0.0025 | 31.60 | 0.158 |
| 3.3 | 12.07 | 0.133 | 0.310 | 0.356 | 4.49 | 5.23 | 4.65 | 1.93 | 6.53 | 0.0038 | 30.21 | 0.188 |
| 4.9 | 16.19 | 0.179 | 0.463 | 0.275 | 5.88 | 7.80 | 6.24 | 2.36 | 8.77 | 0.0056 | 28.62 | 0.220 |
| 7.6 | 21.59 | 0.239 | 0.717 | 0.235 | 8.42 | 12.08 | 8.32 | 2.93 | 11.69 | 0.0087 | 26.54 | 0.262 |
| 10.3 | 26.99 | 0.298 | 0.972 | 0.210 | 10.79 | 16.36 | 10.40 | 3.41 | 14.61 | 0.0118 | 24.46 | 0.299 |
| 13.0 | 31.25 | 0.345 | 1.226 | 0.176 | 12.45 | 20.65 | 12.04 | 3.83 | 16.92 | 0.0149 | 22.82 | 0.335 |
| 18.4 | 38.48 | 0.425 | 1.735 | 0.167 | 17.16 | 29.22 | 14.82 | 4.56 | 20.83 | 0.0211 | 20.03 | 0.410 |
| 23.8 | 46.59 | 0.515 | 2.244 | 0.180 | 23.05 | 37.78 | 17.95 | 5.19 | 25.22 | 0.0273 | 16.91 | 0.492 |
| 29.2 | 55.04 | 0.608 | 2.753 | 0.183 | 28.55 | 46.35 | 21.20 | 5.74 | 29.80 | 0.0335 | 13.65 | 0.578 |
| 34.6 | 63.46 | 0.701 | 3.261 | 0.157 | 31.35 | 54.92 | 24.45 | 6.25 | 34.36 | 0.0397 | 10.41 | 0.666 |
| 40.0 | 69.53 | 0.768 | 3.770 | 0.129 | 32.75 | 63.49 | 26.78 | 6.72 | 37.64 | 0.0459 | 8.07 | 0.751 |
| 50.8 | 80.77 | 0.893 | 4.788 | 0.097 | 36.04 | 80.62 | 31.11 | 7.57 | 43.73 | 0.0583 | 3.74 | 0.897 |
| 61.6 | 87.31 | 0.965 | 5.805 | 0.047 | 30.61 | 97.76 | 33.63 | 8.34 | 47.27 | 0.0707 | 1.22 | 0.984 |
| 72.4 | 89.49 | 0.989 | 6.823 | 0.017 | 21.69 | 114.90 | 34.47 | 9.04 | 48.45 | 0.0831 | 0.38 | 0.996 |
| 83.1 | 90.48 | 1.000 | 7.840 | 0.000 | 0.00 | 132.03 | 34.86 | 9.69 | 48.99 | 0.0955 | 0.00 | 0.933 |



APPENDIX H (cont.)

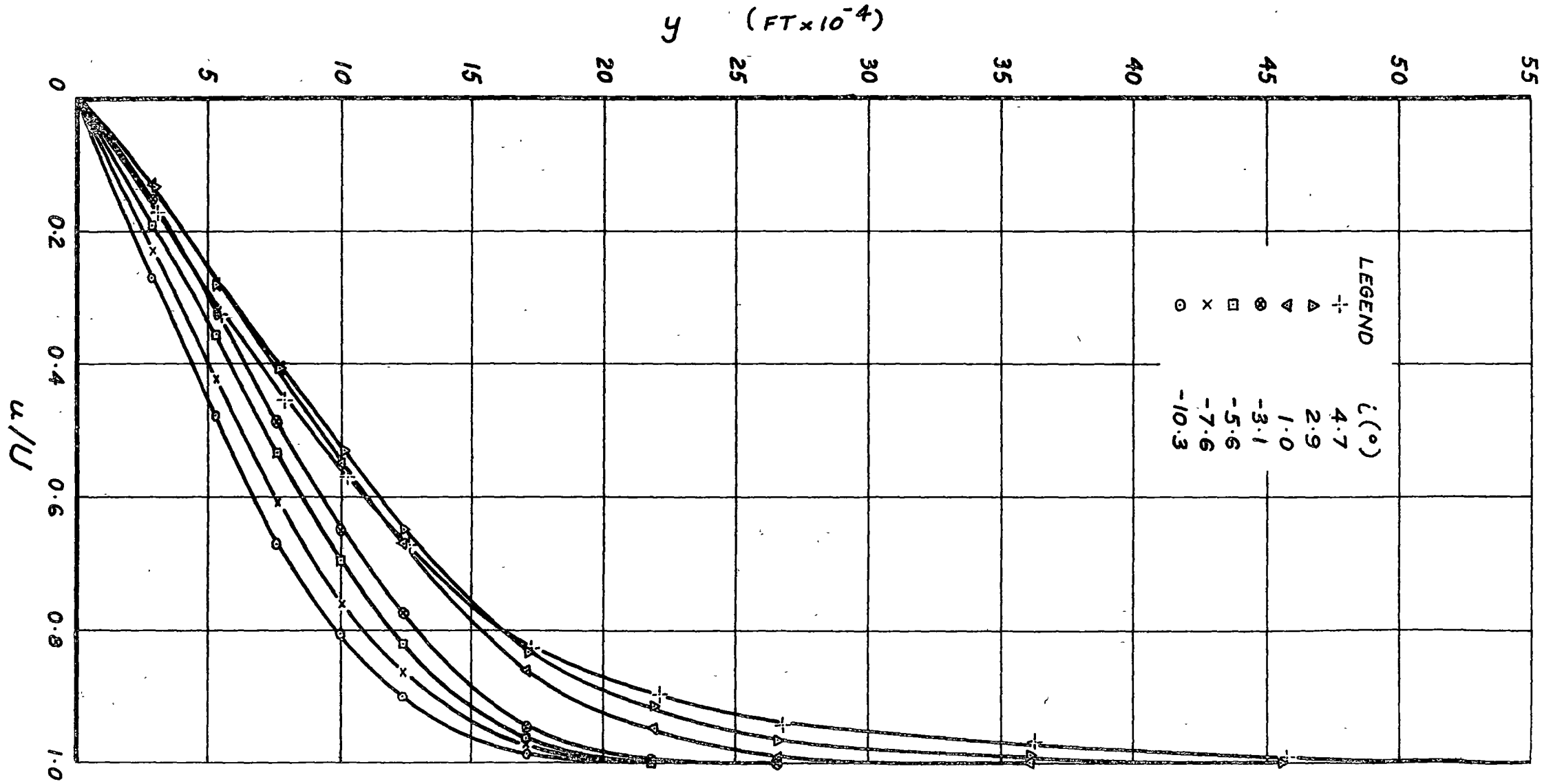


Fig. E.1 Boundary Layer Velocity Profiles from Hot Wire Measurements on Stator Blade Suction Surface: Compressor Speed 500 rpm

x/c = 0.40

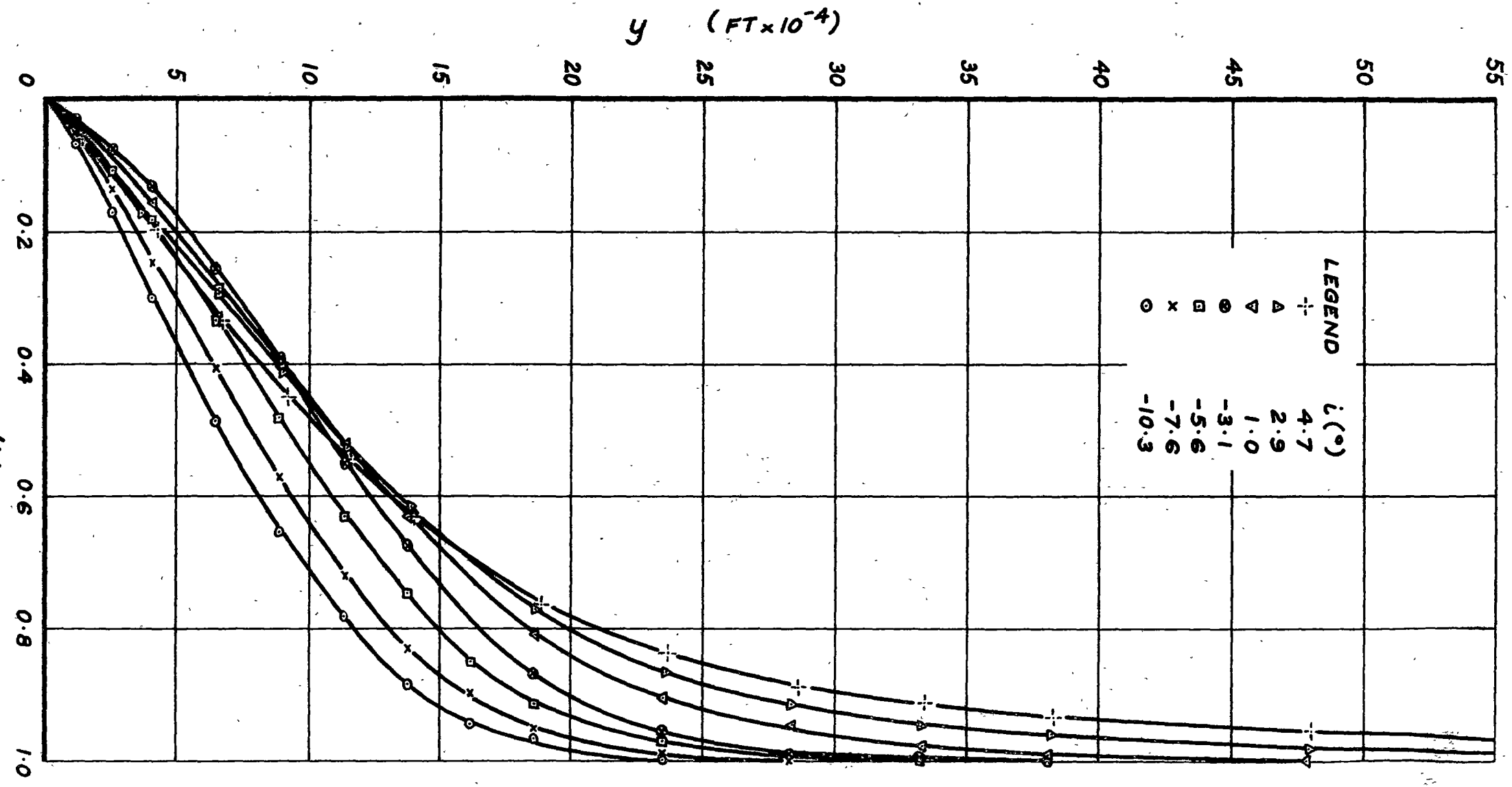


Fig. H.2 Boundary Layer Velocity Profiles from Hot Wire Measurements on Stator Blade Suction Surface: Compressor Speed 500 rpm

x/c = 0.50

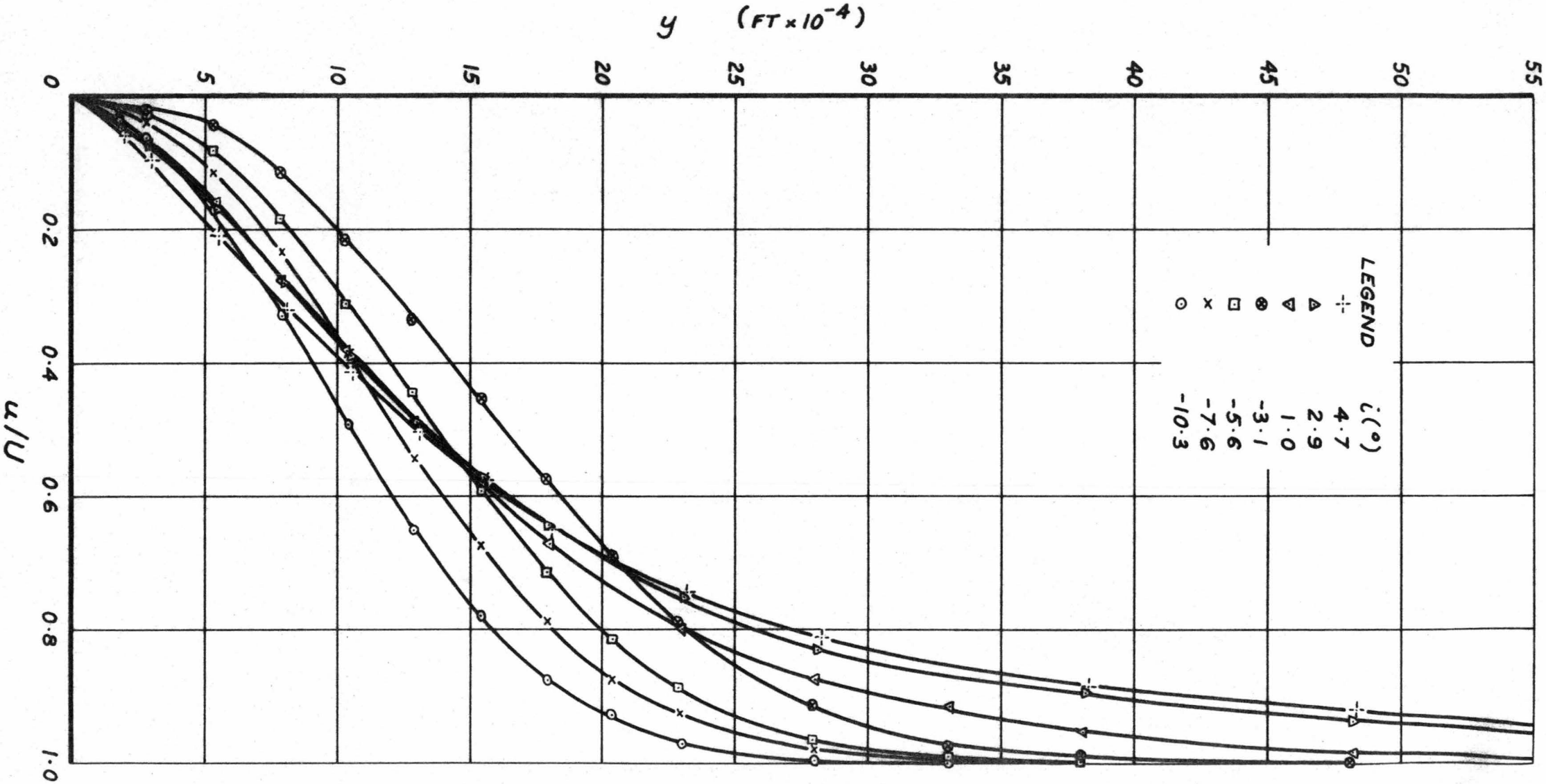


Fig. H.3 Boundary Layer Velocity Profiles from Hot Wire Measurements on Stator Blade Suction Surface: Compressor Speed 500 rpm

x/c = 0.60

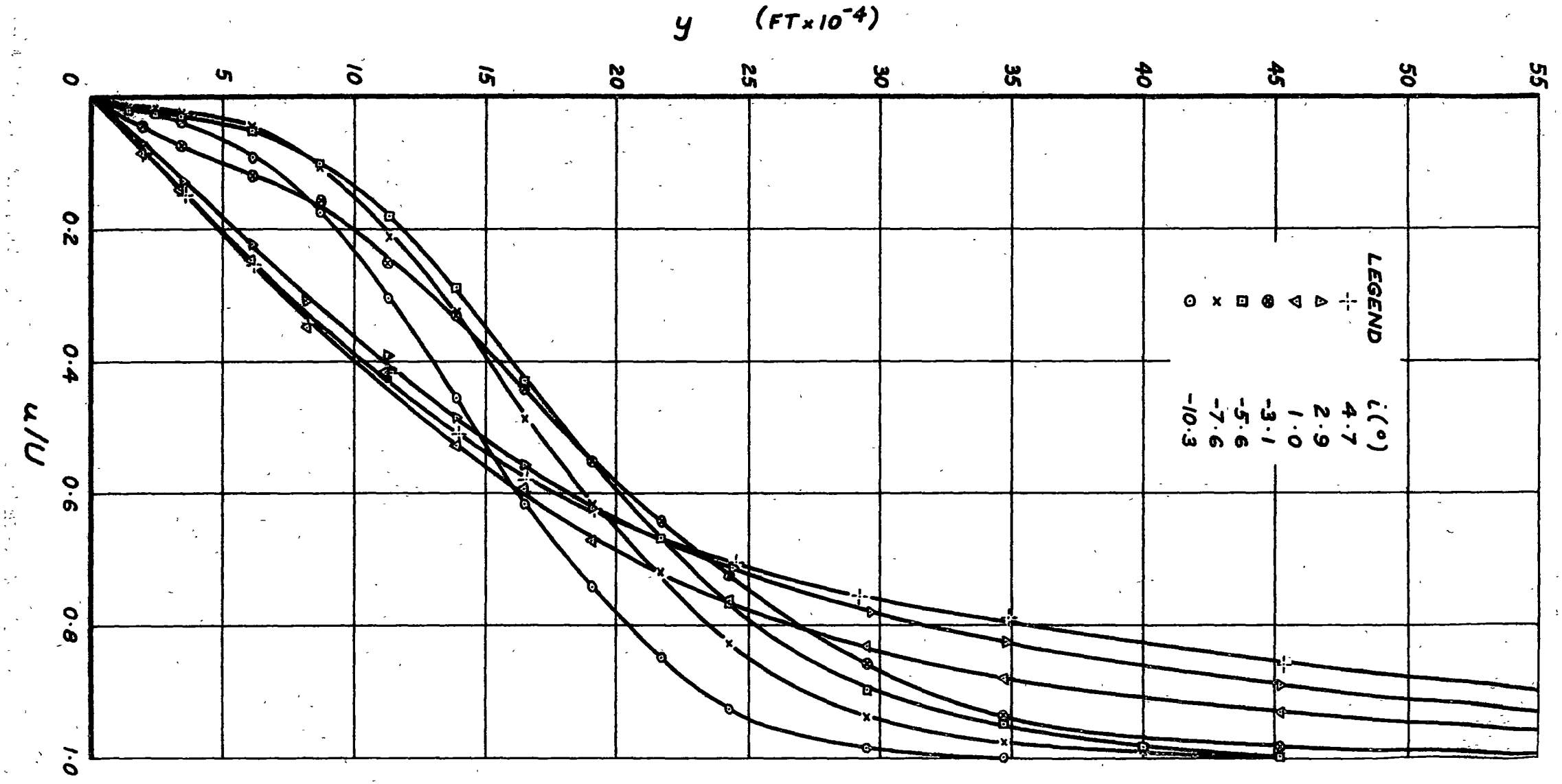


Fig. H.4 Boundary Layer Velocity Profiles from Hot Wire Measurements on Stator Blade Suction Surface: Compressor Speed 500 rpm

x/c = 0.70

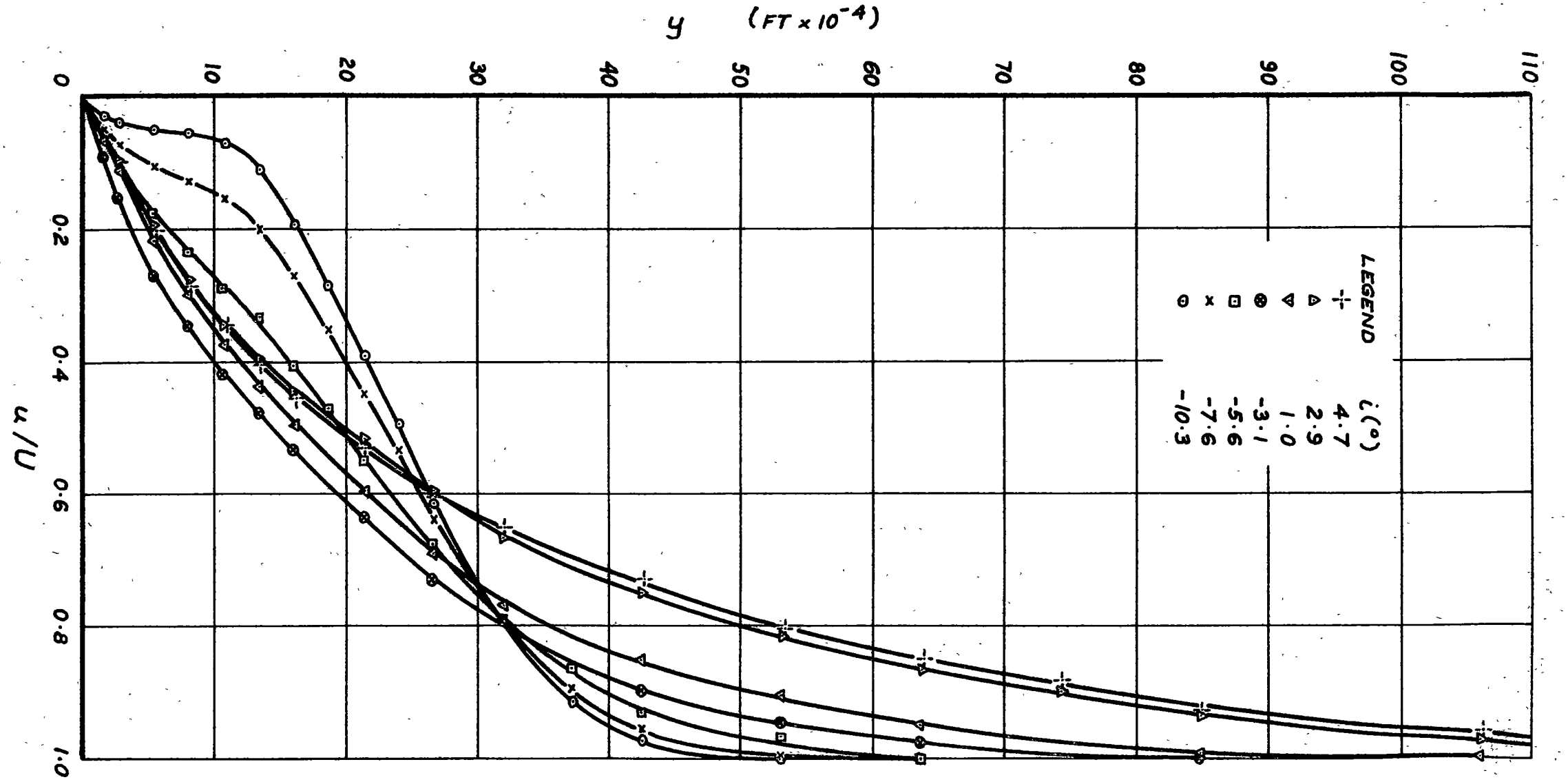


Fig. H.5 Boundary Layer Velocity Profiles from Hot Wire Measurements on Stator Blade Suction Surface: Compressor Speed 500 rpm

x/c = 0.80

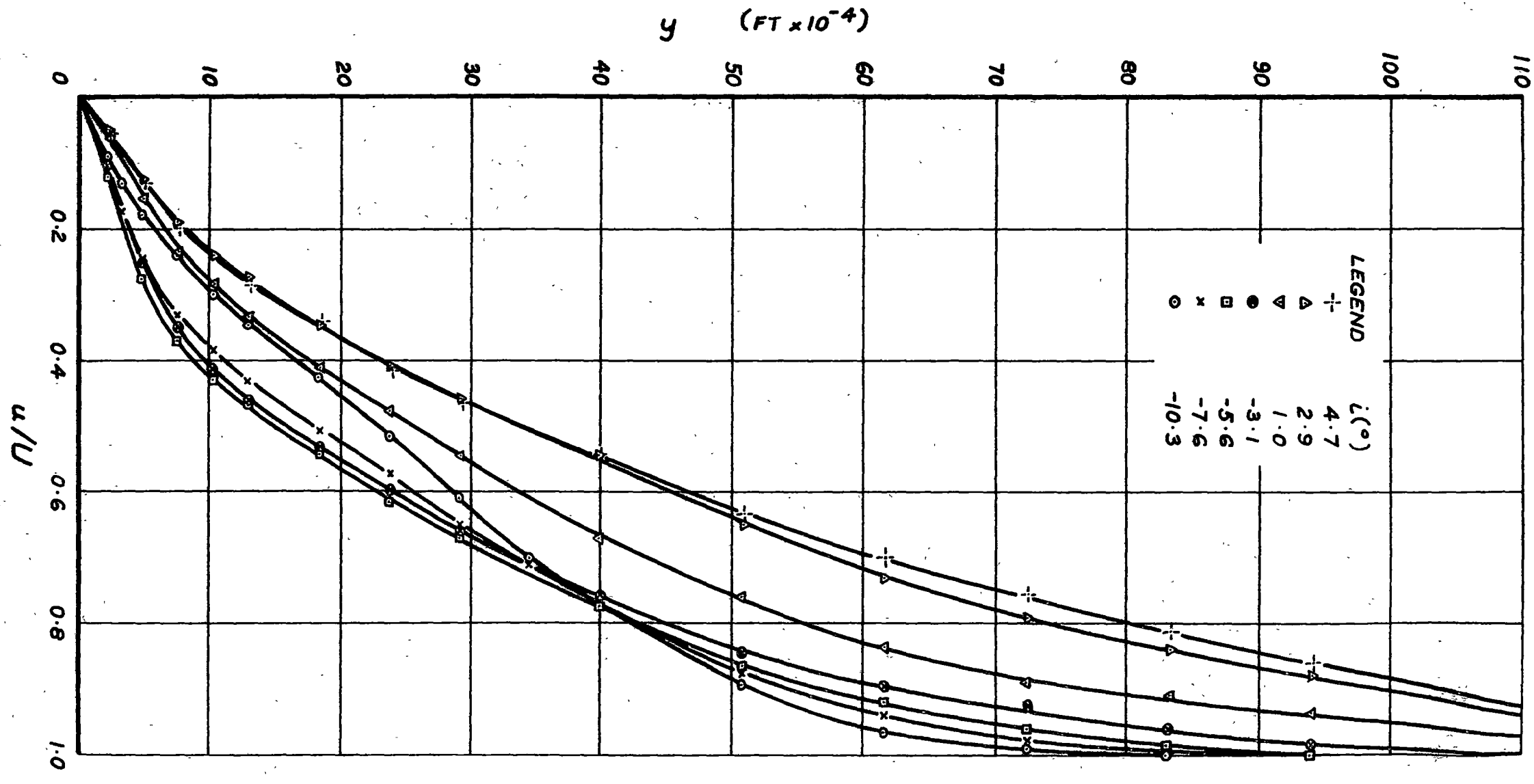


Fig. H.6 Boundary Layer Velocity Profiles from Hot Wire Measurements on Stator Blade Suction Surface: Compressor Speed 500 rpm

x/c = 0.90

# APPENDIX I

## Effect of Change in Wall Proximity Correction on Some Turbulent Boundary Layer Measurements

Due to the uncertainty regarding the correction of hot wire readings for wall proximity effects in turbulent flow (see Sections 3.3.8 and 7.2), this Appendix presents some turbulent boundary layer velocity profiles obtained by using only half of the laminar flow correction given in Table 3.3.

The boundary layer profiles tabulated here were all measured at 90% chord on the stator blade suction surface at a compressor speed of 500 rpm. The values of velocity and other relevant boundary layer parameters can be compared with those for the corresponding profiles in Appendix H, which were all calculated by using the full laminar flow wall proximity correction : this indicates the magnitude of the wall proximity effects, and the possible errors which might arise from them.

X/C = 0.90 4.8 INS THROTTLE 500.0 RPM

| | | | | | | | | |
|---|---|---|---|---|---|---|---|---|
| UE | 61.89 FPS | DUEDX | -151.0 /SEC | H | 2.04 | | | |
| UT | 1.89 FPS | UT/UE | 0.0306 | H** | 1.62 | | | |
| UP | 1.15 FPS | | | PI | 11.74 | | | |
| UB | 31.28 FPS | UB/UE | 0.505 | G | 16.67 | | | |
| CFE | 1.869 $*_{10}$-3 | CTEQ | 7.574 $*_{10}$-3 | GEQ | 20.76 | | | |
| CFLT | 1.681 $*_{10}$-3 | CFE/CFLT | 1.112 | GAMMA | -2.891 $*_{10}$-2 | | | |
| CFNM | 1.746 $*_{10}$-3 | CFE/CFNM | 1.071 | A | 0.934 $*_{10}$4 FT/SEC↑2 | | | |
| CDEL | 1471.52 $*_{10}$-4 FT | DELTA | 137.46 $*_{10}$-4 FT | ALPHA0 | 0.226 | | | |
| DSTAR | 44.99 $*_{10}$-4 FT | REDSTAR | 1699.1 | TH/UE*DUEDX | -5.382 $*_{10}$-3 | | | |
| THETA | 22.06 $*_{10}$-4 FT | RETHETA | 833.1 | K | -4.484 | | | |
| DELTA** | 35.69 $*_{10}$-4 FT | | | NU | 1.638 $*_{10}$-4 FT↑2/SEC | | | |

| Y*$_{10}$4 (FT) | U (FPS) | U/UE | Y/THETA | Z*TH/UE | YY | Y+ | U+ | (Y*)↑0.5 | U* | Y/CDEL | (UE-U)/UT | UC/UE |
|---|---|---|---|---|---|---|---|---|---|---|---|---|
| 0.0 | 0.00 | 0.000 | 0.000 | 0.779 | 0.00 | 0.00 | 0.00 | 0.00 | 0.00 | 0.0000 | 32.71 | 0.000 |
| 2.4 | 4.75 | 0.077 | 0.108 | 0.646 | 2.50 | 2.74 | 2.51 | 1.29 | 4.12 | 0.0016 | 30.20 | 0.192 |
| 5.1 | 9.07 | 0.147 | 0.230 | 0.556 | 4.95 | 5.86 | 4.79 | 1.89 | 7.87 | 0.0034 | 27.92 | 0.250 |
| 7.8 | 13.16 | 0.213 | 0.352 | 0.466 | 6.94 | 8.97 | 6.96 | 2.34 | 11.42 | 0.0053 | 25.76 | 0.284 |
| 13.2 | 17.96 | 0.290 | 0.597 | 0.273 | 9.00 | 15.20 | 9.49 | 3.04 | 15.58 | 0.0089 | 23.22 | 0.331 |
| 18.6 | 21.42 | 0.346 | 0.842 | 0.259 | 12.35 | 21.43 | 11.32 | 3.61 | 18.59 | 0.0126 | 21.39 | 0.368 |
| 24.0 | 25.79 | 0.417 | 1.086 | 0.244 | 15.50 | 27.66 | 13.63 | 4.11 | 22.38 | 0.0163 | 19.08 | 0.401 |
| 29.4 | 28.82 | 0.466 | 1.331 | 0.188 | 16.65 | 33.89 | 15.23 | 4.54 | 25.00 | 0.0199 | 17.48 | 0.434 |
| 40.1 | 33.76 | 0.546 | 1.820 | 0.171 | 21.71 | 46.35 | 17.85 | 5.31 | 29.29 | 0.0273 | 14.86 | 0.502 |
| 50.9 | 39.16 | 0.633 | 2.309 | 0.156 | 26.35 | 58.82 | 20.70 | 5.99 | 33.98 | 0.0346 | 12.01 | 0.573 |
| 61.7 | 43.23 | 0.699 | 2.799 | 0.127 | 28.78 | 71.28 | 22.85 | 6.59 | 37.51 | 0.0419 | 9.86 | 0.647 |
| 72.5 | 46.85 | 0.757 | 3.288 | 0.116 | 32.28 | 83.74 | 24.76 | 7.14 | 40.65 | 0.0493 | 7.95 | 0.721 |
| 83.3 | 50.23 | 0.812 | 3.777 | 0.105 | 35.37 | 96.20 | 26.55 | 7.66 | 43.58 | 0.0566 | 6.16 | 0.793 |
| 94.1 | 53.22 | 0.860 | 4.266 | 0.088 | 36.54 | 108.66 | 28.13 | 8.14 | 46.18 | 0.0639 | 4.58 | 0.857 |
| 115.7 | 57.26 | 0.925 | 5.245 | 0.058 | 36.52 | 133.58 | 30.26 | 9.02 | 49.68 | 0.0786 | 2.45 | 0.956 |
| 137.3 | 60.27 | 0.974 | 6.223 | 0.035 | 33.37 | 158.50 | 31.86 | 9.83 | 52.30 | 0.0933 | 0.85 | 1.000 |
| 158.9 | 61.44 | 0.993 | 7.202 | 0.013 | 23.98 | 183.43 | 32.47 | 10.57 | 53.30 | 0.1080 | 0.24 | 0.981 |
| 180.4 | 61.89 | 1.000 | 8.180 | 0.000 | 0.00 | 208.35 | 32.71 | 11.27 | 53.69 | 0.1226 | 0.00 | 0.908 |



APPENDIX I (cont.)

X/C = 0.90 — 5.2 INS THROTTLE 500.0 RPM

| | | | | | | | |
|---|---|---|---|---|---|---|---|
| UE | 68.38 FPS | DUEDX | -180.0 /SEC | H | 2.07 | | |
| UT | 1.90 FPS | UT/UE | 0.0278 | H** | 1.62 | | |
| UP | 1.26 FPS | | | PI | 14.69 | | |
| UB | 36.32 FPS | UB/UE | 0.531 | G | 18.60 | | |
| CFE | 1.543 *10-3 | CTEQ | 7.795 *10-3 | GEQ | 23.08 | | |
| CFLT | 1.589 *10-3 | CFE/CFLT | 0.971 | GAMMA | -2.973 *10-2 | | |
| CFNM | 1.634 *10-3 | CFE/CFNM | 0.945 | A | 1.231 *10^4 FT/SEC↑2 | | |
| CDEL | 1550.01 *10-4 FT | DELTA | 129.17 *10-4 FT | ALPHA0 | 0.295 | | |
| DSTAR | 43.06 *10-4 FT | REDSTAR | 1793.8 | TH/UE*DUEDX | -5.479 *10-3 | | |
| THETA | 20.82 *10-4 FT | RETHETA | 867.2 | K | -4.752 | | |
| DELTA** | 33.75 *10-4 FT | | | NU | 1.641 *10-4 FT↑2/SEC | | |

| Y*10^4 (FT) | U (FPS) | U/UE | Y/THETA | Z*TH/UE | YY | Y+ | U+ | (Y*)↑0.5 | U* | Y/CDEL | (UE-U)/UT | UC/UE |
|---|---|---|---|---|---|---|---|---|---|---|---|---|
| 0.0 | 0.00 | 0.000 | 0.000 | 0.669 | 0.00 | 0.00 | 0.00 | 0.00 | 0.00 | 0.0000 | 36.00 | 0.000 |
| 2.3 | 4.81 | 0.070 | 0.111 | 0.592 | 2.53 | 2.69 | 2.53 | 1.34 | 3.80 | 0.0015 | 33.47 | 0.197 |
| 5.0 | 9.66 | 0.141 | 0.241 | 0.506 | 5.05 | 5.81 | 5.09 | 1.97 | 7.64 | 0.0032 | 30.91 | 0.251 |
| 7.7 | 13.78 | 0.201 | 0.371 | 0.417 | 7.05 | 8.93 | 7.25 | 2.44 | 10.90 | 0.0050 | 28.75 | 0.283 |
| 10.4 | 17.04 | 0.249 | 0.500 | 0.298 | 8.05 | 12.05 | 8.97 | 2.83 | 13.48 | 0.0067 | 27.03 | 0.307 |
| 13.1 | 19.06 | 0.279 | 0.630 | 0.243 | 9.14 | 15.17 | 10.04 | 3.18 | 15.08 | 0.0085 | 25.96 | 0.327 |
| 18.5 | 23.89 | 0.349 | 0.889 | 0.254 | 13.21 | 21.42 | 12.58 | 3.78 | 18.89 | 0.0119 | 23.42 | 0.364 |
| 23.9 | 28.08 | 0.411 | 1.148 | 0.215 | 15.67 | 27.66 | 14.78 | 4.29 | 22.21 | 0.0154 | 21.22 | 0.398 |
| 29.3 | 31.50 | 0.461 | 1.408 | 0.196 | 18.35 | 33.91 | 16.58 | 4.75 | 24.92 | 0.0189 | 19.42 | 0.433 |
| 40.1 | 38.67 | 0.566 | 1.926 | 0.184 | 24.30 | 46.40 | 20.36 | 5.56 | 30.59 | 0.0259 | 15.64 | 0.506 |
| 50.9 | 44.51 | 0.651 | 2.444 | 0.160 | 28.78 | 58.88 | 23.43 | 6.26 | 35.21 | 0.0328 | 12.57 | 0.584 |
| 61.7 | 50.01 | 0.731 | 2.963 | 0.133 | 31.84 | 71.37 | 26.33 | 6.89 | 39.56 | 0.0398 | 9.67 | 0.666 |
| 72.5 | 53.96 | 0.789 | 3.481 | 0.104 | 33.10 | 83.86 | 28.41 | 7.47 | 42.68 | 0.0468 | 7.59 | 0.746 |
| 83.3 | 57.40 | 0.839 | 4.000 | 0.085 | 34.42 | 96.35 | 30.22 | 8.01 | 45.41 | 0.0537 | 5.78 | 0.821 |
| 94.0 | 60.01 | 0.878 | 4.518 | 0.069 | 34.85 | 108.84 | 31.59 | 8.51 | 47.47 | 0.0607 | 4.41 | 0.887 |
| 115.6 | 64.16 | 0.938 | 5.555 | 0.046 | 35.13 | 133.82 | 33.78 | 9.44 | 50.75 | 0.0746 | 2.22 | 0.978 |
| 137.2 | 66.55 | 0.973 | 6.592 | 0.030 | 33.48 | 158.80 | 35.04 | 10.28 | 52.64 | 0.0885 | 0.96 | 0.999 |
| 158.8 | 68.38 | 1.000 | 7.629 | 0.000 | 0.00 | 183.77 | 36.00 | 11.06 | 54.09 | 0.1025 | 0.00 | 0.948 |



APPENDIX I (cont.)

X/C = 0.90 6.0 INS THROTTLE 500.0 RPM

| | | | | | |
|---|---|---|---|---|---|
| UE | 72.52 FPS | DUEDX | -365.0 /SEC | H | 2.01 |
| UT | 2.17 FPS | UT/UE | 0.0299 | H** | 1.64 |
| UP | 1.63 FPS | | | PI | 18.95 |
| UB | 36.26 FPS | UB/UE | 0.500 | G | 16.82 |
| CFE | 1.785 *10-3 | CTEQ | 7.367 *10-3 | GEQ | 26.09 |
| CFLT | 1.816 *10-3 | CFE/CFLT | 0.983 | GAMMA | -4.386 *10-2 |
| CFNM | 1.923 *10-3 | CFE/CFNM | 0.928 | A | 2.647 *10↑4 FT/SEC↑2 |
| CDEL | 1124.87 *10-4 FT | DELTA | 104.08 *10-4 FT | ALPHA0 | 0.427 |
| DSTAR | 33.60 *10-4 FT | REDSTAR | 1485.1 | TH/UE*DUEDX | -8.412 *10-3 |
| THETA | 16.71 *10-4 FT | RETHETA | 738.7 | K | -6.214 |
| DELTA** | 27.42 *10-4 FT | | | NU | 1.641 *10-4 FT↑2/SEC |

| Y*10↑4 (FT) | U (FPS) | U/UE | Y/THETA | Z*TH/UE | YY | Y+ | U+ | (Y*)↑0.5 | U* | Y/CDEL | (UE-U)/UT | UC/UE |
|---|---|---|---|---|---|---|---|---|---|---|---|---|
| 0.0 | 0.00 | 0.000 | 0.000 | 0.659 | 0.00 | 0.00 | 0.00 | 0.00 | 0.00 | 0.0000 | 33.47 | 0.000 |
| 2.3 | 6.11 | 0.084 | 0.136 | 0.583 | 2.81 | 2.99 | 2.82 | 1.50 | 3.74 | 0.0020 | 30.66 | 0.222 |
| 5.0 | 12.40 | 0.171 | 0.297 | 0.507 | 5.75 | 6.55 | 5.73 | 2.22 | 7.60 | 0.0044 | 27.75 | 0.281 |
| 7.7 | 17.98 | 0.248 | 0.458 | 0.376 | 7.64 | 10.12 | 8.30 | 2.76 | 11.02 | 0.0068 | 25.17 | 0.317 |
| 10.4 | 21.21 | 0.292 | 0.620 | 0.284 | 8.98 | 13.68 | 9.79 | 3.21 | 13.00 | 0.0092 | 23.69 | 0.344 |
| 13.1 | 24.63 | 0.340 | 0.781 | 0.273 | 11.09 | 17.24 | 11.37 | 3.60 | 15.10 | 0.0116 | 22.10 | 0.368 |
| 18.5 | 30.07 | 0.415 | 1.104 | 0.215 | 13.91 | 24.36 | 13.88 | 4.28 | 18.43 | 0.0164 | 19.60 | 0.412 |
| 23.8 | 34.70 | 0.478 | 1.427 | 0.204 | 17.53 | 31.49 | 16.02 | 4.87 | 21.27 | 0.0212 | 17.46 | 0.455 |
| 29.2 | 39.64 | 0.547 | 1.750 | 0.206 | 21.60 | 38.61 | 18.30 | 5.39 | 24.29 | 0.0260 | 15.18 | 0.499 |
| 40.0 | 48.86 | 0.674 | 2.395 | 0.165 | 26.48 | 52.86 | 22.55 | 6.31 | 29.95 | 0.0356 | 10.92 | 0.592 |
| 50.8 | 55.13 | 0.760 | 3.041 | 0.124 | 29.14 | 67.11 | 25.45 | 7.11 | 33.79 | 0.0452 | 8.03 | 0.689 |
| 61.6 | 60.50 | 0.834 | 3.687 | 0.099 | 31.47 | 81.36 | 27.93 | 7.83 | 37.08 | 0.0548 | 5.55 | 0.783 |
| 72.4 | 64.37 | 0.888 | 4.332 | 0.057 | 28.00 | 95.60 | 29.71 | 8.49 | 39.45 | 0.0644 | 3.76 | 0.868 |
| 83.2 | 65.80 | 0.907 | 4.978 | 0.038 | 26.36 | 109.85 | 30.37 | 9.10 | 40.33 | 0.0740 | 3.10 | 0.936 |
| 94.0 | 67.92 | 0.937 | 5.624 | 0.040 | 30.60 | 124.10 | 31.35 | 9.67 | 41.63 | 0.0836 | 2.12 | 0.981 |
| 115.6 | 70.68 | 0.975 | 6.915 | 0.021 | 26.94 | 152.60 | 32.63 | 10.72 | 43.32 | 0.1027 | 0.85 | 0.993 |
| 137.2 | 71.77 | 0.990 | 8.206 | 0.010 | 22.09 | 181.09 | 33.13 | 11.68 | 43.99 | 0.1219 | 0.35 | 0.905 |
| 158.7 | 72.52 | 1.000 | 9.498 | 0.000 | 0.00 | 209.59 | 33.47 | 12.56 | 44.45 | 0.1411 | 0.00 | 0.761 |

X/C = 0.90 8.0 INS THROTTLE 500.0 RPM

| | | | | | | | |
|---|---|---|---|---|---|---|---|
| UE | 76.95 FPS | DUEDX | -252.0 /SEC | H | 1.85 | | |
| UT | 2.86 FPS | UT/UE | 0.0372 | H** | 1.66 | | |
| UP | 1.48 FPS | | | PI | 5.84 | | |
| UB | 30.53 FPS | UB/UE | 0.397 | G | 12.35 | | |
| CFE | 2.762 *10-3 | CTEQ | 6.085 *10-3 | GEQ | 15.17 | | |
| CFLT | 2.456 *10-3 | CFE/CFLT | 1.125 | GAMMA | -2.176 *10-2 | | |
| CFNM | 2.647 *10-3 | CFE/CFNM | 1.043 | A | 1.939 *10^4 | FT/SEC↑2 | |
| CDEL | 662.57 *10-4 FT | DELTA | 85.20 *10-4 FT | ALPHA0 | 0.138 | | |
| DSTAR | 24.62 *10-4 FT | REDSTAR | 1142.5 | TH/UE*DUEDX | -4.363 *10-3 | | |
| THETA | 13.32 *10-4 FT | RETHETA | 618.3 | K | -2.698 | | |
| DELTA** | 22.10 *10-4 FT | | | NU | 1.658 *10-4 | FT↑2/SEC | |

| Y*10^4 (FT) | U (FPS) | U/UE | Y/THETA | Z*TH/UE | YY | Y+ | U+ | (Y*)↑0.5 | U* | Y/CDEL | (UE-U)/UT | UC/UE |
|---|---|---|---|---|---|---|---|---|---|---|---|---|
| 0.0 | 0.00 | 0.000 | 0.000 | 0.854 | 0.00 | 0.00 | 0.00 | 0.00 | 0.00 | 0.0000 | 26.91 | 0.000 |
| 2.2 | 10.29 | 0.134 | 0.166 | 0.757 | 3.59 | 3.81 | 3.60 | 1.40 | 6.97 | 0.0033 | 23.31 | 0.273 |
| 4.9 | 21.16 | 0.275 | 0.369 | 0.578 | 6.96 | 8.47 | 7.40 | 2.09 | 14.34 | 0.0074 | 19.51 | 0.348 |
| 7.6 | 28.29 | 0.368 | 0.571 | 0.371 | 8.65 | 13.12 | 9.89 | 2.60 | 19.17 | 0.0115 | 17.02 | 0.392 |
| 10.3 | 32.72 | 0.425 | 0.773 | 0.259 | 9.78 | 17.77 | 11.44 | 3.03 | 22.17 | 0.0156 | 15.47 | 0.426 |
| 13.0 | 36.35 | 0.472 | 0.976 | 0.212 | 11.18 | 22.42 | 12.71 | 3.40 | 24.62 | 0.0196 | 14.20 | 0.455 |
| 18.4 | 41.69 | 0.542 | 1.381 | 0.158 | 13.66 | 31.73 | 14.58 | 4.05 | 28.24 | 0.0278 | 12.33 | 0.508 |
| 23.8 | 46.22 | 0.601 | 1.786 | 0.151 | 17.23 | 41.03 | 16.16 | 4.60 | 31.31 | 0.0359 | 10.75 | 0.559 |
| 29.2 | 51.08 | 0.664 | 2.191 | 0.143 | 20.63 | 50.34 | 17.86 | 5.10 | 34.60 | 0.0441 | 9.05 | 0.610 |
| 40.0 | 58.45 | 0.760 | 3.001 | 0.111 | 24.86 | 68.94 | 20.44 | 5.97 | 39.60 | 0.0603 | 6.47 | 0.714 |
| 50.8 | 64.91 | 0.844 | 3.811 | 0.085 | 27.61 | 87.55 | 22.70 | 6.72 | 43.98 | 0.0766 | 4.21 | 0.814 |
| 61.6 | 69.04 | 0.897 | 4.621 | 0.050 | 25.66 | 106.16 | 24.14 | 7.40 | 46.77 | 0.0929 | 2.77 | 0.900 |
| 72.4 | 71.13 | 0.924 | 5.430 | 0.039 | 26.53 | 124.77 | 24.87 | 8.03 | 48.19 | 0.1092 | 2.04 | 0.963 |
| 83.1 | 73.85 | 0.960 | 6.240 | 0.037 | 29.88 | 143.38 | 25.82 | 8.60 | 50.03 | 0.1255 | 1.09 | 0.997 |
| 93.9 | 75.75 | 0.984 | 7.050 | 0.024 | 26.92 | 161.99 | 26.49 | 9.14 | 51.32 | 0.1418 | 0.42 | 0.999 |
| 115.5 | 76.95 | 1.000 | 8.670 | 0.000 | 0.00 | 199.20 | 26.91 | 10.14 | 52.13 | 0.1744 | 0.00 | 0.916 |

X/C = 0.90 10.0 INS THROTTLE 500.0 RPM

| | | | | | | | |
|---|---|---|---|---|---|---|---|
| UE | 81.72 FPS | DUEDX | -273.0 /SEC | H | 1.87 | | |
| UT | 3.20 FPS | UT/UE | 0.0392 | H** | 1.65 | | |
| UP | 1.54 FPS | | | PI | 4.95 | | |
| UB | 32.09 FPS | UB/UE | 0.393 | G | 11.87 | | |
| CFE | 3.067 $*_{10}$-3 | CTEQ | 6.239 $*_{10}$-3 | GEQ | 14.16 | | |
| CFLT | 2.387 $*_{10}$-3 | CFE/CFLT | 1.285 | GAMMA | -2.018 $*_{10}$-2 | | |
| CFNM | 2.584 $*_{10}$-3 | CFE/CFNM | 1.187 | A | 2.231 $*_{10}$4 FT/SEC↑2 | | |
| CDEL | 580.54 $*_{10}$-4 FT | DELTA | 77.89 $*_{10}$-4 FT | ALPHA0 | 0.111 | | |
| DSTAR | 22.74 $*_{10}$-4 FT | REDSTAR | 1136.0 | TH/UE*DUEDX | -4.064 $*_{10}$-3 | | |
| THETA | 12.16 $*_{10}$-4 FT | RETHETA | 607.8 | K | -2.470 | | |
| DELTA** | 20.02 $*_{10}$-4 FT | | | NU | 1.635 $*_{10}$-4 FT↑2/SEC | | |

| Y*$_{10}$4 (FT) | U (FPS) | U/UE | Y/THETA | Z*TH/UE | YY | Y+ | U+ | (Y*)↑0.5 | U* | Y/CDEL | (UE-U)/UT | UC/UE |
|---|---|---|---|---|---|---|---|---|---|---|---|---|
| 0.0 | 0.00 | 0.000 | 0.000 | 0.932 | 0.00 | 0.00 | 0.00 | 0.00 | 0.00 | 0.0000 | 25.53 | 0.000 |
| 2.2 | 12.59 | 0.154 | 0.182 | 0.761 | 3.91 | 4.33 | 3.93 | 1.44 | 8.18 | 0.0038 | 21.60 | 0.268 |
| 4.9 | 24.50 | 0.300 | 0.404 | 0.528 | 7.23 | 9.61 | 7.66 | 2.15 | 15.91 | 0.0085 | 17.88 | 0.347 |
| 7.6 | 31.72 | 0.388 | 0.625 | 0.317 | 8.68 | 14.89 | 9.91 | 2.68 | 20.61 | 0.0131 | 15.62 | 0.394 |
| 10.3 | 35.99 | 0.440 | 0.847 | 0.200 | 9.34 | 20.17 | 11.25 | 3.11 | 23.38 | 0.0178 | 14.29 | 0.431 |
| 13.0 | 38.98 | 0.477 | 1.069 | 0.165 | 10.70 | 25.45 | 12.18 | 3.50 | 25.32 | 0.0224 | 13.36 | 0.463 |
| 18.4 | 44.96 | 0.550 | 1.513 | 0.161 | 14.97 | 36.01 | 14.05 | 4.16 | 29.21 | 0.0317 | 11.49 | 0.521 |
| 23.8 | 50.67 | 0.620 | 1.956 | 0.138 | 17.89 | 46.56 | 15.83 | 4.73 | 32.91 | 0.0410 | 9.70 | 0.578 |
| 29.2 | 54.94 | 0.672 | 2.400 | 0.117 | 20.24 | 57.12 | 17.17 | 5.24 | 35.69 | 0.0503 | 8.37 | 0.635 |
| 40.0 | 63.30 | 0.775 | 3.287 | 0.109 | 26.74 | 78.24 | 19.78 | 6.13 | 41.12 | 0.0689 | 5.75 | 0.748 |
| 50.8 | 70.73 | 0.866 | 4.174 | 0.081 | 29.22 | 99.36 | 22.10 | 6.91 | 45.94 | 0.0875 | 3.43 | 0.853 |
| 61.6 | 75.00 | 0.918 | 5.061 | 0.053 | 28.62 | 120.47 | 23.43 | 7.61 | 48.71 | 0.1061 | 2.10 | 0.936 |
| 72.4 | 78.36 | 0.959 | 5.948 | 0.038 | 28.41 | 141.59 | 24.48 | 8.25 | 50.90 | 0.1246 | 1.05 | 0.988 |
| 83.1 | 80.44 | 0.984 | 6.836 | 0.023 | 25.66 | 162.71 | 25.13 | 8.85 | 52.25 | 0.1432 | 0.40 | 1.002 |
| 93.9 | 81.72 | 1.000 | 7.723 | 0.000 | 0.00 | 183.83 | 25.53 | 9.40 | 53.08 | 0.1618 | 0.00 | 0.978 |



APPENDIX I (cont.)

X/C = 0.90 13.0 INS THROTTLE 500.0 RPM

| | | | | | |
|---|---|---|---|---|---|
| UE | 84.77 FPS | DUEDX | -385.0 /SEC | H | 2.00 |
| UT | 3.25 FPS | UT/UE | 0.0384 | H** | 1.62 |
| UP | 1.75 FPS | | | PI | 7.20 |
| UB | 37.62 FPS | UB/UE | 0.444 | G | 13.01 |
| CFE | 2.942 *10-3 | CTEQ | 7.206 *10-3 | GEQ | 16.61 |
| CFLT | 1.961 *10-3 | CFE/CFLT | 1.500 | GAMMA | -2.634 *10-2 |
| CFNM | 2.138 *10-3 | CFE/CFNM | 1.376 | A | 3.264 *10↑4 FT/SEC↑2 |
| CDEL | 607.96 *10-4 FT | DELTA | 73.92 *10-4 FT | ALPHA0 | 0.155 |
| DSTAR | 23.32 *10-4 FT | REDSTAR | 1209.5 | TH/UE*DUEDX | -5.308 *10-3 |
| THETA | 11.69 *10-4 FT | RETHETA | 606.1 | K | -3.217 |
| DELTA** | 18.90 *10-4 FT | | | NU | 1.634 *10-4 FT↑2/SEC |

| Y*10↑4 (FT) | U (FPS) | U/UE | Y/THETA | Z*TH/UE | YY | Y+ | U+ | (Y*)↑0.5 | U* | Y/CDEL | (UE-U)/UT | UC/UE |
|---|---|---|---|---|---|---|---|---|---|---|---|---|
| 0.0 | 0.00 | 0.000 | 0.000 | 0.892 | 0.00 | 0.00 | 0.00 | 0.00 | 0.00 | 0.0000 | 26.07 | 0.000 |
| 2.2 | 12.31 | 0.145 | 0.189 | 0.642 | 3.74 | 4.40 | 3.79 | 1.54 | 7.04 | 0.0036 | 22.29 | 0.229 |
| 3.3 | 16.86 | 0.199 | 0.282 | 0.541 | 5.10 | 6.55 | 5.19 | 1.88 | 9.65 | 0.0054 | 20.89 | 0.267 |
| 4.9 | 22.51 | 0.266 | 0.420 | 0.429 | 6.77 | 9.77 | 6.92 | 2.29 | 12.88 | 0.0081 | 19.15 | 0.307 |
| 7.6 | 29.20 | 0.344 | 0.651 | 0.278 | 8.45 | 15.14 | 8.98 | 2.85 | 16.71 | 0.0125 | 17.09 | 0.355 |
| 10.3 | 33.38 | 0.394 | 0.882 | 0.202 | 9.76 | 20.50 | 10.26 | 3.32 | 19.10 | 0.0170 | 15.81 | 0.393 |
| 13.0 | 37.11 | 0.438 | 1.113 | 0.180 | 11.61 | 25.87 | 11.41 | 3.73 | 21.24 | 0.0214 | 14.66 | 0.427 |
| 18.4 | 43.26 | 0.510 | 1.574 | 0.149 | 14.97 | 36.60 | 13.31 | 4.44 | 24.76 | 0.0303 | 12.77 | 0.491 |
| 23.8 | 48.79 | 0.576 | 2.036 | 0.155 | 19.76 | 47.34 | 15.01 | 5.04 | 27.92 | 0.0391 | 11.07 | 0.554 |
| 29.2 | 55.43 | 0.654 | 2.498 | 0.147 | 23.60 | 58.07 | 17.05 | 5.59 | 31.72 | 0.0480 | 9.03 | 0.619 |
| 34.6 | 60.32 | 0.711 | 2.960 | 0.130 | 26.29 | 68.81 | 18.55 | 6.08 | 34.52 | 0.0569 | 7.52 | 0.685 |
| 40.0 | 65.61 | 0.774 | 3.421 | 0.127 | 29.99 | 79.54 | 20.18 | 6.54 | 37.55 | 0.0658 | 5.89 | 0.749 |
| 50.8 | 74.19 | 0.875 | 4.345 | 0.089 | 31.92 | 101.01 | 22.82 | 7.37 | 42.46 | 0.0835 | 3.26 | 0.866 |
| 61.6 | 79.56 | 0.939 | 5.268 | 0.053 | 29.98 | 122.48 | 24.47 | 8.11 | 45.53 | 0.1013 | 1.60 | 0.953 |
| 72.4 | 82.55 | 0.974 | 6.191 | 0.028 | 25.33 | 143.95 | 25.39 | 8.80 | 47.25 | 0.1190 | 0.68 | 0.998 |
| 83.1 | 83.88 | 0.989 | 7.115 | 0.014 | 20.86 | 165.41 | 25.80 | 9.43 | 48.01 | 0.1368 | 0.27 | 0.994 |
| 93.9 | 84.77 | 1.000 | 8.038 | 0.000 | 0.00 | 186.88 | 26.07 | 10.02 | 48.52 | 0.1545 | 0.00 | 0.947 |

X/C = 0.90 22.0 INS THROTTLE 500.0 RPM

| | | | | | | | |
|---|---|---|---|---|---|---|---|
| UE | 90.48 FPS | DUEDX | -426.0 /SEC | H | 2.31 | | |
| UT | 3.16 FPS | UT/UE | 0.0350 | H** | 1.57 | | |
| UP | 1.85 FPS | | | PI | 9.52 | | |
| UB | 50.28 FPS | UB/UE | 0.556 | G | 16.20 | | |
| CFE | 2.444 *10-3 | CTEQ | 9.345 *10-3 | GEQ | 18.84 | | |
| CFLT | 1.215 *10-3 | CFE/CFLT | 2.012 | GAMMA | -2.491 *10-2 | | |
| CFNM | 1.234 *10-3 | CFE/CFNM | 1.981 | A | 3.855 *104 FT/SEC↑2 | | |
| CDEL | 707.14 *10-4 FT | DELTA | 68.08 *10-4 FT | ALPHA0 | 0.199 | | |
| DSTAR | 24.72 *10-4 FT | REDSTAR | 1368.1 | TH/UE*DUEDX | -5.047 *10-3 | | |
| THETA | 10.72 *10-4 FT | RETHETA | 593.3 | K | -2.995 | | |
| DELTA** | 16.80 *10-4 FT | | | NU | 1.635 *10-4 FT↑2/SEC | | |

| Y*10⁴ (FT) | U (FPS) | U/UE | Y/THETA | Z*TH/UE | YY | Y+ | U+ | (Y*)↑0.5 | U* | Y/CDEL | (UE-U)/UT | UC/UE |
|---|---|---|---|---|---|---|---|---|---|---|---|---|
| 0.0 | 0.00 | 0.000 | 0.000 | 0.725 | 0.00 | 0.00 | 0.00 | 0.00 | 0.00 | 0.0000 | 28.61 | 0.000 |
| 2.2 | 10.79 | 0.119 | 0.206 | 0.430 | 3.30 | 4.28 | 3.41 | 1.58 | 5.84 | 0.0031 | 25.20 | 0.154 |
| 3.3 | 14.05 | 0.155 | 0.307 | 0.324 | 4.25 | 6.37 | 4.44 | 1.93 | 7.61 | 0.0047 | 24.17 | 0.189 |
| 4.9 | 17.76 | 0.196 | 0.458 | 0.251 | 5.59 | 9.50 | 5.61 | 2.36 | 9.61 | 0.0069 | 22.99 | 0.227 |
| 7.6 | 22.70 | 0.251 | 0.710 | 0.222 | 8.14 | 14.72 | 7.18 | 2.93 | 12.29 | 0.0108 | 21.43 | 0.274 |
| 10.3 | 27.87 | 0.308 | 0.961 | 0.202 | 10.53 | 19.94 | 8.81 | 3.41 | 15.09 | 0.0146 | 19.80 | 0.314 |
| 13.0 | 31.90 | 0.353 | 1.213 | 0.169 | 12.15 | 25.16 | 10.09 | 3.83 | 17.27 | 0.0184 | 18.52 | 0.352 |
| 18.4 | 38.84 | 0.429 | 1.716 | 0.163 | 16.90 | 35.60 | 12.28 | 4.56 | 21.03 | 0.0260 | 16.33 | 0.427 |
| 23.8 | 46.80 | 0.517 | 2.220 | 0.179 | 22.88 | 46.04 | 14.80 | 5.19 | 25.34 | 0.0337 | 13.81 | 0.506 |
| 29.2 | 55.15 | 0.609 | 2.723 | 0.184 | 28.44 | 56.48 | 17.44 | 5.74 | 29.86 | 0.0413 | 11.17 | 0.588 |
| 34.6 | 63.54 | 0.702 | 3.226 | 0.159 | 31.29 | 66.91 | 20.09 | 6.25 | 34.40 | 0.0489 | 8.52 | 0.671 |
| 40.0 | 69.59 | 0.769 | 3.730 | 0.130 | 32.70 | 77.35 | 22.00 | 6.72 | 37.67 | 0.0565 | 6.61 | 0.752 |
| 50.8 | 80.78 | 0.893 | 4.736 | 0.097 | 35.99 | 98.23 | 25.54 | 7.57 | 43.74 | 0.0718 | 3.07 | 0.891 |
| 61.6 | 87.31 | 0.965 | 5.743 | 0.048 | 30.59 | 119.11 | 27.60 | 8.34 | 47.27 | 0.0871 | 1.00 | 0.979 |
| 72.4 | 89.49 | 0.989 | 6.750 | 0.017 | 21.69 | 139.99 | 28.30 | 9.04 | 48.45 | 0.1023 | 0.31 | 1.000 |
| 83.1 | 90.48 | 1.000 | 7.756 | 0.000 | 0.00 | 160.87 | 28.61 | 9.69 | 48.99 | 0.1176 | 0.00 | 0.953 |

REFERENCES


1. Howell, A.R. — Fluid Dynamics of Axial Compressors. Proc. I. Mech. E., Vol. 153, No. 12, 1945, pp. 441-452.

2. Johnsen, I.A. & Bullock, R.O., eds. — Aerodynamic Design of Axial-Flow Compressors. U.S.A. National Aeronautics and Space Administration, Special Publication No. SP-36, 1965.

3. Lighthill, M.J. — A Mathematical Method of Cascade Design. Gt. Britain. Aeronautical Research Council Reports and Memoranda, R & M No. 2104, 1945.

4. Blight, F.G. & Howard, W. — Tests on Four Aerofoil Cascades, Parts I & II. Australia. Dept. of Supply, Reports E74, E75, Aeronautical Research Labs., July 1952.

5. Crooks, P.V. & Howard, W. — Low Speed Tests on Three Aerofoil Cascades Designed for Prescribed Surface Velocity Distributions. Australia. Dept. of Supply, Report E76, Aeronautical Research Labs., June 1954.

6. Crooks, P.V. & Howard, W. — Preliminary China Clay Tests on Rotary Cascade Blade Surfaces. Australia. Dept. of Supply, Aeronautical Research Labs., Mech. Eng. Note No. ME196, Dec. 1954.

7. Hawthorne, W.R. ed. — Aerodynamics of Turbines and Compressors. Princeton, N.J. Princeton Univ. Press, 1964. (High Speed Aerodynamics and Jet Propulsion Series, Vol. X) p. 6.

8. Close, D.J. — Boundary Layer Tests on the Rotor Blades of the Vortex Wind Tunnel. Australia. Dept. of Supply, Aeronautical Research Labs., Mech. Eng. Note No. ME243, Nov. 1960.

9. Salter, P.A. — Further Boundary Layer Tests in the Vortex Wind Tunnel. Australia. Dept. of Supply, Aeronautical Research Labs., Mech. Eng. Note No. ME255, March 1963.

10. Thwaites, B. — Approximate Calculation of the Laminar Boundary Layer. The Aeronautical Quarterly, Vol. I, 1949, pp. 245-280.

11. Oliver, A.R. — Comparison Between Sand Cast and Machined Blades in the Vortex Wind Tunnel. Australia. Dept. of Supply, Aeronautical Research Labs., Mech. Eng. Report No. ME103, Sept. 1961.

12. Close, D.J. — Further Tests of Cast C4 Blades in the Vortex Wind Tunnel.
Australia, Dept. of Supply, Aeronautical Research Labs., Mech. Eng. Note No. ME239, June 1960.

13. Wills, J.A.B. — Correction of Hot Wire Readings for Proximity to a Solid Boundary.
Jour. Fluid Mechanics, Vol. 12, 1962, pp. 388-396.

14. King L.V. — On the Convection of Heat from Small Cylinders in a Stream of Fluid.
Phil. Trans. A, Vol. 214, 1914, pp. 373-432.

15. Collis, D.C. & Williams, M.J. — Two-dimensional Convection from Heated Wires at Low Reynolds Numbers.
Jour. Fluid Mechanics, Vol. 6, 1959, pp. 357-384.

16. Almquist, P. & Legath, E. — The Hot-Wire Anemometer at Low Air Velocities.
DISA Information, No. 2, July 1965, pp. 3-4.

17. Hilpert, R. — Wärmeabgabe von geheizten Drähten und Rohren in Luftstrom.
Forsch. Arb., Ing. Wes., Vol. 4, pp. 215-224.

18. Pinkel, B. — A Summary of NACA Research on Heat Transfer and Friction for Air Flowing Through Tube with Large Temperature Difference.
Trans. A.S.M.E. Vol. 76, 1954, pp. 305-317.

19. Sovran, G. ed. — Fluid Mechanics of Internal Flow.
Amsterdam, Elsevier, 1967, pp. 110-151, paper entitled Measurements in a Turbulent Boundary Layer Maintained in a Nearly Separating Condition, by W.G. Spangenberg, W.R. Rowland and N.E. Mease.

20. Hoole, B.J. & Calvert, J.R. — The Use of a Hot-Wire Anemometer in Turbulent Flow.
J. Royal Aero. Soc., Vol. 71, 1967, pp. 511-513.

21. Van Thinh, N. — Sur la mesure de la vitesse dans un écoulement turbulent par anémométrie à fil chaud, au voisinage d'une paroi lisse.
Académie des Sciences (Paris), Comptes Rendus, Série A - Sciences Mathematiques, Vol. 264, 1967, pp. 1150-1152.

22. Tritton, D.J. — Note on the Effect of a Nearby Obstacle on Turbulence Intensity in a Boundary Layer.
Jour. Fluid Mechanics, Vol. 28, 1967, pp. 433-437.

23. Merrington, G.L. — A Study of the Hub Boundary Layer in an Axial Flow Compressor.
Ph.D. Thesis, University of Tasmania, May 1970.

24. Johnston, I.T. & Lockhart, R.C. — Unpublished data, University of Tasmania.

25. Carter, A.D.S. — Blade Profiles for Axial-Flow Fans, Pumps, Compressors, etc. Proc. I. Mech. E., Vol. 175, No. 15, 1961, pp. 775-806.

26. Howarth, L. — On the Solution of the Laminar Boundary Layer Equations. Proc. Roy. Soc., London, A164, p. 547, 1938.

27. Curle, N. & Skan, S.W. — Approximate Methods for Predicting Separation Properties of Laminar Boundary Layers. Aero. Quart., Vol. 8, 1957, pp. 257-268.

28. Görtler, H. — A New Series for the Calculation of Steady Laminar Boundary Layer Flows. Unpublished report of the Mathematisches Institut Universität Freiburg i. Br. See also J. Math. Mech. Vol. 6, 1957, pp. 1-66.

29. Curle, N. — A Two-Parameter Method for Calculating the Two-Dimensional Incompressible Laminar Boundary Layer. J. Royal Aero. Soc., Vol. 71, No. 674, pp. 117-123, Feb. 1967.

30. Owen, P.R. & Klanfer, L. — On the Laminar Boundary Layer Separation from the Leading Edge of a Thin Aerofoil. Great Britain, Aeronautical Research Council Current Papers, C.P. No. 220, 1955.

31. Crabtree, L.F. — The Formation of Regions of Separated Flow on Wing Surfaces. Great Britain, Aeronautical Research Council Reports and Memoranda, R. & M. No. 3122, 1959.

32. McGregor, I. — Regions of Localised Boundary Layer Separation and Their Role in the Nose-Stalling of Aerofoils. Ph.D. Thesis. Queen Mary College, University of London, 1954.

33. Gaster, M. — On the Stability of Parallel Flows and the Behaviour of Separation Bubbles. Ph.D. Thesis. Queen Mary College, University of London, 1963.

34. Gaster, M. — The Structure and Behaviour of Laminar Separation Bubbles. Great Britain, National Physical Laboratory, Aero. Report No. 1181 (Revised), 1967.

35. Wallis, R.A. — The Turbulent Boundary Layer on the Articulated Nose of a Thin Wing Provided with Air Jets. Australia, Dept. of Supply, Aeronautical Research Labs., Aero. Note No. A141, 1954.

36. Walker, G.J. — Unpublished discussion. Commonwealth Advisory Aeronautical Research Council, Specialists' Meeting on Boundary Layers. Bangalore, India, 1967.

37. Woodward, D. — Unpublished note. Queen Mary College, University of London.

38. Horton, H.P. — A Semi-Empirical Theory for the Growth and Bursting of Laminar Separation Bubbles. Great Britain, Aeronautical Research Council Current Papers, C.P. No. 1073, 1969.

39. Stuart, J.T. — Hydrodynamic Stability. Applied Mechanics Reviews, Vol. 18, 1965, pp. 523-531.

40. Schubauer, G.B. & Skramstad, H.K. — Laminar Boundary Layer Oscillations and Transition on a Flat Plate. U.S.A. National Advisory Committee for Aeronautics, Report 909, 1948.

41. Thomson, K.D. — The Role of Streamwise Vortex Bursting in Boundary Layer Transition. Australian Defence Scientific Service, Weapons Research Establishment, Technical Memorandum HSA159, July 1967.

42. Knapp, C.F. & Roache, P.J. — A Combined Visual and Hot-Wire Anemometer Investigation of Boundary-Layer Transition. American Institute of Aeronautics and Astronautics Jour., Vol. 6, 1968, pp. 29-36.

43. Miller, J.A. & Fejer, A.A. — Transition Phenomena in Oscillating Boundary Layer Flows. Jour. Fluid Mechanics, Vol. 18, 1964, pp. 438-448.

44. Obremski, H.J. & Fejer, A.A. — Transition in Oscillating Boundary Layer Flows. Jour. Fluid Mechanics, Vol. 29, 1967, pp. 93-111.

45. Greenspan, H.P. & Benney, D.J. — On Shear-Layer Instability, Breakdown and Transition. Jour. Fluid Mechanics, Vol. 15, 1963, pp. 135-53.

46. Liepmann, H.W. — Investigation of Boundary Layer Transition on Concave Walls. U.S.A. National Advisory Committee for Aeronautics, Advance Confidential Report 4J28, 1945.

47. Emmons, H.W. — The Laminar-Turbulent Transition in a Boundary Layer - Pt. I. Jour. Aerospace Sci., Vol. 18, 1951, pp. 290-298.

48. Schubauer, G.B. & Klebanoff, P.S. — Contributions on the Mechanics of Boundary-Layer Transition. U.S.A. National Advisory Committee for Aeronautics, Report 1289, 1956.

49. Obremski, H.J. & Morkovin, M.V. — Application of a Quasi-Steady Stability Model to Periodic Boundary-Layer Flows. American Institute of Aeronautics and Astronautics Jour., Vol. 7, 1969, pp. 1298-1301.

50. Brown, F.N.M. — The Physical Model of Boundary Layer Transition. U.S.A. David Taylor Model Basin, U.S. Navy Contract NOnr 1623(17), Aug. 1965.

51. Farn, C.L. & Arpaci, V.S. — On the Numerical Solution of Unsteady Laminar Boundary Layers. American Institute of Aeronautics and Astronautics Jour., Vol. 4, 1966, pp. 730-732.

52. Rosenhead, L. (Ed.) — Laminar Boundary Layers. Oxford University Press, 1963, p. 542, in chapter entitled Hydrodynamic Stability, by J.T. Stuart.

53. Obremski, H.J., Morkovin, M.V., & Landahl, M. — A Portfolio of Stability Characteristics of Incompressible Boundary Layers. North Atlantic Treaty Organisation. Advisory Group for Aerospace Research and Development. AGARDograph 134, March 1969.

54. Shaw, R. — The Effects of Reynolds Number, Turbulence Intensity, and Axial Velocity Ratio on Compressor Blade Performance. U.K. University of Liverpool, Mechanical Engineering Dept.

55. Michel, R. — Détermination du Point de Transition et Calcul de la Trainée des Profils d'Ailes en Incompressible. France. Office National d'Études et de Recherches Aéronautiques, Publication No. 58, 1952.

56. Smith, A.M.O. — Transition, Pressure Gradient, and Stability Theory. Proc. 9th Intern. Congress of Applied Mechanics, Brussels, 1957, Vol. 4, pp. 234-244.

57. Smith, A.M.O. & Gamberoni, N. — Transition, Pressure Gradient and Stability Theory. U.S.A. Douglas Aircraft Co., Report No. ES 26388, Aug. 1956.

58. Pretsch, J. — Calculation of the Limit of Stability of Boundary Layer Profiles and of the Amplification of Disturbances. A.V.A. Monographs, British Reports and Translations No. 1004, March 1948.

59. Hartree, D.R. — On an Equation Occurring in Falkner and Skan's Approximate Treatment of the Equations of the Boundary Layer. U.K. Proc. Cambr. Phil. Soc., Vol. 33, Part II, 1937, pp. 223-239.

60. Gaster, M. — On the Generation of Spatially Growing Waves in a Boundary Layer. Jour. Fluid Mechanics, Vol. 22, 1965, pp. 433-441.

61. Jaffe, N.A., Okamura, T.T., & Smith, A.M.O. — Determination of Spatial Amplification Factors and Their Application to Predicting Transition. American Institute of Aeronautics and Astronautics Jour., Vol. 8, 1970, pp. 301-308.

62. Wazzan, A.R., Okamura, T.T., & Smith, A.M.O. — Spatial and Temporal Stability Charts for the Falkner-Skan Boundary Layer Profiles. U.S.A.McDonnell Douglas Corp., Report No. DAC 67086, Sept. 1968.

63. Landahl, M. — A Time-Shared Program for the Stability Problem for Parallel Flows over Rigid or Flexible Surfaces. U.S.A. Massachusetts Institute of Technology, ASRL 116-4, 1966.

64. Spangler, J.G. & Wells, C.S. Jr. — Effects of Freestream Disturbances on Boundary Layer Transition. American Institute of Aeronautics and Astronautics Jour., Vol. 6, 1968, pp. 543-545.

65. Granville, P.S. — The Calculation of the Viscous Drag of Bodies of Revolution. U.S.A. Navy Department, David Taylor Model Basin, Report 849, July 1953.

66. Jones, B.M. — Flight Experiments on the Boundary Layer. Jour. Aero. Sci., Vol. 5, 1938, pp. 81-101.

67. Zalovcik, J.A. & Skoog, R.B. — Flight Investigation of Boundary Layer Transition and Profile Drag of an Experimental Low-drag Wing Installed on a Fighter-type Airplane. U.S.A. National Advisory Committee for Aeronautics, Wartime Report L-94, 1945.

68. Braslow, A.L. & Visconti, F. — Investigation of Boundary Layer Reynolds Number for Transition on an NACA $65_{(215)}$-114 Airfoil in the Langley Two-dimensional Low-turbulence Pressure Tunnel. U.S.A. National Advisory Committee for Aeronautics, Tech. Note 1704, 1948.

69. von Doenhoff, A.E. — Investigation of the Boundary Layer about a Symmetrical Airfoil in a Wind Tunnel of Low Turbulence. U.S.A. National Advisory Committee for Aeronautics, Wartime Report L-507, 1940.

70. Hall, A.A. & Hislop, G.S. — Experiments on the Transition of the Laminar Boundary Layer on a Flat Plate. Great Britain, Aeronautical Research Council, Reports & Memoranda No. 1843, 1938.

71. Dryden, H.L. — Air Flow in the Boundary Layer near a Plate. U.S.A. National Advisory Committee for Aeronautics, Report 562, 1936.

72. Schlichting, H. & Ulrich, A. — Zur Berechnung des Umschlages Laminar-Turbulent. Jahrbuch 1942 der Deutschen Luftfahrtforschung.

73. Tollmien, W. — The Production of Turbulence. U.S.A. National Advisory Committee for Aeronautics, Tech. Memo. 609, 1931. (Translation from 1. Mitteilung, Nachr. Wiss. Göttingen, Math. Phys. Klasse 21-44, 1929.)

74. Gostelow, J.P., Lewkowicz, A.K. & Shaalan, M.R.A. — Viscosity Effects on the Two-Dimensional Flow in Cascades. Gt. Britain, Aeronautical Research Council, Current Paper No. 872, Oct. 1965.

75. Preston, J.H. — The Minimum Reynolds Number for a Turbulent Boundary Layer and the Selection of a Transition Device. Jour. Fluid Mechanics, Vol. 3, 1957-8, pp. 373-384.

76. Shaw, R. & Doyle, M.D.C. — Pressure Distributions on Axial Flow Compressor Blading and Comparison with Distributions on Similar Cascade Blading. Proc. Von Karman Inst. Seminar on Advanced Problems in Turbomachinery 1965, Pt. I, 1.

77. Deverson, E.C., Marsh, H. & Oxford, J.T.B. — The Performance of an Aerofoil in Stationary and Rotating Cascades. Gt. Britain. Aeronautical Research Council, Current Paper No. 1022, 1968.

78. Heilmann, W. — Experimentelle und Grenzschichttheoretische Untersuchungen an Ebenen Verzögerungsgittern bei Kompressibler Strömung, Insbesondere bei Änderung des Axialen Stromdichtverhältnisses und der Zuströmturbulenz. Deutsche Luft-und Raumfahrt, Forschungsbericht 67-88, Dec. 1967.

79. Hebbel, H. — Über den Einfluss der Machzahl und der Reynoldszahl auf die Aerodynamischen Beiwerte von Verdichter-Schaufelgittern bei Verschiedener Turbulenz der Strömung. Forschung auf dem Gebiete des Ingenieurwesens, Vol. 33, 1967, pp. 141-150.

80. Schlichting, H. & Das, A. — Recent Research on Cascade-Flow Problems. Trans. American Soc. Mech. Eng., Series D, Jour. Basic Engg., Vol. 88, 1966, pp. 221-228.

81. Johnsen, I.A. & Bullock, R.O., eds. — Aerodynamic Design of Axial-Flow Compressors. U.S.A. National Aeronautics and Space Administration, Special Publication No. SP-36, 1965, p. 159, in chapter entitled Viscous Flow in Two-Dimensional Cascades, by W.H. Roudebush and S. Lieblein.

82. Walker, G.J. — The Prediction of Boundary Layer Development on Axial Flow Turbomachine Blades. Proc. Third Australasian Conference on Hydraulics and Fluid Mechanics, Sydney, Nov. 1968, pp. 97-104.

83. McCormick, M.E. — An Analysis of the Formation of Turbulent Patches in the Transition Boundary Layer. Trans. American Soc. Mech. Eng., Series E, Jour. App. Mech., Vol. 35, 1968, pp. 216-219.

84. McDonald, H. — The effect of pressure gradient on the law of the wall in turbulent flow. Jour. Fluid Mechanics, Vol. 35, 1969, pp. 311-336.

85. Coles, D.E. — The law of the wake in the turbulent boundary layer. Jour. Fluid Mechanics, Vol. 1, 1956, pp. 191-226.

86. Bull, M.K. — Velocity Profiles of Turbulent Boundary Layers. Aeronautical Jour., Vol. 73, 1969, pp. 143-147.

87. Coles, D.E. & Hirst, E.A. (Eds.) — Computation of Turbulent Boundary Layers - 1968. AFOSR - IFP - Stanford Conference Vol. II.U.S.A. Thermosciences Div. Stanford University, 1969. Paper entitled: The Young Person's Guide to the Data, by D.E. Coles, pp. 1-45.

88. Patel, V.C. & Head, M.R. — Reversion of turbulent to laminar flow. Jour. Fluid Mechanics, Vol. 34, 1968, pp. 371-392.

89. Bradshaw, P. — A note on reverse transition. Jour. Fluid Mechanics, Vol. 35, 1969, pp. 387-390.

90. Stratford, B.S. — The prediction of separation of the turbulent boundary layer. Jour. Fluid Mechanics, Vol. 5, 1959, pp. 1-16.

91. Townsend, A.A. — Equilibrium layers and wall turbulence. Jour. Fluid Mechanics, Vol. 11, 1961, pp. 97-120.

92. Perry, A.E., Bell, J.B. & Joubert, P.N. — Velocity and temperature profiles in adverse pressure gradient turbulent boundary layers. Jour. Fluid Mechanics, Vol. 25, 1966, pp. 299-320.

93. Mellor, G.L. & Gibson, D.M. — Equilibrium turbulent boundary layers. Jour. Fluid Mechanics, Vol. 24, 1966, pp. 225-253.

94. Mellor, G.L. — The effects of pressure gradients on turbulent flow near a smooth wall. Jour. Fluid Mechanics, Vol. 24, 1966, pp. 255-274.

95. Bradshaw, P. — Turbulent Boundary Layers. Jour. Royal Aero. Soc., Vol. 72, 1968, pp. 451-459.

96. Ludwieg, H. & Tillmann, W. — Untersuchungen über die Wandschubspannung in turbulenten Reibungschichten. Ing. Arch., Band 17, pp. 288-299 (Translated as NACA TM 1285).

97. Clauser, F.H. — The Turbulent Boundary Layer. Academic Press. Advances in Applied Mechanics, Vol. IV, 1956, pp. 1-51.

98. Nash, J.F. & Macdonald, A.G.J. — A Turbulent Skin Friction Law for Use at Subsonic and Transonic Speeds. U.K. Nat. Physical Lab., Aero. Report 1206, 1966.

99. Bradshaw, P., Ferriss, D.H. & Atwell, N.P. — Calculation of boundary-layer development using the turbulent energy equation. Jour. Fluid Mechanics, Vol. 28, 1967, pp. 593-616.

100. Nash, J.F. & Macdonald, A.G.J. — A Calculation Method for Incompressible Turbulent Boundary Layer, Including the Effect of Upstream History on the Turbulent Shear Stress. U.K. Nat. Physical Lab., Aero. Report 1234, 1966.

101. McDonald, H. & Stoddart, J.A.P. — On the Development of the Incompressible Turbulent Boundary Layer. U.K. Aeronautical Research Council, Reports and Memoranda No. 3484, 1967.

102. Landweber, L. — Frictional Resistance of Flat Plates in Zero Pressure Gradient. Trans. Soc. Nav. Arch. and Marine Eng., New York, Vol. 61, 1953.

103. Thompson, B.G.J. — A Critical Review of Existing Methods of Calculating the Turbulent Boundary Layer. Great Britain. Aero. Research Council 26109, Aug. 1964.

104. Rotta, J.C. — Critical Review of Existing Methods for Calculating the Development of Turbulent Boundary Layers, in Fluid Mechanics of Internal Flows (ed. G. Sovran), Elsevier, 1967, pp. 80-109.

105. Kline, S.J., Morkovin, M.V., Sovran, G., & Cockrell, D.J. (Eds.) — Computation of Turbulent Boundary Layers - 1968. AFOSR-IFP-Stanford Conference. Vol. I. Thermosciences Div., Dept. of Mech. Eng., Stanford Uni., U.S.A. 1969.

106. Clauser, F.H. — Turbulent boundary layers in adverse pressure gradients. Jour. Aero. Sci., Vol. 21, 1954, pp. 91-108.

107. Nash, J.F. — Turbulent Boundary Layer Behaviour and the Auxiliary Equation. AGARDograph 97, pp. 245-279.

108. Pohlhausen, K. — Zur näherungsweisen Integration der Differentialgleichung der laminaren Grenzschicht. Zeit. ang. Math. Mech., Vol. I, 1921, pp. 252-268.

109. Smith, D.J.L. — Turbulent boundary layer theory and its application to blade profile design. U.K. National Gas Turbine Establishment, Memorandum No. M395, March 1965.

110. Buri, A. — A method of calculation for the turbulent boundary layer with accelerated and retarded basic flow. R.T.P. Translation No. 2073, British Ministry of Aircraft Production, of Thesis No. 652, Federal Tech. Coll., Zürich, 1931.

111. Head, M.R. — Entrainment in the Turbulent Boundary Layer. U.K. Aero. Research Council, Reports & Memoranda No. 3152, 1960.

112. McDonald, H. — The Departure from Equilibrium of Two-Dimensional Turbulent Boundary Layers. Aero. Quart., Vol. XIX, pt. 1, Feb. 1968, pp. 1-19.

113. Küchemann, D. — Inviscid Flow Near the Trailing Edge of an Aerofoil. Zeit.für Flugwissenschaften, Vol. 15, 1967, pp. 292-294.

114. Oliver, A.R. — Definition of Wakes by Vortex Sheets. Inst. of Engineers, Australia, Proc. 4th Australasian Conf. on Hydraulics and Fluid Mech., Melbourne, 1971.

115. Fairlie, B.D. — Separation of Turbulent Boundary Layers. Australian Inst. of Nuclear Science & Engineering, 5th Heat Transfer and Fluid Flow Conference, Lucas Heights, Aug. 1971.

116. Bradshaw, P. — The Analogy between Streamline Curvature and Buoyancy in Turbulent Shear Flow. U.K. Nat. Phys. Lab., Aero Report 1231, May 1967.

117. Thompson, B.G.J. — The Calculation of Shape-Factor Development in Incompressible Turbulent Boundary Layers With or Without Transpiration. AGARDograph 97, May 1965, pp. 159-190.

118. Serovy, G.K. — Recent Progress in Aerodynamic Design of Axial-Flow Compressors in the United States. Trans. American Soc. Mech. Eng., Series A, Jour. Eng. for Power, Vol. 88, 1966, pp. 251-261.

119. Spence, D.A.
Prediction of the Characteristics of Two-Dimensional Airfoils.
Jour. Aero. Sci., Vol. 21, 1954, pp. 577-587, 620.

120. Horlock, J.H., Shaw, R., Pollard, D., & Lewkowicz, A.
Reynolds Number Effects in Cascades and Axial Flow Compressors.
Trans. American Soc. Mech. Eng., Series A, Jour. Eng. for Power, Vol. 86, 1964, pp. 236-242.

121. Bullock, R.O.
Analysis of Reynolds Number and Scale Effects on Performance of Turbomachinery.
Trans. American Soc. Mech. Eng., Series A, Jour. Eng. for Power, Vol. 86, 1964, pp. 247-256.

122. Wassell, A.B.
Reynolds Number Effects in Axial Compressors.
Trans. American Soc. Mech. Eng., Series A, Jour. Eng. for Power, Vol. 90, 1968, pp. 149-156.

123. Wortmann, F.X.
Progress in the Design of Low Drag Aerofoils.
In Boundary Layer and Flow Control, G.V. Lachmann, Ed. Pergamon, 1961, pp. 748-770.

124. Stratford, B.S.
An experimental flow with zero skin friction throughout its region of pressure rise.
Jour. Fluid Mechanics, Vol. 5, 1959, pp. 17-35.

125. Bradshaw, P.
The Response of a Constant-Pressure Turbulent Boundary Layer to the Sudden Application of an Adverse Pressure Gradient.
U.K. Nat. Phys. Lab., Aero. Rep. 1219, 1967.

126. Lieblein, S. & Roudebush, W.H.
Theoretical Loss Relations for Low-Speed Two-Dimensional Cascade Flow.
U.S.A. National Advisory Committee for Aeronautics, Tech. Note 3662, 1956.

127. Lieblein, S.
Experimental Flow in Two-Dimensional Cascades, in Aerodynamic Design of Axial Flow Compressors (I.A. Johnsen & R.O. Bullock, Eds.), NASA SP-36, 1965, pp. 183-226.

128. Fulford, D.
An Investigation into Blade Wake Interaction in an Axial Flow Compressor.
B.E. Honours Thesis, University of Tasmania, March 1968, Unpublished.

## NOTATION

| | |
|---|---|
| $a = d/2$ | Radius of hot wire element (Ch. 3) |
| $a$ | Amplification ratio of small disturbances in the laminar boundary layer (Ch. 6) |
| $a = \partial\tau/\partial y$ | Stress gradient in turbulent wall layer (Ch. 7) |
| $a_o = dp/dx$ | Streamwise pressure gradient (Ch. 7) |
| $b$ | Distance of hot wire element from solid boundary (Ch. 3) |
| $b = v'/u'$ | Ratio of fluctuating velocity components (Ch. 6) |
| $c$ | Aerofoil chord length |
| $d$ | Diameter of hot wire element |
| $dx_1$ | Length of transition region defined by Eqn. 6.25 |
| $dx_2$ | Length of transition region defined by Eqn. 6.26 |
| $e = 2.71828...$ | Constant |
| $h$ | Heat transfer coefficient |
| $i$ | Blade incidence |
| $i^*$ | Blade incidence at Howell nominal operating condition |
| $k = (\theta^2/\nu)(dU/dx)$ | Pressure gradient parameter for laminar boundary layer |
| $k = \overline{u'v'}/u'v'$ | Correlation coefficient (Ch. 6) |
| $k$ | Thermal conductivity of fluid (App. A) |
| $k_o$ | Thermal conductivity of fluid at $T_o$, $P_o$ |
| $l$ | Length of hot wire element (Ch. 3) |
| $l$ | Length of laminar separation bubble (Ch. 5) |
| $l$ | Mixing length (Ch. 7) |
| $l_i = x_t - x_i$ | Instability length |
| $l_1 = x_T - x_S$ | Length of separated laminar shear layer |
| $l_2 = x_R - x_T$ | Length of separated turbulent shear layer |
| $p$ | Static pressure |
| $p_i$ | Static pressure at cascade inlet |
| $q_i$ | Dynamic pressure at cascade inlet |
| $s$ | Aerofoil spacing in cascade |
| $t$ | Time |
| $t^* = t/T_w$ | Non-dimensional time for unsteady flow over stator blade |
| $u$ | Longitudinal velocity component in boundary layer |
| $u_\tau = u_{\tau_w} = \sqrt{\tau_w/\rho}$ | Wall friction velocity |
| $u_{\tau_o} = \sqrt{\tau_o/\rho}$ | Friction velocity based on apparent wall shear stress, $\tau_o$ |

| | |
|---|---|
| $u_\beta$ | Free parameter in the Coles turbulent boundary layer velocity profile, Eqn. 7.29 |
| $u_p = [(\nu/\rho)(dp/dx)]^{1/3}$ | Pressure velocity |
| $u^+ = u/u_\tau$ | Non-dimensional velocity |
| $u^* = u/u_p$ | Non-dimensional velocity |
| $v$ | Velocity component normal to surface |
| $w(y/\delta)$ | Wake function of Coles, Eqns. 7.7, 7.8 |
| $x$ | Chordwise distance from aerofoil leading edge |
| $\bar{x}_i$ | Neutral stability point calculated from time-mean surface pressure distribution |
| $\bar{x}_t$ | Transition point calculated from time-mean surface pressure distribution |
| $y$ | Distance normal to surface |
| $y^+ = yu_\tau/\nu$ | Non-dimensional distance from surface |
| $y^* = yu_p/\nu$ | Non-dimensional distance from surface |
| $A = \pi dl$ | Surface area of hot wire element (App. A) |
| $A = \tau_o/\tau_w$ | Stress ratio (Ch. 7) |
| AR | Aspect ratio |
| AVR | Axial velocity ratio for a cascade |
| $C_D$ | Profile drag coefficient |
| $C_{D_c}$ | Drag coefficient based on total pressure loss coefficient at blade trailing edge |
| $C_{D_u} = D_u/\frac{1}{2}\rho U_\infty^2 c$ | Drag coefficient based on $D_u$ |
| $C_f = C_{f_w} = \tau_w/\frac{1}{2}\rho U^2$ | Skin friction coefficient |
| $C_{f_o} = \tau_o/\frac{1}{2}\rho U^2$ | Friction coefficient based on apparent wall shear stress, $\tau_o$ |
| $C_{f_{NM}}$ | Skin friction coefficient from Nash-Macdonald law, Eqn. 7.37 |
| $C_{f_l} = \tau_l/\frac{1}{2}\rho U^2$ | Viscous shear stress coefficient |
| $C_{L_u} = L_u/\frac{1}{2}\rho U_\infty^2 c$ | Lift coefficient based on $L_u$ |
| $C_p = (p - p_i)/q_i$ | Static pressure coefficient |
| $C_R$ | Propagation velocity of small disturbance waves in the laminar boundary layer |
| $C_\tau = \int_o^\infty (\tau/\frac{1}{2}\rho U^2)\,d(y/\delta)$ | Integral shear stress parameter |
| $D_{loc} = (U_M - U_c)/U_c$ | Local diffusion factor |
| $D_u$ | Drag force/unit width of cascade blade, based on suction surface losses |
| $G = G_w = \sqrt{2/C_{f_w}}\,(1 - 1/H)$ | Boundary layer velocity defect parameter |
| $G_o = \sqrt{2/C_{f_o}}\,(1 - 1/H)$ | Boundary layer velocity defect parameter |
| $\hat{G}$ | Value of G if the boundary layer were in equilibrium with the local value of $\Pi$ |
| Gr | Grashof number |

| | |
|---|---|
| $H = \delta^*/\theta$ | Boundary layer shape factor |
| $H^{**} = \delta^{**}/\theta$ | Boundary layer shape factor |
| $H_1 = (\delta - \delta^*)/\theta$ | Boundary layer shape factor |
| $H_W = \delta_W^*/\theta_W$ | Wake shape factor |
| $I$ | Current passing through hot wire element |
| $K \simeq 0.4$ | Von Karman constant |
| $L = U/\omega$ | Characteristic length for free stream oscillation (Ch. 6) |
| $L$ | Dissipation length parameter in turbulent flow (Ch. 7) |
| $L_u$ | Lift force/unit width of cascade blade, based on suction surface pressure distribution (Eqn. 8.21) |
| $Ma_1$ | Cascade inlet Mach number |
| $N_A = \Delta U/U_o$ | Amplitude parameter for free stream oscillations |
| $Nu$ | Nusselt number |
| $P$ | Ambient pressure (Ch. 3, App. A) |
| $P = (\theta_S^2/\nu)(\Delta U/\Delta x)$ | Pressure gradient parameter for laminar separation bubble (Ch. 5) |
| $P_o$ | Reference pressure |
| $Q = \int_o^\infty u\, dy$ | Volume flux in boundary layer (Ch. 7) |
| $Q = I^2 R_w$ | Heat dissipated in hot wire element (App. A) |
| $R$ | Radius of curvature of streamlines (Ch. 7) |
| $R$ | Radial distance from axis of turbomachine |
| $R_T$ | Blade tip radius of turbomachine |
| $R_w$ | Resistance of hot wire element |
| $R_a$ | Wire resistance at ambient temperature $T_a$ |
| $R_o$ | Wire resistance at reference temperature $T_o$ |
| $Re_c = U_\infty c/\nu$ | Chord Reynolds number based on vector mean velocity |
| $Re_1 = U_1 c/\nu$ | Chord Reynolds number based on inlet velocity |
| $Re_2 = U_c c/\nu$ | Chord Reynolds number based on trailing edge velocity |
| $Re_x = Ux/\nu$ | x-Reynolds number |
| $Re_w = ud/\nu$ | Reynolds number for hot wire element, with fluid properties evaluated at mean film temperature |
| $Re_{l_1} = U_S l_1/\nu$ | Reynolds number based on length of separated laminar shear layer |
| $Re_\delta = U\delta/\nu$ | Boundary layer Reynolds number |
| $Re_{\delta^*} = U\delta^*/\nu$ | Boundary layer displacement thickness Reynolds number |

| | |
|---|---|
| $Re_\theta = U\theta/\nu$ | Boundary layer momentum thickness Reynolds number |
| $Re_{\theta_{crit}}$ | Value of $Re_\theta$ above which amplification of small disturbances may occur in laminar boundary layer |
| $(Re)_{NS} = L\Delta U/2\pi\nu$ | Non-steady Reynolds number for oscillating flow |
| $T = \tau_w\theta/\mu U$ | Wall shear stress parameter for laminar boundary layer |
| $T_a$ | Ambient temperature |
| $T_m = \frac{1}{2}(T_w + T_a)$ | Arithmetic mean film temperature for hot wire element |
| $T_o$ | Reference temperature |
| $T_p$ | Period of Tollmien-Schlichting wave |
| $T_w$ | Period between passage of successive rotor wakes (Ch. 6) |
| $T_w$ | Temperature of hot wire element (Ch. 3, App. A) |
| $U$ | Longitudinal velocity at outer edge of boundary layer |
| $U_1$ | Relative velocity at cascade inlet |
| $U_o$ | Mean velocity of free stream in oscillating flow (Ch. 6) |
| $U_{av}$ | Mean free stream velocity over transition region (Ch. 6) |
| $U_\infty$ | Free stream velocity for isolated aerofoil or vector mean velocity for a cascade |
| $U_{mb}$ | Peripheral velocity of compressor rotor at mid-blade height |
| $V$ | Voltage applied to hot wire element (Ch. 3, App. A) |
| $V_a$ | Axial velocity component in a turbomachine |
| $Y = y(\partial u/\nu\partial y)^{\frac{1}{2}}$ | Non-dimensional distance from wall |
| $\alpha$ | Temperature coefficient of resistance (Ch. 3, App. A) |
| $\alpha$ | Angle of hot wire supporting prongs to local flow direction (Sec. 3.3.9) |
| $\alpha_i$ | Spatial amplification rate for small disturbances in laminar boundary layer (Ch. 6) |
| $\alpha = (\nu/\rho u_\tau^3)(\partial\tau/\partial y)$ | Stress gradient parameter (Ch. 7) |
| $\alpha_o = (\nu/\rho u_\tau^3)(dp/dx)$ | Pressure gradient parameter (Ch. 7) |
| $\alpha' = (\nu/\rho u_{\tau_o}^3)(\partial\tau/\partial y)$ | Stress gradient parameter (Ch. 7) |

| | |
|---|---|
| $\alpha$ | Flow angle relative to axial direction |
| $\alpha_1$ | Relative flow angle at inlet to cascade or inlet to compressor rotor (App. C) |
| $\alpha_2$ | Flow angle at cascade outlet |
| $\alpha_3$ | Flow angle at inlet to compressor stator (App. C) |
| $\alpha_c$ | Flow angle at trailing edge of cascade blade |
| $\alpha_\infty$ | Direction of vector mean relative velocity |
| $\beta$ | Pressure gradient parameter of Hartree |
| $\beta_i$ | Temporal amplification rate for small disturbances in laminar boundary layer |
| $\delta$ | Boundary layer thickness : $\delta = y$ at $u = 0.995\ U$ |
| $\delta^*$ | Boundary layer displacement thickness |
| $\delta^*_W$ | Wake displacement thickness |
| $\delta^{**}$ | Boundary layer energy thickness |
| $\delta_c$ | Boundary layer thickness : distance from wall at which $w = 2.0$ |
| $\varepsilon$ | Kinematic eddy viscosity (Ch. 7) |
| $\varepsilon$ | Flow deflection angle for cascade |
| $\varepsilon^*$ | Flow deflection at Howell nominal condition |
| $\zeta = \partial u/\partial y$ | Vorticity in two-dimensional boundary layer |
| $\eta$ | Efficiency of cascade or axial turbomachine |
| $\theta = T_w - T_a$ | Temperature difference between hot wire element and ambient air (App. A) |
| $\theta$ | Boundary layer momentum thickness |
| $\theta_W$ | Wake momentum thickness |
| $\hat{\theta} = (\theta_W/c)(c/s \cos\alpha)$ | Wake momentum thickness parameter |
| $\mu$ | Dynamic viscosity of fluid |
| $\nu$ | Kinematic viscosity of fluid |
| $\nu_o$ | Kinematic viscosity at $T_o$, $P_o$ |
| $\nu_e$ | Effective kinematic viscosity in turbulent flow |
| $\xi$ | Stagger angle for cascade blading |
| $\pi = 3.14159..$ | Constant |
| $\rho$ | Density of fluid |
| $\sigma = (p_R - p_S)/\frac{1}{2}\rho U_S^2$ | Pressure rise parameter for laminar separation bubble |
| $\tau = \tau_l + \tau_t$ | Total shear stress |
| $\tau_l = \mu \partial u/\partial y$ | Viscous shear stress in boundary layer |
| $\tau_t = -\rho\overline{u'v'}$ | Turbulent shear stress |
| $\tau_w = \mu(\partial u/\partial y)_{y=o}$ | Fluid shear stress at wall |

| | |
|---|---|
| $\tau_o$ | Apparent wall shear stress obtained by extrapolating turbulent shear stress distribution in wall layer to y = 0 |
| $\tau^* = \omega t/2\pi$ | Non-dimensional time in oscillating flow |
| $\phi = V_a/U_{mb}$ | Compressor flow coefficient |
| $\phi_m$ | Value of $y/\delta$ for which turbulent shear stress reaches its maximum |
| $\psi = \Delta P/\frac{1}{2}\rho U_{mb}^2$ | Total pressure rise coefficient for compressor |
| $\omega$ | Frequency of oscillation (Hz or rad/sec as defined in text) |
| $\bar{\omega}$ | Mean total pressure loss measured downstream of a cascade |
| $\Gamma = (\theta/U)(dU/dx)Re_\theta^{\frac{1}{4}}$ | Pressure gradient parameter of Buri |
| $\Delta x = x_R - x_S$ | Length of laminar separation bubble |
| $\Delta U = U_R - U_S$ | Change in free stream velocity over laminar separation bubble |
| $\Delta U = N_A U_o$ | Amplitude of oscillation in free stream velocity (Ch. 6) |
| $\Delta P$ | Total pressure rise from point upstream of compressor inlet guide vanes |
| $\Pi = (\delta^*/\tau_w)(dp/dx)$ | Pressure gradient parameter of Clauser |

Arbitrary functions defined in text

$\Phi, \phi, F, f_1, f_2, f_3, f_4, f_5$

Constants defined in text

$a, a_1, a_2 \ldots a_n, b, b_w, k, k_1, k_2, n, u_s, x_o, A, A^*, B, B^*, B^+, (B^+)^o, (B^+)', C, C_1, C_2, C_3, R_o, U_o, \alpha_1, \alpha_2, \ldots \alpha_n, \delta_o, \theta_o$

Subscripts : applying to subscripted variables not specifically defined above

| | |
|---|---|
| 2-D | Value for two-dimensional flow model |
| EXP | Value measured experimentally |
| a | Value obtained using fluid properties evaluated at ambient conditions |
| b | Value for laminar separation bubble on point of bursting |
| c | Value at trailing edge of cascade blade |
| i | Value at point of neutral stability to small two-dimensional disturbances in laminar boundary layer |
| m | Mean value over interval $x_i$ to $x_t$ |

| | |
|---|---|
| t | Value at point where turbulent flow first appears in boundary layer |
| x | Value at streamwise position x |
| max | Maximum value |
| min | Minimum value |
| M | Value at location of peak velocity in model suction surface velocity distribution for compressor blade |
| R | Value at point of turbulent reattachment |
| S | Value at laminar separation point |
| T | Value at point where boundary layer flow becomes continuously turbulent |

Superscripts

| | |
|---|---|
| ' | Instantaneous fluctuation from time-mean value |
| — | Time-mean value |